1983

Summer Undergraduate Research Fellowships

SURF

Annual Report

California Institute of Technology
Pasadena, California 91125
October 8, 1983

TABLE OF CONTENTS

Brief Background of SURF

The Summer Undergraduate Research Fellowships program at Caltech began in 1979 to encourage creative research, promote interaction between undergraduates and faculty, and improve the undergraduate program. This program was the brainchild of Dr. Fredrick H. Shair, Professor of Chemical Engineering, and Dr. Harold Zirin, Professor of Astrophysics and Director of Big Bear Solar Observatory. In five years the program has grown from 18 students in 1979 to 77 students in 1983. The Caltech Administration has continuously given its enthusiastic support to the program. In 1983 nearly one-third of all faculty in science and engineering participated as faculty sponsors.

A student applies for a fellowship by developing a research proposal in collaboration with a faculty member who has agreed to sponsor him or her. The proposals are reviewed by a committee of faculty members familiar with the fields represented. Fellowships are awarded on the basis of perceived merit.

SURF students are expected to work full time for ten weeks during the summer to complete the projects, and at the end of the ten weeks, each student submits a report of his or her work. In addition to providing an enjoyable learning opportunity, the tutorial relationship between student and sponsor aids in the development of judgment. The program culminates in SURF Seminar Day when each student has the opportunity to present a fifteen-minute oral summary of his or her work to other students, faculty and visitors.

In 1983 a stipend of $2400 was paid each SURF student. Expenses of supplies, equipment, computing travel, etc., are paid by the individual faculty sponsors; this action on the part of Caltech faculty is another indication of their commitment to the training and development of young scientists and engineers.

Acknowledgements

We wish to acknowledge with great appreciation the help of the following people:

Jean E. Cass for conducting Communications Workshops for the SURFellows, proofreading final reports, and general administrative assistance.

Ruth Gilmore for her consultations on the College Work Study funds.

Chris Wood and **Sekhar Chivukula** for their help in the proposal review process.

Carolyn Merkel for administering the program.

Don Browning and **Gordon Imazu** for their work on all the financial aspects of SURF.

Ed Baum and **Elba Smith** for their continued invaluable support in all phases of the program.

Victoria Rose for her assistance with the SURF Annual Report and with SURF Seminar Day.

SURF Board

Corporate Sponsors

Carnation Research Laboratory
Ford Motor Company
General Motors Corporation
IBM Corporation
The O.K. Earl Corporation

Foundation Sponsor

Paul K. and Evalyn Elizabeth Cook Richter Memorial Funds

Individual Sponsors

Mr. Arthur Adams
Mr. Richard Burke
Dr. John N. Cooper
Mr. Richard L. Hayman
Mr. and Mrs. Samuel P. Krown
Mrs. Downie Muir III
Mr. and Mrs. Bruce Nickerson
Mr. and Mrs. Douglas Nickerson
Mr. David Partridge
Mr. and Mrs. Robert Shafer
Mr. and Mrs. George Webster

Faculty Sponsors

Professor Paul Bartlett (Berkeley)
Professor Felix Boehm
Professor William Bridges
Professor Sunney Chan
Professor Noel Corngold
Professor Richard Flagan
Professor George Gavalas
Professor William Goddard
Professor Harry Gray
Dr. Peter Haff
Dr. Eleanor Helin (JPL)
Professor Kenneth Janda
Dr. Satish Khanna (JPL)
Professor Joseph Kirschvink
Professor Masakazu Konishi
Professor Steven Koonin
Dr. John Lamb (JPL)
Professor E. John List
Professor Carver Mead
Professor Jerome Pine
Professor Jean-Paul Revel
Professor Anatol Roshko
Professor Ellen Rothenberg
Professor David Rutledge
Dr. Sten Samson
Professor Fredrick Shair
Professor Frederick Thompson
Professor Thomas Tombrello
Professor David Van Essen
Professor Stanley Whitcomb
Professor Barbara Wold
Professor Yuk Yung
Professor Stewart Zweben

Summer Seminar Speakers

Sally Asmundson, Director, Placement and Career Counseling
John Bercaw, Professor of Chemistry
Christopher Brennen, Professor of Mechanical Engineering
Charles Brokaw, Professor of Biology
Roger Clemens, Carnation Research Laboratory
Geoffrey Fox, Professor of Theoretical Physics
Larry Howell, General Motors Research Laboratories
Paul Hu, IBM General Products Division
Joseph Kirschvink, Assistant Professor of Geobiology
Rudolph Marcus, Arthur Amos Noyes Professor of Chemistry
Robert Mink, Ford Motor Company
Ray Owen, Professor of Biology, Emeritus
Jerome Pine, Professor of Physics
Demetri Psaltis, Assistant Professor of Electrical Engineering
Shirley Thomas, Technical Writer and Consultant

1983 SURF Students and Sponsors

STUDENT	FACULTY SPONSOR
1. Anco, Stephen (GM-SURF)	Lagerstrom, PA
2. Anderson, Robert (GM-SURF)	Roshko, A
3. Asthana, Praveen (IBM-SURF)	Psaltis, D
4. Berman, Stanley A	Yung, Y
5. Bonafede, Daniela M	Konishi, M
6. Bouzari, Alex (IBM-SURF)	List, EJ
7. Brock, Bradley (Richter-SURF)	Ryser, HJ
8. Bronikowski, Michael	Samson, S
9. Butman, John	Pine, J
10. Chan, Susanna M	Hood, L/Wold, B
11. Chang, Joe Chung-Yee (IBM-SURF)	Koonin, SE
12. Chen, Pang-Chieh	Corngold, N
13. Chen, Ze-Hua	Yariv, A.
14. Cheng, Joe K	Haff, P.
15. Cherrey, Kelly D (IBM-SURF)	Tombrello, T
16. Crawford, Glen (Richter-SURF)	Burnett, D/Tombrello T
17. Dunn, James	Revel, JP
18. Fatland, Dennis R (Richter-SURF)	Tombrello, T
19. Fernando, Timothy	Thompson, F/Thompson,B
20. Filmer, Paul E	Kirschvink, J
21. Freymueller, Jeff	Kamphoefner, W
22. Frisch, Josef (Richter-SURF)	Whitcomb, S
23. Fun, David	Rutledge, D
24. Garrett, Brett	Barnes, C
25. George, Ted	Shott, R/Davidson, E
26. Grannan, Eric R (IBM-SURF)	Tombrello, T/Burnett,D
27. Haghi, Mehrdad (GM-SURF)	Flagan, R
28. Hayes, Catherine	McGann, J
29. Houde, John F (IBM-SURF)	Van Essen, D
30. Hui, Kenneth (Ford-SURF)	Goddard, W
31. Ifune, Catherine K	Hamilton, CR
32. Inui, Masahiko (Richter-SURF)	Koonin, SE
33. Jerlstrom, Jennifer	Chan, SI
34. Jones, Stephen E (GM-SURF)	Bridges, W
35. Kong, Steven H (Ford-SURF)	Janda, KC
36. Krishnan, Santosh	Rothenberg, E
37. Kwok, Tak Leuk (Richter-SURF)	Newman, H
38. Lindsay, Mark D	Boehm, F
39. Mahowald, Misha	Konishi, M
40. Mapes, Brian E	Richards, JH
41. Mayhugh, James E	Wold, B
42. McCoy, Candice	Rothenberg, E
43. McGowan, John F (IBM-SURF)	Tombrello, T
44. Minor, Craig N (IBM-SURF)	Thompson, F
45. Murphy, Robert (GM-SURF)	Gavalas, G
46. Myers, Glayde A	Shair, F
47. Nikodym, Lisa A	Scott, R
48. Penn, Matthew (Richter-SURF)	Whaling, W
49. Princen, Norman H (GM-SURF)	Babcock, CD
50. Purtill, Mark (Richter-SURF)	Dean, R
51. Reel, Charles C	Wold, B
52. Remmers, Thomas W (Carnation-SURF)	Herbolzheimer, E
53. Roodman, Aaron J	Zirin, H
54. Ruden, Doug	Parker, C
55. Sadeghi, Behzad	Gray, H
56. Saylor, Janet (Richter-SURF)	Hitlin, D
57. Schaeck, John J	Bartlett, P (Berkeley)
58. Schlom, Darrell G	Wood, DS
59. Shapiro, Cathy	Revel, J-P
60. Shapiro, Lawrence	Chan, SI
61. Skjellum, Anthony (IBM-SURF)	Fox, G
62. Solberg, Teresa	Dervan, P
63. Srinivasan, Aditya	Lamb, J;Khanna, S.
64. Stassen, Clare	Psaltis, D
65. Sutton, Eliza	Dervan, P (Shultz,P)
66. Swanson, Steven R	Helin, E (JPL)
67. Tiller, Christine (Ford-SURF)	Stephanopoulos, G
68. Todorovich, Mira	Brokaw, C
69. Turpin, Barbara J	Munger, ES
70. Villasenor, Jesus N	Zweben, S
71. Wall, John	Hood, L
72. Wingreen, Ned S	Bridges, W
73. Wisanrakkit, Kriengkrai	Gavalas, G
74. Wolf, Sven A	Thompson, P
75. Yo, Christopher	Allman, J
76. Yoda, Minami	Coles, D
77. Yu, Christine HH (Ford-SURF)	Mead, C

September 1, 1983

Perturbation Methods for Autonomizing ODE's

by

Stephen C. Anco

Abstract

Linearization (autonomization) of a differential equation E_1, can occasionally be accomplished by a coordinate transformation which changes E_1 into a linear (autonomous) equation E_2. The problem is studied here qualitatively by simple arguments about solution curves in Cartan space. (The methods actually are taken from differential topology, although very little technical knowledge of this subject is needed here.) Quantitatively, the method of averaging gives approximative coordinate changes for perturbation problems. These ideas were previously used by Chivukula[1] particularly for linearizing equations. Here we deal with autonomization of the Mathieu equation and of the equation for a forced linear oscillator with slowly varying frequency. In doing so we have extended the usual method of averaging. If a Hamiltonian equation is autonomized an invariant is automatically found which is not the classical adiabatic invariant. Thus there exists an exact invariant for a forced oscillator with slowly varying frequency. The classical adiabatic invariance of the free oscillation changes under the influence of the forcing function. It is pointed out that while we deal with linear equations for reasons of analytical simplicity the reasoning used does not in any way depend on linearity. Extension to higher-order equations is discussed briefly.

---

1) R. Sekhar Chivukula, On the Equivalence of Various Second-Order Ordinary Differential Equations, Caltech SURF Report, Aug. 28, 1982 (Faculty Sponsor: P.A. Lagerstrom)

§1. Introduction. Linearization and Autonomization

By linearization (autonomization) of a differential equation E_1 we mean finding another equation E_2 which is linear (autonomous) such that any solutions of E_1 can be obtained from a solution of E_2. If, conversely, all solutions of E_2 can be obtained from the solutions of E_1 we say that the equations are equivalent. The problem to be discussed here is thus a special case of a more general problem: What are the criteria for equations being equivalent and what constructive methods exist for transforming an equation into an equivalent one of a specified form?

The answer to the first (qualitative) problem is essentially given by the ideas of Poincaré of studying the solution of differential equations by methods of geometry, or, to use modern terminology, differential topology. Consider a system of n-first order differential equations

$$S_1: \frac{dv_k}{dt} = f_k(v_1 \ldots v_n, t), \quad k = 1, \ldots n \qquad (1.1)$$

If S_1 is autonomous any solution of S is given by a curve in n-dimensional phase space with coordinates $(v_1, \ldots v_n)$. In the nonautonomous case, (at least one f_k depends explicityly on t) the corresponding statement is true if we enlarge the phase-space to Cartan space by adding t as a coordinate. Even for autonomous systems it is convenient to study the (n + 1) - dimensional Cartan space rather than the n-dimensional phase space. Consider now the solution curves in Cartan space of another n-th order system S_2. If there exists a diffeomorphism[2)] of Cartan space which gives a one-to-one corre-

---

[2)] By this is meant an invertible differentable mapping of Cartan space into itself (subregions might also be considered). This is the only technical term from differential topology we shall use here.

spondence between the solution curves of S_2 and those of S_1 then the two systems are equivalent, they are really the same problem expressed in different coordinates.

We now consider the quantitative problem: Assuming it is qualitatively evident that S_1 is equivalent to a linear autonomous system S_2 how does one find the coordinate transformation which takes S_1 into S_2? Sometimes this is done by clever tricks, sometimes by systematic use of group theory. We shall not deal with such cases here. Instead we consider systems S_1 which are perturbation of linear autonomous systems and use perturbation methods which give the required coordinate transformation to a certain order. The method of averaging turns out to be especially appropriate for our purpose.

The ideas discussed above were also discussed in a previous SURF report which dealt with linearization of second-order dynamical equations. It also briefly considered the classical problem of adiabatic invariants for equations with slowly varying coefficients. In this report we shall make detailed studies of autonomization of equations with more general time dependence and obtain invariants which may be called cousins of the classical adiabatic invariants. We shall still restrict ourselves to second-order Hamiltonian systems, although some qualitative discussion of other cases will be given. Use of the method of averaging for nonautonomous problems was presented by Wm. Kath in a Caltech course on singular perturbations (1982-1983). We shall somewhat modify and extend his methods. The general idea will be given in §2. In §3 we study Mathieu's equation and in §4 the forced linear oscillator with slowly varying frequence in passage through resonance. In §5 we briefly discuss more general cases.

§2. An Extended Method of Averaging

Perturbation problems to be discussed here can be treated by the method of multiple-scales[3]. The results are often easy to interpret physically because the dependent variables are not distorted. However, the coordinate transformation in Cartan space mentioned in §1 amounts to a distortion of the dependent variables (as well as the independent one). For our special purpose the method of averaging, suitably extended and modified, is especially useful[4]. In the present section we present some general ideas, to be illustrated by concrete examples in subsequent sections.

The detailed study will be restricted to simple second-order systems which in polar coordinates may be written

$$\frac{d}{dt}\begin{pmatrix} r \\ \varphi \end{pmatrix} = \sum_{k=0} \varepsilon^{k} \begin{pmatrix} f_k \\ g_k \end{pmatrix}, \tag{2.1}$$

where $f_o \equiv 0$, $g_o = g_o(r,\tau)$; for $k \geq 1$, f_k and g_k may depend on r, φ, t and τ. Here τ is a slow time. $\frac{d\tau}{dt} = O(\varepsilon)$, which may or may not be given a priori. The relation of the polar coordinates to the rectangular coordinates (u,v) will be defined in each special case.

We shall try to find the new polar coordinates (R, Φ) which transform (2.1) into

$$\frac{d}{dt}\begin{pmatrix} R \\ \Phi \end{pmatrix} = \begin{pmatrix} 0 \\ 1 \end{pmatrix}. \tag{2.2}$$

---

[3] See J. Kevorkian and J.D. Cole, Perturbation Methods in Applied Mathematics, Springer, 1982

[4] We believe our methods to be more convenient than the methods of von Zeipel and of Gardner (see Kevorkian-Cole for references), even for the Hamiltonian problems discussed here.

This equation is linear and autonomous which is exactly our aim. In addition we see that R is an invariant; R is a classical adiabatic invariant or a cousin thereof. Thus we are dealing with undamped systems.

The corresponding (distorted) rectangular coordinates are

$$u = R\cos\Phi, \quad v = -R\sin\Phi. \tag{2.3}$$

In rectangular coordinates (2.2) is

$$\frac{d^2u}{dt^2} + u = 0. \tag{2.4}$$

that is the equation for the simple harmonic oscillator, Ocassionally, though expansions will lead to imaginary numbers which transform (2.4) into

$$\frac{d^2u}{dt^2} - u = 0. \tag{2.4b}$$

(An example is Mathieu's equation in unstable regions of parametric space.)

The new coordinates will be introduced in the form

$$r = \sum_{K=0} \varepsilon^K R_K, \quad \varphi = \sum_{K=0} \varepsilon^K \Phi_K. \tag{2.5}$$

where

$$R_0 = R_0(R, t, \tau, \varepsilon), \quad \Phi_0 = \Phi_0(\Phi, t, \tau, \varepsilon),$$

$$R_K = R_K(R, \Phi, t, \tau), \quad \Phi_K = \Phi_K(R, \Phi, t, \tau), \quad \text{FOR } K \geq 1.$$

$$\tau = \text{SLOW TIME}, \quad \frac{d\tau}{dt} = O(1), \quad \tau = 0 \text{ AT } t = 0.$$

In the method of averaging one usually assumes $R_0 \equiv R$, $\Phi_0 \equiv \Phi$; however, the more general form given here will be convenient. In the linear problems dealt with, R_k will contain R only as a multiplicative factor and Φ_k will be independent of R. The slow time τ may or may not be given a priori.

To determine the functions R_K and Φ_k we first compute the (substantial) time derivative in two ways and equate the results. One way is to apply d/dt to (2.5), the other way is to insert (2.5) into the right-hand side of (2.1) and develop into powers of ε: $\sum \varepsilon^k \begin{pmatrix} f_k \\ g_k \end{pmatrix}$ Rearranging the equality gives

$$\frac{d\tau}{dt}\frac{\partial}{\partial\tau}\sum_{k=0}\varepsilon^K\begin{pmatrix} R_k \\ \Phi_k \end{pmatrix} = \sum_{k=0}\varepsilon^k\left[\begin{pmatrix} f_k \\ g_k \end{pmatrix} - J_k\begin{pmatrix} 0 \\ 1 \end{pmatrix} - \frac{\partial}{\partial t}\begin{pmatrix} R_k \\ \Phi_k \end{pmatrix}\right], \tag{2.6}$$

where

$$J_K = \begin{pmatrix} \dfrac{\partial R_K}{\partial R} & \dfrac{\partial R_K}{\partial \Phi} \\ \dfrac{\partial \Phi_K}{\partial R} & \dfrac{\partial \Phi_K}{\partial \Phi} \end{pmatrix}.$$

In the second term of the right-hand side we have used (2.2). Another consequence of (2.2) is that, within an irrelevant constant of integration

$$\Phi = t. \tag{2.7}$$

This leads to various different-looking but equivalent formalisms. For instance, we may treat Φ and t as different variables in a functional expression, form $\frac{\partial}{\partial \Phi}$ and $\frac{\partial}{\partial t}$ as separate derivatives and then use (2.7), or we may use (2.7) immediately.

We shall now use (2.6) to determine the R_k and Φ_k. These functions are not unique; we shall try to choose them so as to give convenient coordinate transformations.

First we note that the left-hand is $o(1)$. Hence the terms of order unity on the right-hand side must vanish,

$$\begin{pmatrix} 0 \\ g_0 \end{pmatrix} - \left(\frac{\partial}{\partial t} + \frac{\partial}{\partial \Xi} \right) \begin{pmatrix} R_0 \\ \Phi_0 \end{pmatrix} = \begin{pmatrix} 0 \\ 0 \end{pmatrix} , \tag{2.8}$$

which can be used to solve for R_0 and Φ_0 (Modifications of this method will be considered). To higher order we first decompose

$$(f_K , g_K) = (f_K^* , g_K^*) + (\tilde{f}_K , \tilde{g}_K) , \tag{2.9}$$

where the starred quantities oscillate with the fast time t $(= \Xi)$ and the rest depends only on the slow variable τ. We then average out the fast oscillations with the modulation equation,

$$\left(\frac{\partial}{\partial t} + \frac{\partial}{\partial \Xi} \right) \begin{pmatrix} R_K \\ \Phi_K \end{pmatrix} = \begin{pmatrix} f_K^* \\ g_K^* \end{pmatrix} - \frac{\partial}{\partial t} \begin{pmatrix} R_\ell^* \\ \Phi_\ell^* \end{pmatrix} . \tag{2.9}$$

Here the index ℓ depends on the order of τ, if for instance $\tau = \varepsilon t$ then $\ell = K - 1$. The solution of the modulation equation may be written

$$\begin{pmatrix} R_K \\ \Phi_K \end{pmatrix} = \begin{pmatrix} R_K^* \\ \Phi_K^* \end{pmatrix} + \begin{pmatrix} \tilde{R}_K (R , \tau) \\ \tilde{\Phi}_K (R , \tau) \end{pmatrix} , \tag{2.10}$$

where R_K^*, Φ_K^* are oscillatory and $\tilde{R}_K$ and $\tilde{\Phi}_K$ are constants of integration, relative to $\Phi (= t)$. When (2.8) and (2.9b) are satisfied (2.6) reduces to

$$\frac{d\tau}{dt} \frac{\partial}{\partial \tau} \left[\begin{pmatrix} R_0 \\ \Phi_0 \end{pmatrix} + \sum_{K=1} \varepsilon^K \begin{pmatrix} \tilde{R}_K \\ \tilde{\Phi}_K \end{pmatrix} \right] = \sum_{K=1} \varepsilon^K \begin{pmatrix} \tilde{f}_K \\ \tilde{g}_K \end{pmatrix} . \tag{2.11}$$

Thus the oscillatory part of (R_K, Φ_K) is determined and the remaining part, constants of integration, can be determined from (2.11) by solving for successively higher order of ε. Rather than computing a power series in ε.

one can sometimes find an answer which to the order considered is equivalent to the power series but which is in compact form. We shall outline the method here and illustrate it in detail in §3.

To fix the ideas assume that $\frac{d\tau}{dt} = \varepsilon$. We may then divide (2.4) by ε and retain only the terms of order unity and those of order ε. Actually (R_0, Φ_0) is known from (2.8). Hence we leave terms of order unity and terms of order ε in one equation and try to bring it into a form which is simple. Actually we decompose

$$\tilde{R}_1 = \tilde{R}_1^{(0)} + \tilde{R}_1^{(1)}, \quad \tilde{\Phi}_1 = \tilde{\Phi}_1^{(0)} + \tilde{\Phi}_1^{(1)}. \tag{2.12}$$

where the second term on the right-hand is a known function chosen as to simplify the relevant part of (2.11) as much as possible when substituted for $\tilde{R}_1$ and $\tilde{\Phi}_1$. The equation, and hence the answer will depend on ε, we shall denote it by $\left(\tilde{R}_0(\tau,\varepsilon),\ \tilde{\Phi}_0(\tau,\varepsilon)\right)$. If developed into powers of ε, the term of order unity is the old (R_0, Φ_0), the term of order ε is $\left(\tilde{R}_1^{(0)},\ \tilde{\Phi}_1^{(0)}\right)$. We are actually not interested in its value, just in ensuring that the method is logically correct: We have taken part of $\varepsilon(\tilde{R}_1, \tilde{\Phi}_1)$ and combined it with (R_0, Φ_0) .

§3. The Mathieu Equation

The Mathieu equation is often written in the form

$$\frac{d^2u}{d\tilde{t}^2} + (\delta + \varepsilon \cos \tilde{t})u = 0 .$$

The interesting values of δ are $\frac{n^2}{4} + \varepsilon\delta_1 + \varepsilon^2\delta_2 + \cdots$

We shall rescale time by $\tilde{t} = \frac{2t}{n}$ and study only the case $n = 1$; furthermore we neglect terms of $o(\varepsilon^2)$. The basic equation is then,

$$\frac{d^2u}{dt^2} + \left[1 + 4\varepsilon(\delta_1 + \varepsilon\delta_2 + \cos 2t)\right]\cdot u = 0. \tag{3.1a}$$

with the Hamiltonian

$$H = \frac{1}{2}v^2 + \frac{1}{2}u^2\left[1 + 4\varepsilon(\delta_1 + \varepsilon\delta_2 + \cos 2t)\right], \quad v = \frac{du}{dt}. \tag{3.1b}$$

In polar coordinates, with $u = r\cdot\cos\varphi$, $v = -r\sin\varphi$,

$$\frac{d}{dt}\begin{pmatrix} r \\ \varphi \end{pmatrix} = \begin{pmatrix} 0 \\ 1 \end{pmatrix} + \varepsilon\begin{pmatrix} 2r(\delta_1 + \cos 2t)\sin 2\varphi \\ 2(\delta_1 + \cos 2t)(1 + \cos 2\varphi) \end{pmatrix}$$
$$+ \varepsilon^2\begin{pmatrix} 2r\delta_2 \sin 2\varphi \\ 2\delta_2(1 + \cos 2\varphi) \end{pmatrix}. \tag{3.2}$$

We now introduce (R, Φ). Since the equation is linear we may assume that r is linear and homogeneous in R and that φ is independent of R. Thus we write

$$r = RR_0(\tau) + R\sum_{k=1}\varepsilon^k R_k(\Phi, t, \tau), \tag{3.3a}$$

$$\varphi = \Phi + \Phi_0(\tau) + \sum_{k=1}\varepsilon^k \Phi_k(\Phi, t, \tau). \tag{3.3b}$$

The notation differs from (2.6) since R_k there is now written $R\cdot R_k$. The leading terms of order unity in (2.6) cancel. The expression for the slow time is not known a priori. Solution of the first modulating equation gives us

$$R_1 = R_0\left[-\delta_1 \cos 2(\Phi + \Phi_0) - \frac{1}{4}\cos 2(t + \Phi + \Phi_0)\right] + \tilde{R}_1(\tau), \tag{3.4a}$$

$$\Phi_1 = \left[\delta_1 \sin 2(\Phi + \Phi_0) + \sin 2t + \frac{1}{4}\sin 2(t + \Phi + \Phi_0)\right] + \tilde{\Phi}_1(\tau). \tag{3.4b}$$

We do not integrate the equations for R_2 and Φ_2 since we would be left with unknown constants of integration $\tilde{\tilde{R}}_2$ and $\tilde{\tilde{\Phi}}_2$ which could only be determined from $O(\varepsilon^5)$ equation. However, assuming that the oscillatory terms in R_2 and Φ_2 have been averaged out (2.6) reduces to

$$\frac{d\tau}{dt}\frac{\partial}{\partial\tau}\left[\begin{pmatrix} R_0 \\ \Phi_0 \end{pmatrix} + \varepsilon\begin{pmatrix} \tilde{R}_1 \\ \tilde{\Phi}_1 \end{pmatrix}\right] = \varepsilon\begin{pmatrix} R_0 \,\mathrm{SIN}\, 2\bar{\Phi}_1 \\ 2(\delta_1 + \frac{1}{2}\cos 2\bar{\Phi}_0) \end{pmatrix}$$

$$+\ \varepsilon^2\begin{pmatrix} \tilde{R}_1 \,\mathrm{SIN}\, 2\bar{\Phi}_0 + 2R_0\tilde{\tilde{\Phi}}_1 \cos 2\bar{\Phi}_0 - 2\delta_1 R_0 \,\mathrm{SIN}\, 2\bar{\Phi}_0 \\ 2\delta_2 - 2\delta_1^2 - \frac{1}{2}\Phi_1 \,\mathrm{SIN}\, 2\bar{\Phi}_0 - 2\delta_1 \cos 2\bar{\Phi}_0 \end{pmatrix}. \qquad (3.5)$$

Clearly $\frac{d\tau}{dt}$ must be of order ε. We shall make the simple assumption

$$\tau = \varepsilon t. \qquad (3.6)$$

The leading terms of (3.5) then give us first order equations for R_0 and Φ_0. The equation for Φ_0 can be integrated in closed form and R_0 can then be found in terms of Φ_0.

$$R_0 = \left(\frac{A(0)}{A(\tau)}\right)^{1/2}, \quad A(\tau) = \delta_1 + \frac{1}{2}\cos 2\bar{\Phi}_0(\tau). \qquad (3.7a)$$

$$\tan\Phi_0 = \begin{cases} \left(\dfrac{\delta_1 + \frac{1}{2}}{\delta_1 - \frac{1}{2}}\right)^{1/2} \tan\left[2\tau(\delta_1^2 - \frac{1}{4})^{1/2}\right], & |\delta_1| > \frac{1}{2}. \\ \left(\dfrac{\delta_1 + \frac{1}{2}}{\frac{1}{2} - \delta_1}\right)^{1/2} \tanh\left[2\tau(\frac{1}{4} - \delta_1^2)^{1/2}\right], & |\delta_1| < \frac{1}{2}. \end{cases} \qquad (3.7b)$$

This gives us the classical term of order ε for the stability boundary.

The terms of order ε^2 give us equations for $\tilde{R}_1$ and $\tilde{R}_2$ with the general solution,

$$\tilde{R}_1 = \mathrm{CONST.}\cdot R_0 + \frac{R_0\left[-\delta_1(\delta_2 + \frac{1}{8})\log A - \frac{1}{4}(\delta_2 + \delta_1^2 - \frac{1}{8})A(A - 2\delta_1)\right]}{\frac{1}{4} - \delta_1^2} \qquad (3.8a)$$

$$\tilde{\Phi}_1 = \text{const}\cdot A + \frac{\frac{1}{4}(\delta_2 + \delta_1^2 - \frac{1}{8})\sin 2\Phi_0 - 2\delta_1(\delta_2 - \delta_1^2 + \frac{3}{8})A\tau}{\frac{1}{4} - \delta_1^2} . \tag{3.8b}$$

Here A is given from (3.7a). We shall use the notation,

$$\omega_2 = \delta_2 - \delta_1^2 + \frac{3}{8} . \tag{3.9}$$

The statement $\omega_2 = 0$ on the stability boundary is equivalent to the classical result that there

$$\delta_2 = -\frac{1}{8} . \tag{3.10}$$

Obviously (3.9) and (3.10) are equivalent if $\delta_1^2 = \frac{1}{4}$. For this value of δ_1 the right-hand sides of (3.8) become infinite unless (3.10) holds. It is also known that on the stability boundary there is at least one periodic solution with period π or 2π (in t). However, (3.8b) will have a term proportional to τ unless $\omega_2 = 0$. This will give a frequency shift which is not allowed on the stability boundary hence ω_2 must be zero there.

So far the result of our computations is the determination of the stability boundary to $O(\varepsilon^2)$. We now return to the problem of finding (r, φ) as a function of R, Φ. We shall only compute as far as R_1 and an Φ_1. This would be completed if we determined the constants of integration in (3.8) which can be done with the aid of the initial conditions, that is the value of r and φ at t = 0 (cf. 3.7). We shall, however, use the method outlined in §2. We decompose $\tilde{R}_1$ and $\tilde{\Phi}_1$ according to (2.12) and pick

$$\tilde{R}_1^{(1)} = \frac{1}{2}\Phi_{0\tau} R_0 , \qquad \tilde{\Phi}_1^{(1)} = -\frac{1}{2} R_{0\tau}/R_0 . \tag{3.11}$$

and insert these values for $\tilde{R}_1$ and $\tilde{\Phi}_1$ into (3.5) which reduces to

$$\frac{\partial}{\partial\tau}\begin{pmatrix} \tilde{R}_0 \\ \tilde{\Phi}_0 \end{pmatrix} = \begin{pmatrix} \tilde{R}_0 \sin 2\tilde{\Phi}_0 \\ 2(\delta_1 + \varepsilon\omega_2) + \frac{1}{2}\cos 2\tilde{\Phi}_0 \end{pmatrix} . \tag{3.12}$$

This is the same equation as that for R_0 except that the constant δ_1 has been replaced by the constant

$$\tilde{\delta}_1 = \delta_1 + \varepsilon \omega_2 . \tag{3.13}$$

Thus

$$\begin{pmatrix} \tilde{R}_0 \\ \tilde{\Phi}_0 \end{pmatrix} = \begin{pmatrix} R_0 \\ \Phi_0 \end{pmatrix}, \qquad \text{with } \delta_1 \text{ replaced by } \tilde{\delta}_1 . \tag{3.14}$$

Here $\tilde{R}_0$ and $\tilde{\Phi}_0$ depend on ε. We could develop in powers of ε and find

$$\begin{pmatrix} \tilde{R}_0 \\ \tilde{\Phi}_0 \end{pmatrix} = \begin{pmatrix} R_0 + \varepsilon \tilde{R}_1^{(c)} \\ \Phi_0 + \varepsilon \tilde{\Phi}_1^{(c)} \end{pmatrix} + O(\varepsilon) . \tag{3.15}$$

The particular value of the ε-term is not interesting, the form (3.14) is much more concise. This illustrates the use of (2.12). We have picked the second component of (2.12) to get a concise equation resembling that for (R_0, Φ_0) but including the terms of order ε. We call the solution $(\tilde{R}_0, \tilde{\Phi}_0)$ Its term of order unity is the old (R_0, Φ_0). Its term of order ε is one term of $(\tilde{R}_1, \tilde{\Phi}_1)$, the other term is given by (3.11). The terms of higher order do not influence the calculations. The term $(\tilde{R}_0(\tau, \varepsilon), \tilde{\Phi}_0(\tau, \varepsilon))$ agrees to the order considered with what we would have obtained by doing the calculations strictly in orders of ε, but it has a much more concise form. It also gives the stability boundary. In $|\delta_1| = \frac{1}{2}$ we replace δ_1 by $\tilde{\delta}_1$ and get

$$|\delta_1 + \varepsilon \omega_2| = \frac{1}{2} \Longrightarrow |\delta_1| = \frac{1}{2}, \quad \delta_2 = -\frac{1}{8} . \tag{3.16}$$

The left and right boundaries of the unstable region are

$$\delta_L = \frac{1}{4} - \frac{\varepsilon}{2} - \frac{\varepsilon^2}{8} + O(\varepsilon^3), \quad \delta_R = \frac{1}{4} + \frac{\varepsilon}{2} - \frac{\varepsilon^2}{8} + O(\varepsilon^3) . \tag{3.17}$$

We have left one question unanswered: Why did we choose (3.11) One way would be to manipulate the equation for $(\tilde{R}_0, \tilde{\Phi}_0)$ till it takes a form similar to the equation for . There are other ways of finding it by a posterioro hindsight which will not be discussed here. Our final result is, to order ε,

$$r = R\left(\frac{\tilde{A}(0)}{\tilde{A}(\tau)}\right)^{\frac{1}{2}}\left[1 + \varepsilon\left(-\tilde{\delta}_1 \cos 2(\Phi + \tilde{\Phi}_0) - \frac{1}{4} \cos 2(\tau + \Phi + \tilde{\Phi}_0)\right)\right]$$

$$\varphi = \Phi + \tilde{\Phi}_0 + \varepsilon\left[\tilde{\delta}_1 \sin 2(\Phi_0 - \tilde{\Phi}_0) + \sin 2(\tau - \text{[illegible]}) + \frac{1}{4} \sin 2(\tau + \Phi + \tilde{\Phi}_0) - \frac{1}{4} \sin 2\tilde{\Phi}_0\right] \quad (3.18)$$

where $\tilde{A}(\tau) = A(\tau)$ with δ_1, replaced by $\tilde{\delta}_1$. In vesting we find

$$R = R(r, \varphi, t, \varepsilon) = r\left(\frac{\tilde{A}(\tau)}{\tilde{A}(0)}\right)^{1/2}\left(1 - \varepsilon\left[-\tilde{\delta}_1 \cos 2\varphi - \frac{1}{4} \cos 2(\tau + \varphi)\right]\right) + O(\varepsilon^2)$$

$$\Phi = \Phi(r, \varphi, t, \varepsilon) = \varphi - \tilde{\Phi}_0 + O(\varepsilon^2). \quad (3.19)$$

where $\tilde{\Phi}_0$ is given by (3.14). These new coordinates autonomize the Mathieu equation within terms of order ε^2. The corresponding Hamiltonian $\tilde{H}$ is then an invariant to the same order

$$\tilde{H} = \frac{R^2}{2} = \frac{r^2}{2} \frac{\delta_1 + \varepsilon\omega_2 + \frac{1}{2} \cos 2\tilde{\Phi}_0(\tau)}{\delta_1 + \varepsilon\omega_2 + \frac{1}{2} \cos 2\tilde{\Phi}_0(0)}\left[1 + \varepsilon(2\delta_1 \cos 2\varphi + \frac{1}{2} \cos 2(\tau + \varphi) + 2\tilde{A})\right] \quad (3.20)$$

This actually includes both the stable and the unstable case. Without carrying out the calculations we see that the two parts of (3.7b) are the same formula if we allow imaginary numbers, resulting from the taking the square root of negative numbers. This idea can be carried through systematically to the introduction of imaginary values of time.

The invariant (3.2c) is not an adiabatic invariant in the usual sense of the word but is obviously of a similar kind.

4. Linear Oscillator with Slowly Varying Frequency. Passage through Resonance.[†]

Introduction. The equation to be discussed is

$$\frac{d^2u}{dt^2} + \omega^2(\tau)\cdot u = \mu(\varepsilon)\cdot\cos t, \quad \tau = \varepsilon t. \tag{4.1}$$

We shall assume $\mu(0)=0$ but otherwise leave the order of $\mu(\varepsilon)$ open for the time being. The frequency $\omega(\varepsilon t)$ is bounded above and below by positive constants.

Three types of equations are considered in this report: (A) (4.1) with $\mu = 0$; (B) Mathieu's equation; (C) (4.1) with μ not identically zero. In all cases the systems are Hamiltonian. For $\varepsilon = 0$ they reduce to a simple harmonic oscillator whose trajectories in the phase-plane are circles (in (A) one would have to replace t by ωt). In case (A) it is known that for $0 < \varepsilon \ll 1$ the motion is nearly periodic. In (B) however a special resonance phenomenon takes place in certain regions of the (δ, ε)-plane such that the solution is unstable. In (C) the classical type of resonance may occur, for arbitrarily small ε , for instance if $\omega = 1$, $\mu = \varepsilon$.

Our main interest here is the problem of passage through resonance. Resonance occurs when $\omega = 1$. Without loss of generality we assume that this occurs when $t = 0$. We make the restricitve assumption that $\omega' \equiv \frac{d\omega}{d\tau} \neq 0$ at $\tau = 0$. Loosely speaking this means that the system does not stay in the resonant condition too long. The problem of passage through resonance was first studied by Kevorkian in connection with problems in space dynamics. Kevorkian studied various model equations, of which (4.1) is the simplest. His original results were improved by himself and others. Our treatment of the problem will, however,

---

[†] For reasons of space and time we can here only give a survey of the results obtained for the problems studied.

not follow that given in the book by Kevorkian and Cole (the reader is referred to this book for various references). Instead our starting point is the presentation given by Wm. Kath in his course[†] on Singular Perturbations, Caltech 1982-83, although our view points and technique will differ from his in various respects.

Free Oscillations. We give a brief survey of the results for $u = 0$. The basic question may be written,

$$\frac{d}{dt}\begin{pmatrix} r \\ \varphi \end{pmatrix} = \begin{pmatrix} 0 \\ \omega(\tau) \end{pmatrix} + \varepsilon \begin{pmatrix} \omega' \cdot \omega^{-1/2} \cdot \frac{r}{2}(\cos 2\varphi - 1) \\ -\omega' \cdot \omega^{-1/2} \cdot \sin 2\varphi \end{pmatrix}, \tag{4.2}$$

where the polar coordinates are related to the rectangular coordinates by

$$u = r \cdot \cos\varphi, \qquad \frac{du}{dt} = -\omega r \sin\varphi .$$

The Hamiltonian is

$$H = \frac{\omega^2(\tau)\cdot r^2}{2}. \tag{4.3}$$

We introduce distorted polar coordinates (R, Φ) with the usual autonomizing requirement $\frac{dR}{dt} = 0$, $\frac{d\Phi}{dt} = 1$.

Straightforward calculations give

$$r = R\sqrt{\frac{\omega(0)}{\omega(\tau)}}\left[1 + \varepsilon\left(\frac{\omega'}{4\omega^2}\sin 2\Phi_0\right)\right], \tag{4.4a}$$

$$\varphi = \Phi_0 + \varepsilon\left[-\frac{1}{8\varepsilon}\int_0^{\tau}(\omega'(\tau'))^2\,\omega(\tau')^3\,d\tau' + \frac{1}{4}\,\omega'\omega^{-2}\cos 2\Phi_0\right] \tag{4.4b}$$

where

$$\Phi_0 = \frac{1}{\varepsilon}\int_0^{\tau}\omega(\tau')\,d\tau'. \tag{4.4c}$$

[†] This incorporates some material due to John Neu.

Inverting gives R and $\bar{\Phi}$ as functions of r and φ. In particular, the new Hamiltonian is

$$\tilde{H} = \frac{1}{2} R^2 = \frac{r^2 \omega(\tau)}{2\omega(0)} \left[1 - \varepsilon \left(\frac{\omega'}{4\omega^2} \sin 2\varphi \right) \right] + O(\varepsilon^2)$$

$$= j \left[1 + \varepsilon \left(\frac{\omega'}{4\omega^2} \sin 4\pi w \right) \right] + O(\varepsilon^2), \tag{4.5}$$

where j and w are classic action-angle variables

$$j = \frac{\omega r^2}{2}, \qquad w = -\frac{\varphi}{2\pi}. \tag{4.6}$$

The slow time, τ, is here given a priori by (4.1). The function $\bar{\Phi}_0$ is the same fast time as used by Kevorkian and Cole. The method of averaging gives it automatically. We may regard φ as a fast time corrected to higher order. The classical adiabatic invariant is given by (4.5). Our view point is, however, different from the usual. We believe: 1) Geometric arguments show that in principle there exists a transformation which autonomizes (4.1), with $\mu = 0$ exactly; 2) Exact autonomization implies automatically the existence of an exact adiabatic invariant; 3 & 4) The method of averaging autonomizes the equation to any desired order in ε, hence it also gives the adiabatic invariant to that order ε.

Forced Oscillations. Assume now $\mu \neq 0$. Then we may pose two problems: First we note that (4.1) is Hamiltonian and that it can be autonomized. This may be carried out approximately by the method of averaging, which thus will give an invariant for the full equation. Secondly, we note that the function of u,v,t, which is an adiabatic invariant (exact or approximate) for $\mu = 0$ will

$$j = \sum_{k,\ell} \varepsilon^k \mu^\ell J_{k\ell}, \qquad \varphi = \sum_{k,\ell} \varepsilon^k \mu^\ell \Phi_{k\ell},$$

where

$J_{k\ell}$, $\Phi_{k\ell}$ are functions of J, Φ, t, τ

and may in addition depend on ε. Calculations, which resemble those of §3 but which we shall have to omit, give

$$J = J(r, \varphi, t, \varepsilon)$$

$$= j \times \left[\left(\frac{1}{2}\frac{\mu}{\varepsilon}\int_0^\tau \omega^{-1/2}\sin(\tau^{+}-t)\,d\tau + 1\right)^2 + \left(\frac{1}{2}\frac{\mu}{\varepsilon}\int_0^\tau \omega^{1/2}\cos(t^{+}-t)\,d\tau'\right)^2\right]^{-1}$$

$$\times \left[1 + \varepsilon\left(\frac{1}{2}\omega'\omega^{-2}\sin 4\pi W\right) - \mu\frac{\cos(t-2\pi W)}{(\omega j)^{1/2}(1+\omega)}\right] + O(\varepsilon^2, \mu^2, \varepsilon\mu)$$

Possibility of Generalizations. We first consider Hamiltonian systmes of one degree of freedom. As an example take

$$\frac{d^2u}{dt^2} + \omega^2(\varepsilon t)u + a v^2(\varepsilon t)u^3 = 0. \tag{5.1}$$

Clearly, our geometric approach to problems of adiabatic invariants shows that under suitable conditions on ω and v (5.1) must have an exact adiabatic invariant. For this reason we consider much the classical treatment of oscillators with slowly varying frequency very unsatisfactory. It depends on the linearity of the equations which is an irrelevant feature from a deeper point of view. Of course, linearity simplifies computations. However, if a in (5.1) is of order ε we can use the method of averaging to linearize and autonomize (4.1).

Some obvious extensions can be made to cases of oscillators with damping, we shall not discuss them here. For higher order equations the problem becomes much more interesting. We believe with R.L. Anderson (private communicaions) that completely integrable Hamiltonian systems may be linearized. His arguments are group theoretical, a point of view we have not discussed here. The situation can be illustrated for two degrees of freedom with a time-independent Hamiltonian. By assumption of complete integrability there exist a second integral which is functionally independent of the Hamiltonian In the case corresponding to oscillatory motion each solution curve is confined to a two-dimensional torus. The topological closure of the curve may be the entire torus. Action-angle variables may then be introduced and the Hamilton-Jacobi equation is separable. (This is a nonlinear analogue finding the normal modes of a linear oscillator. The geometrical argument for linearization may then be extended. For perturbation problems the method of averaging may be used. However, assume that the Hamiltonian is the only integral. The motion is then, for a generic curve, completely ergodic and the topological closure of the solution curve is a complete energy surface. Thus the solution curve cannot be diffeomorphic to the solution curve of two linear oscillators . Also, if the nonlinearity is small, say $O(\varepsilon)$, then we believe any perturbation method will fail for sufficient large times. The same ideas apply to non-Hamiltonian systems. A third-order system whose solution exhibits chaotic gehavior for large times can probably not be linearized, and perturbation methods cannot be valid for times too large.

Finally, we consider a completely integrable Hamiltonian evolution equation. Can the above ideas be extended to infinitely many dimensions?

WATER CHANNEL TESTS OF TRAPPED VORTEX HIGH-LIFT AIRFOILS

Robert C. Anderson

SURF Sponsor: Prof. Anatol Roshko, Aeronautics

Lift and drag of dual flat plate trapped vortex airfoils were measured in the GALCIT low speed free surface water channel. Lift coefficients as high as 2.2 were obtained. Lift dropped off at angles of attack mostly above 15° and in some cases above 40°. Lift was observed to increase when shorter upper plates, upper plate leading edge curvature, or a trailing edge extension flap were introduced. These trends agree with theoretical predictions. Cavity resonance and concave streamline phenomena were observed and are discussed.

INTRODUCTION

The purpose of this SURF/GM/NSF funded research was to investigate the flow past a uniquely designed high-lift airfoil to determine its characteristics, and to optimize these characteristics (high lift, high angles of attack, etc.) to provide an appraisal of various airfoil configurations for use at low speeds.

When stalling occurs in conventional airfoils, the flow separates from the leading edge and does not reattach until far downstream. It was felt that if an additional plate were introduced above an initial flat plate and its leading edge were placed in the free-streamline of the separation layer from the lower plate, that a high lift inducing vortex would develop in the gap between the two plates. The airfoil design used is pictured in Figure 1a and the ideal (reattached) flow pattern in Figure 1b. The design resembles an elongated hinge with an upper plate bend at the leading edge and an upper plate trailing edge extension flap also. The model is constructed out of plexiglass and stainless steel. The lower plate has a dye injection tube which extends to its leading edge. Various lengths of upper (U-) plates can be attached at the trailing edge of the lower (L-) plate by a 15" length of stainless steel piano hinge.

The L-plate is bolted on each side to two large plexiglass discs which are pseudo-walls for the model. The upper plate however is supported by exterior struts which can raise or lower the angle of the U-plate with respect to the L-plate. Similarly the two supporting discs can be turned by supports to vary the angle of attack, α.

Extensive checks and rechecks of the flow were performed to insure that no adverse effects were present in the flow field.

The entire model hangs from a force balance which utilizes three strain gauges (two to measure lift, one drag). Digital readout of the force on the strain gauges is made using an amplifier console calibrated to measure pounds.

Testing of the airfoil was conducted in the CALCIT low speed free surface water channel, the test section of which has an 18" x 20" cross-section and a 20" x 50" viewing window. Top speed in the tunnel is 50 cm/sec, but the experiment was conducted at 30 cm/sec, thus the Reynolds number was calculated as 42,000 based on lower plate chord.

This airfoil design as stated above has only been approached by a handful of scientists. Hurley and Ruglen (Reference 1) studied a similar design without trailing edge flap nor U-plate leading edge bend; however, they employed boundary layer control techniques (a U-plate leading edge blow slot) to force the separated layer to reattach on the upper face of the U-plate. Their lift coefficients were high, but at a cost of high power to the blowing mechanism.

In 1978, Rossow (Reference 2) investigated airfoils with leading edge and trailing edge flaps, but also employed BLC techniques.

The present paper is concerned with the characteristics of the design without boundary layer control. Although drag coefficients are high (above 0.4 in most notable cases) because the flow reseparates from the U-plate for $\alpha \geq 15°$, the high lift coefficients encountered are a significant result.

EXPERIMENTAL RESULTS

High Lift

The lift characteristics of the airfoil were found to be superior to conventional airfoil lift. Numerous configurations were found which had lift coefficients above 1, and three configurations were found with lift coefficients above 2. The highest of these had $C_\ell = 2.2$ (based on ℓ_2 area 6" x 15") for $\alpha = 30°$, $\beta = 53°$, $\ell_1/\ell_2 = 0.67$, bend angle $\phi = 40°$, bend length $\ell_b = 7/8"$ and tail length $\ell_t = \frac{1}{2}"$ (See Figure 3b). The best conventional airfoil can achieve a lift coefficient no greater than 1.6, therefore experiments show a 38% improvement in lift by using the trapped vortex airfoil design.

High Angles of Attack

A typical characteristic of stalling for conventional airfoils is a drop off of lift as angle of attack increases. Here, it was found in most cases, that for β fixed at a moderate value around 5°, the lift would increase without dropping off for α above 15° (where lift drops for most conventional airfoils) and even up to 40° (See Figure 2a).

The only reason for the upper bound of 40° in this study is that the model structure was designed to go up to 40° angle of attack maximum, obviously underestimating the incredible lift drop off characteristics that would be encountered.

High Lift Features

In comparison testing of three lengths of upper plate it was found that as the length ratio decreases with fixed α, that the β angle of lift drop off for the airfoil increased (See Figure 2b). Thus small plates with $\ell_1/\ell_2 \leqq 0.50$ are preferred for high lift over long upper plates.

Also, for the case of $\ell_1/\ell_2 = 0.67$, introduction of an upper plate leading edge bend increases the lift by 22% (See Figure 2c). This result is supported by theory which proposes that leading edge curvature relieves the adverse pressure gradient which is present on the upper face of the U-plate. Although reattachment of the flow on the upper face did not occur above $\alpha = 15°$, the lift of the airfoils was substantial.

It was also found that introduction of a trailing edge extension (of 8% chord for a $\ell_1/\ell_2 = 0.83$ case) increases the maximum lift by 25% over the no tail case (See Figure 2d). This agrees well with theoretical predictions as put forth in Reference 3.

Resonance Configurations

In order to optimize the high lift of the airfoil, the L-plate was fixed at a measured angle of attack and the separation streakline as visualized by dye injection was examined with $\beta = 0$. In this configuration, comparable to a single flat plate, small (approximately 1/20 chord) vortices are visible (See Figure 3a). When the U-plate is raised so that the leading edge is directly in the separation layer, a configuration can be found where the separation layer vortices become about 1.5 times larger in size and well defined in structure.

Due to strong and coherent impingment of these vortical structures on the leading edge of the U-plate, structural resonance of the airfoil was observed. The phenomenon seems to be a cavity resonance effect similar to those described in Reference 4.

Concave Free-Streamline Effect

As seen in Figure 3b, the free-streamline of the maximum lift configurations (i.e., also resonance cases) evidence a convex free-streamline between the L and U-plates; however, for β approximately 10° to 20° above optimum, it was found that the free-streamline was concave and radically lower in speed (by a factor of approximately four from optimum free-streamline speed).

The explanation of this effect is that the stagnation point of the flow has moved onto the upper edge of the L-plate as can be seen in Figure 3c. Remarkably, positive lift was often measured in such cases; however, such a configuration is obviously a stalled case.

CONCLUSION

The lift and drag of high-lift trapped vortex airfoils were measured in the GALCIT low speed free surface water channel. Lift coefficients as high as 2.2 were obtained. Lift dropped off at angles of attach mostly above 15° and in some cases above 40°. Lift was observed to increase when shorter upper plates, upper plate leading edge curvature, or a trailing edge flap were introduced. These results agreed with theoretical predictions. Cavity resonance and concave streamline effects were observed and discussed.

REFERENCES

1. Hurley, D.G., and Ruglen, N. "The Use of Boundary Layer Control to Establish Free Stream-Line Flows Being an Introduction to the Free Stream-Line Flap," Report A.R.L./A.109, April 1958.

2. Rossow, V.J. "Lift Enhancement by an Externally Trapped Vortex," Journal of Aircraft, Vol. 15, No. 9, Sept. 1978, pp. 618-625.

3. Saffman, P.G., and Tanveer, S. "Vortex Induced Lift on 2-D Airfoils," Submitted to Journal of Fluid Mechanics.

4. Gharib, M. "The Effect of Flow Oscillations on Cavity Drag, and a Technique for Their Control," Ph.D. Thesis, California Institute of Technology, 1983.

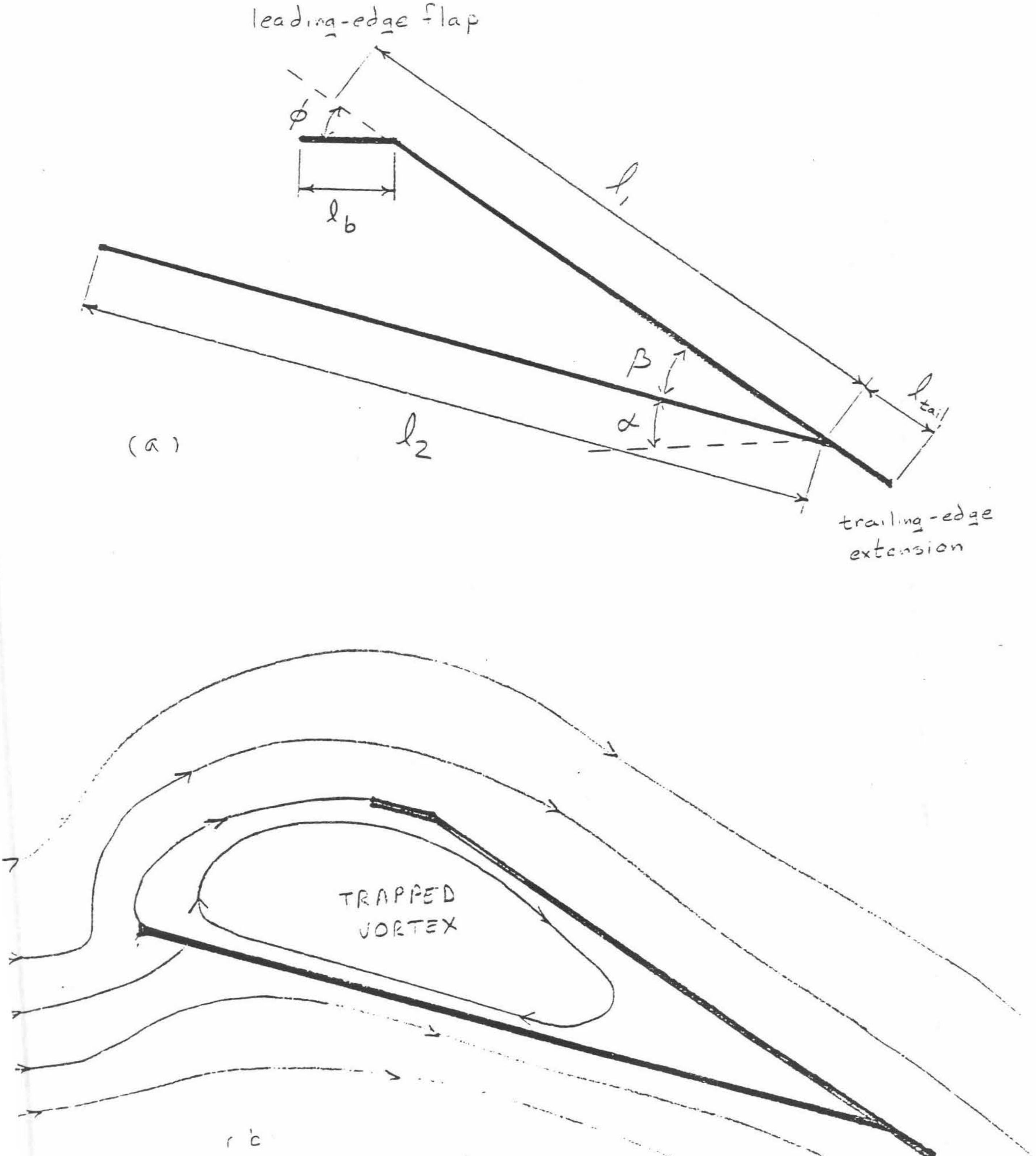
leading-edge flap
φ
l_b
l_1
β
α
l_{tail}
l_2
(a)
trailing-edge extension
TRAPPED VORTEX

FIGURE 1

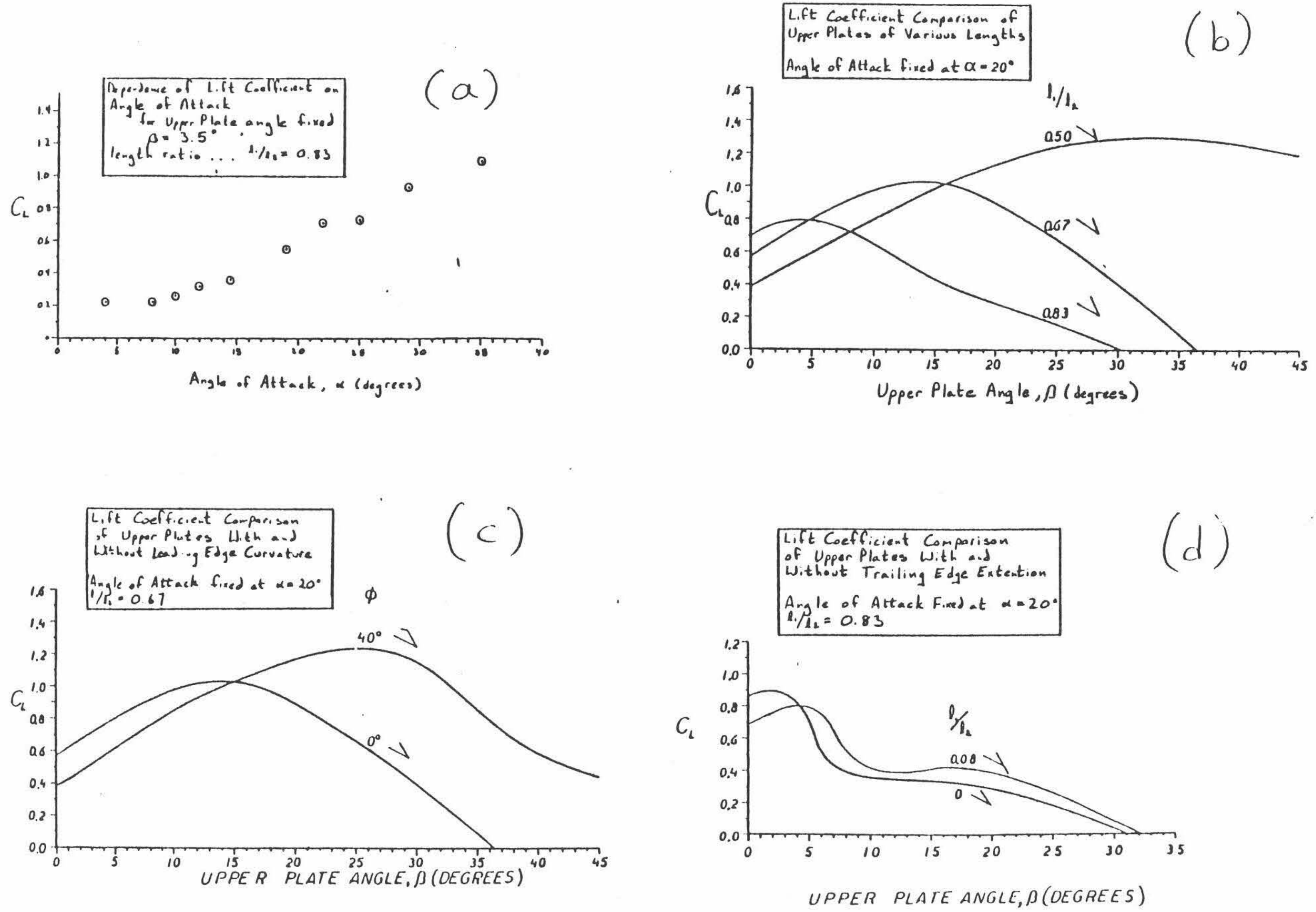(a)
Dependence of Lift Coefficient on Angle of Attack for Upper Plate angle fixed β = 3.5°, length ratio ... l1/l2 = 0.83
C_L
1.4
1.2
1.0
0.8
0.6
0.4
0.2
0
0
5
10
15
20
25
30
35
40
Angle of Attack, α (degrees)
(b)
Lift Coefficient Comparison of Upper Plates of Various Lengths
Angle of Attack fixed at α = 20°
l_1/l_2
0.50
0.67
0.83
C_L
1.6
1.4
1.2
1.0
0.8
0.6
0.4
0.2
0.0
0
5
10
15
20
25
30
35
40
45
Upper Plate Angle, β (degrees)
(c)
Lift Coefficient Comparison of Upper Plates With and Without Leading Edge Curvature
Angle of Attack fixed at α = 20°
l_1/l_2 = 0.67
φ
40°
0°
C_L
1.6
1.4
1.2
1.0
0.8
0.6
0.4
0.2
0.0
0
5
10
15
20
25
30
35
40
45
UPPER PLATE ANGLE, β (DEGREES)
(d)
Lift Coefficient Comparison of Upper Plates With and Without Trailing Edge Extention
Angle of Attack Fixed at α = 20°
l_1/l_2 = 0.83
l/l_2
0.08
0
C_L
1.2
1.0
0.8
0.6
0.4
0.2
0.0
0
5
10
15
20
25
30
35
UPPER PLATE ANGLE, β (DEGREES)

FIGURE 2

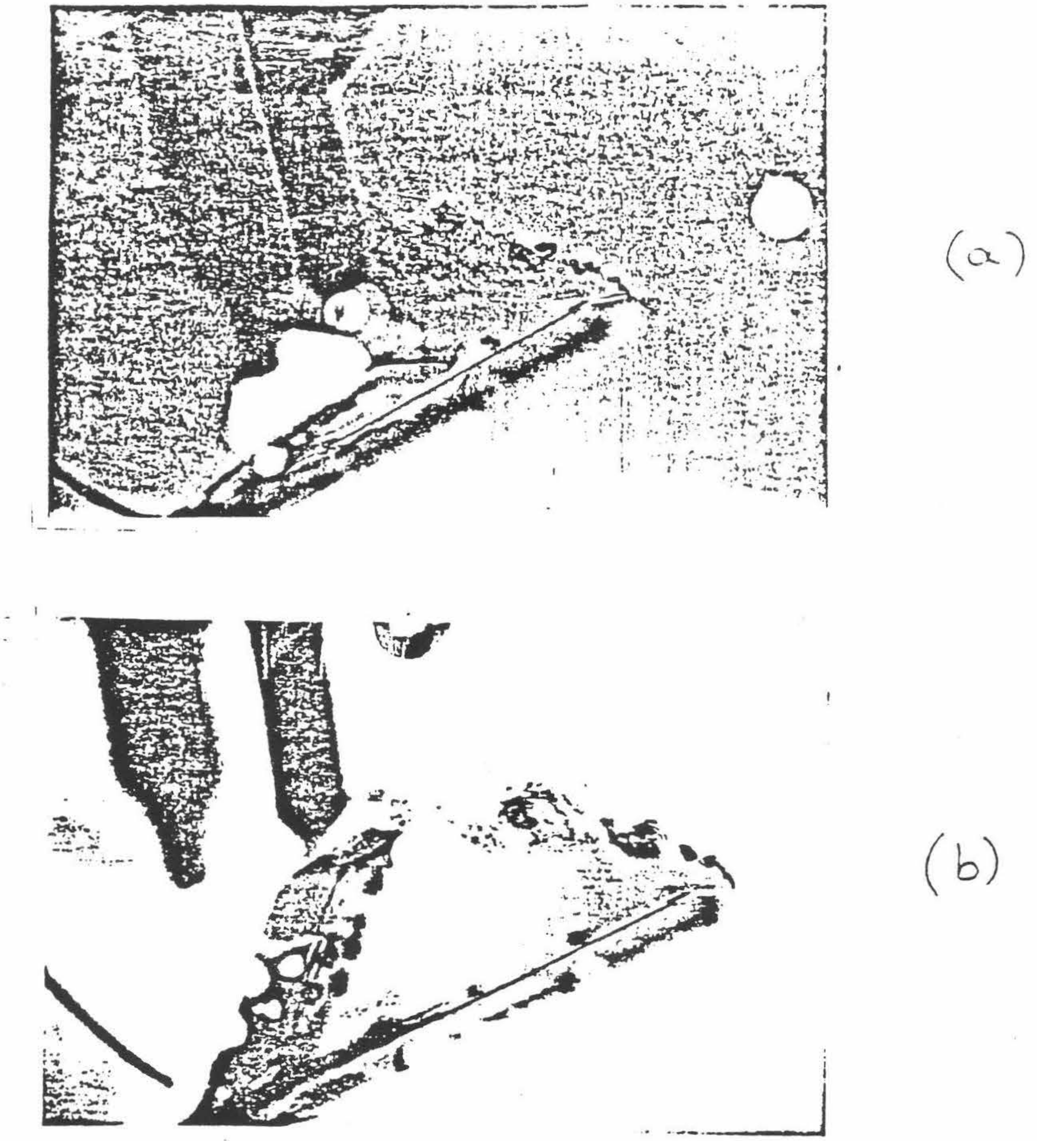

FIGURE 3

Acousto-optic experiments with BSO crystals

Praveen Asthana

Dr. D. Psaltis

Abstract

The objective of the project was to build an acousto optic device with a $Bi_{12}SiO_{20}$ crystal, to look at its acousto optic properties, and to study its optical activity. After ten weeks it can be said that some insight was gained into the acousto-optic interaction, primarily that involving the optical activity of the $Bi_{12}SiO_{20}$ (BSO).

Introduction

Recently wide interest has developed in optically nonlinear crystals for their use in phase conjugate optics and in optical signal processing and computing. A good choice for such a crystal would be the BSO crystal which is of good optical quality, photorefractive, electro-optic and easily available. Acousto-optics is an estabilished method of optical signal processing. It could be useful to study acousto-optical interactions in a nonlinear crystal like BSO.

Presentation

The first task was to build the acousto-optic (AO) device. Considering the difficulty of bonding a transducer to the BSO crystal, I decided to use an available Quartz crystal that already had a Lithium Niobate piezoelectric transducer attached. It was found that the transducer sent out longitudinal acoustic waves in the quartz. Thus the quartz could be used much as a wave guide: held tightly against the BSO crystal, it would channel the acoustic impulses into the BSO.

It was decided attenuation in the quartz would be quite small.

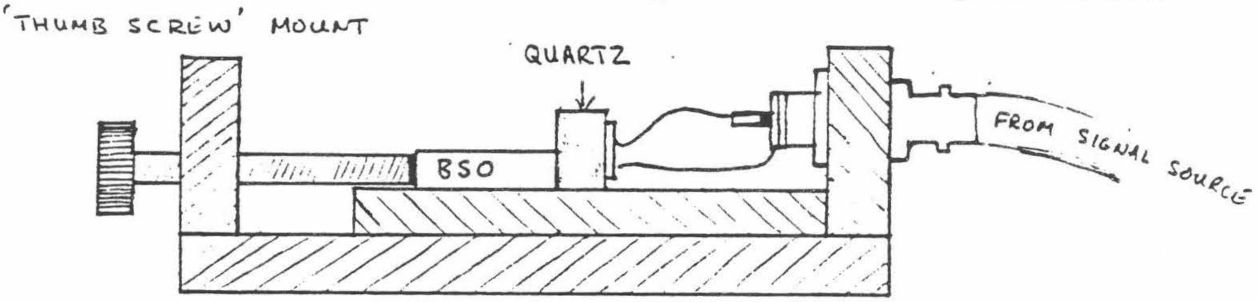

For electrical impedance matching between transducer and signal source, an LC impedance matching network was designed with a centre frequency of 50 MHz. But despite this network, diffraction spots appeared for certain discrete frequencies and not continuously as was expected. This was somewhat baffling until the possibility was investigated that the quartz might be acting as a resonant cavity, an acoustic Fabry Perot, so to speak. Taking the length of the crystal and the sound wavelength used, it was figured in theory that if this were a resonant cavity then the frequencies at which diffraction occured would be separated by 0.34 MHz. The experimental results agreed closely with this. The fact that the quartz was a resonant cavity was a handicap but one that could be lived with.

The refractive index variation grating set up in the BSO crystal by the acoustic waves diffracted light quite well with acoustic frequencies ranging from 8 MHz to 140 MHz. I was unable to locate experimentally the Bragg angle of the BSO acousto-optic cell.

Studying the optical activity of the crystal proved to be fruitful. Linearly polarized light is a superimposition of left-handed and right-handed circularly polarized light. A crystal with optical activity allows the two kinds of circularly polarized light to pass through at different speeds resulting in a phase difference between them. When now superimposed they form linear light polarized at a different angle from the input light. For BSO I discovered the rotary power was 46° per cm of interaction length.

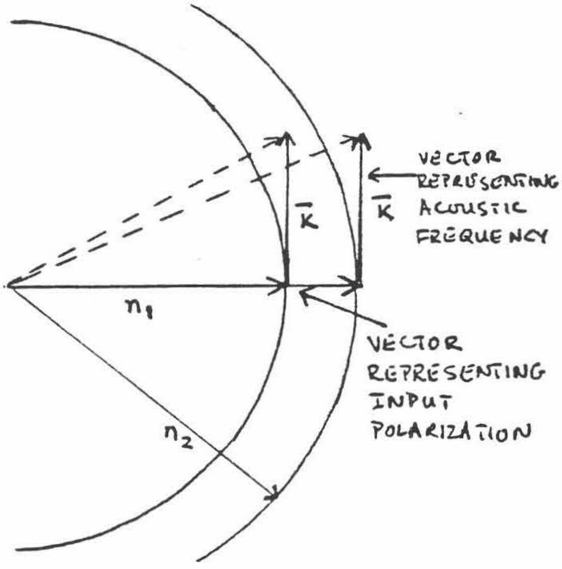

The index of refraction of BSO is $\bar{n}=2.55$. The rates at which the two different kinds of polarized light pass through BSO can be represented by n_1 and n_2, indices of refraction such that:

$$n_1 = \bar{n} + \frac{G}{2\bar{n}} , \quad n_2 = \bar{n} - \frac{G}{2\bar{n}}$$

G represents the Gyration which is a measure of the rotary power.

$$G= \frac{0.4x6328E-10x2.55}{0.005x\pi} = 4.109 \text{ E-5}.$$

Thus n_1= 2.550008 and n_2= 2.5499919. $n_1-n_2 = \Delta n$ = 1.6E-5. n_1 and n_2 can be thought of as radii for two concentric circles. The K vector representing acoustic power cuts across these circles. The coupling of energy from one kind of circular polarization to another was attempted using acoustic waves. To be sure of accurately detecting small changes in the polarization of the light coming out of the BSO crystal, the output light was focused on to a CCD Reticon scanning system with an oscilloscope display.

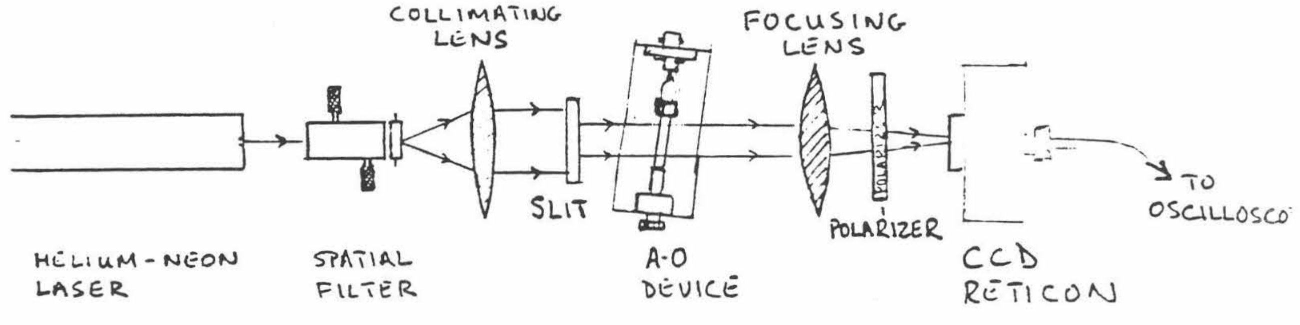

Some time was spent looking for circularly polarized light output at different crystal orientations while sweeping through the frequencies. The input light was lineraly polarized at 0°. At a crystal angle of 3.9° and a frequency of 20.19 MHz, I saw the results shown in photos 1 and 2. The +1 order didn't change at all as I rotated the polarizer. The zeroeth and -1 orders had their minimums.

The vector diagram looks something like this:

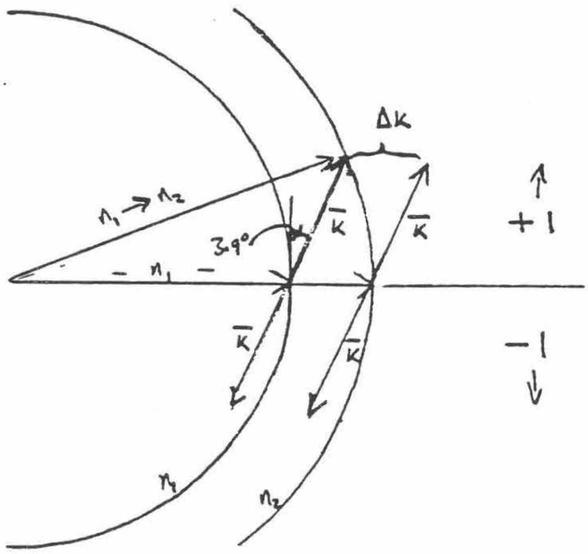

The K vector is in two parts-the part pointing upwards affects the +1 order of the diffraction while the one pointing downwards affects the -1 order. $+n_1$ and $+n_2$ represent the indices of refraction associated with the +1 diffracted order. Likewise $-n_1$ and $-n_2$ are associated with the -1 order. From the diagram it is seen that for the +1 order the polarized light represented by n_1 is coupled to the n_2 circle. The phase mismatch, Δk, of the +1 n_2 vector is large enough for it to adversely affect the +1 n_2 polarization. Meanwhile for the -1 order, the phase mismatch for both n_1 and n_2 is small enough that it can be ignored, allowing the two vectors to add up and form linearly polarized light.

To see if experiment would agree with theory, a vector diagram for 33 MHz was tried. This would mean a crystal orientation angle of 2.5° or 87.5° with respect to incident light. The experiment gave the results shown in photos 3 and 4. The crystal angle was 2.7° and the frequency was 33.76 MHz. The intensity of the peaks was low, perhaps because exact phase matching could not be achieved.

These were the explainable results. There were a few that I haven't been able to explain: For example at certain frequencies, diffraction spots arose between the zeroeth and first orders or the first and second orders. And at 57.46 Mhz, a large number of diffraction spots arose where basically they had no right to do so. Notable also is that these spots were usually differently linearly polarized from each other. See photo on next page showing the result at 57.46 MHz. Each peak represents a diffraction order.

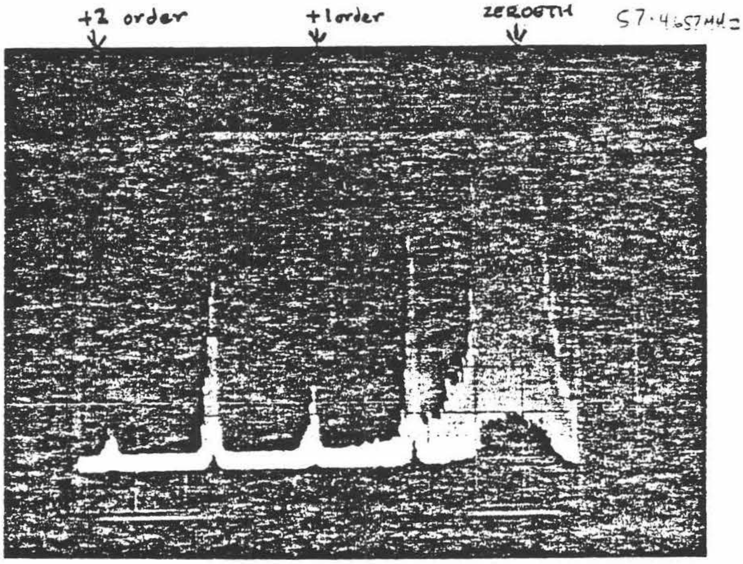

The acoustic waves set up a grating in the BSO, thus light is diffracted by this grating into many orders. However it is not clear why diffraction spots appear in between normal 0th, 1st and 2nd orders.

Conclusion and Discussion

It is possible to couple energy from linearly polarized light to circularly polarized light or from left handed to right handed circularly polarized light in a BSO crystal using acoustic waves. With this ability, BSO crystals can be used as components in an optical computer. True, they can be used as "gates" similar to the ones in electronic computers, but the beauty of the optical computer is that it would be able to incorporate sophisticated techniques like fourier transformation, spatial filtering, phase conjugation and holography into computer functions. BSO crystals are used for phase conjugation and optical storage, making them even more attractive.

I would like to continue this research by looking into the phenomena causing some of my unexplained results. I would also like to look at optical activity in itself--it can be very useful for signal processing as it is possible to control this optical activity by many means (for different results) ranging from light intensity to electric potential. This is a fascinating and resourceful subject.

Photo 1

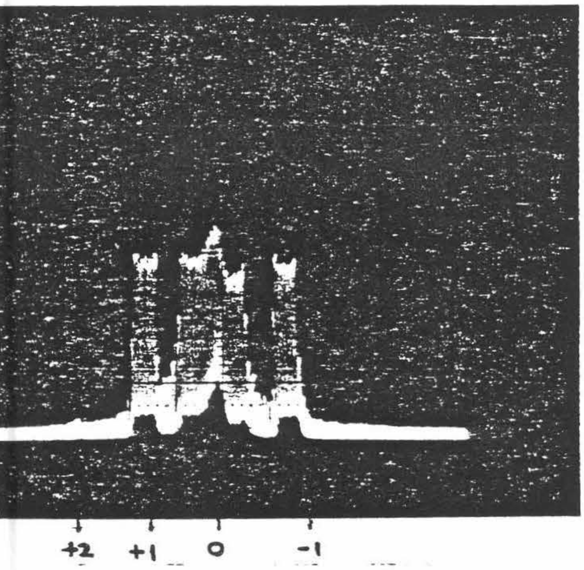

Photo 2

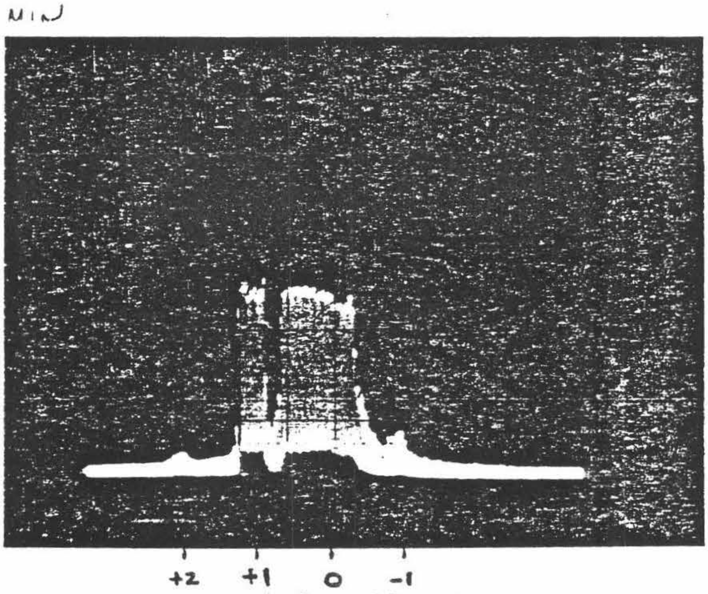

These photos show the output of the CCD onto the oscilloscope screen. The polarizer just before the CCD was rotated and the effect observed. Photo 1 was taken when all orders were maximum and photo 2 was taken when the -1 order was a minimum. The +1 order did not change in intensity while the polarizer was rotated.

Photo 3

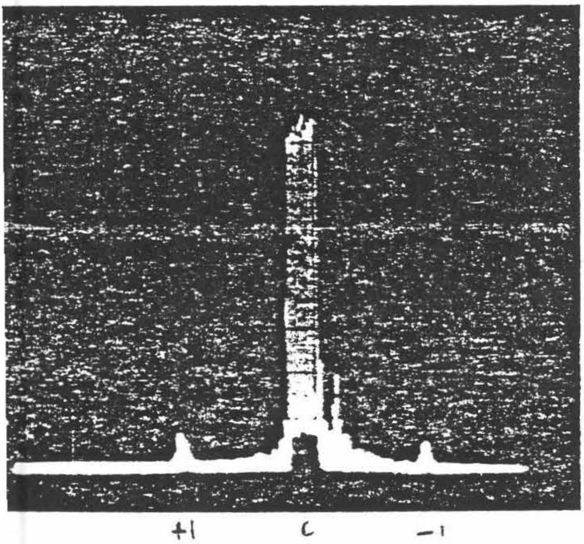

Photo 4.

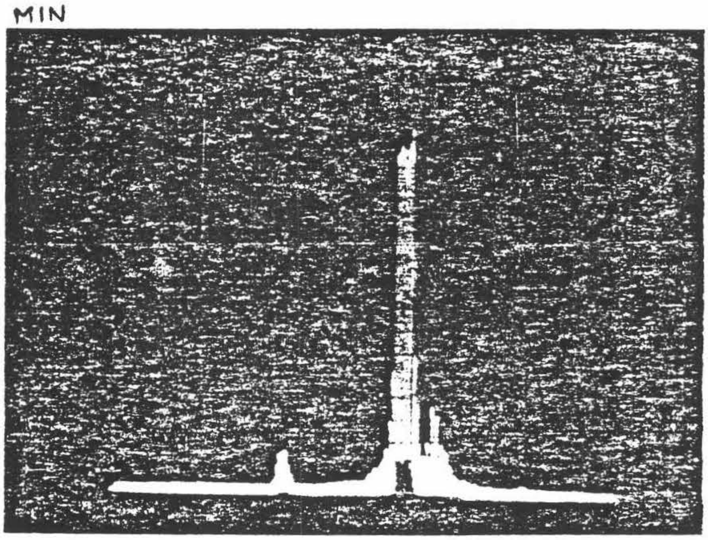

An Analysis of Satellite Observations of Ozone and Related Species

Stanley A. Berman

SPONSOR: Professor Yuk L. Yung

ABSTRACT:

A study was done on data obtained by the LIMS experiment aboard the NIMBUS 7 spacecraft. Assuming photochemical equilibrium, analytic expressions for the concentration of ozone as a function of the data retrieved by LIMS were derived. Differences between the model and observed data show that further investigation is necessary.

Ozone is perhaps the most important constituent of the earth's stratosphere, the region of our atmosphere between the altitudes of 20 km and 60 km. Its abundance affects both chemical and dynamic processes occurring in the atmosphere; it is of major importance in regulating the thermal structure of the atmosphere; and, also, its absorption of harmful solar ultraviolet radiation is necessary for the continued presence of life on earth.

The pioneering work on ozone was done by Chapman and published in 1930. He explained all of ozone's chemistry with four reaction involving the various oxygen species: O, O_2, O_3. It was not until twenty years later that it was realized that other species, though negligible in abundance compared to ozone, could play an important part in the destruction of ozone. The reason is a variety of catalytic cycles which consume these trace species, but then regenerate them later in the cycle. The first cycles discovered were those involving HO_x (H, OH, and HO_2). In later years it was found that NO_x (NO and NO_2) and ClO_x (Cl and ClO) also play a part in the destruction of ozone. Current models of the stratosphere may contain over 30 species and over 130 reactions, but it is believed that the ozone photochemistry may still be adequately explained using only the production and loss mechanisms of Chapman and the catalytic loss cycles involving HO_x, NO_x, and ClO_x.

One reason why work on this subject has proceeded so slowly was the lack of large bodies of data with which to compare to model calculations. Measurements were normally made from spectroscopes mounted on balloons or rockets. These experiments could only be of short duration, and they were very limited geographically. Large planetary variations in ozone are to be expected, and temperature variations at a given point may also alter the ozone concentration, so this data was not very useful. We now, however, have access to data retrieved from the LIMS (Limb Infrared Monitor of the Stratosphere) experiment carried aboard NASA's NIMBUS 7 spacecraft. This contains simultaneous measurements of pressure, temperature, and mixing ratios for ozone, water vapor, nitric acid, and nitrogen dioxide at various times of year and at various latitudes and longitutes.

Assuming photochemical equilibrium (i.e. assuming that the photochemistry is much more important than vertical transport processes such as diffusion) a set of solvable simultaneous equations containing temperature, ozone, water vapor, and nitrogen dioxide were derived for seven pressure levels in the atmosphere corresponding to the altitudes from 35 km to 65 km in 5 km steps. Also input into these equations were several other variables that were not measured by LIMS. Chemical rate constants are calculated using the most recent laboratory measurements. Photochemical rate constants which depend on solar illumination, and thus the geographic location and local time, were calculated using a stratospheric modeling program used by atmospheric researchers at Caltech. This had to be modified slightly for use on a new computer. Also necessary were the concentrations of a few species which LIMS unfortunately did not measure. These include ClO and CO. These values were taken from a standard atmosphere and thus do introduce some uncertainty into the calculation.

These equations have been put into a package that determine the concentration of ozone from the input quantities. Analysis of the returned ozone values show that because of the temperature dependences of the various rate constants there exists a rather simple relationship between the concentration of ozone and the temperature (T).

$$[O_3] \propto \exp(C/T)$$

The constant C depends on the pressure level in the atmosphere, the location, and the local time. A package has also been created that can statistically analyze the LIMS data and determine various relationships between the measured quantities. It turns out that in the observed data there also exists in most places that simple relation between the concentration of ozone and the temperature. In Table 1 can be seen a comparison between the values of C obtained at various pressure levels for data taken between 30 and 35 degrees North latitude. There are also values returned from the theoretical model run at 32 degrees longitude and close pressure levels. It can be seen that there is not good agreement.

There are several possible reasons for the disagreement. One reason is the assumption that ozone is in photochemical equilibrium. Although this is believed to be a good approximation at higher altitudes, it is known to be wrong in the lower stratosphere. At about the 35 km level the observed value of C switches signs which is what one would expect if transport processes were becoming important. Several other sources also report this as the level where transport becomes important. Another possible source for this difference is uncertainties in the values of the chemical rate constants that we are using. A similar study to this has already made predictions for better values of rate constants that were later confirmed in the laboratory. Also it is possible that the values being used for some of the species not measured by LIMS might be in gross error.

OBSERVED VALUES		THEORETICAL VALUES		CORRESPONDING
PRESSURE (MBAR)	C	PRESSURE (MBAR)	C	ALTITUDE (KM)
.1	1694 +/- 356	.094	1145 +/- 4	65
.2	949 +/- 310	.219	1128 +/- 4	60
.4	754 +/- 207	.373	1175 +/- 4	55
.8	928 +/- 127	.797	1359 +/- 4	50
1.5	838 +/- 175	1.313	1454 +/- 4	45
3.0	749 +/- 51	2.870	1462 +/- 3	40
5.0	53 +/- 14	4.984	1380 +/- 3	35

TABLE 1. C AS A FUNCTION OF PRESSURE IN THE MIDLATITUDES

There is still a lot more work to be done before this project is completed. By manipulating the analytic program the actual importance of each of the various loss cycles to the theoretical model may be determined. Then the rate constants may be changed slightly to see if one can force the model to agree with the observed data. By doing this it may be possible to get a better picture of what the important reactions affecting ozone really are. And we might get a feel for what the chemical rate constants really should be.

The photochemistry of ozone is both a very important subject and a poorly understood subject. The differences between the model and the satellite measurements show at the very least that we do not have a quantitative guage on all of the important reactions. The further work on this project should yield something more of value, at least some rough idea of what the relative importance of the various reactions is. Until we get simultaneous measurements of all important species, however, rather than just a select few, we will not have a perfect understanding of what´s really happening up there.

BIBLIOGRAPHY

Allen, M., J.I. Lunine, and Y.L. Yung, The vertical distribution of ozone and related species, 1983.

Barnett, J.J., J.T. Houghton, and J.A. Pyle, The temperature dependence of the ozone concentration near the stratopause, *Quart. J. Roy. Meteor. Soc.* ,101, 245,257, 1975.

Johnston, H.S., and J. Podolske, Interpretation of stratospheric photochemistry, *Rev. Geophys. Space Phys.* , 16, 491-519, 1978.

WMO, *The Stratoshere 1981: Theory and Measurements* ,WMO Global Ozone Research and Monitoring Project Report No. 11, World Meteorological Organization, Geneva, Switzerland, 1981.

Title: Neuronal connectivity in the song system control nuclei of the zebra finch (*Poephila guttata*) brain.

Author: Daniela M. Bonafede

Faculty Sponsor: prof. Masakazu Konishi

Abstract: An experiment assessing the connectivity of HVc cells showed that there are at least two nonoverlapping populations of HVc neurons: X projecting neurons and premotor, RA projecting neurons. The anatomical diversity of the two populations suggests that they may play distinct roles during song acquisition and production.

Introduction

The song of the zebra finch (*Poephila guttata*) is controlled directly by a number of brain nuclei which, through their individual and combined activity, lead to motivation for and production of song. Both anatomical and physiological studies carried out in the past decade in the laboratories of Konishi at Caltech and of Nottebohm at Rockefeller have elucidated the connections between the various nuclei and their possible roles in song learning and production.

Song is an exclusively male behavior in the zebra finch, which is learnt by young birds from their conspecific adult males during a critical period of about 45 days. Young zebra finches need to hear examples of conspecific song in order to make what might be called an "auditory template" of it. At a later time during the critical period these birds start vocalizing and keep correcting their own song pattern against the template by an auditory feedback mechanism. When the desired song pattern is acquired, the song is said to have crystallized: it can no longer change and will persist unaltered throughout the bird's lifetime, even if deafness should occur (1, 5).

The song of an adult male does not occur at random, but is a very specific and integral part of courtship: an adult male zebra finch will always sing when courting a female.

In view of what is known about the modalities of song learning and production, it is possible to infer that there must be at least three major types of neuronal specializations in the zebra finch song nuclei, which, properly coordinated and interconnected, can account for the observed behavioral patterns.

Because the first step towards song learning is listening to conspecific song and because the young bird needs to hear its own imperfect vocalizations in order to acquire song, some of the neurons or brain areas involved in song control must be of an auditory type. The auditory area or areas must be able to respond to conspecific song and keep a "memory" of it, or template, to respond to the bird's own vocalizations and to compare them with the template. Furthermore, there must be a mechanism through which this or these auditory areas can communicate with those more directly involved in song production, such as motor and premotor ones, in order to correct the output.

Second, because song production, as pointed out earlier, does not occur randomly, but is elicited by the presence of a female, it seems likely that there be some sort of neuronal motivational centers, whose activity stimulates song production.

Third, there must be centers devoted to encoding the motor program for the crystallized song and to executing it upon proper stimulation from the motivational centers.

It is an interesting and useful intellectual game to try and deduce *a priori*, before doing any anatomical work, how the various types of neuronal specializations described above could be connected to each other in order to produce a system that works like the zebra finch song system.

I tried to build a schematic model, illustrated in fig.1, that might serve as a guideline for future experiments. I view the song system as a construction enterprise: with several departments in charge of particular tasks and a main office that coordinates and directs their work. The model requires that there be in the zebra finch brain an area that [illegible] as the stimulator to initiate song from the mot[illegible] center in the adult bird and a developmental order to start singing behavior early in life: that has access to both the template and the bird's own song during the critical period and possesses the capacity for comparing the two inputs, that can effectively stimulate activity of the motor control areas during development and simply turn on the song program during adult life.

This requires a plastic system, which allows communication and interaction between the "auditory" and "premotor" neurons in the control area during song development, but shuts it off once the behavior is acquired. It also requires both a motor and a premotor area: one for the actual production of song every time the behavior is started, the other to store the motor program corresponding to the bird's mature song. Accordingly, the control area would stimulate the premotor area only, which would in turn direct the activity in the motor area itself.

If we now go back to the anatomical and physiological data available from previous investigators, we can see whether the model fits the data and even make predictions, or at least suggest experiments that would test it.

Beginning at the bottom of the hierarchy and working our way up, we find nucleus **nXII** (nucleus Hypoglossus, pars tracheosyringealis), which has been repeatedly and conclusively shown to be the motor area (5).

nXII receives projections, other than from nucleus **DM**, from nucleus **RA** (nucleus Robustus Archistriatalis) (6): this area shows activity during song production and its lesion results in severe damage to the bird's song (5). This nucleus may be thought of as a premotor area, particularly in view of the fact that it displays activity shortly before actual vocalizations are initiated.

Moving another step higher in the hierarchy, we find nucleus **HVc** (Hyperstriatum ventrale, pars caudale), which has been shown anatomically to project to **RA** (6) and physiologically to have intense song related activity (5). Its lesion, as that of **RA**, results in severe impairement of song. Physiological studies have shown that **HVc** contains premotor type neurons, whose activity leads by small intervals the production of song (and by even smaller intervals activity in **RA**), but which do not respond to any auditory stimuli; and auditory neurons, which respond to noise and to playback of the bird's own song, but whose activity is suppressed by activity of the premotor neurons, that is prior to and during adult song production (4). Auditory neurons in **HVc** have been shown to project to area **X** only, and not to **RA** (2).

The highest ranking nucleus in the hierarchy of the song system has been found to be nucleus **NIf** (Nucleus Interfacialis): it sends projections to **HVc**, leads all other nuclei in premotor activity and may have auditory responses, although this has not been clearly shown. Its lesion, or lesion of its projection to **HVc**, as expected, results in inability to produce stereotyped song (5).

NIf receives input from nucleus **Uva** (6), a thalamic structure which is apparently not involved in adult song production, since lesion of it or of its projection to **NIf**, has no effect on song. No activity has been detected in **Uva** immediately prior to, during or immediately after song production. **Uva** projects to **HVc**, as well as to **NIf**, but the function of this pathway is just as obscure.

Another nucleus which is anatomically connected to the song system, but whose function is still unknown, is area **X**. It receives input from **HVc**. Its lesion does not appear to have any effect on song behavior and no song related activity has been detected in it.

Nucleus **MAN** (Magnocellular nucleus of the Anterior Neostriatum) is also known to project to **HVc** (6). But, again, its lesion has no effect on song behavior and no song related activity can be detected within it (5). Interestingly, this nucleus has been found to accumulate male hormone more than any other area so, since song learning and crystallization is known to be under hormonal control (1), it is possible that **MAN** play an important role during song acquisition.

There are several ways to approach the problem of further analyzing how the song system is wired up: one of them is to define as precisely and as completely as possible, for each demonstrated or presumtive song nucleus, the types of neurons that make it up, both on physiological and on anatomical basis.

I decided to start with **HVc** for two reasons: one is that it is the nucleus on which more studies have been done so far, and therefore one of which it is more likely to succeed in obtaining a complete description; the other is that it is the one with the most afferent and efferent pathways, and certainly central to the architecture of the song system.

It is known that **HVc** projects to **RA** and **X**, and that it has both premotor and auditory neurons. Auditory neurons are inhibited during song production and at least some of them have been shown to project only to **X**.

A hypothesis that arises from these data is that early in development, when song is being learnt, the exclusively **X** projecting auditory neurons have connections (either direct or through interneurons) with the exclusively **RA** projecting premotor neurons; later on, once the song is crystallized, these connections would be lost or inactivated and the two populations of **HVc** neurons would become physiologically, as well as anatomically, separated. The premotor neurons and/or the interneurons (if there were any) could, upon song crystallization, develop inhibitory synapses on the auditory neurons, which would account for the physiological oservations reported above, as well as for the fact that no changes can be made to the crystallized song, since auditory feedback is turned off in adult birds.

This model has the advantage that it avoids the paradoxical conclusion that there are indeed auditory neurons in the song nuclei, as the auditory feedback hypothesis for song learning requires, but the premotor ones have no acces to the information they relay.

The first step to testing this model is to show that the **RA** and the **X** projecting neurons in **HVc** are indeed two distinct, nonoverlapping populations. This is the simpler step. The next steps are to show that there is activity of the auditory neurons during vocalizations of young birds (before song crystallization) and that lesion of **X** or of the fibers going from **HVc** to **X** in very young birds has an effect on song acquisition.

It is worth carrying out a similar experiment on the projections of Uva to **NIf** and **HVc** for two reasons: one is that it would give more information on the anatomy and connectivity of this nucleus, about which very little is known; the other, more important one, is that it would allow to decide whether **Uva** is part of the song acquisition system and, possibly, with what function and at what stage.

Presentation and discussion of results

In order to distinguish between two populations of neurons within one nucleus with different projections I relied on the retrograde transport of two different and visually discernible tracer substances from the innervated nuclei.

One of the tracers used is a suspension of red fluorescent latex microspheres (beads) (3). Approximately 0.1 µl are injected with a micropipette in the desired nucleus using a stereotaxic apparatus; as soon as 24 hours later there is extensive labelling of the projecting nucleus. Label does not diffuse out of cells and does not fade unless particular chemicals are applied to the sections.

The other tracer used is the enzyme Horseradishperoxidase (HRP). HRP is used as a 10-30% solution in H_2O and approximately 0.1 µl are injected as with beads. Best results were obtained with 48 hour survival time. The DAB reaction was used to process brain sections.

In all experiments zebra finches received simultaneous injections of beads in one nucleus and of HRP in the other, were allowed to survive for 48 hours and sacrificed by cardiac perfusion with 1.25% glutaraldehyde, 0.1% paraformaldehyde in 0.1 Molar phosphate buffer followed by cold 10% sucrose in phosphate buffer. The brains were removed and sunk overnight in 30% sucrose in phosphate buffer at 4C°. The fixed brains were cut sagittally into 30 µm thick sections on a freezing microtome, treated for HRP, mounted on Gatenby slides and coverslipped with minimal immersion ((30") in xylene (to avoid dissolving the beads).

The analysis of the sections was carried out with a Zeiss compound microscope equipped for both light and fluorescence illumination. Cells in the retrogradely labelled nucleus were checked for double labelling: they were projecting to both nuclei if positive, to one only if negative.

A control experiment was also designed and performed to show that double labelled cells could be unequivocally identified. This consisted of injecting a mixture of beads and HRP in one nucleus only. Preliminary experiments also involved injecting only one tracer in one nucleus only, to show that retrograde transport was effective, to establish best stereotaxic coordinates for the various nuclei and to decide how much tracer should be injected for optimal labelling and confined injection site.

So far, 28 zebra finches have been used for these experiments: 3 of these were injected with other fluorescent tracers that did not give satisfactory retrograde labelling; 9 were unusable because of problems arising during surgery, perfusion or histology; 9 were successfully used to establish parameters and 7 gave good data.

The first experiment involved distinguishing between **HVc** neuron populations: beads were injected in **X** and HRP in **RA**; as a control, beads and HRP were injected as a mixture in **X**. In the experiment, out of 263 bead labelled neurons and over 100 HRP labelled ones analyzed, none was double labelled. Most of the labelled neurons in the control were double labelled. Unfortunately, no quantitative analysis is available at present for the control, since the sections had lost the bead labelling when I went back to them for reexamination after two months of exposure to coverslipping fluid.

The results of this experiment clearly confirm the hypothesis that **X** and **RA** projecting neurons in **HVc** are two distinct, nonoverlapping populations of functionally different cells.

The second experiment involves distinguishing between **Uva** neuron populations: beads were injected in **HVc** and HRP in **NIf**; as a control, beads and HRP will be injected as a mixture in **HVc**. So far, I have succeded in establishing good stereotaxic coordinates for **HVc**. but I am still in the process of optimizing my **NIf** coordinates.

Conclusions

A double label experiment which featured HRP and red fluorescent latex microspheres (beads) as retrograde neuronal markers was devised and executed to establish the nature of **X** and **RA** projecting cells in **HVc**. The results indicate that there are at least two distinct, nonoverlapping populations of neurons in **HVc**: **X** projecting neurons, some of which are auditory and are not known to be involved in adult song production, although they may have a role in song acquisition; and **RA** projecting neurons, which are premotor and essential for adult song production.

Experiments that will address the question of the morphology of the neurons belonging to each of these populations by use of *in vitro* brain slice preparations have already been planned and will be started soon. Pending successful use of another fluorescent retrograde tracer to be used for double labelling with beads, eventual interneurons between **RA** and **X** projecting cells will be searched for.

Experiments directed to assess eventual changes in connectivity between **RA** and **X** projecting neurons during song acquisition and crystallization, as well as others involving lesion experiments of area **X** of young birds (age <45 days), may present serious difficulties because of the small size of the song nuclei in chicks.

No conclusions can yet be drawn from the experiments on **Uva** projections, since these are still in progress.

Bibliography

(1) GURNEY, Mark E.: Sexual differentiation of brain and behavior in the zebra finch (Poephila guttata): a cellular analysis.
Ph.D. Thesis Caltech, 1980

(2) KATZ, Lawrence C. and GURNEY, Mark E.: Auditory responses in the zebra finch's motor system for song.
Brain Res.211: 192-197, 1981

(3) KATZ, Lawrence C. et al.: Fluorescent latex microspheres: a new retrograde tracer of neuronal pathways.
manuscript to be submitted to Nature, 1983

(4) McCASLAND, James S. and KONISHI, Masakazu: Interaction between auditory and motor activities in an avian song.
PNAS 78,12: 7815-7819, 1981

(5) McCASLAND, James S.: Neuronal control of bird song production.
Ph.D. Thesis Caltech, 1983

(6) NOTTEBOHM, Fernando et al.: Connections of vocal control nuclei in the canary telencephalon.
J.Comp.Neur.207: 344-357, 1982

Figure legends:

Fig.1 A possible theoretical model for the song system.

Fig.2 Schematic diagram representing a sagittal section of the zebra finch brain and showing the relative positions and the connectivity of the song nuclei considered in this study.

Fig.3 Cresyl violet stained, 30 um thick sagittal sections of zebra finch brain; arrows delimit song nuclei. In all cases, to the left is the anterior and to the top the dorsal part of the nucleus. he magnification factor is 100.
a) song nucleus X
b) song nucleus RA
c) song nucleus HVc

Fig.4 Retrogradely labelled neurons in HVc following injection of beads in X.
a) Arrows delimit HVc. Magnification factor: 160.
b)and c) Labelled neurons. Magnification factor: 1000.
d) particularly well labelled neuron: solid arrow tip points to cell body, long arrow to nucleus (not labelled) and little arrows to neurites.

Fig.5 Retrogradely labelled neurons in HVc (a), magnification factor: 160 and (b), magnification factor:1000, following injection of beads in RA (c), magnification factor:100.

Fig.6 Retrogradely labelled neurons in HVc (a), magnification factor: 160 and (b), magnification factor 1000, following injection of HRP in RA (c), magnification factor:100.

Fig.7 Retrogradely labelled neurons in HVc following injection of HRP in RA; magnification factor:1000. In (c) it is possible to distinguish the cell body (solid arrow tip) and the neurites (little arrows))

Fig.8 Cresyl liolet stained, 30 um thick sagittal sections of zebra finch brain; arrows delimit song nuclei.
a) song nucleus HVc; magnification factor:160. To the left is the anterior and to the top the dorsal part of the nucleus.
b) song nucleus NIf; magnification factor:160. To the left is the anterior and to the top the dorsal part of the nucleus.
c) song nucleus Uva; magnification factor: 160. To the right is the anterior and to the top the dorsal part of the nucleus.
d) same as (c); magnification factor:250.

Fig.9 Retrogradely labelled neurons in Uva (a), magnification factor: 250 and (b,c,d), magnification factor: 1000.

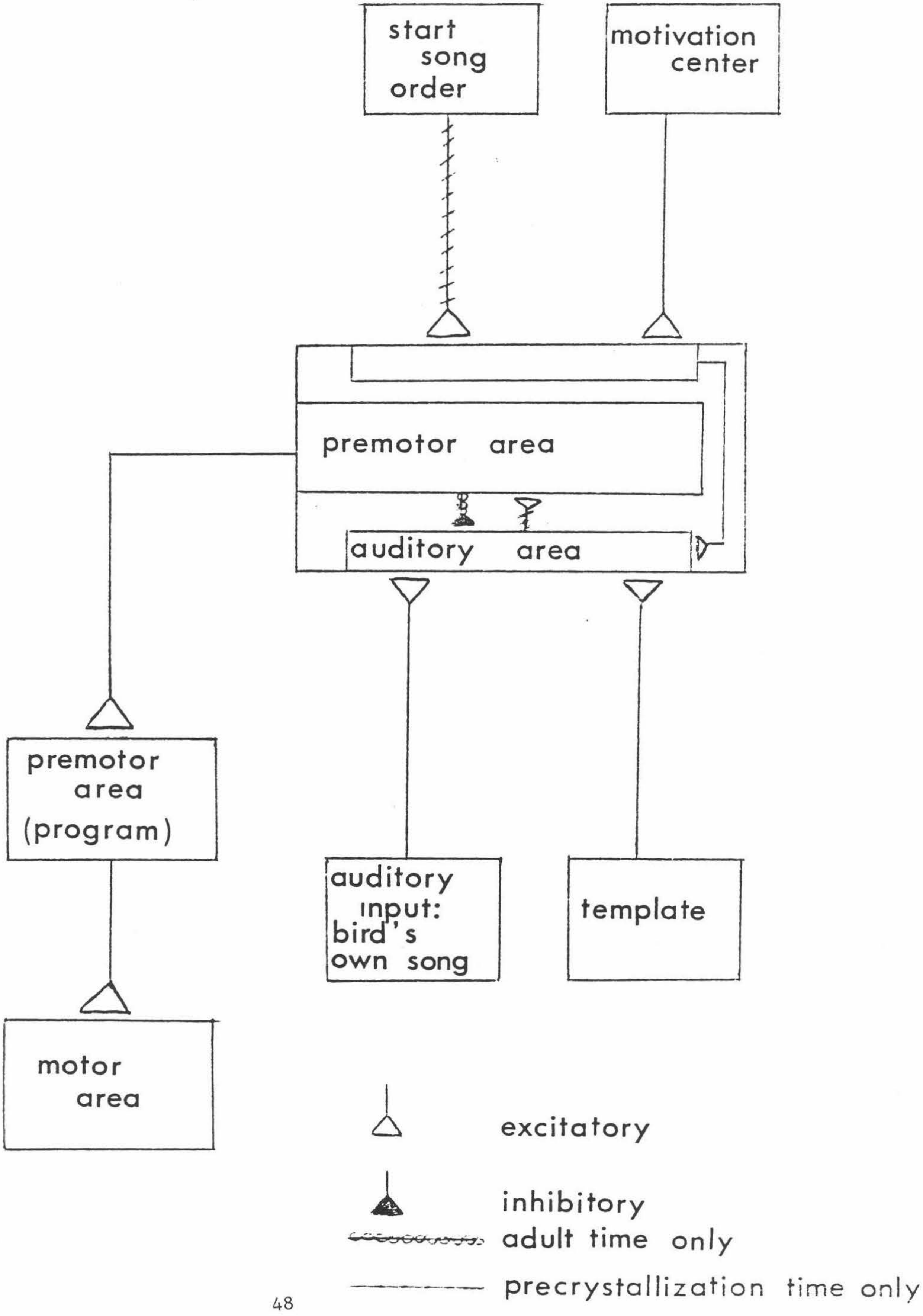
start song order
motivation center
premotor area
auditory area
premotor area (program)
motor area
auditory input: bird's own song
template
excitatory
inhibitory
adult time only
precrystallization time only

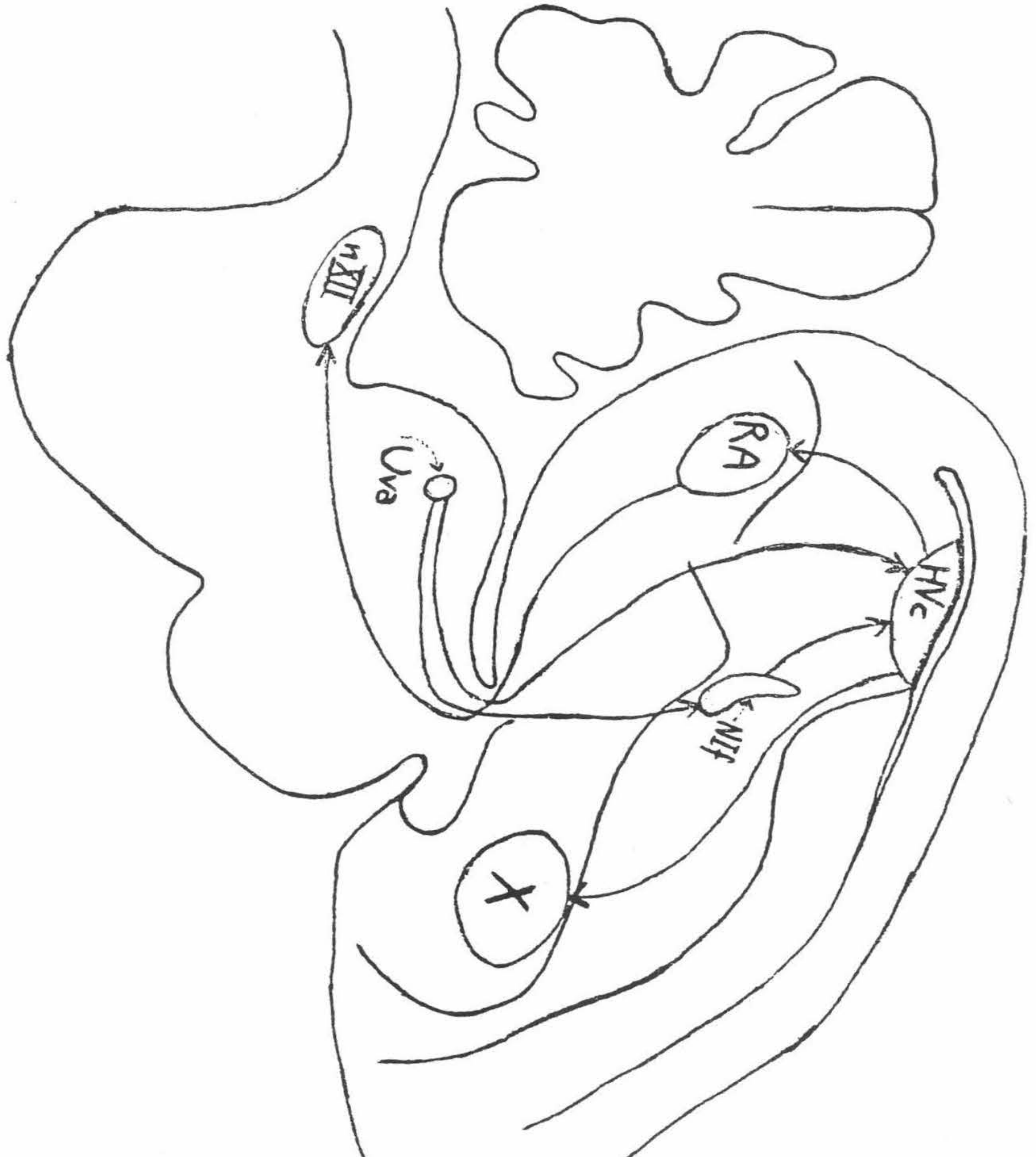

Fig. 2

Fig.

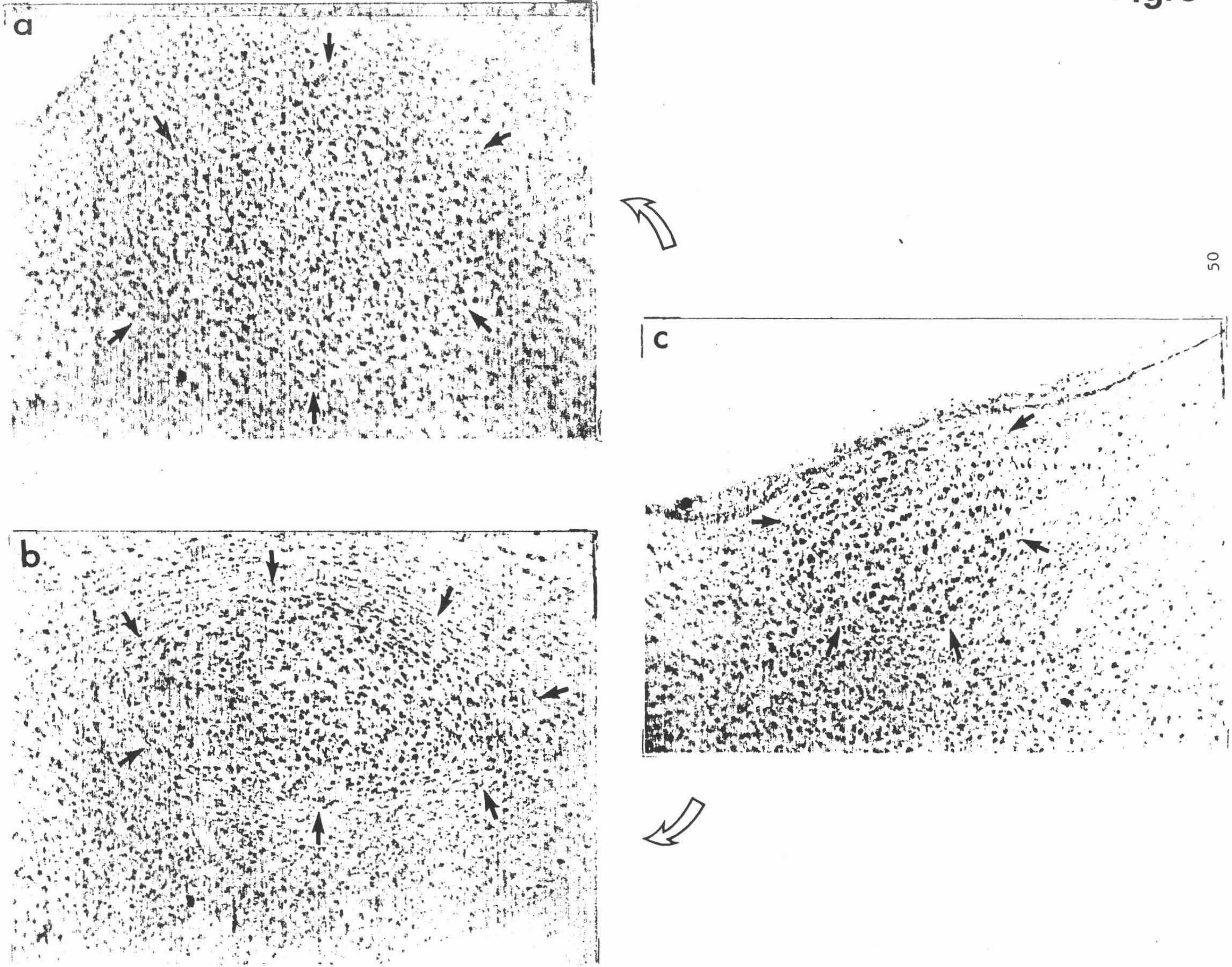

Fig.4

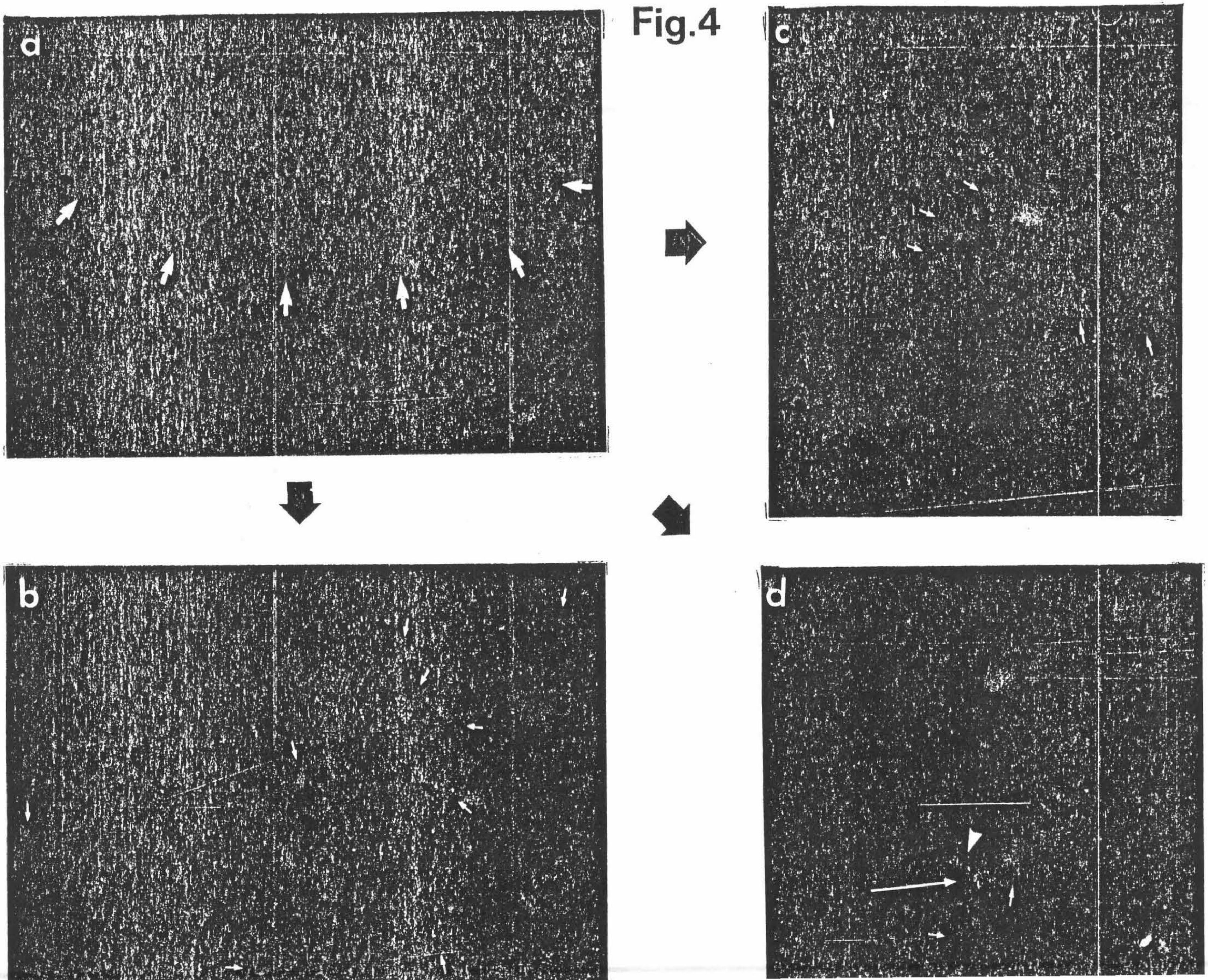

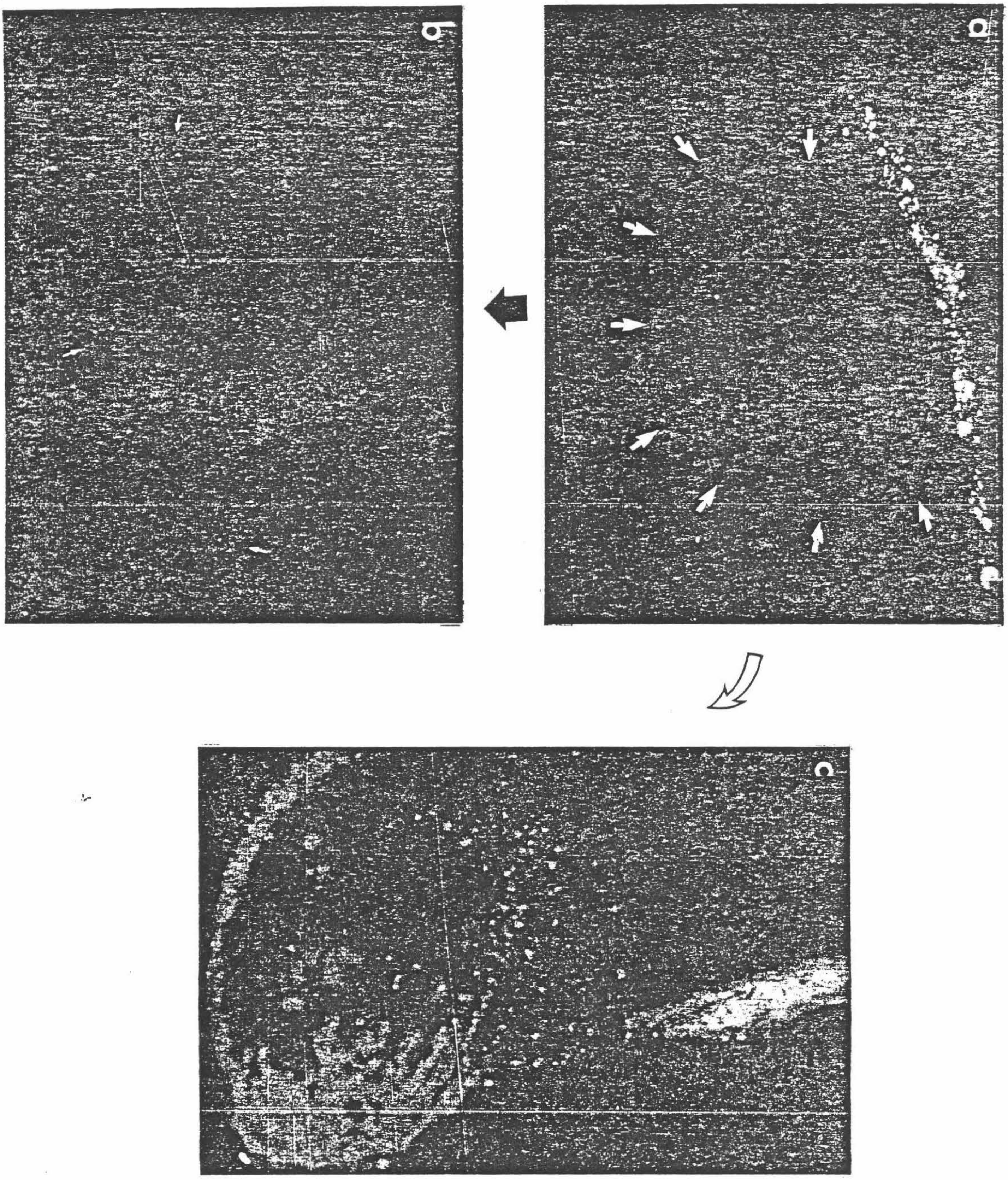

Fig.5

Fig.6

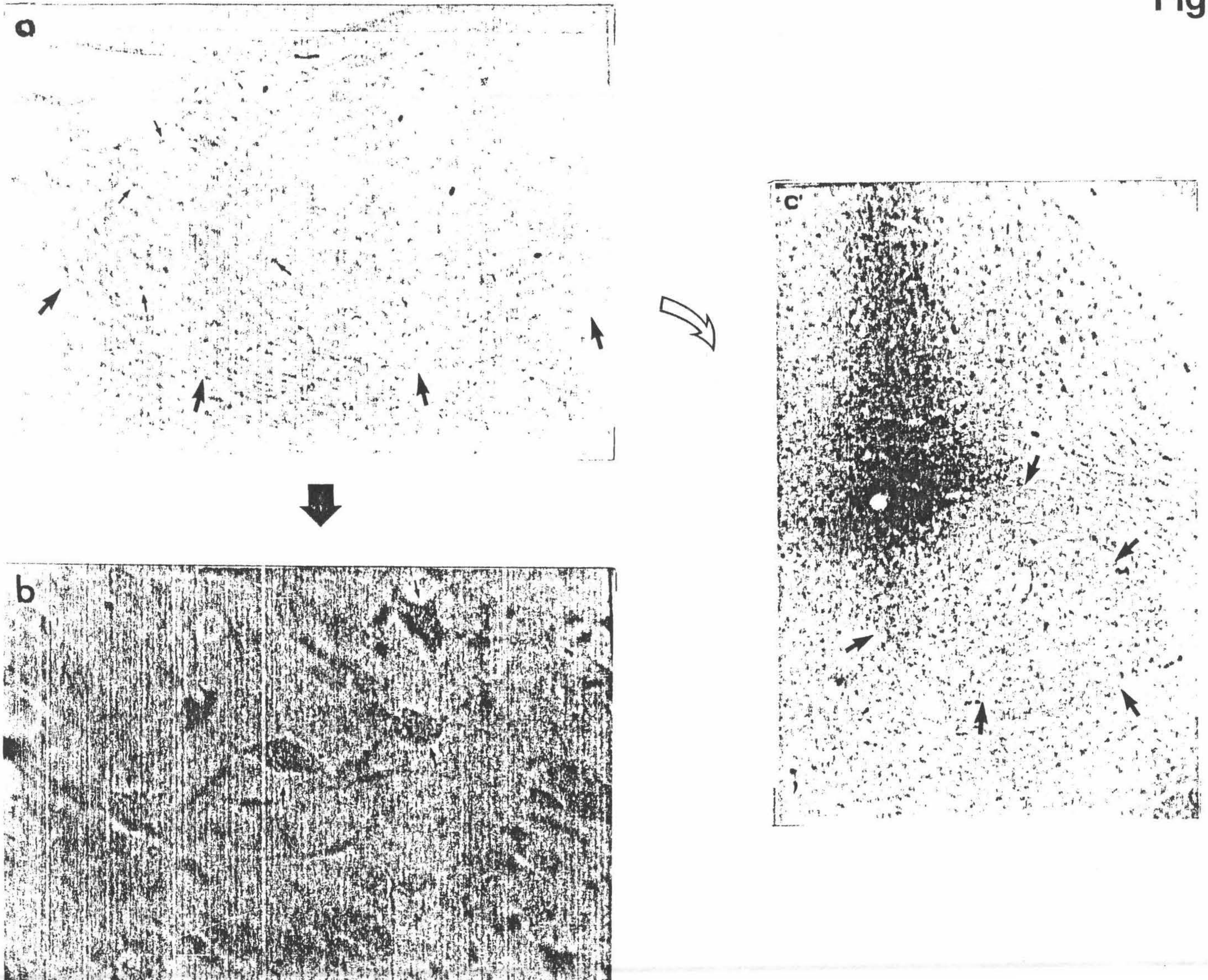

Fig.7

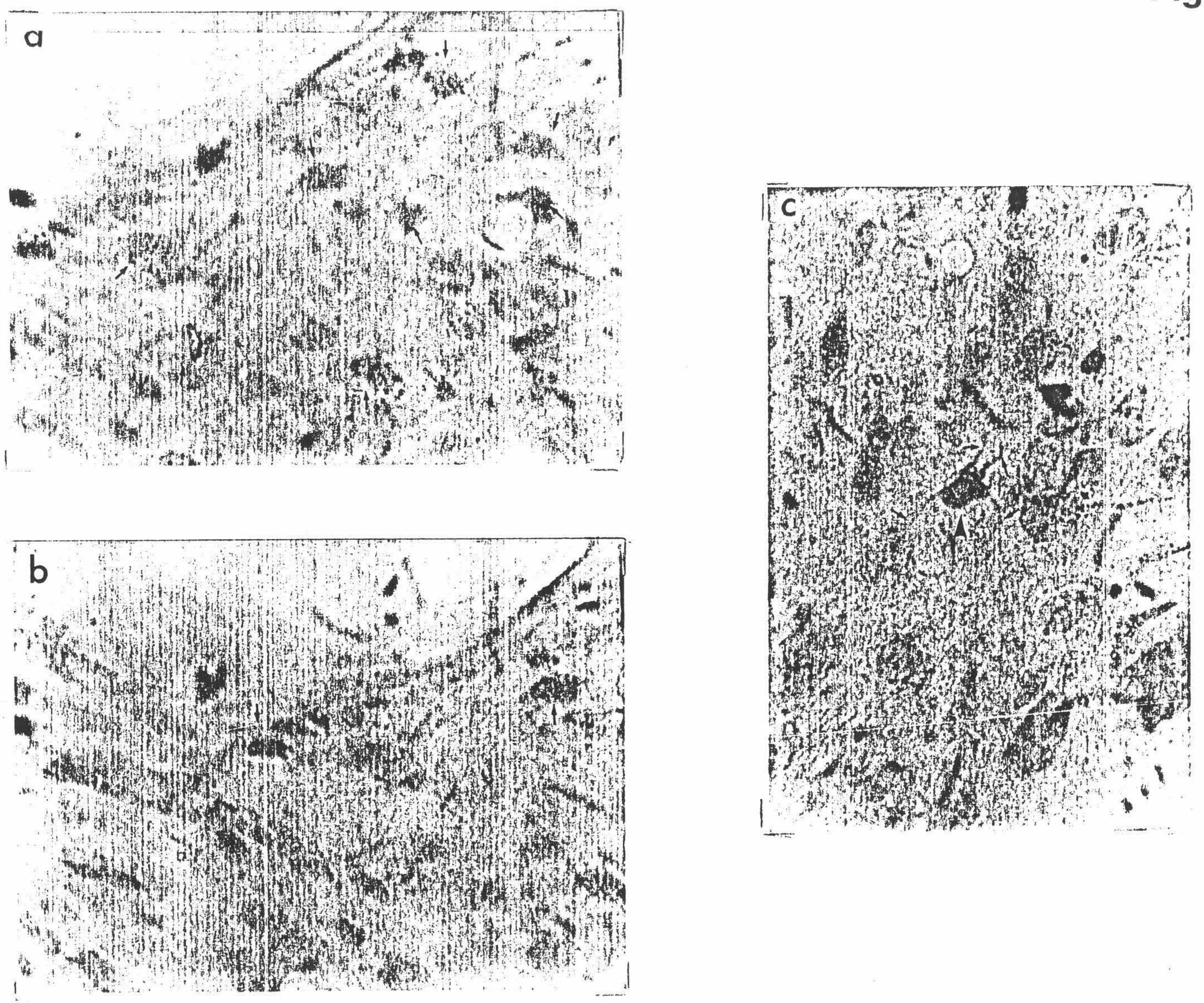

Fig.8

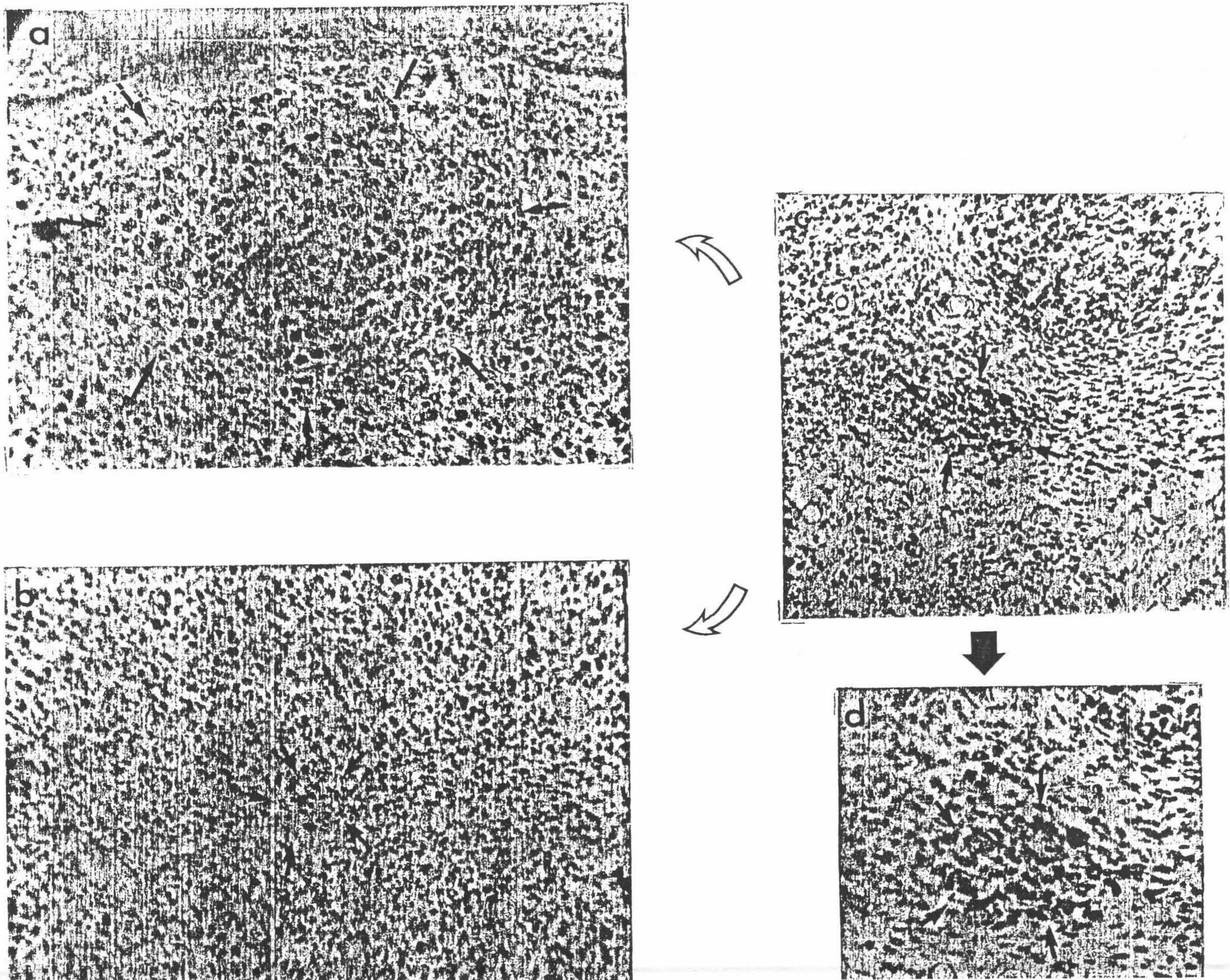

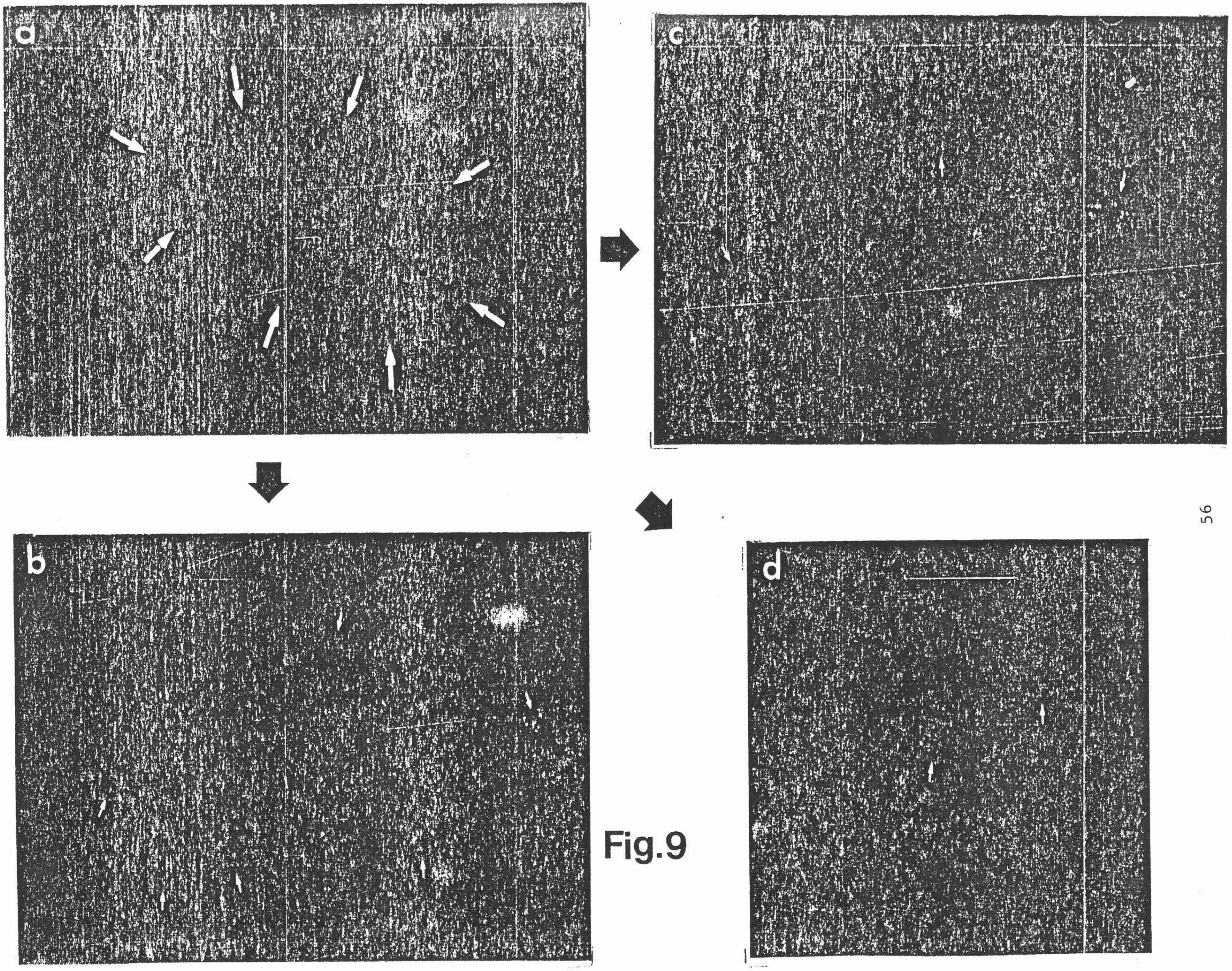

Fig.9

ALEX BOUZARI

NO REPORT SUBMITTED

BRADLEY BROCK

NO REPORT SUBMITTED

The Phase III Crystal Structure of Hexamethylbenzene

Michael Bronikowski

Sponsor:

Dr. Sten O. Samson

Abstract

The approximate phase III crystal structure of hexamethylbenzene (HMB) has been determined. Thus the crystal structures of all three solid phases of HMB are now known. Below the phase three transition temperature the HMB lattice appears to be trigonal or pseudotrigonal, corresponding very nearly to space group $P3_1$ or $P3_2$. There are three molecules per unit cell arranged, as nearly as we can yet determine, in a helical pattern. We attempted to determine exactly the transition temperature but were relatively unsuccessful; the transition from phase II to phase III showed hysteresis from 113.7 K to 120.0 K.

Introduction

Previous work has determined the phase I and phase II crystal structures of HMB to be orthogonal and trigonal, with four and one molecules per unit cell, respectively. However, the low temperature phase III structure had remained unknown owing to technical difficulties: namely, that crystals of HMB tended to shatter on going through the phase III transition. In undertaking this project, our hope was that a new low temperature diffractometer, developed here at Caltech, would enable us to cool an HMB crystal below the transition temperature without its shattering, and collect a complete low temperature data set.

Procedure and Discussion

Before any data could be taken on the diffractometer, it was necessary to obtain and mount a satisfactory HMB crystal. This proved difficult for several reasons. First, we found good, single crystals of HMB difficult to obtain, as twinning was quite common. Several methods of growing satisfactory crystals were tried, and we were eventually able to obtain good crystals by recrystalization from a toluene solution of HMB.

Another difficulty we encountered was that HMB sublimes at room temperature, and does so especially rapidly in the X-ray beam. This problem was solved by insulating the crystal from the surrounding air with a coating of white glue, which proved quite satisfactory in protecting the crystal in normal air and in the vacuum of the low temperature chamber of the diffractometer. This coating may also have helped hold the crystal intact on going through the phase transition.

For data collection we used a four circle diffractometer equiped with a low temperature crystal chamber and precise thermostat. We obtained unit cell constants for the HMB crystal lattice at a variety of temperatures both above and below the phase transition. These measurements are summarized in Table 1.

Table 1. Unit cell constants of HMB at various temperatures

Temp.	204 K	134 K	103 K	81 K	47 K	19 K
a	8.90669	8.8734	8.8120	8.8077	8.79271	8.7881
b	8.8195	8.7916	8.8120	8.8077	8.79271	8.7822
c	5.2587	5.2410	10.782	10.742	10.7352	10.728
alpha	44.313	43.975	90.0	90.0	90.0	90.07
beta	117.230	117.185	90.0	90.0	90.0	89.947
gamma	119.751	119.805	120.0	120.0	120.0	119.996

By measuring and indexing several sets of 15 reflections we determined that the phase III crystal lattice was trigonal or pseudo-trigonal (possibly monoclinic), and further investigation of systematic equivalences and absences of reflections indicated that the space group symmetry is very close to $P3_1$ or $P3_2$. Using this information, we collected two complete equivalent sets of reflection data (+h, +k, ±l and +h, -k, +l). By repeated least squares refinements we obtained a rough electron density map for the HMB unit cell from which we obtained the approximate positions of the carbon atoms in the cell. At the time of this writing, the atomic positions have not been determined with a great deal of accuracy or certainty. Also, we have not yet attempted to determine the positions of the methyl hydrogen atoms. Further refinements are intended, and it should eventually be possible to determine the positions of all of the atoms to within 0.005 angstroms.

The molecules of HMB are arranged helically with each molecule related to another above it by a 120 degree rotation around the c-axis followed by an upward translation of 1/3 of the length of the c-axis. This arrangement may only be approximate, however, and slight tilts in the molecules' orientation are possible.

Conclusion and Summary

To summarize, then, we have discovered the following about phase III hexamethylbenzene:

lattice: trigonal or pseudo-trigonal
space group: $P3_1$, possibly with some distortion
cell constants at 19.0 K: $a = b = 8.78$ A, $c = 10.728$ A,
alpha = beta = 90.0 degrees,
gamma = 120.0 degrees
approximate atomic and molecular configurations determined

A paper describing all the structural details of phase III HMB will be published after completion of additional computational work.

References

Brockway, L.O., and Robertson, J.M. (1939) J. Chem. Soc., 1324

Watanabe, T., Saito, Y., and Chihara, H. (1949) Sci. Papers Osaka Univ., 1, 9.

GROWTH OF SYMPATHETIC NEURONS IN CULTURE

John Butman

Jerome Pine

Abstract: The growth of small numbers of rat sympathetic neurons in culture was recorded on video tape. Neurite outgrowth was observed with emphasis on advancing and retracting, growth cone motility, and interactions with neighboring cells. Evidence indicated that growth cones were not the only site for affecting the length of the neurite. The speed of elongation was limited by the rate new membrane could be added to the growing neurite rather than the speed of the advancing growth cone. Neurites appeared to facilitate cell aggregation in early stages.

Introduction: Early development of neurons is an interesting topic of study as far as mechanisms of growth and the motivations for the final structural pattern of the growth are concerned. There is great difficulty in monitoring the growth of a single neuron on vivo due to the numbers of neurons found. It is also difficult to vary the various controlling factors in vivo in order to see the eventual effect these may have on the growth. For these reasons it is useful to observe nerve cells in vitro where small numbers of cells can be watched and influenced easily.

The original purpose of this project was to observe the morphological variations in growth patterns among neurons grown normally in culture, with electrical stimulation, and with chemical factors. Due to difficulties in culturing the neurons and time considerations, I decided to photograph neuronal growth on dry collagen and collagen gel, foregoing the other possibilities.

Whereas similar work concerning the early development of neurons has been done by Bray, Letourneau, Wessels, and others, a number of interesting phenomena were observed. Branch points were found to move, both toward and away from the soma. Neurites were also found to extend and retract up to 100 microns over a period of a few hours. Cells were seen to be pulled across the substrate by moving growth cones and were also drawn into clusters by neurite action.

This evidence suggests that retraction, as well as elongation, of the neurite occurs, and that the growth cone is not the only site where the growth of the neurite is affected. Neurite elongation is also limited by the ratē at which new membrane is added to the growing neurite rather than the speed at which the growth cone can move across the substrate. Finally, the role of the neurite in the aggregation of cells suggests that it may have structural significance.

Materials and Methods: Superior cervical ganglia were dissected from newborn rats and the cells were dissociated. They were then plated immediately or frozen down for future use. The culture medium used was MEM-1X supplemented with 6mg methocel/ ml of medium, 10% fetal bovine serum, penicillin, streptomycin, glutamine, and NGF. Holes of 7mm diameter were drilled in the center of 35mm plastic dishes and cover slips were glued to the bottom of the hole with sylgar to form a well in which the neurons were placed. The cover slips were either blank glass or were provided with a grid of 10 by 10 lines per sq. mm. The grid was made by evaporating 50Å of nichrome followed by 150Å of gold onto the glass. The cover slip was coated with either dry collagen or collagen gel and sterilized with ultraviolet light before plating.

Approximately 5000 cells were suspended in 100microliters of medium and plated on the dish. Two incubators were used. One was designed to fit on the stage of the microscope, and could only contain one dish, which it kept at 36.5-37.5°C and 5% CO_2. The other was a large incubator kept at 37°C and 5% CO_2 also, but could hold many dishes. Several dishes were made at each plating and were placed in both incubators. Three to four hours after plating, 2ml of medium and 20µl of 10^{-5}M Ara-C were added to the dish.

At this time, the dishes were examined for growth and the dish with neurons that had started to grow, or looked the most interesting, was placed in the stage incubator. Photographs were taken at regular intervals of from 15-30 minutes with 35mm Tri-X Pan film. These were developed and printed and made into a time-lapse video using the audio-visual equipment at J.P.L.

Results: Four sets of time-lapse pictures covering the first few days of SCG neuron growth were made. Three of these were made into a video tape as well.

The first video documents the growth of freshly prepared neurons on dry collagen. Typical growth rates for extending neurites ranged from 9 to 30 microns per hour. A neurite of one cell branched at 50 microns from the soma. While the two new growth cones continued to advance at rates of 9-12 µ/h, the branch point moved towards the soma at a rate of 2-3µ/h until it was internalized within the soma.

The same neurite underwent a fourth branching 126u from the third branch point, which was 150µ from the soma. The fourth branch point moved farther away from the third, reaching a distance of 245µ four hours later. Meanwhile, the third branch point retreated 15µ towards the soma. Beyond the fourth branch point, both of the neurites extended 48µ during this time.

Adifferent cell was observed to extend a neurite 35µ, only to retract it and lie dormant without extending processes for four hours. It then extended neurites which pulled the soma along at 20-30µ/h, the soma moving a total distance of 150µ while the neurites extended a much lesser amount. It was difficult to measure how far they had extended as they grew along a previously existing neurite for part of this time. Eventually, the soma of this cell was drawn all the way to this other neurite and remained there.

A large cluster of 6or7 cells was initially located 100µ away from a group of two cells. The larger group extended many processes and moved to within 50µ of the smaller group. At this point, processes from the large group contacted the other group which had as yet grown no processes. Three hours later the two groups were united, the larger group moving insignificantly during this time.

Finally it was observed that some growth cones would, upon coming into contact with another neurite, move along it, although in other cases the growth cone would simply cross over the obstructing neurite.

The second video documents cells which were frozen down ten days earlier, thawed out and grown on collagen gel.

Cells on this substrate showed virtually no movement during the time of observation. Growth rates varied from 20-30µ/h for neurites which grew continuously. Some neurites exhibited very slow growth, one cell extended a process at 6µ/h. Another cell had a period of dormancy during which its two processes underwent very little change, remaining about twenty microns long. After this period, which lasted several hours, the neurites resumed normal growth.

Another neurite (whose soma was outside of the field of view) displayed ehat appeared to be 'probing' activity, its growth cone moving back and forth within a 25µ by 25µ square for five hours before extending another 45µ in the next twohours. It then showed similar activity for the next three hours after which it appeared to grow and branch normally.

The third video documents the growth of freshly prepared neurons on collagen gel. I suspect that the gel was accidentally destroyed prior to plating as the cells had difficulty adhering to the bottom of the dish and there was considerable cell movement, often covering hundreds of microns. This contrasts with the cells of the second video which were also grown on collagen gel.

Despite the poor adhesion to the substrate, the cells' growth was not inhibited noticeably. The cells did have a noticeable tendency to clump together. Cells, both individually and in groups, moved quite rapidly over the dish, attaining speeds of over 50µ/h. The cause of this movement was not clear in many cases. In some cases the movement of the neurites seemed to be the major influence on cell movement. Nonneuronal cells, possibly fibroblasts or gliaalso moved, and could be seen to move the neurons. In one case it appeared that one group of cells extended a neurite and then retracted it with the growth cone fixed, thus pulling the clump of cells along.

The amount of clumping can be seen in the following table:

Numbers of clumps of various sizes at different times.

Hours after plating	Cells/ Clump						
	16+	11-15	8-10	5-7	3-4	2	1
8	0	0	0	1	4	5	8
16	0	0	1	3	2	1	3
24	0	1	0	3	2	0	2
32	1	0	0	1	2	0	2
40	1	0	0	2	0	1	2

Finally, three cells in this series were seen to reteact processes at distances of up to 100µ.

There was no significant evidence to indicate specific influences on direction of growth found in any of the videos.

Discussion: The branch point which moves back to the soma could be the splitting of a fascicle of neurites rather than the branching of a single neurite. However, if this is not the case then neurites cannot be the only location for neurite growth action, this would require that branch points remain fixed (Bray 70). Unfortuneately, photographs were started just after the branch was formed, so it is impossible to tell whether the two bifurcating growth cones are the result of the splitting of a single growth cone or not. In addition, the advancing growth cones suggest that branch points may retain some of the properties of active growth cones. Sprouting of new neurites from branch points has been observed (Bray 73) suggesting that branch points may be 'dormant' growth cones in some respects.

It is possible that pull from the advancing growth cones result in a strain which tears either the fasciculated neurites apart, or a single neurite in half. The latter is highly unlikely due to the continued growth of the neurite. The ad vancing branch point could be due to pull from the advancing growth cones also. Thus the increased length of the neurite behind the branch point could be due to stretching of the membrane rather than the addition of new membrane. The neurite would then have nearly doubled in length due to stretching alone, which seems unlikely. Information on the diameter of the stretched neurite was lost due to the low magnification used.

This indicates that growth cone speed is limited by the speed at which new membrane can be inserted into the elongating neurite rather than the speed at which the growth cone could advance independent of the neurite to which it is attached. This is supported by the numerous instances in which cell bodies wer pulled along at faster rates than the neurites were extending.

Neurites were found to be very plastic in their first stages of growth, extending and withdrawing over distances of 100µ. This could involve the existence of machinery to disassemble as well as assemble membrane, and this would not necessarily be located in the growth cone. The addition of membrane at the growth cone alone does not seem to explain the phenomena.

The observation of clustering clearly shows the tendency for neurons to aggregate in preference to attaching to a low adhesivity substrate. This clustering was found to occur through the use of the neurites; very little clustering was seen before processes had begun to emerge. Thus neurites may have developmental roles other than simply seeking out and enervating targets.

Nothing conclusive can be said of neurites seeking out targets with any directionality, and neurites seemed to ignore each other's presence at least as often as they fasciculated.

It would be worthwhile to make further studies of the early growth of neurons in culture as these few videos contained interesting data. It would still be interesting to see if growth could be influenced by various agents such as electrical stimulation. Unfortunately, the time scale of the project did not allow me to carry these experimants out.

This research was conducted as part of the SURF '83 program.

Bibliography:

Bray, D. (1970) Proc. Nat. Acad. of Sci., 65, 4, 905.
Bray, D.,(1973), J. Cell Bio., 56, 702.
Johnston, Randal N. and Norman K. Wessels,(1980)Cur. Top. Dev. Biol., 16, 165.
Letourneau, Paul C. (1975) Dev. Biol., 44, 77.
Letourneau, Paul C. (1975) Dev. Biol., 44, 92.
Sidman, Richard L. and Norman K. Wessels (1975) J. Exper. Biol., 48, 3, 237.
Wessels, Norman K. (1982) Cell Behaviour., 225.
Wessels, Norman K. and Robert P. Nutall (1978) Exp. Cell Res., 115, 111.

DHFR GENE EXPRESSION CONTROLLED BY ANTI-SENSE DNA

Susanna Chan

Faculty Sponsors: Leroy Hood, Barbara Wold

ABSTRACT A technique was devised, whereby the expression of a cloned gene could be conditionally controlled, that is "turned on or off " at will. The technique was applied to the dihydrofolate reductase (DHFR) gene, a control used for my experiment involving the rearranged gene, c-myc, a major factor in growth transformation (tumorigenesis). No definite conclusions were able to be drawn at this point, as to the effectiveness of the technique.

Although with our present technology, genes can now be mapped and sequenced, much remains to be known as to their function within the cell. A technique has now been devised to determine this function, and in particular, the function of c-myc, an "oncogene." Oncogenes control cell growth and are important in causing cancer in such cases as Burkitt's lymphoma. These genes are also present in all cells.

One proffered explanation of the involvement of cellular oncogenes in the formation of tumors is that specific chromosomal abnormalities occur at the site of cellular oncogenes and somehow activate them. More specifically, it has been observed that the oncogene c-myc, translocated next to the antibody gene, C_a, induces growth transformation in certain types of cells. This c-myc is different from that found in normal cells.

My project began at this point. I began to investigate the effects of the rearranged c-myc at the RNA level by first looking at a control using a new approach - that of involving anti-sense DNA. DNA is made up of two complementary strands. The anti-sense strand is the strand not used as a template for transcription into RNA. If anti-sense RNA is now copied from this anti-sense DNA, this new RNA may hybridize with the normal RNA in the cell to form a double-helical, which may no longer be translatable into protein. This "turning off" of what may be the major gene causing growth transformation, may cause the "cancerous state" to disappear.

For the control, dihydrofolate reductase (DHFR) was used. DHFR is the enzyme responsible for the reduction of folic acid and dihydrofolic acid to tetrahydrofolic acid, a cofactor required for one-carbon transfers in various biosynthetic reactions. The way anti-sense DHFR was made follows: the gene sequence was cut out by two enzymes and "flipped" around so that the anti-sense strand of the DHFR sequence was now adjacent to the rest of the continuous sense strand. A restriction enzyme map ensured that the sequence had flipped. A promoter taken from the metallothionine gene and thus chemically induced by cadmium or zinc was located upstream with respect to the coding region. The presence of either metal activated transcription to produce anti-sense RNA. The anti-sense DHFR was then transfected (brought into) into L cells.

Once the proper cells had been selected for and grown, two different assays were employed to determine how effective the anti-sense RNA was in binding to the normal DHFR RNA. The first was a functional assay which measured the rate at which a cell extract reduced folic acid (by measuring substrate optical density). Unfortunately, the assay suffered from rather high background levels. This made it difficult to accurately quantitate low levels of DHFR activity. To avoid this problem, a ^{3}H-MTX (tritiated methotrexate) binding assay following the procedure of Johnson and Urlaub was used. Methotrexate is a strong, competitive, "stoichiometric" inhibitor of DHFR with an extremely high binding affinity for this enzyme. Cytoplasmic extracts of the cells grown were combined with this radioactively-labelled MTX solution, added to a charcoal suspension, and then centrifuged. What is happening here is that the ^{3}H-MTX is binding to all the DHFR enzyme present and the charcoal is binding to all the free, unassociated ^{3}H-MTX in the next step. This latter charcoal complex is then pelleted out in the centrifugation. The radioactivity of the supernatant was then measured (the amount of radioactive ^{3}H should correlate stoichiometrially with the amount of DHFR enzyme present). To normalize the amount of enzyme in the different assays, a colorimetric Lowry assay was performed.

In the initial set of measurements, where approximately two million cells were used, no marked differences were detected between the anti-sense DHFR and normal cells, with the exception of one anti-sense cell line. But these data turned out to be invalid when it was found that a linear binding response was not obtained till a one-eight dilution was made of the original cell extract used. Thus, the problem encountered above was an excess of enzyme over substrate. After several assays where proper dilutions of the original cell extract were used, the following data were obtained:

<u>Cells Used</u>
L = normal L cell with no anti-sense DHFR DNA.
1,2,3,4,5 = five different L cell lines with anti-sense DHFR, cell lines 3,4,5 were transfected with more anti-sense DNA.

Cell Growth Conditions (Cd and Zn are anti-sense inducers):
A = HTNeaa (Selective media) for 5 days
B = HTNeaa for 5 days + low level Cd 5 hrs before assay
C = Both HTNeaa + low level Cd for 7 days
D = Both HTNeaa + high level Zn for 7 days

In the three assays below, the enzyme measured in the anti-sense cells were normalized according to the normal L cell grown under similar conditions. Thus, all normal L cells represent 100% and the figure next to its parentheses is the amount of enzyme/mg:

	Condition A	Condition B	Condition C	Condition D
#1	L(100%)1.6 1(10.7%)	L(100%)3.46 1(101.2%)	L(100%)2.04 1(33.0%)	———
#2	L(100%)2.11 3(64.0%)	———	———	L(100%)1.80 2(105.5%) 2(87.2%) 3(60.6%)
#3	L(100%)1.09 3(44.0%)	———	L(100%)1.03 3(217.7%) L(100%)1.55 4(130.4%) 3days→5(6.8%)	L(100%)0.905 3(54.9%) 3(194.2%) 4(101.3%) 5(9.7%)

Different levels of metals were used in the growth conditions for two reasons. One was to detect any differences in the amounts of anti-sense DHFR produced. Another was that heavy metals are known to be toxic to cells at certain concentrations for long periods of time. Thus, the range tested informed us on this aspect. Additionally, zinc is less toxic than cadmium.

Looking at the results under uninduced conditions, the DHFR level in the anti-sense cells was lower than the normal cells. This unexpected result may have been due to two causes. One cause may be that cell lines 1 and 3 were cell lines from clones simply having a lower production level of DHFR. A more complex cause would involve the concept of the repressor, a substance not allowing the transcription of a particular sequence of DNA by binding specifically to its promoter. Thus, the introduction of many anti-sense DHFR promoters into a cell could perhaps overcome the fixed quantity of repressor in the cell. This decreased concentration of repressor surrounding the anti-sense DHFR would result in an active, unbound promoter giving rise to anti-sense RNA which in turn could bind to the DHFR RNA, bringing the levels of enzyme down. But one contrasting fact to this second reason is that cell line 3 has supposedly more anti-sense DNA than cell line 1, so that this cause remains inconclusive.

Due to the uninduced results, we cannot be sure that the same situation is occuring with the lowered DHFR levels under the induced conditions of low cadmium, high cadmium, and high zinc. As for the high or equivalent levels of induced anti-sense cells (as compared to normal L cells), these can be explained again by the different clonal production of enzyme above. Other reasons are that the anti-sense message was not being produced or was unable to hybridize to its complementary RNA. Furthermore, DHFR levels could be rising in the anti-sense cells due to the heavy metals, though this is not understood.

Another aspect to notice is the overall fluctuation of enzyme in the assay. It appears that the normal L cell enzyme level in the first assay, rises with low cadmium and rises even higher with high cadmium. In the second assay, there is a slight decrease in the enzyme level for normal L cells from zinc. And in the third assay, the uninduced, low cadmium, and high zinc conditions result in approximately equivalent L levels except for the increase in one L cell in low cadmium. Perhaps these increases seen with the cadmium are also a reflection of a rise in DHFR level due to some effect the metal is exerting on the DHFR biosynthetic pathways. Als there are fluctuations of the normal L cells among the different aszsays - this is true for the anti-sense cell levels as well. These fluctuations may be due to differences in the original cell densities. There are additionally contrasting percentages in supposedly similar cell lines and conditions. For example, in the third assay where cell line 3 was induced by zinc, we see levels of 50% as well as almost 200%.

Also, although cell line 5 appears to have worked, this datum is not valid as the cells were taken from an aminopterin selective media for only three days, whereas the other cells had the aminopterin diluted out for a longer period of time. Aminopterin inhibits DHFR so that the low levels seen may be due strictly to this inhibition. Further tests must be done.

Due to the low levels of anti-sense cells that were uninduced as well as the fluctuations in the data, no absolute conclusions were able to be drawn at this point as to whether the technique will work. Further experiments must be performed before we can interpret the data correctly. For example, the DHFR anti-sens construction will be "flipped" back to check for normal DHFR activity to ensure that the promoter is actually being induced by cadmium and zinc, and that the DNA is transcribing properly.

Through this experiment, we will gain a better understanding of the function of the oncogene, and thus, the nature of tumorigenesis. Furthermore, through the development of the anti-sense technique, other gene functions may be examined as well.

1. Barth, Crews, Kim, Perlmutter, Takahashi, Hood, Oncogenes and Chromosome Translocations in Lymphoid Tumors, Unpublished, 1983.

2. Johnson et al, Regulation of DHFR Gene Expression in Mouse Fibroblasts during the Transition from the Resting to Growing State, J. Cell Physiol, 1978, 97: 397-406.

3. Mulligan and Berg, Expression of a Bacterial Gene in Mammalian Cells, Science, Vol. 209, Sept. 19, 1980, 1422-1427.

4. Urlaub et al, Isolation of Chinese Hamster Cell Mutants Deficient in DHFR Activity, PNAS, Vol. 77, No. 7, 4216-4220, July 1980.

Hartree-Fock Calculations of Neutron-rich Nuclei in the s-d shell

J. Dobaczewski[†], J. Chang[‡] and S. E. Koonin
W. K. Kellogg Radiation Laboratory, California Institute of Technology, Pasadena, California 91125

I. INTRODUCTION

The properties of nuclei far from the line of β-stability are of interest for several reasons. One, of course, is the new dimension that extreme isospin imbalance offers in understanding nucleon structure, the nature of the nuclear force, and the nuclear many-body problem. A second, more practical motivation for considering such exotic nuclei is their importance in astrophysical circumstances. In particular, for nucleosynthesis by rapid neutron capture (the "r-process" of Burbidge *et al.*), the properties of very neutron rich nuclei (those near the neutron drip line) are of crucial importance.

Experimentally, very neutron rich nuclei can be studied by two methods. One very successful approach has been the chemical separation methods of the products of proton spallation. This has, in fact, allowed measurement of mass for Na isotopes out to the neutron drip line (^{35}Na)[1,2] the farthest off the β-stability line to date. However, such techniques are limited to the alkali elements. A very recent experimental method, the fragmentation of relativistic heavy ion beam, appears to be a very general method for producing exotic nuclei and, indeed, initial

---

[†] Supported in part by the National Science Foundation [Phy 79-23638]. On leave from the Institute of Theoretical Physics, Warsaw University, Hoża 69 Pl-00681 Warsaw, Poland.

[‡] Caltech Summer Undergraduate Research Fellow

studies in the s-d shell via ^{48}Ca fragmentation have proved very promising[3].

Theoretically, there has been growing confidence in our understanding of the systematics of nuclear properties, if not their underlying causes. The Hartree-Fock description of nuclei, when used with the appropiate effective interaction, has been shown to provide an excellent description of the nuclear ground state, near-equilibrium, and dynamical properties for systems near the β-stability line throughout the periodic table. Moreover, in one of the few cases where such calculations were extended to off the β-stability line[4],the binding energies of the very neutron-rich Na isotopes were very well reproduced.

It is both experimental and theoretical considerations such as these which motivated the present HF calculations of nuclei in the s-d shell. We have systematically calculated nuclear ground-state properties (binding energy, radii and quadrupole moments) for nuclei from Z= 10 to Z= 20 for neutron even numbers from N= Z (Z+1 for odd Z) to the neutron drip line. It is hoped these such calculations can be used to guide future experiments. Preparations to extend these calculations to the f-p shell are in progress.

In Section 2, we present a brief summary of the methods used in our calculations. In Section 3, we present our results, together with some discussion of the systematics observed.

2. METHOD OF CALCULATION

We use the standard method[4-8] of describing nuclear ground states in the HF approximation. The Skyrme effective interaction SIII[9] is used in our calculations. We impose axial and reflexion symmetry of the single-particle wave-functions which are approximated by a finite expansion in a cylindrical harmonic oscillator basis truncated to $N = 10$ major shells.

The standard basis parameters $b = (m/\hbar)^{1/2}(\omega_z \omega_\perp^2)^{1/6}$ and $q = \omega_\perp / \omega_z$, which characterize the oscillator frequencies along and transverse to the symmetry axis, ω_z and $\omega_\perp$, are determined by a minimization of the total energy for a given nucleus[8]. Minimization has been performed on mesh points in b and $\alpha = (q-1)/(q+1)$ spaced by 0.005 fm^{-1} and 0.01, respectively. By performing five iterations with $N = 4$ followed by one iteration with $N = 10$, we can correctly probe the dependence of the total energy of a given nucleus on b and α; the values of b found from the automatic minimization procedure have to be, however, increased by 0.01 fm^{-1} to approach the true minimum.

In our calculations we use fixed occupations of the single-particle states with the filling approximation[4] applied to the protons in the odd-Z elements. Since only the time reversal pairs of single particle orbitals are degenerate in deformed nuclei, there are often two or more viable configurations for the ground state occupation of levels in each nucleus. To illustrate the problem, we present in Figure 1 the dependence of neutron single-particle energies on the mass quadrupole moment Q_m for the nucleus ^{46}Ar obtained by using a quadratic constraint on the mass quadruploe moment[8] Apart from an overall scale shift, this diagram is independent of A and similar to the level diagram for proton single particle energies in this mass region. One reason is that on the prolate side of

Figure 1 (Q_m>0) the single particle level energies of a subshell increase with the projection of angular momentum on the z axis, Λ, but on the oblate side (Q_m<0) the ordering is reversed. Whenever a partial occupation of the spherical multiplets is necessary, filling the states with the lowest value of Λ results in a prolate shape. while filling the states with the highest value of Λ results in an oblate shape. Since there is no reason to believe any one configuration to be correct we chose that with the largest B to be the ground state. In order to avoid local minima in the case of a completely filled multiplet, the minimization has been performed separately from the prolate ($\alpha > 0$) and oblate ($\alpha < 0$) side.

Another possible configuration comes from the crossing of the single particle states of neighboring subshells at large deformations. For example, in a nucleus of 28 neutrons we can fill the $1f_{7/2}$ subshell in the usual way or we can occupy the $1/2^-$ state associated with the $2p_{3/2}$ subshell instead of the $7/2^-$ state. The normal configuration will lead to a quasispherical shape (Q_m small). The switched configuration will have a very large prolate deformation. In ref.[4] it was found that the switched configuration at the N= 20 level crossing on the prolate side was not only energetically favored in ^{31}Na but also the extra stability could explain the experimentally observed upturn in S_{2n} at N= 20. For this reason we have investigated level crossings both on the oblate and the prolate side. In the case that there are more than one level crossing between neighboring subshells on either side we try the one occuring at the smallest absolute value of Q_m for each element. If that crossing results in a nucleus energetically favored to the normal configuration we then proceed outward to the next crossing. We have indicated with a circle in Figure 1 where we have found a level crossing favored for atleast one element. Otherwise we do investigate further level crossings for that particular element.

The Hartree-Fock binding energies have been corrected for each nucleus by adding the rotational correction $\Delta E_R = \hbar^2 < J^2 > / 2I$ with the mean value of the total angular momentum squared $< J^2 >$ and the rigid body moment of inertia I calculated microscopically. The corrected binding energies have been taken into account when deciding which level occupation sequence gives the highest binding.

3. GROUND STATE SOLUTIONS

In Table 1 we have tabulated our calculated values of the binding energy B, the proton quadrupole moment Q_p, and the isotopic shift $\delta<r^2>$. We have indicated those nuclei where we found the ground state to be in the switched configuration with a ×. Figure 2 shows a comparison between the calculated mass-excesses and the experimental values from ref.[10]. The vertical scale has been shifted by $10\times(Z-10)$MeV for the isotopes of each element. Overall the odd Z isotopes are overbound in our calculations because we have used no pairing interaction. Otherwise the B-values are very good except for the sulfur (Z=16) isotopes. The mean curvature and the valley of stability are also well reproduced.

We present in Figure 3 the two neutron separation energies. The calcium isotopes best exhibit the features of a spherical shell model, S_{2n} declines smoothly except at shell closures where there is a sudden drop. It is clear that the N= 20 isotopes of neon, sodium and magnesium are bound more tightly than the spherical shell model would predict. This is due to the switched occupation. In the sodium isotopes we do not see a jump in the calculated value of S_{2n} as in ref.[10] because the odd N isotopes are not included. We have also found some level crossings on the oblate side of Figure 1. The N= 34 crossing is favored for Z= 17,18 and 19 and the N= 40 crossing for Z= 18. However there are no such dramatic upturns in S_{2n} as in the prolate transitions.

In Figure 3 we present the calculated values of Q_p for the ground state. Since the prolate and oblate configuration often led to almost degenerate solutions but very different quadrupole moments, we connect with a dashed line the Q_p of the less bound configuration in cases where the differences in B was less than 400 keV. From the sawtooth behavior in the Z= 13 and 14 isotopes we can conclude that the neutron numbers 14 and 18 prefer an oblate deformation while 16 prefers a prolate deformation. However the proton numbers 10-12 also prefer a prolate deformation. As result the nuclei with Z= 10-12 and N= 14 and 18 could be either oblate or prolate. In the range Z= 10 to 17 all nuclei with neutron number between N= 22 and 26 have a large prolate deformation due to incomplete filling of the $1f_{7/2}$ subshell. The isotopes of argon and potassium do not appear to be effected by the neutron number.

References

1) C.Thibault, R.Klapisch, C.Rigaud, A.M.Poskanzer, R.Prieels, L.Lessard, and W.Reisdorf, Phys.Rev. **C12** (1975) 644

4) X.Campi, H.Flocard, A.K.Kerman, and S.E.Koonin, Nucl.Phys. **A251** (1975) 193

5) D.Vautherin and D.M.Brink, Phys.Rev. **C5** (1972) 626

6) D.Vautherin, Phys.Rev. **C7** (1973) 296

7) H.Flocard, P.Quentin, A.K.Kerman, and D.Vautherin, Nucl.Phys **A203** (1973) 433

8) H.Flocard, P.Quentin, and D.Vautherin, Phys.Lett. **46B** (1973) 304

9) M.Beiner, H.Flocard, N.Van Giai, and P.Quentin, Nucl.Phys. **A238** (1975) 29

10) A.H.Wapstra and K.Bos, At. and Nucl.Data Tables **19** (1977) 177

TABLE I. Binding energies, proton quadrupole moments and isotope shifts for nuclei with $10 \le Z \le 20$.

Z	A	B	Q_p	$\delta\langle r^2\rangle$	Z	A	B	Q_p	$\delta\langle r^2\rangle$	Z	A	B	Q_p	$\delta\langle r^2\rangle$
		[MeV]	[fm^2]	[fm^2]			[MeV]	[fm^2]	[fm^2]			[MeV]	[fm^2]	[fm^2]
10	20	159.9	41	0.00	14	36	293.0	24	0.60	18	36	303.5	-43	0.00
	22	179.6	41	0.07		38	301.5	38	0.86		38	325.2	-23	0.05
	24	193.4	-21	-0.10		40	308.2	33	0.96		40	342.8	-37	0.23
	26	203.2	25	0.05		42	314.4	-43	1.22		42	358.8	-41	0.37
	28	208.5	-20	0.20		44	315.6	-30	1.24		44	373.6	-42	0.50
×	30	212.7	45	0.80		46	315.8	1	1.30		46	387.1	-41	0.61
×	32	215.0	54	1.10		48	315.0	0	1.45		48	394.9	-44	0.80
	34	216.1	44	1.10		50	311.4	-29	1.78		50	400.9	-45	1.00
	36	213.8	41	1.10		52	306.5	-21	1.96	×	52	405.4	-56	1.32
×	38	211.8	44	1.30							54	407.6	-47	1.40
	40	207.4	-24	1.20	15	31	261.1	21	0.00		56	409.0	-42	1.58
						33	279.8	-26	0.24	×	58	409.8	-55	1.82
11	23	189.1	48	0.00		35	296.1	0	0.35	×	60	409.5	-60	2.03
	25	204.9	-24	-0.20		37	307.2	32	0.61		62	408.8	-44	2.08
	27	217.9	34	0.01		39	318.2	46	0.86		64	407.8	-46	2.24
	29	225.5	29	0.17		41	326.9	44	0.99					
×	31	232.0	52	0.70		43	333.6	-12	0.92	19	39	333.4	-11	0.00
×	33	236.9	62	1.05		45	337.0	36	1.22		41	351.9	-24	0.15
	35	239.9	50	1.01		47	338.5	20	1.29		43	369.5	-27	0.27
	37	240.1	47	1.09		49	338.4	25	1.50		45	386.2	-25	0.37
×	39	239.6	52	1.34		51	336.2	-30	1.74		47	401.9	-17	0.46
	41	236.8	37	1.22		53	333.2	28	1.93		49	410.6	-25	0.65
						55	329.9	11	2.09		51	418.0	-18	0.81
12	24	197.9	56	0.00						×	53	422.7	-38	1.11
	26	216.2	38	-0.22	16	32	268.4	40	0.00		55	427.3	-32	1.26
	28	232.1	41	0.02		34	288.4	-29	0.14		57	430.7	-28	1.45
	30	241.8	34	0.13		36	306.2	-10	0.24		59	433.6	-6	1.63
×	32	250.6	58	0.66		38	320.8	41	0.51		61	434.3	-24	1.78
×	34	257.9	69	1.02		40	334.3	55	0.76		63	434.9	-29	1.94
	36	263.0	56	0.96		42	345.2	54	0.90		65	435.2	-29	2.09
	38	265.4	54	1.06		44	352.3	35	0.87		67	435.3	-23	2.21
×	40	266.7	60	1.36		46	358.4	49	1.14		69	435.6	0	2.34
	42	264.5	44	1.21		48	360.1	37	1.22		71	431.7	-23	2.47
	44	261.9	33	1.22		50	362.0	44	1.48					
	46	258.9	32	1.35		52	360.3	-35	1.62	20	40	341.4	0	0.00
						54	359.3	39	1.85		42	361.3	11	0.11
13	27	226.1	-32	0.00		56	356.9	25	1.98		44	380.4	20	0.24
	29	243.1	29	0.10		58	354.7	42	2.22		46	399.0	-9	0.32
	31	256.6	-26	0.31							48	417.2	0	0.42
	33	267.6	-7	0.42	17	35	296.1	-37	0.00		50	426.5	-9	0.60
	35	274.8	35	0.75		37	316.0	17	0.07		52	435.9	0	0.77
	37	282.4	48	1.04		39	331.1	-32	0.25		54	441.3	17	0.99
	39	287.0	44	1.13		41	346.6	47	0.48		56	446.7	-17	1.18
	41	290.0	-39	1.27		43	359.4	46	0.60		58	452.1	-13	1.36
	43	290.2	-30	1.32		45	369.4	-33	0.64		60	457.6	0	1.57
	45	289.2	-19	1.39		47	375.9	41	0.85		62	459.1	11	1.71
	47	287.1	-10	1.49		49	380.6	-39	1.03		64	460.7	22	1.87
	49	282.1	-28	1.82	×	51	383.2	-52	1.37		66	462.4	26	2.01
						53	384.1	-40	1.43		68	463.9	19	2.13
14	28	235.3	-38	0.00		55	384.0	-35	1.62		70	465.5	0	2.24
	30	253.6	0	-0.10	×	57	383.3	-51	1.87		72	462.1	11	2.37
	32	270.6	-27	0.26		59	381.5	36	1.95		74	458.8	14	2.50
	34	284.5	0	0.36		61	380.7	50	2.17					

Figure 1

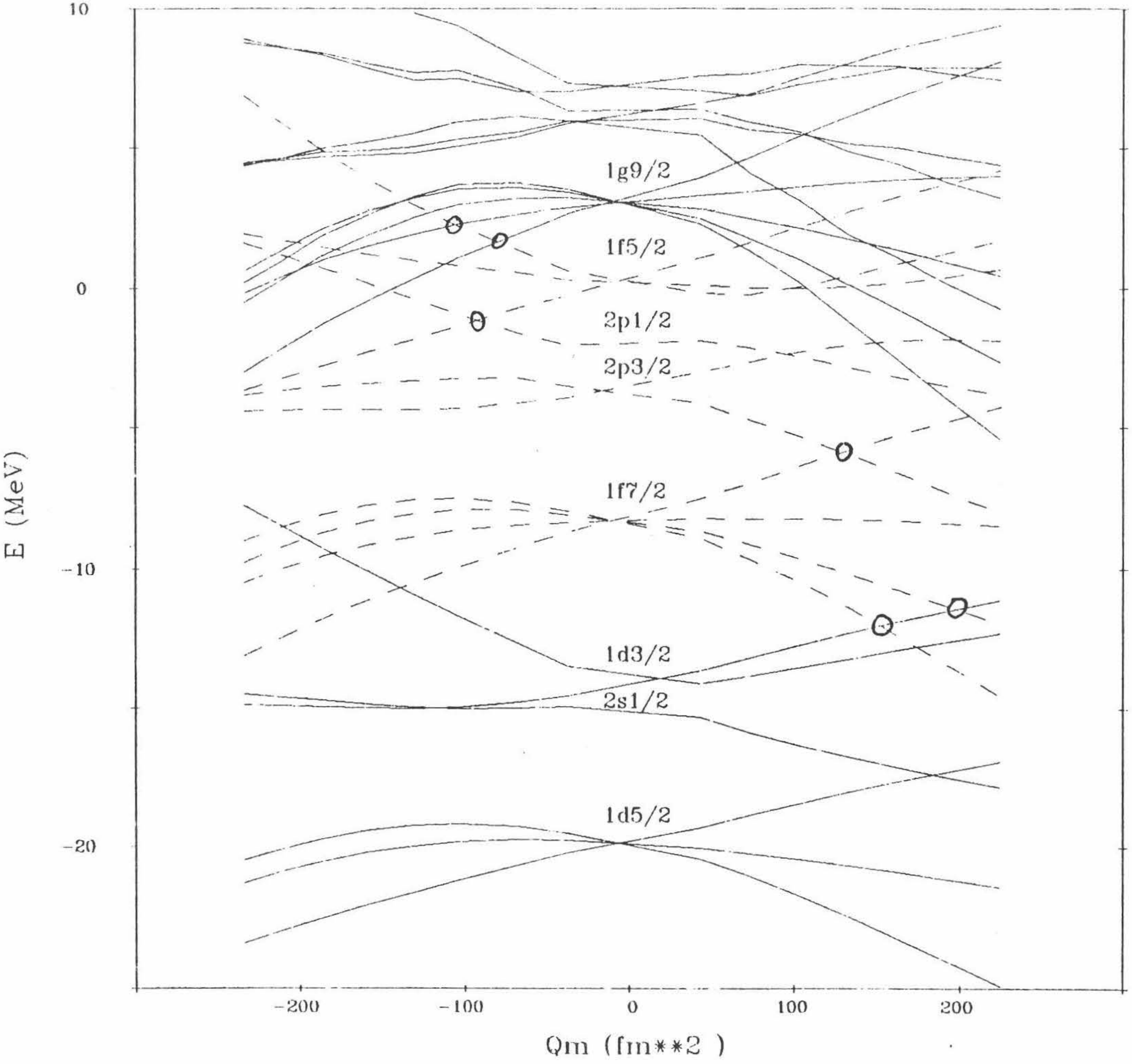
1g9/2
1f5/2
2p1/2
2p3/2
1f7/2
1d3/2
2s1/2
1d5/2
E (MeV)
10
0
-10
-20
-200
-100
0
100
200
Qm (fm**2)

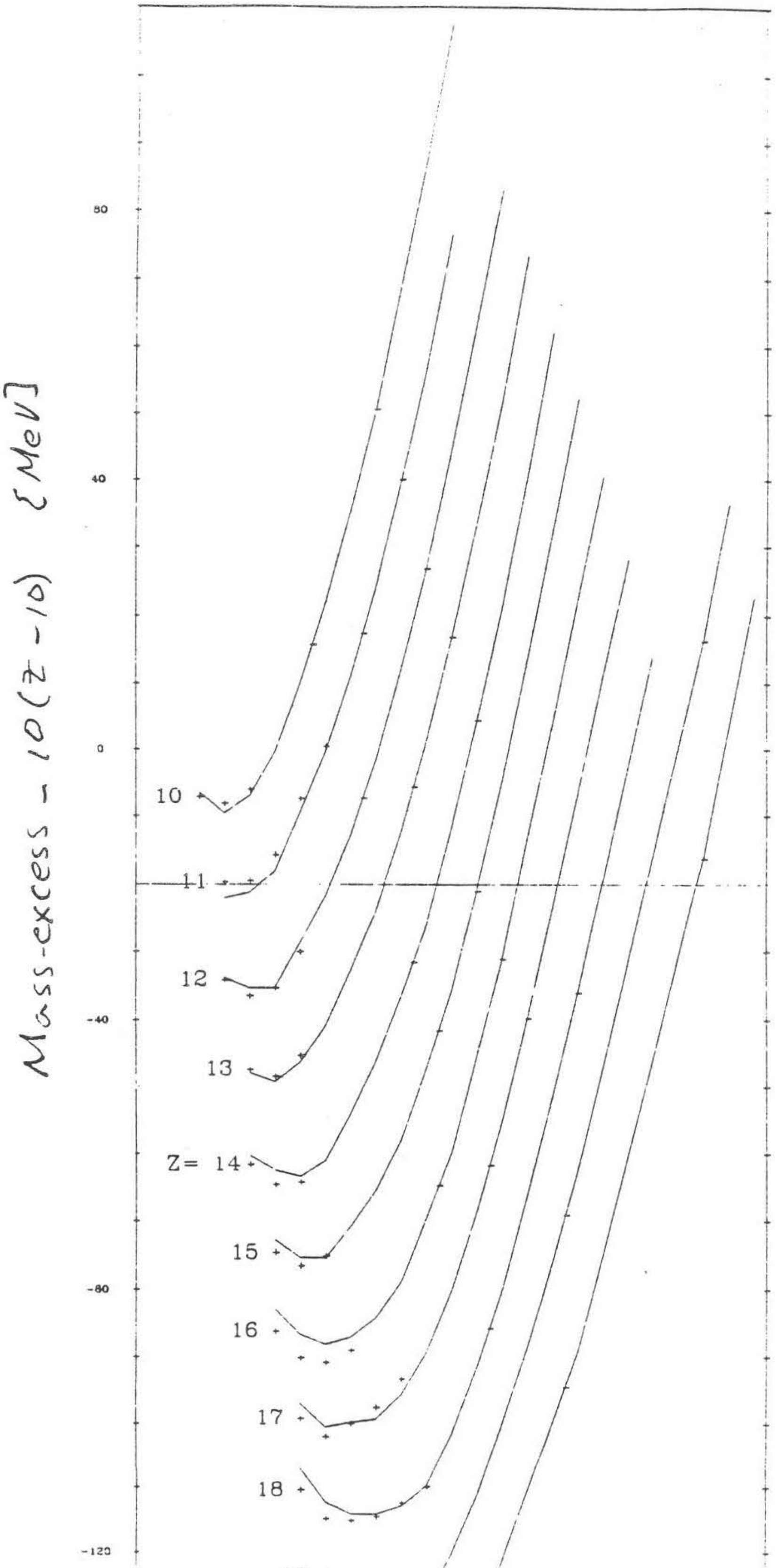

Fig 2
Mass-excess
Solid line : calculated value
+ : experimental value
- : last bound odd N isotope and last bound even N isotope.

Fig 3

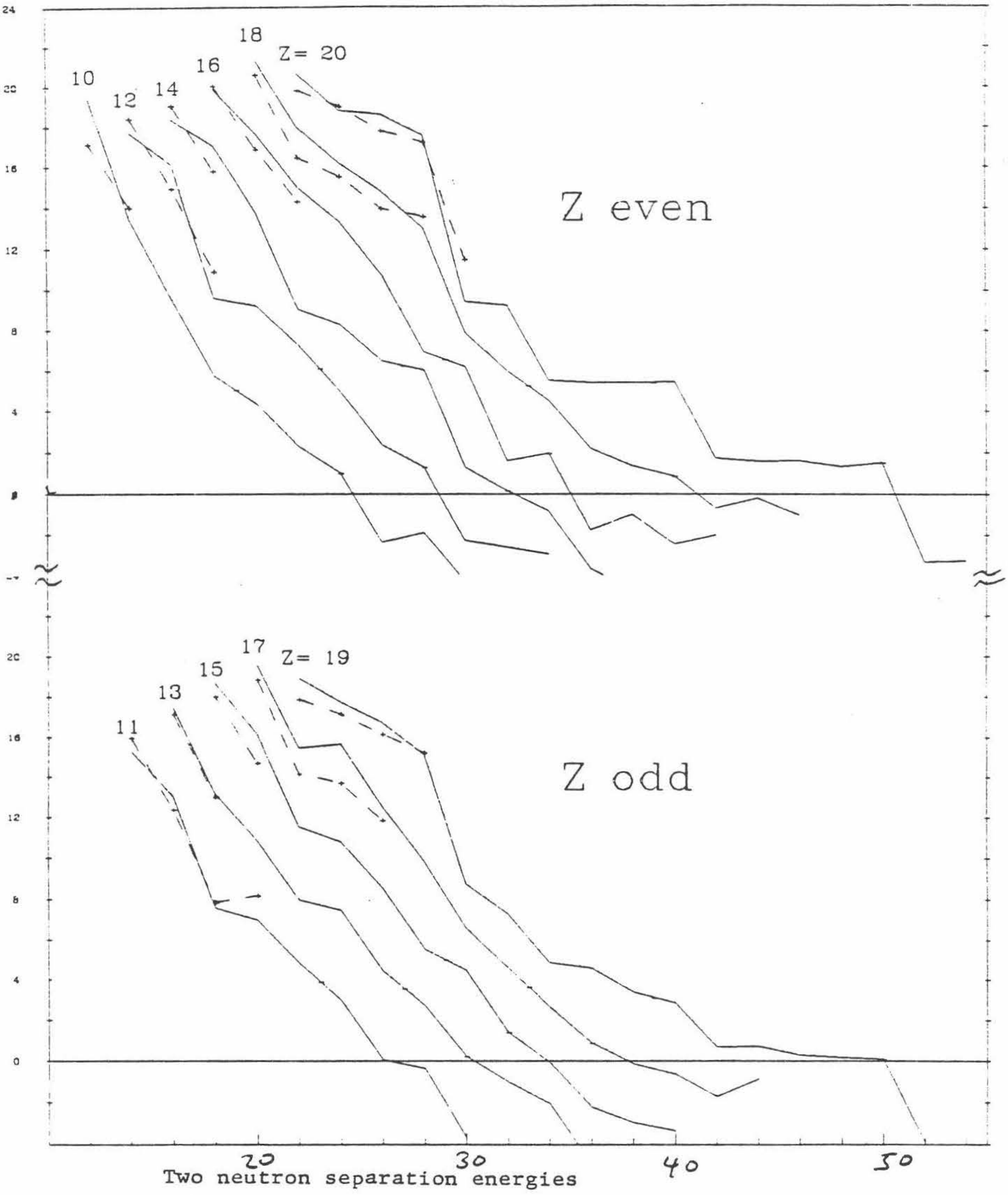

Two neutron separation energies

+: experimental value
-: last bound odd and even N isotope

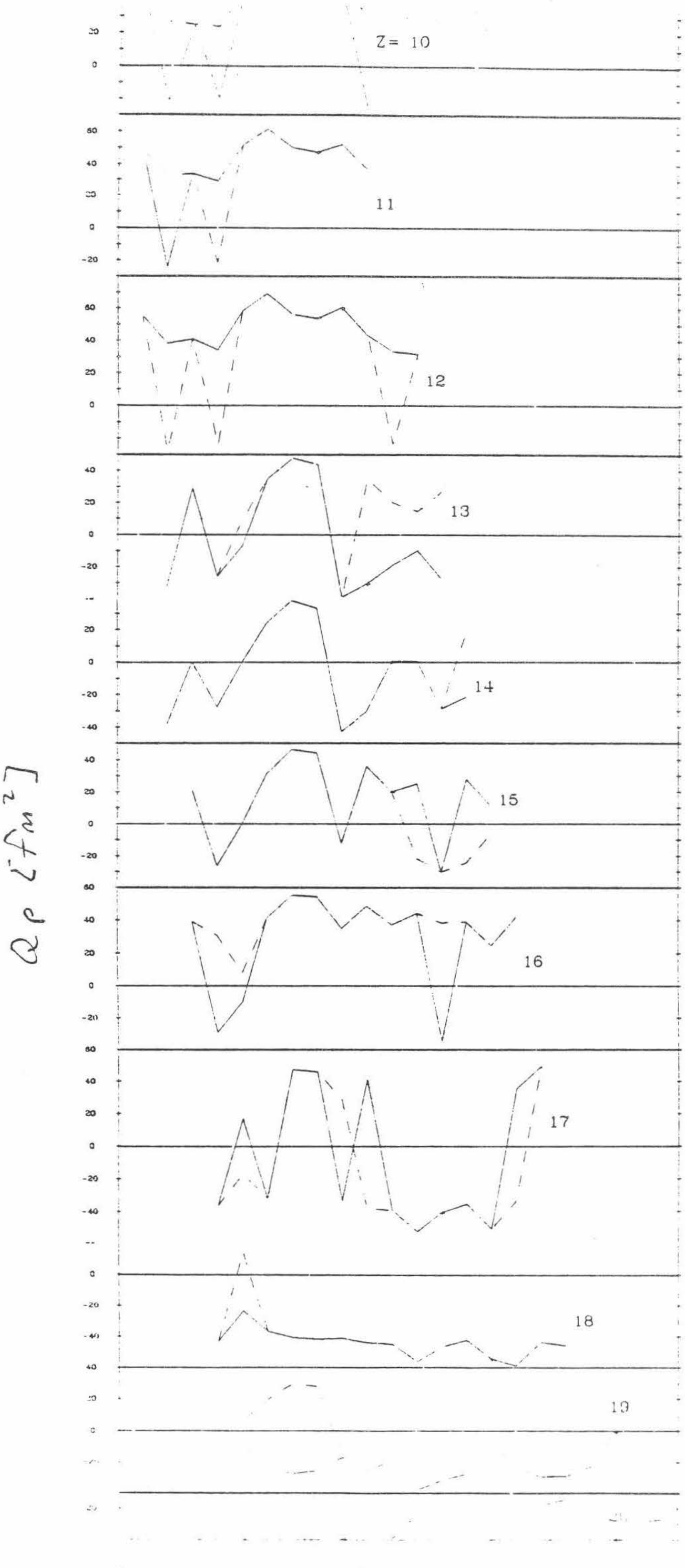

Fig 4

Proton Quadrupole moment vs. neutron number

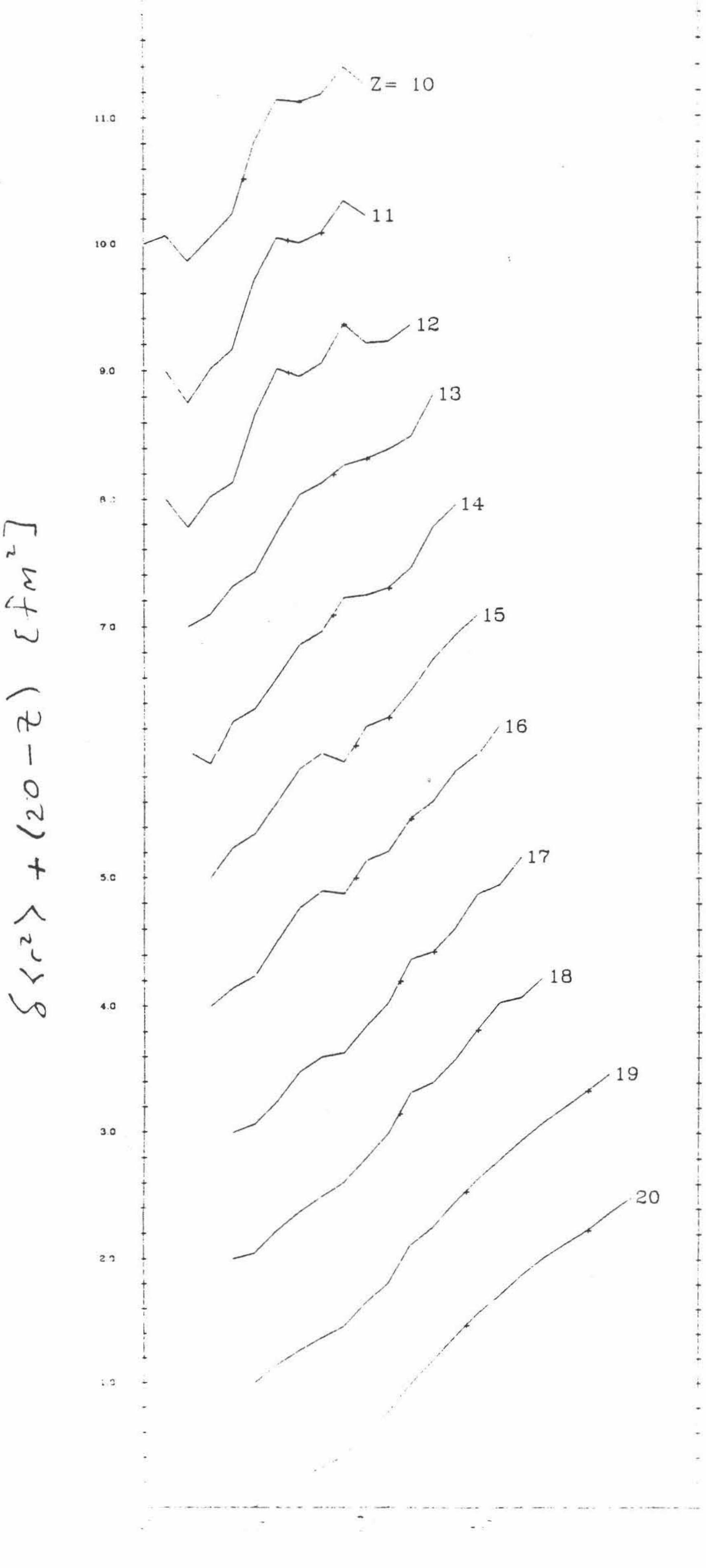

Fig. 5
isotopic shift vs.
neutron number

The Electron Runaway Phenomenon

SURF Project, 1983

Pang-Chieh Chen
Dr. Noel Corngold, Advisor
California Institute of Technology

ABSTRACT: To better understand the electron runaway phenomenon, a simple model containing some of the runaway features is proposed and studied. The solution to this model is obtained in closed form and its asymptotic behavior is explored.

BACKGROUND: In studying the properties of the plasma state, one uses a model consisting of a collection of host particles (ions) and a collection of guest particles (electrons) with their distributions as functions of space, velocity, and time coordinates. When the distribution function of the host particles remains unaltered, the governing equation for the electron distribution is known as a Fokker-Planck differential equation:

$$\frac{\partial f}{\partial t} + \vec{u} \cdot \frac{\partial f}{\partial \vec{r}} + \vec{F} \cdot \frac{\partial f}{\partial \vec{u}} = \frac{\partial}{\partial \vec{u}} \tilde{D} \cdot \left[\frac{\partial}{\partial \vec{u}} + 2\vec{u} \right] f \, ,$$

where $\vec{F}$ is an external force parameter, and $\tilde{D}$ is a tensor. An interesting phenomenon that can be described by the F-P equation is known as the electron runaway effect. This effect results from the fact that the drag a guest particle experiences moving through the medium of host particles actually decreases to zero as its speed tends to infinity. Thus, in the presence of a constant electric field, the speeds of sufficiently fast electrons will be accelerated to infinity. The main problem in solving the F-P equation is that even under the assumption of no spatial dependence and constant external force field, the equation is essentially two-dimensional in velocity space. The equation has unfortunately not been separated. Nevertheless, there are useful some one-dimensional approximations to this equation.

FORMULATION OF A SIMPLER MODEL: In this research project, the relation between the runaway effect and the vanishing drag is under investigation. To understand the nature of the runaway effect, a much more simplified model, rather than the full F-P equation, is being studied. The following assumptions are made so that an analytical solution could be obtained:

1) Neglect spatial variation and work in a one-dimensional model.

2) Define the drag coefficient to be $D = \begin{cases} 1 - \dfrac{|u|}{u_0} & |u| < u_0 \\ 0 & |u| > u_0 \end{cases}$

This assumption allows the drag coefficient to vanish linearly in a finite region, as opposed to the D tensor in the original F-P equation which vanishes at infinity. Nevertheless, the present model contains all three regions of interests: a) the region of diffusion where D dominates the external force field parameter F; b) the region of free motion where D=0; and c) the connection region where the effects of D and F are comparable.

3) Remove the 2u term from the original equation. This assumption corresponds to a situation in which the mass ratio of the electron to the ion tends to zero. (the 'Lorentz model')

The equation we have now is

$$\frac{\partial f}{\partial t} = \frac{\partial}{\partial u}\left(D\frac{\partial}{\partial u} - F\right)f \equiv -\frac{\partial j}{\partial u},$$

where j is defined as the runaway current in velocity space.

RESULTS AND DISCUSSION: The general solution to the above equation is found through the use of Green's function for the D nonzero region. The integral representation of the Green's function is provided by the inversion formula for the Laplace transform.

$$g(x,\xi,t) = \frac{1}{2\pi i}\int_{c-i\infty}^{c+i\infty} ds\; e^{st}\,\frac{\gamma}{u_0}\,p(x)q(\xi)\left\{\frac{1}{J_\nu(\gamma)\,J'_\nu(\gamma)} + \frac{\pi\gamma Y_\nu(\gamma)}{J_\nu(\gamma)}\,H_x^\xi\right\}$$

$$\text{where } p(x) = J_\nu(\gamma v^{1/2})\left[v^{-\frac{\nu}{2}}H_- + v^{\frac{\nu}{2}}H_+\right] \;;\; q(\xi) = J_\nu(\gamma v'^{1/2})\left[v'^{\frac{\nu}{2}}H_- + v'^{-\frac{\nu}{2}}H_+\right]$$

$$\nu = Fu_0;\;\; v = 1 - \frac{|x|}{u_0};\;\; v' = 1 - \frac{|\xi|}{u_0};\;\; \gamma = 2u_0\sqrt{-s}\,;$$

$$H_x^\xi = 1 \text{ for } x\xi > 0\,,\; = 0 \text{ for } x\xi \le 0$$

and H_+ is the Heaviside step function with $H_-(x)=H_+(-x)$

F is assumed to be nonnegative without loss of generality. By collecting residues, we can represent the function as a sum of eigenfunction with exponential decay in time. The eigenfunctions form two groups, odd and even, with their corresponding sets of eigenvalues.

As an application of this Green's function, we study the time evolution of the runaway current at u=u_0 with the initial distribution a delta function centered at u=0. Taking F fixed, and allowing u_0 to be >> 1, we find the asymptotic form of the solution to contain three time regimes (t small, moderate, and large). Defining the variable $\alpha = \frac{Ft}{u_0}$, we have

$$f(u_0,t) \approx \sqrt{\frac{F}{2\pi u_0}}\,\exp\begin{cases} -\nu(\frac{1}{\alpha} - 1) - (\nu + 1)\ln\alpha & \text{if } \alpha \ll 1 \\ -\frac{\nu}{2}(1 - \alpha)^2 & \text{if } \alpha = O(1) \\ -.78 + \nu(1 - \ln 2) - \frac{F^2 t}{4} & \text{if } \alpha \gg 1 \end{cases}$$

The computer plot attached shows the smoothness of the matching regions. Overall, the runaway current as a function of time resembles a Gaussian curve during the intermediate time regime, and decays exponentially for the very long time regime. For the short time regime, the runaway current behaves like the tail of a widening Gaussian curve (from sharply peaked to more bell shaped). The smoothness of the runaway current in the matching region for the large u_0 case indicates a perhaps very good approximation to the exact solution. However, due to the slow convergence and high cancellation of the exact series solution, the results could not be compared.

The asymptotic behavior of the runaway current with u_0 fixed and F vanishing has not been fully explored. Nevertheless, the behavior for very large time is that

$$f(u_0,t) \approx \frac{1}{2u_0} \exp\left[-\frac{Ft}{2u_0}\right]$$

CONCLUSION: The project of analyzing the proposed simple model has been successfully carried out. However, the relation between this model and the original F-P equation and/or the physical world remains to be investigated. The asymptotic behavior for the vanishing F case should perhaps be explored more since it corresponds to a somewhat more realistic picture than the large u_0 case.

ACKNOWLEDGEMENT: I would like to thank the SURF program for giving me this research opportunity. Also, I am very grateful to Professor Noel Corngold for all the time and patience he has given in educating me.

$u_o = 20$, $F = 1$, $\nu = 20$

COMMENT: No forced matching is used.
The graph simply displays the three functions extended over their respective region of validity.

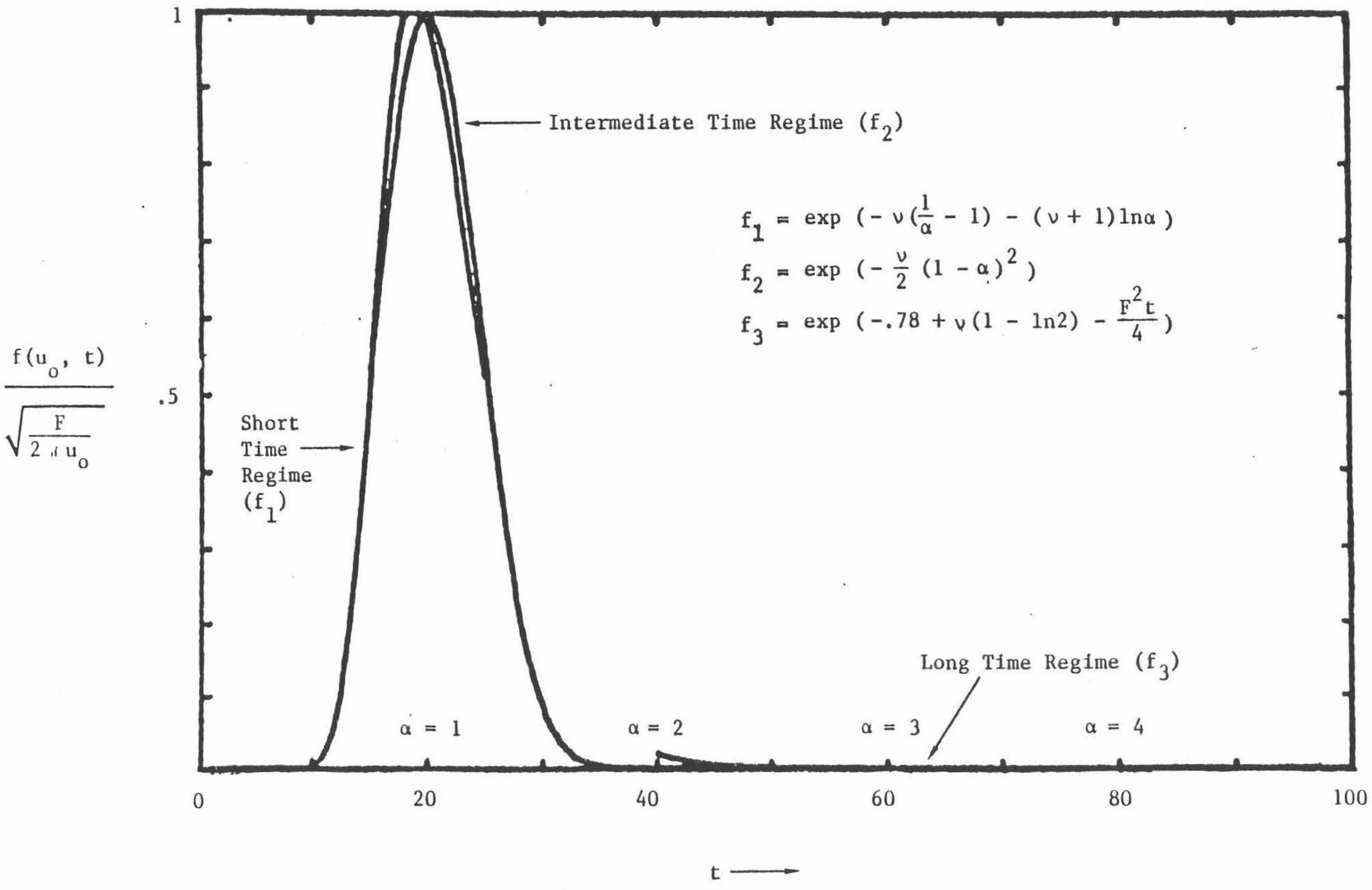

Hot Electron Transport In a Proposed GaAs-Al-GaAs transistor

Z.H.Chen, L.C.Chiu, S.Smith, A.Yariv
California Institute of Technology
Pasadena, California 91125

Abstract

The distribution function of hot-electrons in an Al layer is obtained by solving the Boltzmann's equation subject to certain boundary conditions. The collector-emitter current gain constant in an GaAs-Al-GaAs transistor structure is calculated for different values of the barrier height difference and the base width. A discussion is presented involving the fabrication of such a transistor using Molecular-Beam-Epitaxy.

1 Introduction

Hot electron transistors with a thin film metal base have been proposed for very high frequency operations. which can be used in the high speed logic and parallel processing in computer engineering [1]. It was not possible until the advent of Molecular-Beam-Epitaxy, developed several years ago to fabricate good epitaxial semicoductor-metal-semiconductor transistors. The growth of a single-crystal aluminum Schottky barrier diodes prepared on MBE was studied by Cho [2] in 1978 and rekindled the interest in metal base semiconductor transistors.

Spratt [3] and his coworkers in 1961 measured the collection efficiency for hot electrons in an Al layer of the width 100Å, and they measured a more than 90% collection. They concluded that the hot electron mean free path was longer than 1000Å. Quinn[4] in 1962 also calculated the mean free path of a hot electron $E \approx 1\text{eV}$, and his result was in good agreement with Spratt's measurement.

A thorough theoretical investigation was performed by Sze in 1966 [5] and Crowell [6] in 1968. Sze's expression of the current gain constant is $\alpha=\exp(-\frac{d}{L})$, where d is the base thickness and L is the mean free path. His conclusion concerning the current gain constant, which was less than 0.3 for some metal films of thickness larger than 100Å (Au included), was based on the assumption that the electron-optical phonon scattering was very important. The difference between the two metal-semiconductor interfaces was ignored. In this paper, a new theoretical investigation is carried out which shows that when optical phonons are not present, (as is the case in Al,)the energy loss, due to each collision with acoustic phonon, is much smaller. Hence the effect on the collection efficiency due to the difference between two Schotty barriers can no longer be ignored. The current gain constant is calculated in a number of cases.

2 Qualitative Description of Hot electron Transport In Metals

It is very important to distinquish two different conduction mechanisms in metals for "cold" electrons and "hot" electrons. A "cold", nearly free electron ($E \approx 0$), a few collisions with ions will cause the electron to transit to one of the bulk electron states. The bulk electron system will absorb phonons emitted by that electron during its collisions and emit a new electron. Essentially, a cold electron will be thermalized immediately after it is injected, and an equilibrium Fermi distribution function can be used.

A hot electron($E \approx 1$eV)on the other hand, can suffer many collisions before making a transition to the bulk electron states so that it can travel a relatively long distance before being thermalized. Therefore it is reasonable to assume a distribution function $f(\vec{r},\vec{p})$ describing the hot electron density in both coordinate and momentum space.

Since the hot electron transport is a purely non-equilibrium problem, we must evaluate the rate of change of the distribution function $f(\vec{r},\vec{p})$ due to collisions with phonons in order to solve the Boltzmann's equation. Aluminum has a monatomic f.c.c structure so that it has no optical phonons[7]. The rate of change of the ditribution function, due to electron acoustic phonon scattering can be calculated in many different ways. Of these the one by Yamashita [8] is the most appropriate for the present case.

3 The Solution of The Distribution Function

The following symbols are to be used. V_o= the crystal volume of a unit cell of Al = $5.52510^{-24}(cm)^3$at 300 K. C = an energy parameter describing the coupling between the electrons and phonons = 5eV calculated by BCS theory. u_o=sound velocity = 1.6510^6 (cm/sec) calculated by Bohm-Staver relation. m = effective mass of conduction of electrons = 1.2710^{-27}g. M = mass of ions = 4.4810^{-23}g. Following the conventional theory of metals by Wilson and the work of Yamashita, we can calculate using expansion in spherical harmonics $[\frac{df}{dt}]_{collision}$ for the following coordinate system:

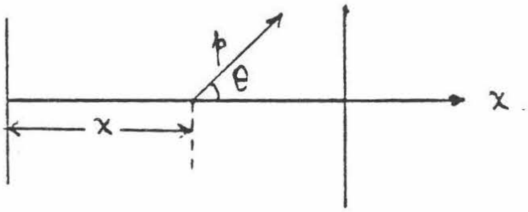

Fig 1

$$f(\vec{r},\vec{p})=f_0(x,E)+f_1(x,E)\cos\vartheta$$

and the collision integral is given by Yamashita [8]:

$$[\frac{df}{dt}]_{colli}=\frac{V\pi C^2}{8\pi^3 M u_0 2\lambda k}\int d\varphi\int\frac{q^2dp}{\exp(x_q)-1}$$

$$[\exp(x_q)f(\vec{k},+\vec{q})-f(\vec{k},-\vec{q})+\exp(x_q)f(\vec{k})] \tag{1}$$

where $x_q=\frac{\hbar\omega_q}{KT}$ and $\lambda=\frac{\hbar^2}{2m}$, k is the norm of $\vec{k}$ and $\omega_q=u_0q$. If we take the first two terms in the Taylor expansions of $\exp(x_q)$, $f_0(E+\hbar\omega)$and$f_0(E-\hbar\omega)$, and assume that $f_1(E+\hbar\omega)=f_1(E-\hbar\omega)$ then we will get:

$$[\frac{df}{dt}]_{colli}=A(T)((2mE)^{1/2}[E\frac{\partial f_0}{\partial x}+(\frac{E}{KT}+2)\frac{\partial f_0}{\partial x}+\frac{2}{KT}f_0]-\frac{E^{1/2}}{(u_0)^2}f_1\cos\vartheta) \tag{2}$$

where $A(T)=(V_oC^2m(2m)^{1/2}KT)/(\pi M(\hbar)^4)$ and the transport equation is :

$$[\frac{df}{dt}]_{colli}=(2E/m)^{1/2}\cos\vartheta\frac{\partial f_0}{\partial x}+(2E/m)^{1/2}(\cos\vartheta)^2\frac{\partial f_1}{\partial x} \tag{3}$$

Now if we equate (2) and (3), and multiply them by $\int \sin\vartheta d\vartheta$, integrate from 0 to π, we get :

$$6mA(T)[E\frac{\partial^2 f_0}{\partial E^2}+(\frac{E}{KT}+2)\frac{\partial f_0}{\partial E}+\frac{2}{KT}f_0]=(2/m)^{1/2}\frac{\partial f_1}{\partial x} \tag{4}$$

Multiply both side by $\int \sin\vartheta\cos\vartheta d\vartheta$ and integrate from 0 to π and differentiate with respect to x we get :

$$(2/m)^{1/2}\frac{\partial f_1}{\partial x}=-\frac{2(u_0)^2}{mA(T)}(\frac{\partial^2 f_0}{\partial x^2}) \tag{5}$$

Substitute (5) into (4) we get the following partial differential equation :

$$E\frac{\partial^2 f_0}{\partial E^2}+(\frac{E}{KT}+2)\frac{\partial f_0}{\partial E}+\frac{2}{KT}f_0+D\frac{\partial^2 f_0}{\partial x^2}=0 \tag{6}$$

Where $D^{-1} = 6(\frac{V_o C^2 KT}{\pi M})^2(\frac{m^5}{\hbar^8 u_0^2})$. Since the distribution function $f(\vec{r},\vec{p})$ is normalized, we can perform a Fourier transform action in x and denote $F[f(x)] = F(y)$. The boundary conditions for f_0 are : $f_0(0,E)=\frac{JV}{qv}$ and $\frac{\partial f_0}{\partial x}(0,E)=\frac{JV}{qvL_p}$ where J is the input current, V is the base volume, v is the carrier velocity, L_p is the diffusion length in Al. Taking the Fourier transform of (6) we get :

$$E\frac{\partial^2 F(y,E)}{\partial E^2}+(\frac{E}{KT}+2)\frac{\partial F(y,E)}{\partial E}+(\frac{2}{KT}-Dy^2)F(y,E)-D(\frac{2}{\pi})^{1/2}(\frac{JV}{qvL_p})=0 \tag{7}$$

The general solution is :

$$F(y,E)=a\exp[-(\frac{E}{KT}+2+((\frac{E}{KT}-2)^2+4DEy^2)^{1/2}]+b\frac{DKTJ}{qvL_p(2-DKTy^2)}(\frac{2}{\pi})^{1/2} \tag{8}$$

where a and b are two different normalization constants to be determined. The inverse Fourier transform of the first term is :

$$\frac{E/2KT-1}{(DE+x^2)^{1/2}}K_1[(E/KT-2)(1/4+\frac{x^2}{4DE})^{1/2}](\frac{2}{\pi})^{1/2}\exp(-1/2(\frac{E}{KT}+2)) \tag{9}$$

where K_1 is the Bessel function of the first kind and that of the second term is :

$$\frac{J}{qvL_p}(DKT/2)^{1/2}\exp(-x(2/DKT)^{1/2}) \tag{10}$$

Therefore the solution of $f_0(x,E)$ is :

$$f_0(x,E)=a\frac{E/2KT-1}{(DE+x^2)^{1/2}}K_1[(E/KT-2)(1/4+\frac{x^2}{4DE})^{1/2}](\frac{2}{\pi})^{1/2}\exp(-1/2(\frac{E}{KT}+2))$$

$$+b\frac{J}{qvL_p}(DKT/2)^{1/2}\exp(-x(2/DKT)^{1/2}) \tag{11}$$

which is the desired result. Numerical calculations show that $f_1(x,E)=10^{-11}f_0$, therefore we can take $f(\vec{r},\vec{p})=f_0(x,E)$ to a good approximation.

4 The Current Gain Constant (11)

The current gain constant is defined as the ratio of the rate of electrons exit the base at x_2 (See Figure 2), to the rate of electrons entering at x_1. (11)

Approximations can be made to simplify $f_0(x,E)$ since we know that $DE \approx 10^{-9}$ in MKS so that DE is much smaller compared with x^2, then (11) is reduced to :

$$f_0=\frac{1}{2}\exp(-(\frac{x}{L})^2-\frac{E}{KT})+2^{-3/2}(\frac{JAd}{qvL_p})L\exp(-2^{3/2}(\frac{x}{L}) \tag{12}$$

which is already normalized. $L = 2(DKT)^{1/2}$ is the effective mean free path due to electron-electron and electron-phonon collisions. The expression for the collection efficency α referring to Fig 2 in terms of the normalized distribution function is ($x_1=E_2=0$) :

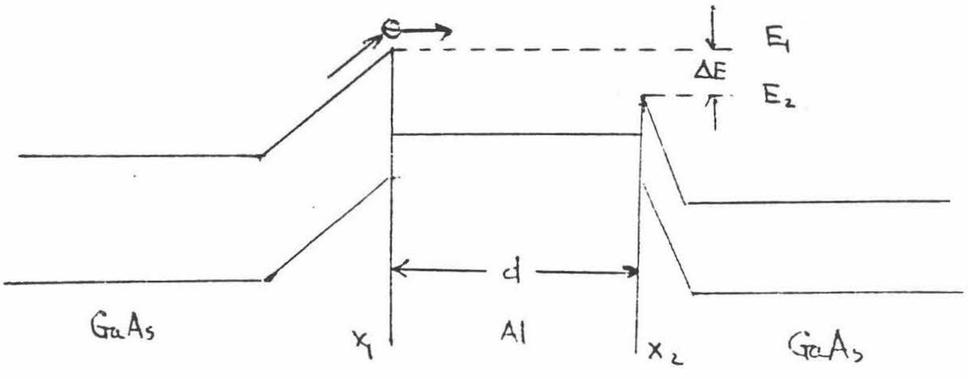

Fig 2

$$\alpha=\frac{2^{1/2}\exp(-(\frac{d}{L})^{2})+Ld\frac{JA}{qvL_p}\exp(-2^{3/2}(\frac{d}{L}))}{2^{1/2}\exp(-\frac{\Delta E}{KT})+(Ld\frac{JA}{qvL_p})} \quad (13)$$

We can see that when d is very large, the first two terms can be neglected and we get Sze's result, $\alpha=\exp(-2^{3/2}\frac{d}{L})$ which is the bulk property in equilibrium. But when d is small (Today we can grow a 50A layer easily), the term involving ΔE becomes important. The dependence of α on ΔE is plotted in Fig 3. The data of the mean free path for hot electrons in Al is summerized by Heiblum [11], for different values of the excess energy. The mean free path for a hot electron with 0.7eV energy is about 150Å, and that of an electron with 1eV is about 80Å. The value of $\frac{JA}{qvL_p}$ for E = 0.7eV is taken as 1.86 in MKS unit. The value of ΔE is 0.06eV at most according to Cho.

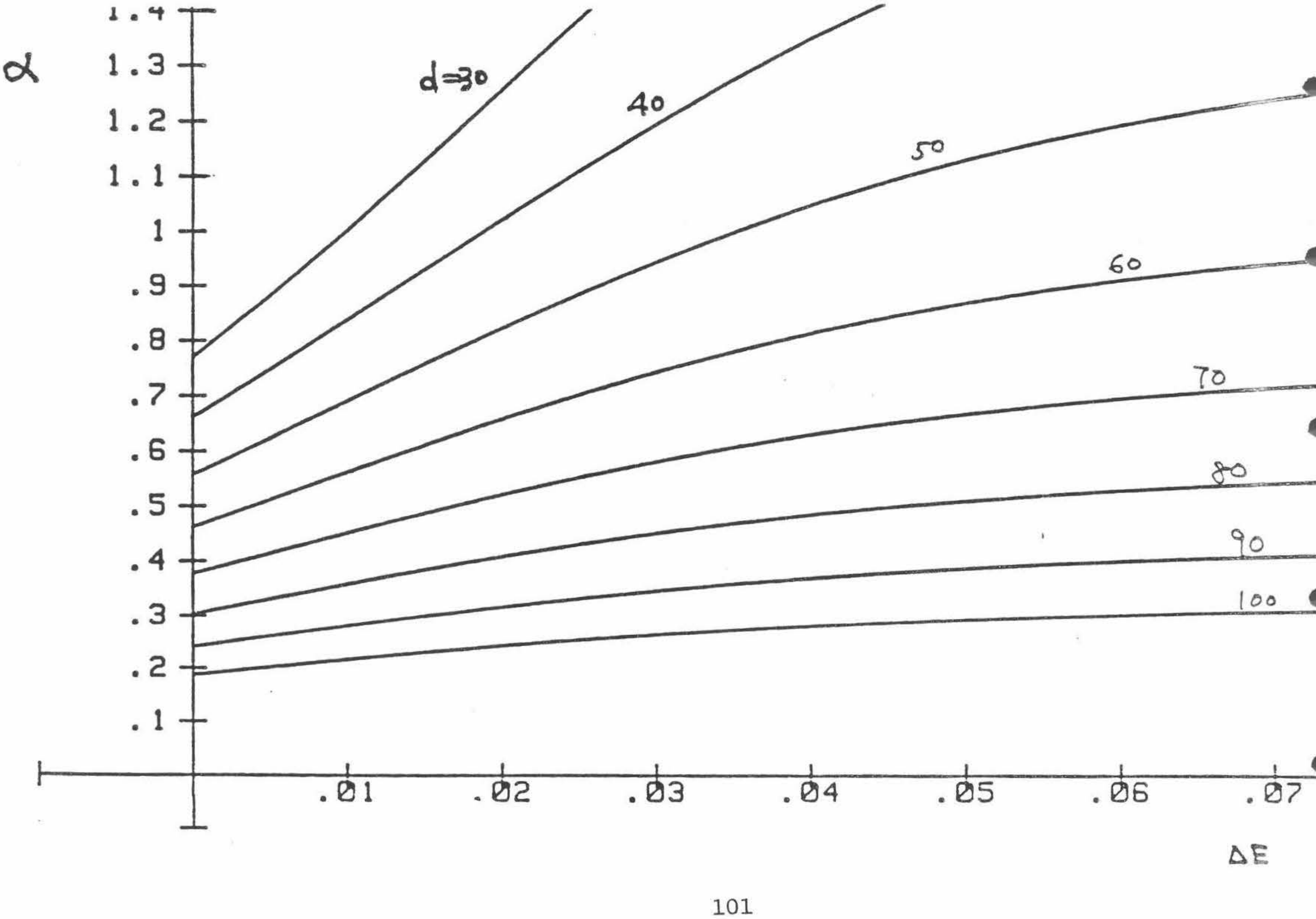

5 Summary and Conclution (13)

Theoretical and experimental studies have shown that the factor due to the difference of two Schottky barriers is important when the base width d is small and one can always get a high current gain constant by making a reasonably large barrier difference and sufficiently thin base layer on MBE. A transistor like this has obvious advantages over others. For exmple, the cutoff frequency f_{out} which is given by Sze[10]

$$f_{out}=\frac{1}{2\pi[\frac{KT(C_e+C_c+C_p)}{qI_c}+\frac{d^2}{\eta D_b}+\frac{x_c-d}{2v_s}]} \qquad (14)$$

becomes larger because now we can grow a thin layer on MBE. The swiching time t_{swich} which is given by Solomon

$$t_{swich}=\frac{1}{2}[(C_{in}+C_{out}+3C_f)\frac{V_L}{I}+3t_b+R_b(C_{out}+C_f)] \qquad (15)$$

becomes smaller because we have a small resistence R_b and a short base transient time t_b.

References

1. Paul M.Solomon Proceedings of IEEE, Vol. 70, No.5, May 1982

2. A.Y.Cho J.Appl.Phys.49(6), June 1978

3. J.P.Spratt Phy.Rev.Lett Vol.6, No.7 April 1961

4. J.J.Quinn Phy.Rev Vol 126, No. May 1962

5. S.M.Sze and H.K.Gummel, Soli.stat.elec Vol 9

6. C.R.Crowell and Sze, Phys.Thin Films

7. Ashcroft and Mermin, Solid State Physics

8. Yamashita and Watanabe, Prog.Theo.Phy, Vol. 12, No.4, 1954

9. M.Heilum Soli.Stat.Elect. Vol 24, 1981

10. Sze, Physics of Semiconductor Devices

Io's atmospheric density as a function of aura's density distribution

Author: Joe K. Cheng
Faculty Sponsor: Dr. Peter Haff
Summer Undergraduate Research Fellowship,
California Institute of Technology, Pasadena, California 91125

ABSTRACT

A computer model is developed to simulate aura density distribution as a function of atmospheric mean free path. The atmospheric pressure can then be calculated from the mean free path. By comparing the simulated results with observed phenomena, a mean free path of 200 km is determined, which corresponds to a pressure of 0.3×10^{-13} bar.

I. Introduction

The nature of Io's atmosphere is an interesting subject. Post-. *Voyager* studies of Io have considered a wide range of models for Io's atmosphere. It is important that Io's atmosphere be studied and ultimately understood because it appears to play key roles in

(1) the supply of ions to the Jovian magnetosphere, (2) the fate of sputtered ejecta from Io's surface, and (3) the closure of flux tube currents at Io.[1]

Bright surface markings are often found in close association with volcanic features on Io. In some localities, topography and seemingly unrelated surface markings can be seen faintly as though mantled by a thin translucent deposit, while in others, the deposit appears to have covered the underlying terrain and to be optically thick. The bright surface markings are called auras, and they suggest a superposition of high albedo material on a pre-existing surface. These studies of auras have been published by S.M Baloga, D.C. Pieri, and D.L. Matson.[2]

In this paper a computer model is developed to simulate an aura's density distribution as a function of the atmospheric mean free path. By comparing the simulations with observed phenomena, the order of magnitude of Io's mean free path is determined. By assuming that Io's atmosphere is composed of thermalized SO_2 molecules, and by knowing the order of magnitude of the mean free path, the order of magnitude of Io's atmospheric pressure is calculated.

Many auras are laterally symmetric with respect to the associated flow, that is, the extent and relative brightening is approximately equal on both sides, as is seen at *Vaugahn Patera*. In other cases, such as *Ra Patera*, the aura effect is clearly and distinctly observed only on one side of the flow. In order to explain these phenomena, the formation of auras must first be understood. Our model describes auras as SO_2 deposits. As the hot lava flows on top of the SO_2 frost on Io's surface, some of these SO_2 molecules sublime. This process only occurs where the lava, SO_2 frost, and atmosphere meet (Fig. 1). If Io does not have an atmosphere, these SO_2 molecules would simply enter ballistic trajectories and then deposit themselves on the surface (Fig. 2). An aura is formed by these deposits. Sometimes the lava covers one boundary of the SO_2 frost, so that no SO_2 can escape (Fig. 3). It is because of this geometry, that an aura is observed only on one side of the flow.

This observation implies that the atmospheric pressure of Io is very small. If the atmospheric pressure is high, the SO_2 molecules would collide with the molecules in the atmosphere, and enter into a three-dimensional random walk, so it is possible to observe some SO_2 molecules which have landed on the other side of the flow. Knowing that this process occurs rarely, if at all, an upper limit on Io's atmospheric density can be established.

II. Actual computer modelling

Typical lava width is about 20 km, and typical height is between 1 and 5 m. Because the lava flow length is vastly longer than the width of the flow and the lateral extent of the observed aura, and also because the flow is believed to have sharp edges, the flow is modelled as an infinitely long rectangular flow with finite width. The source of the escaping SO_2 is placed at a distance arbitrarily close to the lava edge (Fig. 4). It turns out that the simulated aura density distribution is strongly dependent on this distance Δy. In this paper, Δy is taken to be 0.1×10^{-4} m.

III. Analysis

The initial velocity vector $\vec{V}_i$ of the escaping SO_2 molecule uniquely defines its trajectory. The projection of $\vec{V}_i$ on the x-y plane is also a vector; call it $\vec{v}_{xy}$. φ is the angle between the x-axis and $\vec{v}_{xy}$, and ϑ is the angle between the z-axis and $\vec{V}_i$. These are just the usual cylindrical coordinates. The probability density functions of $|\vec{V}_i|$, φ, and ϑ are:

$$f_V = 4\pi\,(\frac{m}{2\pi kT})^{3/2}\,V^2\,e^{\frac{-mV^2}{2kT}} \tag{1}$$

$$f_\vartheta = \cos(\vartheta) \tag{2}$$

$$f_\varphi = \frac{1}{2\pi} \tag{3}$$

where m is the mass of SO_2, k is the the Boltzmann constant, and T is 166 K, the characteristic temperature of SO_2 [3]. By using various techniques including the Monte Carlo method, $\vec{V}_i$ is generated according to the above probability density functions. The probability of a particle travelling a distance s before colliding is

$$P(s) = 1 - e^{-s/l} \tag{4}$$

where l is the mean free path. If s is long enough, the particle would land before it had a chance to collide. If collision does take place, the particle is assumed to scatter with equal probability in any directions and with its original speed.

In order to estimate what kind of mean free path should be picked before the frequency in collision decreases, the effects of the lava flow are temporarily neglected. By letting $0 < \varphi < \pi$, SO_2 can only escape on one side. It is found that $l \approx 200$ km, which corresponds to a pressure of

0.3×10^{-13} bar, before a significant decrease in collision frequency is observed (Fig. 5). When the lava flow is taken into account, the result is similar (Fig. 6).

In calculating the above mean free path, the change of pressure as a function of altitude is neglected since

$$P = P_0\, e^{\frac{-mgh}{kT_a}} \tag{5}$$

where P_0 is the pressure on Io's surface, m is the mass of SO_2 in the atmosphere, g = $1.76\frac{m}{s^2}$, the acceleration due to gravity on Io, T_a = 130 K, the atmospheric temperature, and h is height over the surface.

Fortunately the vertical distance of particle travelled is small enough, so that the linear correction factor is only 1.3, and the change in l is insignificant (Fig. 7).

IV. Discussions

This paper assumes the atmosphere of Io is mainly composed of thermalized SO_2 molecules. This is a questionable assumption. However, Matson, *et al.*, demonstrated that SO_2 is a good candidate. Since aura is observed only on one side of the flow at *Ra Patera*, an upper limit of atmospheric pressure is determined. Therefore this method does not yield the actual atmospheric pressure. However, in any case, the actual atmospheric pressure is expected to be very low.

V. Conclusions

By modelling SO_2 particles as having ballistic trajectories, and assuming random scattering in the atmosphere, the aura density distribution is simulated as a function of the mean free path. The lower limit of the mean free path is found to be 20 km, which corresponds to an upper limit of atmospheric pressure of 0.3×10^{-13} bar. This is extremely small, considering the atmospheric pressure on earth is about 1 bar.

VI. Acknowledgements

I would like to thank my faculty sponsor, Dr. Peter Haff, for lengthy discussions and for special advice when I ran into problems. I would also like to thank Mr. Eric Kawamoto for offering special insights and assistance. This work was supported by the Summer Undergraduate Research Fellowship at the California Institute of Technology.

References

1. D. L. Matson and D. Nash,"Io's atmosphere: Pressure Control by Regolith Cold Trapping and Surface Venting," 1983.
2. S. M. Baloga, D.C. Pieri, and D.L. Matson,"The Auras of sulphur Flows on Io," 1983.
3. S. M. Baloga, D. L. Matson, and D.C. Pieri,"Auras and Io Regolith Outgassing by Sulphur Flows," 1983.

Figure Captions

Figure 1.

This geometry allows SO_2 to sublimate into the atmosphere. This sublimation process can only occur where the lava, SO_2 frost, and atmosphere meet.

Figure 2.

Sublimated SO_2 molecules enter ballistic trajectories and deposit themselves on Io's surface to form an aura.

Figure 3.

When the lava covers one boundary of the SO_2 frost, no molecules on this side can escape into the atmosphere.

Figure 4.

The geometry of the SO_2 source and the lava flow. Δy is taken to be 0.1×10^{-4} m.

Figure 5.

The effects of the lava are neglected here. A computer simulation with mean free path = 200 km. Frequency of collisions begins to decrease at this mean free path, which corresponds to a pressure of 0.3×10^{-13} bar.

Figure 6.

The effects of the lava are taken into account here. The result is similar to that of Figure 5.

Figure 7.

The change of atmospheric pressure due to the change in altitude is considered. The result is similar to that of Figure 6.

Figures

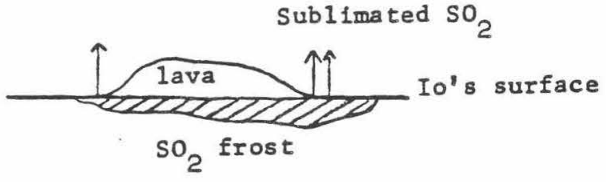

Figure 1

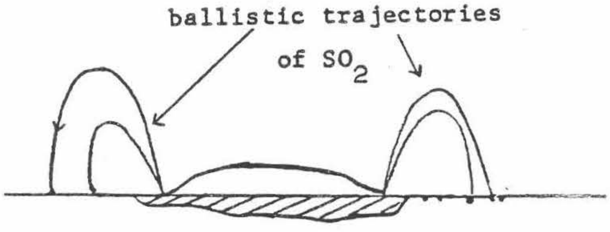

Figure 2

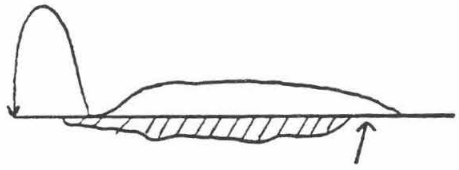

This side of the boundary is completely covered.

Figure 3

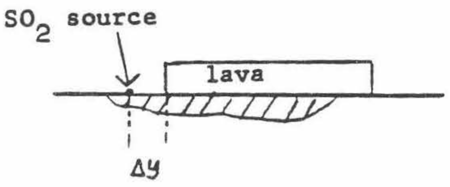

Figure 4

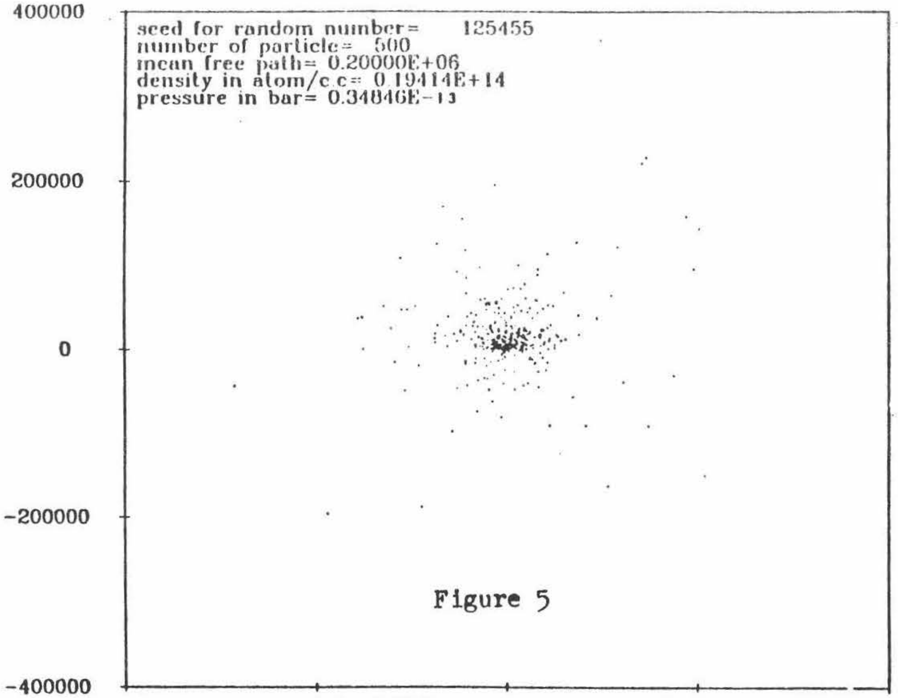

Figure 5

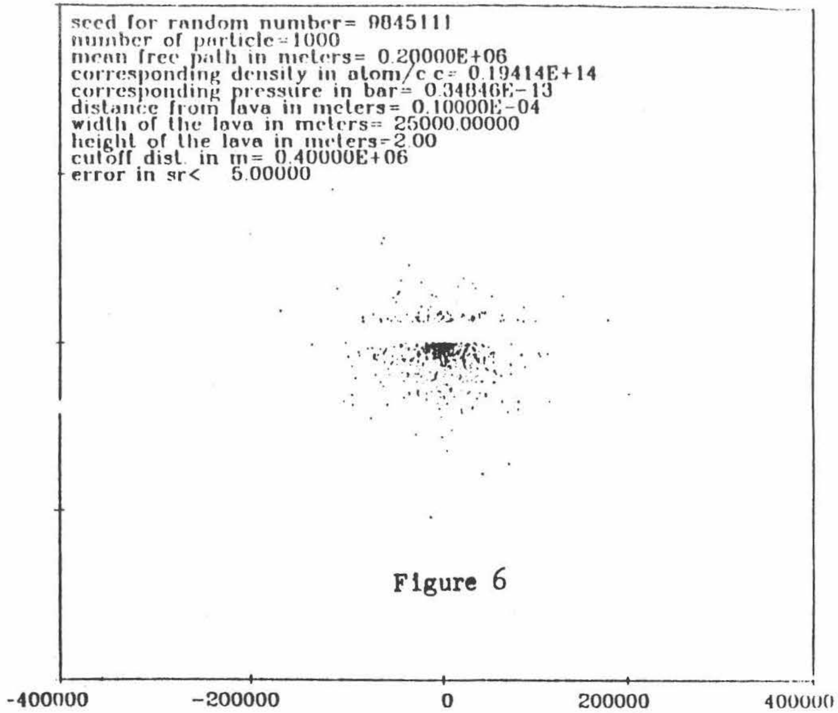

Figure 6

Scatter plot of S02 on Io with correction

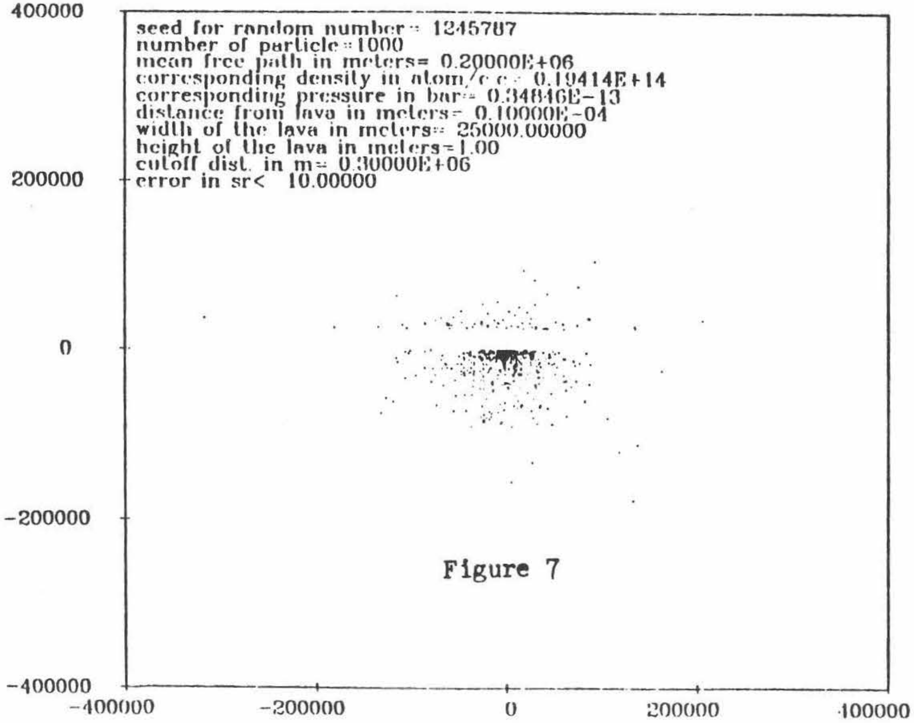

Figure 7

Investigations of the Sputtering Processes in Semi-Conductors and Insulators *

Kelly D. Cherrey

California Institute of Technology, Pasadena, California 91125

ABSTRACT

The sputtering process is well known in metals where the Sigmund theory has been successfully used to explain the experimental results. However, the observed sputtering in insulators is not well explained using the Sigmund theory. Other sputtering theories, most notably those of Tombrello, et. al., have been more successful in explaining the observed sputtering yields in a wide range of insulators. Certain insulators and semiconductors such as CaF, InP and GaAs exhibit departures from these more successful models. An attempt is made to examine more closely the sputtering processes in these types of substances.

*Supported in part by an IBM SURF grant

ONE OF THE SUMMER UNDERGRADUATE RESEARCH FELLOWSHIPS UNDER THE GUIDANCE OF PROFESSOR TOM A. TOMBRELLO

Summer 1983

Investigations of the Sputtering Processes in Semi-Conductors and Insulators *

Kelly D. Cherrey

California Institute of Technology, Pasadena, California 91125

I. Introduction

Sputtering is the process where material is ejected from a target substance upon projectile bombardment. Early work in this field was done by Sigmund[1], where the sputtering of a target was assumed to result from cascades of atomic collisions. While the Sigmund theory explains the sputtering process in metals well, the observed behavior in insulators and semi-conductors is not well predicted. Haff[2] pointed out in 1976 that the "ion explosion" model put forth by Fleischer, et. al.[3] to explain the production of nuclear tracks in insulators by ionizing particles would also predict higher sputtering yields in insulators than the Sigmund theory. Nuclear tracks are regions of damaged material in a substance after particle bombardment. Tracks can be observed by small angle x-ray or neutron scattering or they can be preferentially etched by

---

* Originally my SURF project was entitled ***The Sputtering of GaAs and InP.*** I had planned on doing the actual experiments on GaAs and InP using a beam line on an accelerator at the Oak Ridge National Lab in Tennessee after preliminary trial runs on the ONR Tandem accelerator at the Kellogg Radiation Laboratory at Caltech. However, it became evident after about 5 weeks into the SURF program that Oak Ridge wasn't ready and probably won't be until sometime this December. With this news, we decided to concentrate our efforts on the theoretical models of sputtering that these experiments will hopefully help gain additional insight into. Since the main idea behind the sputtering of GaAs and InP was to understand sputtering in semi-conductors better and since certain insulators exhibit unexplained sputtering properties also, we decided to concentrate our efforts on insulators as well as semi-conductors. Therefore the name of my SURF project was changed to include a broader range of experimental materials. Specifically, we thought it would be worthwhile to sputter CaF and quartz as well as InP and GaAs. Some experiments will be conducted at Kellogg when time on the ONR Tandem accelerator is made available and as materials and expertize needed to carry out the experiments are gained.

chemicals to make them observable with a microscope. The interested reader is referred to the work of Fleischer, et. al.[4]

The mechanism discussed by Haff[2] is referred to as enhanced ion erosion (sputtering) since it represents a component of the erosion process that is largely independent of the collisional ejection of atoms which mainly depends on nuclear stopping (energy deposition of the incident particle per unit path length) in the theory of Sigmund. Watson, et. al.[5] point out that track formation and sputtering may have a more subtle relationship since enhanced sputtering has been observed in both materials that register tracks and ones that apparently do not.[6]

Tombrello[7] has discussed that enhanced adhesion of thin films to a substrate after fast heavy ion bombardment may also have a subtle connection to the sputtering mechanism.

II. Theoretical Models of Enhanced Sputtering

In Watson, et. al.[5], it is pointed out that "many of the models discussed in the literature have either been based on some quantitatively implausible assumption concerning the dynamics of the electronic energy dissipation, or else have simply neglected some link in the chain of energy transfer between the ion and the ejected atom." This should be kept in mind for the next three models.

The Ion Explosion Model. [2,8,9] This model assumes that the incident ion causes electrons to be scattered out of the ion's path. The resulting positive ion pairs repel via coulomb repulsion thus imparting motion to the atoms. The sputtering yield (no. of atoms sputtered / no. of incident ions) is proportional to the energy deposited in the electrons. This energy is proportional to $\left(\frac{dJ}{dx}\right)^2$, where $\frac{dJ}{dx}$ is the no. of ionizations per unit ion path length.

The Thermalized Spike Model. [10,11] This sputtering model assumes that the energy given to the electrons by the incident ion is transferred to the atoms by collisions, causing a core of thermalized material to be formed. If the time that it takes to transfer energy from the electrons to the atoms is shorter that the time for the heat to conduct away from the core, sputtering is initiated by the evaporation of material out of this thermalized core. It has been shown that insulators with very different thermal diffusivities show comparable sputtering yields.[6]

The Thermalized Ion Explosion Model. [12] This model is a combination of the previous two. Heat flow rates in this model are less of a problem since it is postulated that the coulomb repulsion accelerates the atom, then the electrons can reenter the core as the excited atoms thermalize as in the thermalized spike model. It is predicted by this theory that the sputtering yield would go as $\left(\frac{dJ}{dx}\right)^4$.

The Modified Lattice Potential Theory. [5] This is the model which uses no undetermined parameters and is the main subject of my theoretical investigations. This theory takes into account the change in the interatomic potential caused by the incident ion. The potential is changed by the electronic excitation and causes the equilibrium interatomic distances to likewise change. This changes the kinetic energy of the atoms if the electronic excitation lasts long enough to result in heating of the atoms and subsequent ejection.

III. Theoretical Results

I have been making an attempt at extending the ideas of Tombrello[7] to the modified lattice potential theory of sputtering. In reference 7, Tombrello has pointed out connections between nuclear tracks and the sputtering process. He shows that there is a remarkable similarity between the damage profile along the ion's track in a solid and the yield of ejected atoms at the energy that corresponds to each point on the track.

In the modified lattice potential theory, the expansion force acting between molecules is estimated using the Thomas-Fermi statistical atomic model for a molecule confined to a Wigner-Seitz cell. In the theory of Tombrello[7], Young's modulus is used to relate the stress in the core region to the sputtering yield. An effort is being made to make a connection at these points in the two models. Work is continuing in this area but is presently halted due to problems of reproducing some of Watson's calculations in reference 5.

IV. Experimental Results

Unfortunately I have no experimental results to report. If all goes well I hope to have sputtered materials and results by October. Measurements of some of the electronic properties of mica will also be attempted since Dartyge, et. al.[13] have made extensive measurements of nuclear tracks in mica. These electrical properties (band gap and surface binding energy) are important since they will allow another comparison of the modified lattice potential theory to experimental nuclear track measurements.

V. Conclusions

Continued study of sputtering processes promise to be very interesting because of the applications: generation of anti-reflection surfaces, enhanced adhesion of thin films to a substrate, how planetary atmospheres are formed and a better understanding of radiation damage (e.g. "soft" failure of semiconductor memory devices). More has to be learned about the physics behind the sputtering process in order to take full advantage of these uses and perhaps discover more.

Acknowledgements

The author would like to thank Dr. P. K. Haff for introducing me to the field of sputtering research and Prof. T. A. Tombrello for providing an excellent environment in which to learn physics. Dr. C. C. Watson has helped clear up a few misunderstandings in the modified lattice potential theory.

Finally, I am indebted to the SURF committee and IBM for providing this research opportunity.

References

[1]P. Sigmund, *Phys. Rev.* **184** (1969) 383.

[2]P. K. Haff, *Appl. Phys. Lett.* **29** (1976) 473.

[3]R. L. Fleischer, P. B. Price and R. M. Walker, *J. Appl. Phys.* **36** (1965) 3645.

[4]R. L. Fleischer, P. B. Price and R. M. Walker, *Nuclear Tracks in Solids* (University of California Press, Berkeley, 1975).

[5]C. C. Watson and T. A. Tombrello, *Rad. Eff.* (1983) submitted.

[6]Y. Qiu, J. E. Griffith and T. A. Tombrello, *Rad. Eff.* **64** (1983) 111.

[7]T. A. Tombrello, *Track Damage and Erosion of Insulators by Ion - Induced Electronic Processes*, (1983).

[8]J. E. Griffith, R. A. Weller, L. E. Seiberling and T. A. Tombrello, *Rad. Eff.* **51** (1980) 223.

[9]J. Stiegler and T. S. Noggle, *J. Appl. Phys.* **33** (1962) 1984.

[10]R. W. Ollerhead, J. Bottiger, J. A. Davis, J. L'Ecuyer, H. K. Haugen and N. Matsunami, *Rad. Eff.* **49** (1980) 203.

[11]R. D. Macfarlane and D. F. Torgerson, *Phys. Rev. Lett.* **36** (1976) 486.

[12]L. E. Seiberling, J. E. Griffith and T. A. Tombrello, *Rad. Eff.* **52** (1980) 201.

[13]E. Dartyge, J. P. Duraud, Y. Langevin and M. Maurette, *Phys. Rev.* **23B** (1981) 5213.

An Electrostatic Lens for Focussing High Energy Ions in the Solar Wind

Glen Crawford

Faculty Sponsors: Dr. T. Tombrello
Dr. D. Burnett

Summer Undergraduate Research Fellowship
California Institute of Technology, Pasadena, California, 91125

ABSTRACT

This paper describes the design of an electrostatic lens that will magnify the flux of high energy (40 keV and above) ions present in the solar wind by factors of 50X to 100X or better, while also eliminating the background "noise" of H and He ions present.

Introduction

The "solar wind" is a energetic plasma of electrons, protons and ions that is ejected from the sun due to shock waves generated in the solar corona. This plasma propagates outward through the solar system; its existence was predicted by E.N. Parker in early 1958 and first observations of the solar wind were made by Pioneer I in Oct. 1958. Since that time, many experiments have been done to determine the properties of the solar wind and its constituents. It has been found that most of the solar wind is ionized H and He (H/He ratio is about 20/1), with traces of heavier ions. To learn more about the composition of the solar wind (and, by implication, the composition of the solar corona and the sun itself), we wish to study the abundances of the heavier ions in the solar wind. To do this we must eliminate the H and He "noise" and magnify the flux of the heavier ions, since even the most abundant heavy ions exist in a ratio of 1/30,000 with respect to H. This design attempts to accomplish those goals by use of an electrostatic lens, such as is commonly used in high energy beam optics.

Results

The design of the electrostatic lens was undertaken using the SLAC Electron Optics Program (SLAC Report 226), written by W. Hermannsfeldt. This program takes given boundary conditions with either cylindrical or rectangular symmetry and then solves Laplace's Equation at up to 9000 mesh points on the boundary and in the interior, connects the solutions and thus finds all the equipotentials. Then trajectories of incoming particles with known energy and mass/charge ratio can be calculated using the Runge-Kutta Method.

The design goal was to eliminate all H and He ions from the lens and to magnify the flux of high energy ions (specifically, we looked at the case of ^{56}Fe) by a factor of 100X so that abundances and isotopic ratios of the high energy ions could be more easily studied. Previous solar wind measurements have not been able to eliminate H and He "noise" so that most data on heavy ion abundances is not believed to be very good.

Several restrictions were placed on the design of the lens as well. Ultimately, the lens, if acceptable, would have to fly in space (presumably launched off the Space Shuttle), and thus could be no more than 1 meter long for practical reasons. Further, an upper limit of ±20kV was placed on the voltages allowable to operate the device (this limit, an empirical result, was placed by Marcia Neugebauer of the Jet Propulsion Laboratory, an expert on flying electrostatic devices in space). An incoming flux area of 200-300 cm^2 was desired, as was cylindrical symmetry for ease of calculation. Finally, the design should be kept as simple as possible.

Several lens configurations were tried with little to no success in focussing ^{56}Fe (though several were found to effectively focus ^{16}O and lighter ions). See Figs. 1-3 for designs and comments. The factor chiefly affecting focussing was the incoming energy of the ions; the higher the energy of the ions, the less focussed they were by the various lenses, which makes sense intuitively. For focussing, one needs about potentials in kV commensurate with the particle's energy in keV. For solar wind ions, typical energies are on the order of 1 keV/amu, so ^{56}Fe particles have typically 56 keV of energy. Being restricted to 20kV of potential, we found it hard to find a lens that focussed appropriately.

Of the early designs, a Unipotential or "Einzel" Lens proved to be the most successful. The Unipotential Lens is so named because it consists of three coaxial cylinders aligned in series, with the outer two charged to the same potential while the middle one is held at ground. With no modifications, it only provided an area magnifaction factor (the amount by which the incoming flux is "squeezed") of 9X. By blocking out both a small inner circular region and a small outer ring (leaving a cylindrical annulus for the effective "shape" of the lens) where little focussing was achieved, area magnification was increased to 45X-50X. However, this increased magnification was achieved with a 33% loss in total flux due to ions being blocked out. See Figs. 4-5.

A slight modification of the basic Einzel lens produced the best results to date and the most promising design. The modification introduced is charging the central cylinder to -20kV instead of keeping it at ground while the outer cylinders remain at +20kV. The effective voltage range of the lens has thus been doubled from 20kV to 40kV, a factor crucial in facillitating the focussing of ^{56}Fe and other heavy ions. The lens proved very sucessful in focussing ^{56}Fe. It provided an area magnification factor of just under 400X at maximum flux (i.e. total area of the lens was used-no blocking apertures); an area magnification factor of almost 1600X was obtained if the flux was reduced by blocking out the outer, "overfocussed" ions. These apertures reduced the flux to about ½ that of maximum, or $\sim$ 150 cm^2. Figure 6 shows a plot of ion trajectories in this lens.

It should be borne in mind that the rather impressive focal properties of this lens only work for this particular ion, ^{56}Fe. Ions of higher energy, whether due to increased mass or higher velocity in the solar wind, will not be as well focussed. This problem is known as "chromatic aberration" by analogy to light optics. Optical lenses focus different wavelengths (and hence different energies) of light at different points, so that blue and red light are not focussed at the same point-a chromatic aberration. The ion lens similarly focusses well only in a given energy range; outside this range, incoming particles are not focussed. The problem is much worse for ions than light: while visible light only occupies a small band of energy ranges, the ions in the solar wind range from ^{1}H to ^{238}U, an energy range of 1 to 200 keV and beyond. Needless to say, chromatic aberrations are a major -if unavoidable-problem in this design.

A graph of Magnification Factor (in terms of area) vs. Incoming Energy is plotted in Fig. 7 to show the effects of chromatic aberration. All magnifications are calculated at maximum flux; no portion of the beam has been blocked.

From Figure 7, we see that magnification factors of 50X or greater are available for an energy range of about 50keV, from ~40keV to ~90keV. This is adequate for studying ions in this range, but any ions outside of this band will go unfocussed. One solution to this problem is obvious: if we desire to focus lower energy ions, we merely need to lower the voltages on the cylinders. Lower energy ions will no longer be "bounced" or overfocussed by the fields. Focussing higher energy ions proves more difficult. One possible solution is a "stacked" Einzel lens, as shown in Fig. 8; the conventional optical analogue is just two lenses placed in series for greater focal power.

Such a "stacked" lens was found to effectively focus energies in the range of ~40keV to ~120keV, as can be seen in Fig. 9, a plot of Magnification vs. Energy for the stacked lens. Comparing this plot to Fig. 7, we note that the stacked lens effectively broadens the well-focussed region by 30keV. Note also that the peak of the magnification curve is not as high for the stacked lens as for the single lens; the stacked lens offers peak magnification of only 170X @60keV as opposed to 400X @56keV for the single lens. This result is probably due to some overfocussing caused by the extra length and focussing power of the stacked design.

Both the single and the stacked lens designs eliminated H and He ions by simply "bouncing" them out due to their strong electric fields. See Fig. 10 for a graphic example. In fact, both lenses rejected particles of up to 16keV, working effectively as a mirror for such low energy particles.

Another advantage of this design was its insensitivity to changes in the mass/charge ratio in a given energy range; this means that all of the ionization states of ^{56}Fe in the solar wind (there are many-from +8 to +14- and all occur fairly frequently) would be focussed in the same place. The lenses also accepted rays incident at angles of ±10° with respect to the axis and focussed them adequately. The only major unresolved problem with either of the lens designs is the fringe fields, which may scatter some of the ions before they even reach the lens proper. The only feasible solution to eliminating the fringe effects (if this is necessary) is to place mesh grids (as per Fig. 1) in front of the lens to prevent leakage of the +20kV field. Probably ≥2 such grids would be needed; further, the grids may cause problems with charge buildup and sputtered material from off of the grids. Since an adequate computer approximation of the fringe fields could not be arrived at, this remains the only unsolved problem of the lens design.

Conclusions

An electrostatic lens that meets the design goals while staying within the necessary limitations is feasible to build. H and He ions are rejected, and area magnification is easily greater than 100X for the energy band of interest (around 60keV), at least theoretically, and even accounting for fringe field effects, angular dispersions and other practical considerations, the actual lens, if built, should still offer satisfactory magnification. The lens suffers some rather severe chromatic aberrations, so adequate magnification will occur in only a limited energy range. The lens is fortunately rather insensitive to variations in the mass/charge ratio for a given energy.

Acknowledgements

I would especially like to thank my SURF advisors, Dr. T. Tombrello and Dr. D. Burnett, for their questions, suggestions and helpful information. Thanks are also due to Marcia Neugebauer of JPL, and Richard Milner and Rick Kremer of the Kellogg Lab for their assistance.

Bibliography

Geiss, Johannes, "Abundances in the Solar Wind and Some Applications to Astrophysics and Geophysics," presented at Leningrad Seminar on Solar Cosmic Rays, June 1973.

Harting, E. and Read, F.H., **Electrostatic Lenses**, Elsevier, NY 1976.

Hermannsfeldt, William B., **Electron Trajectory Program**, SLAC Report 226, Stanford, 1979.

Klemperer, O., and Barnett, M.E., **Electron Optics**, University Press, Cambridge, 1971.

Moore, John A. et. al., **Building Scientific Apparatus**, Addison-Wesley, NY 1983.

Ross, John; and Adler, Lawrence, "The Chemical Composition of the Sun," *Science*, **191**, 4233.

Zworykin, V.K., et. al., **Electron Optics and the Electron Microscope**, John Wiley & Sons, NY, 1945.

Figure Captions

Figure 1.

The Grid or Mesh design. Almost no focussing power. It has the further problem of sputtering from off of the grid.

Figure 2.

The Electrode or "Gap" Lens was found to have some focussing power, but not much (only about 4X area magnification). Further, focussing was acquired at the cost of flux: the electrodes block much of the incoming ion beam.

Figure 3.

The Unipotential or Einzel Lens.

Figure 6.

A typical plot of trajectories through the einzel lens. Ions enter at the left, and travel left to right. Unipotentials are superimposed on the trajectories.

Figure 7.

Energy vs. Magnification for a "Single" Einzel Lens.

Figure 8.

"Stacked" Einzel Lens design, and its optical analogue.

Figure 9.

Energy vs. Magnification for a "Stacked" Einzel Lens.

Figure 10.

A typical plot showing low energy ions "bouncing" of the stacked lens. Both 10 keV and 15keV particles are shown here; the 15keV particles are the ones that penetrate farther before being deflected.

Figures 1-3. NOTE ALL HAVE CYLINDRICAL SYMMETRY ABOUT CENTRAL AXIS.

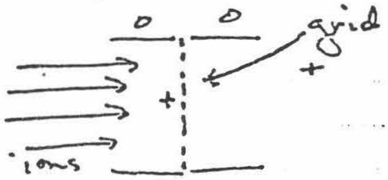

Fig. 1
Grid or Mesh

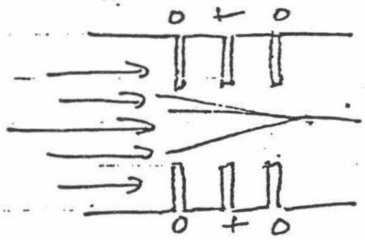

Fig 2.
Electrode or
"Gap" Lens

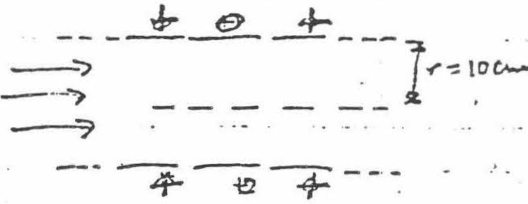

Fig. 3
Unipotential or
"Einzel" lens

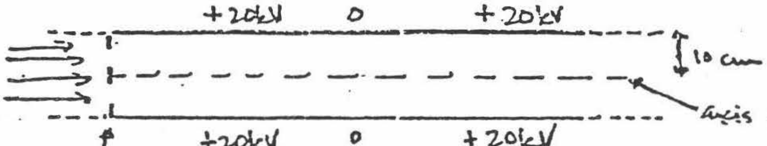

axis of symmetry.

blocking apertures

TO SCALE

Fig. 4

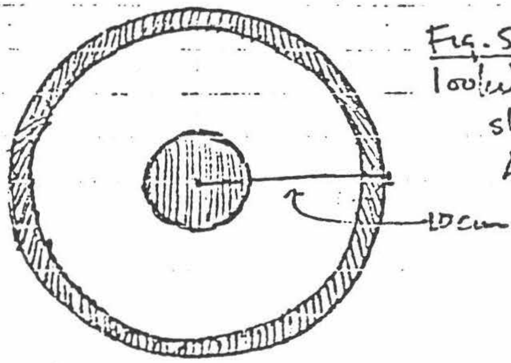

Fig. 5.
looking "down" the lens
shaded areas are blocked.
Approximately to scale.

Figure 6

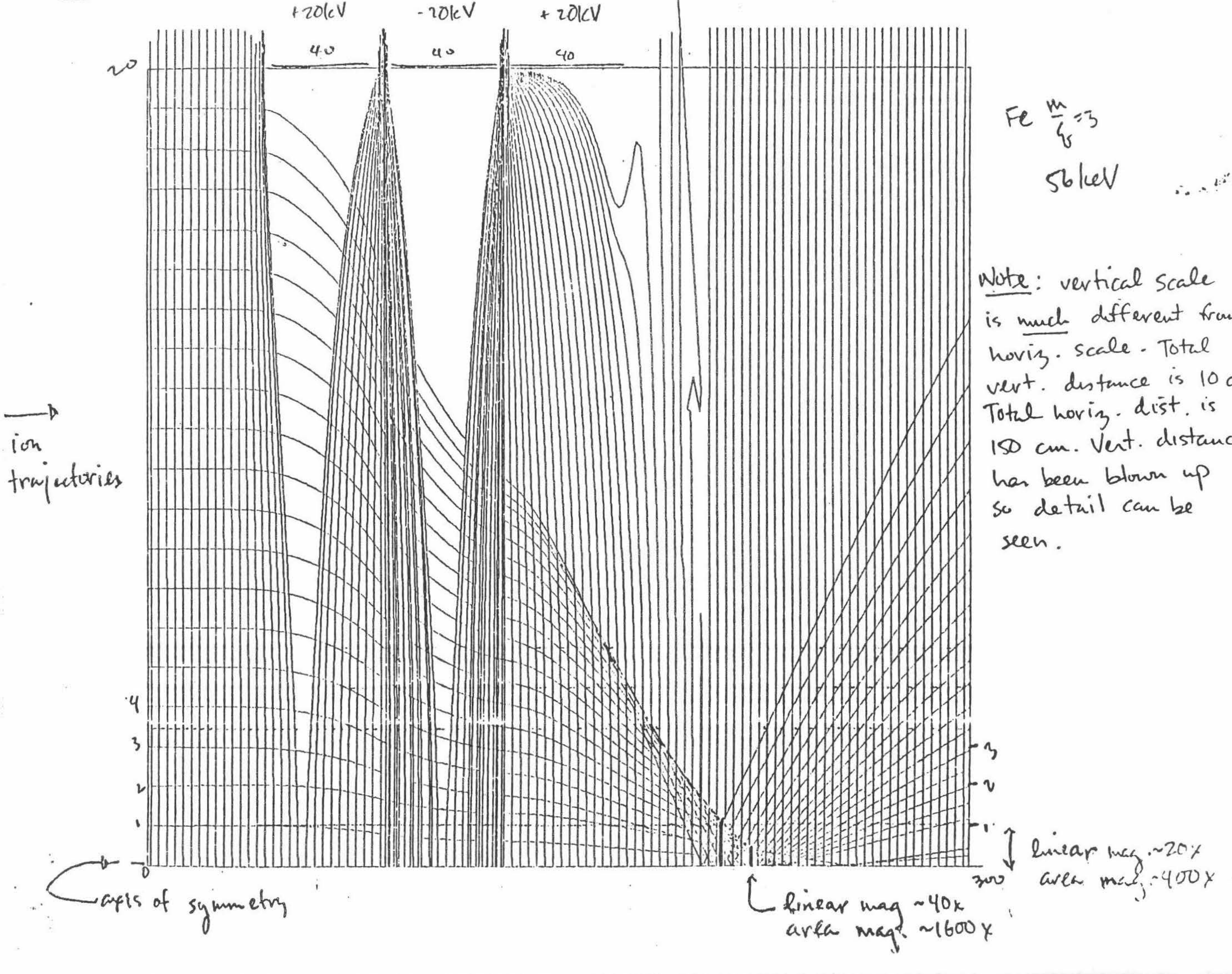

Fe $\frac{m}{q}=3$

56keV

Note: vertical scale is much different from horiz. scale. Total vert. distance is 10 cm. Total horiz. dist. is 150 cm. Vert. distance has been blown up so detail can be seen.

Figure 7.

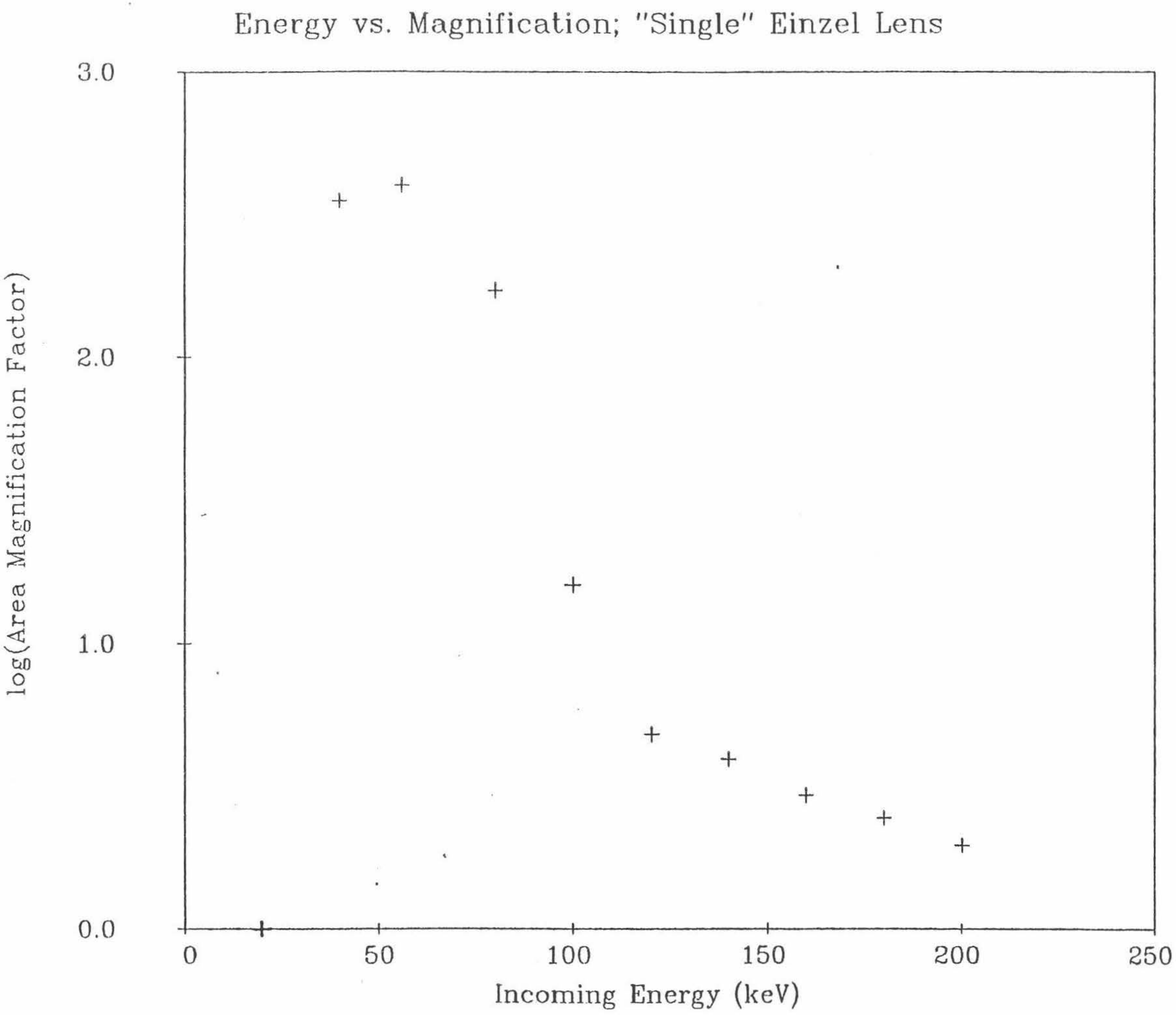

Energy vs. Magnification; "Single" Einzel Lens

Crawford

9/1/83
4

Fig. 8

ELECTROSTATIC LENS.

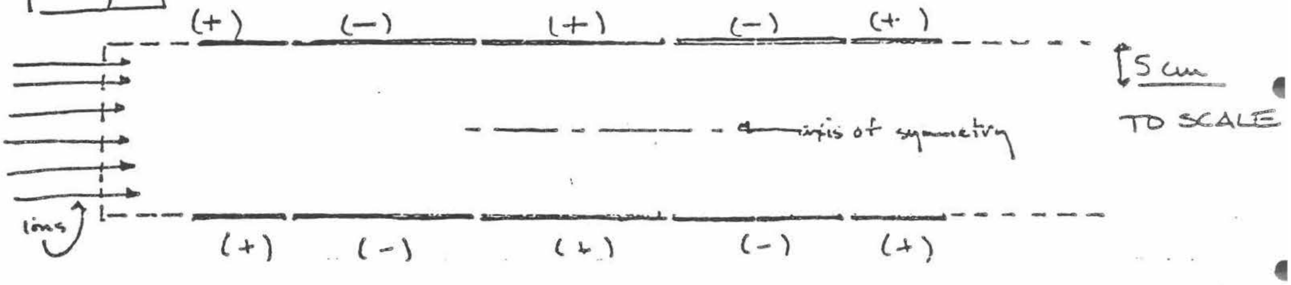

"Stacked" Einzel Lens
all plates charged to ± 20keV, sign as indicated.

Optical Analogue to "Stacked" Lens.

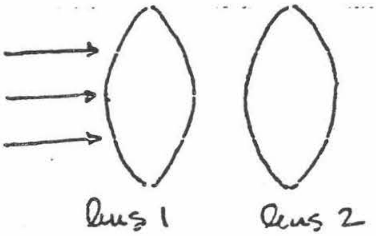

(In an optical analogue, lower energy particle will be well-focussed before they ever reach the ~~se~~ second lens. Middle energy particl not completely focussed by lens 1, will be overfocussed by lens 2).

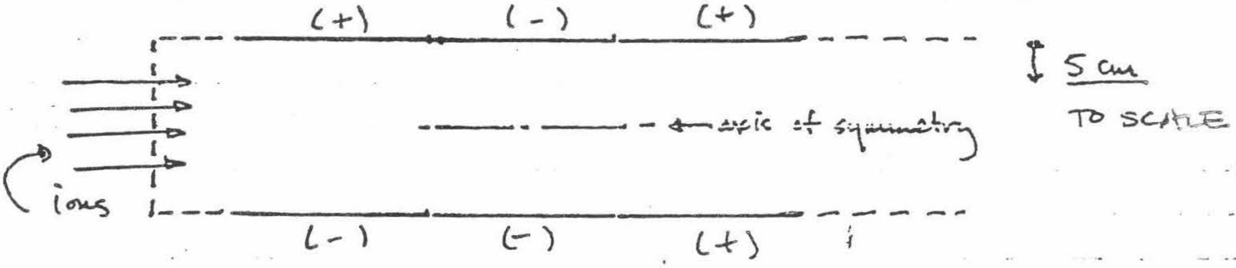

"Single" Einzel Lens
all plates charged to ± 20keV, sign as indicated.

Optical Analogue to "Single" Lens

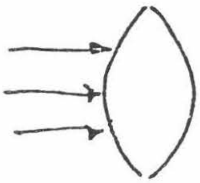

(or, why do we chose to call them "single" + "stacked" lenses.)
[Note: this a somewhat simplified picture. The precise optical analogue of a single einzel lens would be: ].

Figure 4.

Energy vs. Magnification; "Stacked" Einzel Lens

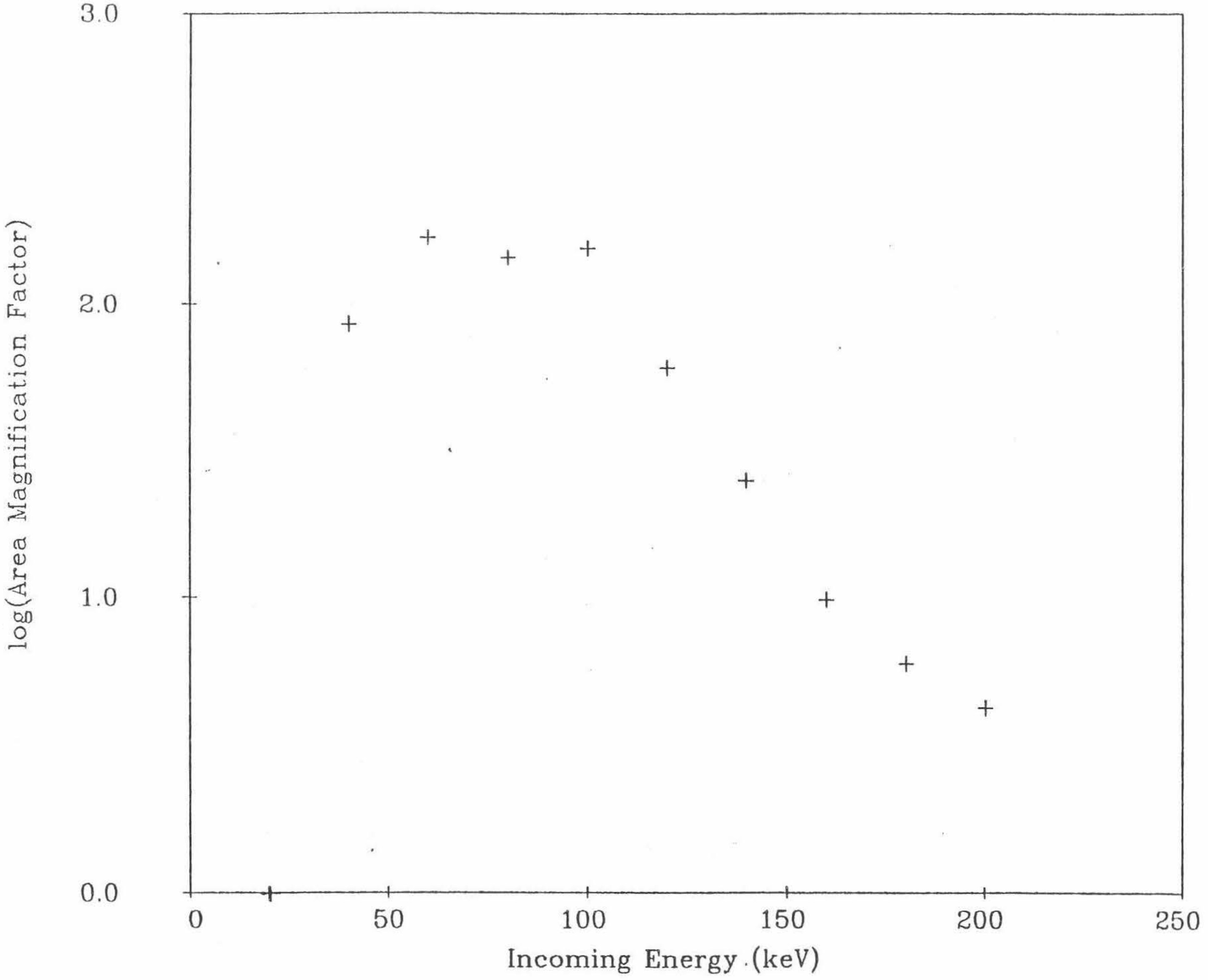

Fig. 10

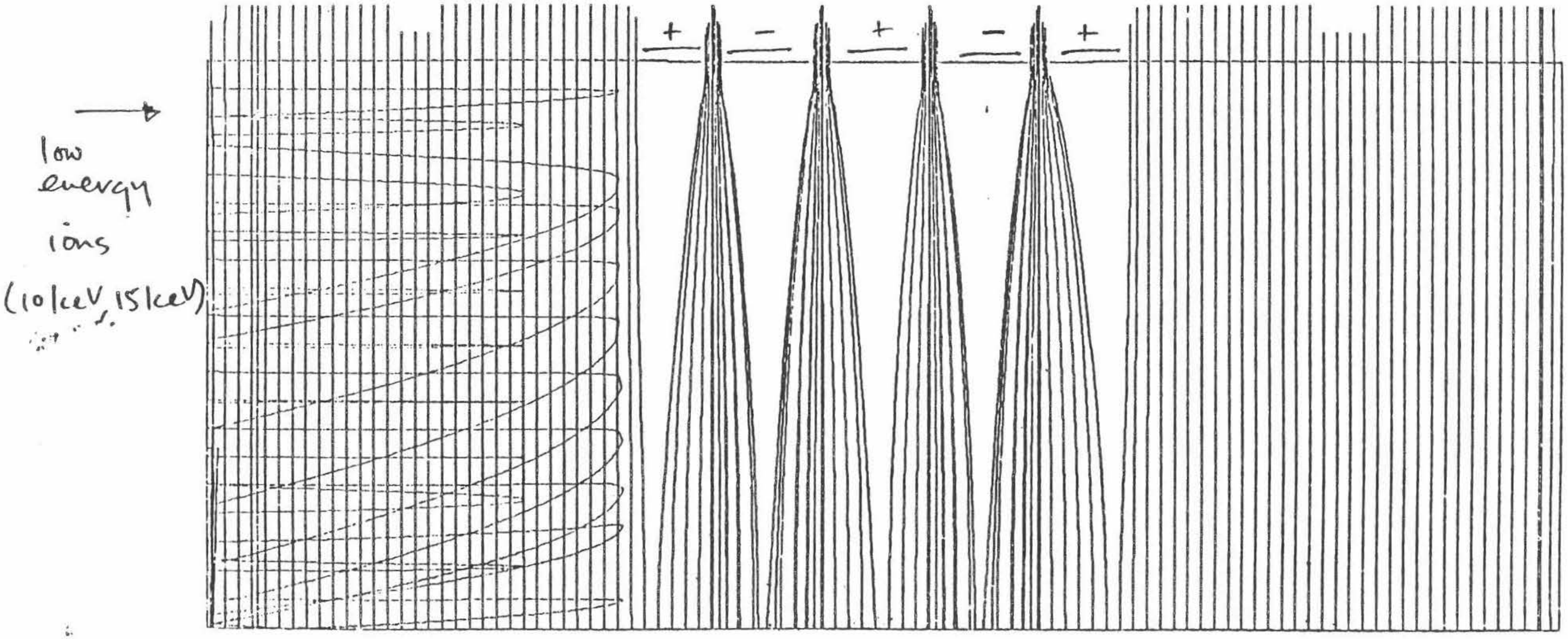

Association Of Gap Junctions With Endoplasmic Reticulum

James Dunn

ABSTRACT

We report the finding that gap junctions, generally believed to be responsible for the direct communication between cells, are seen in association with cisternae of the endoplasmic reticulum in parotid glands of rats. Both freeze fracture and thin sections of the parotid gland reveal close contact between gap junctions and cisternae of the endoplasmic reticulum. Approximately half of the observed gap junctions exhibit this association. This suggests a possible control mechanism for the permeability of gap junctions as well as a possible mechanism in the development of gap junctions.

INTRODUCTION

Gap junctions are channels that allow the passage of ions and small molecules between cells. For example, electrical coupling of heart cells, which is crucial for the synchronous beating of the heart, is mediated by gap junctions. It has been shown by electrophysiology that cells which are normally electrically coupled can be "uncoupled" by various methods, one of which is to increase the concentration of calcium ions. An increase in calcium ion concentration presumably causes a change in the conformation of gap junction channels, which causes cells to uncouple (Unwin and Zampighi, 1980). The mechanism by which the cell actually controls the permeability of gap junctions is not known, although models have been proposed. Endoplasmic reticulum is well-known as one of the calcium ion sinks in a cell (MacLennan, Stewart, Zubrzycka, Holland, 1976). As it will be shown later, cisternae of endoplasmic reticulum are found in close contact with gap junctions. Thus, it is possible that the cisternae are involved in the regulation of permeability of gap junctions.

It is also not well known how gap junctions are formed. It certainly requires the participation of both cells since presumably each half of the gap junction is formed by each cell in contact, but not much is known about how gap junctional protein is inserted into the cell membrane. As mentioned earlier, cisternae with ribosomes attached are found in association with gap junctions. Protein synthesis including membrane proteins is known to take place at the level of endoplasmic reticulum. Thus, it is possible that these ribosomes are involved in the synthesis of gap junctional protein.

The purpose of this project is to investigate the possible relationship of gap junctions with the cisternae of endoplasmic reticulum, in the hope of throwing light on the formation of the gap junction and the regulation of its permeability.

RESULTS

freeze fracture

In freeze fracture, frozen samples are cracked open and a platinum-carbon replica is made from the cracked-open surface. The cleavage plane goes through the cytoplasm of cells as well as the membrane of cells (Fig 1). Once inside the membrane, the cleavage plane goes through the bilayer of the membrane, thus revealing structures that are embedded in the membrane. There are only two types of fracture faces revealed in the cracked-open membrane. After cleavage, the part of the membrane that is in contact with the protoplasm of the cell is called the P face, and the part of the cell that is in contact with the extracellular matrix is called the E face (Fig. 2). Gap junctions in freeze fracture samples appear as densely packed, organized arrays of particles on the P face, and as densely packed, organized arrays of pits on the E face (Revel, Yee, Hudspeth, 1971). For geometrical reasons, gap junction particles on the P face are more easily recognized than gap junction pits on the E face. Normally gap junction particles are arranged roughly in solid circular patches on the P face of the cell membrane. Freeze fracture samples of rat parotid glands reveal such ordinary gap junctions. In addition, structures that have a ring of particles which resemble gap junction particles are also found (Fig 3). The thickness of the ring varies from 1 to 10 particles. The shapes of the rings are similar to those of the gap junction particle patches. Inside these rings, three types of fracture faces can occur. One is the familiar E face of the cell membrane of the opposite membrane of the gap junction; it is on top of the P face, as expected. This piece of E face has no particles. The other two types of fracture faces that can be found inside the ring are structures which have not been seen before. One of them is on top of the familiar E face. This fracture face has a considerable number of particles. As it will be shown later, this is likely to be the P face of a cistern that is in contact with the gap junction. Alternatively, the other unfamiliar fracture face is found below the P face of the cell membrane. It also has particles similar to those found on the fracture face on top of the E face. Again to be shown later, this fracture face is likely to be the E face of an associated cistern.

thin sections

To try to understand the peculiar fracture faces, thin sections of the rat parotid glands were examined. The appearance of gap junctions in thin sections is very different from that in freeze fracture. Because the cell membranes are very close to one another where gap junctions exist, gap junctions are believed to be present wherever the adjacent cell membranes run closely parallel to each other with a gap of the order of 20 angstroms. The exact appearance of gap junctions in thin sections depends on the fixatives and stains used to prepare the sample, as well as the thickness of the sections. For samples that are fixed by glutaraldehyde and osmium tetroxide, gap junctions appear as seven closely-spaced lines (Fig. 4). Thin sections of rat parotid glands but not of normal rat liver often show the presence of endoplasmic reticulum in the vicinity of gap junctions. Very thin sections, approximately 500 angstroms thick, reveal the close association of gap junctions with cisternae of the endoplasmic reticulum (Fig. 5). The cisternae are usually on both sides of the gap junction, with one in each of the apposed cells. The cisternae usually cover almost the entire length of the gap junction, leaving the ends of the gap junction exposed. Ribosomes are found on the side of each cistern away from the gap junction, but not on the side of each cisternae next to the gap junction. The membrane of the cisternae next to the gap junction is very close to the cell membrane. The space between the two membranes appears to have a wavy outline, with a maximum distance of about 100 angstroms between membranes. No other structures have been observed to associate with gap junctions as closely as the cisternae do. Often, there are mitochondria next to the cisternae associated with gap junctions. These mitochondria are about 1000 angstroms away from the cisternae. The mitochondrion from adjacent cells is usually "linked" to the other mitochondrion by desmosomes (Fig. 6).

morphometry

Areas of gap junctions revealed by freeze fracture were measured. Areas measured include the total cell membrane, gap junction particle patches, and the rings of particles (area measured includes the inside of the rings). The result is that the total area of normal gap junction particles is roughly the same as that of the rings of particles. Interestingly, the number of normal gap junctions is considerably more than the number of rings of particles (Table 1). In other words, the rings of particles appear to be larger than gap junction patches on the average. Lengths of gap junctions as revealed by thin section are also measured. The result is that the total length of "normal" gap junctions is about the same as the total length of gap junctions that are associated with cisternae.

DISCUSSION

From the results obtained from freeze fracture and thin sections, it is reasonable to believe that the gap junctions that are associated with cisternae in thin sections give rise to the rings of particles in freeze fracture of rat parotid glands. Recall that three layers of fracture faces can occur inside the rings of particles. The lowest layer is below the P face of the cell membrane. Thus, it is clear that the fracture plane has gone beneath the cell membrane after revealing a few particles and has come back out again to reveal a few more particles, thus giving the appearance of the ring of particles. These particles closely resemble gap junction particles, and the shape of the ring is similar to that of a normal gap junction patch. Therefore, it is reasonable to suggest that these particles are indeed gap junction particles. If this is true, then why are these particles arranged in a ring and why does the fracture plane go beneath the cell membrane? This can be explained by the existence of a subsurface organelle next to the gap junction. It appears that the fracture plane has gone into this subsurface organelle probably because of the close proximity, thus making the inside of the ring lower than the cell membrane. By thin sections, this subsurface organelle turns out to be the cistern of the endoplasmic reticulum. This would also explain the occurence of the three layers inside the rings. The lowest layer is the E face of the cistern; the middle layer is the E face of the cell membrane; the highest layer is the P face of the cistern (Fig. 7). There is one point to be made about the association of gap junctions with cisternae. Parotid gland is a secretory organ; therefore, the cells are packed with endoplasmic reticulum (Fig. 8). It is possible that the cisternae that are associated with gap junctions are simply random occurences; however, this is not likely. First of all, it is not very likely that one cistern of just the right size from each cell associates with a gap junction in the symmetrical fashion shown. Second, there is no such close association of cisternae with cell membrane anywhere else in the cell. Thus, the association appears very specific. Another interesting question that can be asked is whether there are gap junction particles within the ring of particles. It is certainly possible that there are no other particles than the ones revealed since there is no direct evidence for their existence. However, it is possible to imagine that these particles do exist and they are simply "masked" by the way the membrane has fractured (Fig. 7). These particles are either "pulled" out of their place or they are "covered" by the membrane of the cisternae. The latter explanation is more plausible because one does not have to assume the existence of special particles that are arranged in a ring which has never been seen before, though there is no hard evidence for either one.

The association of gap junctions with cisternae leads one to speculate on the possible functions of this complex. One of the speculations is that the cisternae that are associated with gap junctions play an important role in regulating the permeabilty of gap junctions. Endoplasmic reticulum is well-known as one of the calcium-ion sinks in a cell. It has been shown that the concentration of calcium ions is important in determining the permeabilty of gap junctions. Thus, it is reasonable to suggest that the cisternae are involved in regulating the calcium level in the vicinity of gap junctions. The cisternae may release calcium ions so as to close the gap junction, or it may act as a buffer for the gap junction to maintain a low level of calcium ions. Cytochemical detection of ATPase activity associated with calcium ion pumping would support this idea. The cisternae could also act as a physical barrier for the gap junction. It is interesting to note that mitochondria, another calcium sink in the cell, are often present along with this cisternae-gap junction complex (Rose and Lowenstein, 1975). The mitochondria may serve as a secondary calcium buffer. However, if one examines the distribution of mitochondria inside a parotid cell, one realizes that a large portion of the mitochondria are found along the cell surface. Thus, it is possible that the presence of the mitochondria is a random occurence.

Another speculation on the function of this complex is that the cisternae that are associated with gap junctions may be responsible for the formation of gap junctions. There have been many theories on how gap junctions are formed; none is proven. Here one hypothesizes that gap junctional protein is synthesized on the ribosomes of the cisternae that are associated with the cell membrane, and the protein is subsequently inserted into the membrane via the cisternae. This would explain why the gap junction particles are so densely packed, though none of our observation allows specific questions to be answered.

CONCLUSION

If indeed the association of gap junctions with cisternae is important, then one may expect to find similar association in other tissues and animals. Thus far, only one documentation of this association is found. It is observed in the liver of neo-natal mice, but this association disappears after about 10 days (Perissel, Malet, Geneix, 1973). One also sees similar association in liver extracted from either anoxic or ischemic rats (B. Yancey, personal communication), though not much work has been done on those as far as this association is concerned. To conclude then, gap junctions are observed to associate with cisternae of endoplasmic reticulum in parotid glands of rats. This association gives rise to the ring of gap junction particles observed in the freeze fracture samples. This suggests possible control and development of gap junctions. Further investigation is necessary to uncover the functions and specificity of the gap junction-cisternae complex.

Fig. 1 Low magnification view of the freeze fracture replica of rat parotid glands. Structures inside the cytoplasm of the cells are clearly visible. Some nuclei (N) are broken open, while others remain intact. The cells are packed with endoplasmic reticulum (ER) near the basal end. Zymogen granules (Z) are found near the lumen (L) of the acinus. (x1700)

Fig. 2 Membrane of the cells in the parotid gland as revealed by freeze fracture. The E face (E) is on top of the P face (P). Gap junctions (GJ) are present as organized particles on the P face. One of the gap junctions appears as a ring of particles (arrow). (x28000)

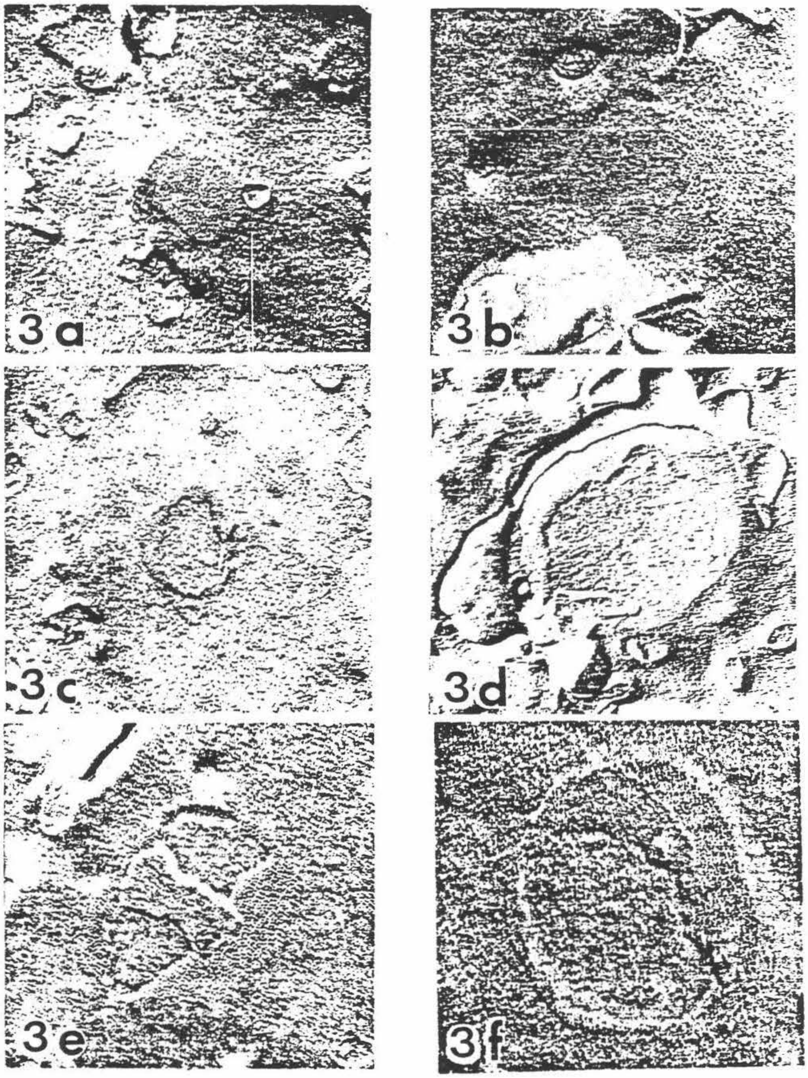

Fig. 3 All samples are taken from the parotid glands of rats.

a. An ordinary gap junction appears as a solid circular patch of particles on the P face. (x37000)

b. A gap junction at the interface between a P face and an E face. Note that the gap junction appears as pits on the E face. (x43000)

c. A ring of particles with the inside below the surface of the P face. Note the similarity in appearance of these particles to that of gap junction particles. (x33000)

d. Same as c. (x33000)

e. A ring of particles with the inside split into parts that are below the P face and parts that are above the P face. (x470000)

f. A ring of particles with the inside split into parts that are below the P face and parts that are the E face. Note that pits can be seen on the E face. (x44000)

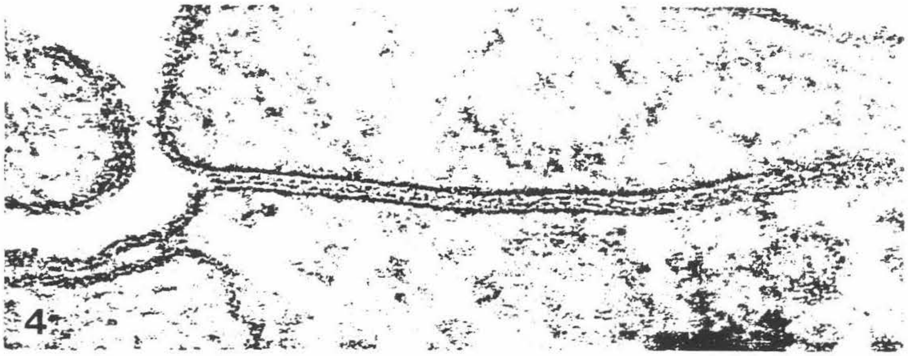

Fig. 4 An ordinary gap junction in rat parotid glands as seen in thin sections. Note the seven lines that are present (4 dark ones and 3 light ones). (x240000)

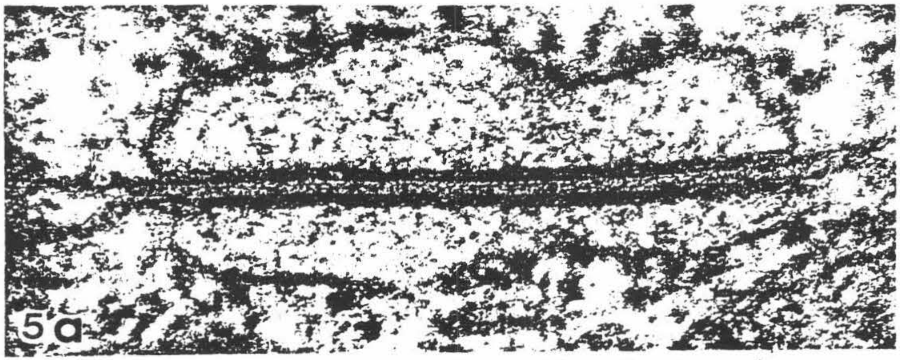

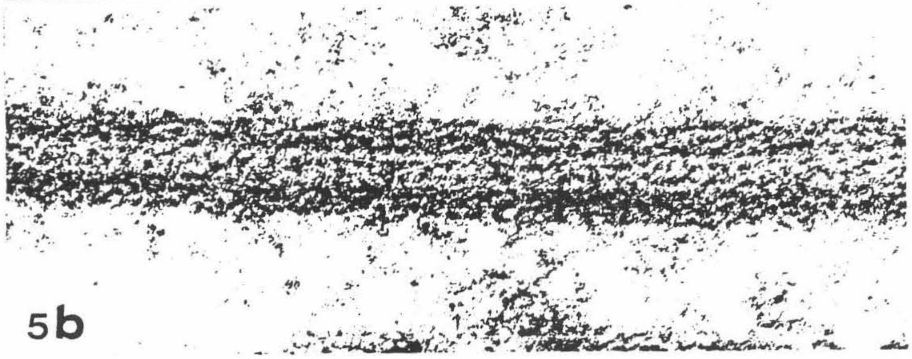

Fig. 5a A gap junction with cisternae next to it. Note the ribosomes on the sides of the cisternae away from the gap junction. (x240000)
Fig. 5b Higher magnification of 5a. Note the closeness of the cisternal membrane and the cell membrane. (x500000)

Fig. 6 Mitochondria (M) in cells of rat parotid glands are often linked to those in the adjacent cells by desmosomes (D) This is a serial section of Fig. 5a. Note that there is only one cistern (C) with no ribosomes next to the gap junction (GJ). (x130000)

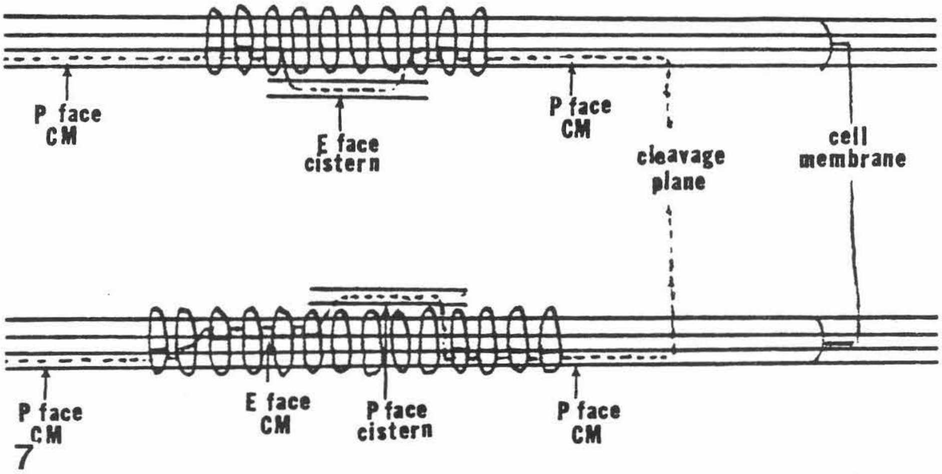

Fig. 7 Schematic diagrams of the cleavage plane that will give rise to the ring of particles in freeze fracture. The one on top diagrams the clevage plane to reveal a ring of particles with its inside below the P face. The one below diagrams the cleavage plane to reveal a ring of particles with its inside split into part E face and part on top of the E face.

Fig. 8 Thin sections of the rat parotid gland. Note the abundance of the endoplasmic reticulum (ER). N: nucleus, M: mitochondrion, GJ: gap junction, CM: cell membrane. (x57000)

Table 1

freeze fracture	membrane	normal gap junctions	rings of particles
area (sq. micron)	1450	10.2	9.50
number	–	71	20

thin sections	normal gap junctions	gap junctions with cisternae
length (micron)	6.42	7.77
number	15	13

BIBLIOGRAPHY

MacLennan, D.H., Stewart, P.S., Zubryzycka, E., and Holland, P.C. (1976) Composition, structure, and biosynthesis of Sarcoplasmic Reticulum. Cell Motility: Cold Spring Harbor Conferences on Cell Proliferation Book A 153-163.

Perissel, B., Malet, P., and Geneix, A. (1973) Associations junctions-organites cellulaires dans le foie neonatal de souris. Z. Zellforsch 140, 77-89.

Revel, J.-P., Yee, A.G., and Hudspeth, A.J. (1971) Gap junctions between electronically coupled cells in tissue culture and in brown fats. Proc. Natl. Acad. Sci. USA 68, 2924.

Rose, B. and Loewenstein, W.R. (1975) Calcium ion distribution visualized by Aequorin: diffusion in the cytosol is restricted due to energized sequestering. Science 190, 1204.

Unwin, P.N.T., and Zampighi, G. (1980) Structure of the junctions between communicating cells. Nature 283, 545-549.

Environmental Effects on Subsurface Radon:
A Lytle Creek Rainfall Anomally Model and a Pacoima Signal Model

by Dennis R. Fatland

Faculty Sponsor: Dr. T.A. Tombrello

Principal Investigator: Dr. M.H. Shapiro

Abstract

The project focused on two aspects of the radon-thoron monitoring network data. The first is a curious post-rainfall signal drop observed at several sites including Lytle Creek. Some simple assumptions have led to an empirical equation which adequately describes this phenomenon. The second aspect is the Pacoima Dam site signal in general over a two year period. Most of this signal can now be constructed from rainfall data, seasonal weather patterns, and daily thermal cycles.

Introduction

Since 1977, Caltech has operated a radon monitoring network as part of an earthquake prediction research program. This network consists of several automated sensing devices which record concentrations of radioactive radon gas dissolved in subterranean water systems, or aquifers. Measurements are taken by means of a vertically drilled borehole, typically three inches in diameter and one hundred feet in depth. Because the radon has a half life of only 3.8 days, it provides an excellent method for examining what happens within the granite these aquifers permeate. There is evidence that seismic strain precursory to an earthquake produces microfractures within the granite. These in turn cause radon concentrations to increase via the greater rock surface area to which the aquifer water is exposed. Thus the eventual aim is to analyze radon signals to help predict earthquakes. The problem is that the radon signal reflects many non-seismic, environmental influences such as daily heating by the sun, rainfall, borehole water level, and seasonal changes in the aquifer. These influences must be filtered out of the signal before seismic effects are to be clearly visible. The network has now collected an appreciable amount of data enabling ever more meaningful analysis of these effects.

There are two purposes to this project. The first is to provide a model for an unusual radon concentration response to heavy rainfall. The second is to reduce the Pacoima Dam site radon signal to low amplitude random noise using a computer and data files on rainfall and borehole water levels.

In February of 1980, the Lytle Creek radon signal suddenly jumped above a previous, fairly smooth, gradually increasing equilibrium level of about 2200 counts (on a relative scale). This increase, to roughly 3300, corresponded to rain storms in the area. Upon reaching this peak the signal plummeted to 650 in 152 hours. Thereafter it began a climb back to equilibrium, reaching 2000 in ten days, just as another rainstorm began. The derivation for the model of this is as follows:

We know that water flows through the underground aquifers at a rate determined by the hydrostatic pressure driving it and the porosity of the granite the aquifer lives in. Picture then a slug or parcel of water moving down this aquifer, carrying an initial concentration of radon, N_o. Since the radon signal does not dwindle to nothing, and yet radon is constantly decaying into Polonium, there must be a constant supply of radon in the rock: As fast as it decays and is sucked out by passing water, it is renewed by the decay of ubiquitous radium. Assume the water slug inhales radon from the rock proportionally to the amount of radon in the rock, R. Let the radon concentration in the water be denoted N, the initial concentration; N_o, and the radioactive decay constant; γ. Then over a period of time, Δt, the concentration N changes by an amount ΔN:

$$\Delta N = -\gamma N \Delta t + rR\Delta t,$$

where r is some proportionality constant. This leads to an equation for N:

$$N = N_o e^{-\gamma t} + \frac{rR}{\gamma}(1-e^{-\gamma t}),$$

and as time goes on the exponentials evaporate, so $N = \frac{rR}{\gamma}$, a stable equilibrium given that there is a steady, constant radon supply in the rock.

But now significant rainfall drains through the upper layers of rock into the aquifer. This water is passing through previously dry rock, collecting radon as it sinks. It also creates greater pressure on the aquifer, so increasing the water velocity. Thus more water, now radon rich, moves through the borehole and gives a higher radon count.

Now the last of the water input from above the aquifer ceases. There is no longer the high hydrostatic pressure, so the water in the aquifer slows down. This case is identical to the previous derivation, with N_0 equal to the radon level just after the rain quits, except that we now assume that much of the radon in the aquifer rock has been washed out. It will recover to its previous concentration eventually, but meanwhile the aquifer water has less radon from which to draw its supply. The radon count correspondingly drops, even far below the pre-rain equilibrium level. After bottoming out it begins a slow climb back to this or perhaps a new equilibrium. We assume that R is not constant, but rather a function of time:

$$R = \frac{\bar{R}}{a}(a-e^{-bt}).$$

($\bar{R}$ is the equilibrium concentration of radon in the rock, and a and b are empirical constants.) Substituting this into our initial equation for N, we get

$$N = -\gamma N\Delta t + rR\Delta t = -\gamma N\Delta t + r\bar{R}\Delta t - \frac{r\bar{R}e^{-bt}}{a}\Delta t.$$

The result is a function for N which describes the drop and recovery curve of the radon signal at Lytle Creek:

$$N = ae^{-\gamma t} - be^{-ct} + d.$$

Here again a, b, c, and d are four empirical constants which can be determined from a given signal.

The first problem at Pacoima is that of the water level in the borehole. There are similarities in the graphs of this water level and water storage in the nearby reservoir, but there is no time lag between corresponding events. Also, while at one point the reservoir storage drops to nothing, the borehole always remains within a four foot depth range. Thus the reservoir is probably not a significant driving force on the borehole, but rather changes in both places are driven by weather.

The Pacoima radon signal is very noisy, filled with high frequency, high amplitude fluctuations. Using a computer these frequencies are analyzed by means of the noise normalized fast fourier transform power spectra of signals over different time intervals. From these we see that throughout the year the signal fluctuates daily. This daily fluctuation becomes more pronounced during the summer months, and fades in the winter. It is likely that solar heating of the granite causes it to expand and increase dissolved radon. The increase may also be due to daily temperature effects on the monitoring device. But regardless of the mechanism, we know that there is a driving force on the signal with a once per day frequency, more prevalent in the summer. This can be low pass filtered out of the data, leaving a smoother but still messy signal.

The next step is to clean out all the signal peaks during the winter, typically five to twelve days in duration, which correspond to rainfall. The Los Angeles County Flood Control District, which operates Pacoima Dam, records the rainfall daily and has provided us with some useful information about the area. Once the rainfall has been filtered out, most remaining peaks correspond to changes in the borehole water level. This includes the annual sinusoidal pattern the radon signal exhibits. Thus we have a solid procedure for filtering a year's data.

Conclusion

Each radon monitoring site has its individual characteristics. Several more years of data will be required before we can conclude just how static these sites are. The problem becomes one of testing whether these and other simple models can consistently explain the physical systems in the field. Working out empirical formulas such as the Lytle Creek anomaly equation and reapplying them to other sets of data is now a procedure for testing the accuracy of our hypotheses.

Bibliography

Callison, Joe. Los Angeles County Flood Control District.

Dr. M.H. Shapiro.

Shapiro, Dr. M.H., et al. Annual Technical Report, USGS Contract No. 14-08-0001-19752, 1981,82.

Dr. T.A. Tombrello.

Rachel Wing.

Verbs in A Simple Knowledgeable System

Timothy Fernando
Dr. Bozena H. Thompson
Dr. Frederick B. Thompson

ABSTRACT

Problems concerning the processing of verbs defined in terms of "to be" and "to have" are discussed, and solutions are described. These center on the implementation of a case grammar and on handling conjunctions.

INTRODUCTION

My work this past summer focused on the framework for handling verbs in A Simple Knowledgeable System (ASK), "a total system for the structuring, manipulation and communication of information." [1] ASK initially recognizes only the copula verbs "to be" and "to have" since the meaning of most, if not all, other verbs depends on the context in which they are used. Non-copula verbs can be introduced by the user through paraphrase. For instance, the verb "know" might be defined as follows:

    >verb: Sylvia "know"s Ann: Ann is a friend of Sylvia

It is instructive to look at verbs involving n nouns as describing n-ary relations of nouns. These nouns can be given labels, which in linguistic circles are called "cases." In the example above, one can assign Sylvia the case agent, and Ann the case object. These same case assignments would then hold for the sentence "Sylvia is known by Ann." That is why we bother to categorize nouns into cases. A case grammar gets us deep into the sentence's structure.

Decisions concerning what cases a case grammar is to recognize and how the assignments are to be made vary from one linguist to another. Some elaborate and complex systems have been developed which handle certain sentences very impressively. As tempting as it is to adopt such systems, it is important to determine whether the gains in verb processing justify the added complexity. For inspite of the tremendous work on this area and the many mechanisms intoduced to extend the capabilities of case grammars, "there seems to be a great deal of irreducible idiosyncracy' [2] in English. Complexity can easily explode (especially because of undesirable side effects) while the resulting gains dwindle.

A major problem which I did not expect when I began my work was the conjunction routine for definitions of verbs with more than two noun cases. The rules for defining verbs are not very restrictive and while this might be desirable from the user's point of view, it means much work in designing the routines for processing verbs. Moreover, a lot can go wrong when the user, who could not be expected to completely grasp how the system responds to his inputs, is allowed to do almost anything he wishes.

These then were the problems which I faced. My work consisted of cleaning up the parsing of verb phrases, modifying the case grammar to include prepositional cases, and improving the conjunction routines.

DISCUSSION

I. A Prepositional Case Grammar

One of the major influences on the design of ASK's case grammar was the concern that the user not be burdened with cumbersome descriptions of objects he introduces to the system. True, more powerful case grammars could have been developed with the machinery available in ASK (e.g., feature checks). However, the present case grammar was chosen largely because of the rather limited demands it makes on the user to be attentive to his language.

ASK recognizes the agent, object, and to_noun cases as well as a number of other prepositional cases. The prepostional cases were introduced simply to allow the nouns preceded by these prepostions to be recognized. With the exception of the to_noun, prepositional case assignments are made solely on the basis of the presence of the preposition in the sentence. The agent, object, and to_noun cases recognize more complex transformations.

Modifications in the case grammar will almost surely be made in the future Changing case assignments would consist for the most part of modifying one small procedure in the verb routine. A number of issues merit consideratio before any change is made, however.

For simplicity, noun features were not used in determining cases. The added burden on the user that this would entail did not seem to justify the rather limited gains which result from it. Moreover, certain undesirable side effects turn up because of it. Consider the sentence "Xerox donated books to the library," where the only reason one might turn on the animate feature for Xerox is so that a question like "Who donated books to the library?" might be answered correctly. But then, "What donated books to the library?" would not be answered correctly since "what" has the animate feature turned off. (In fact, the answer to this question would be "yes" since the agent case would not have been instantiated and the question would have been interpreted the same way as "Are books donated to the library?")

Also, there was little interest in allowing a case to be marked by more than one preposition. In the present system, this would have meant that certain combinations of prepositions could not be parsed since cases can be assigned to no more than one noun group in a simple sentence. Furthermore, the purpose of case assignments in ASK is not to capture semantic similarities among prepositional phrases appearing in different verbs, but to mark where a particular noun belongs in the n-tuple described by a particular verb. That is, the fact that "for <noun phrase>" might be related to "to <noun phrase>" in the verbs "buy" and "give" is of no concern to case assignments in ASK.

II. Verbs with more than two noun cases

Such verbs express n-ary relations where n>2. For various reasons , ASK reduces n-ary relations into binary relations. In particular, if an n-tuple (a1,a2,...,an) has a field ai which identifies the n-tuple uniquely (i.e, a key field), then the n-tuple can be represented in terms of the ordered pairs (ai,a1), (ai,a2),..., (ai,an). (Otherwise, a key field must be introduced.) That is, if R is the n-ary relation underlying a verb, then the statement that (a1,...,an) belongs to R is paraphrased in ASK by the conjunction of sentences (ai,a1) belongs to B1, ..., (ai,an) belongs to Bn, where B1,...,Bn are the appropriate binary relations. (Just what binary relations are "appropriate" will become clear below.)

For example, the verb "carry" can be thought as expressing membership in the tertiary-relation, class of trips, AA x BB x CC, where AA consists of carriers, BB consists of cargo, and CC consists of destinations. Thus, the sentence "Maru carries bananas to Los Angeles" means "there is a trip with Maru as its carrier, bananas as its cargo, and Los Angeles as its destination." [3] A possible problem here, however, is that cargo may be related in one's database not to the trip but to the carrier. (The same can be said for destination.) This is probably because a trip is often uniquely identified by its carrier. That is, usually the carrier is precisely the key field of the trip-le, in which case the concept of trip is unnecessary [4]

To understand how we might approach this problem, familiarity with ASK relations and ASK attributes is necessary. ASK Objects can be associated by binary relations or attributes, where the only difference is that the <attribute> of an <object> has a unique value whereas the <relation> of an <object> need not (e.g., father vs son). In other words, attributes have key fields while relations may not. A conjunction of attribute statements in which each of the non-key entries of the n-tuple is declared as the value of an <attribute> of the n-tuple's key field satisfactorily describes, as we have seen, the n-ary relation a verb underlies. Now, suppose we wish to introduce another field to the n-tuple. It is not difficult to see that the statement that the resulting n+1-tuple belongs to a verb relation is adequately expressed by extending our old paraphrase to includ a relation or attribute statement connecting the n-tuple's key field to the new entry. Since an n+1-tuple (a1,a2,...,a(n+1)) can be rewritten as ((a1,a2,..,an),a(n+1)) where (a1,a2,..an) is uniquely determined by its key field a1, in order to specify (a1,...,a(n+1)), we need only add to the description of (a1,a2,...,an) the proposition that (a1,a(n+1)) belongs to a certain relation. [5]

This means that we can paraphrase "Maru carries mangoes to Manila" by "mangoes are Maru's cargo and Manila is Maru's destination" as long as either cargo or destination is an attribute (since the carrier is a key field of the attribute). [6]

In summary, two conditions must be met in paraphrases of verbs with n noun cases where n>2: (see [4])
i) No more than one relation can be mentioned in the paraphrase. This is illustrated by the trip-les ((carrier),(cargo),(destination)) below:
  (Maru,{bananas,mangoes},{Los Angeles})
  (Ubu,{bananas,mangoes},{Los Angeles,San Francisco})
  (Alamo,{bananas,mangoes},{Los Angeles,San Francisco})
(Note that the first trip-le requires only one binary relation (i.e., the cargo relation) whereas in the second trip-le, destination must also be a relation.) While it is clear that Maru carries bananas and mangoes to Los Angeles, there is some question as to what fruit Ubu carries to what city. Observe that it is not enough to relate cargo to destination, as the third trip-le shows.
ii) The key field a1 of the n-tuple (or of the n-1-tuple) must be linked to each of the other noun cases. Furthermore, a1 must be the key field in all but possibly one of the ordered pairs which describe the n-tuple. The one exception may be the relation pair (if one is involved), or any of the attribute pairs (if there is no relation pair). Note that for attributes which are not one-to-one functions, the argument in an attribute statement is the attribute's key field.

One of the chief problems in processing verbs with more than two cases is designing the routine for handling the conjunctions which define them. A case may appear as an ASK noun_phrase, a wh_word (i.e., who, what, etc.), or as an FVAR (i.e., unmentioned in the sentence being processed). Thus the binary relation statement "A is cargo of B" can occur in 3*3=9 ways. Combining such conjuncts bacomes very complicated. For example, for two conjuncts, there are 9*9 = 81 cases to consider.[7]

The introduction of coordinating quantifiers makes case anlyses for the most part unnecessary. Furthermore, it affords a solution to other problems such as the decomposition of questions like "Who loves and hates Mary?" (compare to "Who loves and who hates Mary?") into simple phrases amenable to semantic analysis.

The coordination utility is rather complicated and an explanation of how it works would take us deeper into ASK than we might like. Essentially, what it does is it intersects nouns with the same coordinating quantifier (where the coordinating quantifiers are distinguished by the case of the noun quantified) and outputs the intersection along with the fields corresponding to it.

To understand the reason for this, consider the processing the question "what ship carries corn to Pasadena?" involves. Suppose the verb "carry" is defined with carrier as the key field:

```
   >verb: ships "carry" coal to London: coal is the ships's cargo and
   London is the ships' destination
```

The question is reduced to "corn is what ship's cargo and Pasadena is what ship's destination"? Note that "what ship" in the first conjunct must be no different from "what ship" in the second conjunct. By intersecting the records of "what ship" in each conjunct, this condition is met.

CONCLUSION

A number of problems remain. The coordination of FVAR's and wh words has yet to be worked out. The details for processing sentences like "Is John the son of Mary and the cousin of Ann?" which require coordination but which are not verb definitions have not been written. The case grammar could stand some polishing. And of course, there is always debugging.

ACKNOWLEDGEMENT

Were it not for the sponsorship of Professor Thompson, I would not have been able to carry out this project. It was his system that I worked on, it was his ideas that I thought about, and it was his patience and encouragement that made it all a pleasant experience.

NOTES

[1]
Bozena H. Thompson, Frederick B. Thompson, "Introducing ASK", in Proceedings of the Conference on Applied Natural Language Processing, February 1983.

[2]
Terry Winograd, Language As A Cognitive Process, Volume 1: Syntax, Addison Wesley, 1983.

[3] The inadequacy of paraphrasing "Maru carries bananas to Los Angeles" by "bananas are Maru's cargo and Los Angeles is Maru's destination" is evident in the following situation. Suppose:
(1) Maru carries bananas to Los Angeles,
(2) Maru carries mangoes to Manila,
(3) Ubu carries mangoes to Los Angeles.
By (1), Los Angeles is a destination of Maru, and by (2), mangoes are its cargo. Thus, by definition, Maru must carry mangoes to Los Angeles. Adding the condition that Los Angeles be the destination of mangoes does not help any since this is true by (3).

[4] In any event, the user might be expected to have the sense to decide whether it is appropriate in his database to define cargo with respect to the carrier or with respect to a trip. For afterall, if Maru's cargo varies depending on the trip, it would seem rather silly not to mention the trip in which Maru's cargo includes bananas.
What follows are no more than guidelines on how verbs might be defined so that they would work when verbs are viewed as underlying n-ary relations. Other ways may seem more natural to a specific database. For instance, if in all trips, carriers have the same cargo, it might be more desirable to define cargo with respect to the carrier, a violation of rule ii) below. At any rate, the user must be cognizant of the limits of his definition.

[5]
Basically what we have is

$$(a1,\ldots,a(i+1)) \Rightarrow ((a1,a2,\ldots,ai),a(i+1)) \Rightarrow (a1,a(i+1))$$

[6] For what it's worth, I am inclined to believe that most paraphrases would mention the key field in each of their relation/attribute statements and that, moreover, whenever it appears as one of the verb's case nouns, the key field would almost always be the agent case.

[7] The situation is actually more complicated because of quantifiers which are handled by routines called crunchers.

PAUL FILMER

This student is extending his SURF project on Geomagnetic Positions of Various Cratons in Morocco. A copy of his final report will be available in the SURF Office at a later date.

JEFF FREYMUELLER

NO REPORT SUBMITTED

LASER BEAM CLEANING WITH SINGLE MODE OPTICAL FIBERS

Josef Frisch
Sponsor: S. Whitcomb

ABSTRACT

This report describes experiments done to determine the usefulness of single mode birefringent optical fibers for reducing lateral motion of a laser beam for use in the Caltech gravity wave interferometer. The fiber beam cleaner was found to be effective and looks practical for this application.

When a gravity wave passes through an area, it produces forces on any masses present. These forces will tend to move the masses closer together in one direction and further apart in a perpendicular direction. The forces on the masses alternate with the frequency of the gravity wave but remain opposite in phase in orthogonal directions. (see figure 1). The strength of a gravity wave can be measured by the resulting change in separation of two masses divided by their initial seperation. For a strong hypothetical source, an extragalactic supernova, the expected strength is

$$\text{change}(L) / L = 10^{-21}$$

Even for masses located a hundred meters apart the detector would have to be able to register a motion of less than 10 E-16 cm, considerably smaller than a nuclear diameter. The type of signal expected is a short (few cycles) pulse at a frequency of about a kilohertz.

The Caltech gravity wave detector has three test masses suspended 40 meters apart in an L- shaped vacuum chamber. (figure 2). The masses hold mirrors and other optics required to form 2 perpendicular 40 meter long high finesse Fabry Perot optical cavities. An argon ion laser is frequency locked in resonance with one of the cavities while its light is fed into the second cavity. The length of the second cavity is controlled (by a piezo-electric element) so as to be in resonance with the frequency of the laser. A gravity wave passing the detector should cause a differential change in the length of the cavities. The laser frequency is changed to stay locked to the resonant frequency of the first cavity. The length of the second cavity will change by a different amount, so it will no longer be exactly at resonance. The electronics will have to feed back a signal to the piezo-electric element in the second cavity. This feedback signal will be recorded and would show the presence of the gravity wave.

When the cavities are in resonance, the light reflected off their input mirrors is at a minimum. The system is then insensitive to intensity variations in the input laser light. If the input beam moves laterally, however, different modes of the cavities will be excited and if the cavities are not perfectly matched, this will cause noise at the output.

The input beam to a cavity can be described by a superposition of modes of the cavity. Optimally one would want the beam to have the form of the lowest order mode of the cavity. It is sufficient, however, for the shape and position (and therefore mode composition) of the input beam to remain constant over a timescale of tens of milliseconds.

In this project I tested a device which reduces the lateral motion of the laser beam. This is achieved by passing the laser beam through a single mode birefringent optical fiber.

Some work has been done with fiber optic beam cleaners at MIT but little quantitative data has been published. Work has been done at Caltech and elsewhere on beam cleaning systems based on resonant cavities. These work but tend to be fairly complex.

An optical fiber is a thin rod of glass which has been manufactured to have several radial layers, the core, the cladding, and several protective layers. The core has a higher index of refraction than the cladding. Light in the core is kept in the core by total internal reflection.

A fiber acts as a dielectric waveguide for optical frequencies. As the size of the fiber is decreased, the number of propagating modes decreases. At some point only one mode of the fiber propagates while the rest decay exponentially. The cross section of this mode has an electric field whose profile is the zeroth order bessel function.

If a laser beam is incident on a single mode fiber only the part of the beam which overlaps the lowest mode of the fiber will be propagated and the beam exiting the fiber will be composed only of this mode. This lowest order mode beam has a well defined and constant shape and position. Therefore it would be useable as an input beam for the Fabry-Perot cavity.

For this experiment I used a special type of single mode fiber which preserves the polarization of the input beam. This fiber was used because the gravity wave detector is, to some extent, polarization sensitive.

Ordinary fiber is cylindrically symmetric so that the two perpendicular polarizations of input light have identical wavelengths. Thus the two polarizations can couple significantly. If you put in one polarization you will get a mixture of both polarizations at the output.

Polarization preserving fiber is manufactured with an elliptical cladding. When the fiber is drawn the core is put under pressure. Because the cladding is elliptical, the pressure is different along the two perpendicular axes. Since the index of refraction of glass is somewhat pressure sensitive this causes the core to be birefringent, ie, it has different indices of refraction for the two perpendicular polarizations of light. The wavelengths of the two polarizations are no longer degenerate and they will not couple. If the input light has its polarization aligned with the major axis of the fiber the light will retain its initial polarization after traveling through the fiber.

One of the major difficulties with using a single mode fiber is coupling the light from the laser efficiently into the fiber. The core of the fiber which I used has a diameter of four microns. The input laser beam must be focused to hit the end of the core with exactly the right divergence for maximum coupling. Most of my experiments were done with about 40% of the light from the laser coupled into the fiber. Newport Research Corporation has reported that it is possible to get 80-90% of the light coupled into the fiber with sufficient care.

There is a related problem with input coupling to the fiber. Some of the light which is not coupled to the core of the fiber will travel down the cladding and outer layers of the fiber. This light is not restricted to only one mode and can therefore introduce noise into the beam exiting the fiber. If the fiber is painted with black paint near its ends these "cladding modes" will be absorbed while the core light is unaffected.

I performed the following experiments to measure the beam cleaning properties of the fiber.

I reflected the beam from a Helium Neon 1mw laser off a mirror mounted on a piezoelectric element and coupled it into the fiber with a microscope objective. The output beam from the fiber was directed onto a position detector. (figure 3)

The piezoelectric mirror was intended to move the beam lateraly to simulate random motions of the beam exiting a laser. The position detector would measure the position of the beam before and after it passed through the fiber to see how well the fiber reduced the motion of the beam.

The position detector consists of two

photo-diodes very close together. The laser beam is aimed so that part of it falls on each of the detecters. I designed circuitry (figure 4) which subtracts the amount of light seen by each of the diodes and divides the difference by the total amount of light seen by the diodes. For small beam motions when the beam is centered between the detectors, this gives a signal proportional to the motion of the beam.

There was a problem with the detector. When the piezo mirror caused the input spot on the fiber to move, the intensity of the light in the fiber fluctuated . The intensity divider circuit in the detector doesn't work perfectly, so even with the spot centered on the diode, intensity fluctuations show up as (very small) lateral beam motions.

To monitor the effect of intensity fluctuations on the position detector's output, I set up a Pockels cell to intensity modulate the light. The Pockels cell did not move the beam laterally to any significant extent.

The experiment was designed to allow switching between applying a driving voltage to the piezo and to the Pockels cell. I adjusted the amplitudes of the driving voltages so that the amplitude of the intensity signal caused by the piezo and that caused by the Pockels cell were similar.

The piezo and Pockels cell driving voltage was always a sine wave at 1000Hz. I drove them at one frequency rather than wideband to allow bandwidth limiting to decrease noise.

I drove the piezo with varying amplitude and recorded both the intensity and position signals from the position detector following the fiber. I then repeated the measurements while driving the Pockels cell. The plots of position signal vs intensity signal were found to be identical straight lines through zero.

I repeated the same experiment except this time the driving signal was switched alternately between the Piezo and Pockels cell. This reduced the time the equipment had to drift between measurements and improved the accuracy of the experiment. The following error signal was calculated.

$$\frac{\text{position signal piezo driven}}{\text{intensity signal piezo driven}} - \frac{\text{position signal Pockels cell driven}}{\text{intensity signal Pockels cell driven}}$$

This error represents the difference in position signal seen for the same amount of intensity signal when the driving voltage was applied to either the Piezo or the Pockels cell. If, as was the case, there was no statistically significant signal, all of the apparent motion of the beam caused when the Piezo was driven, was in fact caused by errors in the circuit not completely eliminating signals from the changing intensity. (figure 5)

The amount of intensity signal seen was known as a function of the drive voltage on the piezo. From the just mentioned calculation, I took the statistical error in the position signal seen as a function of intensity signal as an upper limit on position motion as a function of intensity signal. Combining these gave a maximum position signal as a function of Piezo driving voltage.

I then set up the apparatus so that the detector measured the motion of the beam leaving the Peizo mirror. Corrections were made for the beam size to obtain the ratio of beam motion to beam diameter (the most relevant figure of the position stability of the beam).

The fiber was found to reduce beam motion by at least a factor of 4000. With no driving voltage I measured a total beam motion/diameter of 5.6E-8 . This was about a factor of 3 above the theoretical shot noise limit of the detector. This apparent motion did not appear to be due to intensity noise in the laser output but was probably noise in the detector itself.

Other tests measured the effects of the fiber on the polarization and intensity noise of the laser. The fiber was found to maintain the polarization of the input beam to at least a part in several thousand even when the input beam was moved across the fiber surface with the piezo mirror.

The fiber did increase the intensity noise of the output beam. This was largely due to sound in the room affecting the input coupling to the fiber. At normal room noise levels I found the intensity noise caused by the fiber to be significantly greater than laser noise up to frequencies of about 1500 Hz. The difference increased to about 10db at low frequencies. Under quieter conditions noise caused by the fiber was below laser noise at frequencies above about 300hz. Again the maximum difference (below about 50hz) was about 10db.

In general fiber beam cleaning looks promising for the gravity wave detector project. The fiber beam cleaner appears to greatly reduce lateral motion of the laser at a cost of increased intensity noise at low frequencies. The increased intensity noise, however is largely nulled out by the gravity wave detector's design while the decreased position noise should help improve sensitivity.

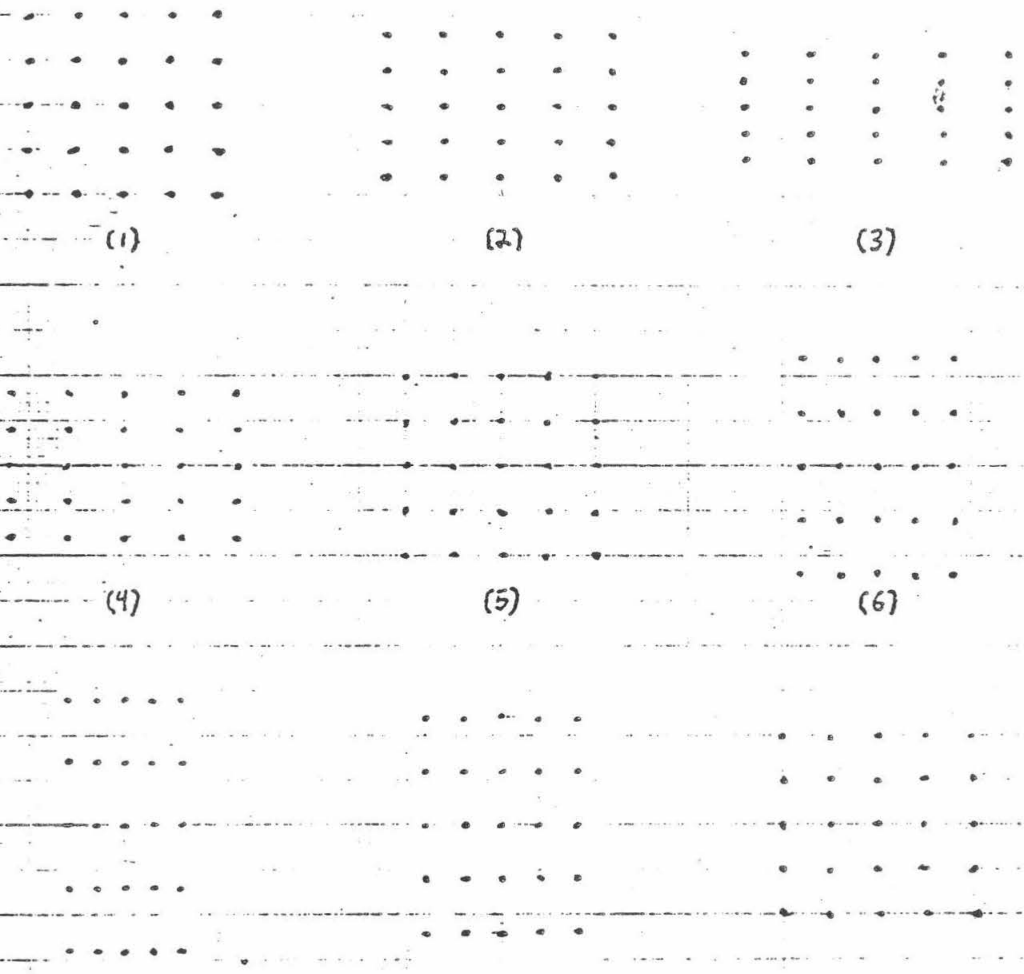

(1) (2) (3)

(4) (5) (6)

(7) (8) (9)

EFFECT OF GRAVITY WAVE ON FREE MASSES

(FIGURE 1)

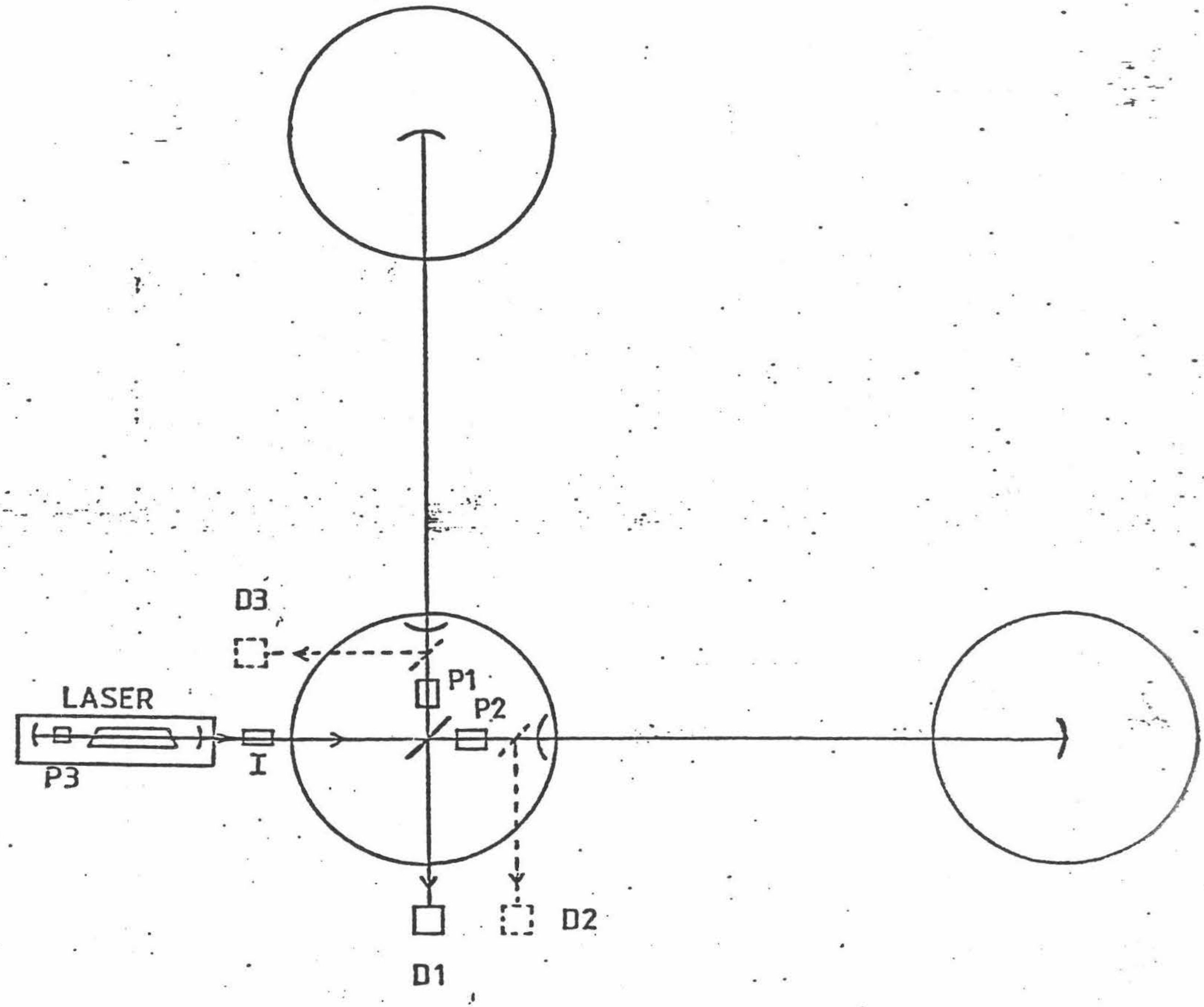

Figure 2. Schematic diagram of a possible optical arrangement for a free mass gravity wave detector using resonant cavities for displacement sensing.

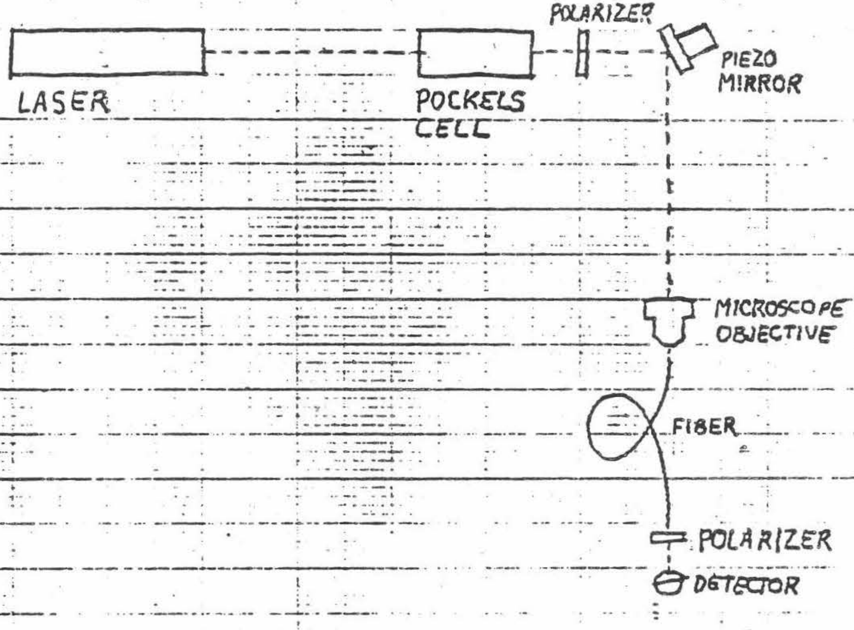

EXPERIMENTAL SETUP

(FIGURE 3)

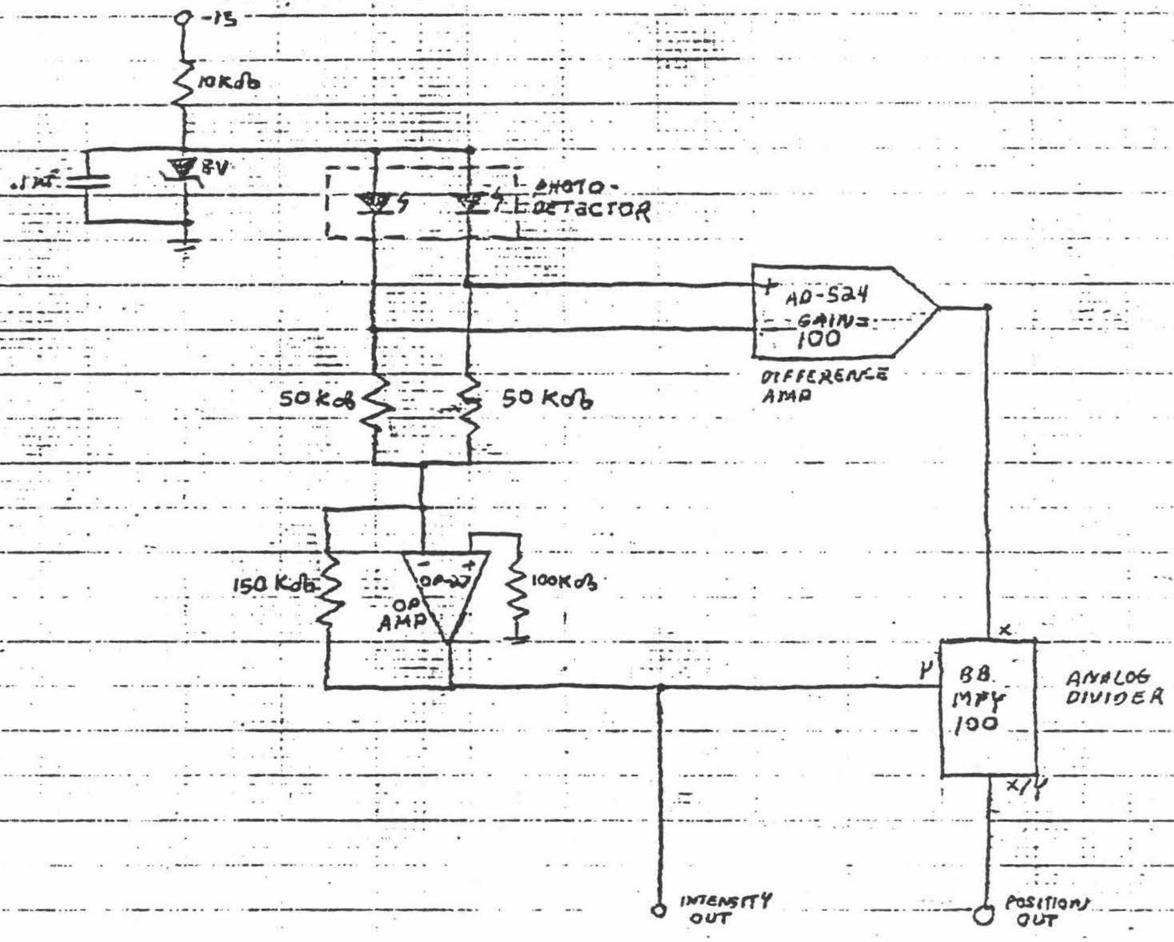

CIRCUIT FOR POSITION DETECTOR
(FIGURE 4)

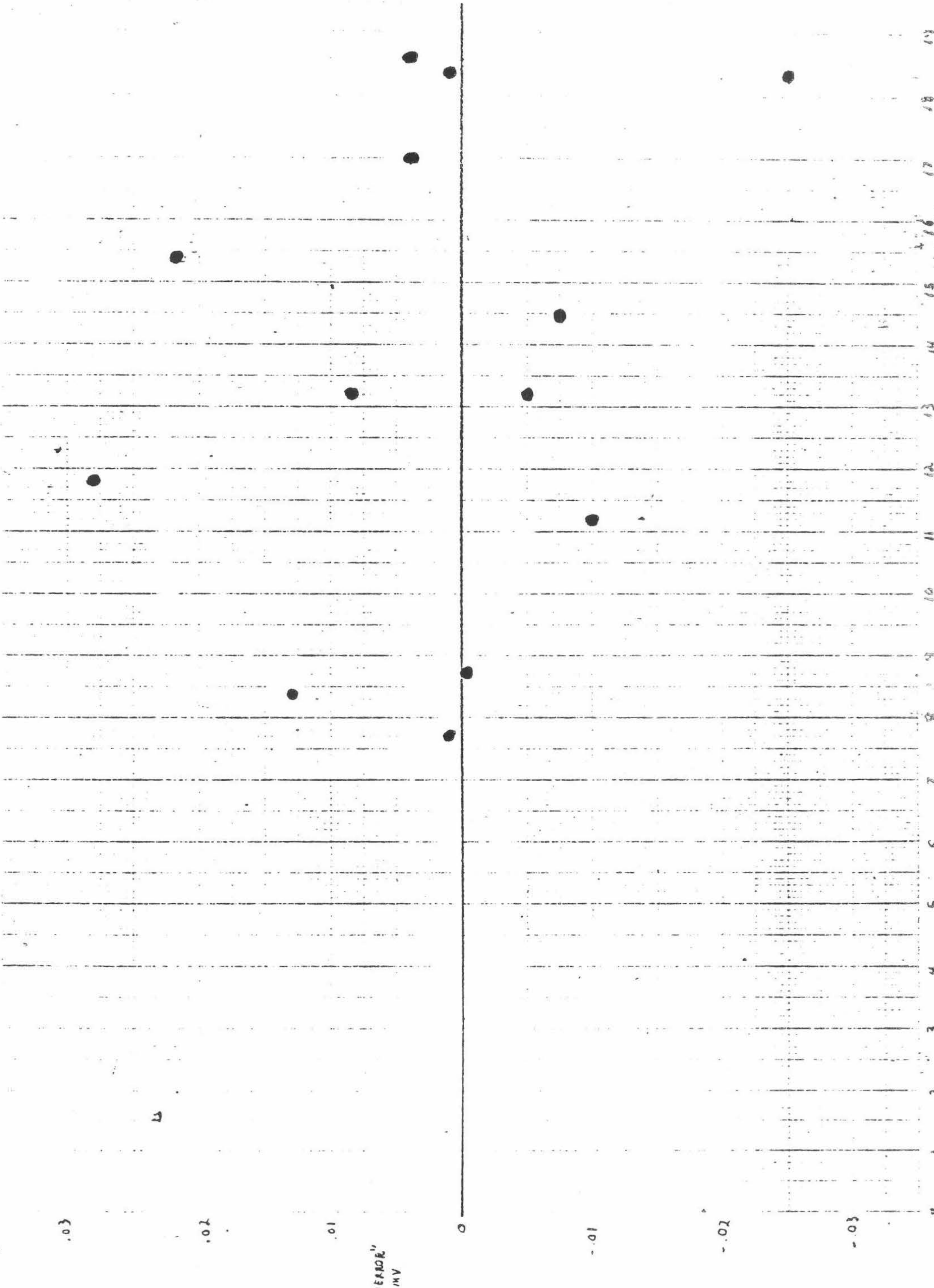
DRIVE VOLTAGE VOLTS
0
1
2
3
4
5
6
7
8
9
10
11
12
13
14
15
16
17
18
19
.03
.02
.01
0
-.01
-.02
-.03
"ERROR"
MV

MICROSTRIP TRANSMISSION LOSSES
AT
MILLIMETER FREQUENCIES

David R. Fun
David B. Rutledge, Faculty Sponsor

ABSTRACT-This report proposes a method of measuring losses in microstrip transmission lines at millimeter frequencies. It is a technique that is not completely proven but provides promise. It is concluded that such a technique could be useful if the losses to be measured are not very high.

There has been much research in the area of microstrip antennas in the millimeter range. However, there has been very little work done in the area of microstrip circuit elements in this range. This paper investigates one aspect of one type of circuit element at millimeter frequencies, losses in microstrip transmission lines.

The main emphasis of the project was to experimentally measure surface-wave losses (Kasilingam and Rutledge). The experiments were set up using microwave modeling techniques. Microwave modeling uses the microwave frequency band to make measurements in. In order to do this, the dimensions of the experiment must have the same ratio of length with respect to the microwave wavelength as to the wavelength of the frequency one is modeling for. Thus, the subtrate for the microstrip was thicker, and the microstrip itself was wider. Manufacture of the test pieces was very easy since instead of using photolithography, strips of copper foil could be pasted onto the substrate. Also since testing was done in the microwave band, there was test equipment readily available. However, problems were incurred due to the impedence mismatch at the junction between the test equipment and the test pieces. Thus the only way to measure the losses accurately was to perform an absolute impedence measurement. However, such a measurement requires an appropriate and frequency independent impedence reference. In this case, a microstrip connector with the pin filed off proved to be an adequate reference.

To determine the attenuation constant, it was assumed that the impedence of the line would spiral down about the characteristic impedence as one made the line longer. If one could measure three points on the spiral, one could determine the rate of spiral and hence, the attenuation constant.

The experiment was set up and run, but it yielded very erratic results. It was finally theorized that the lines were too long, and the losses too high. When the lines are very long, and the losses high, the spiral is very small, and the slightest error in the data could change the perceived rate of spiral and hence, the perceived attenuation constant.

However, the experiments have not been run yet to prove whether or not this theory is true. Hence, the only conclusion to draw is that this method of measure is still possibly valid.

If the results from these future experiments are consistent, then using this method of measurement, one can accurately determine the magnitude of surface wave losses for microstrip transmission lines.

REFERENCES

Kasilingam, D.P. and Rutledge, D.B., (1983) IEEE MTT International Symposium Digest, paper C-5.

Design of Apparatus to Detect ^{16}O Nuclei from the $^{12}C\ (\alpha,\gamma)\ ^{16}O$ Reaction

By

Brett Garrett

SURF 1983

C. A. Barnes

Faculty Sponsor

Abstract.

The purpose of this project is to design a set-up that will enable the detection of the oxygen nuclei produced in the nuclear reaction $^{12}C + {}^{4}He \rightarrow {}^{16}O + \gamma$.

Introduction.

The cross section of the $^{12}C\ (\alpha,\gamma)\ {}^{16}O$ reaction has been measured in the past by shooting a beam of high-energy carbon particles into helium gas, or vice versa, and measuring the resultant gamma radiation. Unfortunately, at lower center of mass energies, various background radiations become more significant, causing serious experimental errors and thus limiting the minimum energies at which the cross section can be measured. The low energy rate of this reaction is important because it is closely related to the ratio of carbon and oxygen produced in stars during the helium burning stage of evolution.

A new proposal is to avert the background radiation problem by observing the resultant oxygen particles in coincidence with the gamma rays. As this experiment will be a major undertaking, my portion of the project concerns only the detection of the ^{16}O nuclei after the reaction occurs.

The elements used for this purpose include a magnetic quadrupole, which focuses the ^{16}O particles; a Wien filter (velocity selector), which eliminates most of the carbon (beam) and alpha (target) particles; and a bending magnet, which focuses the oxygen particles on the detector and eliminates still more unwanted particles, particularly neutrals that passed through the Wien filter. The aim of my research is to design these elements to transmit the maximum fraction of the oxygen nuclei and the minimum fraction of other particles to the detector.

Presentation and Discussion of Results.

Most of the work was done with the computer program BTRANS, which uses matrix methods to calculate the first-order effects of various elements upon the width of the beam. The program calculates both the "phase space," an envelope that contains the entire beam, and a "ray," the trajectory of an individual particle, given its initial position and velocity vector. Our oxygen nuclei will not all have exactly the same momentum; the program was therefore modified to calculate, in addition, rays for particles of slightly different (± 2.5 %) momenta.

We define z as the direction of propagation of the beam, and x and y as the horizontal and verticle positions of the particles in the beam. Each quadrupole creates magnetic fields which effectively focus the beam in the x-direction and defocus in the y-direction, or vice versa. By using a doublet of two quadrupoles of opposite orientation, one after the other, it is possible to achieve focussing for both the x- and y-directions at a given distance from the quadrupole doublet. The program BTRANS was used together with a minimization method to determine the fields necessary to do this.

The Wien filter, or velocity selector, will be placed between the quadrupole doublet and its focus position. This filter consists of electric and magnetic fields crossed in such a way that the forces will cancel for particles of a chosen velocity (the average velocity of the oxygen nuclei), but other charged particles will be strongly deflected. The fields of the Wien filter were chosen for the maximum deflection of the carbon particles consistent with the requirement that they not hit the plates of the filter, as this could cause a background of scattered carbons.

The vast majority of carbon nuclei will pass through the helium target without reacting. The charged carbons will be deflected by the Wien filter and eliminated from the beam by a slit placed at the focus of the quadrupole doublet, near the end of the filter. The slit will be large enough to transmit the focused oxygen nuclei, but it will eliminate the majority of the unwanted particles from the beam.

The next element is the bending magnet, a dipole which bends the beam of oxygen ions so that only one charge state (+4 or +3) will reach the detector. The bending magnet is a very complicated element because it is very sensitive to small differences in the momenta of the particles and because it has many parameters which may be varied. These parameters include the beam entrance and exit angles, the deflection angle, and the magnetic field strength, all of which strongly affect how the magnet focuses the beam. Hundreds of combinations were tested on the computer in order to determine what kind of magnet would best focus the oxygen beam on the detector.

At this point, the elements were fairly well determined, but a "Monte Carlo" calculation was necessary to show exactly what the beam would look like. A thousand rays were chosen at random in accordance with the expected distribution of ^{16}O particles at the end of the helium target. These rays were individually traced through the system to see where they would end up, and the results could be plotted to show the shape and concentration of the ^{16}O beam anywhere along its path.

Later, the computer program TRANSPORT was used to do further calculations. This program is useful because it provides more accurate, second-order calculations, and it can output transport matrices that include momentum terms. These matrices can be used for Monte Carlo calculations which are both faster and more accurate than those done with program BTRANS.

Conclusions.

The system shown on the next page has been tentatively chosen for a beam of oxygen particles of charge +4 and energy 3 MeV. This system results in a beam no wider than four cm diameter at the detector, and possibly much narrower.

Second-order effects appear to be somewhat significant, but just how important they are has not yet been determined.

Bibliography.

Articles:

Penner, S., "Calculations of Properties of Magnetic Deflection Systems," The Review of Scientific Instruments, 32 (February, 1961) 150-160.

Ioanoviciu, D., "Ion Optics of a Wien Filter with Inhomogeneous Fields," International Journal of Mass Spectrometry and Ion Physics, 11 (1973) 169-184.

Computer Programs:

BTRANS, by Dave Wiltzius, National Electrostatics Corp., 1975.

TRANSPORT, as revised by Los Alamos Meson Physics Facility,1981.

Tentative Parameters for 3 MeV Oxygen Nuclei.

Initial Phase Space*	X (max)	3 mm
	X' (max)	27 mrad
	Y (max)	3 mm
	Y' (max)	27 mrad
Drift		50 cm
Quadrupole (First of doublet)	Field at Pole Tip	1.75 kG
	Focusing Plane	Y
	Length	24.8 cm
	Aperture	5.08 cm
Drift		15.9 cm
Quadrupole (Second of doublet)	Field at Pole Tip	1.25 kG
	Focusing Plane	X
	Length	24.8 cm
	Aperture	5.08 cm
Drift		85 cm
Wien Filter	Magnetic Field	1.08 kG
	Electric Field	6.45 kV/cm
	Deflecting Plane	X
	Length	50 cm
Drift		100 cm
Bending Magnet	Magnetic Field	6.24 kG
	Radius of Beam Curvature	40 cm
	Entrance Angle	40 degrees
	Exit Angle	-40 degrees
	Deflecting Angle	45 degrees
	Bending Plane	X
Drift		between 60-100 cm
Detector		

---

*Actually the initial distribution of the ^{16}O particles is much more complicated than a simple phase space, which is why the Monte Carlo calculations are extremely useful.

Plot of BTRANS Output for Phase Space

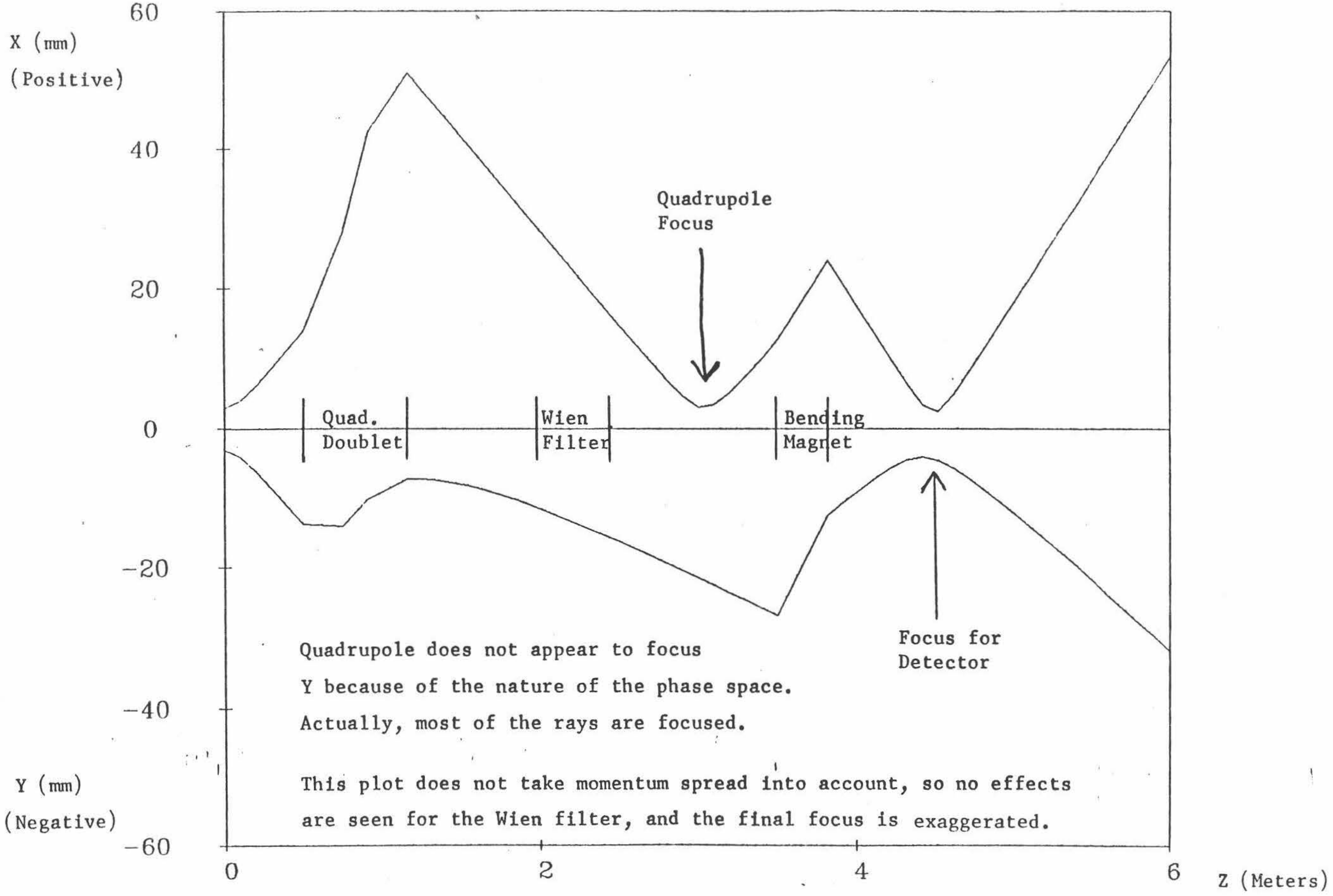

Quadrupole does not appear to focus
Y because of the nature of the phase space.
Actually, most of the rays are focused.

This plot does not take momentum spread into account, so no effects
are seen for the Wien filter, and the final focus is exaggerated.

Comparative Sequence Analysis of Embryonic Actin Genes of the Sea urchin

by Ted George
with
Eric Davidson
Rosemary Shott

Abstract

The 3' non-coding region of the sea urchin cytoplasmic actin gene, cyIIIa, was obtained from a cDNA copy cloned into the plasmid, pUC9. It was end-labelled, and the sequence obtained using Maxam-Gilbert techniques. The sequence was used to detect restriction map differences between cyIIIa, cyIIIb, and cyIIIc.

Introduction

There are eight actin genes in the genome of the sea urchin, Strongylocentrotus Purpuratus.[1] The coding regions of these genes are very similar, but show divergence in their intron DNA sequences, and in their transcribed but untranslated flanking DNA regions. These genes are grouped into four subtypes based on homology in their 3' untranslated region. They are: cyI, cyII (a,b, and c), cyIII (a,b, and c), and M. The M actin gene is actively transcribed in muscle tissue, and the cy genes encode cytoskeletal actin genes expressed both in muscle and non-muscle cells. Of the eight, at least six produce active mRNAs at some point in the sea urchin lifetime.[2]

One of the more interesting subtypes is the cyIII family. These genes are only active in the embryonic stages of development where their expression is enriched in the ectodermal cells.[2] They are not expressed in adult tissues. Therefore, they provide a good example to investigate the mechanisms of gene regulation during development. The sea urchin itself is an ideal system to study regarding developmental gene regulation because its embryology is well characterized, and large quantities of synchronously developing embryos are easily obtained.[3]

During early development, the primary actin transcript is transcribed from the cyIII family. However, due to close sequence homology of this family, it has not been possible to distinguish these genes and thus to identify which one is the major embryonic actin gene. The goal of this project was to distinguish between these genes by DNA sequence comparisons.

The cyIIIa 3' non-coding region was obtained from an embryonic cDNA library, and cloned into the Pst I site of the plasmid, pUC9. From there, the insert was excised, radioactively end-labelled, and sequenced. Its sequence was then compared to the already existing sequence for cyIIIb, and a restriction map search performed to find discernible differences between cyIIIa, cyIIIb, and cyIIIc.

Materials and Methods

The 3' noncoding region of cyIIIa, cloned into the Pst I site of the plasmid, pUC9, was used for sequencing. A resriction map of the resulting plasmid, p9KIa, is shown in figure one. For accuracy sequencing must be performed in both directions; therefore there were two labeling strategies. To sequence 5' to 3', p9KIa was first cut with Ava II, end-labelled, and then cut again with EcoR I. To sequence in the opposite direction, it was cut first with EcoR I, end-labelled, and cut again with Hind III. In both cases, the radioactive fragment was isolated, and sequencing performed according to Maxam-Gilbert sequencing protocol.[4]

Results

The sequence obtained for the 3' transcribed but untranslated flanking sequence of the sea urchin cyIIIa actin gene is shown in figure two. In figure three, the sequence for cyIIIa is compared to the sequence of that same region of gene cyIIIb. This shows that the sequences for cyIIIa and cyIIIb are very similar throughout the first one hundred and fifty base pairs, showing only 14% divergence, but after that they diverge completely.

In the past, it has been impossible to discern how many genes there were in the cyIII family because there were no known restriction map differences. All three genes had an Ava II site at their 3' end. The difference between cyIIIb and the other cyIII genes is that cyIIIb does not have an internal Rsa I site in its 3' flanking region. When the restriction maps of cyIIIa and cyIIIb were compared, it was noted that cyIIIb had a Dde I site that cyIIIa did not have. Upon investigation, it was found that cyIIIc also had this enzyme site. These restriction site differences are shown in figure four.

At this point, then, all of the genes in the cyIII family can be distinguished. Further comparison of the restriction maps of twenty-seven individual cyIII cDNA isolates will determine which gene(s) gives rise to the major embryonic transcript.

Conclusion

In conclusion, sequencing has revealed restriction site differences between genes cyIII a,b, and c. There are definitely three genes in this family, though they seem to have very similar flanking sequences.

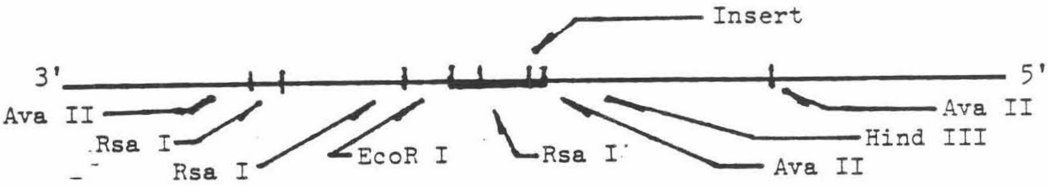

FIGURE 1 Restriction Map of p9KIa. (scale: 1/8" is 100 bp.)

FIGURE 2 The sequence obtained for the 3' transcribed but untranslated region of the cyIIIa actin gene. The ambiguous codons used are: N, any base; P, a purine (G or A); Y, a pyrimidine (C or T). ATAAA is the polyadenylation signal at the end of the transcript.

5'--CAGGPAGTGCZYCTAAACAPCTTGATTTTCTTCNCTTCTNATGAGCAACCCTGATTTGTTTTC

YTCTGTTTTANCYCCTGTTGCACCTNTTPYAAACNATTTGGNTACCGGATGGTNACATGTTATTAGG

ATTTTCTCCTCYNTCTTTATCAAAAAGTGTTCCTTGTATGTCAAACGTGTTCAAGGGTAAATTATAT

ATATTTATTCAGATTTGAAGACAAAATAAAACCTCGCCCPTTATTGATCTCAC--3'

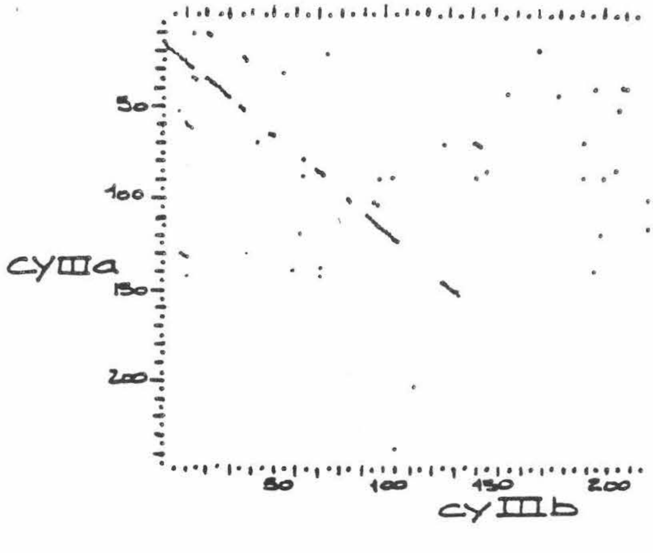

FIGURE 3 Here, the sequence of cyIIIa and cyIIIb are graphically compared. A dot has been placed at those positions where the sequences coincide. If two identical genes are compared in this way, a straight line with a slope of -1 is the result. Obviously then, the sequences of cyIIIa and cyIIIb are very similar through the first 150 bases, at which point the sequences diverge.

FIGURE 4 Below are displayed the restriction site differences between cyIII a,b, and c. The Dde I site disparity was discovered as a direct result of sequencing the gene cyIIIa.

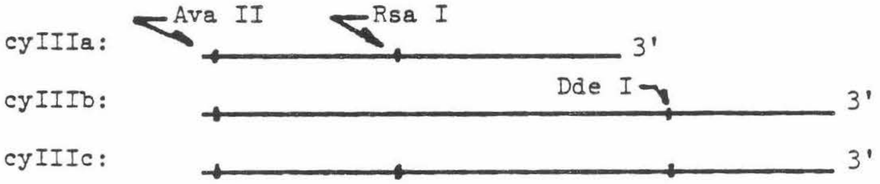

Bibliography

1. Lee J.J., Shott R.J., Rose S.J., Thomas T.L., Britten R.S., and Davidson E.H., (1983), Journal of Molecular Biology, In Press.

2. Shott R.J., Lee J.J., Britten R.J., and Davidson E.H., (1983), Developmental Biology, In Press.

3. Davidson E.H. "Gene Activity in early Development," Academic Press, New York.

4. Maxam A.A., and Gilbert W., in "Methods in Enzymology," Academic Press, New York, pp. 499-560.

Preliminary Report: Conductivity Changes in Carbon Films Induced by Ion Irradiation

Eric Grannan

Sponsor: Dr. Thomas Tombrello

Using the Caltech Van de Graff Tandem Accelerator we have irradiated amorphous carbon films with Flourine ions of 2, 7, and 17 MeV. For all the samples, as the irradiation dose increased the conductivity of the film got larger. The 7 MeV ions were the most effective in raising the conductivity.

Work has been done[1,2] regarding the use of ion irradiation in inducing changes in the conductivity of materials. The conductivity of both polymeric substances and carbon films have been increased by bombardment with 2 MeV Ar^+. Up until now, however, this effect has not been investigated using higher energy ions.

We were visited by Dr. T. Venkatesan of Bell Laboratories in July. He brought thin carbon films evaporated onto Sapphire, and proposed using the Tandem Accelerator to determine how the resistivity change depended on the energy of the bombarding ion. Since Venkatesan was only to be at Caltech for two days we wished to get an overall picture of the energy and dose dependence in order to indicate areas of interest for further research. We used Flourine ions of 2, 7, and 17 MeV. We took a fairly broad range of doses at each energy. The results are shown in Figure 1.

Note that these results are not consistent with the increase in conductivity simply going as the amount of energy deposited in the material. Interestingly the data we have seems to be in very good agreement with sputtering yield experiments. For incident Flourine ions on a variety of materials (such as SO_2, ice, and UF_4) the yield is low for low energy ions, increases rapidly to a maximum at about 7 MeV, and then decreases as the ion energy increased further.[3] This is qualitatively quite similar to our results for conductivity increases, implying that something similar may be going on. This is not really surprising, since although sputtering involves damage produced on the surface, and the conductivity change involves damage in the interior, the mechanism for inflicting the damage could very well be the same. Watson and Tombrello have developed a modified lattice potential model which agreed very well quantitatively with experiments of sputtering yield.[4] Perhaps the same model can be used to explain the damage that causes the increased conductivity.

Since then I have been waiting for Venkatesan to prepare and send us more films so that we can do a more detailed analysis. We finally recieved the films on September 8 and expect to start work with them during the week of September 19-23. We are interested in looking at a more extensive dose dependence going up to higher doses. Also of interest is the energy dependence. It has been hard to do much analysis on the three points we have so far. We wish to take more points, and to go up to higher energies. Another interesting possibility is to see if we can determine an effect due to the charge state of the ion. It has been shown that the sputtering yield has a very strong dependence on the charge state[5], so since a similar mechanism may be involved with conductivity changes, we may see a similar dependence. We will use very thin carbon films, about 50 Å thick, so that the ions will hopefully remain far from charge state equilibrium as they pass through the film. Finally we may vary the ion used to see if there is any effect.

REFERENCES

1. S. R. Forrest, M. L. Kaplan, P. H. Schmidt, T. Venkatesan, and A. J. Lovinger, Appl. Phys. Lett. 41 (1982).
2. T. Venkatesan, R. C. Dynes, B. Wilkens, A. E. White, J. M. Gibson, and R. Hamm, REI Conf. Proc.
3. D. J. LePoire, B. H. Cooper, C. L. Melcher, and T. A. Tombrello, Rad. Eff. 71 (1983).
4. B. H. Cooper and T. A. Tombrello, Rad. Eff. (1983) in press.
5. C. K. Meins, J. E. Griffith, Y. Qiu, M. H. Mendenhall, L. E. Seiberling, and T. A. Tombrello, Rad. Eff. 71 (1983).

Ratio of initial resistivity
to resistivity after irradiation

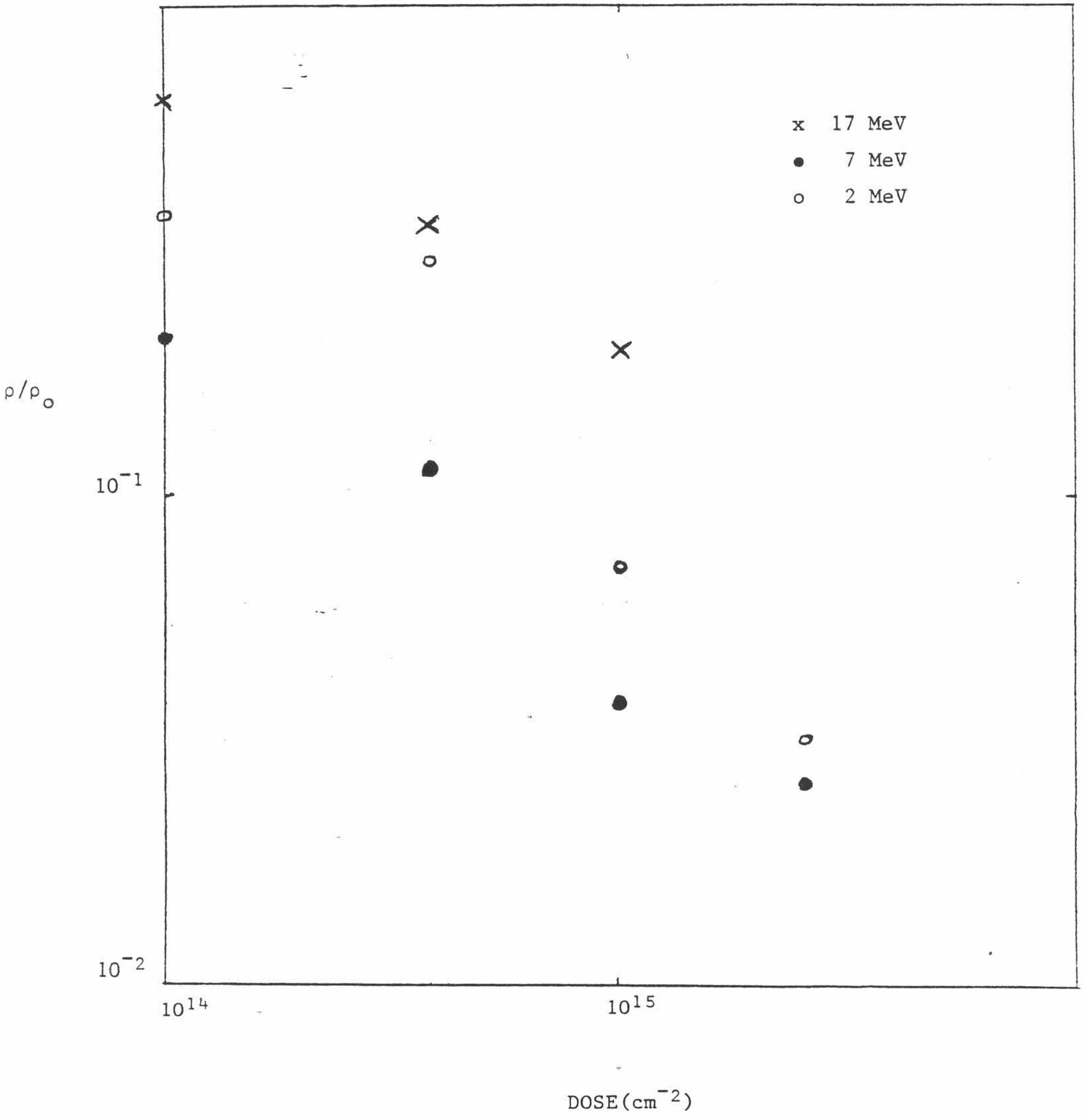

Design and Construction of Screen Based Jet Impaction Fog Collector

Author: Mehrdad Haghi
Faculty Advisor: Professor Richard Flagan

Abstract:

Various Possible designs for a screen based jet impaction fog collector are implemented and tested. A prototype device is constructed for quantitative analysis that uses the aerodynamics of tilted strings to overcome some major device problems.

Introduction:

Recent reports of high acidities in fogs have shown the need for a reliable method of collecting fogwater for chemical analysis. A good fog sampler must be able to selectively separate fog droplets (diam.$\geq 1\mu m$) from the ambient aerosol, collect a relatively large amount of water in a short enough time so that fog characteristics do not change significantly during sampling, and do so while keeping contamination and sampling biases to a minimum. Many samplers have been constructed to date all of which collect fog particles using inertial impaction, through which airstreams are made to navigate an impaction surface; the smaller particles follow the airstreams while the larger particles, due to their higher inertia, impact on the surface and are collected[1]. The current CIT rotating arm collector[2] has at best, a lower cut off of $8\mu m$, and is somewhat cumbersome to operate, requiring constant supervision. The purpose of this project was to create a collector with better size resolution which was also easier to handle, and more readily lent itself to automation. Specifically, an inertial impaction system was to be selected, and a device based on it constructed and optimized through laboratory tests.

Design and Construction:

Of the various possible choices for impaction systems (jet impactors, cyclones, and screen or grid impactors) the screen impactor was selected for several reasons. First, very thorough theoretical studeies of such systems existed in the literature. Second, screen impactors are probably the easiest of these systems to construct. After some preliminary study it was decided to build a see-through, highly modular device, so that many possible designs could be easily tested, their impaction and collection characteristics being directly observable.

The final design for the prototype to be used in quantitative calibration experiments involves eight rows of thirty 11 mil teflon strings, tilted about 38 degrees from the vertical with the bottom ends being downstream of the top ends, in a 3 by 3 inch pipe. The string is threaded through holes in the pipe wall above, and holes in a tilted teflon sheet below. The choice of Teflon for the strings was necessitated by the fact that the collector must be chemically inert. This also meant, however, that the strings could not be glued in since teflon is impossible to glue, and had to be threaded into holes in the device. The bottom teflon sheet both insures against contamination in the collection of the water that has come down, and through the teflon-teflon contact prevents the water from leaking through the thread holes, since teflon is extremely hydrophobic.

This assembly is connected to a high volume air pump (flow rate of about 2.4 m^3/min) through a section of round pipe stuffed with plastic starws to straighten the flow and insure a uniform flow field at the screen.

Satisfaction of Major Criteria:

I) High Sampling Rate:

Two major factors are involved in acheiving high rates of liquid sampling. The first is the efficiency with which water is extracted from the fog, which has to do with the string density in the device. This is the reason behind the eight banks: some 250 strings needed to be in the filter to properly extract the water, but drilling such small holes at a density of 80 per inch was next to impossible, so eight banks were drilled at 10 holes per inch. The second major factor is the sampling rate. For the standard inorganic analysis routinely carried out in the CIT Fog Program at least 10 ml of sample is needed.[3] For a typical fog liquid water content of 0.2 g/m^3, a sampling rate of about 2 m^3/min is required to collect 10 ml in 30 minutes. The current prototype samples between 2 and 2.4 m^3/min with the current pump. However, pumps with much higher flow rates are available, and the collector could easily be made to sample at several times this rate. The problem with doing this in previous string collectors has been that to sample more air, one must either increase the flow velocity past the strings or the screen area, and in previous collectors which have had their strings perpendicular to the flow and have depended on gravity to pull the impacted particles down, the former has led to particles flying off the strings, and the latter in particles evaporating, becoming contaminated or having their chemistry altered otherwise during the long, slow decent. The tilt in the strings in the current design uses the airflow to push the impacted particles down the strings, at about the angle the water droplets would fly off verticle strings. Thus losses due to reintrainment are minimized allowing much higher flow velocities. Furthermore, the particles are quickly removed from the airstream thus minimizing contamination.

II) Size Cut:

The size cut of a screen impactor (ie the smallest particle diam.

impacted with >50% efficiency) is a function of string diameter and flow velocity. For a flow rate of 2.4 m^3/min through a 3 by 3 inch pipe, with string diameter 11 mils, an impactor with its strings perpendicular to the flow would have a size cut of 3.4μm. It is not yet known for certain what the effect of tilting the strings is on the size cut, but preliminary analysis based on potential flow solutions seems to indicate that only the perpendicular component of the flow contributes to impaction(that is, flow perpendicular to the strings), in which case the estimated size cut for the current device would be 4μm. There is another possible source of uncertainty here though: theoretical studies ignore the size of the string in their considerations as much larger than the size of the droplets, but 11 mil string is only about 3 times the diameter af the largest fog droplets. How significant this is will be determined when the device is calibrated. Possible errors in the size cut due to fluctuations of ambient winds should be small since the prototype's duct velocity is probably much larger than most ambient winds(duct vel. aprox. 6.7 m/sec). Measures like regulating the flow to be constant using a flow meter inside the duct to regulate the motor may be taken later, though.

III) Anisokinetic Sampling Error:

Some sampling bias can be caused by the mismatch between ambient and duct air velocities and flow directions, since such a mismatch would cause the streamlines to bend on approach to the duct discriminating against heavy particles through the same inertial processes used to collect them. The extent of this error is determined by the angle between the duct and ambient wind, the ratio of ambient to duct wind velocities and an inlet Stokes number[4]. The directionality problem can be overcome by placing the device on a rotating platform, and though space does not permit detailed discussion, the device geometry is such that with at most minor modification the inlet Stokes number can be lowered to about 1 for the largest particles desired, so that even if ambient winds become significant compared to the duct velocity, the sampling error will remain below 10%.

IV) Thermodynamic Effects:

Affects due to thermodynamic changes caused by the restriction of the flow are kept to a minimum by having the screen as close to the front of the duct as possible. In the current prototype the strings start just 3/8 inch from the front of the duct. The exact extent of these effects is yet to be guaged.

V) Contamination:

If a particle stays on the impaction surface and exposed to the airflow long after it has impacted, it may be contaminated, or its chemical structure or concentration altered through evaporation or condensation. The current prototype uses the airflow itself to push collected particles out of the stream. In preliminary tests particles were cleared of the string about one minute after impaction. On the perpendicular string experiment this time was about five times longer. Experiments were done to see if vibrating the strings helped rapid collection, but the vibrations proved less efficient at moving small particles down the strings and more efficient at shaking large particles clean off the strings than had been hoped for, so this idea was abandoned.

Conclusions:

An impaction system was selected, experiments conducted to optimize device design and a prototype fog collector constructed for quantitative analysis. The prototype should be capable of collecting sufficient fogwater samples in sufficiently short time spans to be a useful field device. Furthermore, in addition to keeping contamination and sampling biases to a minimum, the device is highly portable and should lend itself easily to automation.

REFERENCES

1 Houghton and Radford(1938):"On the Measurement of Drop Size and Liquid Water Content in Fogs and Clouds", Pap.Phys.Ocean. Met. Mass. Inst. Tech. and Woods Hole Ocean. Inst., 6,No.4

May,K.R.(1961):"Fog-droplet sampling using a modified impactor technique",Quart. J. Roy. Met. Soc.,87,535-548

Katz,U.(1980):"A droplet impactor to collect liquid water from laboratory clouds for chemical analysis",Communications de la 8eme Conference sur la Physique des Nuage,Clermont-Ferrand, France,15-19 July 1980

Okita,T.(1968):"Concentration of sulfate and other inorganic materials in fog and cloud water and in aerosol",J.Met.Soc. Japan,46,120-126

Brewer et al(1983):"Chemistry of mist and fog from the Los Angeles urban area, Atmos. Environ. (in press)

*Freidlander,S.K.(1977):Smoke, Dust and Haze,Wiley-Interscience, New York

2 Jacob et al(1983):"Design and calibration of a rotating arm collector for ambient fog sampling",4th International Conference on Perciþitation Scavenging, Dry Deposition, and Resuspension, Santa Monica,CA,Dec.1982, Elsevier, Netherlands and paper currently being written

3 Jacob et al(1983):paper currently being written

4 Watson,H.H.(1954):"Errors due to anisokinetic sampling of aerosols",Ind. Hyg. Quart.,March,21-25

*Freidlander,S.K.(1977): ibid

---

* A usefull general referance concerning almost all discussed in this paper.

CATHERINE HAYES

NO REPORT SUBMITTED

MATHEMATICAL REPRESENTATIONS OF TRANSFORMATIONS OF THE VISUAL FIELD IN THE VISUAL PATHWAY

John Houde
Faculty Sponsor: D. C. VanEssen

Abstract:

The representation of the visual field undergoes major transformations at successive stages of the visual pathway. 2-dimensional geometrical models, based on mathematical descriptions of the visual representation are shown to be a useful way of analyzing these transformations.

Introduction:

In the brain, the visual field is represented in an orderly fashion at each stage of the visual pathway. The transformation of the visual field is highly non-linear, involving a much greater emphasis on central vision than on peripheral vision. The general appearance of this transformation can be seen in fig. 1, which is taken from a paper by Van Essen et al. The standard way this transformation has been mathematically described has been to measure cortical magnification of unit areas or lengths of the visual field as a function of visual field coordinates. The various results of this measure, which is called a cortical magnification factor, suggested that it is proportional to the inverse of radial distance from the fovea and independent of angle in the visual field. Schwartz (1980) and Fischer (1973) realized that this implied the transformation can be represented as a particular analytic function - the complex logarithm of the form f=log(A+z), where A is a real constant and z is a complex variable of the form z=r*exp(i*th),where r and th are polar coordinates in the visual field. Recent evidence (see fig. 1.), however, has shown that the transformation is not precisely conformal, making the complex logarithm description of it inaccurate. Better descriptions of cortical magnification factors were needed. The purpose of my project has been to use geometric transformations to derive more precise expressions for cortical magnification than previously possible.

Presentation and Discussion of Results:

The basic method used for investigating the nature of the mapping transformation was to use a computer (in this case a PDP 11/34) to generate a map of a visual area from mathematical descriptions of the cortical magnification factors. Since there magnification factors are approximately constant over a tiny region an array of points representing the map was constructed in the following iterative manner. Starting at the fovea, the first point in the array, the second point is calculated by moving along the horizontal meridian of the map by an amount proportional to the radial component of the cortical magnification factor at the fovea (fig. 2.). This initial direction is known because the representation of the horizontal meridian of the visual field is also horizontal. The third point is calculated as the vertex of the triangle whose baseline is on the horizontal line from the fovea to the second point and whose two unknown sides are proportional to the radial and angular components of the magnification factor (fig. 2.). This process is then repeated with the third point taking the place of the second and so on, until 180 degrees of the first angular contour in the visual field are done (fig. 3.). The next point P(n) is calculated by moving along the horizontal meridian by an amount proportional to the radial component of the magnification factor at the second point. The next point P(n+1) is calculated by considering it, the last horizontal horizontal meridian point P(n), the second point, and the third point to form a quadrilateral compartment whose sides S1 and S2 (see fig. 4.) are proportional to the radial and angular components of the magnification factor at P(n). In a similar fashion, the rest of the points in the second and succeeding angular contours in the map are calculated (fig. 5.).

The first approach taken in attempting to define the cortical magnification factor was to separately define an angular magnification and a radial magnification factor. Using these factors, the first maps were made. However, this method proved incapable of handling the extreme stretching of compartments in the map that result from trying to approximate the experimentally derived map shown in fig. 1. The reason for this was because it was difficult to maintain the same area of a compartment when the radial and angular sides of it were being independently stretched. This problem created edge distortions of the map (fig. 6.). The best derived formulas for the radial and angular magnification factors were

$$M(\text{angular}) = 10\,Anis/(1+r) \quad \text{and} \quad M(\text{radial}) = 10/(1+r)$$

where r is the radial distance from the fovea and

$$Anis = 1+.1\cos(th \times r/(1+r))$$

which is the factor that stretches the compartments. Both M(radial) and M(angular) have forms which are similar to the derivative of the complex logarithm.

As a result of finding great problems with the first approach, a second approach was introduced in which an areal magnification factor was defined along with its radial component. In this method, the areal magnification factor defines what the area of each compartment will be and the formula for its radial component is adjusted to achieve the desired stretching of the compartments. The angular component is automatically adjusted to maintain the correct area for each compartment. This method was much more successful. By knowing what the area of each compartment would be before being stretched it became easier to predict what would happen to the map when a certain stretching function was imposed upon the radial magnification factor (fig. 7.). The best derived formulas for the areal magnification factor and its radial component again reflect the basically logarithmic nature of the mapping:

$$\mathrm{M(areal)} = 100/(1+r)^2 \qquad \text{Radial Comp.} = \mathrm{F(radial)} \cdot 10/(1+r)$$

where r again is radial distance in the visual field from the fovea and F(radial) is a complicated stretching function.

Conclusions:

From the results of this project it has been verified that the transformation of the visual field is generally logarithmic but that stretching functions are needed to make a more complete description. The areal magnification factor approach is probably the best way of describing the transformation, not only because it provides a flexible system for predictably changing the shape of the map, but also because it expresses the main feature of the transformation - that an area of the visual field is magnified when it is mapped to a visual area. The descriptions of the components of the areal magnification factor are needed only to make the topography of the map approximate that of the actual data.

An important application of the results of this project that has developed is the back-transformation of occular dominance stripes from visual areas to the visual field. Each visual area of the brain receives input from both eyes and the layout of neurons in one which receive input from one eye interlaces with the corresponding layout of those which receive input from the other eye to form a striped pattern on the surface of the visual area. With a good mathematical description of the transformation of the visual field onto a visual area, these stripes can be accurately mapped back to the visual field by inverting the transformation. The resulting distribution of stripes in the visual field can then be accurately examined.

Bibliography:

Fischer B. (1973) Overlap of receptive field centers and representation of the visual field in the cat´s optic tract. *Vision Research* 13, 2113- 2120.

Schwartz E. L. (1980) Computational anatomy and functional architecture of striate cortex: a spatial mapping approach to perceptual coding. *Vision Research* 20, 645-669.

Van Essen D. C., Newsome W. T. and Maunsell J. H. R. (1983) The visual field representation in striate cortex of the macaque monkey: asymmetries, anisotropies, and individual variability.

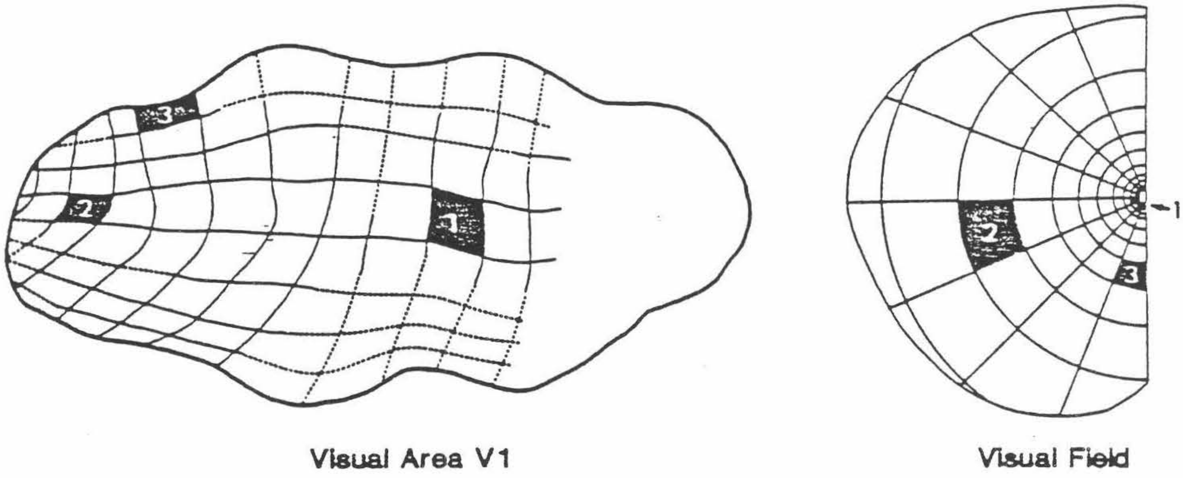

Fig. 1.

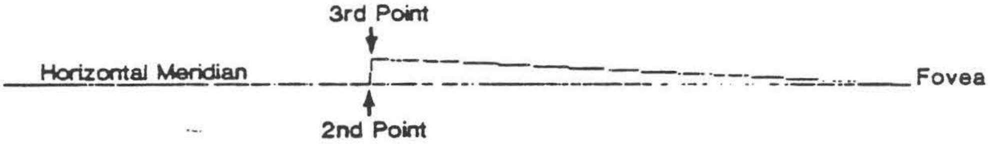

Fig. 2.

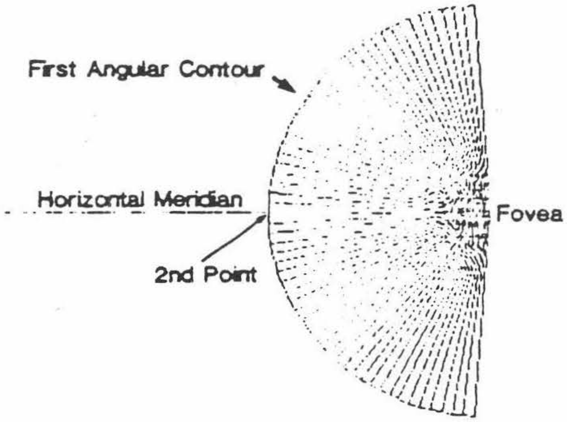

Fig. 3.

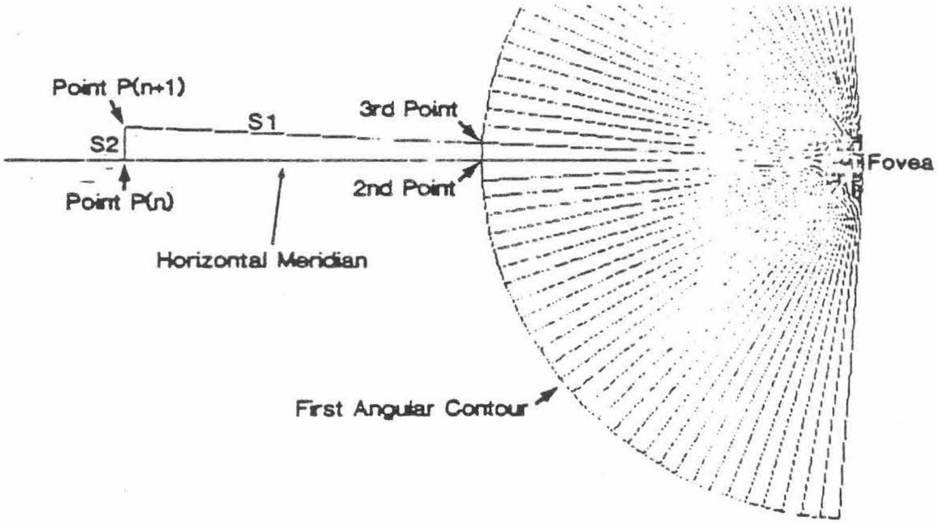
Point P(n+1)
S1
3rd Point
S2
Fovea
Point P(n)
2nd Point
Horizontal Meridian
First Angular Contour

Fig. 4.

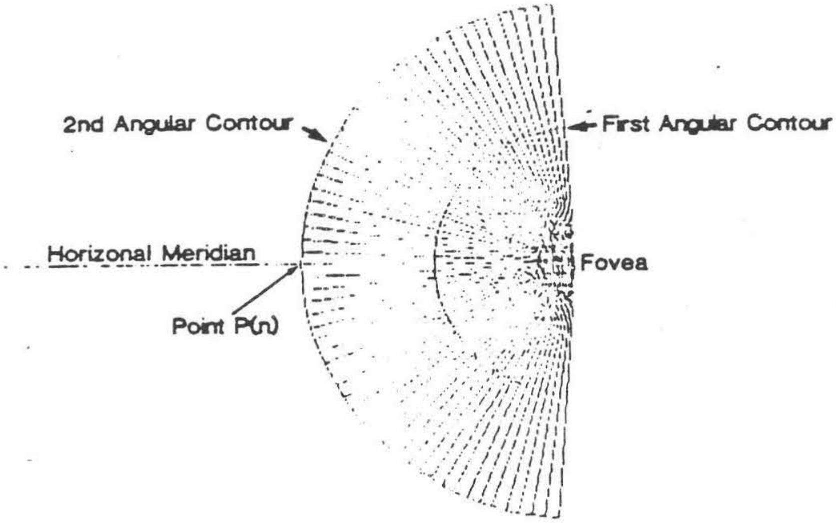
2nd Angular Contour
First Angular Contour
Horizonal Meridian
Fovea
Point P(n)

Fig. 5.

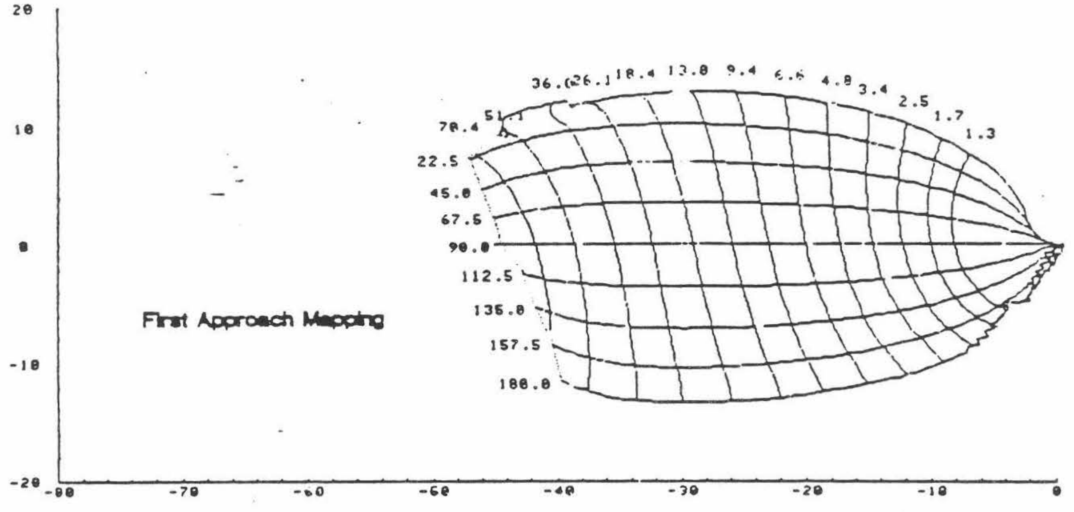
20
10
0
-10
-20
-80
-70
-60
-50
-40
-30
-20
-10
0
36.0
26.1
18.4
13.8
9.4
6.6
4.8
3.4
2.5
1.7
1.3
51.1
70.4
22.5
45.0
67.5
90.0
112.5
135.0
157.5
180.0
First Approach Mapping

Fig. 6.

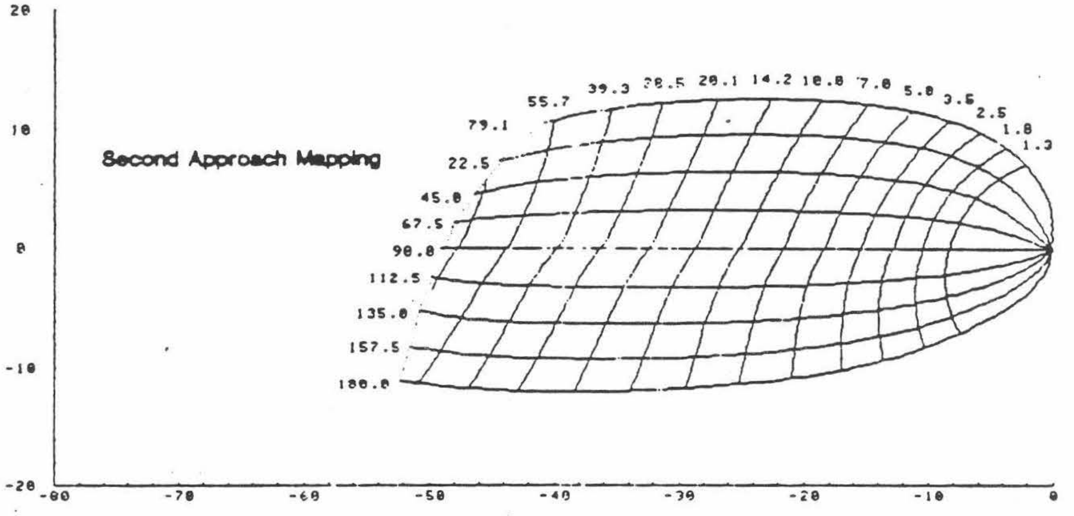
20
10
0
-10
-20
-80
-70
-60
-50
-40
-30
-20
-10
0
55.7
39.3
28.5
20.1
14.2
10.8
7.0
5.0
3.5
2.5
1.8
1.3
79.1
Second Approach Mapping
22.5
45.0
67.5
90.0
112.5
135.0
157.5
180.0

Fig. 7.

TESTING OF THE CLUSTER MODEL APPROACH TO DESORPTION PROBLEMS

by Kenneth Hui

(Faculty Sponsor : William A. Goddard III)

ABSTRACT

The Cluster approach to calculating equilibrium configurations of adsobates on surface and for calculating desorption rates is developed and tested. The maximun practical cluster size which could be examined is about 100 sites. It is found that this size restriction severely limits the applicability of the cluster method and consequently its usefulness in desorption problems is highly questionable. We conclude that Monte Carlo methods provide a more fruitful approach.

Introduction

Redondo *et al.* [1] used the cluster method to calculate the coverage dependence of the desorption rate of Xe on W(111). Since little is known about the accuracy of such cluster calculations, we decided to do an extensive testing of the cluster model and refine it if possible. We applied the cluster method used by Redondo *et al.* [1], and several improved versions of it, to the half coverage square lattice gas with nearest neighbor (nn) coupling. This problem is equivalent to the Ising model [2] with no external field by an exact transformation [3]. Onsager provided the exact analytic solution to this Ising model in 1944 [4]. Thus we are able to compare our cluster results with the exact results. In the following sections we will discuss only the most sophisticated version of the cluster models we have tested. (Which gives the best results).

Results and Discussion

In the square lattice gas model, there are well defined adsorption sites which form an infinite 2 dimensional square lattice (fig. 1). The energy for a particular state of the system consist of the two parts , the interaction between the adsorbed particles (adparticles) and the interaction between the surface atoms and the adparticles . Since the total interaction energy between the surface and the adparticles is a constant for a given coverage, we will take it as zero. The energy for the state i of the system then becomes

$$E_i = \frac{\varepsilon}{2} \sum_j \{ \text{ no. of nn bond for adparticle j } \} \qquad (1)$$

where ε is the nn interaction energy between two adparticles and the summation is over all the adparticles. The thermal average energy of the system is

$$< E > = \frac{\sum_i E_i \exp[-E_i\beta]}{\sum_i \exp[-E_i\beta]} \qquad (2)$$

where $\beta=\frac{1}{k_b T}$. Eqn (2) can be evaluated analytically for the case ϑ = 0.5 where ϑ is the coverage.

In our cluster model, we approximate the infinite system by two 6x6 sites clusters (i.e. 36 absorption sites for each cluster). Each cluster (cluster A and cluster B) is surrounded by 24 mean field sites (fig. 2). Each mean field site for cluster A (B) is assumed to have ϑ_a (ϑ_b) adparticles, where ϑ_a (ϑ_b) is the mean field coverage for cluster A (B). Therefore, M_a, the number of mean field adparticles for cluster A, is equals to $24\vartheta_a$ and similarly for cluster B. The energy for a given state of the system is the sum of total nn interaction energy between the adparticles inside the clusters and half the total nn interaction energy between the cluster and mean field adparticles. To mimic a infinite system with coverage $\vartheta_\infty = 0.5$, we introduce the following constraints to our clusters :

$$N_A + N_B = \vartheta_\infty \times 2 \times 36 = 36 \tag{3.1}$$

$$M_A + M_B = \vartheta_\infty \times 2 \times 24 = 24 \tag{3.2}$$

The thermal average energy of the system is then

$$<E> = \frac{\sum_{N_A=0}^{36} \{ \sum_{M_A=0}^{24} (\sum_i E_A(i,M_A) e^{-E_A(i,M_A)\beta} + \sum_j E_B(j,M_B) e^{-E_B(j,M_B)\beta}) \}}{Z} \tag{4}$$

where Z is the partition function and $E_A(i,M_A)$ is the energy of cluster A in state i, which depends on M_A. Note that the possible states of cluster A depend on N_A. The notation for cluster B is similar to that of cluster A. To carry out the summation in Eqn (4) as it stands by generating all the possible states of the clusters is not possible even with high speed computers. Instead we would like to express the energy states of the 6x6 cluster in terms of the energy states of some 3x3 clusters which is more manageble. Or in other words, we want to reduce the 6x6 cluster to a number of 3x3 clusters. This could be done with the following approximation.

The 6x6 cluster is first divided into four 3x3 clusters (reduced clusters). The energy of the 6x6 cluster for a given state is just the sum of the energies of the reduced clusters. Consider the energy of reduced cluster **1** in fig. 3. The energy depends on (i) the configuration of the adparticles in reduced cluster **1** (ii) the mean field coverage and (iii) the configuration of the adparticles in the 6 sites in reduced cluster **2** and **3** which can have nn bonds with the adparticles in reduced cluster **1** . We apply the mean field approximation to (iii). It is assumed that each of the

6 sites in (iii) has ϑ_1 adparticles where

$$\vartheta_1 = \frac{N^{2+3+4}_{r.c.}}{27} \tag{5}$$

Here $N^{2+3+4}_{r.c.}$ is the number of adparticles in reduced cluster 2, 3 and 4 This simplifies the calculation tremendously since now (iii) depends only on the *number* $N^{2+3+4}_{r.c.}$ but not on *configuration* of those $N^{2+3+4}_{r.c.}$ adparticles. The average energy of a 6x6 cluster with N_{6x6} adparticles and a mean field coverage of ϑ_{6x6} can now be written as

$$< E_{6x6}(N_{6x6}, \vartheta_{6x6}) > = \frac{\sum \{ \prod_{i=1}^{4} Z_i(\vartheta_{6x6}, \vec{N}) \} \{ \sum_{j=1}^{4} < E^{j}_{r.c.}(\vartheta_{6x6}, \vec{N}) > \}}{\sum \{ \prod_{i=1}^{4} Z_i(\vartheta_{6x6}, \vec{N}) \}} \tag{6}$$

where

$$\vec{N} = (N^1_{r.c.}, N^2_{r.c.}, N^3_{r.c.}, N^4_{r.c.}) \tag{6a}$$

and the summation is over all $\vec{N}$ which satisfy

$$N^1_{r.c.} + N^2_{r.c.} + N^3_{r.c.} + N^4_{r.c.} = N_{6x6} \tag{6b}$$

Here Z_i is the partition function for reduced cluster i. Eqn (4) can then be rewritten as

$$< E > =$$

$$\frac{\sum_{N_A=0}^{36} \{ \sum_{M_A=0}^{24} (< E_{6x6}(N_A, \vartheta_A) > + < E_{6x6}(N_B, \vartheta_B) >) \, e^{-\{< E_{6x6}(N_A, \vartheta_A) > + < E_{6x6}(N_B, \vartheta_B) > \} \beta} \}}{\mathbf{Z}} \tag{7}$$

with $E_{6x6}(N_A, \vartheta_A)$ given by Eqn (6). Eqn (7) can now be evaluated numerically.

By similar arguments, we can also obtain an simplified equation for the specific heat of the clusters. We have evaluated Eqn (7) and also the specific heat numerically and the results are shown in fig. 4 and 5 respectively. The exact results and the results from a calculation using the cluster method of Redondo *et al.* are also included in fig. 4 and 5 for comparison. From fig. 4, we see that the energies from our cluster calculations deviate from the exact results by 6% to 10%, the error increasing with decreasing temperature. This is due to the larger correlation length at lower temperature. Our calculations shows a transition temperature at $\frac{T_c}{\varepsilon}$ = 0.55 while Onsager solution gives 0.57. Although this is a significant improvement over results obtained by the cluster method of Redondo *et al*, the error is still in general too large (As one can get a much better result by Monte Carlo methods [5,6]).

Another disadvantage of our cluster method is that for most lattice structures (for example, the hexegonal lattice) it is not possible to reduce a large cluster into smaller clusters unless additional approximations are made. This greatly limits the applicability of this method.

Conclusion

The cluster method has been tested and the results from the cluster calculation is compared with the exact results. In general our results deviate from the exact results by about 8%. Since it is possible to get much better results and greater flexibility by Monte Carlo methods, we now believe that at this time cluster method is not a good approach to the desorption problem.

References

1. A. Redondo, Y. Zeiri and W.A. Goddard III, Surf Sci., submitted for publication.
2. E. Ising, *Z. Physik.* **31,** 253 (1925)
3. T.D. Lee and C.N. Yang, *Phys. Rev.* **87,** 410 (1952)
4. L. Onsnger, *Phys. Rev.* **65,** 117 (1944)
5. For example, see (a) D.P. Landau, *Phys. Rev.* **27,** 5604 (1983) ; (b) D.P. Landau, *Phys. Rev.* **21,** 1285 (1980)
6. For a review on Monte Carlo methods, see K. Binder, in *Monte Carlo Methods in Statistical Physics*, edited by K. Binder (Springer,Berlin,1979).

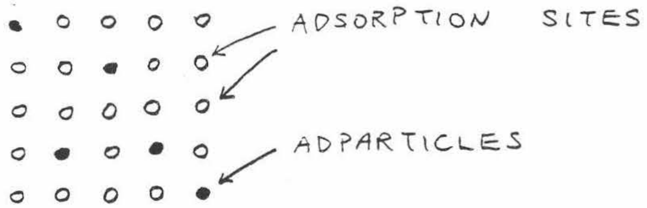

FIG 1

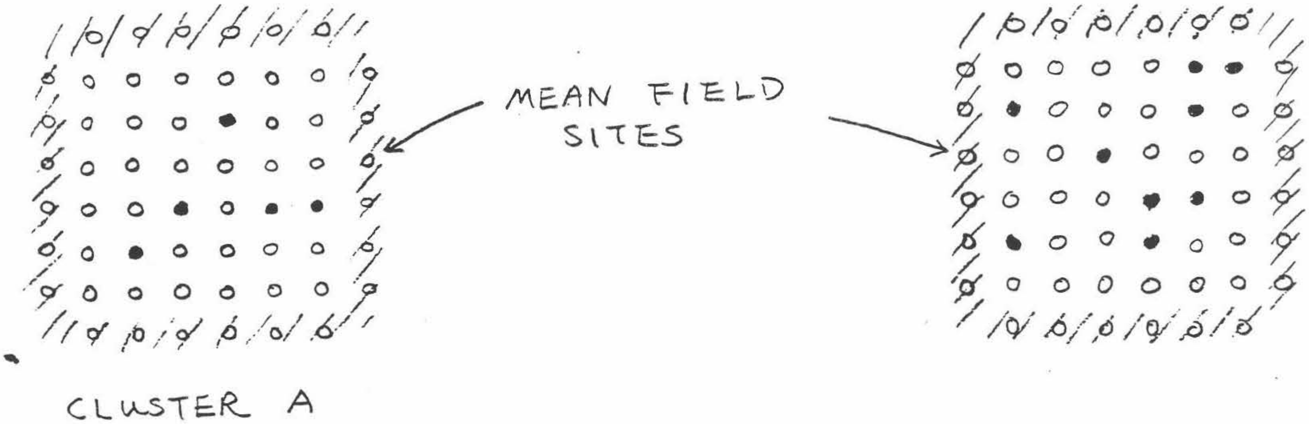

FIG 2

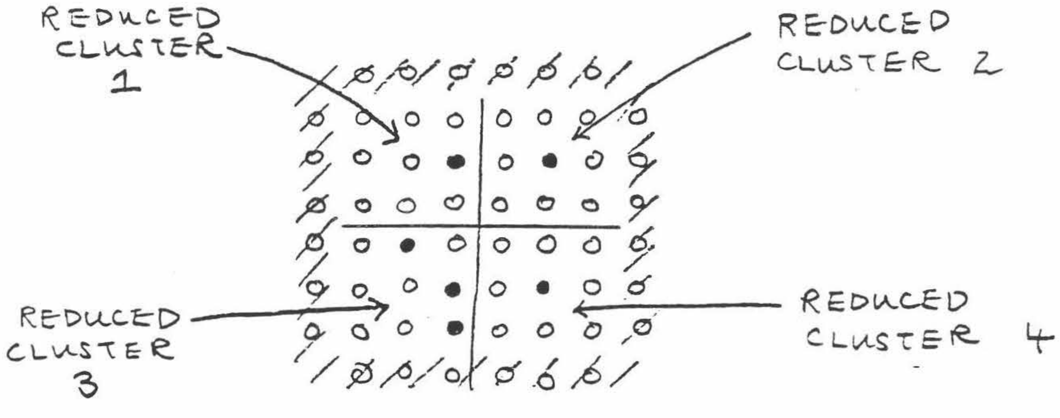

FIG 3

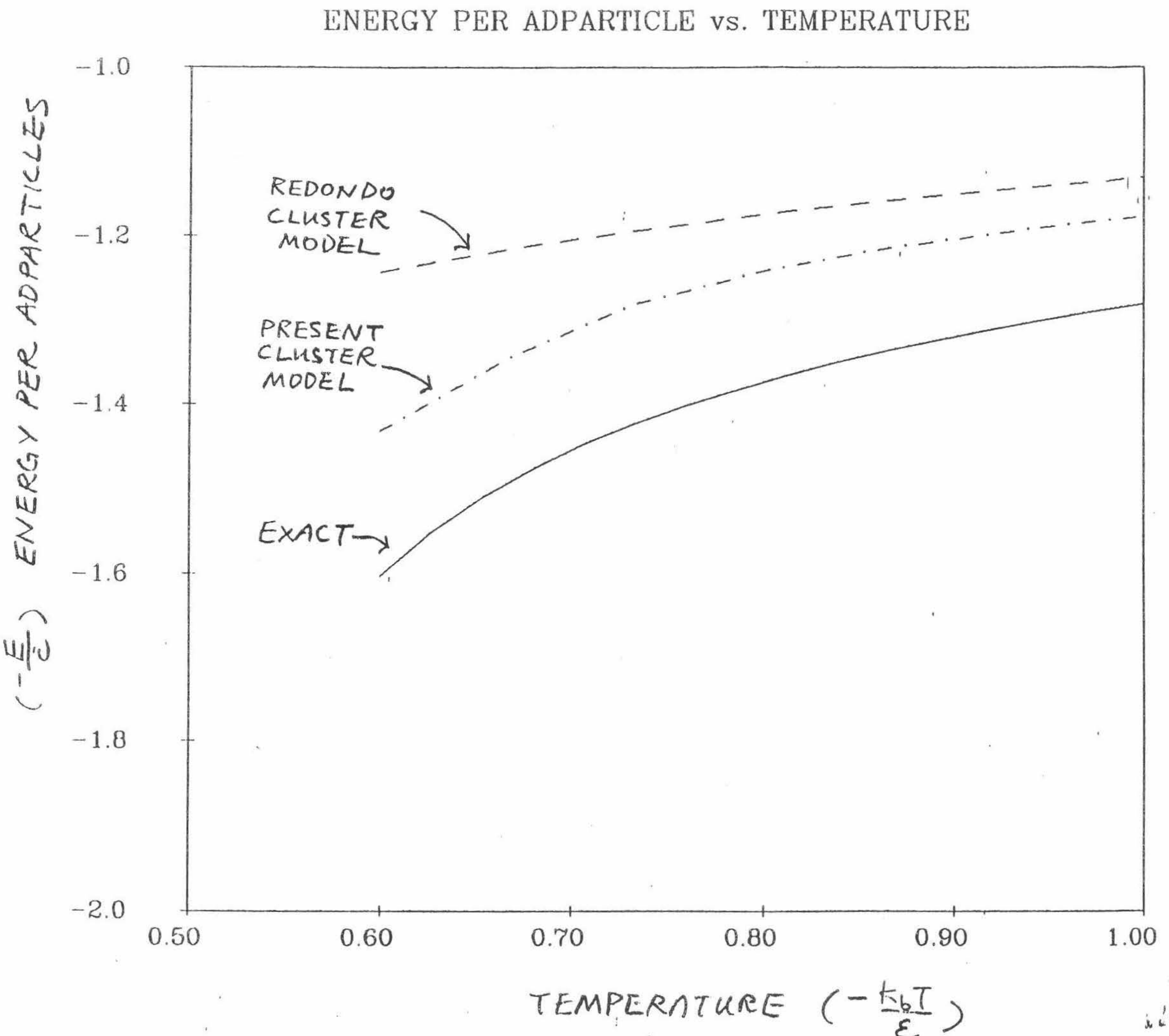
ENERGY PER ADPARTICLE vs. TEMPERATURE
ENERGY PER ADPARTICLES ($-\frac{E}{\varepsilon}$)
−1.0
−1.2
−1.4
−1.6
−1.8
−2.0
0.50
0.60
0.70
0.80
0.90
1.00
TEMPERATURE ($-\frac{k_b T}{\varepsilon}$)
REDONDO CLUSTER MODEL
PRESENT CLUSTER MODEL
EXACT

FIG 4

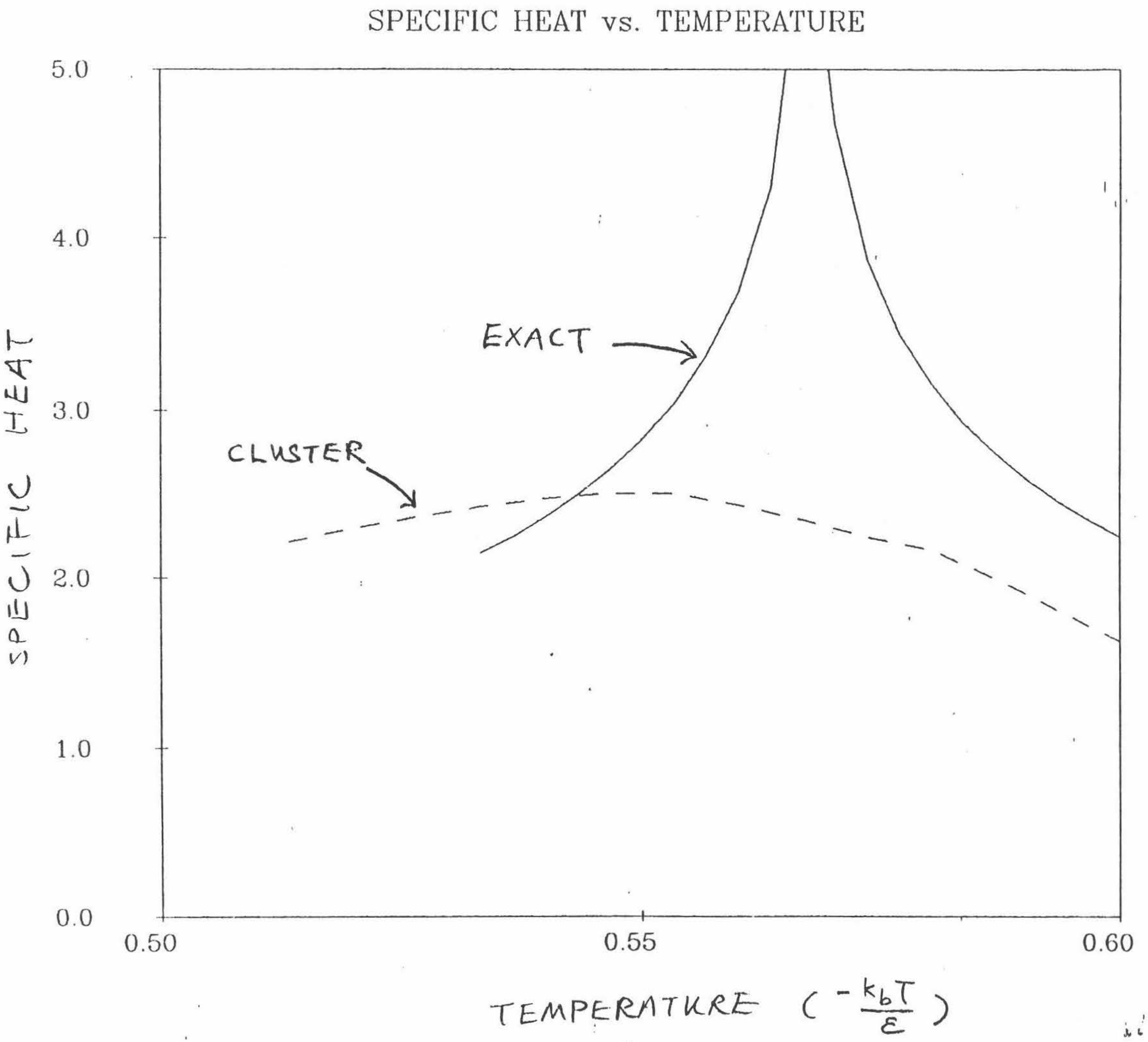
SPECIFIC HEAT vs. TEMPERATURE
5.0
4.0
3.0
2.0
1.0
0.0
SPECIFIC HEAT
EXACT
CLUSTER
0.50
0.55
0.60
TEMPERATURE ($-\frac{k_b T}{\varepsilon}$)

FIG 5

HEMISPHERIC DIFFERENCES IN PREFERENCE AND RESPONSE IN SPLIT-BRAIN MONKEYS

CATHERINE K. IFUNE

Div. of Biology, California Institute of Technology

Charles R. Hamilton and Betty A. Vermeire
Advisors

Abstract- Eight split-brain monkeys, four males and four females, were tested for hemispheric differences in preference and response to color videotape representations of animals, monkeys, people, and scenery. The number of facial expressions elicited from the right hemisphere was significantly greater than the number elicited from the left hemisphere. An almost significantly greater right hemisphere preference was found. In a comparison between monocular and binocular viewing, the right hemisphere showed a significantly greater preference than both hemispheres combined while the preference of the left hemisphere did not significantly differ from the preference of the combined hemispheres.

INTRODUCTION

It is well established that hemispheric asymmetries exist in the human brain. The left side is considered to be sequential, analytical, and linguistic in nature while the right is thought to be more holistic and spatially oriented. Impracticalities in using humans in some aspects of experimentation has provided the impetus behind the search for brain lateralization in non-human primates.

Results of experiments indicate a right hemisphere superiority in humans for face recognition and for the processing of emotional stimuli [1,2]. Can such asymmetries be found in the brain of the monkey? Experiments involving facial discrimination and recognition in monkeys have found no overall significant advantage in learning with either the left or right hemisphere. However, a significant right hemisphere advantage for facial discriminations was found in female monkeys [3]. Other studies have indicated an overall greater preference by the monkey's left hemisphere in viewing colored slides in absence of differential reward [4].

Research carried out by Plimpton, Schwartz, and Rosenblum have shown that differential responses from monkeys are elicited by videotapes of conspecific males and females [5]. The use of color videotape in the presentation of stimuli allows the control and repeatability of the stimuli while ensuring a relatively high level of responsiveness [5]. In this experiment, the use of videotape has been adapted to measure differences in preference and response between the two hemispheres of the monkey brain. The behavioral response and preference of each hemisphere was tested with a selection of videotape segments chosen to elicit a variety of responses. In this way, a comparison can be made between hemispheres of similar genetic and experimental background.

METHODS

The monkeys used in this experiment were Rhesus monkeys (*Macaca mulatta*) and all had undergone a midline division of the optic chiasm, corpus callosum and the anterior and hippocampal commissures. With this commissurotomy, information recieved by one hemisphere cannot be transferred to the other hemisphere. For example, information from the right eye goes only to the right hemisphere and similarly information from the left eye goes only to the left hemisphere. Therefore by presenting visual stimuli to one eye alone and then to the other eye, a comparison between the two hemispheres can be made (see illust).

The visual stimuli shown to the monkeys consisted of two tape sets, A and B. Each tape set was composed of two parts. The first part consisted of ten 1.5 minute segments and the second part was identical to the first part except the ordering of the segments was reversed. The first ten segments for tape sets A and B are listed below:

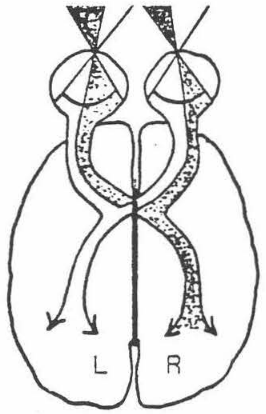

A SPLIT BRAIN

TAPE SET A

Jill (monkey)
Frisbee game
Dash (monkey)
empty cage
rhinoceros
B. Turpin
mandrill
scenery
cartoon
gorillas

TAPE SET B

flamingoes
Gigi (monkey)
empty cage
P. Siracusa and B. Mapes
snake
window view
tigers
cartoon
Nike & Frey (monkeys)
B. Vermeire

Each monkey was tested monocularly and binocularly in a design which balanced sex, the tape set viewed, and binocular-monocular testing order. The following chart presents the testing scheme:

MONKEYS		
BRN (F)	BV (A)	MV (B) [L,R]
EDN (M)	BV (A)	MV (B) [R,L]
ETH (F)	MV (B) [R,L]	BV (A)
ZOR (M)	MV (B) [L,R]	BV (A)
HSH (F)	MV (A) [L,R]	BV (B)
KEF (M)	MV (A) [R,L]	BV (B)
LME (M)	BV (B)	MV (A) [L,R]
YAM (F)	BV (B)	MV (A) [R,L]

BV- binocular viewing
MV- monocular viewing
[R,L]- tested with right eye then left eye
(A)- tape set A
(B)- tape set B

RESULTS

The numbers of responses elicited from each hemisphere are given in Table 1 and graphed in Figure 1 for each monkey. Responses are defined as facial expressions such as lip-smacking, a form of greeting or an appeasing, submissive display; threats, an aggressive or fearful display; fear grimacing, a fearful or submissive response; and yawning, displayed in tense or stressful situations [6]. The dominance index (DI) defined as (L-R)/(L+R), where L is the total number of responses for the left hemisphere and R is the total number for the right, can also be found in Table 1 for each monkey.

MONKEYS	LEFT HEMISPHERE	RIGHT HEMISPHERE	DI
BRN	15	15	0
EDN	7	11	-22.22
ETH	2	16	-77.78
ZOR	11	9	+10.00
HSH	0	28	-100
KEF	0	2	-100
LME	0	0	0
YAM	0	11	-100

(TABLE I)

For each monkey, the total number of responses for each hemisphere and the dominance index (DI)

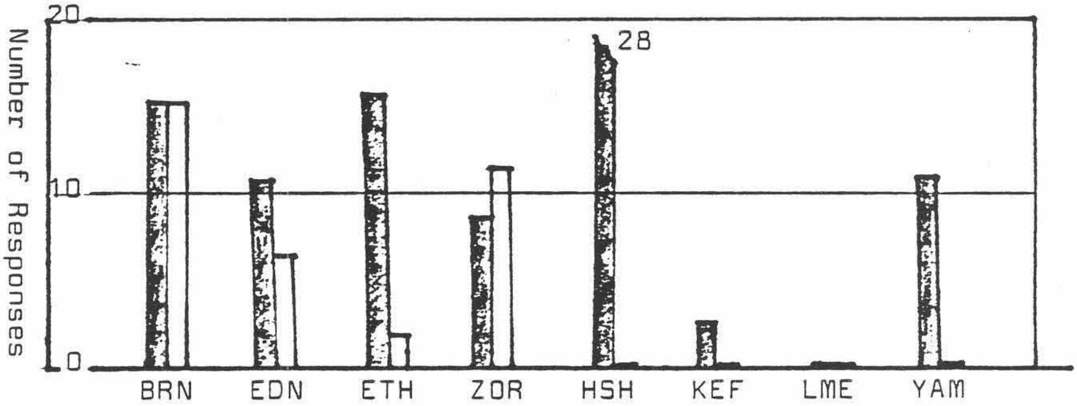

(FIGURE 1)

Total number of responses elicited from each hemisphere. Shaded bins represent the right hemisphere.

Over all the monkeys, the mean of the dominance indices was negative (X= -48.75). In the case of a DI being equal to zero, the right and left hemisphere responded an equal number of times. A negative DI indicates the right hemisphere responded more than the left and in this case, the right hemisphere responded more to a significant degree (t= -2.7475, p .05).

The dominance index for hemispheric preference was calculated using right and left hemisphere watching times. For each monkey a DI was calculated using the left hemisphere and right hemisphere watching times for each of the ten segments. These dominance indices were averaged together to give each monkey an average DI. These average DIs are listed in Table II.

MONKEYS	DOMINANCE INDEX FOR PREFERENCE
BRN	+10.14
EDN	-25.27
ETH	-29.84
ZOR	-11.13
HSH	-22.56
KEF	+8.50
LME	+4.73
YAM	-35.13

(TABLE II)

Average dominance index for preference for each monkey

The average of the dominance indices in Table II is negative, meaning the right hemisphere is viewing for longer periods of time than the left hemisphere. This greater preference by the right hemisphere is almost significant (t= -1.9491, p .10).

The average watching times for the binocular and monocular viewings for each segment are presented in Table III. Overall, the monocular right eye viewing time was significantly longer than the binocular viewing time (t= 2.5425, p .02). The left eye viewing time did not significantly differ from the binocular viewing time (t= -0.2116, n.s.). Although the tape viewed monocularly and the tape viewed binocularly differed for each monkey, an analysis of variance indicated no significant difference between tape sets A and B.

SEGMENTS	RIGHT EYE	LEFT EYE	BINOCULAR
Jill	48.38	35.59	33.45
Frisbee	60.99	56.01	80.29
Dash	65.19	68.11	65.44
empty cage	25.27	17.45	26.65
rhinoceros	62.34	72.82	71.59
B. Turpin	38.12	24.23	29.17
mandrill	84.32	47.68	83.12
scenery	23.64	40.56	25.28
cartoon	57.19	44.69	88.16
gorillas	36.33	20.82	30.76

(TABLE IIIa)

Right eye, left eye and binocular average watching times for each segment in tape set A

SEGMENTS	RIGHT EYE	LEFT EYE	BINOCULAR
Flamingoes	66.79 sec.	57.57 sec.	46.33 sec.
Gigi	65.81	66.01	36.73
empty cage	46.87	35.04	18.46
P. Siracusa & B. Mapes	63.05	52.22	49.16
snake	54.14	31.16	17.41
window view	63.15	38.30	37.29
tigers	31.90	14.65	17.09
cartoon	94.39	79.86	53.00
Nike & Frey	70.13	39.70	49.77
B. Vermeire	40.34	31.22	31.99

(TABLE IIIb)

Right eye, left eye, and binocular average watching times for each segment in tape set B

CONCLUSION

In humans, the results of various studies have shown that the processing of emotional stimuli is lateralized [1,2]. In most humans, this processing takes place in the right hemisphere or the non-dominant hemisphere, the non-dominant hemisphere being ipsilaterl to the preferred hand. In this experiment, the average dominance index across monkeys for the display of facial expressions was negative and significantly different than zero. This seems to suggest in monkeys a greater involvement by the right hemisphere in responding to emotional stimuli. However, it should be noted that the greater number of responses made by the right hemisphere may be related to preference. The more the monkey watches the stimuli, the more opportunities the monkey has to respond.

If monkeys were comparable to humans, one would expect that the non-dominant hemisphere in the monkey to be more emotionally expressive. Since the degree of handedness in monkeys has been reported to be uniformly distributed left to right along a continuum [7], a linear relationship between the degree of handedness and the dominance index for the display of facial expressions may exist. However, in this experiment the correlation between handedness and the dominance, shown in Figure 2, was not significant (r= -0.4449, ns).

An overall greater preference for viewing was found for the right hemisphere. This is interesting because other studies had found an overall greater preference for the left hemisphere for viewing colored slides [4]. This difference may be due to inherent differences between colored slides and colored videotapes or differences in the testing situations.

It is difficult to say what a preference asymmetry between two hemispheres of the monkey brain implies. A greater preference could be due to the emotional content of the stimuli, the hemisphere more apt at handling such stimuli may pay more attention. Or on the other hand, there just may be a hemisphere with a longer attention span. In humans, studies have implied that the capacity for sustained attention lies in the right hemisphere, while the left is more likely to have attention lapses [8]. If monkey brains and human brains were analogous, then one might expect a relationship between handedness and the dominance index for preference. However, the correlation between handedness and the dominance index for preference, presented in Figure 3, was not significant (r=-0.0237, ns).

Finally, the viewing time for the right hemisphere was significantly different than the binocular viewing time. The monkeys, on an average. watched more with their right hemisphere thatn they did when they viewed the videotape with both eyes. The left hemisphere viewing, on the other hand, did not differ significantly from the binocular viewing. This suggests that the preferences of the left hemisphere are more similar to the preferences of the whole monkey and that the right hemisphere viewing may be suppressed by the left hemisphere in binocular viewing.

Although the results of this experiment are encouraging, they should be treated with reserve until these results can be replicated with the testing of an additional number of monkeys.

(FIGURE 2) Handedness vs. Dominance Index for the Display of Facial Expressions

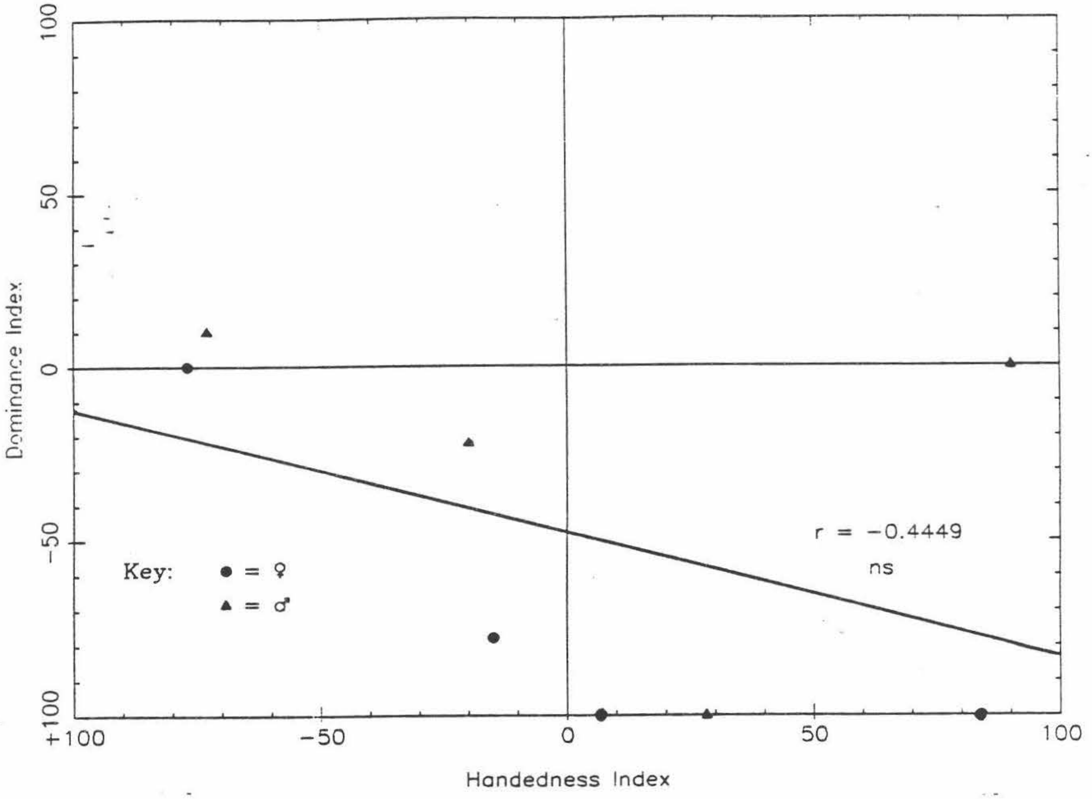

(FIGURE 3) Handedness vs. Dominance Index for Preference

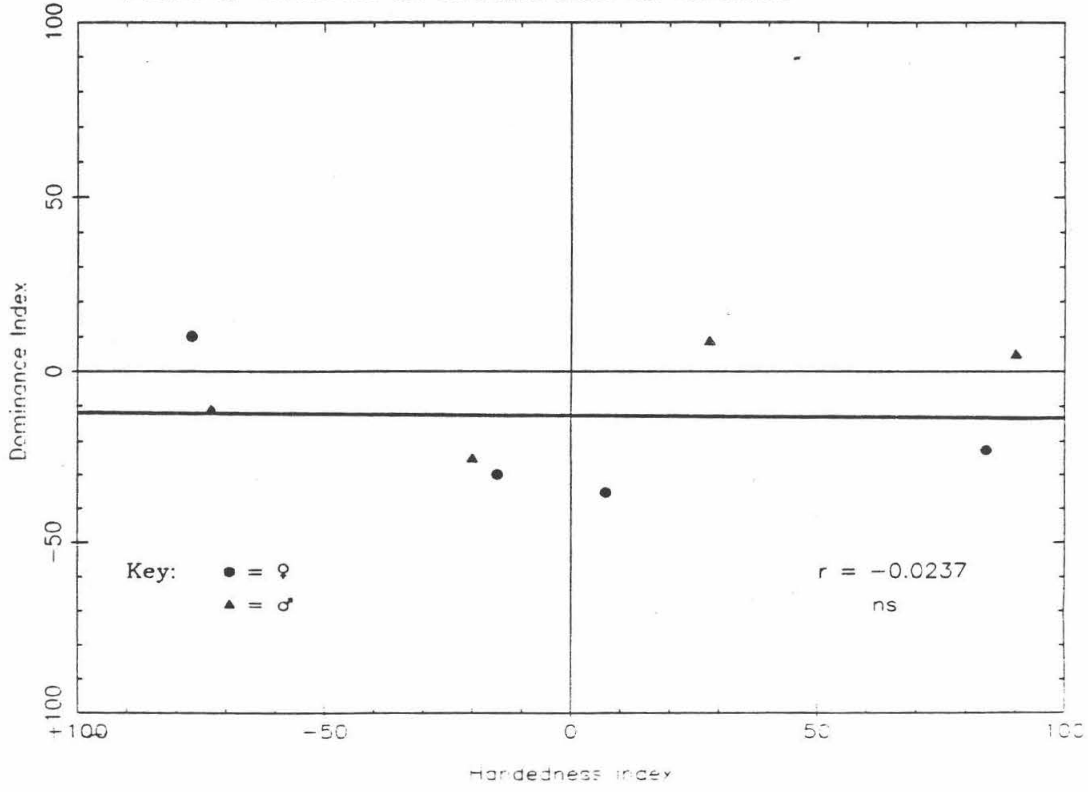

REFERENCES

1. R.G. Ley and M.P. Bryden, <u>Brain and Language</u> 7, 127-138 (1979).

2. W.H.Overman, Jr. and R.W. Doty, <u>Neuropsychologia</u> 20, 113 (1982).

3. C.R. Hamilton and B.A. Vermeire, <u>Discrimination of Monkey Faces by Split-Brain Monkeys</u>, pre-editorial manuscript (1983).

4. B.A. Vermeire, <u>Laterality and Visual Perception in Monkeys</u>, unpublished doctoral dissertation (1980).

5. E.H. Plimpton, K.B. Swartz, and L.A. Rosenblum, <u>Developmental Psychobiology</u> 14(2), 109-115 (1981).

6. W.K. Redican, <u>Primate Behavior</u>, vol. 4 (Academic Press, 1975).

7. R.A.W. Lehman, <u>Neuropsychologia</u> 16, 33-42 (1978).

8. S.J. Dimond, <u>Brain</u> 99, 347-356 (1976).

Determination of the nuclear proximity function from sub-barrier fusion data for p-shell

M. Inui and S.E. Koonin (Sponsor)

Abstract

Sub-barrier fusion cross sections for 12 systems involving p-shell nuclei are analyzed to determine the proximity function of inter-nucleus potentials. We use the previously developed procedure based on WKB approximation, which is proven to be highly accurate. We found that the determination of the function was possible by using the scaling implied by the proximity formulation, and that the function has a roughly exponential form.

I. Introduction

For astrophysical reasons as well as the interest in the internucleus interaction itself, it has been of importance to determine an universal form for nucleus-nucleus potential which can be applied to any pair of nuclei.

One appealing theoretical approach to the problem assumes that the force between two nuclei is proportional to the interaction potential per unit area between two flat surfaces of nuclear matter. Such an assumption leads to a proximity potential between any two nuclei of the form (ref. [1])

$$V_p = 4\pi\gamma\bar{R}\Phi(\zeta) \tag{1}$$

where γ is the surface energy coefficient of the semi-empirical mass formula, $\bar{R}$ is the harmonic mean of the central radii of the nuclei involved (assumed to be spherical), ζ is the separation of the nuclear surfaces in units of the surface thickness b, and $\Phi(\zeta)$ is the dimensionless universal proximity potential function.

There have been attempts made to determine the function, Φ, using elastic scattering and above-barrier fusion data. However, since the elastic scattering data only give the extreme tail of the function and above-barrier fusion data provide only one point per system with large uncertainty, the result of such analyses has not been enough to determine Φ directly.

Recently, it has been demonstrated that it is possible to obtain internucleus potentials from sub-barrier fusion data (ref. [2]), using inversion of a WKB approximation. This method, which is briefly summarized below, has proved to have small uncertainty and to provide extracted points with smaller separation of the surfaces of nuclei, ζ, than elastic scattering data, subject to the assumption that fusion is determined by penetration through a real, one-dimensional, energy independent potential barrier.

In this note, we applied this method to p-shell nuclear fusion data for a systematic determination of proximity funtion, Φ. We found that there seems to be a consistent form of $\Phi(\zeta)$ for p-shell systems which is roughly exponential. Furthermore, we found that the influence on the structure of fusion process is not significant in most of the systems analyzed. Exceptions are $^{12}C+^{12}C$ the very light systems $^{9}Be+^{10}B$ and $^{9}Be+^{12}C$, and the system $^{14}N+^{14}N$.

II. Method

The method of reconstructing the potential barrier between two nuclei from low-energy fusion cross section data is fully explained in ref. [2]. The method can be summarized by the following equations giving the maximum barrier height, B, and the thickness of the barrier, $t(V)$ (the distance between the inner and outer turning points at energy $V<B$) :

$$\frac{d}{dE}\left(\frac{E\sigma}{\pi R^2}\right)\Bigg|_{E=B} = \frac{1}{2}, \tag{2}$$

$$t(V) = -\frac{2}{\pi}\left(\frac{\hbar^2}{2m}\right)^{1/2}\int_V^B \frac{(dS_0/dE)}{\sqrt{E-V}}dE. \tag{3}$$

Here, E is the center-of-mass bombarding energy, $\sigma(E)$ is the fusion cross section, m is the reduced mass, and $R(E)$ characterizes the effective moment of inertia, mR^2. Following the discussion of the ref. [2], we take $R(E)$ to be the average of the barrier radius, R_B, and the Coulomb turning point, $R_C(E)=Z_1Z_2\,e^2/E$; that is,

$$R(E)=\frac{1}{2}(R_B+R_C(E)). \tag{4}$$

Finally, the cross section enters into Eq. (3) through the S-wave action,

$$S_0(E) = \frac{1}{2}\log\left[\left(\frac{d}{dE}\left(\frac{E\sigma}{\pi R^2}\right)\right)^{-1}-1\right]. \tag{5}$$

Equations (2-5) are not complete since the barrier radius, R_B, is not fixed from the data, but must be specified on other basis. Furthermore, Eq. (3) only gives the thickness of the barrier and, to obtain the inner turning point, we must fix the outer turning point in some way. Apart from these points, if R_B and the outer turning point for each energy is specified, we can construct the barrier completely from cross section data, using the above equations.

Once the barrier is obtained, simply subtracting the coulomb potential, $V_C(r)=\frac{Z_1Z_2\,e^2}{r}$, from the barrier height at each r gives the internuclear potential, $V_N(r)$, of the system.

In our analysis, we assume that the outer turning points can be represented by the superposition of the Coulomb potential and an exponentially decreasing nuclear potential, $V_E=V_0\exp\left[-\frac{r-R_B}{a}\right]$ since the the nuclear potential at outer turning point vanishes quickly out side of R_B. However, the barrier radius, R_B, should be chosen so that the the diffuseness of the exponential potential, a, falls in the physically resonable range, when V_0 and a are adjusted to connect the outer turning points smoothly at $V=B$. In practice, we used the potential fitted to the elastic scattering data by Akyüz and Winther (AW) in finding the barrier radius (ref. [3]), since the diffuseness of the potential with such radii turned out to be in the range of 0.4-0.8 fm in most of the cases. The radii obtained with the original proximity function of ref. [1] gave unphysical values of over 1 fm.

We used the following values given in the ref. [1] to scale the potential data to the proximity function, except that we used the nuclear radii, C_i, given in ref. [3].

$$b = 1 \quad fm$$

$$\gamma = 0.9517[1-1.7826I^2] \quad MeV/fm^2$$

$$C_i = 1.20A_i^{1/3}-0.35 \quad fm$$

where $I=\frac{N-Z}{A}$, and N, Z, and A refer to the numbers of combined system's neutrons, protons, and nucleons, respectively. Here, since we have used nuclear radii which are larger than those found in ref. [1], the data have been slightly shifted in the direction of smaller ζ with respect to the original proximity function, $\Phi(\zeta)$.

To verify this method, we have analyzed several sets of fusion pseudodata, created by an Incoming Wave Boundary Condition (IWBC) calculation[+], and we obtained satisfactory results in reconstructing the nuclear potential models used in generating the pseudodata.

III. Discussion of Results

The result of the analysis of 10 p-shell systems is summarized in Fig. 1. We find that the scaling described above put the extracted points into one particular region, indicating some relation between Φ and ζ, and that the points obtained in this analysis are at a smaller surface separation, ζ, than those obtained from elastic scattering data.

The best exponential fit to the data was made to obtain a consistent form for the function Φ. This fit showed somewhat smaller diffuseness than the original function given in ref. [1] as can be seen in the inset of Fig. 1. The numerical values for this fit in the form,

$$\Phi_{fit}(\zeta)=\Phi_0 \exp\left[-\frac{\zeta-\zeta_0}{a}\right] \qquad (6)$$

were

$$\Phi_0 = 0.2210 \pm 0.0037$$
$$\zeta_0 = 2.0727$$
$$a = 0.666 \pm 0.098$$

We must point out that, in our analysis, we eliminated certain systems such as $^{12}C+^{12}C$ and systems which were suspected to show the influence of the structure of the nuclei involved. The analysis was originally performed for 12 p-shell data sets. However, 2 sets of the data involving ^{9}Be nucleus showed anomalously high cross sections, possibly due to the excess neutron, and they were not used in the determination of the proximity function. Also, there were other data sets abandoned before the analysis since they did not have the data in above-barrier region and the evaluation of the integral in Eq. (3), for which we need to determine barrier height, B, from Eq. (2), was impossible.

From the fitted function, Φ_{fit}, we can construct the potential barriers for any p-shell system and compare them with the barriers obtained from fusion data. A few examples of barriers found with Φ_{fit}, the AW potential, and from the fusion data are shown in Fig. 2. It is seen that the fitted potential gives barriers smaller than those obtained with the AW potential and satisfactorily close to the actual barriers. Furthermore, it is interesting to note that the fitted proximity function gives an excellent barrier for the system $^{12}C+^{20}Ne$ even though ^{20}Ne is not a p-shell nucleus.

We are in the process of analyzing the fusion data for nuclei belonging to other shells. So far, we have found that for $^{40}Ca+^{40}Ca$ system, the barrier created from the fitted proximity function obtained above is a few MeV higher than the actual barrier. Moreover, we know from ref. [2] that for even heavier systems such as $^{64}Ni+^{64}Ni$, nuclear structure become too important to obtain a significant result by the method employed here.

[+] An IWBC calculation assumes that to simulate the result of the interactions such as fusion, it is possible to impose the boundary condition that all partial waves are travelling inwards at a particular radius in the interior of the interaction region.

IV. Conclusion

We determined the nuclear proximity function at relatively small surface separation from sub-barrier fusion cross section data for 10 p-shell systems. We found that the p-shell internucleus potentials seem to scale with a roughly exponential form of a proximity nuclear function, Φ. We have made this exponential fit to the proximity function, and found that we could construct the actual potential barriers satisfactorily.

The method of reconstructing potential barriers from sub-barrier fusion data has been tested with several sets of pseudodata, generated by wave mechanical calculations. The result was quite satisfactory.

The structure of the reactions was not significant in most of the cases we have analyzed. However, we expect that it will be a major difficulty for the determinaton of the proximity function Φ from heavier systems.

Analysis of heavier systems, namely $^{40}Ca+^{40,44,48}Ca$, $^{32}S+^{27}Al$, $^{32}S+^{24,25,26}Mg$ and $^{34}S+^{24,25,26}Mg$, is underway. We also hope that more precise measurements of sub-barrier fusion will be performed to refine the analysis presented in this note.

References

[1] J. Blocki, J. Randrup, W.J. Swiatecki, and C.F. Tsang, Ann. Phys. (N.Y.) 105 (1977) 427.

[2] A.B. Balantekin, S.E. Koonin and J.W. Negele, submitted to Phys. Rev. C and to be published.

[3] Ö. Akyüz and A. Winther, Proceedings of the Enrico Fermi International School of Physics, 1979, "Nuclear Structure and Heavy Ion Reactions", as developed in R.A. Broglia and A. Winther, "Heavy Ion Reactions" p.104

Sub-barrier fusion cross section data are from:

$^{12}C+^{11}B$: M.D. High and B. Cujec, Nucl. Phys. A278 (1977) 149.

$^{10}B+^{14}N$: S.C. Wu, J.C. Overley, C.A. Barnes and Z.E. Switkowski, Nucl. Phys. A312 (1978) 177.

$^{12}C+^{14}N$: Z.E. Switkowski, R.G. Stokstad and R.M. Wieland, Nucl. Phys. A279 (1977) 502.

$^{13}C+^{13}C$: S. Trentalange, Caltech Thesis, (1982).

$^{12}C+^{16}O$: B. Cujec and C.A. Barnes, Nucl. Phys. A266 (1976) 461.

$^{14}N+^{14}N$: Z.E. Switkowski, R.G. Stokstad and R.M. Wieland, Nucl. Phys. A274 (1976) 202.

$^{13}C+^{16}O$: B. Dasmahapatra, B. Cujec and F. Lahlou, Nucl. Phys. A394 (1983) 301.

$^{14}N+^{16}O$: Z.E. Switkowski, R.G. Stokstad and R.M. Wieland, Nucl. Phys. A279 (1977) 502.

$^{12}C+^{20}Ne$: G. Hulke, C. Rolfs and H.P. Trautvetter, Z. Physik A297 (1980) 161.

$^{16}O+^{16}O$: S.C. Wu and C.A. Barnes, to be submitted to Nucl. Phys. A.

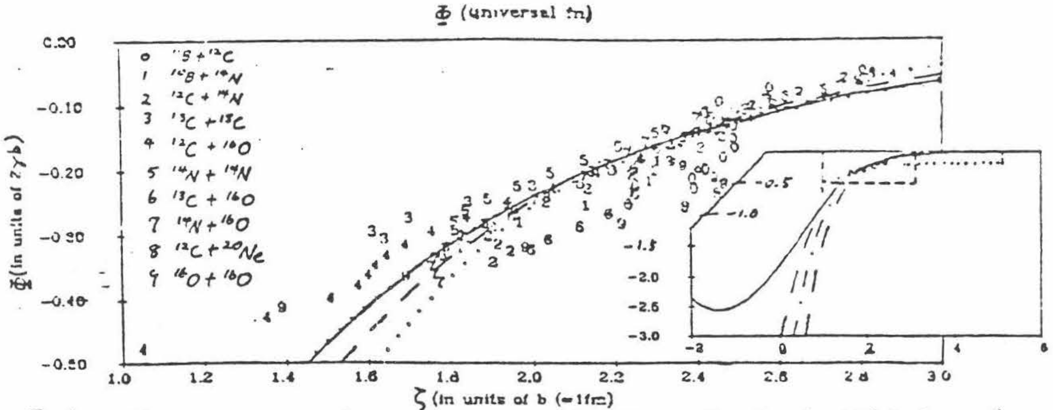

Fig. 1. The extracted points from 10 sets of fusion data. The small inset on the right indicates the rough scale of the original proximity potential [Solid line] and the region of interest [dashed box] with the range of data obtained from the elastic scattering data [dotted box]. The best fit to the data is indicated by a dashed line with the error envelope of dotted lines [dot-dashed line with dashed lines in the Inset].

Fig. 2. The potential barriers of 3 systems.

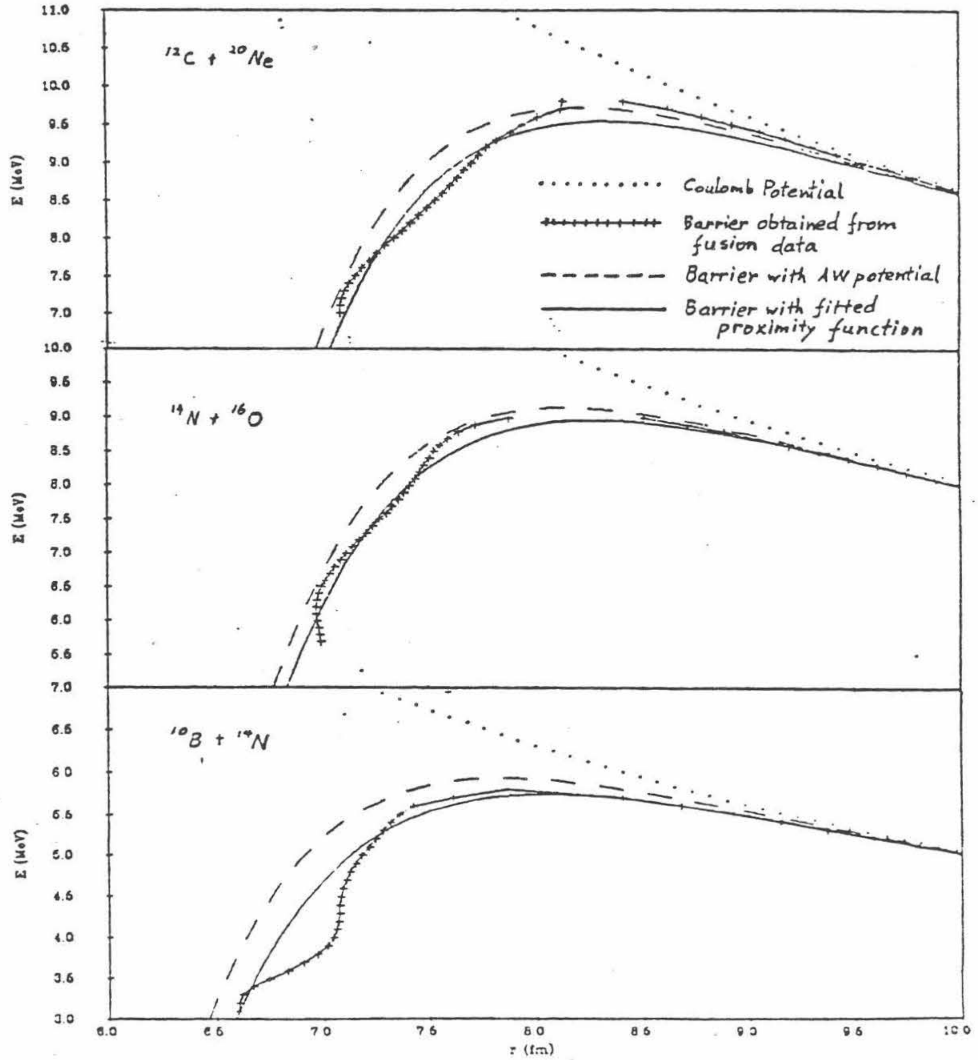

JENNIFER JERLSTROM

NO REPORT SUBMITTED

MEASURING THE COPPER ISOTOPE SHIFT AND HFS USING OPTO-GALVANIC SPECTROSCOPY

Stephen E. Jones

Faculty Sponsor:
Dr. William B. Bridges

Abstract

An experiment was set up to measure isotope shifts using the opto-galvanic effect and a state-of-the-art tuneable dye laser. This experiment successfully measured the isotope shifts in the hyperfine structure of the copper line $\lambda 578.2\text{nm}(3d^9\ 4s^2\ {}^2D_{3/2} - 4p^2\ P_{1/2})$. A hollow-cathode discharge in neon was used as the source of copper atoms.

Introduction

Atomic spectra have been studied since the days of Newton, with each succeeding generation increasing its knowledge of atomic physics by using new technologies to produce spectra of finer resolution. With the advent of lasers, the forgotten phenomena of the opto-galvanic effect (OGE) has been employed with tuneable lasers to realize a spectrometer of high precision. In this paper we report measurements of the isotope shifts and hyperfine structure in copper using this technique.

The OGE occurs when a gas discharge plasma is illuminated at wavelengths corresponding to allowed transitions in the gas atoms. When atomic levels are thus excited, the atoms become more easily ionized and thus the voltage needed to maintain the discharge will change; the result is an optogalvanic signal, (see Bridges 1978 for example).

Dye lasers are well-known for being inherently tuneable and therefore easily lend themselves to excite atoms over a reasonable range of wavelengths. Thus, it was a natural choice to use a state-of-the-art dye laser (the Coherent model 699-21) as the source in an opto-galvanic spectrometer.

Material and Methods

The isotope shift of the strong yellow line in helium was originally proposed as the line to measure. However, it was subsequently discovered that the intended measurement had already been done (Freeman, et al; 1980) and that the shift was small enough to require Doppler-free techniques, something we did not wish to undertake initially. As an alternative, copper meets the requirements of having a strong line in the laser's tuning range (565 nm - 620 nm), of being readily available, and of last being measured 27 years ago with conventional (non-laser) techniques (Murakawa; 1956).

The dye laser used was a CR-699 built by Coherent which was pumped with 5 Watts of 514 nm power from a Coherent CR-10 argon ion laser. The CR-699 has a scan width of 30 GHz with a line width of about 1 MHz. After some investigation of alternative dyes, Rhodamine 6G was chosen as the laser dye since it had the greatest response over a wide range of frequencies.

Many attempts were made to build a hollow cathode copper vapor source; the final version consisted of a 1/4 hollow-copper tube 25 mm long inserted into a hollow glass tube which formed the top of a "T". The glass "T" was 23 mm long and 65 mm tall. A solid copper connecting rod was inserted into the stem of the glass "T" support which was connected to the power supply through an insulated plug protruding through the vacuum system walls (see Fig. 1). Pure neon or a Penning mixture of neon and argon was added as a buffer gas at pressures between 1/2 torr to 10 torr.

To view the signal, the cathode was connected through a capacitor to an oscilloscope connected in parallel with a lock-in amplifier; signals could be seen on the scope, but the lock-in was required to discriminate against noise and ripple. The lock-in amplifier output was connected to an X - Y plotter: the X-axis was swept by the dye laser scan output and the Y-axis was the OGE signal. The plots thus obtained thus measure the strength of the atomic absorption as a function of frequency.

To facilitate finding a specific copper line in the spectral "forest" of neon, a conventional 0.5 meter Jarrell-Ash spectrometer with about 0.05 nm resolution was set up so as to see both the spectrum of the hollow cathode discharge and of the laser. Thus, the dye laser could be mechanically coarse-tuned to a given copper line. Then the dye laser was then electronically fine-tuned to the copper line until the OGE signal was seen. Then the electronic sweep was activated and the hfs spectrum obtained.

The OGE was found to vary with several parameters. 1) The laser beam position radially within the hollow cathode affected the resolution of the spectra such that a beam skimming the inside cathode wall produced higher resolution than a beam going through mid-center. 2) The OGE intensity was found to vary as the square of the discharge current at low currents (< 30mA) and linearly with current at high currents (90mA). 3) The OGE did not vary significantly with the neon gas pressure. 4) The OGE varied with the cathode temperature such that both increased in time. 5) The OGE depended upon the "freshness" of the neon gas fill (contamination) and any amount of argon that may have been present.

The amount of laser power actually absorbed by the hollow cathode discharge was measured to be 3-5% at the peak of the hfs and the maximum discharge current To obtain a stronger OGE we would have to increase the copper atom density by increasing the discharge current (increased sputtering rate) or by making the optical path longer.

A scan of the copper isotope shift and hyperfine structure for the line 578 nm is shown in the top half of Fig. 2, measured with a chopping frequency of 870 Hz. Peaks labeled with unbarred letters are from Cu^{63}; peaks labled with barred letters are from Cu^{65}. Natural copper consists of 69.09% Cu^{63} and 30.91% Cu^{65}. The bottom half of figure 2 shows the results of Murakawa (1956) using a Fabry-Perot etalon. Our measurements are in good agreement, and the top and bottom scans of Fig. 2 are aligned to visually compare the results. Numerically, they compare as follows:

	Wave Number This Paper cm^{-1}		Wave Number Murakawa cm^{-1}		Δ %
a	0		0		
$\bar{a}$	0.0664	.0013	0.0674	.0007	1.5
b	0.1747	.0013	0.1572	.0021	11.1
c	0.1991	.0013	0.1855	.002	7.3
d	0.2897	.0013	0.273	.002	6.1
$\bar{d}$	0.3627	.0013	0.3589	.003	1.1
$\bar{f}$	0.4445	.0013	0.420	.003	6.0

The differences shown were consistent in every scan. A possible explanation is that although Murakawa observed more structure, our modern electronics allows for higher precision.

It is interesting to note that isotopic peak height ratios (.47 ±.1) agree well with the known isotopic ratios (.45)

Discussion and Conclusion

It would be useful to computerize Murakawa's data, apply a gaussian spread (3 GHz Doppler width) to each peak, plot the result, and compare with our plot. This would reveal the hidden influences of the small lines the OGE missed.

One part of the original SURF proposal was to attempt to separate isotopes using selective excitation and catephoresis. To do this, a different discharge tube is required. The present experiment demonstrates that selective excitation is possible and that the different isotopes are resolved in a hollow-cathode discharge. The next step is to design a liquid-cooled cathode such that isotope separation experiments become feasible. This project will be continued as a senior thesis. It would also be interesting to apply this OGE technique to a variety of other elements such as europium, uranium, helium or other copper lines.

[Note: It has just come to our attention that the Cu λ578 nm line has been measured using Doppler-free OGE by Gerstenberger et al; their published result for the non-Doppler free hfs is identical to ours.]

References

Bridges, W. B. "Characteristics of an Opto-Galvanic Effect in Cesium and other Gas Discharge Plasmas", J. Opt. Soc. Am., 68, 352-380, (1978).

Freeman, et al. "Isotope Shift of the 2^3P-3^3D Transition in Helium", Physical Review A, 22, 1516-1516, (1980).

Gerstenberger, D. C., E. L. Latush, and G. J. Collins, "Doppler-Free Laser Spectroscopy of Atomic Copper in a Hollow-Cathode Discharge", Opt. Comm., 31, 28-30, (1979).

Murakawa, K. "Hyperfine Structure of the Spectrum of Cu I and Test of the Hyperfine Structure Formulas", J. Phys. Soc. Japan, 11, 774-777, (1956).

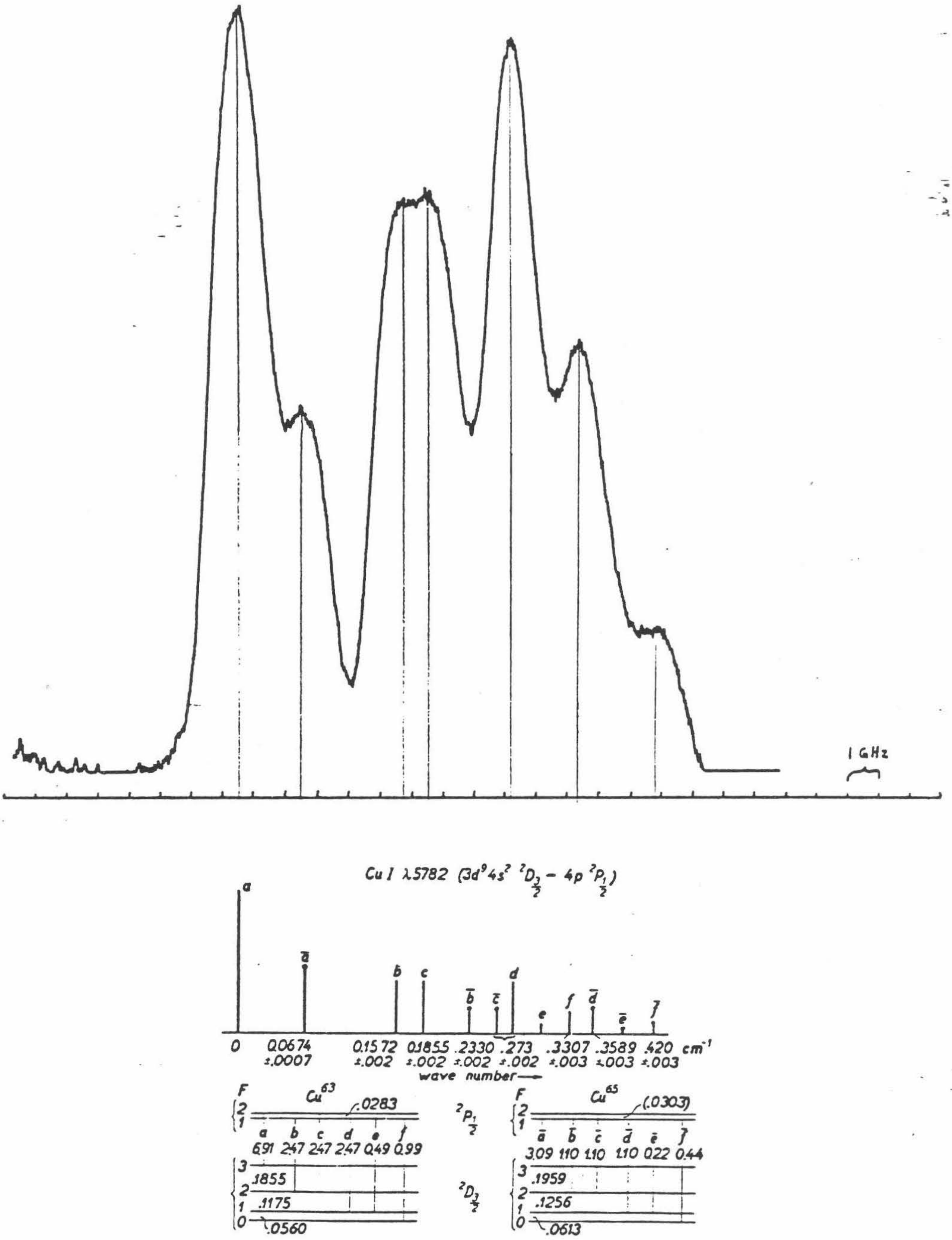

Fig. 2. Hfs of Cu I λ5782.

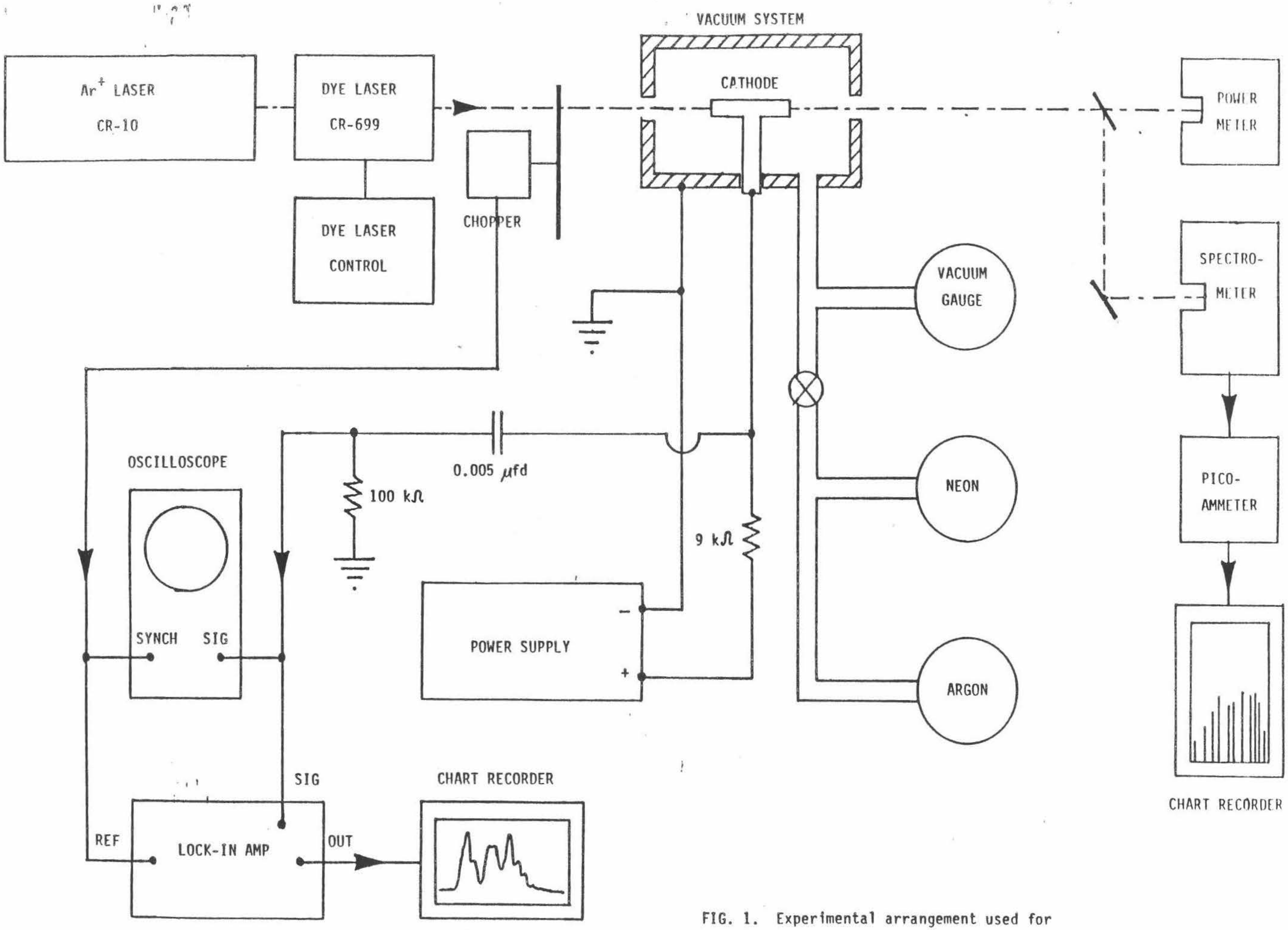

FIG. 1. Experimental arrangement used for opto-galvanic effect measurements.

THE PHOTOCHEMISTRY OF OZONE ON GaAs SURFACES

Steven Kong
SURF 1983
Sponser: Kenneth Janda

To further understand the oxidative properties of GaAs, the photochemistry of GaAs at cryogenic temperatures is the topic of research. A prototypical experiment would be to physiosorb ozone onto the GaAs crystal and stimulate it with a laser. It is hoped that the oxygen resulting from dissociation will react at the site where the ozone physiosorbed and produce a homogeneous oxide layer.

The fabrication of a homogeneous oxide layer on a GaAs surface is of considerable interest since the usual thermal oxidation method used successfully on silicon produces an inhomogeneous oxide layer on GaAs. Such an inhomogeneous oxide layer results in unreliable electronic components. To study this problem, the experiment will be carried out in a stainless steel UHV chamber with a base pressure less than 10^{-10}torr, and with a GaAs surface at cryogenic temperatures. The low temperature will reduce thermal agitation and allow adsorption of a homogeneous overlayer. The GaAs sample is cleaned and mounted on a crystal manipulator and placed inside the UHV chamber. The chamber is pumped down to less than 10^{-10}torr and the crystal is cooled to less than 20 K. The gas of interest is leaked into the chamber and allowed to physiosorb onto the crystal. A CO_2 gas laser, dye, or excimer laser can excite the ozone.

$$O_3 + h\nu \text{ (UV or visible)} \qquad O_2 + O$$

The resulting reaction of the oxygen products with the GaAs surface would be studied.

The experiment requires a great deal of construction and preperation. The UHV chamber requires testing since a sufficient vacuum must be obtained. The chamber must be baked to about 200 C to remove extraneous substances adsorbed on the inner surface of the chamber. The liquid helium refrigerator also requires testing to obtain a sufficiently low temperature so gases may be condensed on the sample's surface. The thermal link between the refrigerator and the sample will also need to be developed. To determine the purity and cleanliness of the sample, Auger spectroscopy is employed. From the spectrum, the degree of contamination of the GaAs crystal may be determined, and so the efficiency of the cleaning process determined. Another major obstacle is the handling and introduction into the UHV chamber of ozone. Ozone is a violently reactive substance and measures must be taken to insure safety and successful transfer of ozone into the chamber.

In assisting in the preparation for the experiment, I have worked on several electronics and electrical components for the Auger electronics, oven control system, thermocouple junctions, and ion gauges. I have also conducted library searches into the handling of ozone and the cleaning of GaAs.

The UHV chamber has been successfully pumped down to 8×10^{-11} torr. The process of pump down is initialized by a sorption pump which reduces the pressure from atmospheric and allows the diffusio pump to be activated. The chamber pressure drops to 10^{-8} torr at this point. Next the chamber is baked to 200 C raising the pressure since adsorbed gas is forced out of the stainless steel. After cooling, the pressure drops below 10^{-8} torr to 10^{-10} torr. The titanium sublimation pump is activated which assists the diffusion pump in obtaining the ultra high vacuum.

The liquid helium refrigerator can cool to about 20 K. The temperature of the refrigerator was measured using chromel and gold thermocouples. To test the validity of the thermocouples, a calibrated diode will be used. A temperature near 15 K should be achievable. A high purity copper strip is used at present to make thermal contact between the refrigerator and the sample.

Auger spectroscopy was adopted as the means of studying the composition of the sample's surface. Auger spectroscopy involves the characteristic energy structure of the elements. An electron beam bombards the sample and ejects core electrons. This results in an imbalance in the electronic structure which causes a valence electron to drop into the core level. The energy released will in turn eject another electron. The energy of these electrons is measured and the characteristic energies are referenced to determine the composition of the surface. The process of determining the energy of the electrons involves several electronic components. A ramped voltage with a 1 Khz sinusoidal modulation superimposed onto it is amplified through a high voltage source. The modulated high voltage output is applied to hemispherical grids inside the UHV chamber. The electric field selectively rejects electrons so that their energies may be determined.

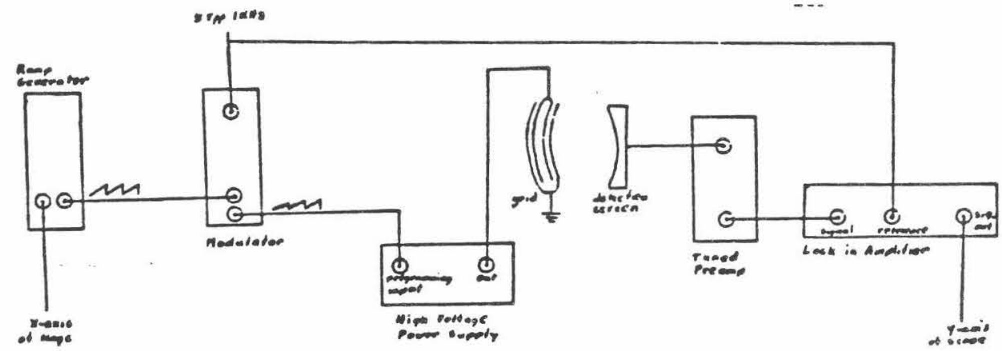

Auger spectroscopy system

Carbon and oxygen are the major contaminants of the GaAs crystal. Oxygen may be removed by heating the crystal to 560 C. There are many methods of removing carbon. The easiest method is by heating the crystal before exposing it to an electron beam. There are various other thermal methods with basically the same technique. One non-thermal method involves UV light and ozone, and another involves H_2 plasma. The thermal method seems the most practical and it will be tested out first.

Ozone may be safely stored while it is adsorbed onto silica gel at liquid nitrogen temperature. A U-shaped glass tube containing silica gel is used to trap and store ozone. The ozone may be introduced into the chamber through a valve. The line from the ozone source to the chamber will be made of glass and a minimum amount of stainless steel, since stainless steel acts as a catalyst in decomposing O_3. Stainless steel can withstand ozone corrosion very well.

In the lab a successful vacuum has been made, a working Auger spectroscopy system constructed, and the refrigerator installed and tested. A sample of GaAs has been mounted and the cleaning technique is being tested. After the sample is properly cleaned and analyzed with Auger spectroscopy, experiments will be conducted. The ozone introduction system still remains to be constructed. After its completion the ozone experiment may be carried out.

Bibliography

Chang, Chin-An. "Thermal removal of surface carbon from GaAs substrate used in molecular beam epitaxy." Journal of Vacuum Science Technology 21 (July/August 1982): 663-5.

Friedel, P, and Gourrier, S. "Interactions between H_2 and N_2 plasmas and a GaAs(100) surface: Chemical and electronic properties." Applied Physics Letters 42 (15 March 1983): 509-11.

McClintock, J. A., Wilson, R. A., and Byer, N. E. " UV-Ozone cleaning of GaAs for MBE." Journal of Vacuum Science Technology 20 (February 1982): 241-42.

Reimschuessel, H. K. "Handling of Ozone." US Patent 3514963 June 2, 1970.

THE PURIFICATION OF MURINE INTERLEUKIN-2

Santosh N. Krishnan

Sponsor: Dr. Ellen Rothenberg
Dr. James P. Lugo

Interleukin-2, IL-2, is a soluble factor produced by T-cells and T-cell precursors. It is classified as a lymphokine, a hormone produced by cells of the immune system. IL-2 has various effects, both in vivo and in vitro. IL-2 was discovered as a necessary factor for maintaining T-cell cultures in vitro, and was thus termed T-cell Growth Factor abbreviated TCGF. It has also been shown that the ability to produce IL-2 is a marker for helper T-cells, which produce this molecule in a lymphocyte activation process triggered by antigen. An analysis of the production and response to this lymphokine raises many interesting questions. Just as the ability to produce IL-2 can be used as a marker for helper T-cell precursors in the thymus, the ability to respond to this molecule may also have developmental significance. In particular, the expression of a receptor for IL-2 and the biochemical and physiological properties of this receptor provide an excellent system for the study of thymocyte differentiation and the mechanism of hormone-receptor interaction. Progress in these studies, however, is severely hampered by the lack of pure IL-2. The presence of unknown factors in sera added to media and the secretion of other factors by Il-2 producing cells preclude any firm conclusions being made as to the exact effect of this lymphokine. For these and other reasons, this laboratory decided to establish a protocol for purifying this molecule.

The purification of Il-2 is complicated by the fact that as a hormone, it is highly active and is found in very small quantities relative to other contaminants in crude supernatants. Furthermore, while rat and human IL-2 are found as monomeric molecules with a molecular weight of about 15,000 daltons, the murine IL-2 is found to exist at a molecular weight of about 30,000 daltons. Moreover, the evidence available indicates that it is a a dimer. These structural dissimilarities between the human and mouse species necessitate vastly different purification procedures. The strategy adopted by this laboratory for the purification of murine IL-2 can be divided into two broad steps. The aim of the first phase is to remove the major contaminants of the IL-2 containg crude supernatant, serum albumin and immunoglobulin, and also to make the preparation sufficiently enriched for IL-2 in order to facilitate a high degree of resolution in the powerful second step of High Performance Liquid Chromatography (HPLC).

Crude IL-2 is obtained by stimulating subclones of the EL4 mouse lymphoma line with 20ng/ml of the potent tumour promoter TPA. After a 24 hour exposure to the TPA in the culture medium, the preparation is subjected to centrifugation and the cell free supernatant is harvested. A second stimulation with the same cells in fresh medium with TPA has been shown to produce enhanced levels of IL-2. The supernatant thus obtained is the crude IL-2. The initial step performed is to concentrate this preparation by precipitation with Ammonium Sulphate. The slurry containing the Ammonium Sulphate is incubated for several hours and then centrifugated to recover a pellet. The precipitate pellet is then resuspended in a minimum quantity of distilled water and then dialyzed to remove the excess of Ammonium Sulphate and re-equilibrate the IL-2 containing medium to a 50mM salt concentration. The concentrated supernatant is then subjected to DEAE-Sephacel chromatography. The IL-2 containing medium is loaded onto the column and washed with a 50mM salt solution. Some proteins don not bind to the column and can be colllected in this wash. One such contaminant that can be found to come through in this wash is IL-3, another lymphokine. Once the protein has been loaded onto the column, a salt gradient from 50mM to 300mM is used to elute proteins from this column. Using DEAE

Sephacel chromatography, IL-2 can be separated from other growth factors such as Colony Stimulating Factor (CSF), IL-3, and contaminants like serum albumin. The fractions collecting significant quantities of IL-2 are collected and then subjected to lectin chromatography. The IL-2 containing medium is loaded onto a column of Concanavalin-A (Con A) coupled to sepharose beads. This column binds glycoproteins that have sugar moieties that bind to Con A. IL-2 binds to this column and can be competed off by the addition of alpha-methyl mannoside, the sugar specific to Con A, to the column. The final step of the initial phase is to pass the IL-2 containing medium over a G-75 sizing column. Based on the size of the beads in the column, proteins can be separated from each other by virtue of their different molecular weights. At this stage, the preparation can be further concentrated by subjecting it to both heat and vaccuum during centrifugation.

After this final concentration, the preparation is ready for further enrichment of the IL-2 containing medium by means of High Performance Liquid Chromatography (HPLC). For this system different kinds of columns can be used, each giving slightly different resolution patterns. Small quantities of the protein are loaded and a gradient of the solvent system used is then applied to elute the protein from the column. In this laboratory the solvent that has been chosen is acetonitrile. Once it has been determined at what point in the gradient the IL-2 is eluted off, the gradient can be manipulated to provide maximum resolution of the HPLC profile. Thus a steep gradient can be employed to get rid of most of the contaminants and as the IL-2 starts to elute from the column, the gradient can be made shallower to ensure additional resolution. The IL-2 recovered from one run on the HPLC can be subjected to further purification on subsequent HPLC runs. With the addition of a carrier molecule like Polyethyleneglycol (PEG) to stabilize the IL-2, the purified molecule can be then stored for further use.

The Ammonium Sulphate precipitation is accomplished by the addition of the compound to 80% saturation. It usually results in a 15-20 fold concentration with no loss of IL-2 activity. Since it is dialyzed, a small reduction in total protein is accomplished. Thus as a result of this step, the specific activity of the IL-2 in units/mg protein remains essentially unchanged at about 750 units/mg protein. In the other steps, further enrichment of the IL-2 is accomplished, but some loss of activity takes place with each step. While all the steps in phase one of the purification protocol have not yet been performed in sequence, individual results indicate that at the end of the first phase, a specific activity of about 20,000 units/mg protein can be achieved even with the loss of 30%-40% of the initial total IL-2 activity.

Analysis of HPLC profiles has shown, however, that this is nowhere near a homogeneous preparation of IL-2. Data from other researchers has indicated that a pure preparation of IL-2 would have a specific activity as high as 10,000,000 units/mg protein. This only serves to indicate the enormous resolving capability of the HPLC system after several runs with a carefully designed gradient system.

While a complete series of purification steps resulting in the pure product has not been carried out in this laboratory, preliminary tests of the steps in the protocol have been completed. These studies have exposed various shortcomings in the system and steps have been taken to correct these. Thus the groundwork has been laid to initiate a full scale deployment of the various procedures in the purification protocol. The entire process, which if conducted with minimal delay takes about two weeks, will be soon set into motion. Thus while a vial of the pure substance cannot be lifted to the light at the end of these ten weeks, it is not unreasonable to hope that it can be done in the near future.

Study of charge asymmetry in the reaction $e^+e^- \to \mu^+\mu^-$ with the forward counters of the MARK J detector at PETRA

California Institute of Technology

SURF Report

Author : Kwok, Tak Leuk
Faculty Sponsor : Professor Harvey Newman
Date : 8/25/83

ABSTRACT

The forward-backward charge asymmetry in the reaction $e^+e^- \rightarrow \mu^+\mu^-$ at $\sqrt{s} \approx 34$ GeV and in the angular range $0.5 < |\cos\vartheta| < 0.8$ has been determined to be:

$$A_{\mu\mu} = -16.3 \pm 3.7\ \%$$

This is in agreement with the standard unified electroweak theory prediction of - 14.2 ± 1.8 %. Attempt has been made to determine the asymmetry down to $|\cos\vartheta| < 0.9$. But a lack of bending power in the detector at the end of the muon acceptance results in insufficient momentum resolution that causes difficulties in the determination of the muon charge with sufficient reliability. Further analysis of the track fitting procedures in this region is needed.

The MARK J experiment has previously reported [1] a charge asymmetry of:

$$A_{\mu\mu} = A^{T} - A^{QED} = -\ 10.4 \pm 2.1\ \%$$

in the angular range $0. \leqq |\cos\vartheta| < 0.8$ at $\sqrt{s} \approx$ 34.6 GeV, which compares favourably with the Glashow-Salam-Weinberg theory (GSW) prediction of:

$$A^{GSW} = -\ 8.6 \pm 0.2\ \% \quad \text{for } \sin^2\vartheta_W = 0.23\ .$$

In the present work the forward counters and chambers are included which then extend the angular range to $|\cos\vartheta| < 0.9$. The GSW unified electroweak theory predicts a maximum charge asymmetry at small angle. By including a large angular range that goes down to smaller angle, the validity of the theory can be tested with greater precision. The present work is an effort to study the efficiency of the counters and analyse data obtained from the detector, attempting to arrive at a value of charge asymmetry to be compared to theoretical prediction.

PETRA AND MARK J

PETRA (Positron Elektron Tandem Ringbeschleuniger Anlage) is currently the world's highest energy e^+e^- colliding machine. At the present moment it reaches a centre of mass energy of 43.5 GeV. It houses four experimental halls, among which is MARK J. Fig.1 shows a schematic layout of PETRA and the experiments.

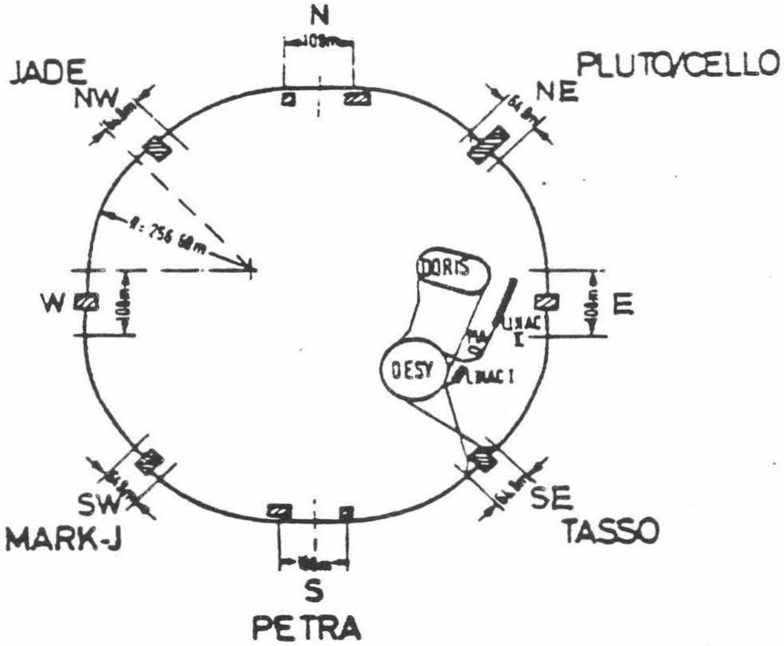

Fig.1 : The PETRA storage ring and the four experimental groups.

The MARK J detector is shown in Figs. 2a and 2b. It is designed to distinguish charged hadrons, electrons, muons, neutral hadrons and photons and to measure their directions and energies. Fig.3 shows the layer structure of the detector as seen by particles emerging from the interaction point. The forward muon trigger counters and chambers (so called E counters and R chambers respectively in Fig.2) have the same function as the part called 'muon detector' in Fig.3 . A detailed description of each individual component of the detector can be found in Ref. 2 . Having a close to uniform efficiency, and with $\sim 4\pi$ acceptance MARK J is capable of fulfilling a broad range of physics objectives, one of which is the measurement of the charge asymmetry in $\mu^+\mu^-$ production.

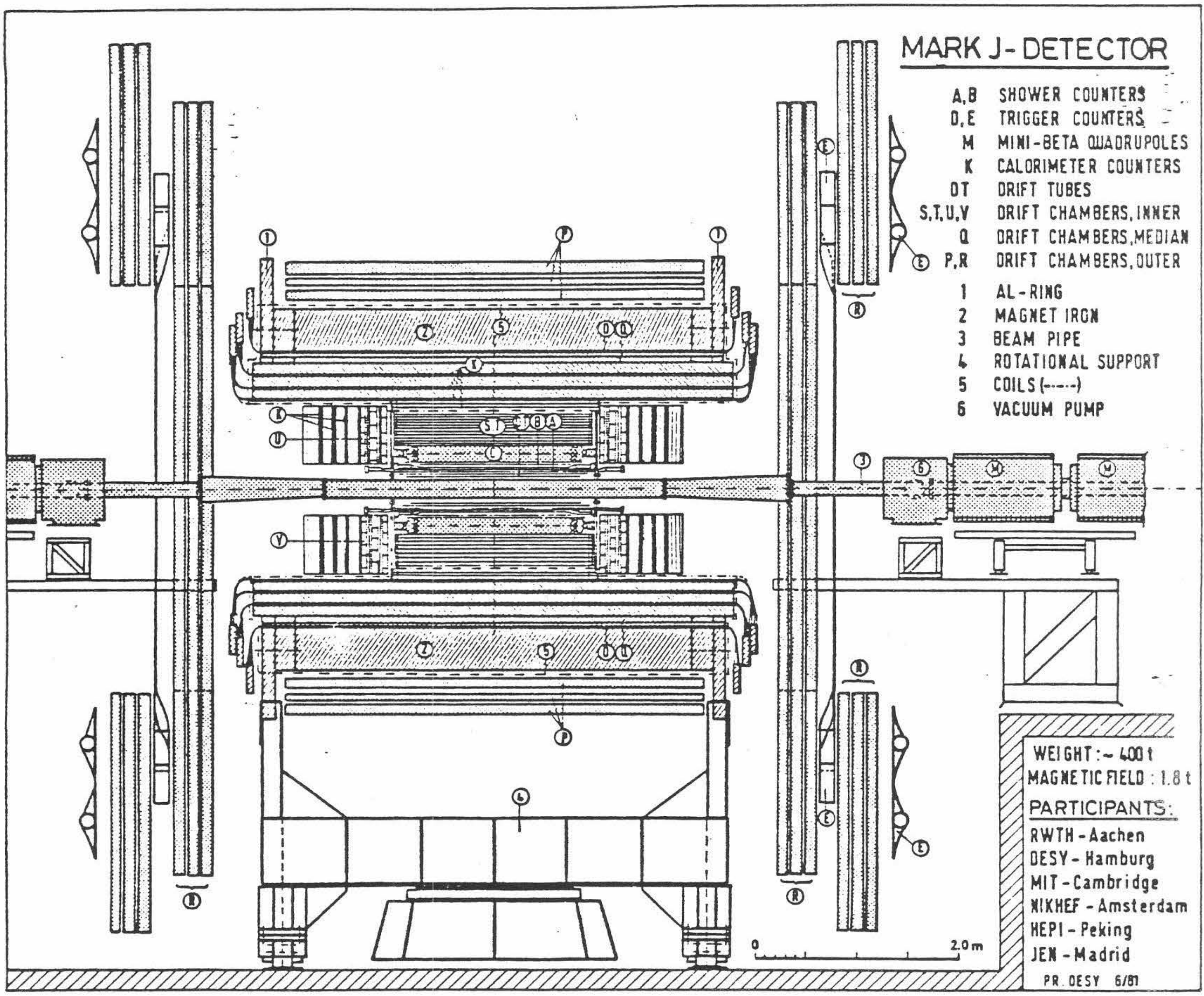

Fig.2a : The MARK J detector (side view).

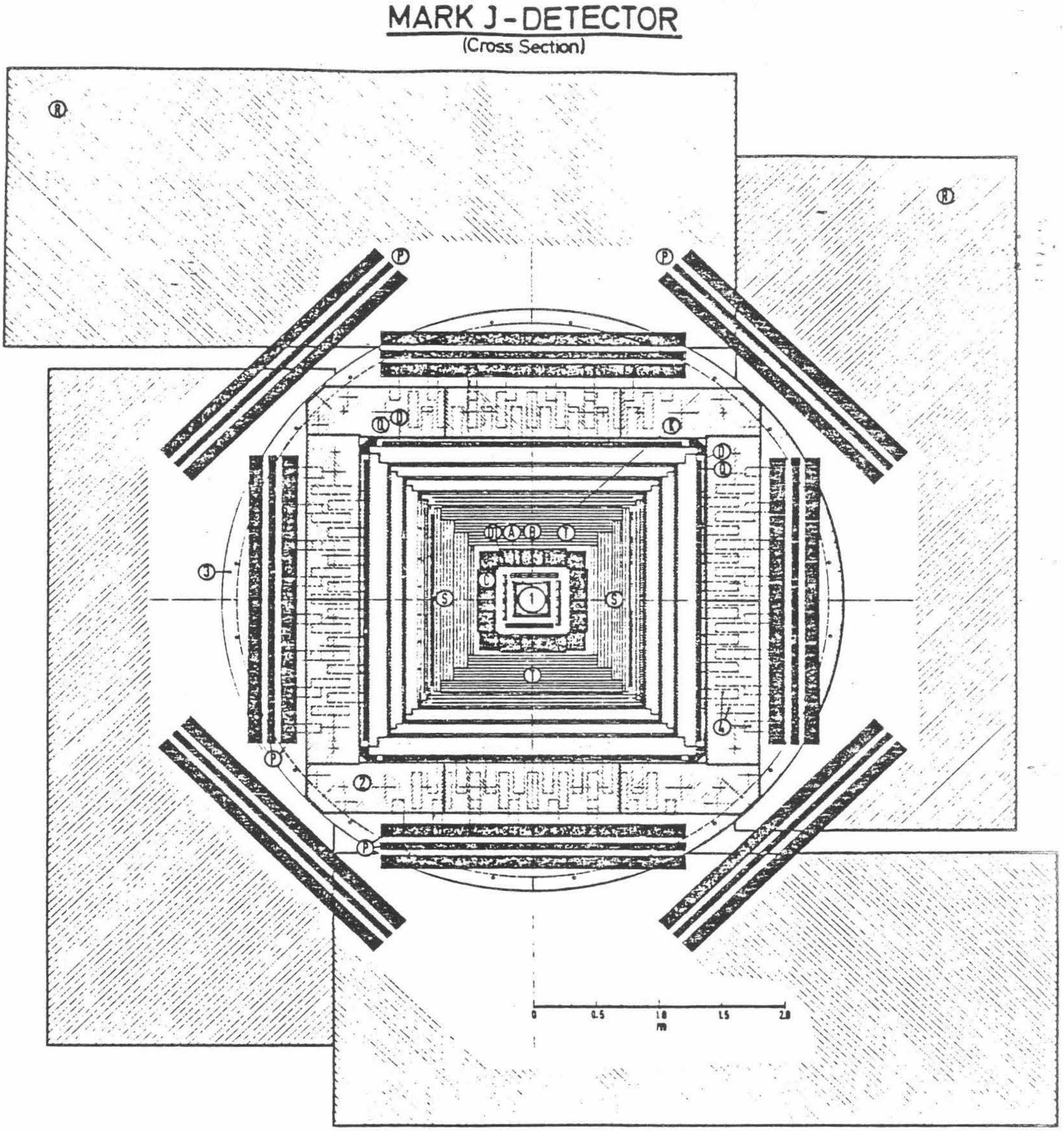

: Fig.2b : The MARK J detector (end view).

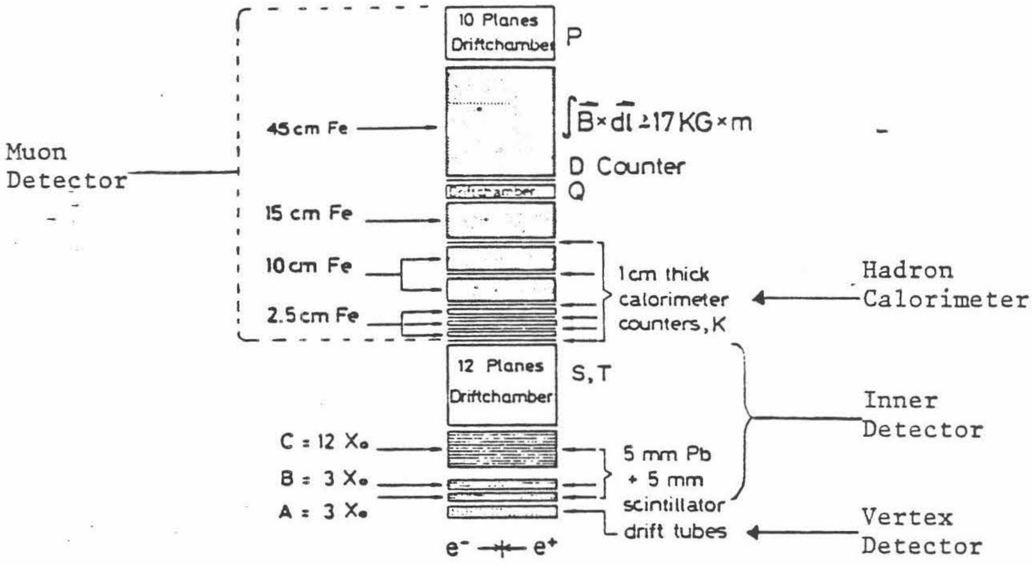

: Fig.3 : Layer structure of the detector as seen by particles emerging from the interaction point.

A. THEORY

The observation of weak neutral currents [3] gave crucial support to the idea that a neutral massive gauge boson is one of the mediators of the weak interaction. The GSW model [4] appears so far to be the most satisfactory unified model of weak and electromagnetic interactions. One of the detectable effects of the neutral weak boson (Z^0) at PETRA is the forward-backward charge asymmetry in e^+e^- annihilation into μ pairs:

$$A_{\mu\mu}(\vartheta) = \frac{N_{\mu^-}(\vartheta) - N_{\mu^-}(\pi - \vartheta)}{N_{\mu^-}(\vartheta) + N_{\mu^-}(\pi - \vartheta)}$$

where $N_{\mu^-}(\vartheta)$ is the number of μ^- in the solid angle $d\Omega$ about the direction (ϑ,φ) (see Fig.4).

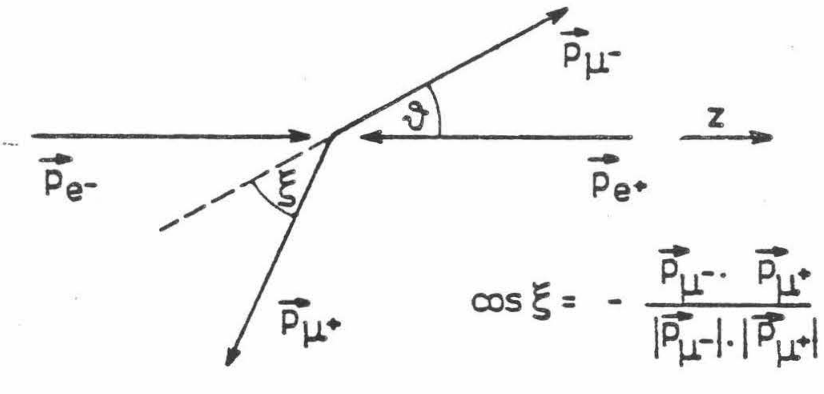

: Fig.4 : Definition of ϑ in $A_{\mu\mu}(\vartheta)$, and of ξ, the acollinearity angle

Since statistics are still low, the number usually quoted is integrated over angle:

$$A_{\mu\mu} = \frac{N_{\text{forward}} - N_{\text{backward}}}{N_{\text{forward}} + N_{\text{backward}}}$$

The reaction $e^+e^- \rightarrow \mu^+\mu^-$ proceeds through both a photon and a Z^0 exchange. The corresponding lowest order Feynman diagrams are shown in Fig.5 .

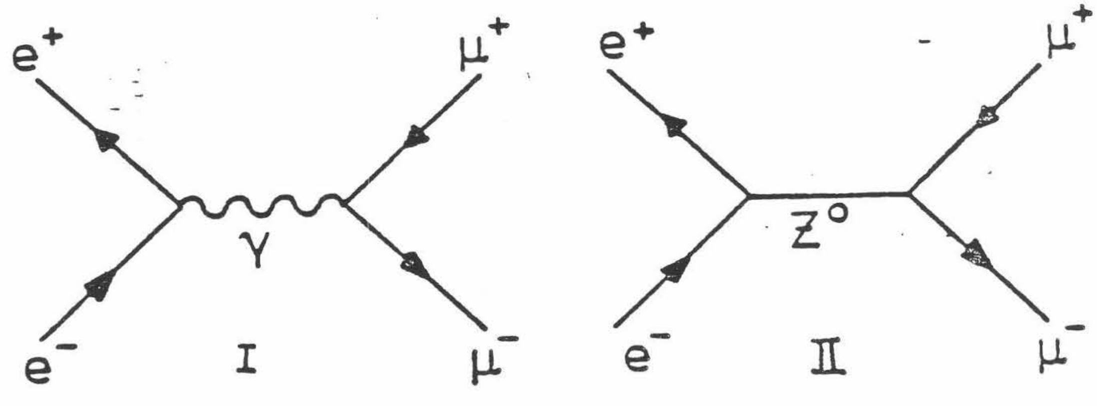

: Fig.5 : Lowest order Feynman diagrams of a γ and a Z^0 exchange

Diagram I represents the pure electromagnetic process and diagram II shows the pure weak process. Using Bjorken and Drell notation, the effective Lagrangian is:

$$\mathcal{L}_{eff} = - \bar{\psi}_e\gamma^\nu(g_v+g_a\gamma^5)\psi_e Z_\nu - \bar{\psi}_\mu\gamma^\nu(g_v+g_a\gamma^5)\psi_\mu Z_\nu$$
$$- e\bar{\psi}_e\gamma^\nu\psi_e A_\nu - e\bar{\psi}_\mu\gamma^\nu\psi_\mu A_\mu$$

where g_v and g_a are the vector and axial vector couplings of the Z^0 to the lepton field, and A_ν is the electromagnetic field. To lowest order then, the differential muon pair production cross section is:

$$\frac{d\sigma}{d\Omega} = \frac{\alpha^2}{4s} \left[F_1 \, (1+\cos^2\vartheta) + F_2 \cos\vartheta \right]$$

where

$$F_1 = \underbrace{1}_{\text{pure QED}} + \underbrace{8sgg_v{}^2\chi}_{\text{electroweak inteference}} + \underbrace{16s^2g^2(g_a{}^2+g_v{}^2)^2\chi^2}_{\text{pure weak}}$$

$$F_2 = \overbrace{16sgg_a{}^2\chi} + \mathcal{O}\,(\chi^2)$$

$$\chi = M_Z{}^2 \, / \, (s - M_Z{}^2)$$

$$g = G_F/8\sqrt{2}\pi\alpha = 4.49 \cdot 10^{-5} \ \mathrm{GeV}^{-2} \quad .$$

The asymmetry part of the cross section is the term proportional to $\cos\vartheta$ The term F_2, which is due to weak electromagnetic interference, is the major factor giving rise to the charge asymmetry. At PETRA energies, the pure weak term is small compared to the pure QED term, but the interference term amplifies the effect of Z^0, producing a forward-backward asymmetry:

$$A_{\mu\mu} \approx 7 \cdot 10^{-4} \ sg_a{}^2\chi\cos\vartheta/(1+\cos^2\vartheta) \quad .$$

This asymmetry is plotted in Fig.6 .

To do the calculation properly, one has to take into account radiative corrections from QED. Diagrams of order α^3 depicted in Fig.7 also give rise to a charge asymmetry, in the opposite direction, as plotted in Fig.8 .

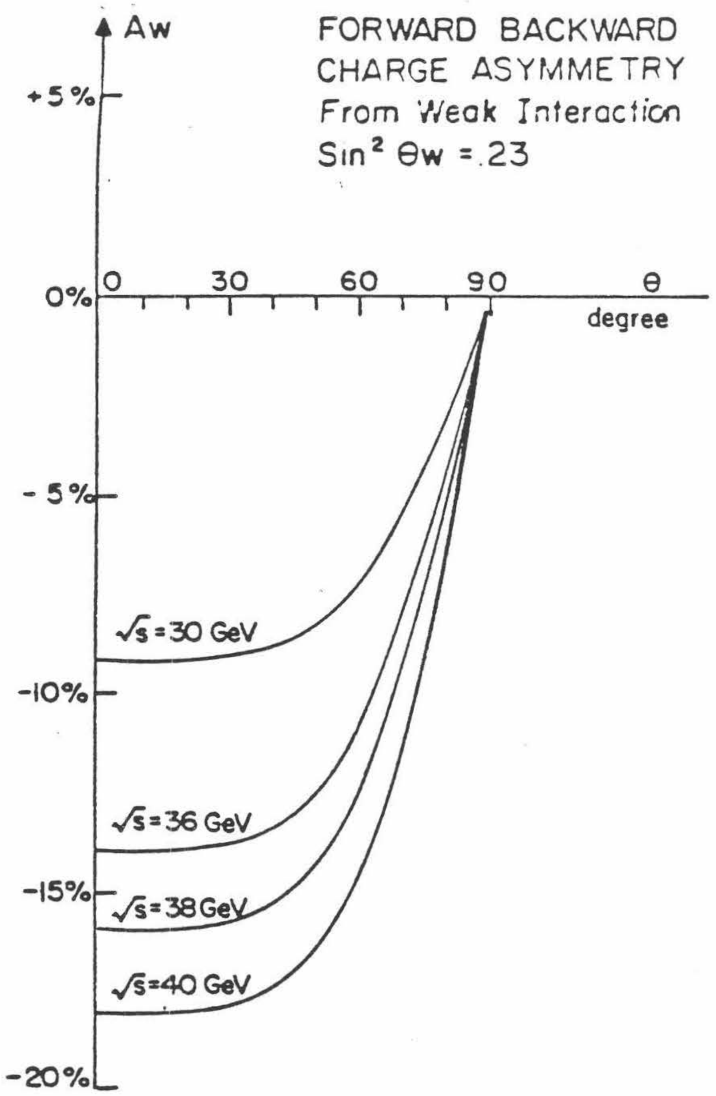

: Fig.6 : Forward backward charge asymmetry from weak interaction

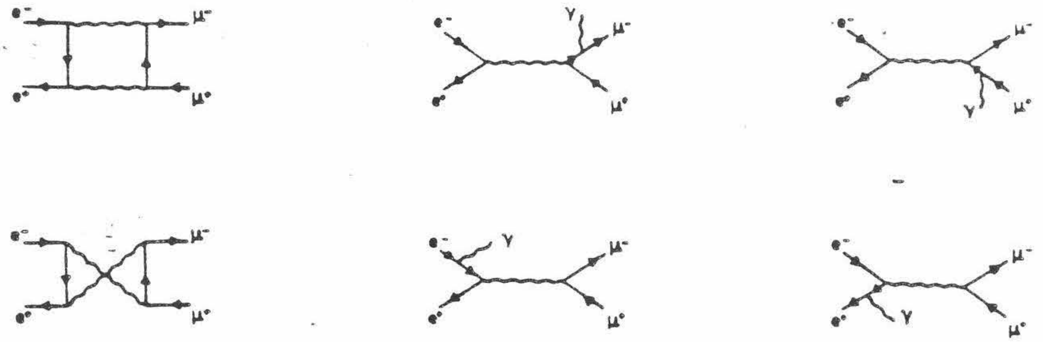

: Fig.7 : Feynman diagrams of order α^3

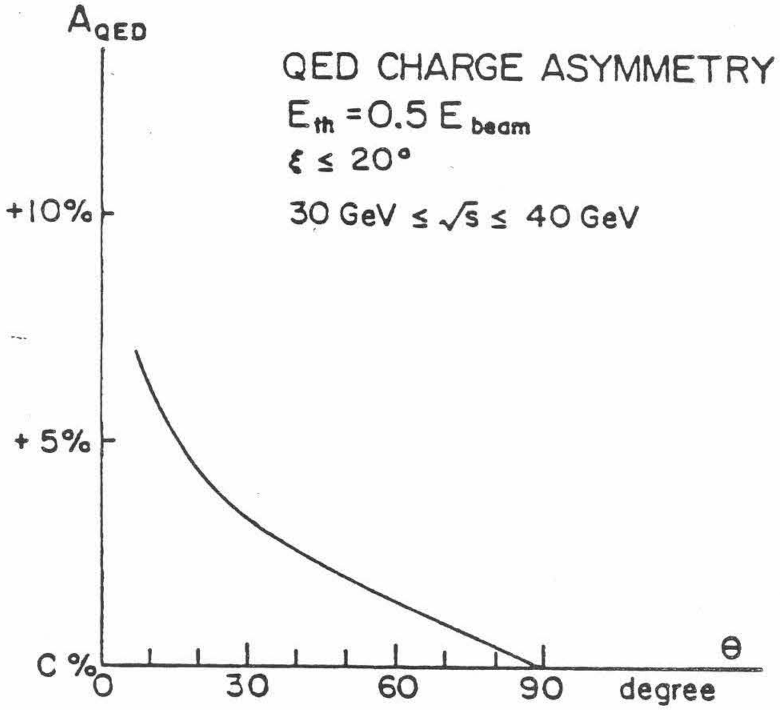

: Fig.8 : QED charge asymmetry

Apart from the direct observation of the Z^0 [5], the precise determination of the charge asymmetry from electroweak interference is the most important verification of the idea of the unified electroweak theory.

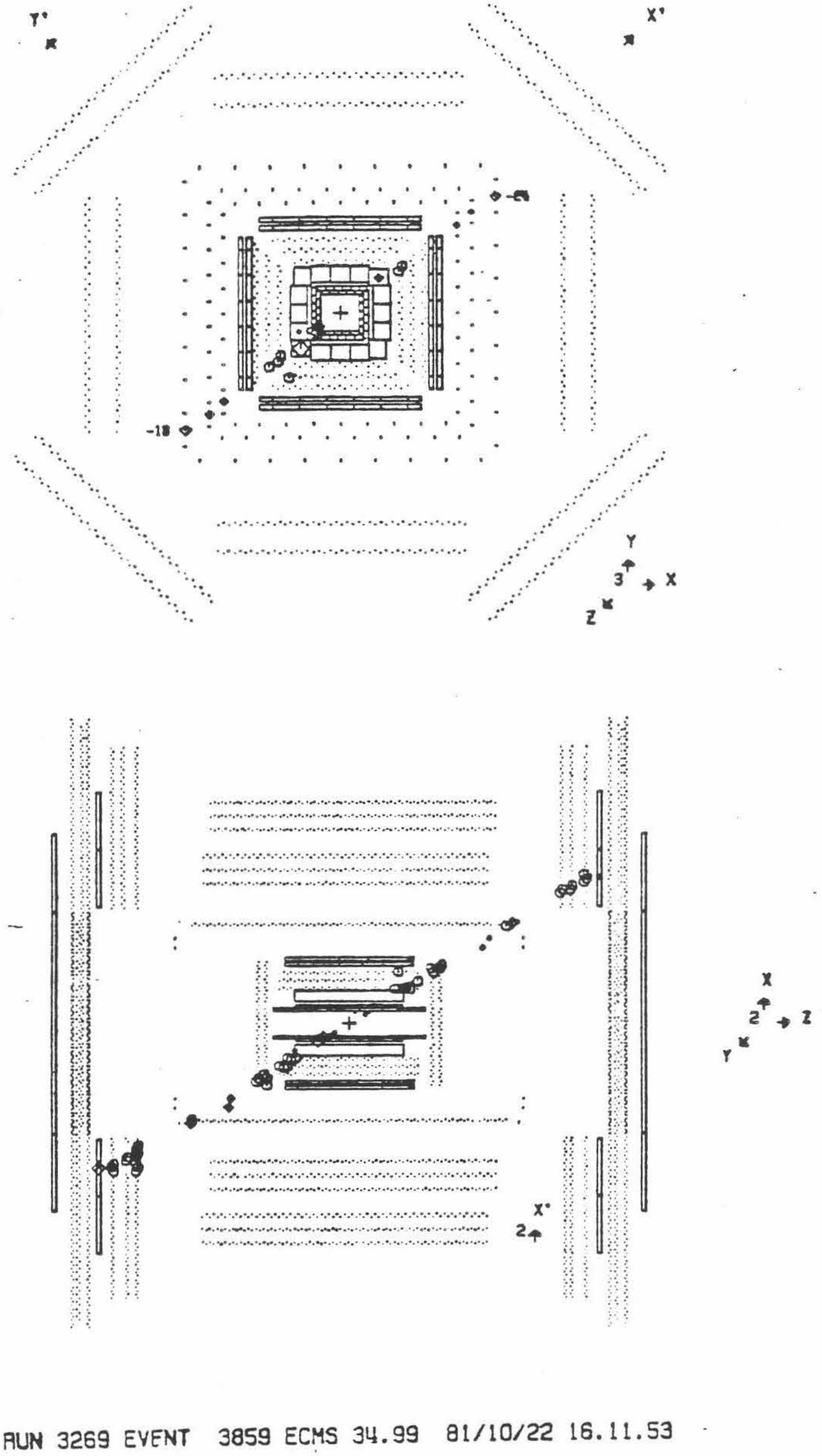

Fig.9 : An example of a 'good' dimuon event.

B. EXPERIMENTAL METHOD

As seen from Fig.6, the weak asymmetry is maximum at smallest angle. In the past the asymmetry has been measured and compared favourably to theory, only that the acceptance of the detector goes down only to $|\cos\vartheta| < 0.8$. It was the main reason for the installation of the forward counters to push the acceptance down to $|\cos\vartheta| < 0.9$, so as to test the theory at smaller angle where asymmetry is bigger.

Muon pair events are selected according to certain criteria [6] . To study the events in the extended angular range offered by the E counters, an off-line program selected those events that have E counters hits. Out of a raw data sample selected by an on-line trigger requirement dimuon events with E counters hits are selected. An interactive graphics routine is available by which individual events can be scanned together with the MARK J detector plotted on the same screen. The routine also provides an interactive monitor that can supply information of momentum fit, energy deposition, hit coordinates and many other details of each event. A good dimuon event is shown in Fig.9 . The signature of a 'good' event candidate is the presence of a nice track in the drift chambers and a good timing in the time of flight counters. Another program operates on this reduced sample to select candidates that have a good R chamber track.

Fig.10 shows the construction of the drift chambers. For a detail description, please refer to Ref.7 .

Fig.12 shows a 3-D view of the E counters with respect to the vertex as the origin. As shown in Fig.11 , each counter consists of a piece of plastic scintillator and a phototube at each end.

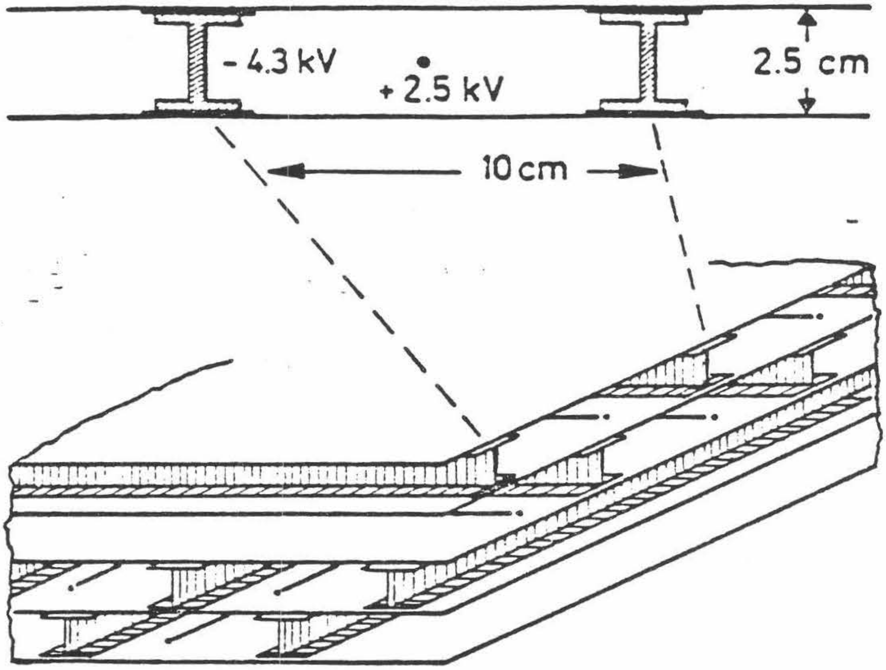

: Fig.10 : Mechanical assembly of the drift chambers.

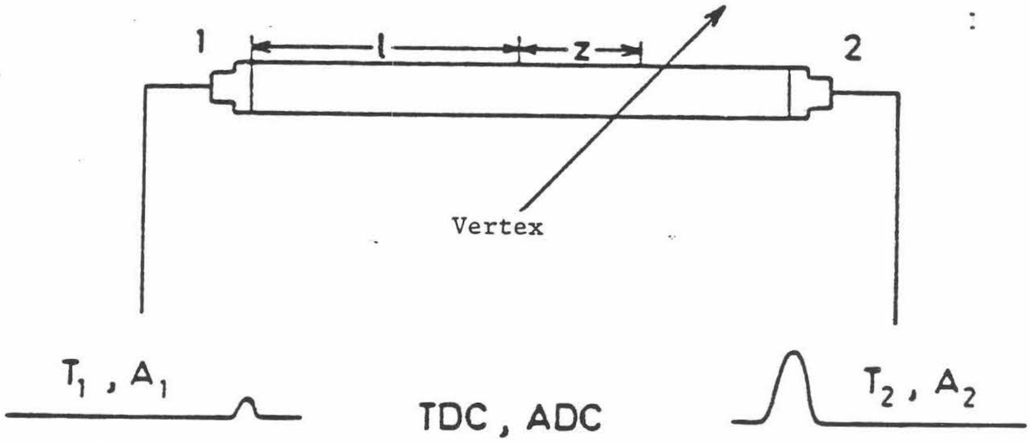

: Fig.11 : ADC and TDC readout of the counters.

The signal from each tube is fed through an ADC and TDC unit, which gives pulse height and timing information respectively. A major effort has been made to understand the systematic bias of the asymmetry measurement and to keep it < 1%. Some examples are given below [8] :

- uncertainty in momentum measurement
- uncertainty in detector acceptance
- trigger inefficiency
- tau pairs
- two photon processes
- cosmic rays

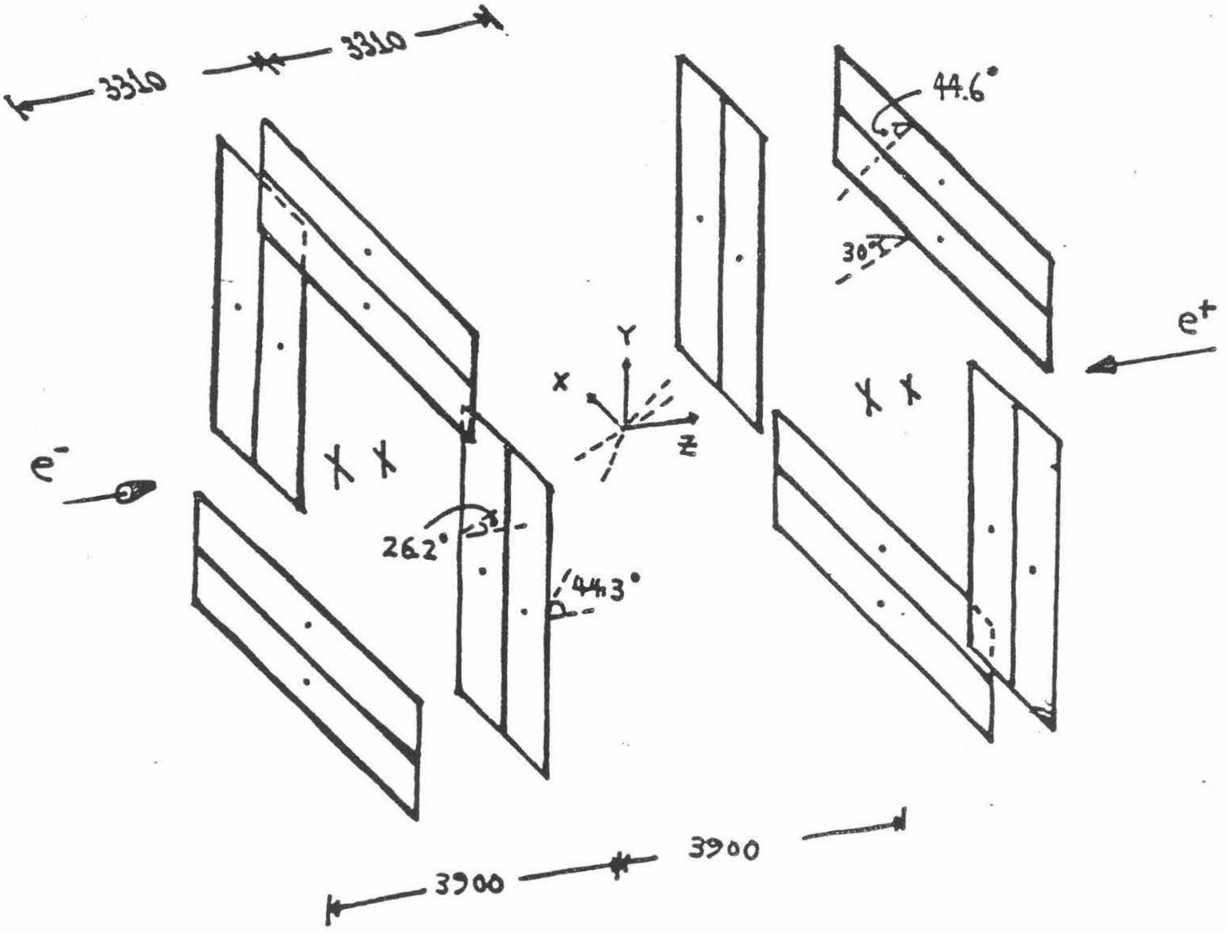

: Fig.12 : Three dimensional view of the forward counters.

An additional problem at energies above $\sqrt{s} \approx 40$ GeV, that is unique to the E counters, is the contamination due to synchrotron radiation as the E counter is not well shielded from the mini-β quadrupoles at the entrances of the particles bunches into the detector. Some beamgate events[1] ($\sqrt{s} \approx 41$ GeV) are scanned and on the average 9 random hits are observed per event. This poses serious problem on the counters because the synchrotron radiation hits which occur in random concidence with muon hits from $e^+e^- \rightarrow \mu^+\mu^-$ ruin the timing.

Like the other counters, the E counters have to be calibrated. The TDC readout has to be corrected for time slew effect, time zero, time of flight and propagation time in the scintillator material. The tracks fitted in the R chambers are also extrapolated to the E counters and the position of the hits along the counters compared to the values determined from ADC and TDC information. The R chamber track fit helps to separate muon hits from random hits, as synchrotron radiation cannot leave very good tracks in the R chambers because of its low energy (typically $\lesssim 1$ MeV) . Fig.13a shows the comparison of the hit position from E counters and R chambers. Fig.13b is a comparison of the timing from the E counter TDC's and that calculated from the positions reconstructed from R chamber tracks. Fig.13c is a histogram of the time sum of the two TDC's, one at each end of each E counter. They all show that the E counters have pretty good timing and spatial resolution. It is also apparent from these histograms that the level of synchrotron radiation effect is not very serious at 34 GeV (which is the main subject of this report). However, the effect is obvious at energies above ~ 40 GeV. Since the effect of synchrotron radiation cannot be well simulated and since we want to have as small a deadtime as possible, it is necessary that at least some substantial additional shielding has to be installed if we want to include the acceptance covered by the E counters in the final $e^+e^- \rightarrow \mu^+\mu^-$ sample.

C. DATA ANALYSIS

To calculate the charge asymmetry, one needs simply to count the number of μ^- in the forward and backward hemispheres. To this end the toroidal magnetic field acts as a charge identifier. The bending of the muon trajectory tells the momentum and charge of the muon. Fig.14 illustrates

---

[1] During each run, at a certain constant interval, all the trigger requirements are suppressed and the gate is opened when the beams collide to record all the hits with completely no bias. This is called a beamgate event.

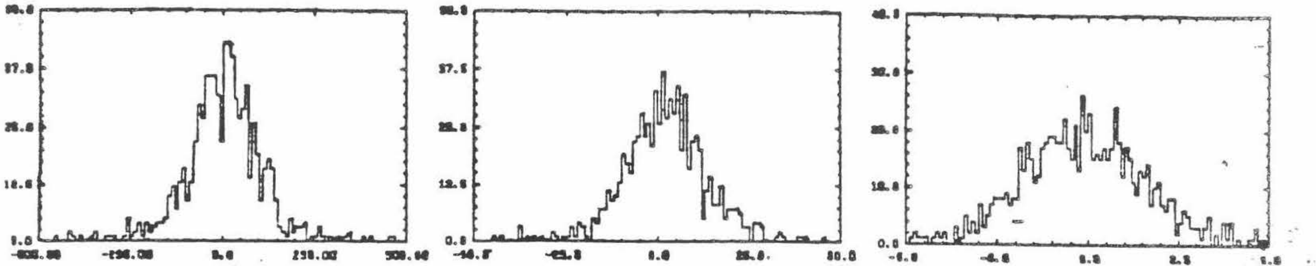

$\Delta Z = Z_R - Z_E$ (mm) $\Delta T = T_R - T_E$ (/20=ns) TSUM = $TDC_1 + TDC_2$ (/2=ns)

$\sigma_{\Delta Z} = 107$ mm $\sigma_{\Delta T} = 0.6$ ns $\sigma_{TSUM} = 0.8$ns

: Fig.13abc : Timing and spatial resolution of the E counters.

how the charge of the muon is related to the polarity of the magnetic field.

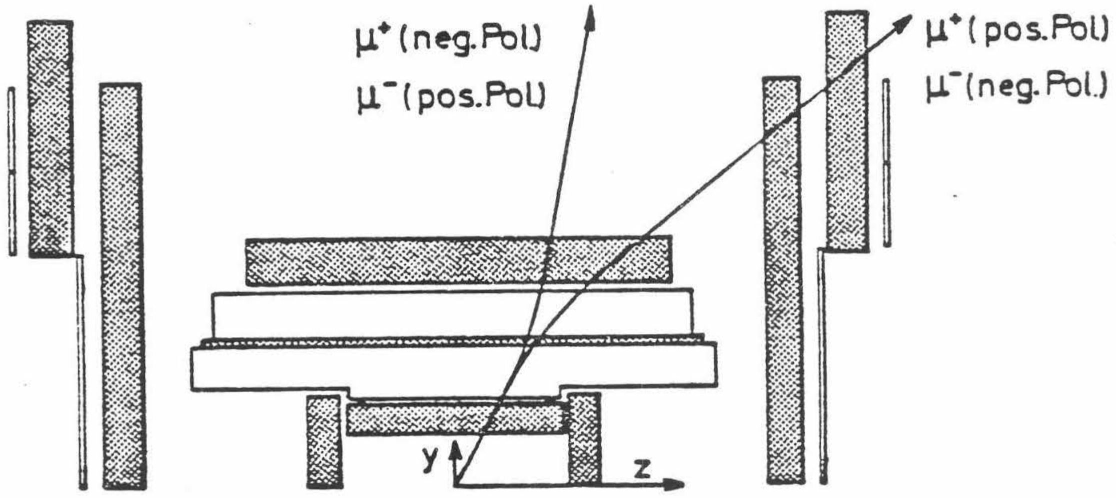

: Fig.14 : Relation of μ charge to magnet polarity.

After momentum determination, one has to consider the acollinearity ξ of the muon pair (ξ is already defined in Fig.4). By applying a momentum cut of $P_\mu/E_b > 0.5$, and an acollinearity cut of $\xi < 20°$, one can separate events due to lowest order γ and Z^0 exchange from those due to two photon process as in Fig.15., and also cut off events due to hard photon bremstrahlung.

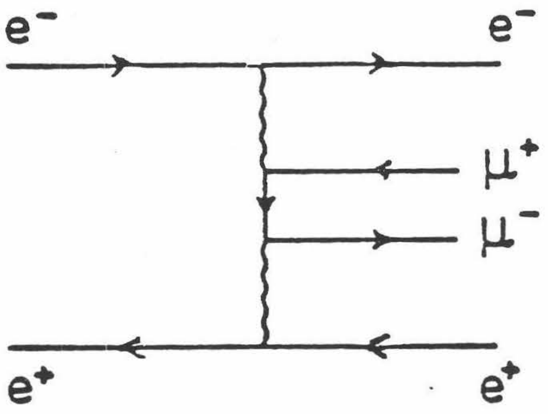

: Fig.15 : Two photon process.

Typically radiative events tend to have high ξ whereas two photon events tend to have small muon momentum with a uniform distribution of ξ. Fig.16 illustrates the P and ξ cut applied. And Fig.17a and 17b illustrate the P and ξ distributions before and after the cuts.

In principle the charge asymmetry is determined by counting the forward and backward μ^- within the sample resulting from the two cuts. But one has to be careful that there is an intrinsic detector asymmetry. It is evident in Fig.18 that the magnetic field causes an asymmetry in the μ^- acceptance. One of the nice features of MARK J is that the magnetic field polarity can be switched. One can thus gather data in both polarities and the detector asymmetry can then be compensated according to the following scheme:

$$A^{POL+} = A + A^{DET}$$

$$A^{POL-} = A - A^{DET}$$

thus

$$A = (A^{POL+} + A^{POL-})/2$$

$$A^{DET} = (A^{POL+} - A^{POL-})/2$$

Data with positive and negative polarities are analysed separately and the asymmetry is determined to be:

$$A^{T} = - 13.3 \pm 3.5 \%$$

$$A^{DET} = - 6.7 \pm 3.5 \%$$

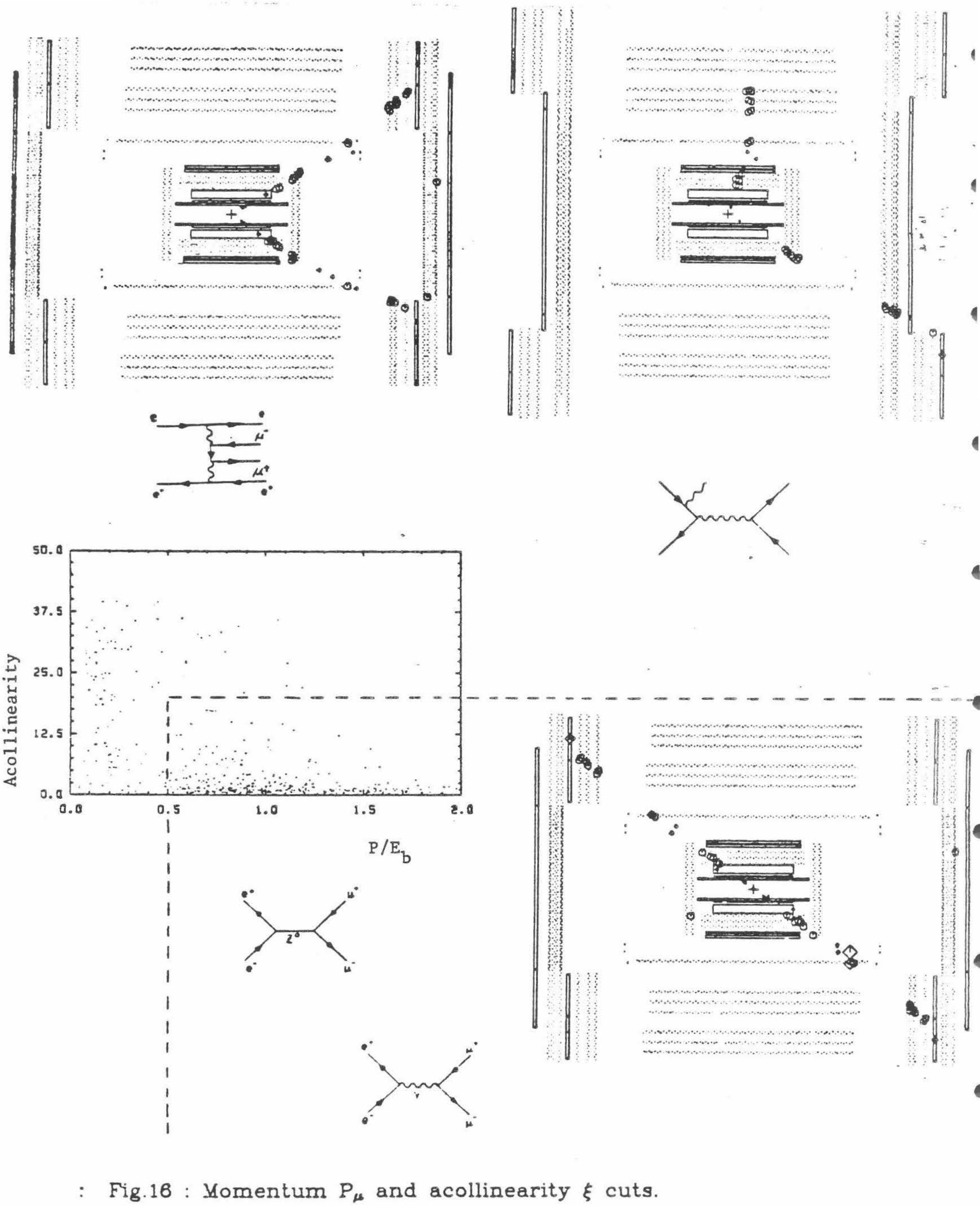

Fig.16 : Momentum P_μ and acollinearity ξ cuts.

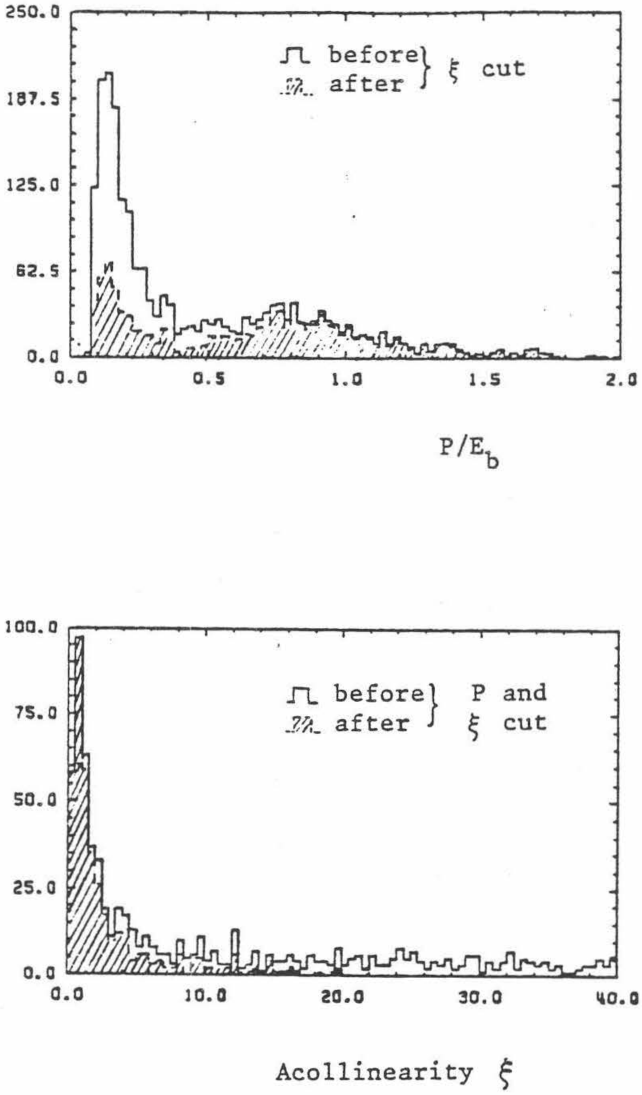

: Fig.17 : Momentum P_μ and acollinearity ξ distributions before and after the cuts.

Note that the charge asymmetry above is the total asymmetry, including $A_{\mu\mu}$ and A^{QED}. Using standard error propagation treatment, the error associated with the asymmetry is given by $\sigma_A = \sqrt{\{(1 - A^2)/(N_f + N_b)\}}$.

To compare with theory, one starts with a Monte Carlo event generator that incorporates the GSW model [8)] and generates events according to the theory involved. The events are then fed through a detector simulation

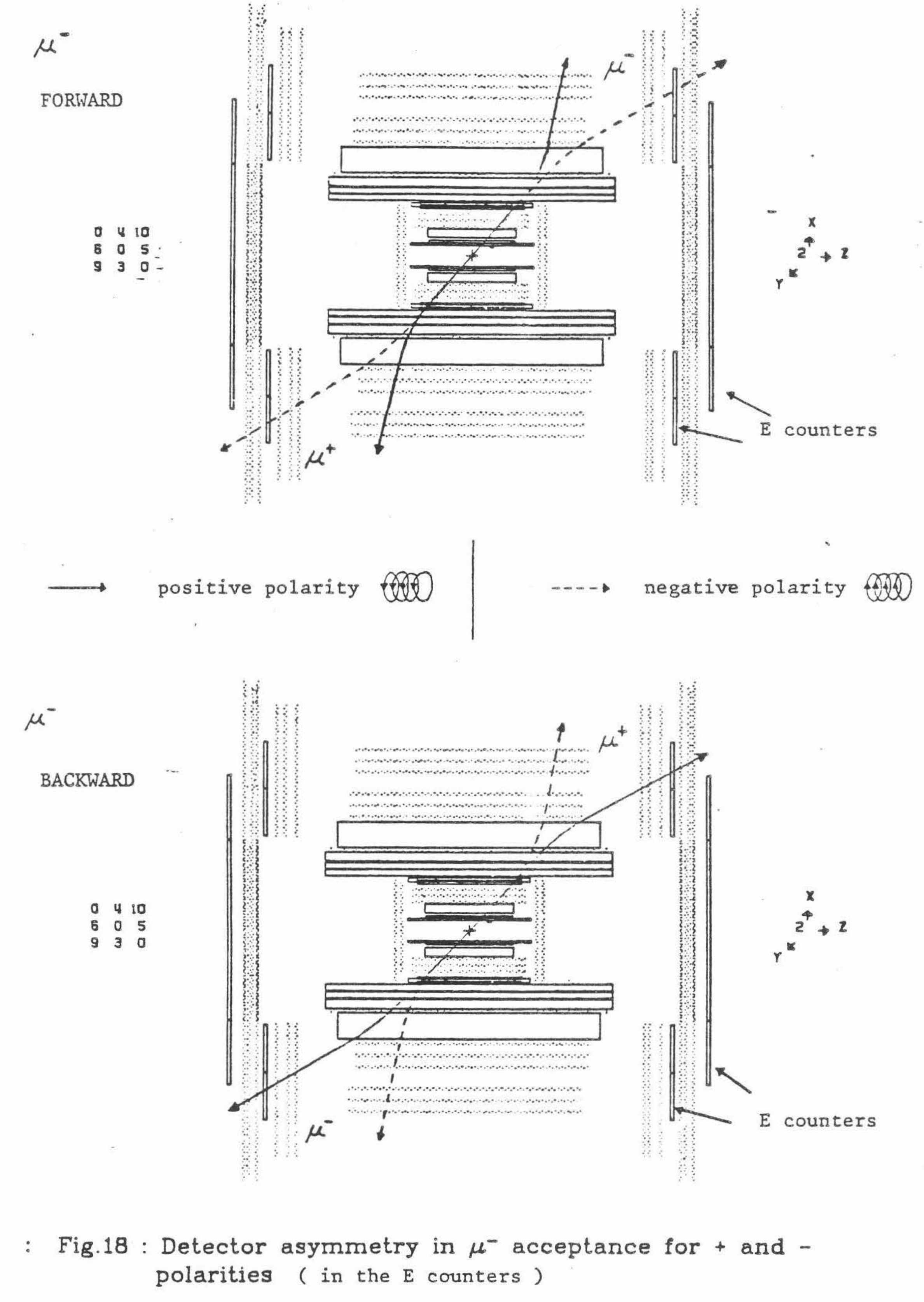

: Fig.18 : Detector asymmetry in μ^- acceptance for + and - polarities (in the E counters) program that simulates the entire detector in detail. This results in a Monte Carlo data file on which the same analysis is performed, namely μ pair event with E counter hits selection, P and ξ cuts, polarity selection, etc. Fig.19a,b and c show the comparison between real data(postitive magnet polarity) and Monte Carlo data (positive magnet polarity) on the momentum distribution, acollinearity distribution - and the forward-backward charge asymmetry respectively. It is evident that they are in good agreement. From the Monte Carlo data the asymmetry is calculated to be:

$$A^{T} = -11.2 \pm 1.3\ \%$$

To get the weak charge asymmetry one has to calculate the contribution from QED. Monte Carlo data files that include only QED process are also generated, one with positive polarity and the other negative. The same analysis is done and the charge asymmetry obtained to be:

$$A^{QED} = +3.0 \pm 1.3\ \%$$

We thus arrive at the final weak charge asymmetry:

$$A_{\mu\mu} = A^{T} - A^{QED} = -16.3 \pm 3.7\ \%$$

$$A^{GSW} = -14.2 \pm 1.8\ \% \quad \text{for } \sin^2\vartheta_W = 0.23 \quad .$$

for the angular range $0.5 < |\cos\vartheta| < 0.8$. The following table summarizes the asymmetry values:

Data	N_f^+	N_b^+	A^{POL+}	N_f^-	N_b^-	A^{POL-}	A^{T}	A^{DET}
Raw	164	246	-20.0±4.8%	176	201	-6.6±5.1%	-13.3±3.5%	-6.7±3.5%
M.C.	1248	1846	-19.3±1.8%	1485	1580	-3.1±1.8%	-11.2±1.3%	-8.1±1.3%

M.C. QED	1454	1587	-4.4±1.8%	1691	1374	+10.3±1.8%	A^{QED}= +3.0±1.3%	-7.4±1.3%

An attempt was made to do the same analysis on those events that do not involve more than one D counter . In other words they are events in the extra angular range covered by the E counters. Only a small percentage of the events is of this kind. But in trying to fit the momentum a serious problem was encountered. Fig.20 shows a possible good candidate and the

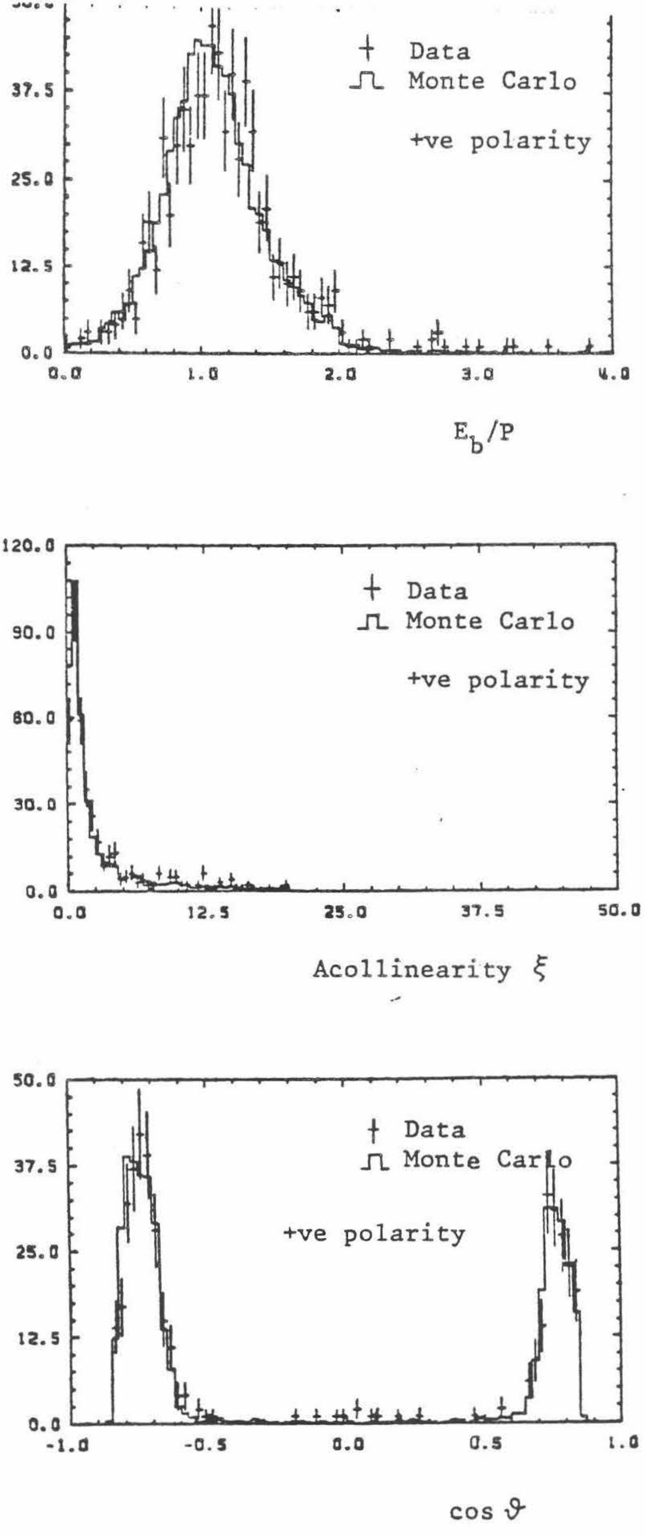

: Fig.19 : Comparison between real data and Monte Carlo data on the P distribution, the ξ distribution, and the forward-backward charge asymmetry.

problem involved: the muon only passes through a small section of the magnet and hence the momentum resolution is insufficient to determine the charge of the muon.

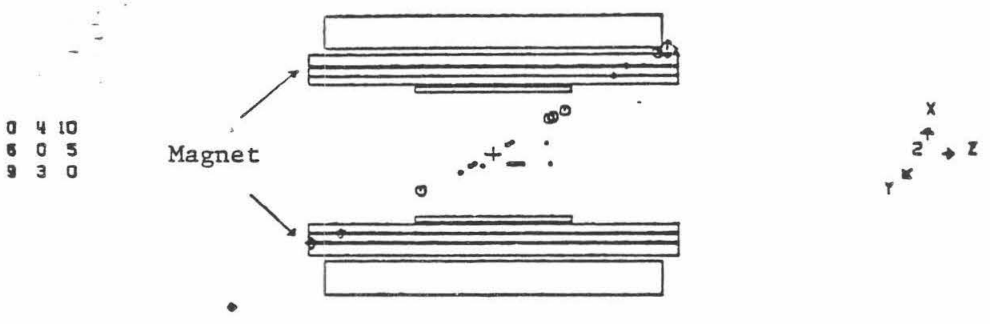

Fig.20 : Problem with event that has no D counter hits.

As a result it is hard to determine the asymmetry from this already small data sample.

Fig.21 is a block diagram summarising all the major steps involved in this work.

FIG.21 :BLOCK DIAGRAM

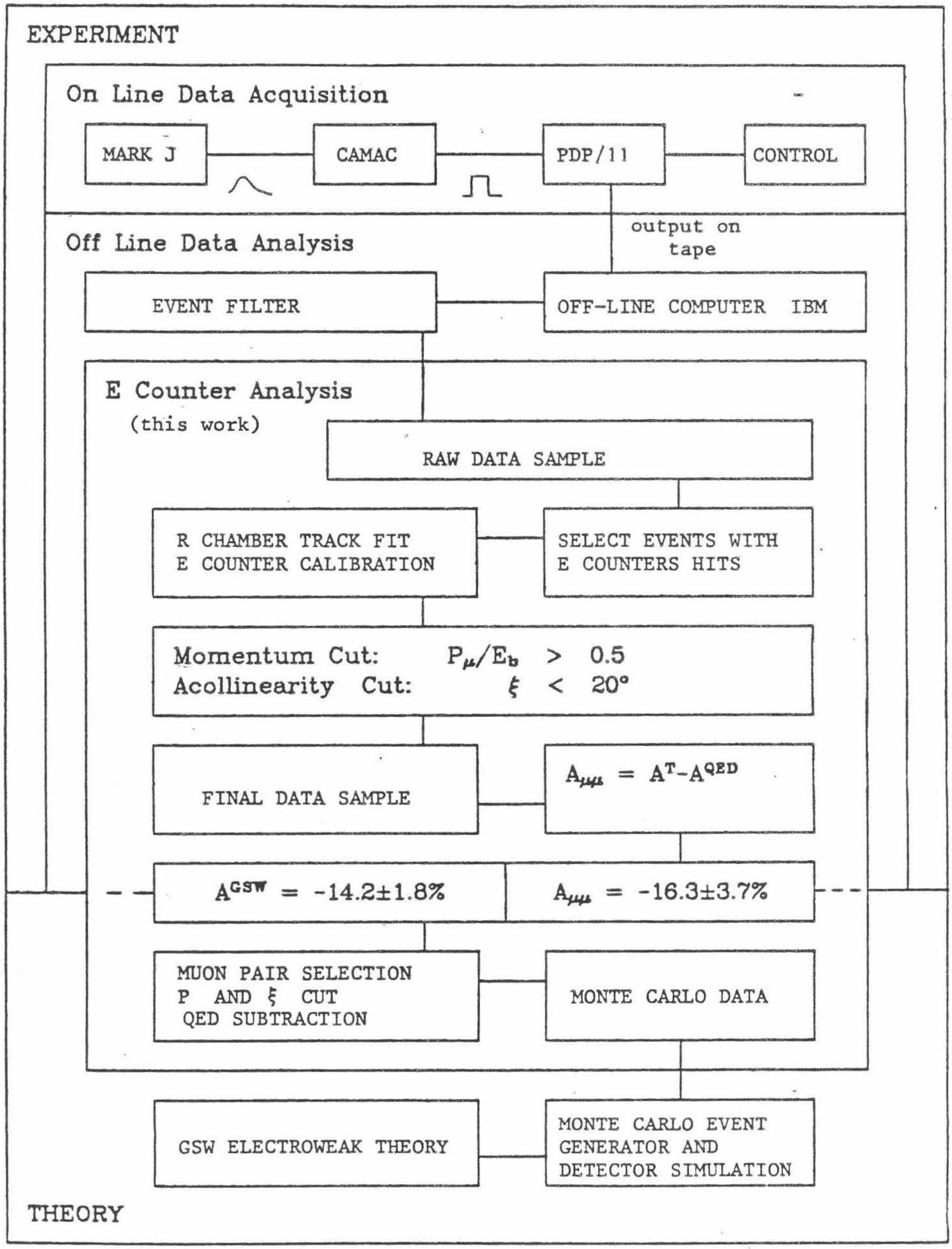

Fig.21 :Block Diagram

The forward counters of the MARK J detector have been studied and found out to have good resolution. The charge asymmetry of the reaction $e^+e^- \rightarrow \mu^+\mu^-$ in the angular range in common to the forward and the side counters compares well with the GSW model prediction. Effort has been made to extend the calculation to the extra angular range offered by the forward counters but a lack of bending power in the forward region made it hard to determine the μ charge with the same reliability as in the central region. Further analysis is required.

It is to be emphasized again that the determination of charge asymmetry provides a test of the GSW theory apart from the direct observation of the intermediate vector bosons themselves. In principle (see appendix) the charge asymmetry allows one to test the relationship between the mass of the intermediate bosons, the vector and axial vector weak couplings in more detail as they are all related through the unique parameter of the unified theory, viz. the Weinberg angle ϑ_W .

Note that the precise test of the theory involves radiative corrections to the $W^\pm$ and Z^0 masses, and $\sin^2\vartheta_W$. Higher order corrections also enter in the definition of G_F and α in ultra-precise low energy experiments (muon decay and the anomalous magnetic moment of e^+ and e^-). It is the self-consistency of all these basic parameters that will determine if the GSW theory is fundamentally correct. The determination of the charge asymmetry thus provides a test on the unified electroweak theory at a more quantitative level than just an identification of a particle.

APPENDIX

In the frame work of the GSW model, the mass of the intermediate bosons, the vector and axial vector coupling constants are all inter-related as follows:

$$M_Z^2 = \kappa \,/\, (\sqrt{2}G_F)$$

$$M_Z^2 = M_W^2 \,/\, (1 - \zeta^2)$$

$$g_v^2 = (1 - 4\zeta^2)\cdot\kappa/4$$

$$g_a^2 = \kappa/4$$

where

$$\zeta = \sin\vartheta_w$$

$$\kappa = \pi\alpha/ \,\{\zeta^2(1-\zeta^2)\}$$

BIBLIOGRAPHY

1) J.G.Branson , DESY 82-078 , (1982)

2) The MARK J Collaboration , Phys. Rep. 63, 337 (1982)

3) F.Hasert et al , Phys. Lett. 46B , 138 (1973)

4) S.Glashow , Nucl. Phys. 22 , 579 (1961) ;
S.Weinberg , Phys. Rev. Lett. 19 , 1264 (1967) ;
A.Salam , in : Elementary Particle Theory , Editor H. Svartholm
(Almquist and Forlag , Stockholm , 1968)

5) The UA1 Collaboration , CERN - EP/ 83-73 , (1983)
The UA2 Collaboration, recent results presented at the
Cornell Conference (1983)

6) B.Adeva et al , Phys. Rev. Lett. , 48 , 1701 (1982)

7) G.Herten, Thesis, RWTH Aachen Third Physics Institute, (1983)
(unpublished)

8) F.A.Berends, R.Kleiss, Nucl. Phys. B177, 237 (1981)

Title: Gamma Ray Background Suppression in Detection of Polarization Asymmetry of Nuclear Beta Rays.

Author: Mark D. Lindsay

Faculty Sponsor: Felix Boehm

ABSTRACT:

A proportional counter and a Si(Li) solid state detector were placed in a telescopic geometry along the path of ^{60}Co beta rays. The proportional counter pulse was used as a coincident gate pulse for the Si(Li) detector. In the presence of a large background of gamma rays the Si(Li) γ-ray count rate was reduced by a factor of 30 by this gating while the Si(Li) count rate for beta rays travelling along the axis was reduced by only 20%

INTRODUCTION:

One of the research projects going on in Dr. Boehm's lab is the search for time-reversal invariance violation in the beta decay of Co^{60} nuclei. A violation is indicated by a correlation in the β-decay distribution of the triple vector product $\vec{J} \cdot \vec{\sigma} \times \vec{p}$, where $\vec{J}$ is the spin of the Co^{60} nucleus, $\vec{\sigma}$ is the spin of the emitted electron (beta ray), and $\vec{p}$ is the momentum of the electron.

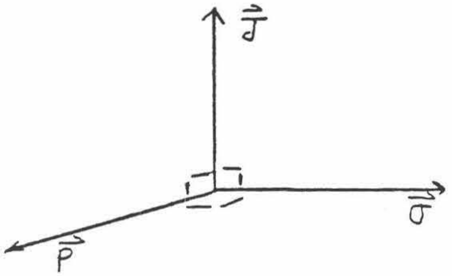

Thus the presence of a transverse polarization of the emitted beta rays perpendicular to the nuclear spin signals time-reversal violation.[1] A standard method to measure beta-ray polarization is to employ the polarization dependent Mott backscattering asymmetry.[2] Mott scattering is ideally a single nuclear scattering so the scattering target (a Au foil) must be very thin to eliminate plural scattering in the foil. Backscattering is an extremely inefficient process; (about 1/10,000 β's scatter at an angle greater than 90^0). Therefore the beta ray detectors positioned at 120 degrees for maximal asymmetry will measure only a very small count rate of backscattered electrons. However, ^{60}Co source emits gamma rays also, and the γ count rate in the Si(Li) will be much larger than the desired beta ray count rate. The gamma-ray pulses must be suppressed. A γ-ray background suppressed Si(Li) detector[3] has been developed using a thin-windowed proportional counter in a telescopic geometry as a gate to eliminate background gamma-ray counts.

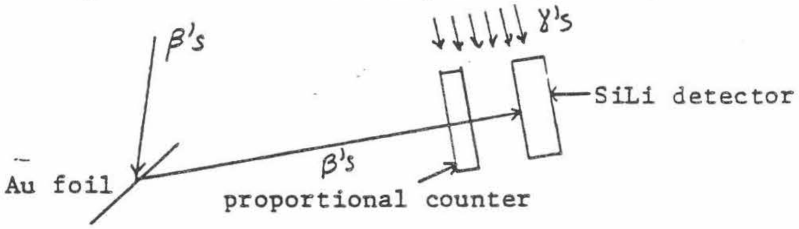

The desired β rays pass through the proportional counter and into the Si(Li) detector while the γ rays do not interact appreciably with the proportional counter.

RESULTS:

The Si(Li) detector obtained commercially had a diameter of 2.5 cm and an active depth of 5 mm. The proportion counter made out of aluminum is shown in Fig. 3. Stainless steel wire (20 μm diameter) was used as the anode. Three anode wires were used, spaced about 0.6 cm apart.

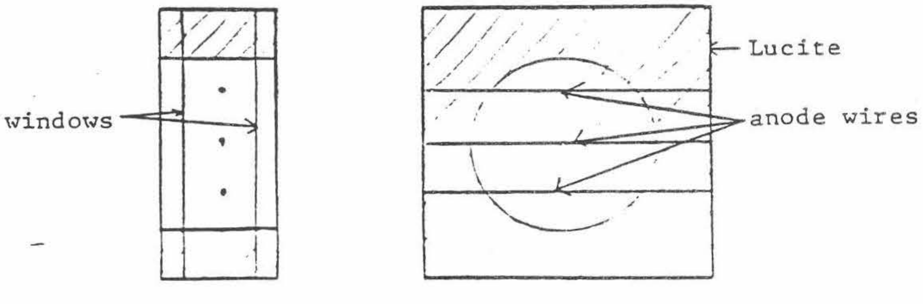

This rather large spacing means the charge collected by the counter (the size of the pulse) will depend not only on the energy of the incident beta ray, but also on its location in the counter. This non-linear response is satisfactory, however, since the pulses from the proportional counter will be converted into <u>logic</u> gate pulses. No energy measurements are made from the proportional counter.

The beta rays are intended to pass completely through the proportional counter and stop in the Si(Li) counter behind. To get accurate energy measurements of the beta rays, they must lose very little energy in the proportional counter. Thus the walls of the counter must be as thin as possible. However the counter which is filled with counter gas (90% Ar, 10% CH_4) at 1 atm must be in vacuum to allow passage of beta-rays. Thus the counter windows must be thick enough to resist one atmosphere of pressure. We have used aluminized Mylar, (25 m thick). The aluminum provided the ground plane for the electric field. A hybrid microcircuit preamp was used and placed in a ground shielded box close by the proportional counter to minimize wire length and outside interference. The typical pulse output of the preamplifier was about one volt with noise observed at about 1 millivolt. Therefore, the noise never triggered a gate pulse.

When a beta-ray source was placed along the axis of the pair of detectors, the gated count rate was 80% of the ungated count rate. This is a 20% loss of efficiency for the detector as a whole, which is acceptable.

The main source of gamma-ray background with the proportional counter operating as a gate was gamma-rays that Compton-scatter in the front surface of the Si(Li), and eject an electron which then goes into the proportional counter. This process mimics the passage of an electron through the proportional counter into the Si(Li(, and to reduce this we moved the proportional counter as far as possible away from the Si(Li) to reduce the solid angle the Compton-scattered electron would have to be ejected into. Gamma-rays can also interact in the walls of the proportional counter, producing a pulse there and then sending a Compton-scattered electron into the Si(Li). We minimized this process by building second proportional counter almost entirely out of Lucite plastic, which has a low Z, and so has a low Compton cross section.

CONCLUSION:

By using a thin-windowed proportional counter and SiLi solid-state detector in a telescopic geometry, it is possible to reduce counts from background gamma-rays by a factor of 30 while preserving 80% of the counts from on-axis beta rays.

ACKNOWLEDGMENTS

I would like to thank the SURF organization for their generous grant, Dr. Boehm for taking me into his research group, and John Markey for many fascinating discussions and a great deal of support.

Footnotes

1) J.D. Jackson, et al., Phys. Rev. 106 (1957) 517.

2) Shin-R. Lin, Phys, Rev. 133A, 965 (1964).

3) T. Toriyama et al., Future Directions in Studies of Nuclei Far From Stability, J.H. Hamilton et al., (eds.), North Holland, 1980, p.97.

APPLICATIONS OF SOUNDSPECTROGRAM ANALYSIS TO BIRDSONG

Misha Mahowald

Sponsor: M. Konishi

ABSTRACT

Soundspectrogram analysis of birdsong was used to investigate problems related to song learning, song maintenance, and synchronization of syringeal output. The song of a masculinized female zebra finch was analyzed in order to determine whether or not females, like males, learn song from their fathers. Because her father's song could not be obtained, no conclusion could be reached. The song of a deafened canary was analyzed and the data suggest that audio feedback is necessary for maintenance of normal song in the canary. The songs of two canaries and two zebra finches whose anterior commissures had been ablated were analyzed. Incomplete and unreliable data from the canaries makes it impossible to form any conclusions at this time. The fact that the songs of the zebra finches remains unchanged after commissurectomy indicates that there is no functional connection through the anterior commissure between the right and left hemispheric song nuclei at the level of the telencephalon which is responsible for integration of sound produced at the syrinx.

Introduction

Birdsong is an ideal animal model for the study of serial order in behavior. It begins to approach in complexity and degree of temporal integration such motor feats as speaking and playing the banjo. The soundspectrogram is useful in the study of birdsong because, by plotting frequency and intensity as a function of time, it translates the acoustic-temporal pattern of song into a visuospatial pattern which is easier to analyze.

Normally, only male birds sing; however, female birds can be masculinized to produce song. Song learning takes place in many species in a two stage process. For example, in the first stage of song learning of the zebra finch, the bird hears the song of his father and stores it as a model. Later the bird uses auditory feedback to develop a sensorymotor pattern for song. Once a bird has learned, or "crystallized", his song, auditory feedback may or may not be necessary formaintenance of normal song. Deafened adult chaffinches, for example, continue to sing a perfectly normal song, while the song of the Common Cardinal will undergo deterioration if the bird is deafened as an adult.

Many of the basic neural pathways and nuclei involved in song production have been delineated through lesion studies and neuroanatomical techniques. Lesion studies have shown that nuclei HVc (Hyperstriatum ventrale, pars caudale), RA (Robustus Archistriatialis), which is efferent to HVc, and nXIIts (Hypoglossus, pars tracheosyringealis) are necessary for normal song production. Neuroanatomical connections between these, and other nuclei implicated in song production are diagrammed in figure 1. The brain is bilaterally symmetrical; therefore, all of the nuclei appear identically on the right side of the brain and the left.

Although these nuclei are implicated in song development and production, their exact function is unknown. The presence of two complete sets of song production apparatus comprising neural and syringeal components, has raised interesting questions concerning the functional significance of the duplicity and the synchronization of the entire system. Coordination of the right and left syringeal halves implies some communication between the right and left neural pathways for song production. The point along the pathway where this communication takes place is unknown. There are a multitude of places where it could take place. For example: Traditional neuroanatomical tracer techniques have not disclosed any direct connections between song nuclei of the telencephalon of the canary. The nucleus intercollicularis (Ico) of the midbrain, which is efferent to the ipsilateral RA, sends projections to the contralateral Ico. Lesion ofIco produces only minor effects on song, however, so this can apparently be eliminated as the site of communication. Nottebohm has postulated that the Commissura Infima, a fiber tract in the medulla which may connect the right and left nXIIts, is the pathway of communication between the two sides. Another possibility is that there are indirect connections of the telencephalic nuclei through the anterior commissure.

It is appparent that birdsong presents a wide variety of topics for investigation. The scope of this project encompassed several aspects of bird song, including song learning, the use of auditory feedback for song maintenance, and the synchronization of the right and left song production pathways.

An interesting question which this project adressed is related to the sexual diamorphism of the song system and song learning. Two masculinized female zebra finches who had been fostered by the same pair of Bengalese finches were employed in an attempt to determine if song learning takes place in the female as it does in the male.

In addition to song learning in zebra finchs, the function of auditory feedback in maintenance of song in canaries was investigated. There is currently a debate about the effect of deafening of a adult canary. Nottebohm (unpublished work) found that a canary's song began to deteriorate as soon as two weeks after deafening and had, by the next season, deteriorated still further. McCasland, however, found little change in the quality of the song of a deafened canary even after one year (personal communication).

The third and final problem which was investigated concerned the possible role of the anterior commissure, the fiber bundle connecting the two hemispheres of the telencephalon, in synchronizing vocalizations from the right and left halves of the syrinx. As was stated earlier, no neuroanatomical evidence has been found to indicate that the commissure plays such a role, but the existence of a pathway through the commisure connecting the two sides of the song system has not been disproven. If the anterior commissure does serve as the site of right-left communication, its ablation would seriously affect song. For example, one might expect parts of elements in canary song to become shifted relative to one another since hypoglossal nerve section experiments indicate that each side of the syrinx may produce independent parts of elements. A different effect might be observed in the zebra finch whose song requires the combined effort of both syringeal halves to produce overlapping fundamentals. In this case, destruction of the pathway allowing for synchronization might cause severe deterioration of song.

METHODS AND RESULTS

Sound spectrograms generated using a Sona-graph machine were used to analyze the songs of the birds used in these experiments. The birds were housed in isolation boxes and song was recorded for analysis. Both pre-operative and post-operative song was analyzed and compared for each bird. Analysis of song was based on division of the songs of zebra finches and canaries into commonly accepted units.

The song of a zebra finch is composed of a sequence of elements. (One element is defined as a blackening on the soundspectrogram that is continuous in time). A set of elements which appear together repeatedly is called a motif. A combination of introductory elements and several consecutive motifs form a strophe. A normal adult male zebra finch sings a well-stereotyped song in which the motif and introductory elements are unchanging.

The song of a canary is also composed of elements. Instead of being grouped into motifs however, one to three elements are said to compose a syllable. A string of identical syllables is called a phrase. Combinations of phrases form songs. A normal adult male canary has approximately thirty syllables in his repertoire which may be grouped to form a very large number of different songs. While phrases may tend to appear in a certain pattern, the song of the canary is not as stereotyped in this sense as the song of the zebra finch.

Masculinized female zebra finches

Two female zebra finches had received subcutaneous implants of estradiol as chicks which served to masculinize the nuclei responsible for song production. Prior to exposure to testosterone as adults, neither of these birds was heard to sing. The birds received subcutaneous implants of approximately 5 mg. of testosterone. Within five days of exposure to testosterone the birds were producing new vocalizations. At first these vocalizations were sung very softly and had an amorphous structure. In the case of bird R439, the song did not progress much beyond this stage. The vocalizations became more recognizable as song elements but they continued to be sung softly and were never formed into a stereotyped song. Bird B474 began producing a well formed song with stereotypy as good as that of a male two to three weeks after exposure to testosterone.

These female finches were foster fathered by a male Bengalese finch. All attempts to prompt him into song by presenting him with female Bengalese finches failed and none of his song was ever recorded. He will be implanted with testosterone and will continue to be monitored for song.

Deafened canaries

Two canaries were deafened by removal of their cochlea and 5mg. pellets of testosterone were implanted subcutaneously in order to induce the birds to sing again as soon as possible after surgical trauma. Bird B52 did not recover from the surgery and did not sing. Bird S14 sang three weeks after surgery.

The post-operative song of S14 differs substantially from his pre-operative song. Before deafening his repertoire included 29 syllables. After deafening his song included only 15 syllables. As expected, with fewer syllables there is less variation in the songs that are sung. Some syllables remained intact while others suffered varying degrees of degeneration. The two syllables which are sung most often post-operatively are unrecognizable as any of the pre-operative syllables.

Commmissurectomy

Two canaries and two zebra finches underwent commissurectomy surgery. The surgery was performed with a 6mm probe made from an etched tungsten wire. The wire was hooked at the end. The probe was inserted into the brain through a hole in the skull and dura whose location was determined using rough stereotaxic coordinates. The probe was directed through the brain tissue in an arc of approximately 90° and withdrawn, cutting the anterior commissure.

Post-operative song was recorded for a period that varied with each bird. The canaries were implanted with testosterone pellets two weeks after commissurectomy. They sang about ten days after exposure to testosterone. Zebra finch NT5 began singing three weeks after commissurectomy. Zebra finch B473 began singing within five days of surgery.

After recordings of post-operative song was completed NT5, B473, and NTS were sacrificed by cardiac perfusion. Histology was performed by slicing the brain tissue into 30micron slices. Tissue sections were stained with cresyl violet dye and examined to determine the effect of the commissurectomy. In all three cases the commissure was severed; however, as a result of the surgical procedure, the lesions were slightly lateral ofthe midline and it is possible that relevent fibers remain intact.

The effect of the surgery on the songs of the canaries is difficult to determine. While collection of data remains incomplete at this time, certain observations can be made. The song of NTS sounds similar to the ear in terms of complexity of phrase arrangement and variety of syllables. Of the post operatively produced syllables which have been analyzed with soundspectrograms, few show substantial deviation from pre-operative syllables. Four syllables which were unobserved pre-operatively have been found to date. Three of these are similar to syllables sung by other canaries housed in the same room.

In-contrast, the post-operative song of R191 sounds much simpler than his pre-operative song. Soundspectrograms demonstrate the dearthof complex trill elements, which characterize canary song, in his post-operative song.

Unlike the songs of the canaries, the zebra finches' respective post-operative and pre-operative songs are identical. This clear-cut absence of any effect of commisurectomy is, in itself, exciting.

CONCLUSIONS

If it is true that ablation of the anterior commissure of a zebra finch has no immediate effect on his song, then one can conclude that any short-term synchronization of the syringeal output does not take place at the level of the telencephalon. This supports the findings of neuroanatomists who were unable to discover any interhemispheric connections. The question of how song is synchronized remains unanswered.

The results obtained through analysis of the song of the deaf canary have also proven interesting. The data seem to support the claim that auditory feedback is necessary for maintenance of intact song in the adult canary. It is difficult, however, to make any conclusive statements because the observed deterioration of the song of the one bird could result from side effects of the surgery or from an indirect effect of the deafening. One example of an indirect effect of deafening was observed by Peter Marler. He found that the size of the song repertoire of the deafened adult canary increased when the deaf bird was exposed to other birds. The theory in this case is that deaf birds lack the environmental auditory stimuli likely to trigger song and that this effect is somehow compensated for by contact with other birds. One effect of deafening then appears to be motivational and is not directly related to neural events which play a role in song maintenance.

Much of the data relevent to this project has not yet been obtained and therefore few conclusions can be drawn. For example The work done with the masculinized female finches agrees with work that was done in the past but the resolution of the problem of whether a female learns her fathers song as does the male awaits analysis of the song of the Bengalese foster father. The data obtained from the canaries which underwent commissurectomy is very inconclusive. The data from the two birds seems to conflict, the song of S14 seemingly much less affected by the surgery than that of R191. Other factors, such as the fact that NTS appeared to have undergone a molt and may have begun to recrystallize a song containing new elements, serve to further complicate the data. It will be interesting to continue to monitor both R191 and S14 and see what effects deafening and commissurectomy have on the development of next season's song.

BIBLIOGRAPHY

Gurney, Mark (1982) Behavioral correlates of sexual differentiation in the zebra finch song system. *Brain Research*. *213*: 153-172.

Marler, Peter (1981) Birdsong: the acquisition of a learned motor skill, *TINS*, April, 88-94.

McCasland, J. (1983) Neuronal Control of Bird Song Production. Ph.D dissertation. California Institute of Technology.

Nottebohm,F. (1975) Vocal Behavior in Birds, In "Avian Biology" (J.R. King and D.S. Farner, eds.), Vol. 5, Chap. 5, pp. 287-332. Academie Press, New York.

Nottebohm, F. (1980) Brain pathways for vocal learning in birds: A review of the first 10 years. *Prog, Psychobiol. Physchol*. *9*: 85-124.

Sossinka, R., and Böhner, J. (1980) Song types in the zebra finch *Poephila guttata castanotis*. *Z. Tierpsychol*. *53*: 123-132.

Figure 1. Schematic diagram of the vocal control system in songbirds. Arrows indicate anterograde connections between nuclei. Lesion studies have shown HVc (Hyperstriatum ventrale, pars caudale) and RA (n. Robustus Archistriatalis) are necessary for normal song production. Hatched areas represent auditory pathways. Other abbreviations: NIf (Nucleus Interfacialis); nXIIts (n. Hypoglossus, pars tracheosyringealis); MAN (Magnocellular nucleus of the anterior neostriatum); X (area X). (original by M. Gurney, slightly modified.)

REPRODUCED FROM REFERENCE 3

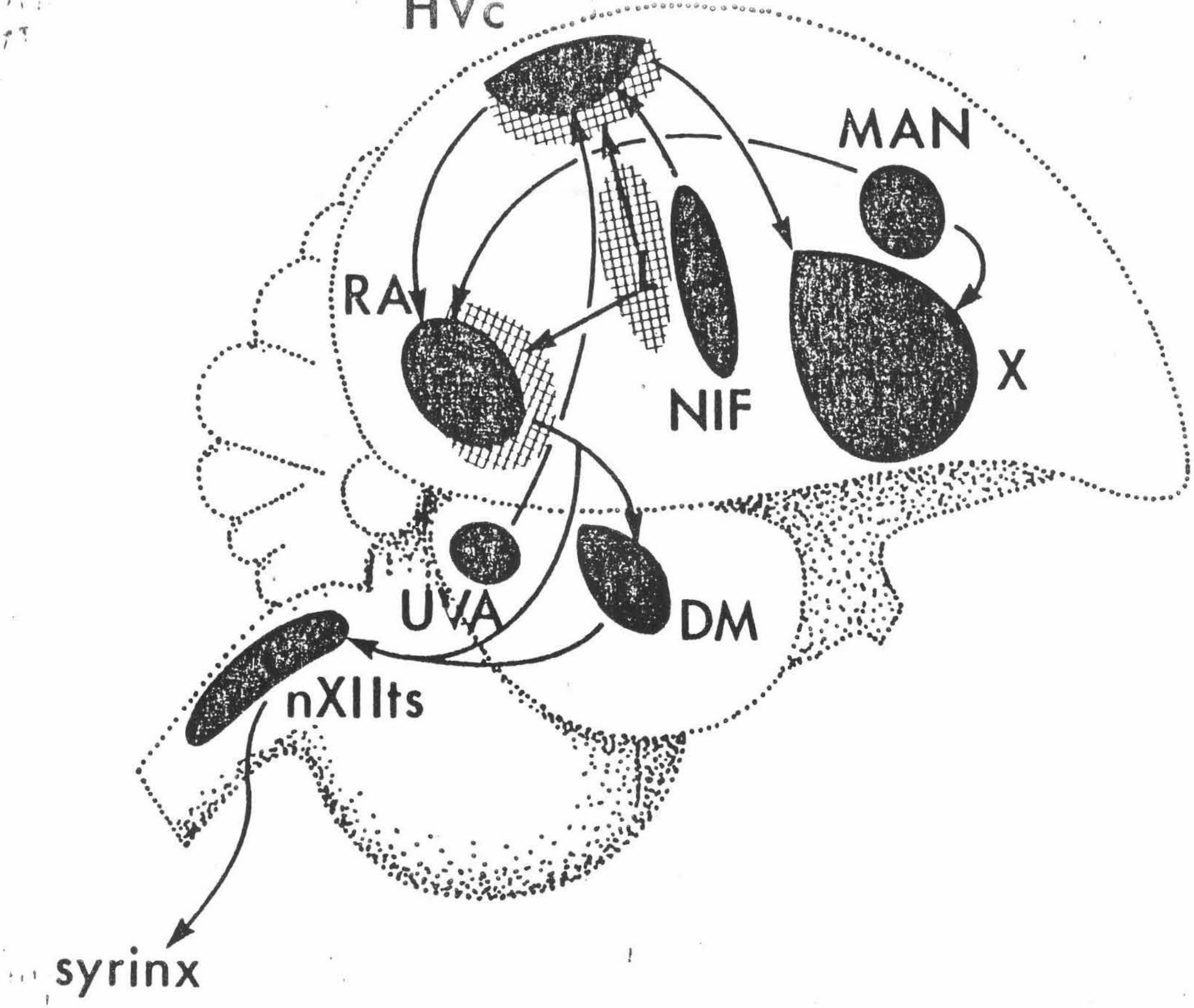
HVc
MAN
RA
NIF
X
UVA
DM
nXIIts
syrinx

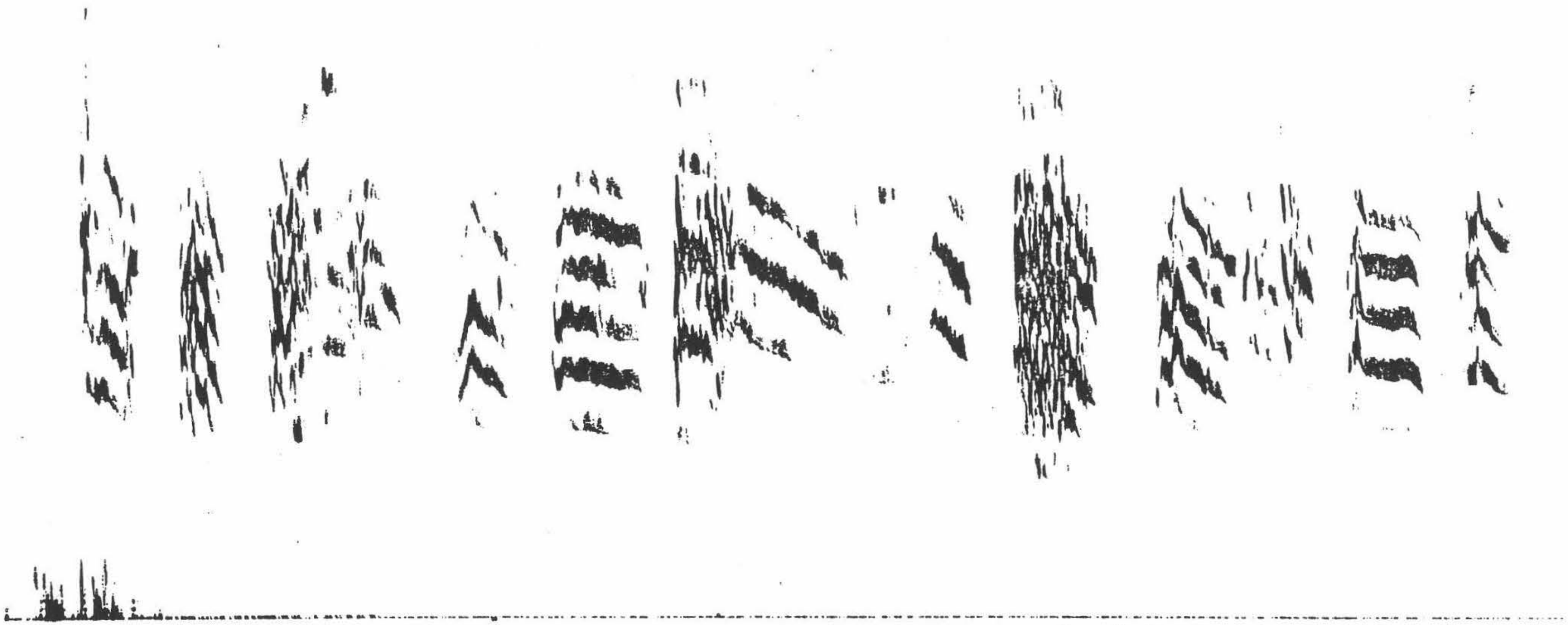

Song of masculinized female zebra finch B474 who was fostered by Bengalese finches.

ZEBRA FINCH NT5

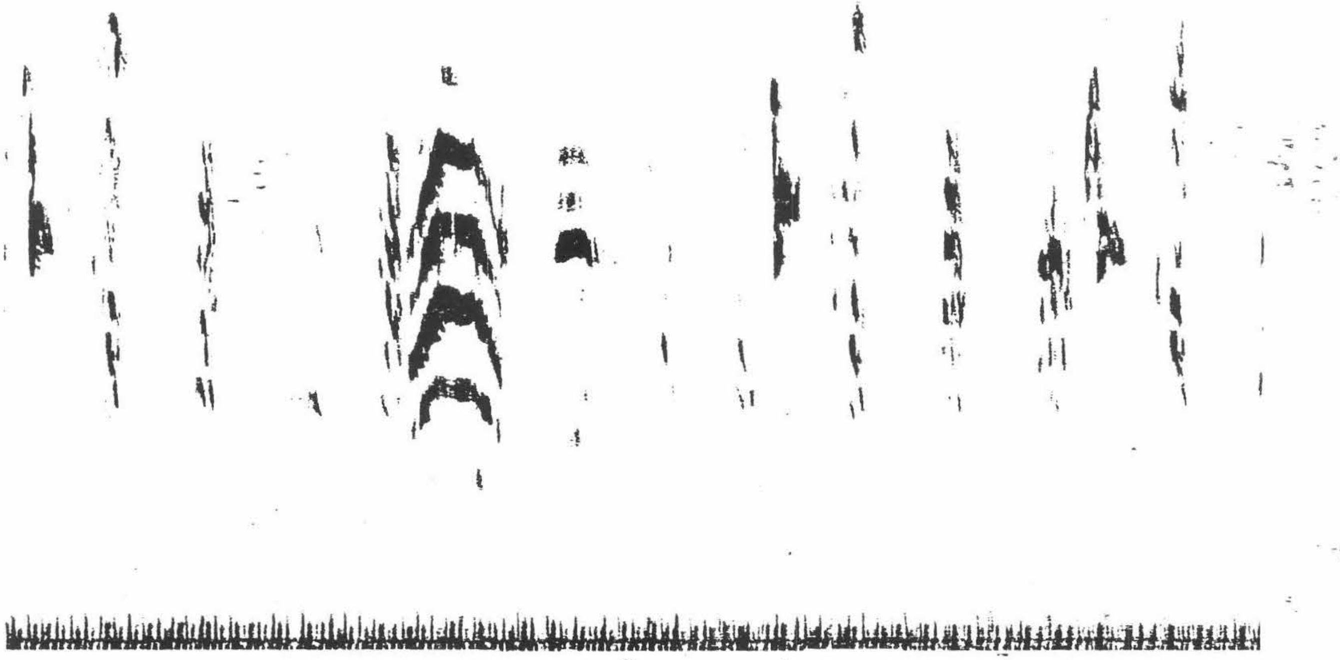

Pre operative song

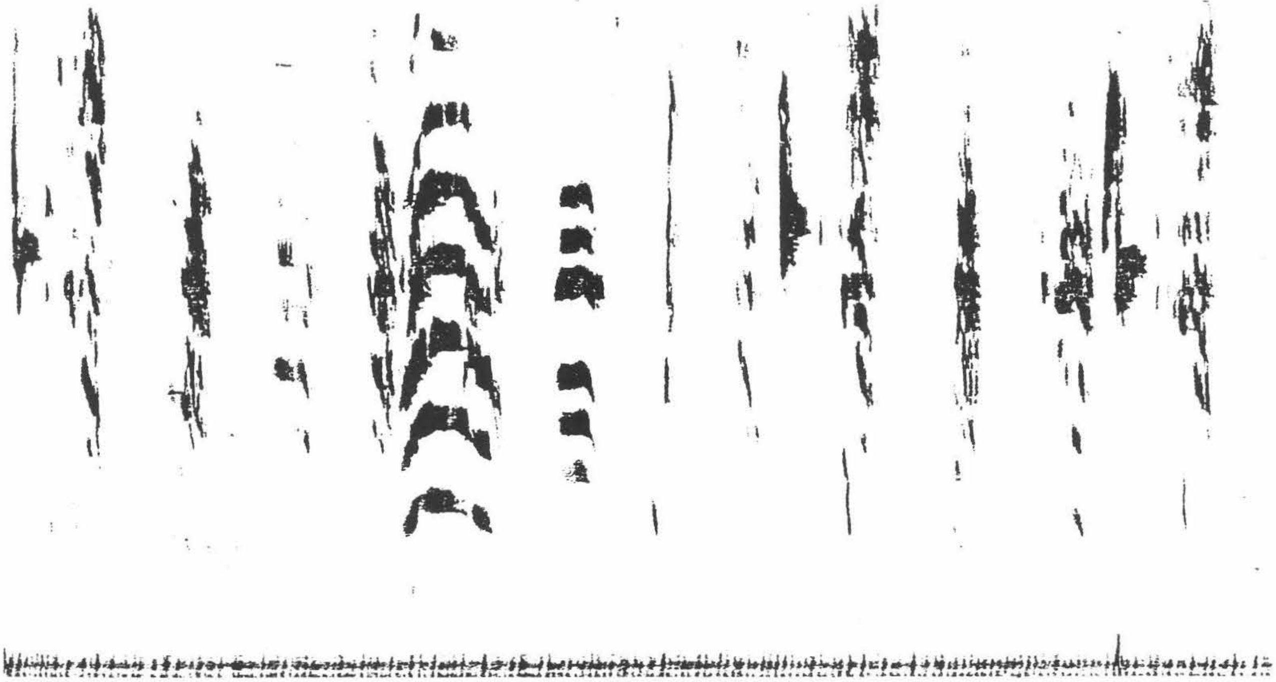

Song approximately three weeks after commissurectomy

ZEBRA FINCH B475

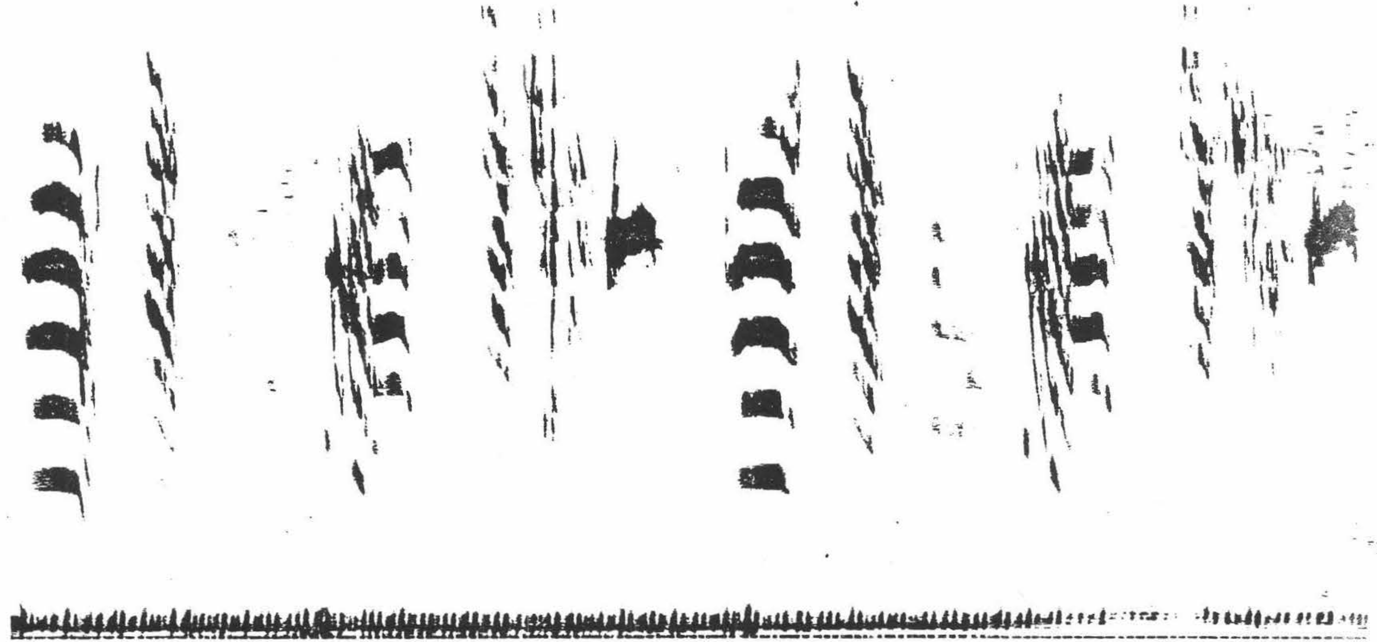

Pre-operative song

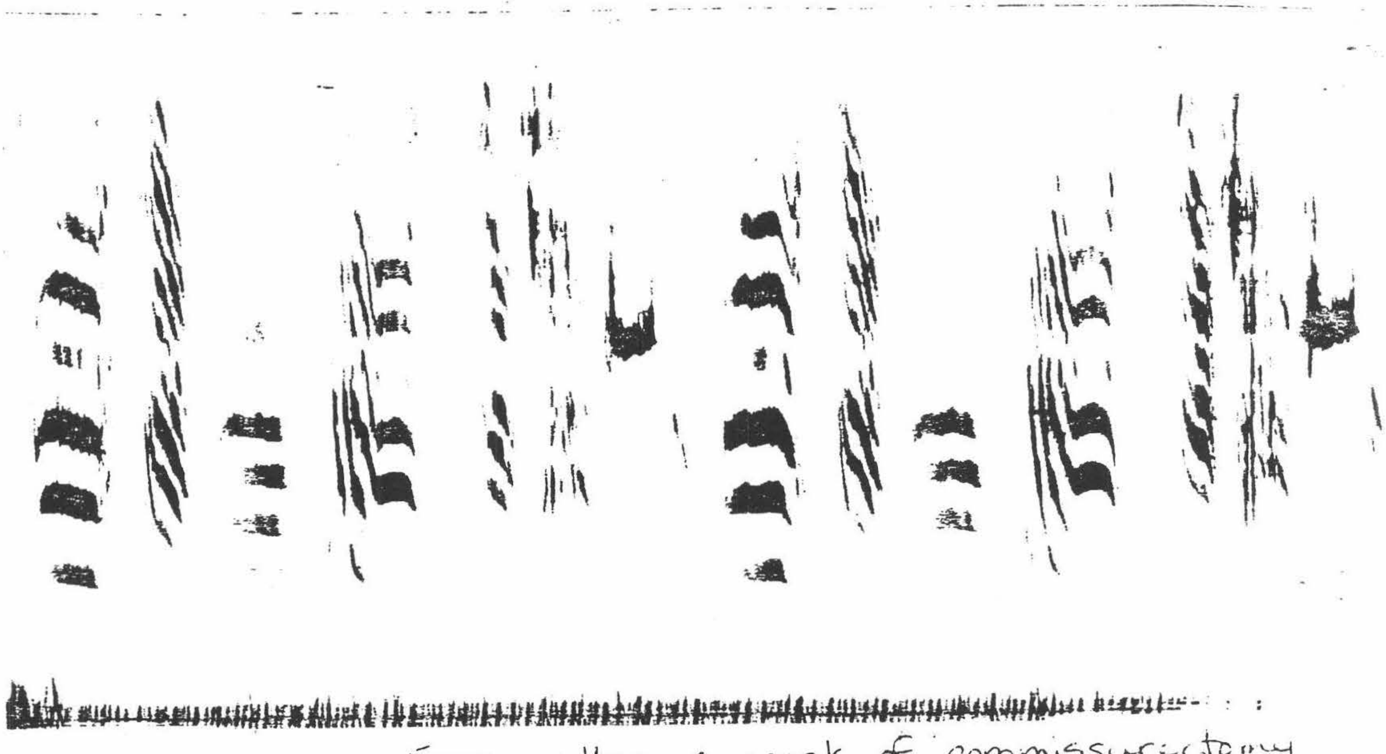

Song within a week of commissurectomy

Activity of β-lactamase and mutant R2

Brian Mapes
SURF '83

Faculty Sponsor:
J.H. Richards

Abstract: Wild-type β-lactamase and mutant R2, with serine instead of threonine at the 71^{st} residue, were biosynthesized and purified. It was found that R2 has only about 15% as much activity as wild-type, and is considerably less stable thermally.

The β-lactamase of this study is the product of a gene found on plasmid pBR322, grown in E. coli. It is linear, 265 amino acids in length, and has a molecular weight of roughly 30,000 daltons. It acts to catalyze the hydrolysis of the β-lactam ring of various antibiotic agents. In this study, penicillin-G was used as a substrate:

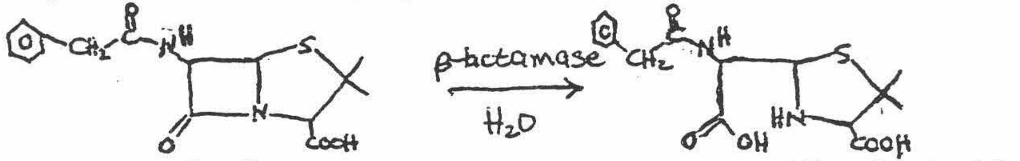

penicillin-G penicillanic acid

This reaction proceeds via an acyl-enzyme intermediate(1) involving the serine at residue 70, which is common to all β-lactamases known. All β-lactamases also have threonine at residue 71. This suggests the experiment of creating mutant enzymes with slightly different amino acids at these key sites and checking their activities. Serine and threonine differ by only a methyl group:

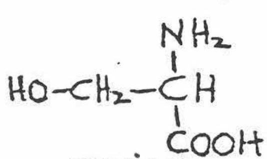

serine

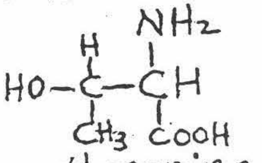

threonine

This small structural difference, though, has a profound manifestation in the chemical activity of B-lactamase.

Among the mutants which have been created are ser 70→thr and the double mutant ser 70→thr, thr 71→ser, both of which are catalytically inactive. However, when the double mutant gene was exposed to random mutation pressure in a medium in which only cells able to produce active β-lactamase could survive, a strain of partially active enzyme emerged. This mutant, in which the threonine at 70 had reverted back to serine, making it simply the single mutant thr 71→ser, was dubbed R2 and was the focus of this project.

Working samples of wild-type and R2 β-lactamase were prepared by the method described in (1). Because β-lactamase is found in the periplasmic space, outside the cell membrane and inside the cell wall, it is easily extruded by osmotically swelling the cell membrane. It is then separated out of the resulting solution of mixed cellular proteins by differential precipitation with $(NH_4)_2SO_4$, then ion-exchange chromatography, and finally elution through a sizing column. After these procedures, the specific activity of my wild-type sample was quite close to the published value for pure β-lactamase, and gel electrophoresis showed both samples to be free from major foreign protein components.

The purest fraction of wild-type β-lactamase I obtained has a specific activity of 57 μkatal/mg, where 1 katal=1 mole of substrate hydrolized/second. The purest R2 fraction has specific activity 8.5 μkat/mg, just 15% as much as wild-type. Also, R2 is significantly less stable thermally than wild-type. Its activity was reduced by $\frac{1}{2}$ by exposing it to 40° C for 9 minutes, while wild-type remained unaffected. It took 13 minutes at 55°C to halve the activity of wild-type.

It is not clear how the deletion of one methyl group from B-lactamase reduces its activity and stability so dramatically. Perhaps the methyl group is crucial to the proper alignment of the substrate, and R2 must wait for it to drift into the correct position for reaction. Perhaps without the methyl group the substrate is bound more securely, and ties up the active site on the enzyme for a longer period of time. These theories wouldn't explain the thermal deactivation, though. Perhaps the change in the linear acid sequence does not affect the activity directly, but rather affects the tertiary structure, the way the molecule folds up, in such a way that the active conformation is less favorable and the enzyme spends less time in its active state, less and less at higher and higher temperatures. It is likely a combination of factors producing this behavior.

Further study of this system will focus on determining what step of the reaction is slowed by R2's mutation, and the study of other mutants may also provide insight into the details of the mechanism of β-lactamase's activity. The hope is to eventually clarify the relationships between linear protein sequence, tertiary structure, and activity.

Footnote:

(1) = Fisher, J., Belasco, J.G.,Khosla, S.&Knowles, J.R.(1980)Biochemistry 19, 2895-2901

Applications of Fluorescent Mevinolin Derivatives to Human Cells in Tissue Culture

James Edward Mayhugh

Dr. Barbara Wold

ABSTRACT

A fluorescent derivative of mevinolin would be valuable for the study of cholesterol level regulation in humans . Five major plans for synthesis were arrived at , each focusing on a different portion of the mevinolin molecule . When future research puts these plans into action , each experimental compound will need to be tested for both activity and stability inside a cell . These tests will use human lung cells maintained as part of this project , including strains which were selected for gene amplification at loci involved in cholesterol biosynthesis .

September 22, 1983

Applications of Fluorescent Mevinolin Derivatives to Human Cells in Tissue Culture

James Edward Mayhugh

Dr. Barbara Wold

Mevinolin was first isolated from the fungus Aspergillus terreus . It has been shown in laboratory tests that this compound can lower the cholesterol levels of many animals and man . Mevinolin acts as a very potent competitive inhibitor of the enzyme 3-hydroxy-3-methylglutaryl-coenzyme A reductase , or HMG-CoA reductase for short . HMG-CoA reductase catalyzes the major rate limiting step in cholesterol biosynthesis . In this step , the enzyme uses up a molecule of NADPH in order to reduce HMG-CoA to mevalonic acid , which is a precursor of cholesterol . Normal human cells exposed to mevinolin concentrations as low as one half micro molar will virtually cease production of mevalonic acid . The strength of mevinolin as a competitive inhibitor of HMG-CoA reductase is so great that a one to one binding relationship between mevinolin and HMG-CoA reductase is assumed .

Mevinolin has potential as a means to study the regulation of HMG-CoA reductase in human cells . Cells grown in media containing mevinolin will take in a quantity of the drug that will reflect the number of active HMG-CoA reductase molecules in the cells being treated . One need only to find a good way to keep track of the number of molecules of mevinolin that are in any given cell in order to use it effectively as a probe .

There exists a form of mevinolin that contains radioactive carbon-14 as a means to detect it . Cells are treated with this radiolabel , then coated with a photographic emulsion . Time is needed for it to develop , then reductase levels can be measured by noting the extent to which the silver grains surrounding a cell have been exposed . This method is unable to observe the behavior of a cell as it changes in time in response to stimuli because the process is lethal to the cells being tested ; only the condition at the time of death can be known . It would be better to follow the mevinolin by using a fluorescent molecular tag . A fluorescent derivative of mevinolin could be seen with optical equipment not lethal to cells , making it possible to watch a cell for a period of time and also leave it alive for it to divide if it is a variant of interest . Fluorescein is a good fluorescent tag to use , because its high quantum yield for fluorescence would maximize the reliability of data collected .

No lab space was available to perform the linkage of fluorescein to mevinolin this summer . However, I did spend many hours researching the problem . I read all the journal articles that dealt with the chemistry of mevinolin and,a related drug, compactin, as well as reading their references . I now am more familiar with the drugs and have written reactions to add a fluorescein tag at five different points on the mevinolin molecule .

I learned many new techniques by working in the tissue culture room . I started with normal fetal lung cells to learn the basics of maintaining human cells in petri dishes. Their media is both their food source and their waste deposit . The cells need to be washed and fed fresh media regularly or they'll die . Cells will also die if they become overcrowded, they must be split and moved to a new dish with a lower population . There is a special sterile technique to learn as well, because of the cell's vulnerability to infection.

Bibliography

1. Roberts, James M.(1982).Gene Amplification and Correction in Somatic Cells. Cell,Vol.29,pp. 109-119.

2. Hirama, Masahiro.(1982).Chiral Total Synthesis of Compactin.J. Am. Chem. Soc.,Vol.104,pp. 4251-4253.

3. Willard,Alvin K.Incorperation of 2(S)-Methylbutanoic Acid-1-Carbon 14 into the Structure of Mevinolin.J.Labelled Comp.and Pharm.,Vol.19,No.3,pp.337-344.

4. Garbisch,Edgar W.,Jr.(1961).Preparation of Some Arylalkenes.

5. Mayashita,Masaaki.(1977).Pyridinium p-Toluenesulfonate. A Mild and Efficient Catalyst for the Tetrahydropyranylation of Alcohols. J.Org.Chem.,Vol.42,pp.3772-3774.

6. McKillop,Alexander.(1979).Organic Synthesis Using Supported Reagents-Part One and Part Two.Synthesis,George Thieme Publishers,pp.401-422 and 481-500.

7. Corey,E.J.(1972).Protection of Hydroxyl Groups as tert-Butyldimethylsilyl Derivatives.J.Am.Chem.Soc.,Vol.94,No.17,pp.6190-6191.

8. Meskens,Frans A.J.(1981).Methods for the Preparation of Acetals from Alcohols or Oxiranes and Carbonyl Compounds.Synthesis,Georg Thieme Verlag,pp.501-522.

9. Lee,Ta-Jyh.(1982).Structural Modification of Mevinolin.J.Org.Chem.,Vol.47, pp.4750-4757.

10. Basha, Anwer.(1977).A Mild ,General Method for Conversion of Esters to Amides. Tetrahedron Lett.,No.48 ,pp.4171-4174.

Cloning the Murine Terminal Transferase Gene Using λgt11, a Unique Phage Expression Vector

Candice McCoy

Dr. Ellen Rothenberg

Abstract: RNA was isolated from the thymuses of B6 TL+ (TdT+) mice and fractionated on sucrose density gradients. The size fractionated RNA of interest (TdT message-containing RNA or TdT-mRNA) was then run over an oligo-dT cellulose column which binds polyadenylated or "messenger" RNA (mRNA). The bound mRNA was eluted from the column and precipitated in ethanol. Previous results from the laboratory had indicated that TdT message was slightly larger than the message encoding the Thymus Leukemia antigens (TL). Therefore, a dot-blot on nitrocellulose of the size-fractionated RNA was probed with a radioactively labelled 6.2 kilobase DNA molecule believed to be homologous to the Tla locus which codes for TL. Sequences homologousto the probe were located in the fraction containing 16S RNA as expected. Thus, we can be reasonably certain that the TdT-mRNA was also located in fractions containing 18.5S RNA. Attempts to translate a small amount of TdT-mRNA <u>in vitro</u> were unsuccessful. However, the RNA appears to be transcribable. Attempts to maximize first-strand cDNA synthesis using splenic polyadenylated RNA (splenic mRNA) have elucidated the presence of cDNA synthesis inhibitors. Progress is now being made to determine whether these inhibitors are generated in the isolation of the RNA, are due to the configuration of the RNA, or are present in the reverse transcriptase itself.

Introduction: Terminal transferase (TdT) is an unusual DNA polymerase in that it can direct the random synthesis of DNA without the use of a template. Biochemically it is characterized as a polypeptide of 58000-60000 daltons, demonstrates no genetic polymorphism, and can be detected serologically with a rabbit antiserum against calf TdT. In molecular biology it is used as a DNA polymerase, but the real interest in TdT centers around its function in T- and B-lymphocyte ontogeny. The purpose of this project was to isolate a cDNA clone of the TdT gene using λgt11, a unique phage expression vector. At present a small amount of TdT-mRNA has been isolated and attempts are being made to maximize the synthesis of a DNA copy of the RNA (cDNA) by first making cDNA from splenic mRNA.

Presentation and discussion of results:

1) Isolation of TdT-mRNA: The isolation of TdT-mRNA was facilitated by work done in Ellen Rothenberg's lab by Loyd Burgess who showed by <u>in vitro</u> translation of size-fractionated mRNA that the peak of TdT-mRNA activity was contained in the 18.5S fraction of a 10-30% sucrose density gradient (S is a sedimentation coefficient called a Svedberg unit. $1S=10^{-13}$ sec.). Thus, 1.196 mg of total thymic RNA were fractionated on two 15-30% sucrose density gradients at 40000 rpm (40K) for 4.5 hours at 25°C and 1.0 mg of total thymic RNA was fractionated in four 15-30% sucrose den-

sity gradients at 24.7K for 17 hours. Gradients were harvested and the optical densities were measured to determine the location of the 28S and 18S peaks of ribosomal RNA (rRNA). Due to problems with RNA aggregation the RNA from all six gradients was pooled, ethanol precipitated, and fractionated again on six 15-30% sucrose density gradients. However, this time the RNA was denatured at 80°C for five minutes in 100 mM NaCl, 10 mM Tris pH 7.5, 1 mM EDTA, 0.5% SDS. This heating step prevented the aggregation of the RNA and promoted its efficient fractionation. Fractions containing 16.5S-21S RNA were pooled, ethanol precipitated, and passed over an oligo-dT cellulose column. Such a column binds the polyadenylated tails of mRNA through complimentary base pairing to the oligo-dT. Any ribosomal RNA passes through the column because it lacks a polyadenylated end. The bound mRNA was eluted by washing with salt-free buffer. The yield of TdT-mRNA was 5.44 ug. The expected yield based on 13.6 ug/fraction was 4.76 ug.

2) RNA dot-blot: Fractionated RNA from one sucrose gradient was ethanol precipitated, dissolved in 5 ul of Tris-EDTA buffer, and dotted on nitrocellulose. The filter was then baked and incubated with a radiolabelled 6.2 kilobase DNA probe which is homologous to the Tla locus and, thus, to the mRNA sequences coding for TL antigens. The first attempt at detection was unsuccessful because too little RNA was dotted on the filter. However, the second time 6.8 ug from each fraction were dotted on the nitrocellulose. As a positive control serial dilutions of unlabeled 6.2 kb DNA were used. The results showed the presence of RNA sequences homologous to the DNA probe in the fraction containing 16S RNA as well as in those containing 28S ribosomal RNA.

3) Detecting TdT on nitrocellulose: In order to screen a λgt11 library replicas of the agar plates on which phage-infected bacteria are growing are made by pressing nitrocellulose filters on the plates. The filters are exposed to chloroform to lyse the bacteria so their contents, including any proteins made, stick to the nitrocellulose. The filters are then incubated with antibody to the protein of interest and then with ^{125}I-protein A which binds to antigen-antibody complexes. Thus, it was necessary to determine if TdT would bind to nitrocellulose and if it could be detected by the above procedure. A thymocyte lysate was immune precipitated with anti-TdT antibody and the precipitated products were run on an acrylamide gel. An attempt was made to transfer the precipitated TdT to nitrocellulose by electrophoresis, a procedure known as Western blotting. The nitrocellulose filters were then incubated with various wash buffers and concentrations of antibody and ^{125}I-protein A in order to determine the best incubation conditions. While some TdT was detected on the filters it was clear from fluorography of the gel that most of the TdT had not been transferred and had remained in the gel. However, these experiments demonstrated which washing procedure would detect TdT but give low background signal in an autoradiography. Another problem with the previous procedure was that it was impossible to determine how much TdT was being detected and how little could be detected by this procedure. Thus, calf TdT was

dotted on nitrocellulose in serial dilutions and incubated with anti-TdT antibody and ^{125}I-protein A using the optimum conditions as established in the previous experiment. Using a 1:250 dilution of antibody and $2x10^5$ cpm/ml ^{125}I-protein A in Tris-buffered saline as little as 3 ng of TdT was detected on the nitrocellulose.

4) _In vitro_ translation of TdT-mRNA: Attempts to translate _in vitro_ 0.2 ug of TdT-mRNA yielded no protein products as determined by TCA precipitation of ^{35}S-methionine labelled products. Thus, it was impossible to immune precipitate the protein products with anti-TdT antibody in order to determine if TdT was synthesized from the TdT-mRNA template.

5) First-strand cDNA synthesis: The first step in making cDNA is to synthesize the first strand of cDNA using an mRNA template. The enzyme reverse transcriptase catalyzes this reaction. The kinetics of reactions involving different lots of reverse transcriptase were studied. From these studies it appeared that two lots may have RNase and/or DNase contamination as the yield of cDNA drops appreciably between 45 and 60 minutes. Optimal levels of oligo-dT and reverse transcriptase were established using splenic mRNA as a template for cDNA synthesis. An appreciable increase in the yield of cDNA appeared to result from an increase in the reverse transcriptase concentration. Yet longer length cDNA resulted when the oligo-dT concentration was kept low (0.5 ug/ug mRNA) and the reverse transcriptase concentration was increased. Yet, it has also been observed that percent yield increases as the concentration of mRNA decreases. This same titration effect has been observed in _in vitro_ translation reactions done by Ellen Rothenberg. Some inhibitor appears to be present in the RNA. It was thought that phenol extracting the mRNA would improve the yield because it would remove any residual proteins. However, the titration effect on yield was consistently observed with phenol extracted mRNA. Thus, experiments are underway to determine what other components of the reaction may be inhibitory. It may be that a high percentage of the "mRNA" is in fact _not_ polyadenylated. This could be the case if rRNA had bound to the oligo-dT column by virtue of the fact that it was somehow bound to mRNA. Any rRNA contaminant could sequester reverse transcriptase as well as other vital reaction components, thus inhibiting the reaction. Thus, the mRNA will be denatured and run over the oligo-dT column again. Formation of aggregated RNA molecules during the reverse transcriptase reaction could also inhibit the reaction. Thus, the mRNA will be heat denatured immediately before the reverse transcriptase reaction. Hopefully these measures will improve the yield of cDNA from the mRNA templates as well as mitigating the titration effect seen in _in vitro_ translation reactions.

Conclusions:
1) TdT mRNA has been isolated from thymic RNA from B6 TL$^+$(TdT$^+$) mice. The location of TdT-mRNA in sucrose density gradient fractions was based on unpublished work by Loyd Burgess.

2) Messenger RNA sequences homologous to the Tla locus were located in sucrose density gradient fraction containing 16S RNA. The fact that fractions containing 28S rRNA also bear homology to the probe is probably due to the fact that there is an abundance of RNA sequences in this peak many of which bear homology to such a large DNA probe. Such a genomic DNA probe may also include some repeated sequences which are homologous to rRNA.

3) As little as 3 ng of TdT can be detected on nitrocellulose. This is very important since screening a λgt11 library is based upon detecting very small amounts of cellular products on nitrocellulose sheets. The fact that immune precipitated TdT could not be seen on a Western blot is probably due to the fact that the transfer to nitrocellulose was not complete, a problem which can be mitigated by running the electrophoresis for up to three times as long as originally run.

4) In vitro translation of TdT-mRNA was unsuccessful. This may also be due to contamination with rRNA which would decrease the actual concentration of TdT-mRNA added to the translation reaction. Ribosomal RNA contaminants could also sequester vital reactants. However, inhibition could be due to protein inhibitors in the mRNA preparation.

5) Characterization of the reverse transcriptase catalyzed synthesis of cDNA from an mRNA template is in progress using splenic mRNA from B6 TL^+ (TdT^+) mice. Progress in this area has been slowed by an apparent inhibition of the reaction at high mRNA concentrations. The inhibitor is probably not a protein complexed to the mRNA or present in the mRNA preparation since phenol extracted mRNA was also inhibitory. However, inhibition could be due to contamination of the mRNA by rRNA or to aggregation of the mRNA. Steps are being taken to elucidate the nature of the inhibitor.

BIBLIOGRAPHY

Efstradiatis, Argiris and Lydia Villa-Komaroff. Cloning of Double Stranded cDNA. Genetic Engineering, Principles and Methods vol. I. Hollander, A. and J. K. Setlow, eds. (Plenum Publishing Corp., New York).

Payvar, Farhang and Robert T. Schimke. Methylmercury Hydroxide Enhancement of Translation and Transcription of Ovalbumin and Conalbumin mRNA's (1979). Journal of Biological Chemistry 254, 7636-7642.

Rothenberg, Ellen. Expression of Differentiation Antigens in Subpopulations of Mouse Thymocytes: Regulation at the Level of de Novo Synthesis (1980). Cell 20, 1-9.

Rothenberg, Ellen and Edward A. Boyse. Synthesis and Processing of Molecules Bearing Thymus Leukemia Antigen (1979). Journal of Experimental Medicine 150, 777-791.

Silverstone, A. E., N. Rosenberg and D. Baltimore. Correlating Terminal Deoxynucleotidyl Transferase and Cell-Surface Markers in the Pathway of Lymphocyte Ontogeny (1978). Differentiation of Normal and Neoplastic Hematopoietic Cells. Clarkson, B., J. Till and P. Marks, eds. (Cold Spring Harbor Laboratory, New York). 433-453.

Towbin, Harry, Theophil Staehalin and Julian Gordon. Electrophoretic Transfer of Proteins from Polyacrylamide Gels to Nitrocellulose Sheets: Procedure and Some Applications (1979). Proceedings of the National Academy of Sciences USA 76, 4350-4354.

Young, Richard A. and Ronald W. Davis. Efficient Isolation of Genes Using Antibody Probes (1983). Proceedings of the National Academy of Sciences USA 80, 1194-1198.

Hydration of Sodium Silicate Glasses
Dependence on Sodium Content

by John F. McGowan

ABSTRACT

Hydrogen diffuses into the surface of glassy materials such as a mixture Na_2O -xSiO_2. This is believed to be described by $X^2=KT$ where x is the depth of hydration, T is time, and K is a constant that varies with temperature in an Arrhenius fashion. The purpose of the experiment is to get some idea of how the rate of hydration, and in particular the activation energy and diffusion constant vary with the sodium content.

At the moment , I am still in the process of getting results. (See next page)

My experimental approach is to make several sodium silicate glasses with different proportions of SiO_2 and Na_2O. These will be broken up into smaller pieces and hydrated for various times and temperatures in distilled water in order to determine the activation energy and diffusion constant. The hydrogen will be profiled using a nuclear resonance interaction between roughly 17 Mev Fluorine 19 and the hydrogen. This will be done with an F^{19} beam from the TANDEM accelerator in Kellog.

The glasses were made by putting a mixture of powdered Na_2CO_3 and SiO_2 in a graphite holder. The holder was heated to about 800 degrees Celsius for 12 hours in a nitrogen filled oven to drive off CO_2 and turn the Na_2CO_3 into Na_2O. Then the mixture was heated to roughly 1400 degrees at which temperature most compositions liquefy and form a glass.

The glass samples will then be hydrated and profiled. The profiling is done with an ^{19}F beam. The energy of the beam is varied over a range. The ^{19}F particles loose energy as they penetrate into the surface of the glass until they reach the energy at which the nuclear interaction occurs and gamma rays are produced. The gamma ray output is proportional to the concentration of hydrogen and it is calibrated using a chlorite sample of known hydrogen content. Thus, by varying the beam energy, it is possible to get a hydrogen concentration versus depth profile.

I have prepared three compositions. Unfortunately, the TANDEM is currently being fixed and will not be available until September 4 or so. Thus I do not expect to be finished until late September or early October if all goes well.

Short Bibliography

R.H. Doremus, Interdiffusion of Hydrogen and Alkali Ions in a Glass Surface, Journal of Non-Crystalline Solids 19(1975)

C.A. Houser, J.S. Herman, I.S. T. Tsong and W.B. White and W.A. Lanford, Sodium-Hydrogen Interdiffusion in Sodium Silicate Glasses, a paper submitted to the Journal of Non-Crystalline Solids

J.F. Ziegler and many others, Profiling Hydrogen in Materials Using Ion Beams,Nuclear Instruments and Methods 149 (1978)

DEVELOPMENT OF A COMPOSER'S AMANUENSIS

Written by: Craig N Minor

SURF Advisor: Dr. Fred Thompson

Abstract:

Using artificial intelligence programming techniques, a piano performance can be interpretted by computer. As a scoring machine, it can produce the same music from unique playings of the same composition. Such a system when coupled with a music editing feature could be a valuable tool for the music composing and publishing industry.

The history of this project begins with the development of a microcomputer dedicated to scan the piano keys and record the keystrokes. The purpose was to learn about timing of the musician's performance hence we recorded a time with each identified keystroke. However, hand analysis was slow and inaccurate for the amount of data, so we invested in a personal computer, the Otrona ATTACHE. Programs were developed to display the data in different ways on the screen allowing immediate visual analysis. We soon became curious as to whether the computer could be taught to reproduce a correct score from the data. The major problem was that the pianist takes many liberties while playing from music, liberties that can't be accounted for by formula. We set a goal to have the computer produce the same score for two different performances of the same music.

The data we obtain from a piano performance is a record of the timing information only. It is organized as a list of presses and releases tagged with times that are accurate to 10 milliseconds. Pairs of key-change and time are referred to as events. Since the keyboard scanning is accomplished via on-off contact switches, no amplitude or velocity information is stored.

The most difficult part of this project was breaking from a musician's view of music and forming a mathematical model from the data. First a method was developed to determine where the beats occurred. These are not the same beats that a musician taps with his foot, but are the finest division of time that we can use to follow the sequence of keystrokes. A statistical modeling was used to develop a method for tracking the beat. The meter followed in most music suggests that note changes (both presses and releases) should occur in groups at even time intervals. Assuming the pianist doesn't rapidly change playing speed, the time between the mean of each group is roughly the same. The first several groups can be separated by using an autocorrelation technique. By comparing all intervals between events, we can select the shortest interval that occurs a significant number of times. By defining the mean of the first group as the first beat location, the second beat can be predicted using the computed interval.

Given a beat length, the location of the following groupings of notes are guessed by extrapolation. By evaluating the differences between the guess and the actual groupings in the data, the correctness of the guess can be determined. If the guessed beat is significantly different from the actual then we use the difference to calculate the basis for a second guess. Evaluation of each guess reveals which is the best choice for this beat. Each succeeding beat and beat length is determined by this method and used as the basis for guessing later beats.

Once the beat has been selected, further checks are made to detect errors in beat placement. If a note starts and ends without a beat occurring in between, then we may have to revise previous guesses. If the time until the next chosen beat is more than an arbitrary percentage (10% presently) of the current beat length then it is handled as an exception, making the note a staccato. These are the notes played too briefly with respect to the rest of the performance to be evaluated properly. Otherwise backtracking is invoked to rework old guesses with smaller beat lengths until the exception is alleviated.

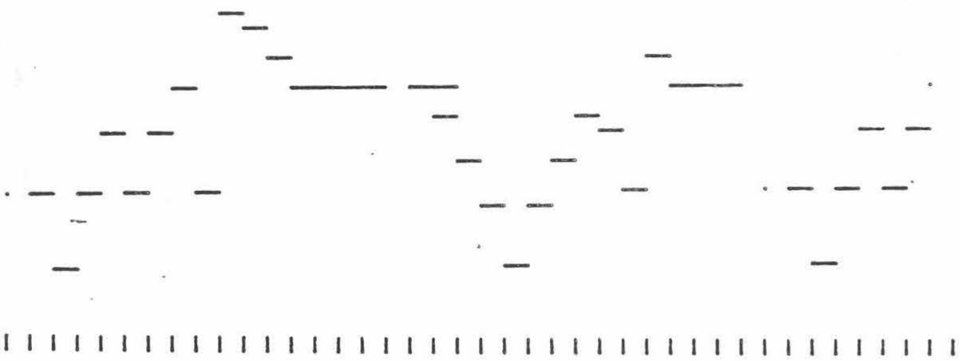

Fig. 1 Intermediate Form

When the position of each beat has been determined, the event list is converted into sub-lists of notes played on the same beat. Each keystroke is listed as the number of the note on the keyboard and the number of beats the note was held. An intermediate output form was developed to assist evaluation of the beat tracking. (Fig. 1) Appearing like a piano roll, it uses bars to represent notes on a graph of time vs. frequency. Since the source data can be plotted in the same manner, comparisons can be made to insure all notes are accounted for and mapped onto the correct beats. A mechanical routine can convert the note-of-keyboard to a position on the staff given the key and offset of the data. Notes can then be plotted from this data directly, converting beat-length to note-value. (Fig. 2)

Simple rests and measure bars are the most advanced symbols that can be produced by the program to date. More complex musical constructs are starting to be implemented but another level of computation needs to be performed on the data to map more complicated features on the staff. Other additions should include decisions about stem direction, perhaps by using a melody tracking scheme. Bars on eighth and smaller notes needs to be implemented but there are some complicated rules to be followed.
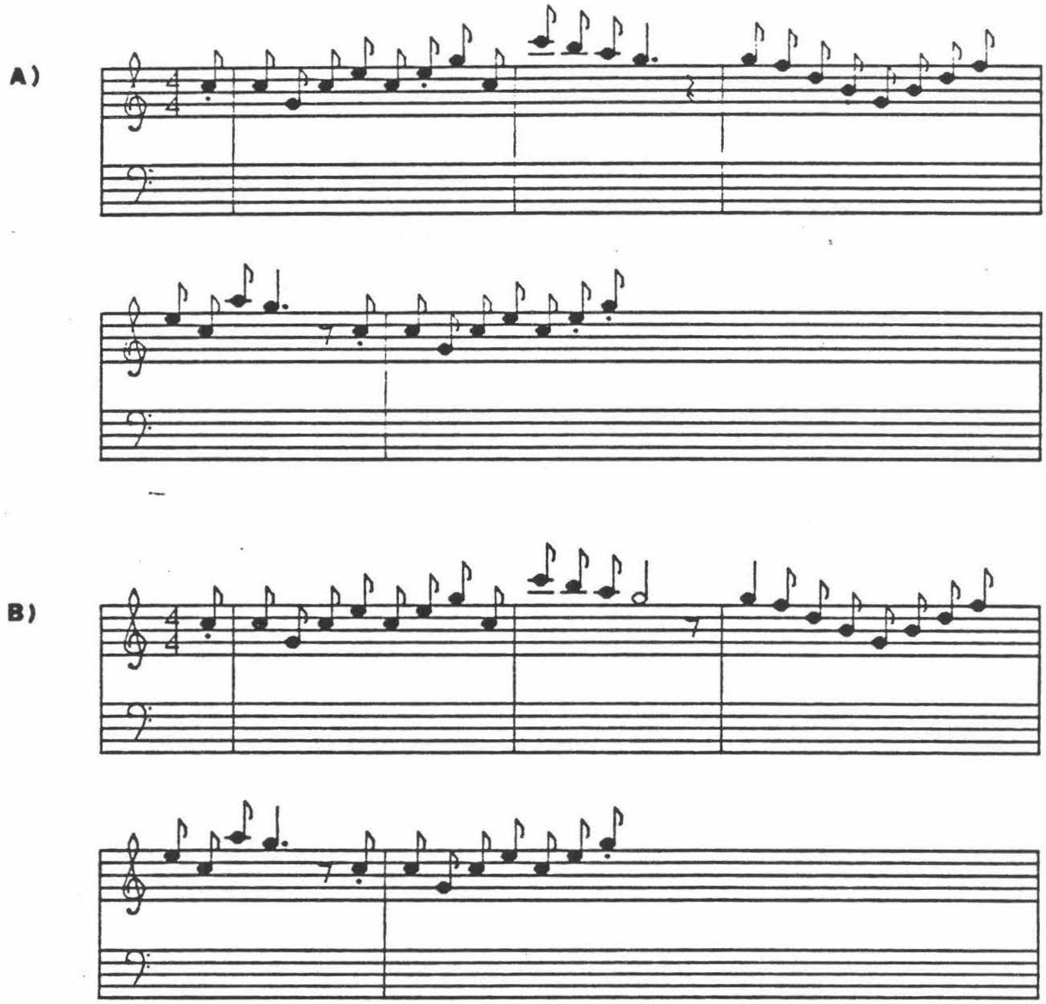
Fig. 2 Resulting Scores

For this system to become useful as a musician's amanuensis, there needs to be more exception handling routines for glissandos, syncopation, trills, etc. There should also be a music editor to allow corrections for those things the computer cannot understand or that the musician cannot play. Facilities to allow transposition (fig. 3) and score splitting may also be important to composers for band and orchestral works. These additions would require a high quality graphics display system to allow more than one line of music to be displayed on the screen at one time.
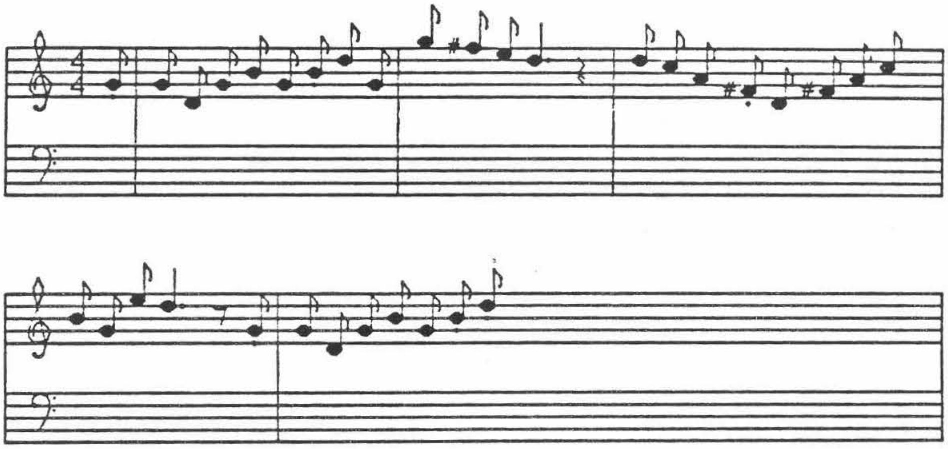
Fig. 3 Transposition of 2A

Conclusions

Programming a computer to interpret the data from a musical performance requires artificial intelligence techniques. Methods used to do the analysis include confidence of estimation and backtracking. Although further work is required to make a commercially useful system, a basis for this system is complete.

The Reduction Of Sulfur Dioxide To Elemental Sulfur

Robert Murphy, Dr. George Gavalas Faculty Sponsor
California Institute Of Technology
September 1, 1983

Abstract

A 25% conversion of SO_2 to elemental sulfur has been observed with the system:

$SO_2 + 1/2O_2 + Na_2O \longrightarrow Na_2SO_4$; $Na_2SO_4 + CO \longrightarrow Na_2O$, elemental sulfur, CO_2, SO_2, COS, Na_2S

The sodium containing compounds are supported in alpha alumina and the reactions occur at 800° C . The conversion of SO_2 to sulfur was raised to 30% by adding iron to the system via the reactions:

$SO_2 + Na_2O + Fe_2O_3 + O_2 +$ iron sulfides $\dashrightarrow Na_2SO_4$, $FeSO_4$; $Na_2SO_4 + FeSO_4 + CO \dashrightarrow$ elemental sulfur, Na_2O, iron sulfides, Fe_2O_3, COS, Na_2S, CO_2, SO_2.

The addition of iron to the system hinders the release of sulfur due to the formation of stable iron sulfides. Therefore, iron does not substantially improve the system from the standpoint of efficiently reducing SO_2 from pollution sources to salable sulfur because of the energy needed to thermally abstract the sulfur from the sulfides.

1 Introduction

The emission of SO_2 from coal burning power plant and sulfide smelter waste gases into the atmosphere is causing serious environmental problems such as acid rain. Therefore, the reduction of gaseous SO_2 to salable and nonvolatile products like sulfur is recieving considerable attention.

The following process for the conversion of SO_2 to sulfur has been examined by graduate student Theresa Weston and was further evaluated in this project. The absorptioncycle consists of,

$$Na_2O + 1/2O_2 + SO_2 \longrightarrow Na_2SO_4.$$

This is followed by the regeneration cycle,

$$Na_2SO_4 + CO \longrightarrow Na_2O,\ CO_2,\ \text{sulfur},\ Na_2S,\ COS,\ SO_2.$$

The sodium containing compounds are supported in alpha alumina and the reactions are occuring at 800° C. The system removes SO_2 well since Na_2O is completly converted to Na_2SO_4 and the alumina has a high surface area to retain the products. Na_2O, NaS, and Na_2SO_4 form a melt at these reaction conditions. The mecahnism by which CO interacts with the melt to form these products is unknown. Reviews of molten salt chemistry are in references 3 and 4.

The main purpose of this project was to evaluate the effect of iron on this system above with regard to the system's ability to efficiently reduce SO_2 to elemental sulfur. Work by Kahalafalla(1,2) shows that the addition of iron to hydroxylated alumina catalytically increases the yield of sulfur from the reactions; $SO_2 + 2CO \dashrightarrow 2CO_2 + 1/2S_2$, and $2COS + SO_2 \dashrightarrow 2CO_2 + 3/2S_2$. The gaseous reactants react on solid Al_2O_3 and iron. This work gives some promise that iron could increase the yield of sulfur when added to the Na_2O/AL_2O_3 sorbent above, however, little comparison can be made since the system to be discussed involves a molten salt whereas Kahalafalla's system does not.

2 Experimental

Three sulfated sorbents were prepared by mixing known amounts of water, Na_2SO_4,$FeSO_4$, and 35-60 mesh alumina with a pore volume of .27 cc/gm. Assuming the pores of the alumina were filled with the solutions, the resulting sorbents were: .108gm Na_2SO_4/gm Al_2O_3, .108gm Na_2SO_4 and .0004gm $FeSO_4$/gm AL_2O_3, .108gm Na_2SO_4 and .0043 gm $FeSO_4$/gmAL_2O_3. The sulfated sorbents were seperately reacted with 10% CO and air by volume at 800° C for four hours in a fixed bed reactor. The reactor consisted of a quartz tube mounted vertically in a furnace. 1.5 to 2 gms of sorbent were packed in the tube and the temperature was measured by a thermocouple. The reactor effluent gases passed through a trap immersed in ice to precipitate any sulfur formed. The concentrations of COS and SO_2 in the flue gases were measured at four minute intervals with a flame photometric detector. Total COS and SO_2 production during the four hour reaction with CO was calculated by numerical integration of the concentration vs. time curves. The sulfur produced was measured by a simple titration technique. Following the reactions with CO, the sorbents were reacted at 800° C with 10% SO_2 and air by volume for 3 hours to convert everything to Na_2SO_4 and $FeSO_4$. Complete conversion to sulfates was assured when the inlet and outlet concentrations of SO_2 were the same. Sulfur production was also monitored during the sulfation period.

3 Results and Discussion

3.1 Sulfur Production

The table below shows the percentage of the sulfur in the sulfate form which was converted to elemental sulfur (labelled % conversion) during the four hour reduction with CO and the three hour sulfation with SO_2. The sorbents are labelled by the ratio of moles Na to moles Fe in the sorbent.

Table 1 Sulfur Production

Sorbent	Run	%Conversion
Na/Fe=1/0	1	25%
Na/Fe=1/0	2	20%
Na/Fe=587	1	6%
Na/Fe=587	2	4%
Na/Fe=27	1	30%
Na/Fe=27	2	30%

The data above is misleading because of an experimental difficulty. It was found that for the sorbent without iron, almost all of the sulfur was produced during the reduction with CO and very little was produced during the passage of N_2 at 800° C through the reactor following reduction. However, for the sorbents containing iron, most of the elemental sulfur was produced during the passage of N_2 following reduction. This was not observed until the Na/Fe=27 sorbent was tested after the sorbent with less iron. Since the sorbent with less iron was not heated with N_2 as the sorbent with more iron was, no comparison can be made with the lower iron sorbent. Despite this error, the higher iron sorbent shows that iron increases sulfur production but it delays the accumulation of sulfur. A possible explanation for this delay is that the iron binds the sulfur in the sorbent in the form of stable iron sulfides which slowly release sulfur during the post reduction heating with inert N_2.

3.2 COS and Sulfur Dioxide Production

The table below shows the production of COS and SO_2 during the four hour reaction with CO. The columns % S as COS and SO_2 refer to the percentage of the sulfur in the original sulfate form which was converted to the COS and SO_2 forms.

Table 2 COS and SO_2 Production

Sorbent	Run	%S as SO_2	%S as COS
Na/Fe=1/0	1	3%	14.4%
Na/Fe=1/0	2	3.5%	16%
Na/Fe=587	1	2.9%	13.7%
Na/Fe=587	2	4.2%	25%
Na/Fe=27	1	1.3%	19.7%
Na/Fe=27	2	1.03%	16%

The only distinctive feautures shown in this table are the decrease in SO_2 production for the higher iron sorbent and the fact that the COS to SO_2 ratio is about four. Without a knowledge of the chemistry of the system, the decreased SO_2 production can't be explained. A major reason for measuring COS and SO_2 production was to test the feasibility of using the COS and SO_2 produced to form more sulfur via the Claus process. The Claus process consists of the rection, SO_2 + 2COS--> CO_2 + 3/2&S_2 with solid alumina and iron as catalysts. A COS/SO_2 ratio of four may make the Claus process a feasible addition to this system.

3.3 Carbon Deposition

It was noticed that the sorbents had a black coating on them following reduction with CO. This carbon was possibly formed by the reaction, 2CO--> solid carbon + CO_2. It was hypothesized that the loss of CO through this reaction could retard the reduction of the sulfates to sulfur. To test this hypothesis CO_2 was added to the CO and air mixture to inhibit this reaction. The CO/CO_2/air mixture was tested on the sorbent without iron with the result that no significant change in sulfur production occured. A possible explanation is that an insignificant amount of the CO is lost to carbon deposition.

4 Conclusion

This project has shown that the effect of iron on the Na/Al_2O_3 sorbent has been to increase the production of sulfur at the expense of forming stable iron sulfides which slow down the evolution of elemental sulfur. From an industrial standpoint, the iron is probably detrimental to the sorbent because the energy required to thermally decompose the iron sulfides to sulfur costs more than the extra sulfur obtained. The COS/SO_2 production ratio of 4/1 during reduction with CO may make the Claus process a feasible addition to this system. Further progress toward increasing sulfur yields will depend upon how much can be learned about the chemistry of the melt formed and the interaction of CO with this melt.

Modeling of Indoor Air Quality

Glayde A. Myers
SURF Fellow

Dr. F. H. Shair
SURF Advisor

Summer Undergraduate Research Fellowship Report
California Institute of Technology
Pasadena, California 91125

Abstract

Indoor air quality is of rapidly increasing concern. Efforts to cut energy costs by decreasing outside air infiltration may result in the accumulation of pollutants inside. Accurate modeling is required to help determine the best trade-off. Data for an EPRI sponsored field study were analyzed and modeled.

Introduction

Indoor air quality is of increasing concern and has been affected by recent efforts to reduce energy costs. In order to decrease the costs of heating and cooling the infiltration of outside air must also be decreased. However, without adequate ventilation, harmful concentrations of pollutants can accumulate inside. Thus modeling of indoor air quality is also of increasing concern. These models serve four major purposes.

Models are used to relate indoor air quality to various infiltration, source, and sink parameters. Second and most important, a model provides a means to accurately predict functions of concentration such as peak concentration and dosage for places and conditions other than those tested experimentally. Third, models can be used to determine the accuracy and precision to which various quantities must be measured if a desired accuracy of prediction is to be achieved. Fourth, they are often useful in sorting out trends in experimental data.

The first part of this work involved determining the variation of the air exchange rate with respect to location within a typical room.

The second part involved determining the influence of temporal variations which might occur throughout a 24-hour period in the air exchange rate upon peak concentrations and dosages associated with an indoor source.

The third part of this work involved setting up a numerical least squares procedure to determine the values of the internal and external exchange rates for a two compartment model. Actual tracer data from an EPRI sponsored field study were analyzed by means of this technique.

Theoretical Development

Variation of Air Exchange Rate with Respect to Location

The Single Compartment Model

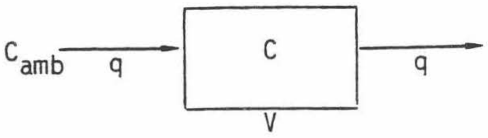

$$\frac{dC}{dt} = \frac{q}{V} C_{amb} - \frac{q}{V} C$$

The sampling unit integrates over a ten minute interval. C^* is the theoretical value that the samples should yield.

$$\ln\left(\frac{C^* - C_o}{C_{amb} - C_o}\right) = k - \frac{q}{V} t \ ; \quad \text{where k is a constant}$$

Linear regression was performed to obtain the best values for C_{amb} and q at each of nine locations in the room. We allowed C_{amb} to be different in each location.

Variance of Dosages With Varying Infiltration

Several empirical relations exist which relate air infiltration rates with inside-outside temperature difference and wind speed. A situation in which these two factors are not constant would give rise to an infiltration rate that changes with time. When linearized and with an indoor source, the model becomes:

$$\frac{dC}{dt} = \frac{q_o(1 + \alpha t)}{V} C_{amb} - \frac{q_o(1 + \alpha t)}{V} C + k$$

The equation was made dimensionless with the following substitutions and solved.

$$\tau = \frac{q_o}{V} t \qquad \beta = \alpha \frac{V}{q_o} \qquad R = \frac{k}{q_o}$$

$$C(\tau) = C_{amb} + (C_o - C_{amb})\, e^{-(\frac{1}{2}\beta\tau^2 + \tau)} + e^{-(\frac{1}{2}\beta\tau^2 + \tau)} \int_0^{\tau} R e^{\frac{1}{2}\beta\tau^2 + \tau} d\tau$$

The integral on the right cannot be solved analytically and must be solved numerically. If the infiltration rate is averaged these much simpler equations are obtained.

$$\frac{dC}{dt} = \frac{q}{V} C_{amb} - \frac{q}{V} C + k$$

$$C(t) = C_{amb} + (C_o - C_{amb})\, e^{-\frac{q}{V} t} + \frac{k}{q}(1 - e^{-\frac{q}{V} t})$$

These two functions for C are to be used to calculate the maximum hour dosage and the 24-hour average given a typical day's weather and source patterns. The results will be compared to determine if the simpler version is accurate enough.

The Two Compartment Model

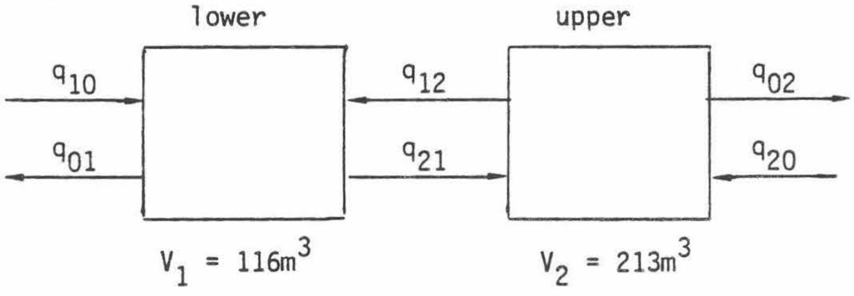

$$\frac{d(V_1C_1)}{dt} = q_{10}C_o - (q_{10} + q_{12})C_1 + q_{12}C_2$$

$$\frac{d(V_2C_2)}{dt} = q_{20}C_o + q_{21}C_1 - (q_{20} + q_{21})C_2 + S$$

Presentation and Discussion of Results

Variability of Air Exchange Rate with Respect to Location

32	5	29	4.7	3.0	5.0
29	17	29	4.4	4.1	5.0
37	23	27	5.3	4.4	4.7
	a.			b.	

a. Ambient concentrations determined such that the correlation coefficients are maximized.
b. The air exchanges per hour at each of the nine locations subject to the above backgrounds.

Mean air exchange per hour	4.5
Standard deviation	0.6
Maximum deviation	33%

Variance of Dosages With Varying Infiltration.

See the weather and source scenario included in Appendix II. This was used to describe the infiltration rate and source behavior for the entire day. The non-linear case was linearized over one-hour intervals.

Volume	$198\ m^3$
Source(CO)	0.7 cc/sec
C_{out}	1 ppm

Achenbach and Coblentz:

$$I = 0.315 + 0.0273\cdot V + 0.0105\cdot|T_a - T_r|$$

Average I = 1.030

24 hour dosage	2.539 ppm
Approximate 24 hour dosage	2.543 ppm
Maximum hour dosage	7.445 ppm
During interval	18.5 to 19.5
Approximate maximum hour dosage	7.417 ppm
During interval	18.5 to 19.5

Malik:

$$I = 0.23 + \frac{0.169}{40} \cdot \frac{2}{\pi} \cdot |T_a - T_r| \cdot V + 0.0146 \cdot |T_q - T_r|$$

Average $I = 0.8326$

24 hour dosage	2.884 ppm
Approximate 24 hour dosage	2.905 ppm
Maximum hour dosage	8.060 ppm
During interval	18.5 to 19.5
Approximate maximum hour dosage	8.115 ppm
During interval	18.5 to 19.5

The Two Compartment Model

See Appendix III for graphical results. From the graphs we can notice a quite good fit. This is good evidence that the houses being tested are well represented by the two compartment model. Earlier attempts to model using the single compartment model yielded very poor results.

Conclusions

The spatial variability in the air exchange rate for a given room may be as high as 33%.

Typical temporal variations which result from diurnal changes in outside temperature and wind speed were found to give rise to relatively low variations in the peak one-hour dosage and the 24-hour dosage. That is using the average air exchange rate in a constant coefficient model yields results very nearly equal (i.e. ± .73%) to those obtained from the variable coefficient model which requires a numerical solution.

A least squares numerical method was developed and used to determine internal and external air exchange rates so that tracer data could be analyzed via a two compartment model.

Acknowledgments

I would like to express my myriad thanks to my advisor Dr. F. H. Shair for his guidance and tolerance. I would also like to thank Dr. Shair again and all others without whom SURF would not be possible.

I would like to take this opportunity to thank the men and women of Fleming House for making me who I am today. Finally, I would like to thank a small group of high school students without whom this summer would have been less interesting.

Bibliography

Richard A. Wadden and Peter A. Scheff, "Indoor Air Pollution - Characterization, Prediction, and Control," John Wiley & Sons, 1983.

"Energy Use, Infiltration, and Indoor Air Quality in Tight Well-Insulated Residences," GEOMET Technologies, Inc., Rockville, Maryland, August 23, 1982.

APPENDIX I

DILUTION

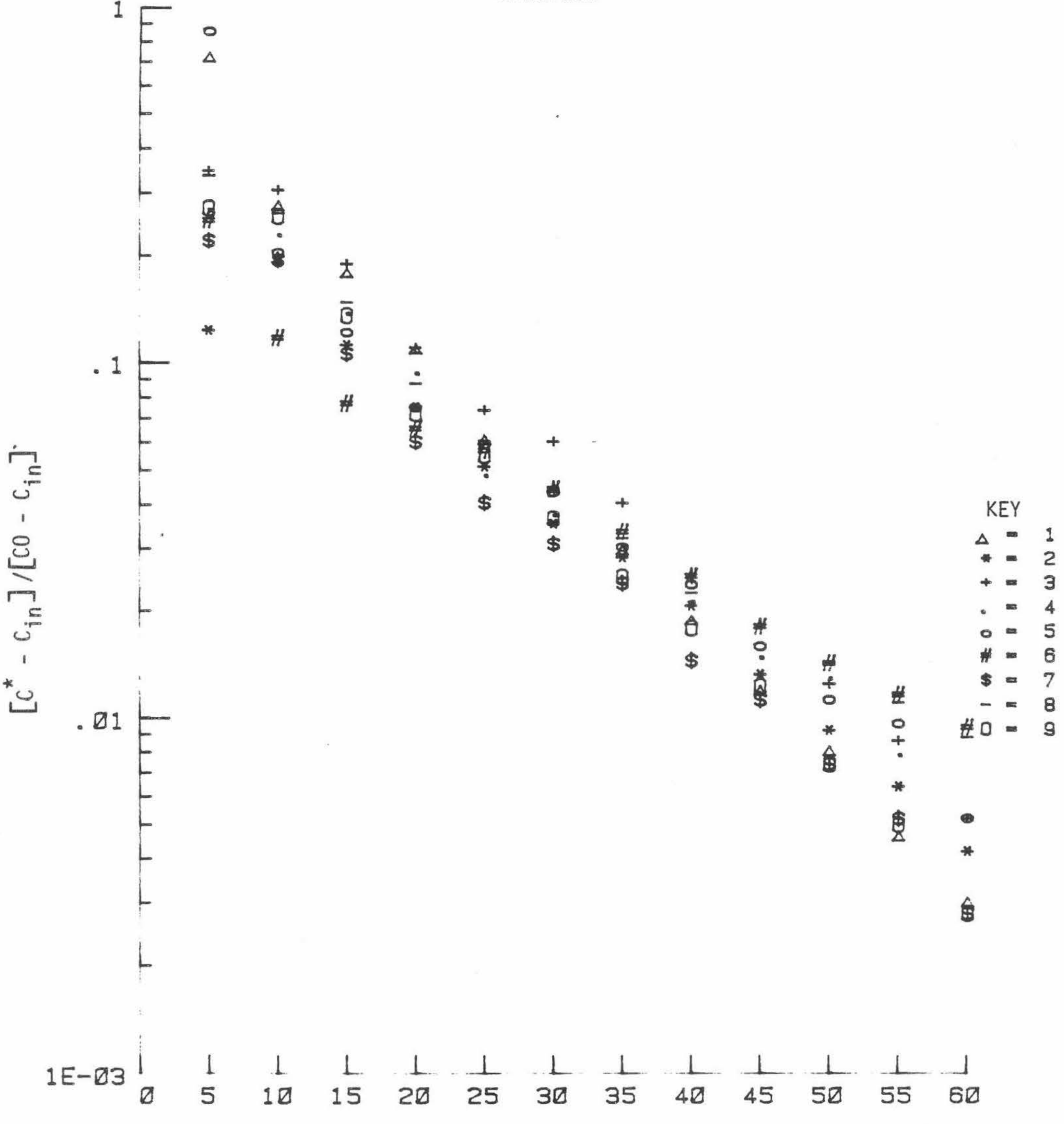

RELEASE LOCATION: AIR VENT RM. 236 SPALDING
RELEASE TIME: 9:00 6-21-83

APPENDIX II

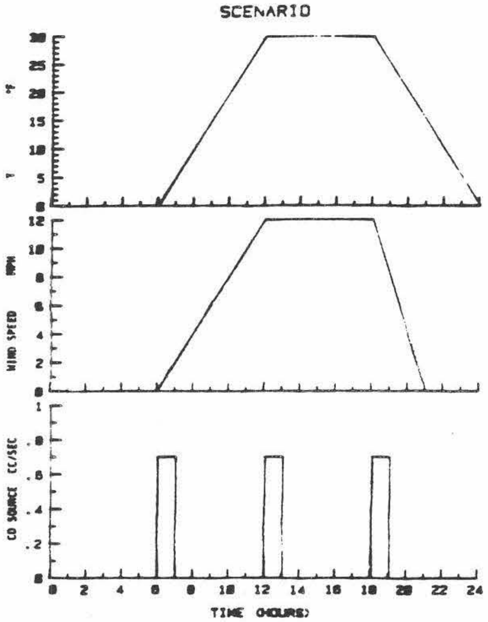

SCENARIO

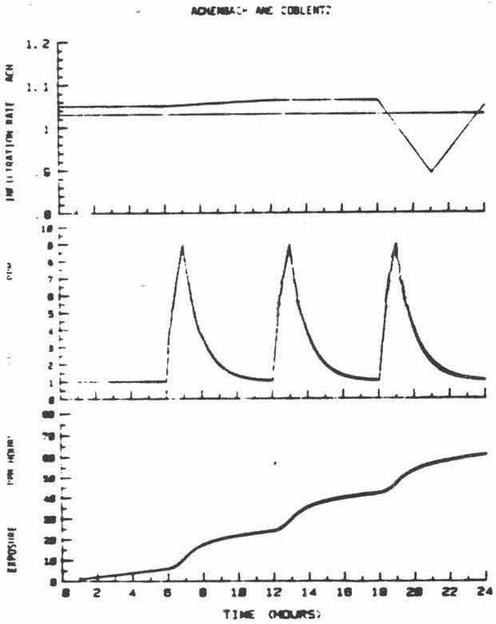

ACHENBACH AND COBLENTZ

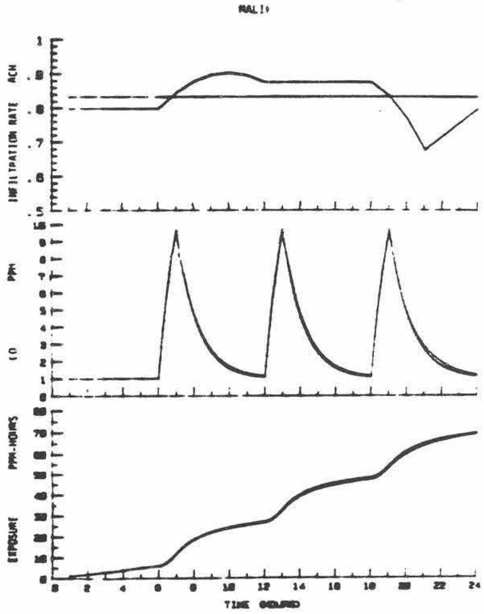

MALIK

APPENDIX III

House A Downstairs

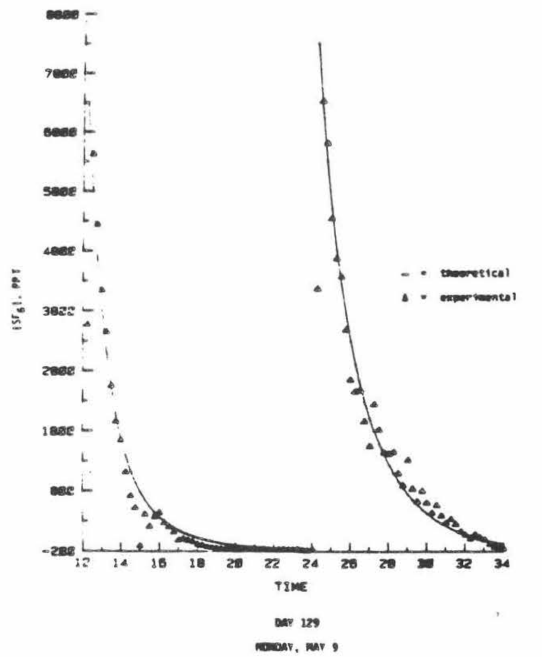

House A Upstairs

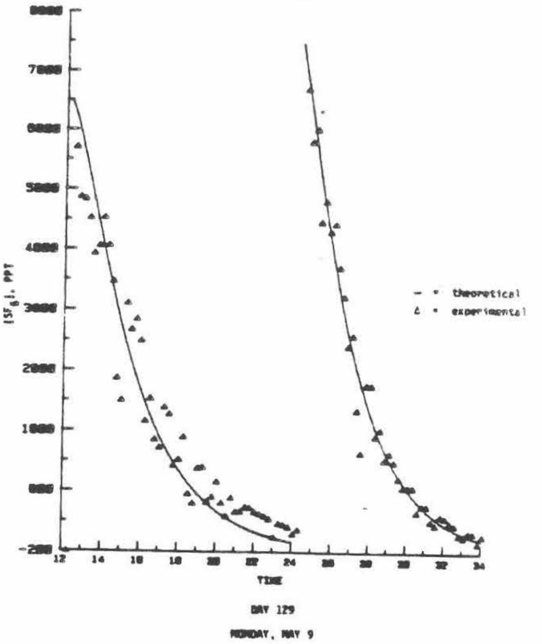

House B Downstairs

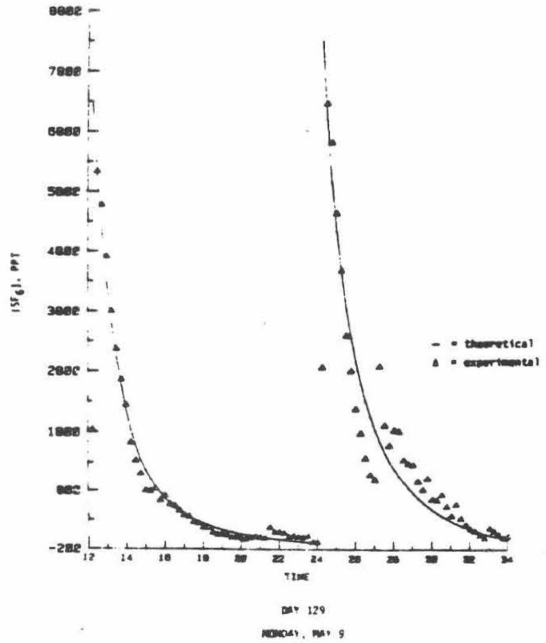

House B Upstairs

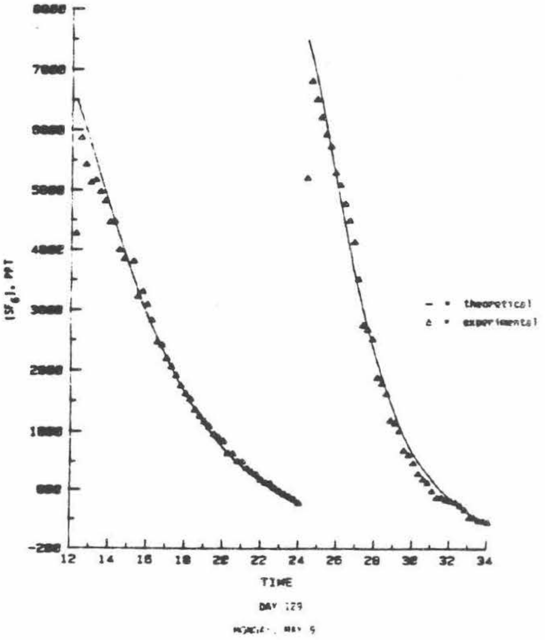

AN EXPERIMENTAL STUDY OF SOIL SLOPE FAILURE USING A CENTRIFUGE

Lisa Nikodym
Faculty sponsor: Dr. Ronald F. Scott

ABSTRACT

A centrifuge was used to examine the behavior of damp sand slopes experiencing earthquake-like vibrations. A sand slope was put on the centrifuge and "spun up", increasing its apparent weight, until it failed. It was rebuilt, spun up to a lower acceleration, and an earthquake-like vibration was added. Failure behavior was recorded, and compared both to the static experiment and to theory (from a computer program).

-I-

INTRODUCTION

The behavior of soil slopes and dams subjected to earthquakes is not very predictable quantitatively. A number of approximate methods exist to predict slope failure, but none work well under all conditions for all soils. For earthquake conditions, especially, no really reliable methods exist.

In this project, the failure of a simple earth slope experiencing earthquake-simulating vibrations was examined. The results were compared both to current theory and to static (no earthquake) slope failure.

Because it is impractical to build full-scale slopes, the Caltech centrifuge was used. A small slope in the centrifuge experiences a centrifugal acceleration, increasing its apparent weight, so that it behaves like a much larger slope.

-II-

GENERAL PROCEDURE

1) Soil Testing

The soil used in this project is called "Nevada Fine sand". Laboratory tests were run to determine its strength parameters. Further details are given in section III.

2) Predictions from Theory

Using the strength parameters found in the soil tests, a computer program was used to predict the failure conditions for the slopes built later in the project. Further details are given in section IV.

3) Centrifuge-Testing the Slopes

A 70-degree slopes was put on the centrifuge and "spun up" until a thick surface layer over most of the slope slid off, which is defined as failure. The slope was rebuilt and run at a lower acceleration and an earthquake-like vibration was added. The experiment was repeated to check reproducibility.

4) Analyzing the Results

The slope on the centrifuge is a small one; to determine how large a slope it is behaving like, multiply all dimensions of the experimental slope by the number of gravities of acceleration at which the centrifuge is spinning. The number of gravities at failure and the geometry of the failure surface for the static case were compared to the program results to determine the accuracy of the program for this slope. The failure surfaces for the dynamic experiments were examined to determine, if possible, how failure occurred. Again, the geometry of the failure surfaces was compared to the program results. The dynamic failure behavior was also compared to static failure behavior, and generalizations made about dynamic failure.

-III-

SOIL TESTS

The two most often used measures of a soil's strength are its cohesion, c, and its angle of internal friction (or friction angle), ϕ . A completely dry sand has no cohesion; as water is added, its cohesion increases. Clays have negligible internal friction. Silts have both cohesion and internal friction.

These parameters may be found by a number of tests, though all give only approximate values. The "direct shear test" was used on the sand. The soil sample is placed in a box consisting of two separate halves, and a vertical normal force, P_v, is applied to the top. During the test, the top half of the box is mechanically displaced slowly sideways (see figure 1) and the horizontal shear force, P_h, measured by a load cell connected to a recorder. The test is run for various values of P_v, and a graph is made of P_h/A versus P_v/A (where A is the horizontal cross-sectional area of the sample). The friction angle is the angle of inclination of the resulting straight line, and the cohesion is its intercept on the ordinate axis. For all tests, a calculator program was used to find the best-fit line.

The water content (i.e. the ratio of weight of water to weight of solids) used for all experiments was 7%. The approximate density used was 106 pounds per cubic foot (0.0613 pounds per cubic inch, or 28 grams per cubic inch). These are fairly average natural values for this sand.

For the direct shear test data, see table 1. A graph of the data with the best-fit line appears in figure 3. The results were:

$c = 1.7$ lbs./sq. in. $= 245$ lbs./sq. ft.

$\phi = 27.5$ degrees

-IV-

THEORETICAL FAILURE CONDITIONS

A computer program using the Bishop method of slices computed the theoretical failure conditions for all slopes used in the experiment. Given a two-dimensional slope geometry, an assumed circular failure surface, and the cohesion, friction angle, and density of the soil, the program finds the slope's factor of safety, FS. For a given potential failure surface,

$$FS = \frac{\text{sum of resisting forces along potential failure surface}}{\text{sum of driving forces along potential failure surface}}$$

The factor of safety for the slope is the minimum of the factors of safety for all potential failure surfaces. By trying many circle centers and radii, one can find the most likely failure surface and its factor of safety. Because this method assumes a circular failure surface, which is roughly true for most materials and not true at all for some, this result is considered to be only a maximum possible value and not necessarily accurate. Other approximations in the method further add to the uncertainty.

In order to analyze the effect of earthquakes, the program uses pseudo-static methods which are approximate at best. One simply gives it the pseudo-static earthquake coefficient, k, which is the maximum horizontal ground acceleration (in number of gravities). The maximum k generally assumed in earthquake engineering design in the U.S. is about 0.15. I used the values k = 0.1 and k = 0.2 in the program to give a general indication of how the slope acts in this range.

To find the acceleration on the centrifuge at which the slope is expected to fail, one adjusts the "theoretical" soil density until FS = 0.95 to 1.00. Then,

$$\text{number of gravities at failure} = \frac{\text{"theoretical" density at which FS} = 0.95 \text{ to } 1.00}{\text{true density of the soil}}$$

The height of the slope one is attempting to simulate is the height of the experimental slope times the number of gravities it is spun at. The slopes used in this experiment were 5.5 inches high, so the slope size they were behaving like was 5.5 inches times the number of g's of acceleration.

If the circle center is at a lower altitude than the crest of the slope, the program assumes that the circle "curves back on itself" before reaching the top of the slope. Because this is unrealistic, it was assumed that the failure surface remains vertical rather than curving back (for an example, see figure 2). This is equivalent to the formation of a tension crack near the crest of the slope.

A listing of the theoretical number of gravities at failure and corresponding theoretical slope height for each slope appears in table 2. For graphs of the slopes and the theoretical failure surfaces, see figures 4 and 5. Included in figure 4, the static case (k = 0), is the failure surface found in the static centrifuge experiment.

-V-

THE CENTRIFUGE

The centrifuge consists of a spinning arm with "buckets" attached to either or both ends. The arm is mechanically spun at adjustable speed to impart centrifugal acceleration to the buckets. An electronic noise generator was used as the source of the "earthquake" acceleration. The actual earthquake acceleration felt by the slope is difficult to control at all precisely, but the maximum acceleration produced generally corresponds to k = 0.2 to 0.3. Several accelerometers were placed on the slope in order to measure its acceleration at various points, but equipment problems prevented the recording of any useful data.

The bucket containing the slope was 22 inches long, 7 inches wide, and 9.75 inches deep. All slopes were 5.5 inches high and 2 inches wide.

The slope was "spun up" until it failed, and the failure acceleration and geometry of the failure surface recorded. The slope was then rebuilt and spun up to the acceleration at which the computer program predicted failure for k = 0.2 and earthquake-like vibrations were added for around one and one-half seconds. The dynamic experiment was repeated to check reproducibility. (I have found by previous experience that static tests are adequately reproducible, so, in the interests of time, the static test was not repeated.)

-VI-

EXPERIMENTAL RESULTS

The static slope (k = 0) failed at a centrifuge acceleration of 63 gravities. The program predicted failure at, to the nearest five, 60 gravities; this prediction, then, was quite reasonable. The experimental failure surface, however, was much shallower than that predicted (see figure 4). It may be guessed that the dynamic failure would also be shallower than predicted.

For both dynamic tests, the centrifuge was spun up to 40 gravities. Horizontal lines of darker sand were placed in the sand every half inch along the glass face of the bucket to make the failure surfaces easier to see. Figures 6 and 7 are sketches of the failure surfaces. Test 1 had three obvious slides; test 2 had two, plus more beginning to form. The program was obviously not equipped to predict slides of such complexity, and hence was inherently inaccurate.

The chronology of test number one (figure 6) is difficult to follow. It is probable, though by no means certain, that the rightmost failure mass was the first to slide, followed by the leftmost (deepest) slide, with the upper failure mass the last to go. (With the exception of the last slide, this follows the general pattern of the second slide.) The program predicted that the failure surface would meet the surface of the slope at one-quarter to one-half of an inch (measured diagonally) above the base; the actual distance was between one-half and three-quarters of an inch (with lines only every half-inch, it was impossible to tell more precisely). As in the static case, this experimental failure surface was considerably shallower than that predicted by the program. Notice the "bumps" along the slope at the crest and toe of each individual slide; the ones at the crests are the relatively undisturbed "corners" of each subsequent crest, while the ones at the toes are from the piling up of the failed slides where they come to rest.

Test number two (figure 7) is of a more classic failure pattern. The rightmost slide occured first. This failure mass settled to the right of the slope with the crest still higher than the toe. Another failure surface began forming near the new crest, spread, and slid away. Part of the first failure mass was still resting on it, and was pushed farther to the right, with the toe of the second slide beneath the first slide. Note the tension cracks forming near the crest of the slope. If the earthquake had lasted longer, these probably would have spread downward and outward, one by one, to become more failure surfaces and produce more slides; thus the pattern started by the first two slides would continue. This phenomenon occurred, with many repetitions, in the Turnagain Heights, Alaska, slide of 1964 (see The Great Alaska Earthquake of 1964; Engineering, listed in the bibliography, for more details). Again, as predicted, the failure surfaces developed completely above the base of the slope. (For comparison, the failure surface in a clay or silt slope will often go well below the base of the slope.)

-VII-

CONCLUSIONS

1) The centrifuge can be used to adequately model large slopes. The failures of both the static and dynamic slopes were similar in form to those occurring under real conditions.

2) A slope experiencing an earthquake has a considerably lower factor of safety than a static slope. In the sand tested, once failure begins, more slides develop for as long as the earthquake lasts.

3) Pseudo-static theory predicts that dynamic failure surfaces extend farther into the slope than static failure surfaces. This turned out to be true experimentally even if only one slide occurs in the dynamic case.

4) The method of prediction used can give a rough estimate of the factor of safety for a static slope (generally an upper bound), but cannot make a reasonable estimate for dynamic failure, which is too complex for the program to handle.

TABLE 1 : DIRECT SHEAR TEST DATA FOR NEVADA FINE SAND

= P /A   = P /A   A = 4.87 sq in

Trial #	P (lb)	P (lb)	(lb/sq in)	(lb/sq in)
1	30	24	6.2	4.9
2	50	32	10.3	6.6
3	60	40	12.3	8.2
4	75	52	15.4	10.7
5	100	58	20.5	11.9

TABLE 2 : THEORETICAL FAILURE CONDITIONS

k	# of g's at failure	corresponding slope height (ft)
0	60	27.5
0.1	50	23
0.2	40	18

FIG. 1: DIRECT SHEAR BOX (SCHEMATIC)

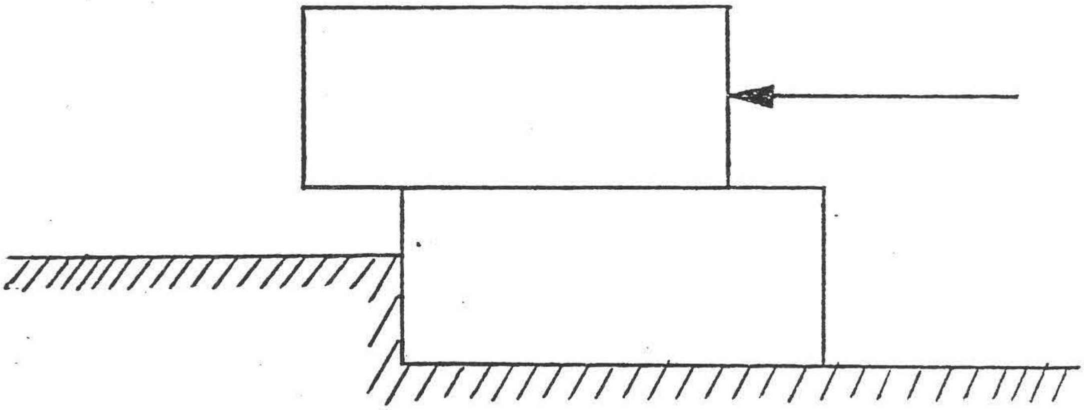

FIG. 2: BISHOP PROGRAM ASSUMPTION

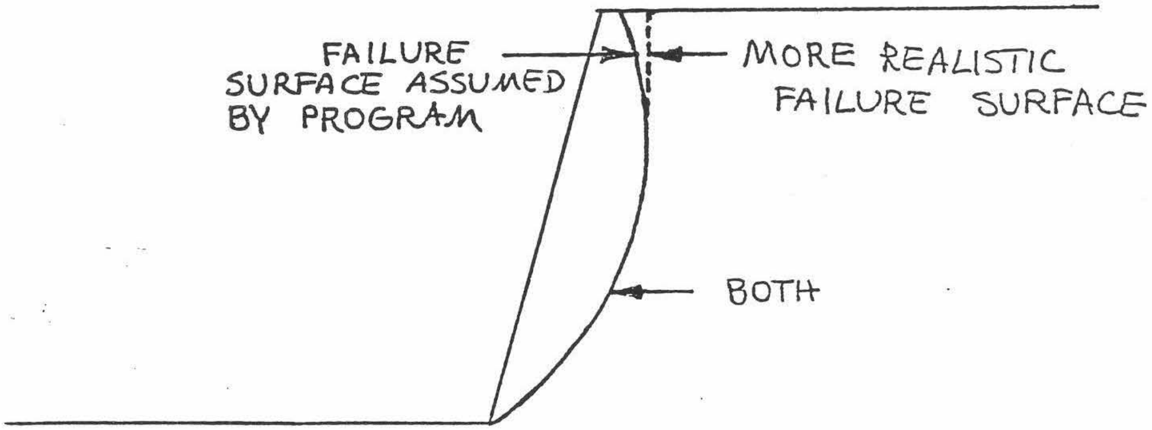

FIG. 3 : DIRECT SHEAR TEST DATA

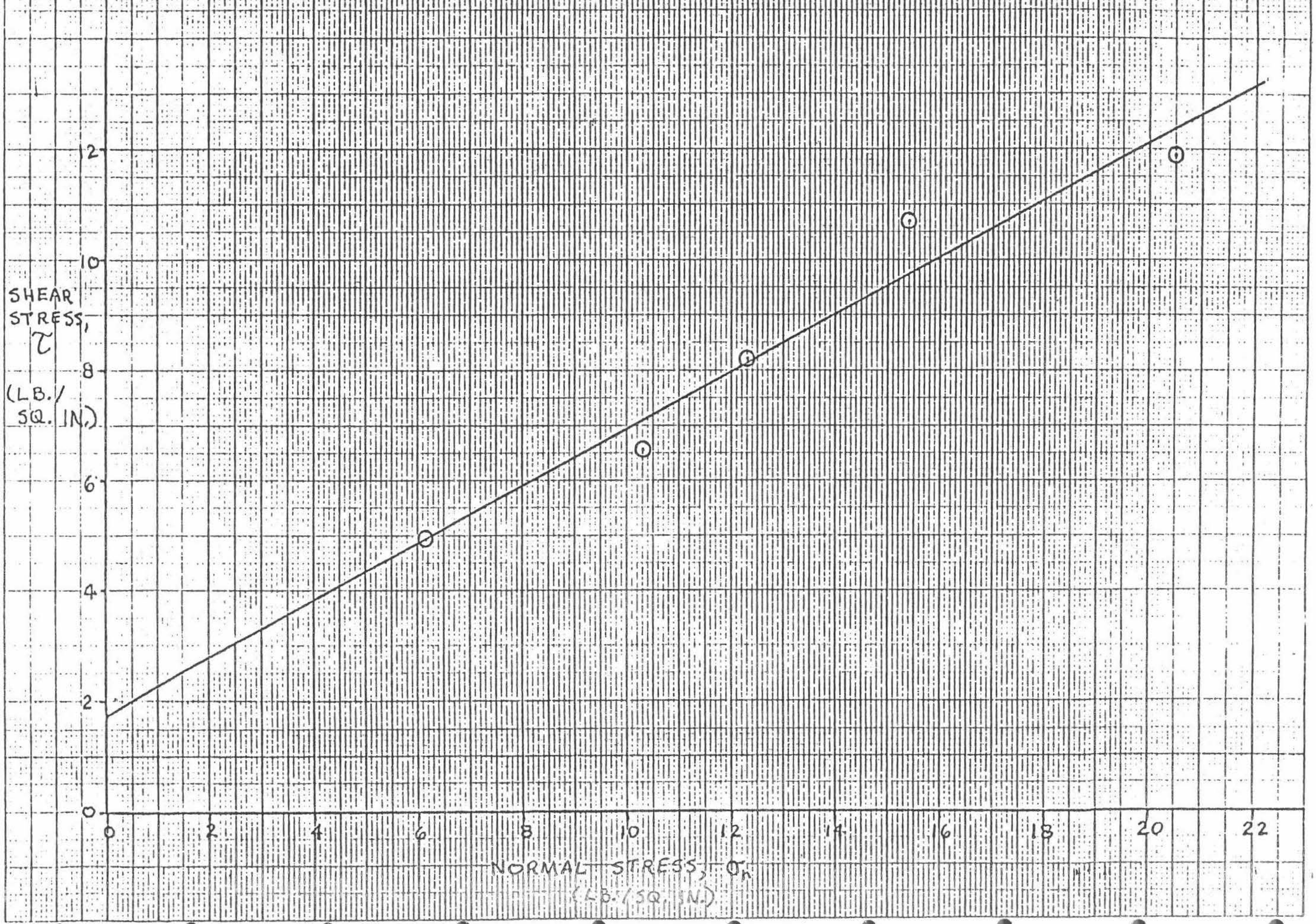

FIG. 4: STATIC SLOPE FAILURE

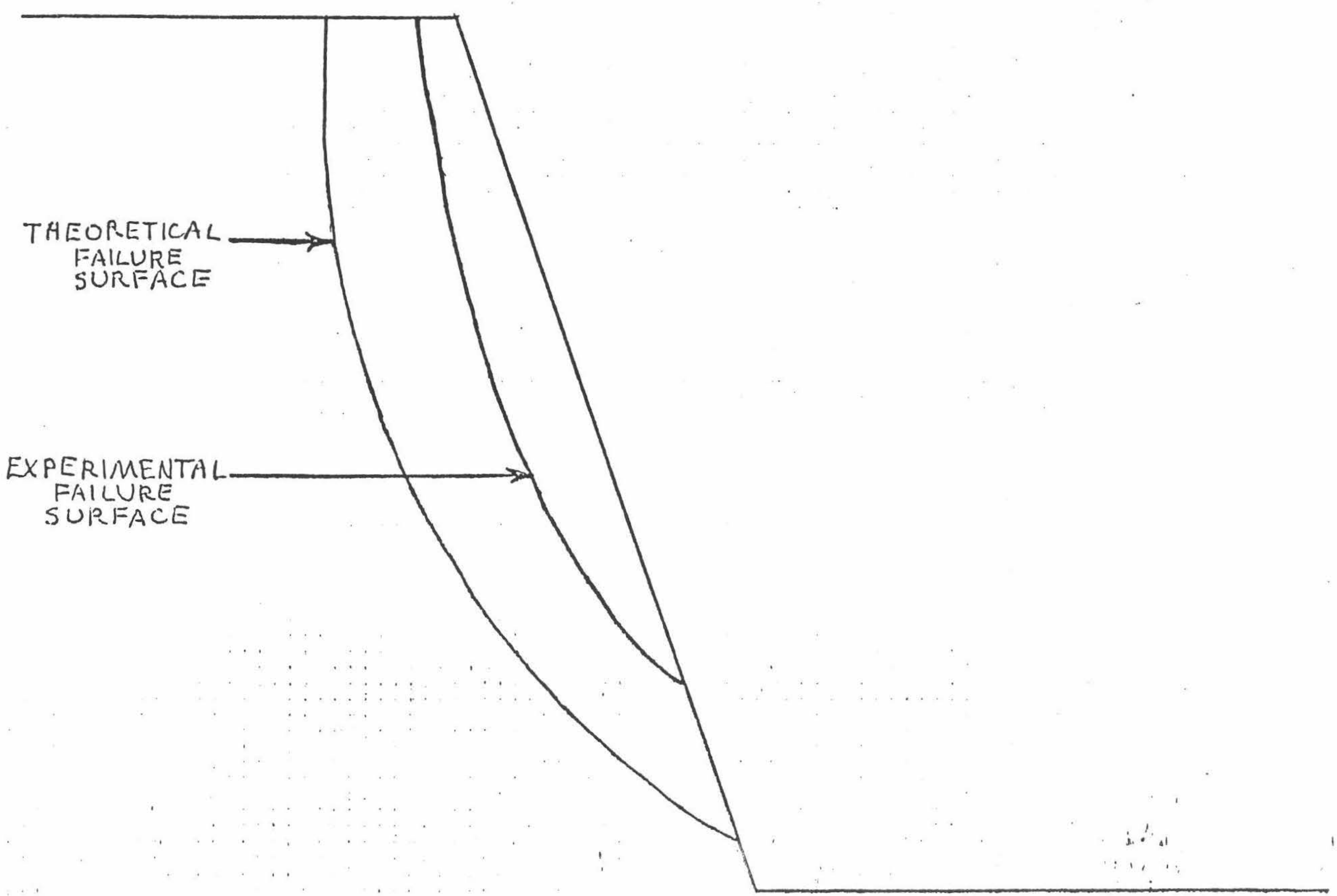

FIG. 5: DYNAMIC SLOPE FAILURE

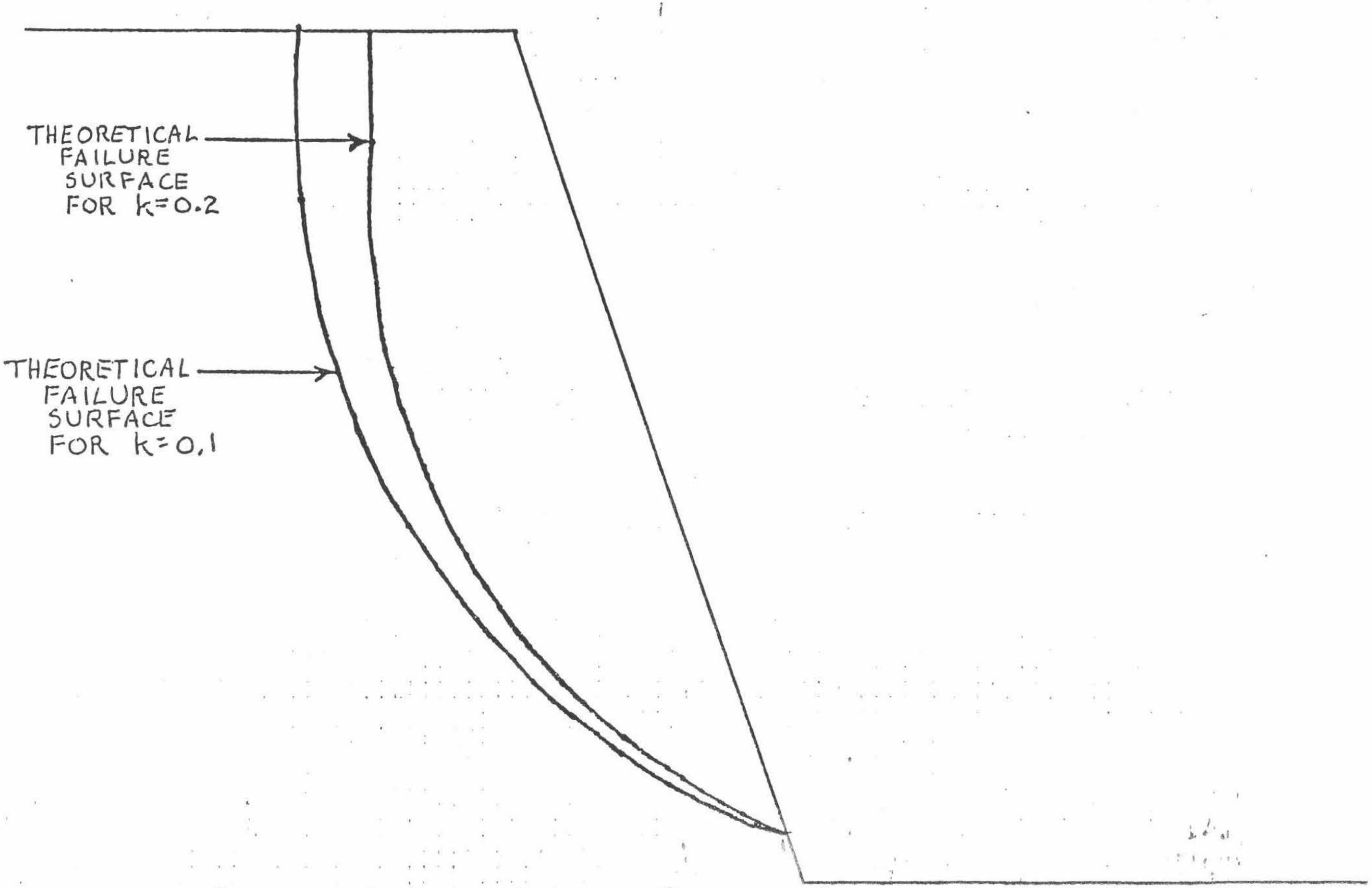

FIG. 6: TEST #1, FINAL CONFIGURATION

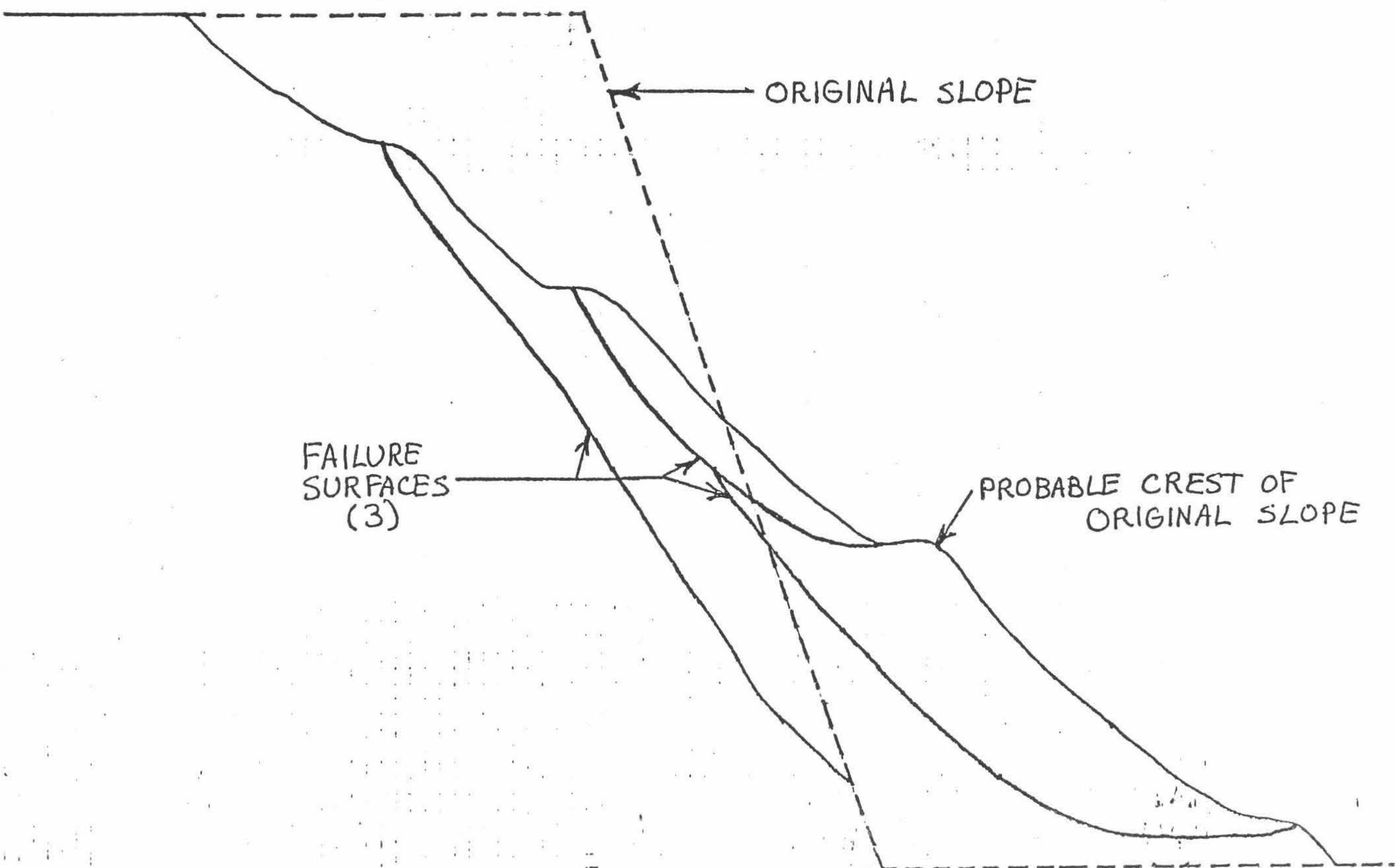

FIG. 7: TEST #2, FINAL CONFIGERATION

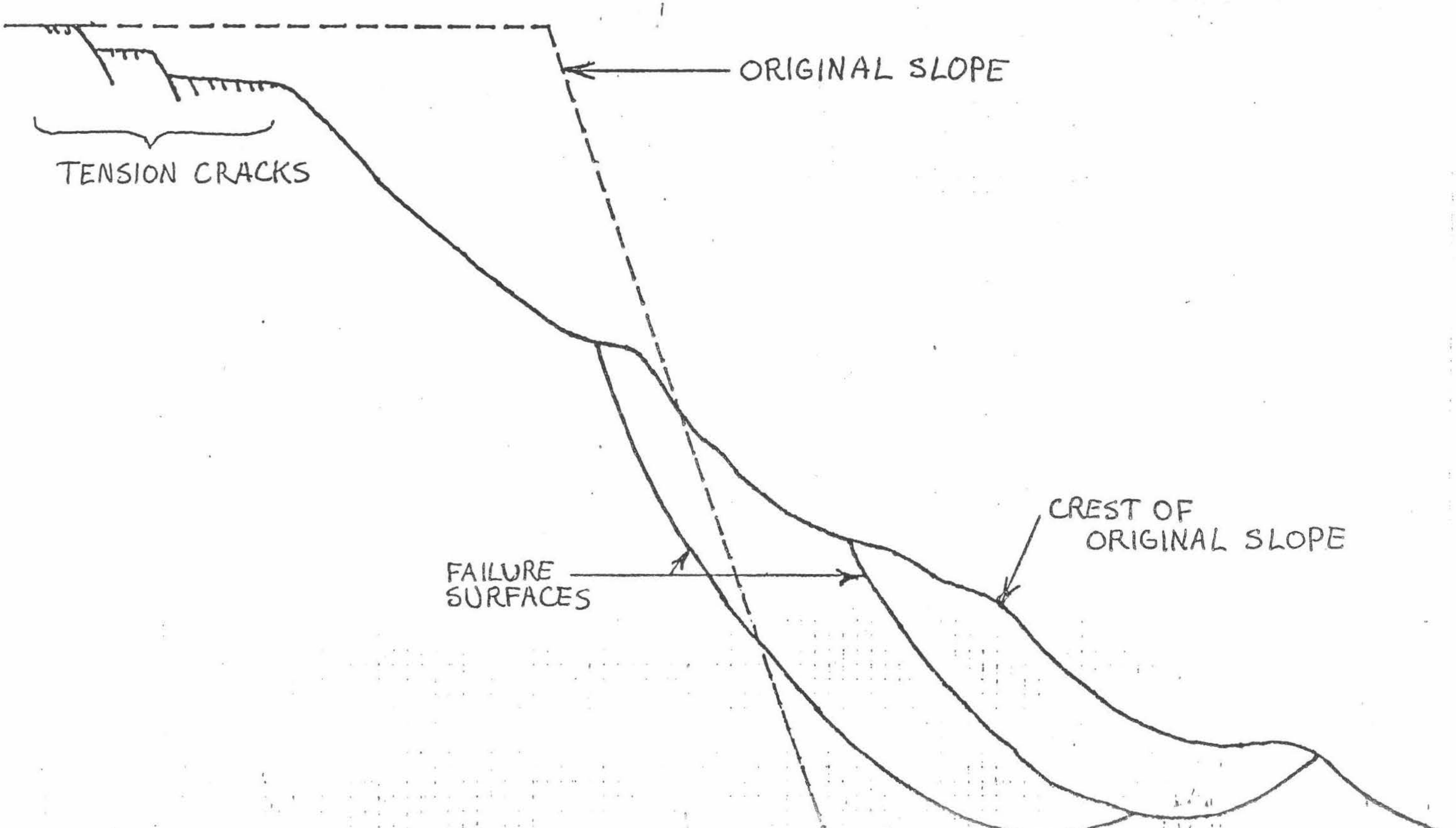

BIBLIOGRAPHY

BOOKS

Joseph E. Bowles
ENGINEERING PROPERTIES OF SOILS AND THEIR MEASUREMENT
Second Edition
McGraw-Hill Book Company 1978

T. William Lambe and Robert V. Whitman
SOIL MECHANICS
John Wiley & Sons, Inc. 1969

Shunzo Okamoto
INTRODUCTION TO EARTHQUAKE ENGINEERING
John Wiley & Sons, Inc. 1973

Ronald F. Scott
PRINCIPLES OF SOIL MECHANICS
Addison-Wesley Publishing Company, Inc. 1963

Ronald F. Scott and Jack J. Schoustra
SOIL MECHANICS AND ENGINEERING
McGraw-Hill Book Company 1968

Donald W. Taylor
FUNDAMENTALS OF SOIL MECHANICS
John Wiley & Sons, Inc. 1948

Robert L. Wiegel, coordinating editor
EARTHQUAKE ENGINEERING
Prentice-Hall, Inc. 1970

REPORTS

G. I. Pokrovsky and I. S. Fyodorov
CENTRIFUGE MODEL TESTING IN THE CONSTRUCTION INDUSTRY, VOLUMES 1 & 2
Translated by Building Research Establishment Library Translation Service, U. K. 1975

A. N. Schofield
USE OF CENTRIFUGE MODEL TESTING TO ASSESS SLOPE STABILITY
University of Cambridge Department of Engineering 1976

H. Bolton Seed, Ignacio Arango and Clarence K. Chan
EVALUATION OF SOIL LIQUEFACTION POTENTIAL DURING EARTHQUAKES
UC Berkeley Earthquake Engineering Research Center
Report No. EERC 75-28 October 1975

ATOMIC ABUNDANCES IN A HOLLOW CATHODE DISCHARGE

Matthew Penn
Advisor -- Prof Ward Whaling

ABSTRACT

Hollow cathode discharge (HCD) spectra, taken with a 1-m Fourier transform spectrometer at Kitt Peak and with a 5-m Paschen-Runge spectrometer in Bridge Lab, were analyzed to investigate atomic energy level populations in various discharge regions and under different gas pressures. A relation between energy level populations in the z3P term and gas pressure was found.

INTRODUCTION

One source that has been used to produce high quality emission line spectra is the hollow cathode discharge (HCD). This device consists of a hollow, cylindrical metal electrode to which a negative voltage is applied. Our cathode was placed in a low pressure atmosphere, in which a steady flow of an inert gas is run.

Previous investigations of an HCD system using an iron cathode and argon gas have been made, and results of these investigations, especially by Humphrey in 1982 SURF work, have shown curious features. If the discharge in an HCD were to follow the standard statistical models, one might expect the populations of the energy levels to decrease with increasing energy, roughly corresponding with e^(-E/kT). This e^(-E/kT) dependance is generally seen when one compares populations of the different terms of iron; for example, since the z5D term (at 26000 cm^-1) is less energetic than the z3P term, (at 34500 cm^-1), the z5D has a larger population. Levels within some terms, such as the z3P term, behave differently. One sees the opposite behavior; i.e. the higher energy levels in the z3P term have greater populations than the lower energy z3P levels. The study of this phenomena was the purpose of this investigation.

DISCUSSION

One theory for this unique behavior involves different mechanisms in different regions of the discharge. Data exploring this possibility was taken at Kitt Peak using a 1-m Fourier transform spectrometer. Scans of different regions of an HCD were taken using various masks in the imaging system of the spectrometer. (see Figure 1) Two scans were taken of the central region of the cylindrical cathode discharge, and two scans were taken of the annular region of the discharge, the region nearest the cathode surface. Data from these spectra were recorded on magnetic tape, and then reduced with the help of a PDP 11 processor. Existing software was used to plot the spectra, and then integrate the spectral lines of interest. A set of nineteen lines were chosen to be studied, from which populations for eight atomic energy levels could be calculated.

Figure 1 -- System used for Kitt Peak spectra

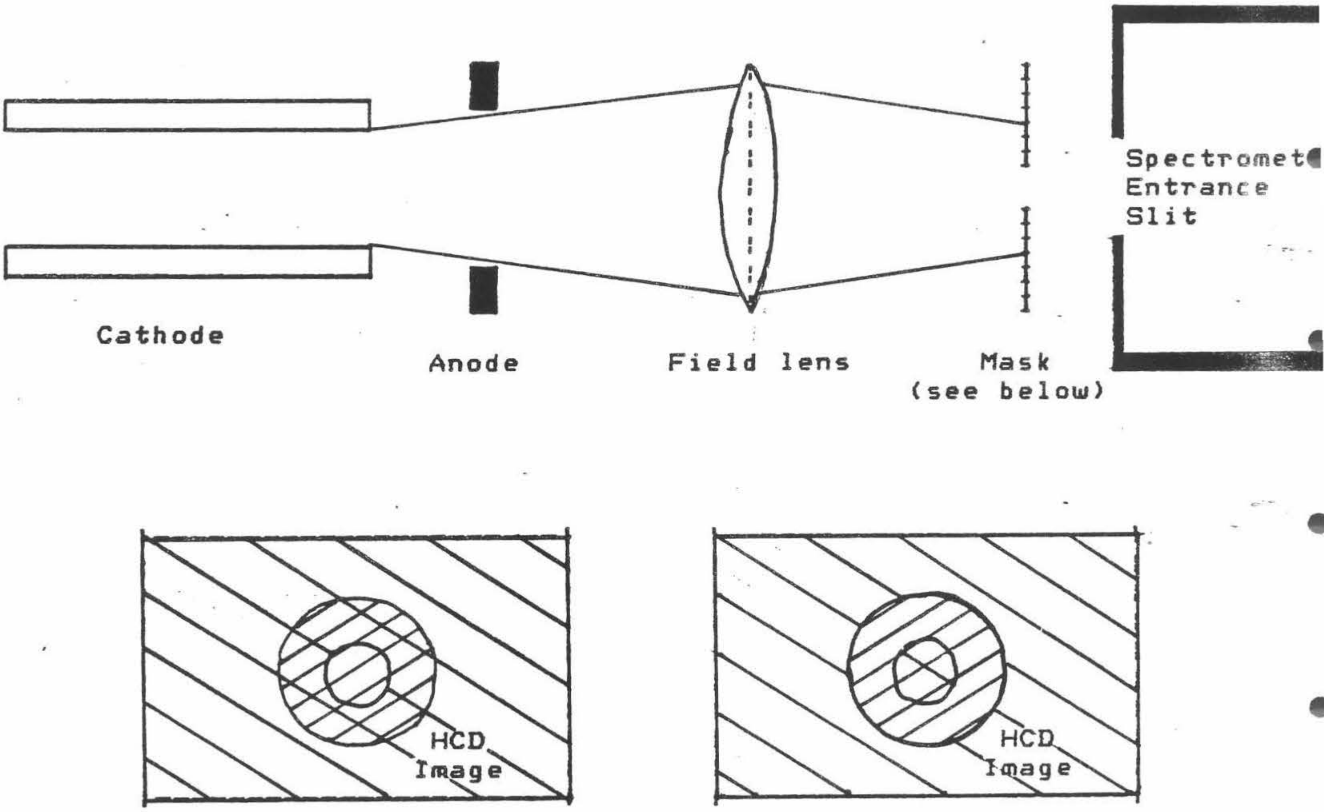

"Central" Mask

"Annular" Mask

The photon intensity (photons/sec) of a spectral line, I(u), is related to the population N(u) of the level u from which the photon is emitted by the following formula:

$$N(u) = \frac{I(u)}{A(ul)}$$

where A(ul) is the transition probability from the upper to lower level. A factor of 2J+1 was also used in the data reduction to calculate the population of a magnetic substate of the upper level;

$$N(ms) = \frac{N(u)}{2J+1}$$

it is this value, the population of a magnetic substate of the upper level which was used for comparisons in this investigation.

The actual photon intensity I(u) is related to the observed intensity I(obs) by;

$$I(u) = \frac{I(obs)}{\text{FTS efficiency}}$$

where the spectrometer's efficiency is a function of wavelength. Several calibrations of the KPNO data using argon emission lines showed that the efficiency curve of the spectrometer was flat in this region, and therefore the efficiency function was assumed to be 1 for the reduction of all KPNO data.

The KPNO data did not reveal any significant differences between the central and annular regions of the discharge. The populations of the z3P term displayed the "non-kinetic" or inverted form where the highest energy level was most populated in both sets of central and annular scans.

In the second part of this investigation, the effects of power and gas pressure on energy level populations was studied. The HCD used contained a 99.999% pure iron cathode, and an atmosphere of argon gas which was varied in pressure. Spectra of this HCD were taken in Bridge Lab, using a 5-m Paschen-Runge spectrometer. This spectrometer employs a scanning photomultiplier tube which outputs to a chart recorder, providing a detailed line spectra of the HCD. Such line spectra do not usually lend themselves to line integration; however, an oversized entrance slit was used in the spectrometer, producing flat-topped spectral lines and thereby providing a simple integration method. The spectrometer's photomultiplier tubes provided a zero signal "dark current" of about 1.5 nanoamps, and the HCD produced a continuum of about 0.5 nanoamps. These background signals were subtracted from the lines studied, though the average lines were two orders of magnitude stronger than this background. A set of nine lines, from three different terms were observed (see Table 1). These lines were chosen within a narrow wavelength range (75 Å), and since the efficiency curve of the spectrometer was flat in this small region, the efficiency factor was ignored in the subsequent data reduction.

Spectra were taken at Argon pressures between 3.2 and 0.3 Torr. During all runs, a continuous flow of Argon was maintained, and attempts were made to keep the running current of the cathode within a small range. After pressure and current conditions were set for the HCD, the system was allowed to stabilize ~~for~~ a very long time, up to six hours. Thirty-three scans of the HCD were taken using these techniques. The relative level populations, N(r), were calculated using the formula:

$$N(r) = \frac{I(u)\ \Lambda^2}{(gf)}$$

where gf is a value proportional to $g(u)A(ul)\Lambda^2$. The gf values for the observed transitions were taken from Blackwell et al. (see REFERENCE 2)

TABLE 1 -- Spectral lines examined in Bridge Lab

	J value	Level Energy (cm^-1)	Wavelength (Å)
y5D term			
	2	33801.6	3834.22
	1	34017.1	3840.44
	0	34121.6	3849.97
y5F term			
	4	34039.5	3799.55
	3	34328.8	3795.00
	2	34547.2	3787.88
z3P term			
	2	33947.0	3850.86 and 3812.96
	1	34342.9	3790.14
	0	34555.6	3786.71

For two of the observed terms, the y5D and y5F terms, the variations of the energy level population distributions seemed totally independant of variations of argon pressure in the HCD. However, for the z3P term, a relation was present. In general, as the argon pressure increased, the energy level populations also increased. At low pressures, with P<= 1.0 torr a distribution similar to that seen by Humphrey was present; i.e. the higher energy levels were more populated. However, at high pressures, with P>=2.5 torr, the situation reversed, and the lower energy levels were more populated; as would be expected for a statistical equilibrium. This reversal was more prominent for the z3P$_2$ level than for the J=1 level, presumably because the A plot of level populations from both a high and a low pressure HCD run is presented in Figure 2.

CONCLUSION

We have found that the energy level populations seem to be in a statistical equilibrium when gas pressures of about 3.0 torr are present in te HCD; the lower energy levels are more populated than the higher levels. However, at low gas pressre, near 0.5 torr, the energy level populations do not follow a statistical equilibrium, instead the level populations are inverted, with the highest energy levels having the highest populations. This behavoir is still unexplained. More detailed study of the effect of distance from the cathode on the energy level populations may involve the use of newly shaped cathode, perhaps involving nonconcentric shapes. Such future investigations may help to explain the inverted populations of the z3P term.

FIGURE 2 -- z3P level populations at high and low pressures

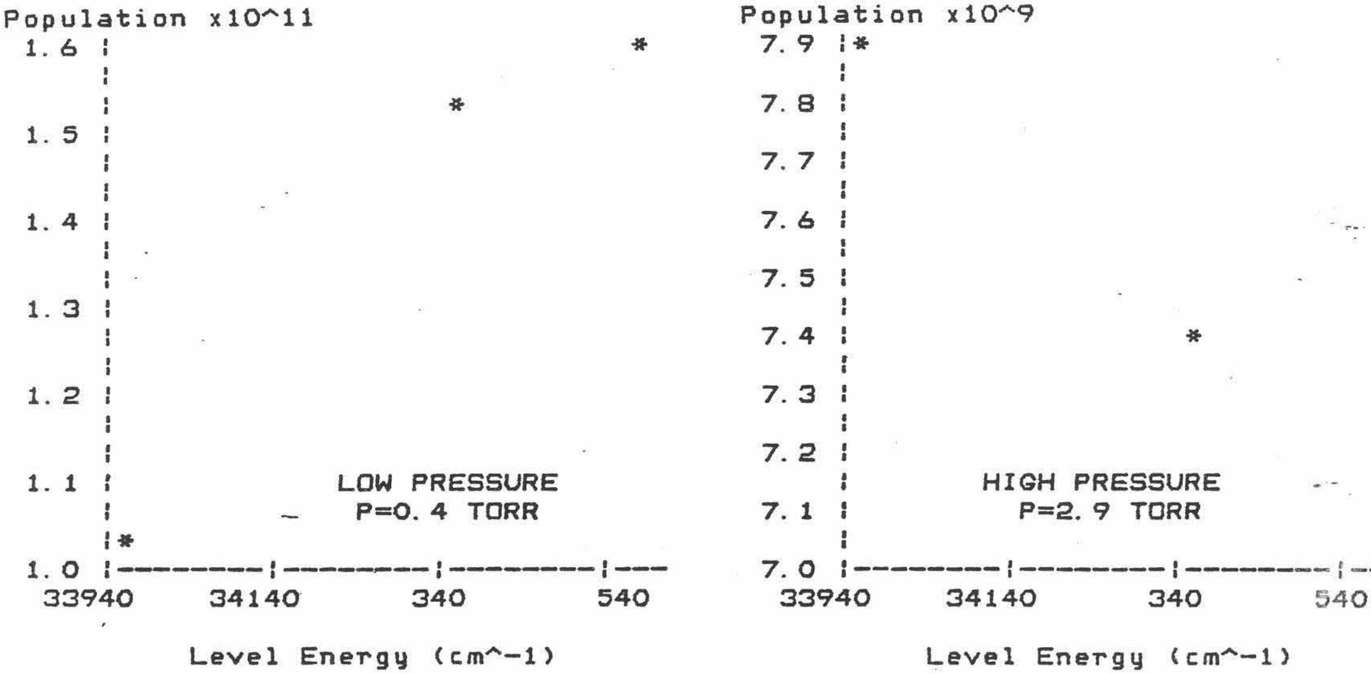

REFERENCES

(1) Adams, D.L. and Whaling, W.; LEVEL LIFETIMES AND BRANCHING RATIOS IN THE Z3PO TERM OF NEUTRAL IRON; Journal of Quantitative Spectroscopy and Radiative Transfer, vol 25, pp 233-236

(2) Blackwell, D.E., et al.; Monthly Notices of the Royal Astronomical Society, vol 199, pp 43

(3) Humphrey, J.N., Adams, D.L., and Whaling, W.; ATOMIC LEVEL POPULATIONS IN THE HOLLOW CATHODE DISCHARGE; to appear in Journal of Quantitative Spectroscopy and Radiative Transfer, October 1983

STRUCTURAL DESIGN AND ANALYSIS OF A SPACE SHUTTLE PAYLOAD

SURF Final Report 1983

Research performed by Norman Princen under the supervision of Professor Charles Babcock.

Abstract

A structure for a Small Self-Contained Payload (SSCP) has been designed to fly aboard the Space Shuttle. Calculations were performed to verify that critical elements of the design would meet the stringent requirements. More accurate modeling utilizing finite element methods has been begun and will continue as the design of the experiment hardware is finalized.

Introduction

The rigors of space flight can play havoc with the delicate instruments often needed to carry out meaningful scientific research in space. The launch of a space vehicle is probably the most severe environment which these instruments need to endure. Typical accelerations created by launch are in excess of 3g's and fairly severe vibrations are caused by the operation of the rocket motors. The purpose of the structural designer in this case is to create a structure that not only survives this punishment, but also provides maximum protection for the instruments on board and is weight and volume efficient.

The standards that affect the design of the structure are set down by NASA to include an adequate safety margin that compensates for differences between theoretical analysis and actual practice. According to these standards, the payload may not have any major resonant frequencies below 35 Hz, must withstand 10g in the X-Y plane, and 14g in the Z direction. Verification of compliance with these requirements is necessary for safety approval of the payload and can be accomplished either by analysis or by testing.

The structure that was designed this summer is part of the second experiment package developed by the Student Space Organization (SSO). This package is designed to fit inside a SSCP canister provided by NASA for Space Shuttle flight. The SSCP canister has internal dimensions of 20" in diameter and 31 1/4" in length. The second SSO experiment package is predicted to fly in the fall of 1984.

The thermal control system for the first SSO payload was designed as a result of work carried out during my SURF project last year. Similar thermal controls to those outlined in my final report last year were also incorporated into the design of the structure for the second payload.

Presentation and Discussion of Results

In the initial design phase, many different structures were evaluated in an attempt to find a structure that would meet the NASA requirements and would incorporate the lessons learned from experiences with our first payload structure. Some of the problems with the first payload included poor access to experiment equipment and the need to build many specialized mounting clamps. These problems have been avoided in the new design by using a large aluminum I-beam as the major structural element. Experimental hardware can be bolted directly to the central web of this beam without the use of special brackets and clamps. Access to the hardware is also made simple since hardware can be assembled and disassembled in any order.

The space and weight efficiency of the payload structure is improved by combining the structure's function with other functions in the payload. The bulkheads that attach to either end of the I-beam and the cylindrical side panels of the payload are constructed of polyurethane foam cores covered in Kevlar-epoxy composite laminate. Aluminum inserts laminated into the bulkheads provide attachment points for mounting other structural elements. These materials were not only chosen for their structural properties, but also because they exhibit low thermal conductivities that are beneficial to good thermal control.

Another example of duality of purpose is the payload battery box which bolts onto the primary bulkhead on one face and the central web of the I-beam on a second face. This box was designed to contain the batteries that run the payload equipment. These batteries represent the single largest mass in the payload, weighing 60 pounds. They also vent hydrogen gas upon being discharged, which means that the box must also be a pressure vessel. The box must not only carry these loads, but also must transfer some of the laods from the I-beam to the bulkhead.

Attachmant of the payload to the SSCP canister is aacomplished by brackets from the primary bulkhead to the end plate of the canister. Pads that extend from the outer edge of the secondary bulkhead contact the inner walls of the can to provide lateral support at the bottom of the payload.

Calculations were done in order to determine material thicknesses that were appropriate in order to meet the NASA requirements. These calculations were performed using formulas derived from classical plate theory and resulted in a rough approximation as to the performance of the structure. Based on these estimates and prior experience gained from the first payload's structure, the design was finalized and construction of the hardware was begun by other members of the SSO. By the end of the summer, all pieces of the structure had been fabricated, but some finishing work still needed to be done. This precluded the possibility of any verification testing as of the writing of this report.

After the design of the payload was finalized, my attention was focussed on learning to use the SDRC finite element software implemented on the Cadre system. This familiarization took much longer than expected and was not completed until nearly the end of the summer. This made it impossible for me to include a finite element analysis in the results of this report. Work on this part of my project is continuing, however, so that results might be obtained by the SURF Seminar Day. These results will not be entirely accurate since the mass distribution in the payload is not entirely known. This must wait until the final experiment hardware is designed.

Conclusions

A usable structure for the second SSO payload has been designed. This structure can be easily modified to meet the NASA requirements if testing or finite element analysis shows that is is inadequate. More work needs to be done in the analysis area before any conclusions can be drawn as to the soundness of the design. Alternatively, testing can be carried out assuming a particular payload mass distribution. Work will continue in both of these areas.

STRUCTURAL ELEMENTS

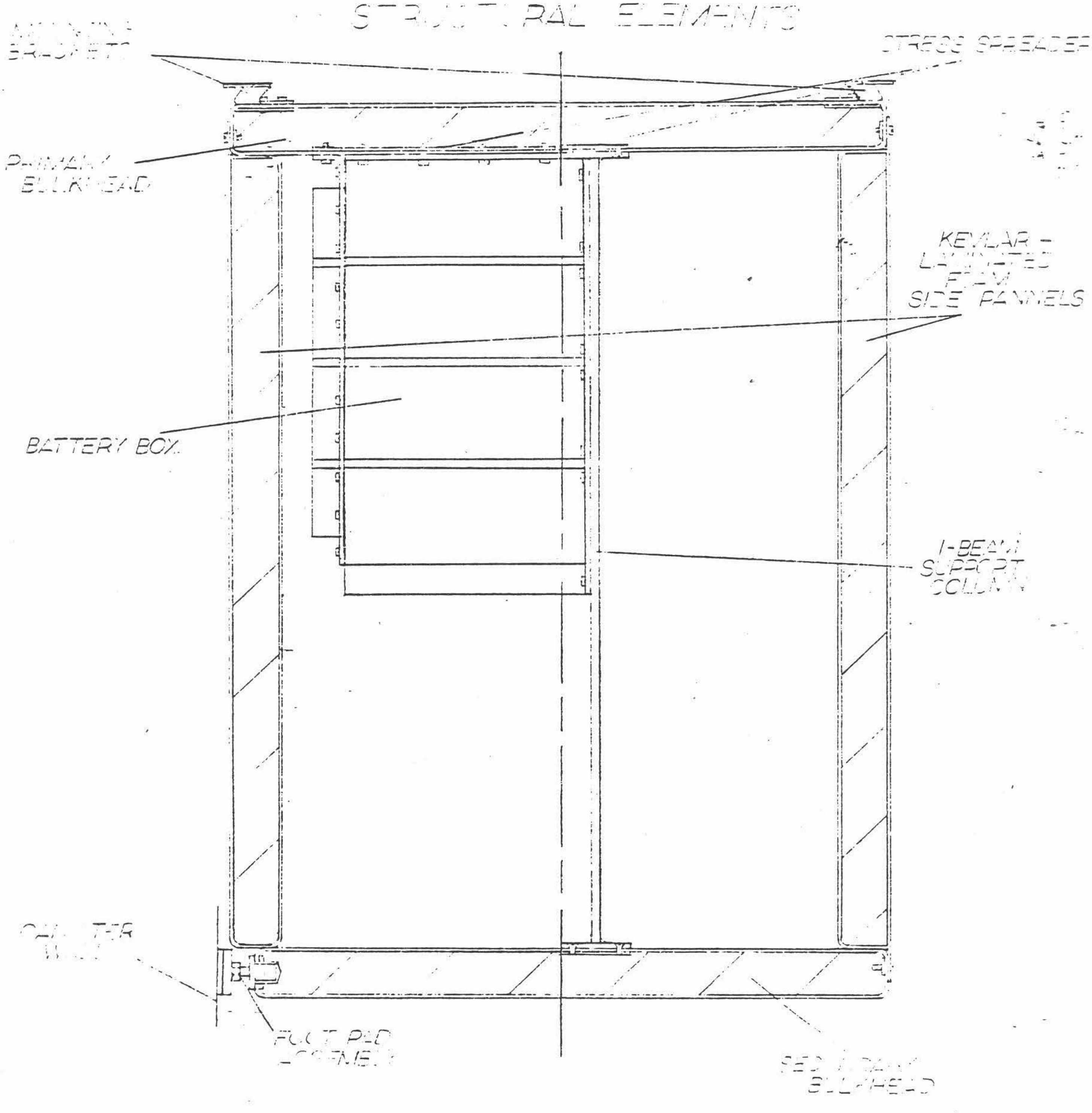

On Moufang Loops of Even Order pq^2*

Mark Purtill
R. M. Wilson (advisor)

Abstract. For p prime, we show all Non-Associative Moufang Loops (NAMLs) of order $2p^2$ are groups, and the uniqueness of the NAML of order $4p$.

1. Introduction

Moufang Loops are loops which satisfy the Moufang Law, $(xy)(zx) = (x(yz))x$. For background, see [1], whose notation we in general follow. In particular, note that the order of an element of a Moufang Loop divides the order of the loop [1.V.1.2]. We also need Moufang's Theorem, which states that if L is a Moufang Loop, then for any pair of elements of L generated a group, and that any three elements of L which associate (any one way) generate a group [1.VII.4].

Chein [2] showed that all Moufang Loops of orders p, p^2, p^3 and pq, (p, q prime) are groups, and in [5] the author showed Moufang Loops of orders pq^2 and pqr (p, q, r odd primes) where groups. The results of this paper mean that only the case $2pq$ remains to be considered for Moufang Loops of order the power of three primes.

We also require, from [3], Lemma 0, which states that if $H<L$ and $x \in L$ such that d is the smallest positive integer such that $x^d \in H$, then $|<H,x>| \geq |H| \cdot o(x)$. We refer to this as Chein's Lemma. From the same source, we need:

THEOREM 0: *If L is a NAML for which every minimal set of generators contains an element of order , then there exists G, a nonabelian group and x, an element of order* 2, *such that every element of L is expressible uniquely as gx^α, $g \in G$, $\alpha=0,1$ and*

$$(g_1 x^\delta)(g_2 x^\varepsilon) = (g_1^\nu g_2^\mu)^\nu x^{\delta+\varepsilon} \tag{1}$$

with $\nu=(-1)^\varepsilon$, $\mu=(-1)^{\varepsilon+\delta}$.

Conversely, given any nonabelian group G and an element x of order 2, *the multiplication above defines a NAML.*

---

*This research was supported by grants from the Richter Foundation and Caltech's Summer Undergraduate Research Fellowship Program.

We refer to this result as Chein's Theorem.

2. Results

LEMMA 1: *Let L be a NAML of order $2p^2$. There exists an element x of order 2 and an element y of order p in L.*

Proof: The existence of x follows from the fact that there are an even number of elements of any odd order (a fact easily proved by induction on the number of prime factors) and the uniqueness of 1. If there were no element of order p, then all elements would be of order a power of 2, hence we would have a 2-loop, so by [4] we would have $|L|$ a power of 2, # (contradiction). ■

In what follows, we let L be a NAML of order $2p^2$, and x, y be elements of L of orders 2 and p respectively.

LEMMA 2: *There does not exist an element z of $L-\langle y\rangle$ of order p.*

Proof: Suppose there is such a z. Clearly $\langle y,z\rangle\cong C_p\times C_p$. Let u be any element of order p. $o(xu)\in\{2,p,2p\}$. $o(xu)=2$ means $\langle x,u\rangle\cong D_p$. $o(xu)=2p$ means $|\langle xu,z\rangle|\geq 2p^2$, so by Moufang's Theorem, L is a group, #. If $o(xu)=p$, either $x\in\langle u\rangle$, #, or $\langle x\rangle\cap\langle xu\rangle=1$, whence $|\langle x,u\rangle|\geq 2p^2$, #. So for every u of order p, $\langle x,u\rangle\cong D_p$. Then:

$$(xy)z=((((xyx\cdot x)z)x)x=((xyx)(xzx))x=((x^2y^{-1})(x^2z^{-1})x)=x(y^{-1}z^{-1})^{-1}=x(yz). \tag{2}$$

(Moufang Loops satisfy $((ab)c)b=a(b(cb))$. [1.VII.3.1]) So by Moufang's Theorem, we have a group, #. ■

COROLLARY 3: *For all x of order 2, y of order p in L, $\langle x,y\rangle\cong D_p$ or C_{2p}.*

Proof: By the proof of Lemma 2, all we need to do is show that if $o(xy)=2p$, $\langle x,y\rangle\cong C_{2p}$. Suppose not, then there is a $k\neq 1$ such that $xyx=y^k$, as inner mappings preserve order and by Lemma 2. Then $y=x^2yx^2=xy^kx=(xyx)^k=u^{k^2}$. Then $k^2\equiv 1 \pmod p$, so $k\equiv -1 \pmod p$. But then $xyxy=x^2y^{-1}y=1$, so xy is of order 2, but it was assumed to be of order $2p$, #. ■

LEMMA 4: *There exists a minimal set of generators of L, $G=\{g_1g_2,\ldots,g_k\}$, such that $o(g_i)=2p$ for all i, $1\leq i\leq k$.*

Proof: The hypothesis of Chein's Theorem cannot hold, as there is no nonabelian group of order p^2. Hence there is a minimal generating set with elements of order p and $2p$ only. By Lemma 2, the square of any element of order $2p$ generates $\langle y\rangle$, as do all elements of order p. Hence we may dispense with any elements of order p, by minimality. ■

LEMMA 5: *For any g, h distinct elements of L of order $2p$, $\langle g,h\rangle\cong C_2\times C_{2p}$.*

Proof: If the subgroup is abelian, result follows, so assume nonabelian. Let $a=g^p$, $b=h^p$, elements of order 2. Look at $o(ab)$ to give us $\langle a,b\rangle$. If $o(ab)=2$, $\langle a,b\rangle\cong C_2\times C_2$. If $o(ab)=p$,

$\langle a,b\rangle \cong D_p$. But then $g^p h^p = y^k = g^{2k}$, $g^{2k-p} = h^p$, so g^{2k-p} is of order 2. But this implies $k \equiv 0$ (mod p), whence $g^p h^p = 1$, so $g = h$, #. If $o(ab) = 2p$, $\langle a,b\rangle \cong D_{2p}$. Suppose $g \in \langle a,b\rangle$. By the orders of elements, $\langle g\rangle = \langle ab\rangle$, so $g^p = a = (ab)^p$. In D_{2p}, this is impossible, #. So $g \notin \langle a,b\rangle$, and similarly $g^k \notin \langle a,b\rangle$ for all $k \in \{1,2,\dots,k\}$, and by Chein's Lemma,

$$|\langle g,h\rangle| \geq p \cdot |D_{2}p| = 4p^2 > 2p^p = |L|, \tag{3}$$

contradicting the fact that $\langle g,h\rangle \leq L$, #.

So $\langle a,b\rangle \cong C_2 \times C_2$. Also,

$$\langle a,y\rangle = \langle g\rangle \cong \langle b,y\rangle = \langle h\rangle \cong C_{2p}. \tag{4}$$

Hence a, b and y all commute with one another. Since $\langle a,b,y\rangle = \langle g,h\rangle$, $\langle g,h\rangle$ is abelian, #. So $\langle g,h\rangle \cong C_2 \times C_{2p}$. ■

LEMMA 6: *For any a in L, there is an element g of order $2p$ in L so that a is a power of g.*

Proof: Let C be the set of $a \in L$ satisfying the Lemma. Clearly $C \supset G$, the set of generators of Lemma 4. Take a, b in C. Then there are g, h in L so that a, b are powers of g, h respectively. But $\langle g,h\rangle \cong C_2 \times C_{2p}$, and examining this group, we find that there is an m in $\langle g,h\rangle$ so that ab is a power of m. Thus C is closed, so $C = L$, proving the lemma. ■

COROLLARY 7: *The elements of order* 2 *of L, along with* 1, *form a subloop of L.*

Proof: We need to show closure, and this follows from the above Lemma and the fact that in $C_2 \times C_{2p}$, the elements of order 2, along with 1, form a subgroup. ■

THEOREM 8: *There are no NAMLs of order $2p^2$.*

Proof: Suppose L is one such. Clearly, by Lemma 2, the elements of order p form a subloop, with 1. And by Cor. 7, the elements of order 2 form a subloop. Hence, the elements of order the (nonnegative) powers of any prime form a subloop of L. Cor. 1 of [4] states that this condition implies the L is the direct product of p-loops for some primes. The only primes can be 2 and p and we know that L is not such a loop. The only possible orders of such loops are 2, p, $2p$ and p^2, and we know all loops of these orders are groups [2]. Therefore, L is the direct product of groups and hence is a group. ■

Contrast Thm. 8 with

THEOREM 9: *There is a unique NAML of order $4p$ (to isomorphism).*

Proof: Let L be such a subloop. (One such exists by Chein's construction, with G equal to D_p, which is the unique nonabelian group of order $2p$. This loop is denoted $M(D_p,2)$.) As in Lemma 1, there exist x, y in L of order 2 and p respectively, and there is obviously only one subloop of order p. Hence, all elements of L not in $\langle y\rangle$ are of order 2 or of order $2p$.

There cannot be any element of order $2p$, z as there would be an element of order 2, x, not in $<z>$, and then $<x,z>$ would be L, #. Hence, any generating subset must include elements of order 2 and by Chein's Theorem we have $M(D_p,2)$. ∎

Remark: In the case of Moufang Loops of order $2pq$, if $p \mid q-1$, we get a NAML by Chein's construction. It is not obvious that this is unique, or that there are not NAMLs if $p \nmid q-1$.

3. Conclusions

For Moufang Loops of order the product of three primes, then, we have only groups, except for the orders $4p$ and $2pq$. In the $4p$ case, the unique loop is formed by Chein's construction. The case $2pq$ is unsolved except for the remark above.

4. Bibliography

[1] Bruck, R.H., *A Survey of Binary Systems*, (corrected third printing) Springer-Verlag, New York, 1971.

[2] Chein, Orin, "Moufang Loops of Small Order I," *Trans. Amer. Math. Soc.*, **188** (1974), 31-51.

[3] ——, "Moufang Loops of Small Order," *Memoirs Amer. Math. Soc.*, **13** (1978), number 197.

[4] Glauberman, George, "Nilpotence of Finite Moufang 2-Loops," *J. Algebra*, **8** (1968), 415-417.

[5] Purtill, Mark, "On Moufang Loops of Odd Order pq^2," (submitted for publication).

ISOLATION OF THE LOW DENSITY LIPOPROTEIN RECEPTOR GENE

Charles C. Reel
Barbara Wold

Division of Biology
California Institute of Technology
Pasadena, California 91125

ABSTRACT

A sensitive system is being developed to isolate and clone the bovine low density lipoprotein receptor gene, using antibody screening. The cloning vector, λgt11, has been refined by treatment with calf alkaline phosphatase (CAP) to increase the efficiency of cDNA incorporation. An *in vitro* packaging extract procedure has been modified to provide increased packaging yields. Experiments are continuing toward the end of isolating the LDL receptor gene.

INTRODUCTION

Cholesterol is required by mammals for biosynthesis of cell membranes. The source of cholesterol can be of extracellular origin or intracellular de novo synthesis. Extracellular cholesterol in the form of low density lipoprotein (LDL) is incorporated into the cell via receptor mediated endocytosis (1-3). The receptor, which mediates the uptake of LDL, acts in concert with the de novo pathway to maintain a cellular cholesterol homeostasis. The genes associated with the receptor structure and with enzymes of the de novo pathway have not been isolated.

The receptor structure, believed to be a single 1.6×10^5 dalton polypeptide (4), has dual functions for binding and localizing LDL in coated pits for internalization. Both binding and internalization must occur for successful transport of LDL. In the human genetic disorder Familial Hypercholesterolemia, mutations of the receptor system occur, resulting in deficient LDL endocytosis. Distinct defects in the receptor's binding and localization roles have been identified, providing a model for investigations of the LDL system.

The research this paper focuses on is the isolation of the receptor gene. The approach our lab has chosen involves DNA mediated transfer of wild type bovine receptor gene to bacteria (5,6). Bacteria expressing the wild type gene can be identified in culture. DNA transfer is effected by insertion of cloned sized fractions containing the receptor gene into an expression vector. The expression vector is used to infect bacteria in culture. Conformation of expression is provided by polyclonal antibody screening for the vector receptor protein in bacterial plaques (5,7).

MATERIALS AND METHODS

λgt11 (LAC5 NIN5 CI857 S100)

λgt11 was prepared, as described by Maniatis et al. (1982) (8), with modifications, from a temperature inducible lysogen (SS314) provided by R. Young (Stanford University). Overnight and inoculated cultures were 0.5% in glucose and grown at 30°C. Cultures were induced at $OD_{600} = .5$, for 15 min at 43°C. Bacteriophage pellets were run on CsCl equilibrium and step gradients to purify their DNA. Formamide dialysis was used to remove CsCl from this recovery. The resulting λ DNA was isopropanol precipitated and resuspended.

Vector Preparation

Concatemers were formed from λgt11 arms by ligation with T-4 ligase for 30 min at 25°C. The ligase was killed at 70°C and the DNA was Eco RI cut at 37°C for 30 min. The DNA was organically extracted in four stages (phenol, 50/50 phenol/sevag, sevag, ether) and precipitated with ethanol. A pellet was recovered from centrifugation, washed and resuspended in low TE.

CAP Assay

Five 10 μg aliquots of vector DNA were prepared with 5×10^{-3} (1X), 1×10^{-2} (2X), 2.5×10^{-2} (5X), 5×10^{-2} (10X) units of calf alkaline phosphatase (CAP) 3 units/ml). The fifth sample, a control, had no enzyme added. The reactions were incubated at 37°C for 30 min and then killed at 68°C for 5 min. λ DNA was extracted in three stages (50/50 phenol/sevag, sevag, ether) and precipitated with ethanol. The pellets were recovered from centrifugation, washed and resuspended in low TE. The vector preparations were assayed on plate titers as described below.

pBR322 Insert Preparation

pBR322 was Eco RI cut, extracted and resuspended in low TE.

Insert-Ligation Assay

Aliquots of λ DNA reacted with 2X level of CAP and the non-enzyme treated control were ligated with pBR322 inserts in molar ratios (inserts:λ arms) of 4:1, 2:1, 1:1, 1:2, 1:6. A control without insert was also prepared for each vector. Reactions were incubated for 8 hr at 4°C with T-4 ligase. Preparations were packaged in vitro and plate titered as described below.

In Vitro Packaging Extract Preparation

MMS A345 (E. coli lysogen) was provided by F. Stahl (U. of Oregon). A modified version of Stahl's protocol was used in preparing extracts. MMS A345 was streaked onto Luria plates and incubated overnight at 30°C and 42°C. A colony from the 30°C plate was used to inoculate Luria broth and grown at 34°C overnight. A 34°C culture from the overnight was grown to OD_{550} = .6, induced at 44°C for 15 min and incubated at 37°C for 90 min. The preparations were cooled in ice and bacterial pellets collected by centrifugation. Pellets were washed, centrifuged and collected. Aliquots of resuspended bacteria in CH buffer were frozen in liquid nitrogen for storage.

In Vitro Packaging

Vector-insert recombinant DNA was packaged as described by Maniatis et al. (10) with the modification of incubations carried out at 25°C instead of 37°C.

Plating Bacteria Preparation

LE392 was grown overnight in Luria broth (.2% maltose) at 37°C.

Plate Titers

In vitro packaging preparations were titered to yield ~ 10^4 λ/plate. λ dilutions were pre-adsorbed with LE392 aliquots for 30 min at 25°C. The pre-adsorbed bacteria were suspended in Luria top agar, plated and incubated for 8-12 hr at 37°C.

RESULTS

The λgt11 preparation yielded 45 µg of phage DNA. (CsCl buoyant density = 1.46) UV spectroscopy revealed a pure product, free of contaminating proteins (OD 260:280 = 1.8).

CAP Assay

Results of plate titers for CAP-ing efficiency, using pBR322 test inserts, revealed maximal insertion (> 95%) at the 2X CAP level with diminishing insert incorporation at 1X, 5X and 10X levels. The non CAP-ed (0X) control vector showed less then 1% insert incorporation, resulting from self-ligation of λ ends (see Discussion).

Insert Ligation Assay

Analysis of plate titers for insert:arm ratios demonstrated highest levels of insert incorporation with molar excesses of pBR322. Greater than 95% of packaged vector contained single or multiple inserts for 4:1, 2:1 and 1:1 ratios (insert:arm). 1:2 and 1:6 ratios resulted in < 10% and < 3% vectors with inserts respectively.

Packaging Extracts--In Vitro Packaging

MMS A345 derived extracts were found to package between 0.1 and 1% of λ chromosomes present in vitro. 50 µl of extract packaged up to 4 µg of exogenous λ DNA.

FIGURE 1.

λgt11 (-pBR322 Insert) Plate Titer

10^{-3} μg (1.9 x 10^7 Phage) λgt11 Plated on LE392

CAP Level	2X					0X	
Insert:Arm Ratio	4:1	2:1	1:1	1:2	1:6	4:1	1:1
Plaques (#)							
w/Insert(s)	~5×10^3	~5×10^3	~3×10^3	~10^2	31	11	1
%Total	~97%	~98%	~95%	<10%	<3%	<1%	<1%
No Insert	189	~10^2	166	~10^3	~10^3	~10^3	~10^3
% Total	~3%	~2%	~5%	>90%	>97%	>99%	>99%
Totals	~5×10^3	~5×10^3	~3×10^3	~10^3	~10^3	~10^3	~10^3

Note: X-GAL overlays were used to distinguish insert from non-insert containing plaques.

DISCUSSION

Low yields of λgt11 are believed to reflect deficiencies in the host strain (SS314) related to this E. coli's lysogenic characteristics. A pure product, however, was recovered in sufficient quantities to construct a cDNA library.

CAP effects the removal of terminal 5' phosphate from double stranded DNA, thus inhibiting the self-ligation of linear λ phage. CAP-ing the expression vector clearly is shown to increase the proportion containing insert, by commensurately decreasing λ self-ligation. The decrease in efficiency noted with higher levels of CAP may be attributable to the action of an exonuclease contaminant present in this enzyme.

Ideally, the insert tc arm ratio of a recombinant λ phage preparation should reflect a 1:2 relationship (insert:arm). However, in practice factors effecting insert cohesive ends, the occurrence of multiple inserts and vector self-ligation act to require relative molar excess of insert in a ligation reaction. The results presented here demonstrate the saturating effect on insert incorporation with insert excesses (i.e., 4:1, 2:1, and 1:1 ratios), and may represent recombinants with a high percent of multiple inserts. The 1:2 (insert:arm) ratio represents a moderate level of single inserts, frequently encountered (see Fig. 1).

Package extracts provided an *in vitro* efficiency of high order. Representing between 10^7 and 10^8 plaque forming units per microgram of λ DNA plated.

CONCLUSIONS

Early work by Brown and Goldstein (1-4) led to the isolation of the LDL receptor protein. From studies of the receptor on the cellular level much has been learned about the regulation of cholesterol homeostasis. In order to arrive at a complete understanding of this modulation, our lab is actively studying the molecular genetics of the cholesterol system. A key goal in this work is the isolation of the LDL receptor gene.

To date progress has been made along this line in the experiments reported here. An expression vector, λgt11, has been produced, refined and assayed for its efficiency in incorporating a receptor gene-carrying cDNA library. *In vitro* packaging extracts have been prepared which incorporate high levels of recombinant DNA. The cloning system as a whole shows promising efficiency. It remains, upon the completion of the cDNA library, to screen for the LDL receptor gene with this system.

ABBREVIATIONS

kb - Kilobase
LDL - Low Density Lipoprotein
CAP - Calf Alkaline Phosphatase
λgt11 - Lambda Bacteriophage (LAC5 NIN5 CI857 S100)
pBR322 - 4.3 kb Plasmid (*E. coli*)
MMS A345 - *E. coli* Lysogen C Su$^-$ (λ cos2 RED$_3$ CI857 SA_)
LE392 - *E. coli* Strain [F$^-$, HSD R514 (R$^-$ M$^-$)]
Low TE - 10 mM Tris, pH 7.5, 1 mM EDTA

REFERENCES

1. Brown, M. and Goldstein, J. (1979). Proc. Natl. Acad. Sci. USA **76**, 3330-3337.
2. Brown, N. et al. (1981). Science **212**, 628.
3. Goldstein, J. et al. (1982). CIBA Symposium **92**, 77-95.
4. Schneider, W. et al. (1982). J. Biol. Chem. **257**, 2664-2673.
5. Young, R. and Davis, R. (1983). Proc. Natl. Acad. Sci. USA **80**, 1194-1198.
6. Okayama, H. and Berg, P. (1983). Mol. Cell. Biol. 3, 280-289.
7. Anderson, R. et al. (1982). J. Cell. Biol. **93**, 523-531.
8. Maniatis, T. et al. (1982). CSH Molecular Cloning Manual, p. 78.
9. Feiss, M. et al. (1983). Proc. Natl. Acad. Sci. USA **80**, 955-959.
10. Maniatis, T. et al. (1982). CSH Molecular Cloning Manual, p. 262.

SEDIMENTATION IN SHEARED SUSPENSIONS

THOMAS W. REIMERS

SPONSOR: PROF. ERIC HERBOLZHEIMER

ABSTRACT: The SURF research consisted of measuring the sedimentation velocity of quiescent and sheared suspensions as a function of concentration and shear rate. The concentration varied from 0 to 0.25; and the dimensionless shear from 0 to 11. The sedimentation velocity increased with shear at concentrations up to 0.14, in agreement with theory.

INTRODUCTION: The velocity of a particle settling in an infinite fluid under low Reynolds number conditions is given by Stoke's law:

$$U_0 = \frac{2}{9} a^2 (\rho - \rho_s) g/\mu$$

where U_0 is the Stoke's velocity, a is the particle radius, ρ is the fluid density, ρ_s is the particle density, g is the gravitational constant, and μ is the fluid viscosity. When there are many particles distributed throughout the fluid, the settling velocity decreases as a result of multiparticle hydrodynamic interactions. Recently it has been proposed that in dilute quiescent (non-sheared) suspensions a microstructure develops in which the particles become in some sense well-spaced. In this case, the leading order correction to the settling velocity is given by:

$$u/U_0 = 1 - bc^{1/3}$$

where u is the settling velocity at a given concentration, c is the volume fraction of particles and b is some constant. However, when the suspension is sheared, the ordering of the particles becomes random, and the theory predicts the leading order correction term should be O(c). Professor Herbolzheimer has shown that for pure-straining flow (a flow which unfortunately cannot be realized in practise) the settling velocity is given by:

$$u/u_0 = 1 - 4.52c$$

The primary goal of the research was to provide experimental results to support the proposed theory.

The settling velocity at a given concentration is also a function of the shear rate. As the magnitude of the shear is increased, the settling velocity increases to an assymptotic limit. This limit is taken to be the "sheared velocity" previously mentioned for a particular concentration. The proposed dimensionless shear is:

$$\overline{\tau}_* = 8.01 \frac{\Omega a}{u_0}$$

To verify that $\overline{\tau}_*$ is indeed the correct dimensionless group, u_0 will be varied by changing the particle radius and the fluid viscosity. The plots of dimensionless settling velocity (u/u_0) versus dimensionless shear should collapse upon each other for different u_0 at a given concentration.

EXPERIMENTAL: To create a simple shear flow, a couette device of two vertical concentric cylinders with a 1/4" gap and a 4.975" inner radius was employed. The inner cylinder of anodized aluminum was kept stationary, while the outer cylinder of pyrex was rotated to reduce radial concentration gradients caused by centrifugal forces. A naturally averaged sedimentation velocity was measured by aligning the crosshairs of a cathetometer on the clear fluid-suspension interface. To account for temperature variations between experiments, all velocities were multiplied by a ratio of the oil viscosities at a standard temperature to that at the temperature of the individual experiment.

The fluid viscosity was measured with a Cannon-Fenske routine viscometer. The fluid density was measured with a hydrometer; and the particle density was obtained by noting volume and mass change of particles in water. The fluid was UCON lubricating oil HB-500; and the particles were spherical glass beads of 50-55 micron size. As the temperature of the couette experiments could not be controlled closely, the properties were measured over a wide temperature range (10-25 °C). A thermocouple was used to measure the temperature of the suspension before and after velocity measurements were taken. To counter thermocouple readout drift, the probe was continuously calibrated by immersing it in oil of a known temperature. The readout slope was fairly linear in the temperature range of the experiments; temperature values obtained were accurate to 0.1 °C.

Previous experiments did not produce outstanding results primarily because particle size was nonuniform. A microscope revealed that many of the particles were of significantly smaller diameter than the mean. Since the settling velocity is proportional to the radius squared, these small particles settle much slower than the bulk of the suspension. As a result, the interface spreads out and becomes indistinct making measurement of its position extremely difficult.

After several experiments, it was found that by entering the particles into a vertical fluidized bed the smaller, lighter particles would be carried out the top of the system in preference to the larger, heavier ones. The device constructed to filter the particles was a 40" by 1.1 cm o.d. pyrex tube with an entrance port attached 20" from the top of the tube. A vacuum flask was attached at the bottom to collect the filtered particles and to provide a mechanism for connected compressed air to create the fluidized bed. Approximately 20% of the particles were removed in this manner; a microscope revealed the collected particles were indeed of a much more uniform size than the nonfiltered particles. Empirically, at a concentration of 0.08, the interface achieved was noticably sharper using the filtered particles.

RESULTS: Figure 1 shows dimensionless settling velocity versus concentration; the shear values are on the asymptotic limit.

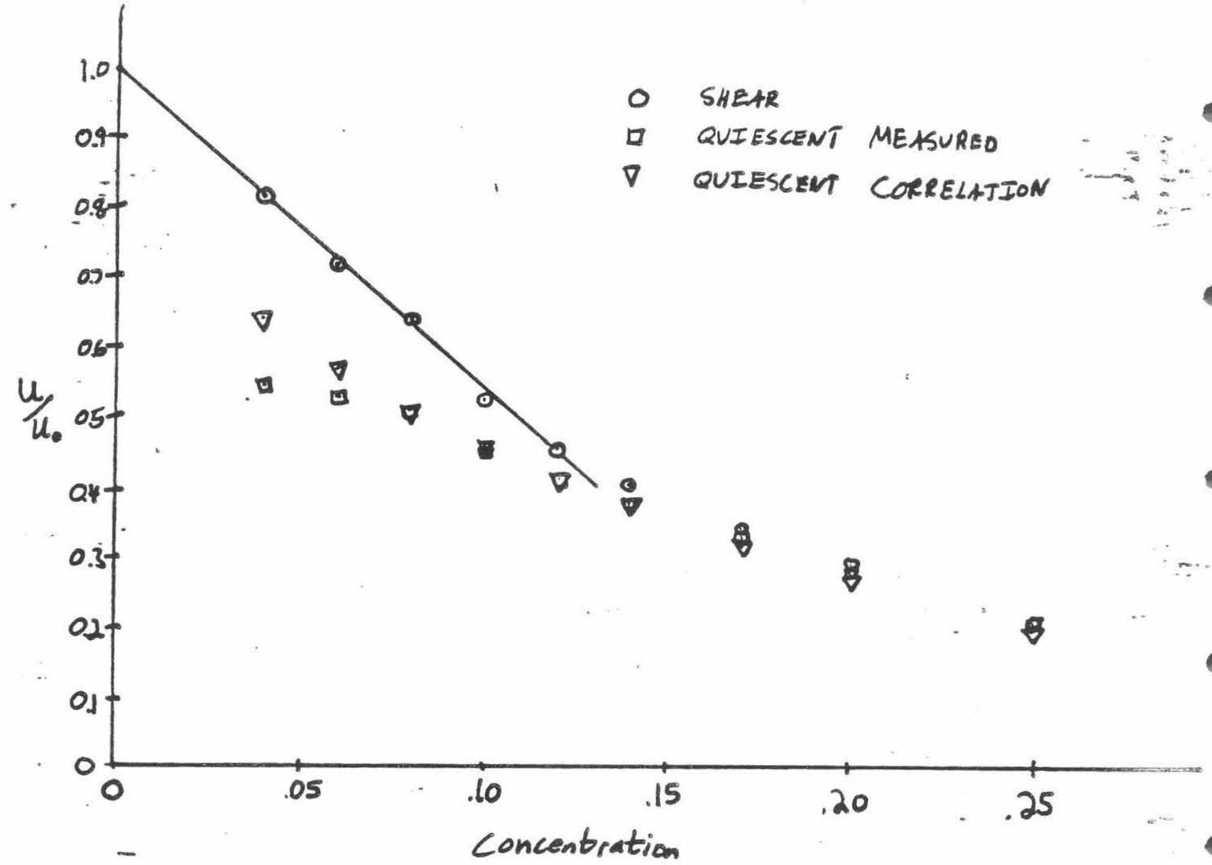

The line drawn is the theoretical curve for pure-straining motion. The shear values fit very well at concentrations to 0.12. Beyond that concentration, the quiescent and shear curves intersect, and the settling velocities are essentially the same for both. The only points significantly deviating from theoretical values are the quiescent settling velocities at 0.04 and 0.06 concentration. These deviations can probably be attributed to the difficulty obtaining accurate measurements at low concentrations. Extending a least squares fit of the points in the linear range to zero concentration should give the Stoke's velocity. Knowing the rheological properties, the Stoke's velocity calculated in this manner corresponds to a particle radius of 55.0 microns.

Among other effects noticed was the sharpening of the interface upon shear at concentrations above 0.10. Any particles which settle above the interface will be in a suspension of lower concentration. These particles, especially in shear flow, are in a regime where ther settling velocity is much greater than in the bulk causing the interface to sharpen. Experiments at a different Stoke's velocity have yet to be done.

CONCLUSION: The results indicate that the proposed theory to describe the sedimentation of sheared suspensions is valid. As predicted, the settling velocity did increase upon shear at low concentrations. Interestingly, the theory for pure-straining motion is quantitatively accurate for simple shear.

REFERENCE: "Sedimentatipn in Quiescent and Sheared Suspensions", Edward D. Lynch, Master's thesis, Caltech, 1981.

A determination of the Solar Period in the Calcium K-line and the Sun as a star.

Aaron J. Roodman

Sponsored by Dr. Harold Zirin

Abstract: Our initial goal was to duplicate studies of stellar rotation periods in the Calcium K-line using the sun. We took 93 full disk digitized solar images in the K-line spread out over 140 days, isolated the intensity excess due to plage regions- and did a power spectrum analysis of the excess. Preliminary results point to a period of between 31 and 37 days, significantly greater than the well known value of 27 days.

1. Introduction

A substantial amouunt of work has been done on the subject of solar rotation and activity cycles. Techniques to determine the solar period fall into two categories : 1) measuring the movement of a discernable object, a sunspot perhaps, on the disk, or 2) analyzing a time series of some solar flux for periodicity. The latter is a technique that has become popular recently- and has spawned research efforts towards finding the rotation periods of stars as well. Vaughan et al. have found the periods of stars by looking at the variations of the Calcium K-line in spectra.

This is a logical choice as the bright plage regions that appear in active regions, and frequently surround sunspots are easily seen in the K-line. Here, then, is the point at which we begin: to see if a similar study can be done with the sun.

2. Discussion

For my analysis I used full disk images that were taken with a simple fixed camera and filter at the Big Bear Solar Observatory from September 1982 to March 1983. These images were subsequently digitized into frames of 512 by 481 pixels. A contour plot of one of these images is shown in Fig. 1). One should note the visibility of a number of active regions, and the considerable limb-darkening that occurs.

The first task at hand was to remove the background due to limb- darkening, so that only the plage regions, or the Calcium line excess remained. This was done by dividing each image into 40 radial strips, themselves separated into 110 bins. I fitted 20 of the radial strips to 6th order polynomials (using values from every 4th bin) as a function of radius. Then I took the coefficients of these 20 polynomials and fit those each as a 6th order polynomial as a function of theta. This gives an equation of form: Intensity= F(theta)*G(radius)
for each image.

Finally this function is calculated for all pixels and the result subtracted from the original value- (an example of a subtracted image is shown in Fig. 2). Notice that the active regions remain, although there is an amount of low level noise that persists. Therefore to sum up the intensities- and avoid including the noise- I only sum those values that exceed a cutoff. The cutoff varies linearly from 15% of the images maximum value- at the sun center ,to 30% at the sun's edge. This type of cutoff is used to help compensate for the greater occurance of noise around the sun's edge.

3. Results

Unfortunately this summer I was only to analyze 2/3 of the data I had. The values of the integrated Ca excess intensity are shown in Fig. 3a; also in Fig. 3b are the area's occupied by the plage regions for the same period. Now to determine what frequencies are present in this time series I did a power spectrum analysis as described in "Digital Time Series Analysis" by Otnes et al, p270-1. The results of this analysis are shown in Fig. 4a for the integrated intensity, and Fig. 4b for the area excess.

Note that in neither of these spectra do we see a clear 27 day peak that might represent the solar rotation period as it is commonly accepted. Instead both spectra have peaks at 15.5 and 39 days. So possibly the smaller peak is a half-period peak, which would point to a period around 31 days- a fairly believable result, more so than a period of 39 days. So the question for now is just what do all these numbers mean, which peaks are real and which are artifacts.

One source of the problem is evident. My sample is just not large enough to avoid a ringing effect that produces peaks at frequencies at integral fractions of the entire time series. As a kind of control I did the power spectrum analysis on 10cm flux data for two different lenghts of time. In Fig. 5a we see the power spectrum for 3yrs worth of data, while in Fig 5b is a spectra for 4 months of data- about the same length of time I used for my Ca K-line data. The first spectra shows a clear rotation period of 27 days, while the second instead displays a small peak at about 15 days and a larger one at 40 days. This seems to indicate that a sample of about 120 days is just not adequate in finding a 27 day periodicity, at least with this statistical technique.

Also note the similarity in spectra between the 10cm flux and my Ca excess- which may mean that in both cases we are seeing both the 27 period and a ringing effect due to the small sample size. This similarity gives me some justification for being optimistic in finding a believable period from the data.

4. Conclusions

At this point my project is far from complete, as I still have several options to proceed with. I will definitely analyze my remaining data in the hope that with a longer time series any period that exists will appear in a power spectrum analysis. Also I have not really had a chance to examine my images in detail to check for problems in the summing of the values. In addition other statistical techniques exist, such as cross-correlation, which might prove fruitful in this instance.

But for now I believe we have shown the following :(1) that there is not an easily identifiable period present in the sun's Calcium K-line excess; (2) that with statistical analysis it is possible to determine a rotation period; and (3) that we can indeed fit the sun's limb darkening to a variable separable equation. The first of these is significant in that in Vaughan et al. many stars did exhibit an easily seen period. This is not to imply that I will not be able to pinpoint the solar period; only that I have not been able to do so as of yet. But I am optimistic that I will be able to get a reasonable, if not consistent result.

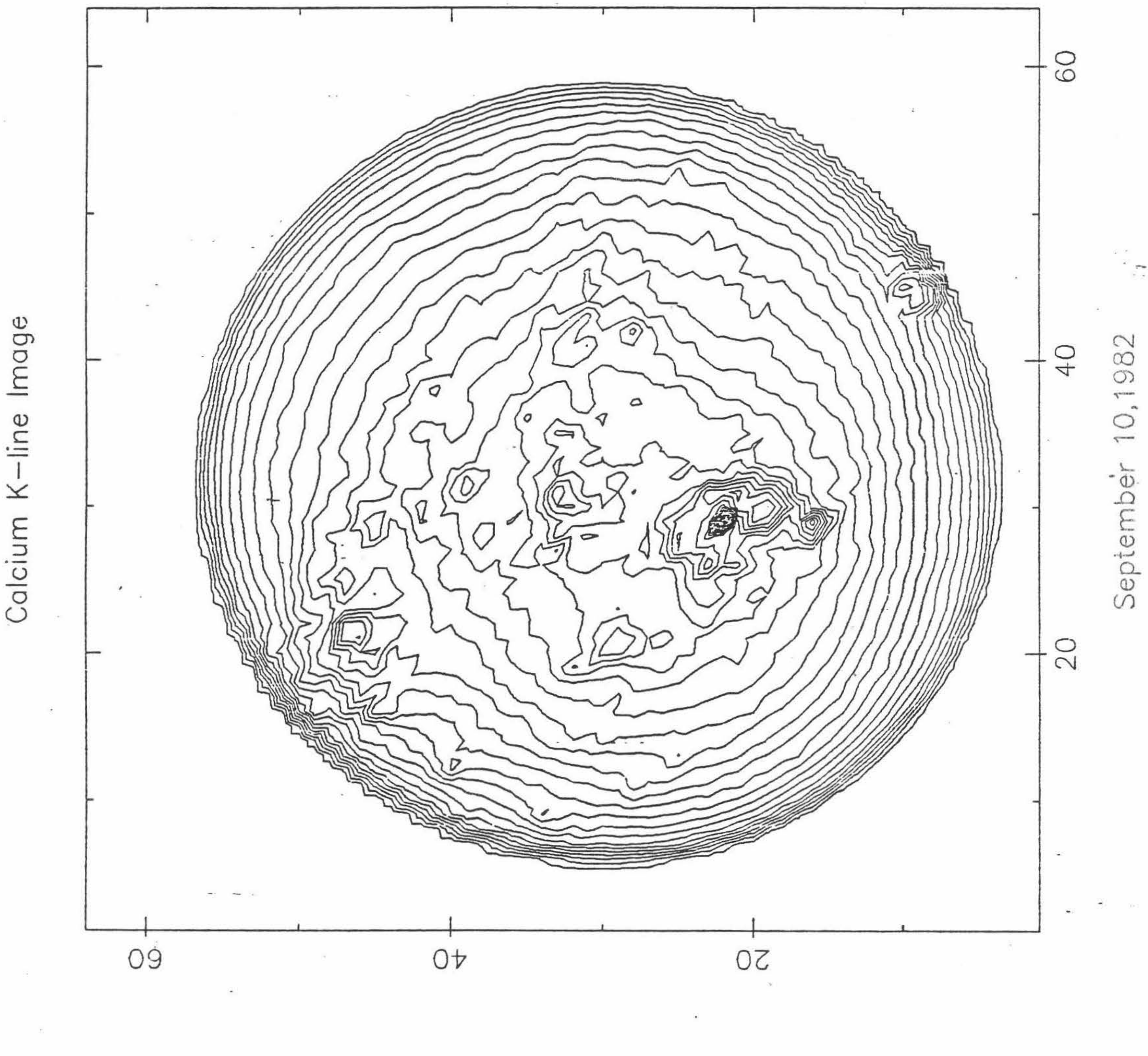

Fig 1

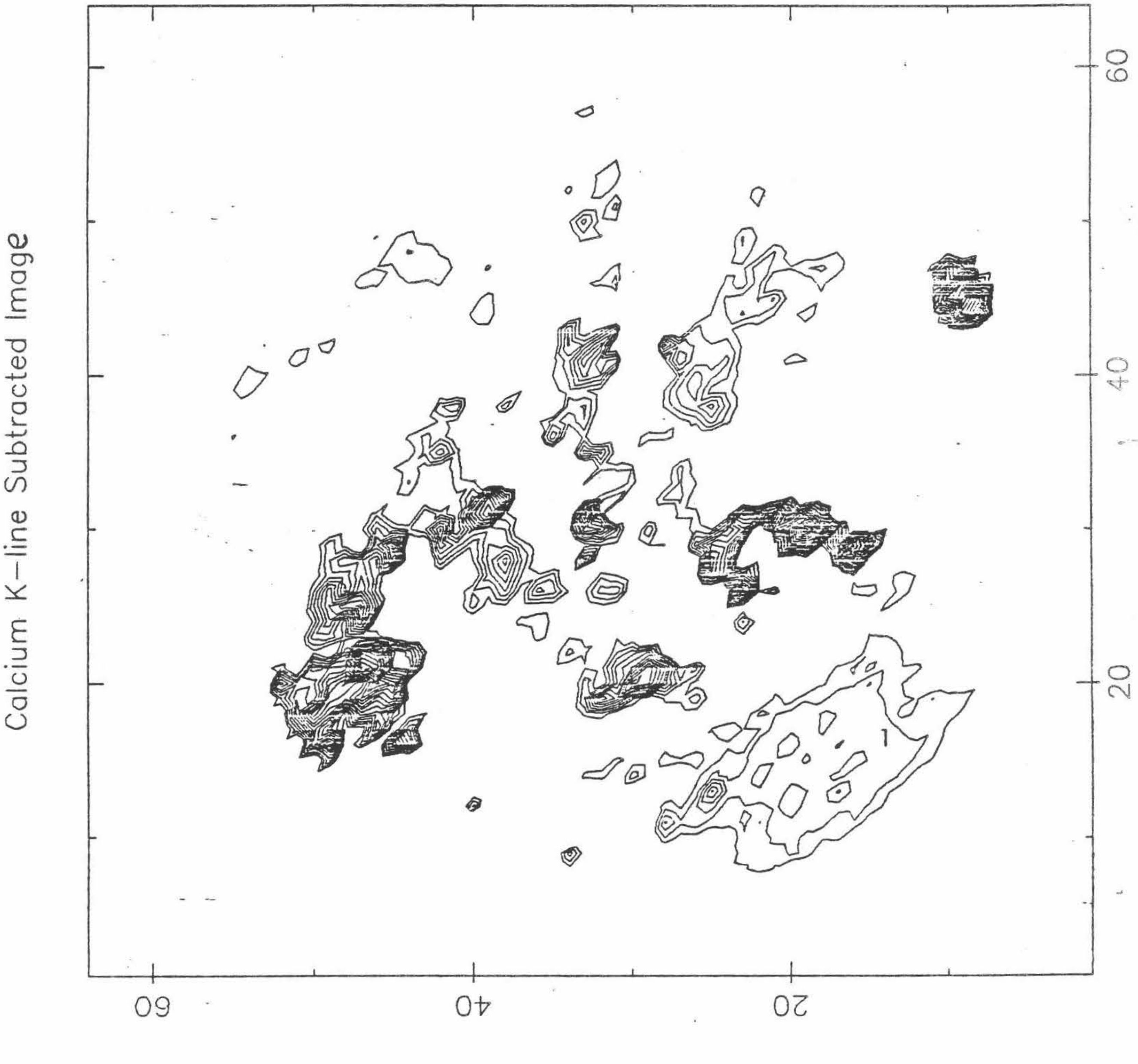

Fig 2

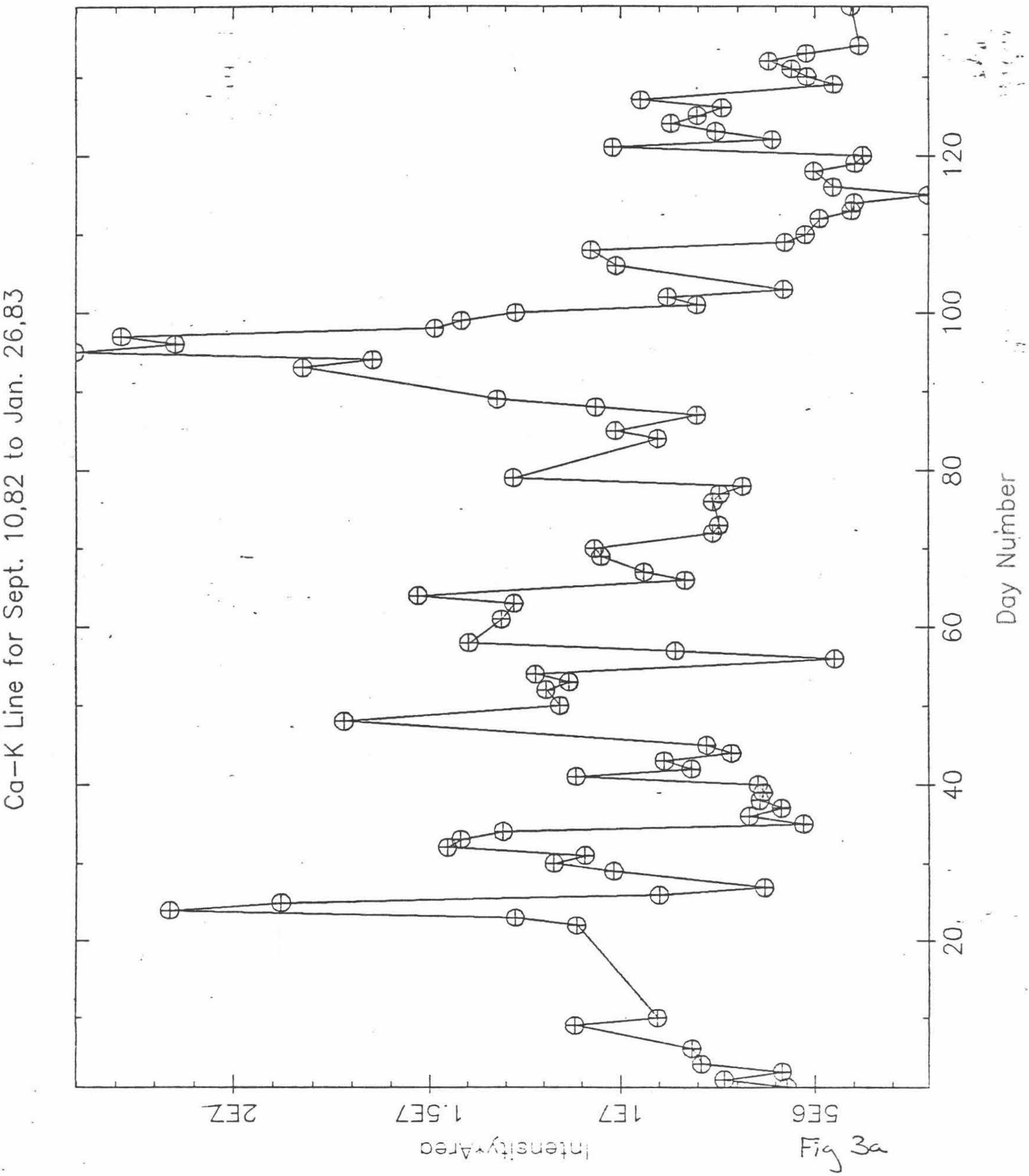
Ca–K Line for Sept. 10,82 to Jan. 26,83
Intensity*Area
2E7
1.5E7
1E7
5E6
Day Number
20
40
60
80
100
120

Fig 3a

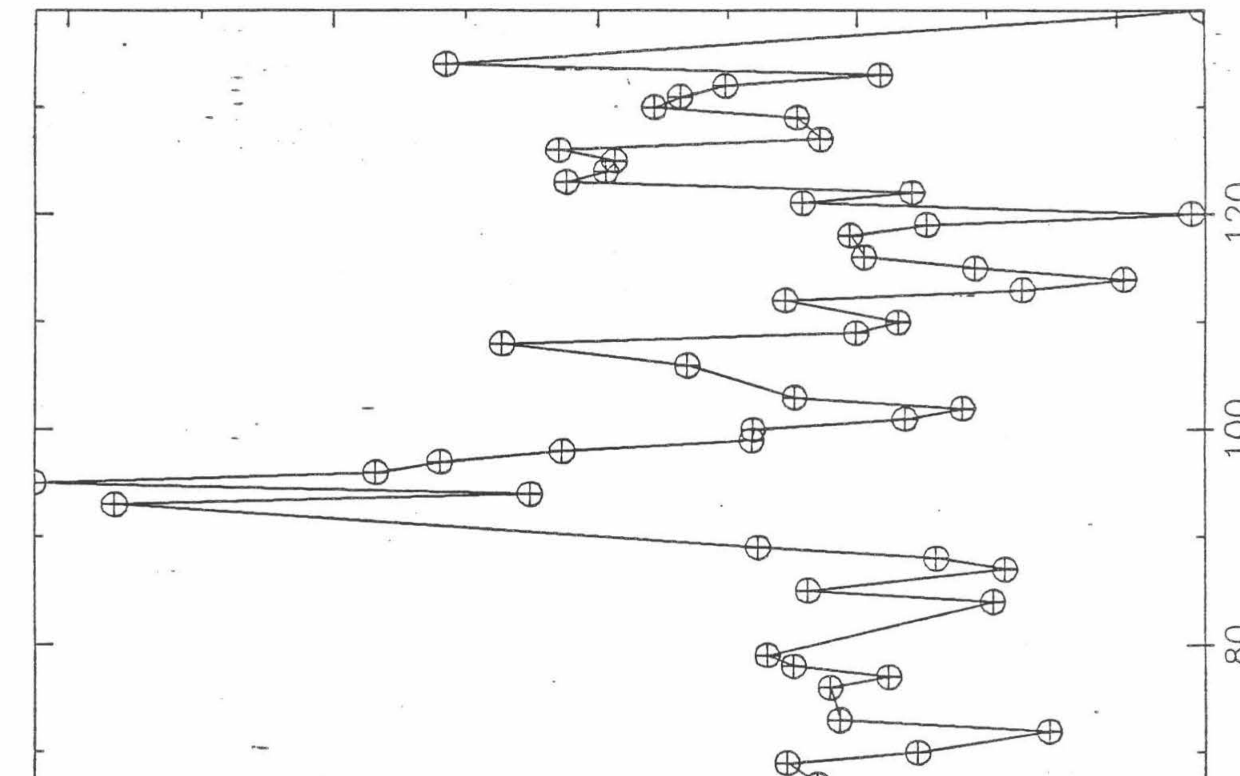

Ca-K Line for Sept. 10,82 to Jan. 26,83

Fig 3b

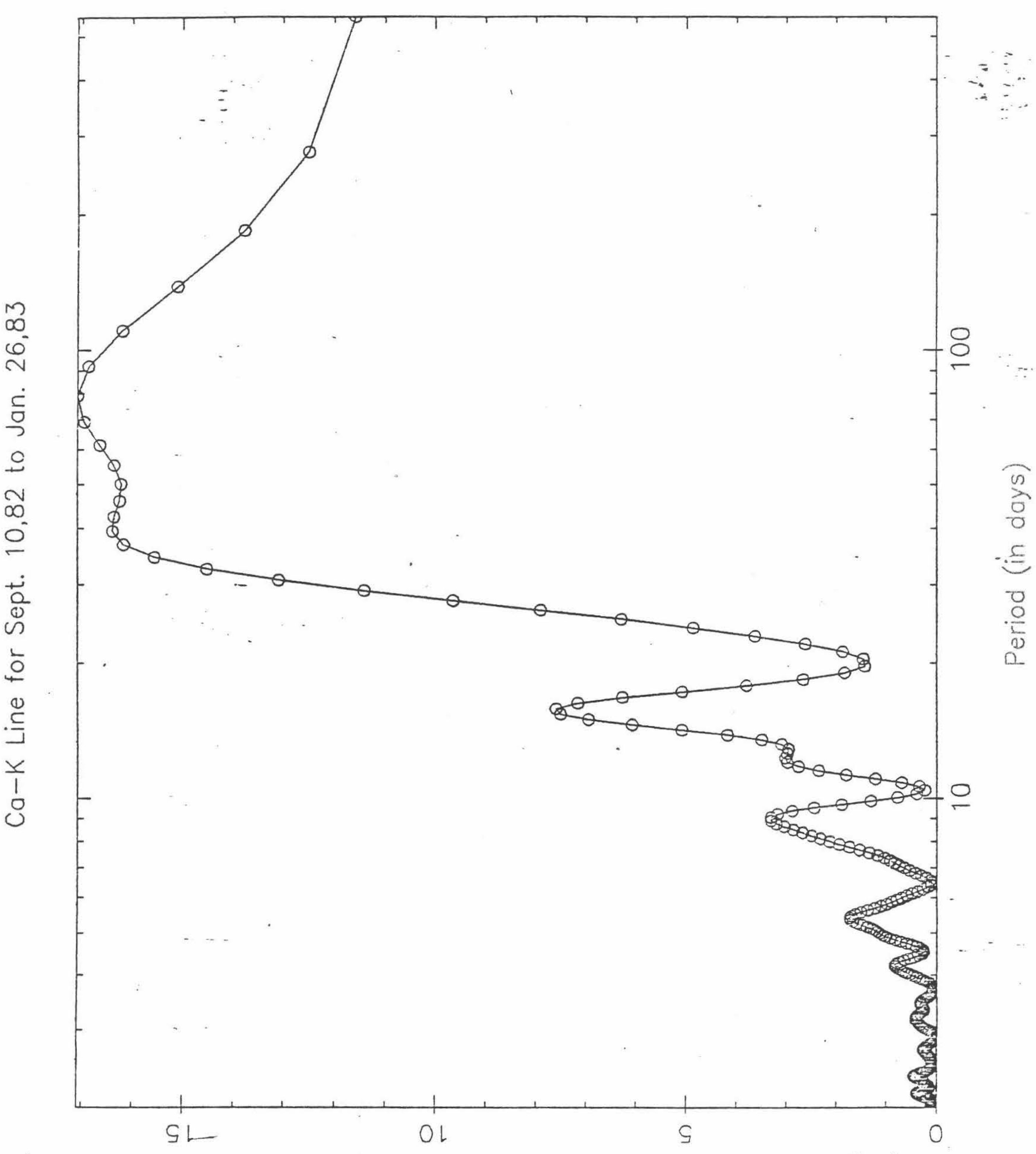
Ca-K Line for Sept. 10,82 to Jan. 26,83
Power Spectrum Density
0
5
10
15
Period (in days)
10
100

Fig 4a

Spectral Analysis of Plage Area from 10/9/82 to 26/1/83

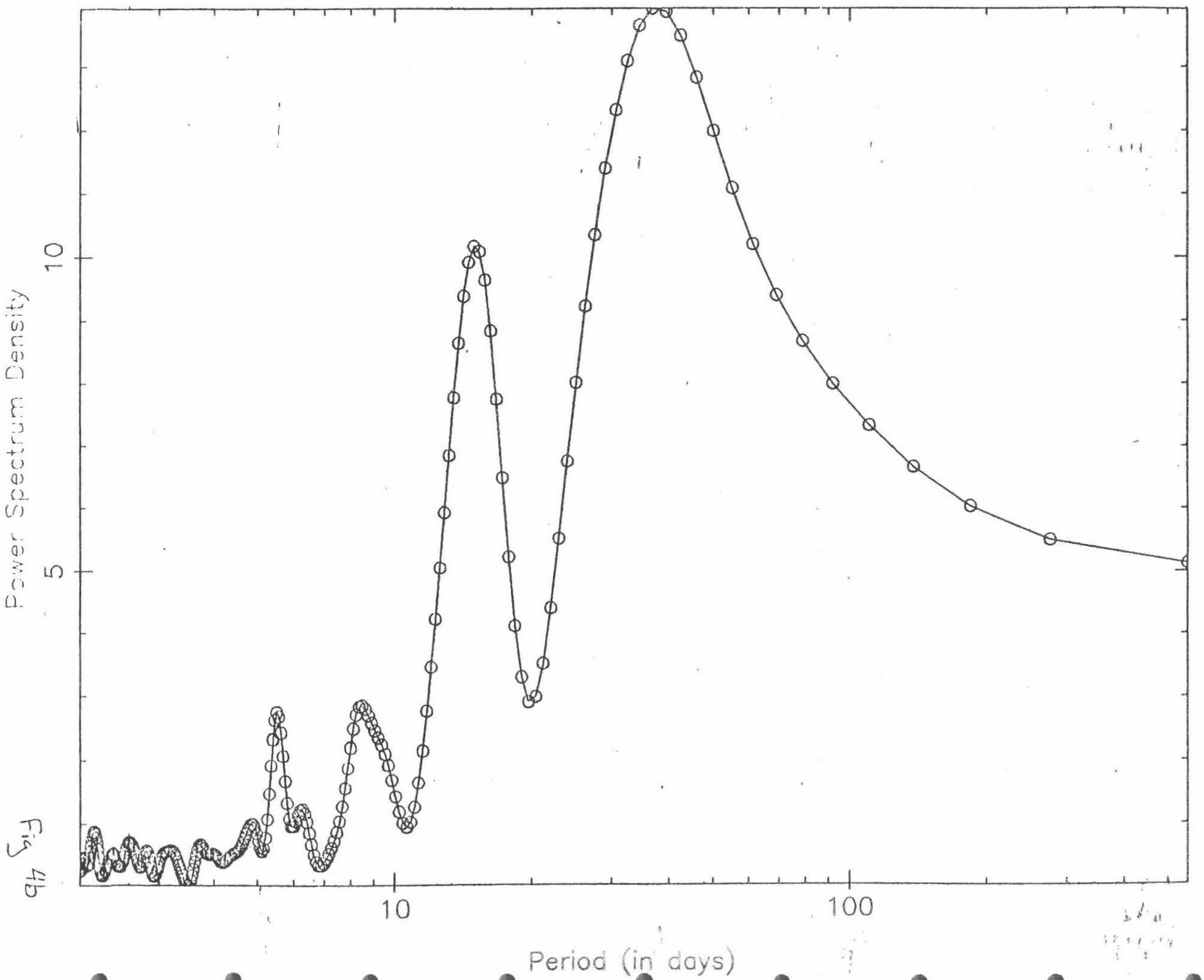

Fig 4b

10CM Flux (1980–82)

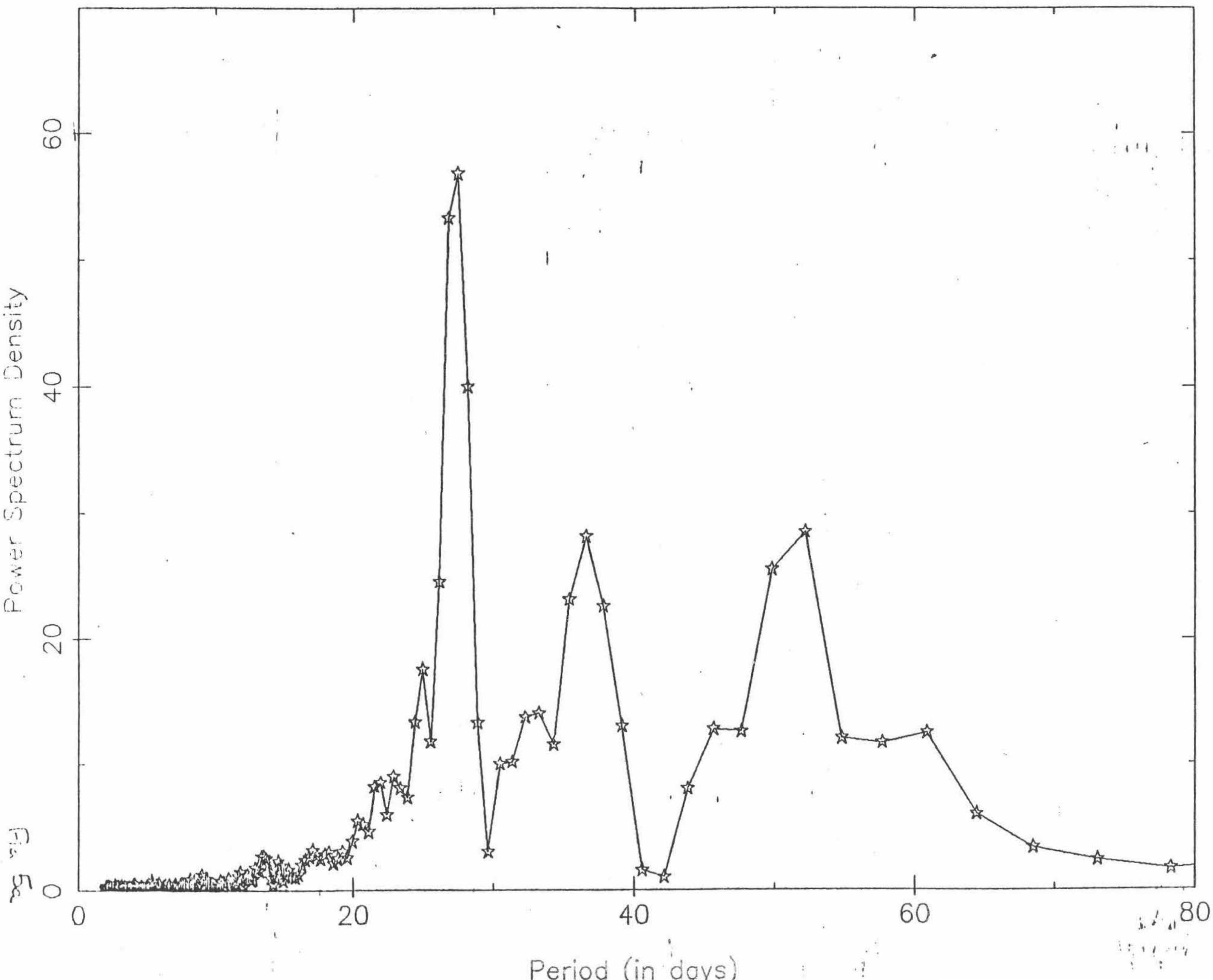

Fig 5a

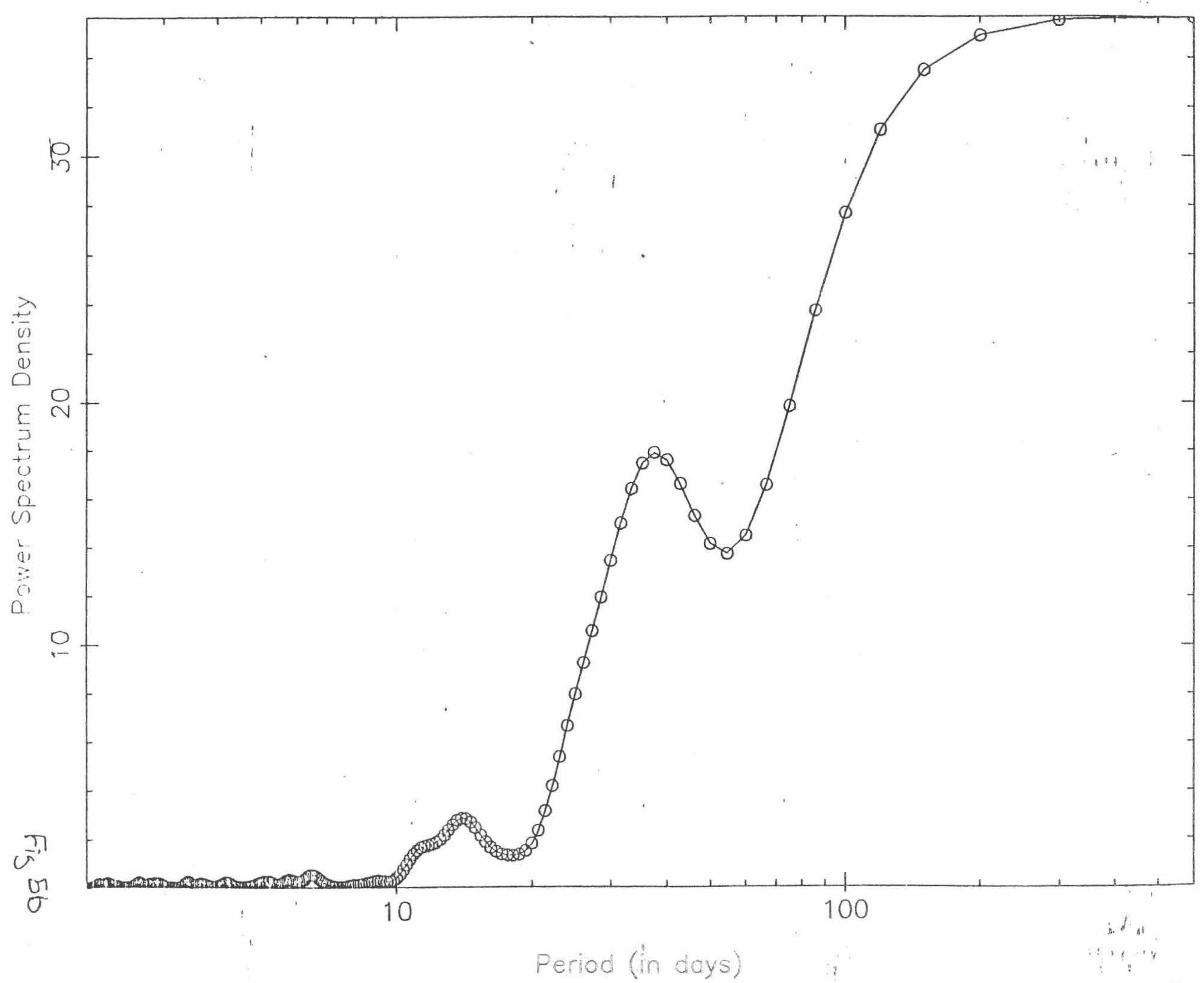

Spectral Analysis of the 10.7 cm Line

Fig 5b

ISOLATING THE GENE FOR A DROSOPHILA TRANSCRIPTION FACTOR

Author: Doug Ruden

Faculty Sponsor: Carl Parker

Abstract: A Heat-Shock specific transcription Factor (HSF) has been purified through a series of column chromatography steps, gel purified from a polyacrylamide gel and injected into a rabbit for antibody production. The antibody will eventually be used to screen a Drosophila λgt-11 expression library in order to identify the gene for this protein.

Introduction: My advisor, Carl Parker, is studying the regulation of transcription of eukaryotic structural genes. He has identified a series of factors which enable Drosophila RNA polymerase II to initiate transcription *in vitro*. One factor, the Heat-Shock specific transcription Factor (HSF), is required for the transcription of Drosophila heat-shock genes. Carl found that this HSF binds to DNA in a region adjacent to the startpoint of transcription of Drosophila heat-shock genes. (see Figure) Evidently, in order for RNA polymerase II to transcribe heat-shock genes, this factor must first bind to the recognition site.

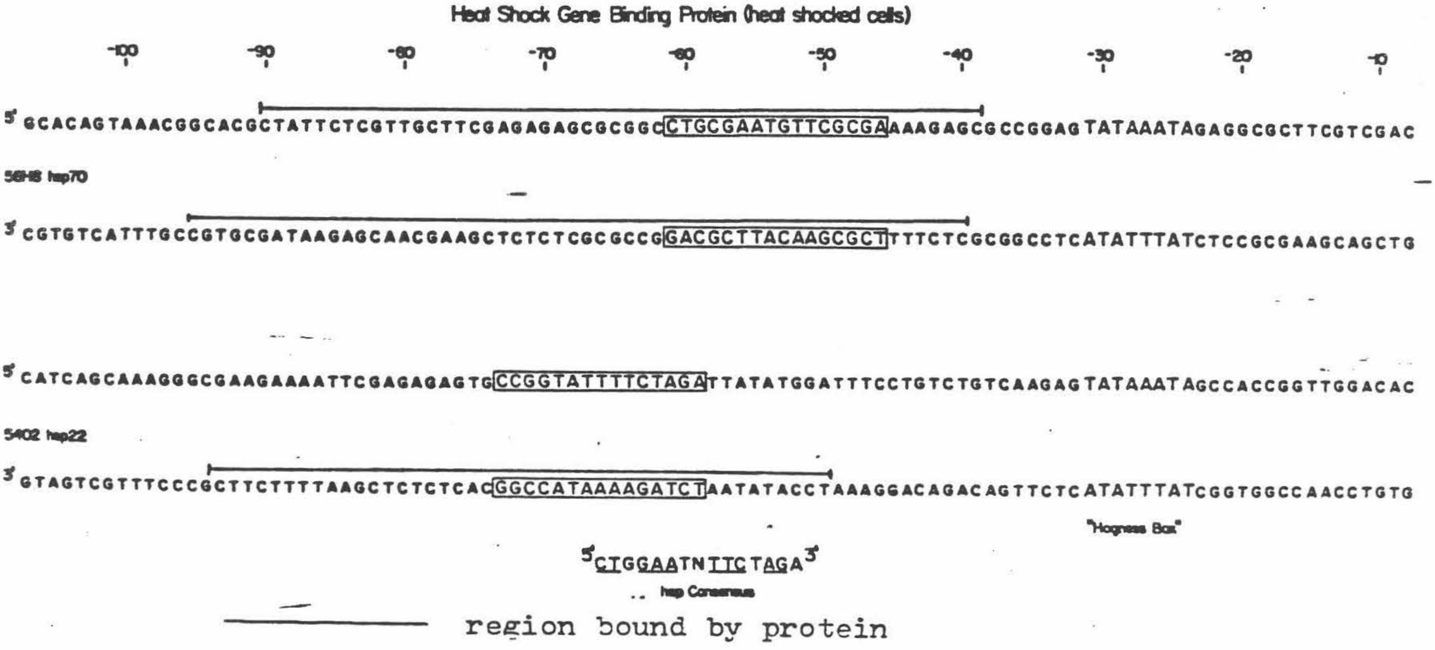

In vivo, transcription of heat-shock genes is stimulated when the organism is heat-shocked or subjected to some other stress, such as chemical uncouplers to the respiratory cycle like sodium azide. In cultured Drosophila cells, heat-shock genes' transcription is also only stimulated after a stress. This stress-dependent transcription of the heat-shock genes has been observed *in vitro* by making crude nuclear extracts from both shocked and non-shocked Drosophila tissue culture cells. By showing that only heat-shock genes are efficiently transcribed in a heat-shock extract, it is thought that the HSF protein is uniquely active in the heat-shocked cell.

The HSF protein is present in both extracts but is particularly active in enhancing transcription of the heat-shock genes when it is purified from the heat-shocked cells. A possible explanation for this is that during heat-shock, the HSF protein is modified from a less active to a more active state.

The purpose of my research last summer was to generate antibodies against purified HSF protein and to isolate the gene for this factor by screening a λgt-11 expression library with this antibody.

Results: The first step in purifying HSF protein is to prepare a crude nuclear extract of Drosophila tissue-culture cells. The non-shocked extract is made by growing the tissue culture cells at 25°C, the normal growth temperature for these cells. The cells are harvested by centrifugation and resuspended in a hypotonic buffer and homogenized to lyse them. The cytoplasmic material is separated from the nuclear material by centrifugation. Chromosomal proteins present in the isolated nuclei are dissociated from the DNA by a salt-extraction step. Finally, proteins present in the crude nuclear extract are concentrated by ammonium sulfate precipitation. The heat-shocked extract is made identically except that the cells are first briefly heated to 37°C immediately before being harvested.

The HSF protein is purified from the crude extract through a series of column chromatography steps. First, the crude extract is chromatographed through a DEAE (diethylaminoethyl) cellulose column. DEAE cellulose is a positively charged resin which binds to negatively charged amino acids in proteins, hence it is referred to as an anion exchanger. Next, the fractions containing the

HSF protein are chromatographed through a Biorex 70 cation exchanger. The third column is a DEAE sephadex (A-25) anion exchanger. The fourth column is a phosphocellulose cation exchanger. The fifth purification step is a glycerol-sucrose gradient which separates proteins on sedimentation properties or size. The next step is a DNA cellulose affinity column. Finally, the highly purified protein is run on a polyacrylamide denaturing gel and the protein band containing the HSF is cut out with a razor.

The gel slice containing the HSF protein is homogenized with an equal amount of 1% agarose, dialazed overnight in saline solution and injected into a rabbit. The rabbit is boosted at weekly intervals with gel purified HSF and next month it will be bled to determine if any anti-HSF antibodies are generated.

Discussion and Conclusions: The HSF protein from the shocked and the non-shocked cells chromatographed identically except for the Biorex 70 column. The active HSF breaks through this column while the nonactive HSF binds.

When the rabbit anti-HSF antibodies are available, a Drosophila λgt-11 expression library will be constructed and then screened with the antibodies. Once this is accomplished, we will have isolated, for the first time, the gene for a eukaryotic transcription factor.

BEHZAD SADEGHI

NO REPORT SUBMITTED

JANET SAYLOR

NO REPORT SUBMITTED

Work on a Synthetic Sequence in the Synthesis of Tirandamycin.

John J. Schaeck

Paul A. Bartlett

The synthesis of tirandamycin is desirable for the insight gained in attaining a specific molecular stereochemistry. The synthetic sequence undertaken sets four of the seven chiral centers of tirandamycin using a variety of techniques. The techniques employed have great promise in other natural product syntheses.

Tirandamycin (I) is a 3-acyl tetramic acid antibiotic which acts as an inhibitor of RNA polymerase in bacterial and mammalian cell-free test systems[1]. It is thought that the bicyclic ring system is largely responsible for the large activity relative to other tetramic acids, making the ring system an interesting target for study. The seven chiral centers of the ring present a challenge in selectivity since only one of the one hundred twenty-eight isomers is desired. It was the synthetic methods required for the selectivity which motivated the project and its particular synthetic sequence since any methods developed could have wide application for important natural product syntheses.

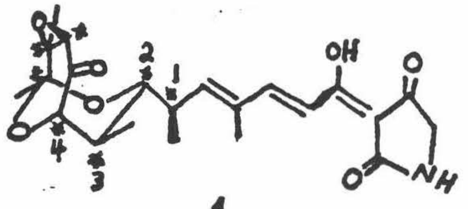

1

The sequence performed in the SURF project was part of a slightly modified version of a synthesis of the bicyclic portion of tirandamycin which was outlined in Joel Myerson's[2] unpublished PhD thesis. Subsequently Ireland[3] has reported synthesizing tirandamycic acid (2) from D-glucose. Most recently DeShong[4] has reported the synthesis of racemic 3 from 4 and 5 which gave tirandamycic acid in four additional steps.

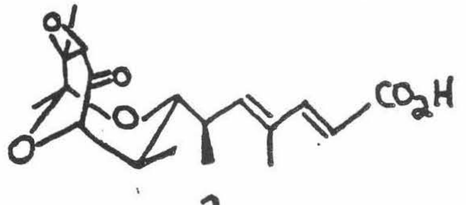

2

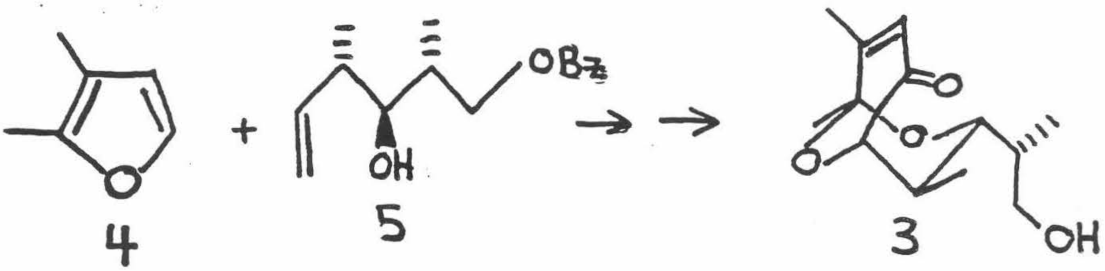

4 5 3

The target of the sequence performed was the lactone 6 which shows four of the seven chiral centers of the bicyclic product. The corresponding chiral centers have been labled in both 1 and 6. The product 6 is to be taken on to 7

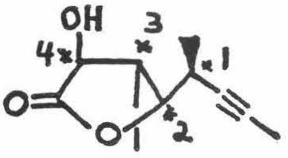

6

by other researchers who had originally proposed the sequence shown in scheme 1, but which has since been modified.

SCHEME I

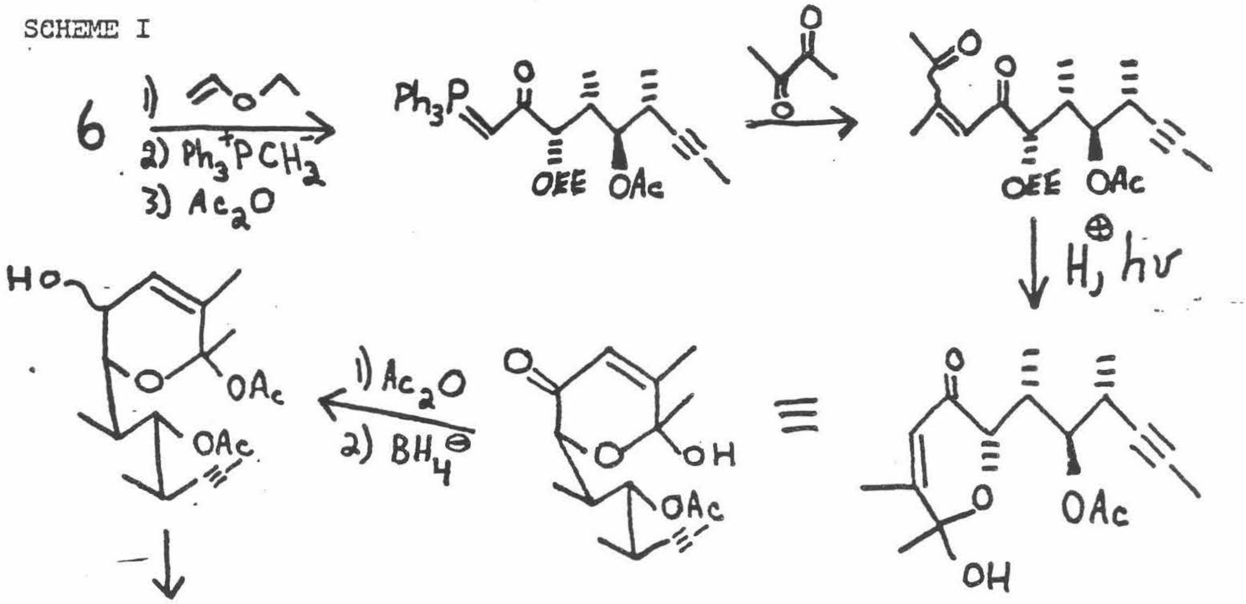

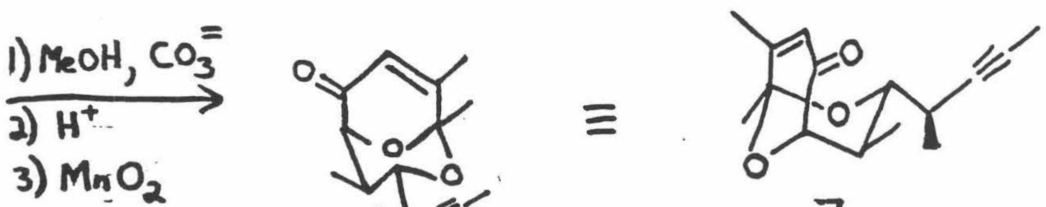

7

The reaction sequence undertaken in this project began with the reaction of 8 and 9 to give the allane 10. The remaining series is shown in scheme II. The commercially available epoxide 11 is reacted with the allane to add

$$\underset{8}{-\equiv} \quad + \quad \underset{9}{Et_2AlCl} \xrightarrow{a} \underset{10}{Et_2Al-\equiv-}$$

SCHEME II

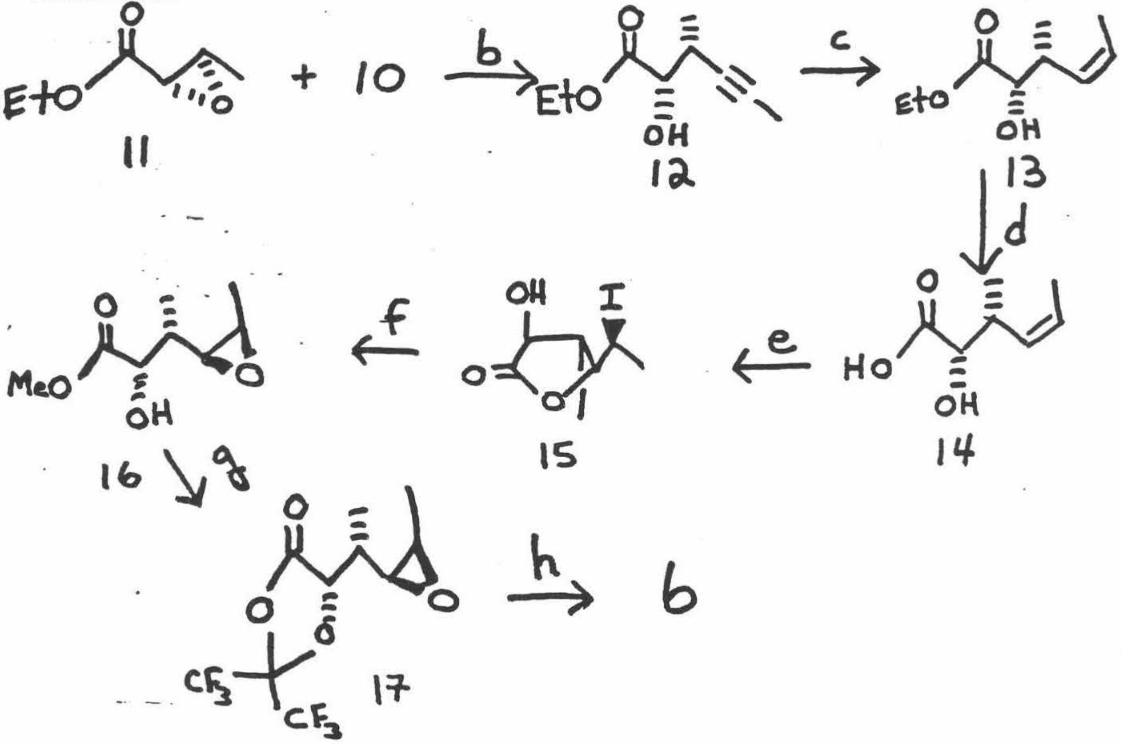

further to the carbon chain and set two of the chiral centers. Next the alkyne is hydrogenated to the alkene which is then saponified to the acid in preparation for the centerpiece reaction—the iodolactonization.

Much of Myerson's work dealt with acyclic stereocontrol via iodolactones.

The present pathway was designed to utilize this method for the insertion of an oxygen functionality stereospecifically under kinetic conditions. In the next step the ring oxygen displaces the iodine, adding another oxygen of set stereochemistry. This then is protected by hexafluroacetone and then reacted again with the allane to give the lactone 6. This sequence was followed through once and then followed through step (d) twice more. At step (e) these two runs were combined and carried through to 6 together. The results given in the experimental section are based on these second two runs.

Conclusions

I found the introduction of the oxygen functionality by the iodolactone to be quite interesting and of great potential. The other methods of achieving stereocontrol were also of interest. Though the yields were not as high as desired, the laboratory experience I gained was of great value and provided me with a first hand view of university research. In all an enjoyable summer's work.

Experimental

a) (8) was condensed into 500 mmol nBuLi in toluene/hexane at 0°C and stirred under N_2 for 1.5 hrs. (9) was then added and stirring was continued at 0°C for another 4 hrs.

b) (11) was added to the allane solution by syringe and stirring was continued for another 5 hrs. at zero degrees during which time the solution turned yellow. The mixture was then placed in the refrigerator overnight. The reaction was quenched with 800 ml 5% (v/v) sulfuric acid solution. The aqueous phase was extracted with ether and the organic phase washed with brine. Dried magnesium sulfate. Removed solvent. The orange oil was purified by high pressure liquid chromatography (HPLC) (4:1 hexane:ether) yielding an orange product oil. Run A=34%, B=45%.

c) One-twentieth equivalent of $Ni(Ac)_4 \cdot 4H_2O$ was dissolved in 95% ethanol under nitrogen. A one-twentieth equivalent of 1 M sodium borohydride solution was then added by syringe turning the blue solution black. Then one-fifth eqiv. of ethylenediamine followed by the alkyne (12) was added by syringe. Flushed with hydrogen and placed under a balonn of hydrogen overnight. Filtered through celite/charcoaland diluted with ether and water. Separated and washed the org. with water. Washed combined aq. with ether and dried org. with magnesium sulfate. Obtained a crude orange oil after solvent removal.

d) (13) was dissolved in 95% ethanol with 1 M sodium hydroxide and stirred for eighteen hrs. Removed solvent, added water, extracted with ether, extracted org. with water, acidified aq. to pH=2, extracted acidified water with ether, dried org. with magnesium sulfate. Yield over last two steps for A=67%, B=66%.

e) Dissolved (14) in acetonitrile with ten eqiv. sodium bicarbonate at zero degrees. Three eqiv. of iodine was added and the solution was stirred using an overhead stirrer for four hours protected from light. Poured into sat. sodium bicarbonate, diluted with ether and sodium thiosulfate, separated layers and washed org. with sat sodium thiosulfate, extracted combined aq. with ether, dried org. with magnesium sulfate. Got 99% of an orange solid.

f) Dissolved (15) in methanol with 1.3 eqiv. sodium carbonate and stirred for eight days. Removed solvent, dissolved in sat. sodium chloride, extracted with ether, dried org. with magnesium sulfate. HPLC (2:1 hexane/ether) gave an orange-red oil 60%.

g) Condensed hexafluroacetone into (16) dissolved in carbon tetrachloride. Monitored by NMR. Added sodium carbonate, stirred overnight, washed water, washed sat. sodium chloride. Obtained 55% crude oil which could not be cleaned by chromatography.

h) Ran reaction described in (a) but let lithium salts settle overnight. Cannulated in (10) to (17) dissolved in toluene at zero degrees under nitrogen. Stirred three hrs. Added 300 ml 1M hydrochloric acid, diluted with ethyl acetate, washed with water, washed with sat. sodium carbonate, washed with water, washed with sodium chloride solution, extracted comb. aq. with ether. Dried org. magnesium sulfate. Through a combination of recrystallizations (dichloromethane/pentane) and flash chromatography (12:1 dichloromethane:acetone) 48% clean and some remaining crude was obtained.

NOTE: The reaction sequence was done on a much larger scale than literature and thus the lower yields.

Acknowledgement: I would like to thank the SURF program for its financial aid for a project away from Caltech. I would also like to thank Dave Richardson and Chris Newcome for their advice and help. Most of all I would like to thank Paul A. Bartlett for giving me the opportunity to work at a first rate research institute and in a first rate research group.

Bibliography

(1) Reusser, Fritz. Infec. Immun. 1970,2,77.

(2) Myerson, J. PhD thesis. 1980. University of California Berkeley.

(3) Ireland, R.E.; Wutz, P.G.M.; Ernst, B. J. Am. Chem. Soc. 1981,103, 3205.

(4) DeShong, P.; Ramesh, S.; Perez, J.J. J. Org. Chem. 1983,48, 2118.

UNIDIRECTIONAL CRYSTAL GROWTH FROM SOLUTION WITH NEGLIGIBLE CONVECTION

SURF Project 1983

Research performed by Darrell Schlom under the supervision of Professor David S. Wood.

Abstract

The goal of this research is to make a crystal growth experiment to be flown aboard the Space Shuttle. A 5 3/4" x 5" x 1 1/4" nickel plated aluminum prototype crystal growth cell was designed and constructed. A temperature control system has been "calculated" out. Testing of the crystal growth cell awaits delivery of fused silica windows.

Introduction

Crystallization from solution is a process involving a simultaneous mass and heat transport between a crystal surface and the surrounding fluid, causing a reduction in the density of the fluid. Consequently, in the presence of gravity, a growing crystal is usually surrounded by a rising convection current (5). It has been suspected that growth in a microgravity environment, which greatly reduces these convection currents, might produce a superior quality crystal. The only crystal growth from solution experiment performed in space to date was done by Dr. Ichiro Miyagawa of the University of Alabama (2). His experiment was performed aboard Skylab-4. Parts of his space grown crystals were of excellent quality and other parts showed highly regular, elongated tubular voids. Crystals grown under the same conditions on earth showed much less regularity in defect structure.

The Student Space Organization (SSO) at Caltech has purchased several five cubic foot self contained payloads ("Getaway Specials") from NASA. My work this summer has been on the continuing development of a crystal growth experiment to be flown on or shortly after STS 18 in September 1984 in the second of these SSO payloads.

The goals of this experiment are to determine whether crystals grown in a convectionless environment in space are indeed superior to ones grown on the earth under otherwise equivalent conditions, and to see how closely the observed growth follows the predictions of a model of crystal growth dynamics proposed by Dr. W.R. Wilcox (4). His growth model predicts the unidirectional growth rate, and concentration profile for the unidirectional growth of a single crystal face in a solution (free of thermal gradients) which is being cooled at a constant rate.

In order to perform an experiment that could be compared to theory, I chose to grow a single crystal face in an isothermal crystal growth cell. Potassium dihydrogen phosphate (KDP) was selected as the crystal to be grown because it is labile, it can be greatly supercooled before it spontaneously nucleates, and it is commercially important. Unfortunately, it is corrosive to many common construction materials. Many materials have been tested in order to find suitable construction materials compatible with KDP.

Last year I used a simplified diffusion equation (one that neglected the convective term and interface kinetics) to predict how much KDP would grow during the space experiment. With 35 degrees Celsius supercooling, about 1mm of crystal will grow in 5 days. Since Space Shuttle missions last from 3 to 7 days, this is about all the growth that can be expected. Laboratory experience indicates that more than 35 degrees Celsius supercooling will result in spontaneous nucleation elsewhere in the crystal growth cell.

A possible experiment sequence is as follows. Initially the crystal will be mounted in the growth cell with its (100) or (101) crystallographic face exposed. An inflated rubber-encapsulated "flipper" separates the crystal from the solution (saturated at 70 degrees Celsius). Once the payload is in orbit, the crystal growth cell is heated to 75 degrees Celsius. The flipper is deflated and rotated back and forth to stir the heated solution, dissolving any nuclei that might have formed during storage. The stirring also sets up a uniform concentration everywhere within the crystal growth cell. The flipper is then locked in its upright position. As soon as the fluid motion of the solution is damped out by viscous forces, the growth cell will be slowly cooled (less than 1/2 degree Celcius per hour) down to about 35 degrees Celsius. The growth cell temperature is held at 35 degrees Celsius until the end of the at least 90 hour experiment. The experiment is concluded by the flipper being rotated back to its horizontal position and inflated. Oil is squirted across the crystal face to displace any remaining solution.

Once the experiment is returned to earth, the results of the experiment will be compared to Dr. Wilcox's theory. The defect structure and quality of the crystal will be compared to crystals grown on earth under identical conditions to the space experiment (with the exception of gravity).

Presentation and Discussion of Results

This year's prototype (see attached drawings) reflects several design improvements over the growth cell that I made last year. After much testing, I found that last year's prototype suffered two major flaws: it leaked, and its glass windows either broke or became unbonded from their frame as the cell was assembled. So, instead of bonding the windows into their frames, I decided to use O-ring seals. This design also incorporates a "flipper" used to separate the crystal from the solution before and after the experiment, and to stir the solution at the start of the experiment.

In order to make the circular contours in the design (i.e. the three O-ring grooves), a computer controlled milling machine was used to make the prototype. I wrote the computer programs necessary to machine the cell pieces and machined all the parts. Insaco Inc. agreed to fabricate and donate the fused silica windows. However, at the time of this writing, the windows have not arrrived. Consequently, final machining of the cell interior has not ocurred. To test the sealing of the cell, I assembled the cell using rough cut glass windows. The O-ring seals worked well.

I performed order of magnitude type calculations to get an idea how stringent of temperature control was necessary in order to keep a convection negligible at the 10^{-4} to 10^{-6} g microgravity levels expected on the Space Shuttle. The result is that between one-tenth and one-hundredth of a degree Celsius temperature control is necessary. In order to accurately control the temperature of the cell to these levels, a preliminary temperature sensor and heater layout has been devised. In order to have the heat flow symmetrically out of the cell windows, a 2 1/2" thick layer of low density polyurethane foam will be used to cover all metal surfaces. This insulation makes is so that only one-hundredth of the heat flowing out of the cell flows through the insulation on the metal cell block. The rest flows out through the cell windows and thermoelectric coolers mounted on the cell block. The outside of the fused silica windows will be evaporator coated with 12.2 angstroms thick gold film (20 ohms/square resistivity, 81% visible light transmission). One 1/2" x 1 1/4" thermoelectric heater/cooler will be positioned on each of the four sides of the aluminum cell block. The foam above the thermoelectric heater/cooler will be removed, allowing it to convect heat away.

Calculations indicate that the temperature difference between the outside of the windows and the solution is only about .006 degrees Celsius, assuming perfect temperature control. Thermistor temperature sensors will be placed on the outside of the cell windows and inside the cell block. The block heater will be controlled to a slightly higher temperature than the outside of the cell windows. This "calculated" thermal control system will be altered as indicated by actual experimentation.

Conclusions

An improved crystal growth cell with O-ring seals has been fabricated. Final assembly and testing await the delivery of fused silica windows. A temperature control system has been "calculated" out and will be experimentally refined.

Some of the mechanical difficulties have been conquered. However, there are still many problems that must be overcome before the experiment reaches a feasible state. Perhaps the most important of these is the ability of the "flipper" to work properly.

Acknowledgements

I would like to thank Dr. Paul J. Shlichta of JPL for his unceasing advice and for the use of his laboratory; Dr. David S. Wood for his detailed and understandable explanations and encouragement; Dr. George R. Rossman for his enthusiastic suggestions and the use of his laboratory facilities; Dr. Jane G. Raymond for her loans of needed equipment; Mike Miranda and the division of biology for the use of 07 Beckman as my wet lab; Dr. Brad Sturtevant and Dr. Charles Babcock for their qualitative explanations and continued interest; Dr. Thomas Caughey, Dr. Rolf Sabersky, and Dr. Eric Herbolzheimer for their suggestions on thermal control; Elmer Szombathy for his many machining tips; the entire SSO for their constructive criticisms, suggestions, soliciting for the donation of the materials and products I used this summer, and for building the structure and electronics that will contain and control this experiment aboard the Space Shuttle; and to Great Western Inorganics for their $10,000 donation paying for the SSO's second payload canister (which this experiment will fly in).

REFERENCES

1. W.R. Wilcox, Preparation and Properties of Solid State Materials, Vol.2, Dekker, New York, 1976.

2. I. Miyagawa, Final Report: Investigation of Crystal Growth from Solutions, NASA, 1975.

3. Wok, Burton, N. Cabrera, F.C. Frank. The Growth of Crystals and the Equilibrium Structure of their Surfaces, Phil. Trans. Royal Society of London, A.243, pp. 299-358, 1951.

4. W.R. Wilcox, Computer Simulation of Growth of Thick Layers from Solutions of Finite Solute Concentration without Convection, Journal of Crystal Growth, Vol. 56, pp. 690-698, 1982.

5. P. S. Chen, P. J. Shlichta, W. R. Wilcox, and R. A. Lefever, Convection Phenomena During the Growth of Sodium Chlorate Crystals from Solution, Journal of Crystal Growth, Vol. 47, pp. 43-60, 1979.

6. P.J. Shlichta, Third Semiannual Report: Crystal Growth in a Spaceflight Environment, JPL, 1980.

CRYSTAL GROWTH CELL

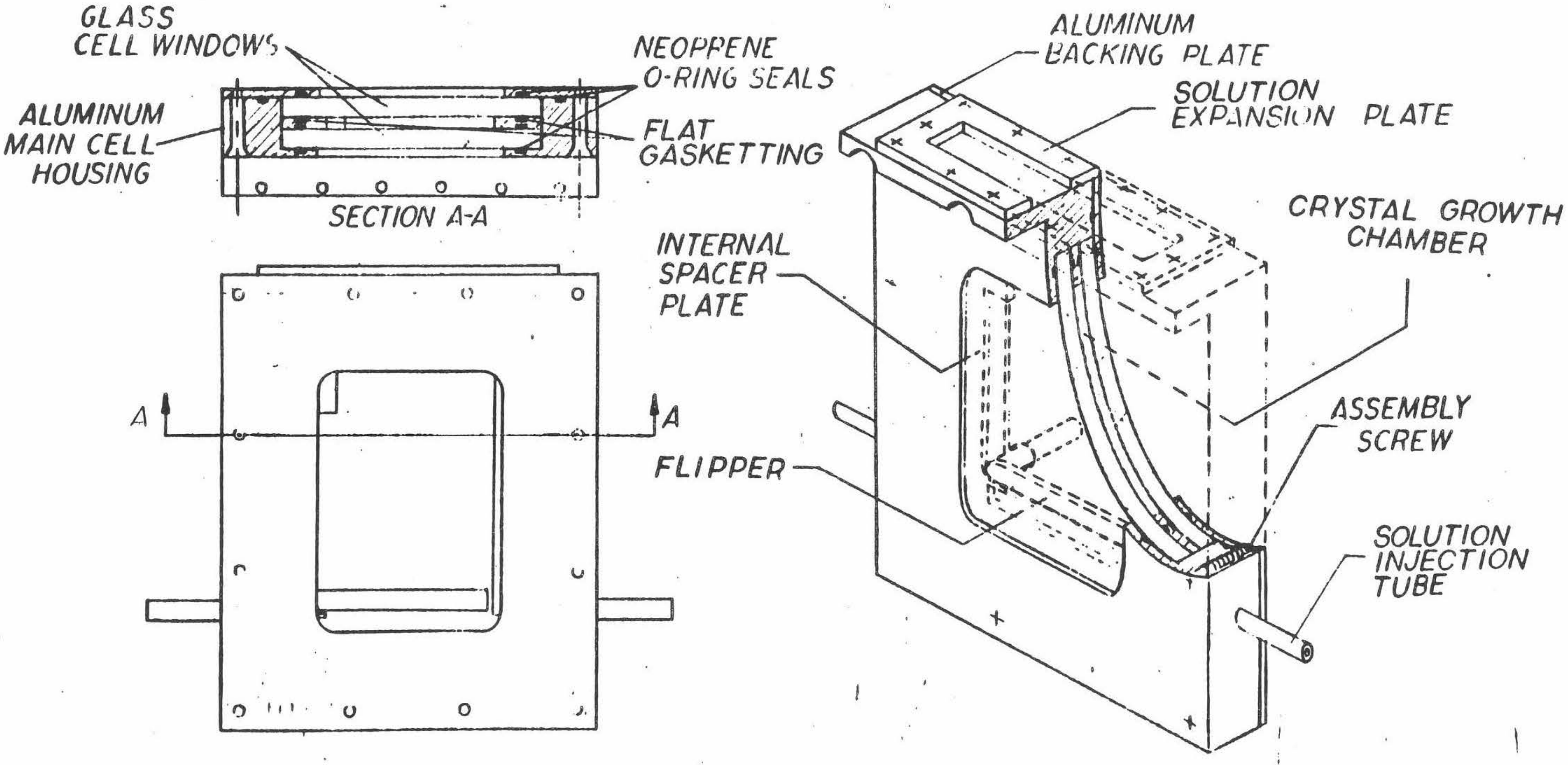

HALF SCALE

CATHY SHAPIRO

NO REPORT SUBMITTED

Two-Dimensional Nuclear Magnetic Resonance Studies of Polymyxin B at 11.75 Tesla

Lawrence S. Shapiro

ABSTRACT: The peptide antibiotic Polymyxin B has been subjected to study by two-dimensional NMR techniques at 11.75 Tesla. The proton spectrum has been completely assigned by scalar J-correlation spectroscopy as well as two-dimensional J-resolved spectroscopy. Partial assignment of the natural abundance ^{13}C resonances was achieved via proton-carbon heteronuclear shift-correlation spectroscopy. Two-dimensional nuclear Overhauser effect spectroscopy yields data suggestive of a constrained configuration of the acyclic portion of the molecule.

FACULTY ADVISOR: Sunney I. Chan

In "normal" one-dimensional Fourier-transform NMR spectroscopy, a single radio-frequency pulse "flips" the magnetization vector of the observed nuclei to an axis of a coordinate system (y) perpendicular to H_0, the vector of the external field along the z axis. The magnetic moment of the nuclei now precesses in the laboratory xy plane at the nuclear Larmor frequency ω_0. The magnetization in the xy plane decreases exponentially with time constant T_1 as the spins relax back to the prepulse Boltzmann distribution (for an $I = 1/2$ system) with more spins parallel than antiparallel to H_0. Moreover, magnetization of the same Larmor frequency exponentially dephases in the xy plane with time constant T_2 particular to the chemical environment of the observed nucleus. The trace of the magnetization undergoing these processes is known as free-induction decay and is observed as rf oscillations in routine spectroscopy. Fourier transformation of the FID along the time axis gives a frequency spectrum with peak positions determined by ω_0, and linewidths, ideally, determined by T_2.

In two-dimensional NMR spectroscopy, a sequence of multiple rf pulses is used to generate a set of FID's, each differing by a constant time interval, e.g., between pulses, thus making the data amenable to representation as a two-dimensional matrix $S(t_1, t_2)$ where t_2 is the real-time axis of the FID and t_1 is the time axis of the delay time increasing by a constant interval with each FID. Fourier transformation of the matrix $S(t_1,t_2)$ along both the two time axes leads to a data matrix, or spectrum $F(\omega_1,\omega_2)$ of two orthogonal frequency axes ω_1 and ω_2, corresponding to t_1 and t_2. Each element of $F(\omega_1,\omega_2)$ is a number specifying the "absorbance" at the two-dimensional frequency coordinate (ω_1,ω_2). The physical meaning of the two-frequency axes is completely dependent upon the pulse sequence used as will now be illustrated in

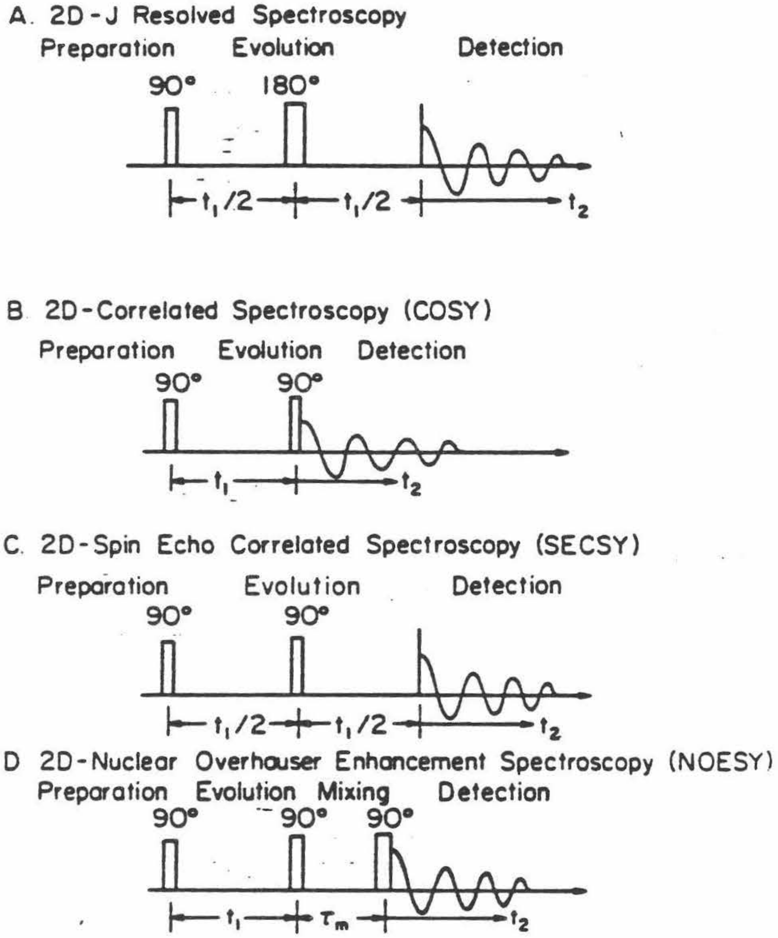

Figure 1

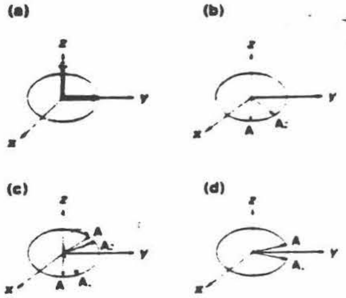

Figure 2

in the case of two-dimensional homonuclear J-resolved spectroscopy.

Many NMR spectra exhibit complicated homonuclear spin-spin splitting patterns which may elude analysis through such complications as chemical shift degeneracy of multiplets or falsely implied multiplets through fortuitously shifted uncoupled resonances. Many spectral analyses would be greatly simplified by, say, separation of chemical shift and coupling constant information along two separate frequency axes, i.e., ω_1 and ω_2 of the previous section. The pulse sequence $(\text{RD}-\pi/2-t_{1/2}-\pi-t_{1/2}-\text{FID})_\eta$ is shown graphically in Figure 1. Consider a weakly coupled I = 1/2 homonuclear AX spin system which will have resonant frequencies

$$\eta_{A_1} = \eta_A + J/2 \text{ for } |X\rangle = \alpha$$

$$\eta_{A_2} = \eta_A - J/2 \text{ for } |X\rangle = \beta$$

$$\eta_{X_1} = \eta_X + J/2 \text{ for } |A\rangle = \alpha$$

$$\eta_{X_2} = \eta_X - J/2 \text{ for } |A\rangle = \beta$$

where η_A and η_X are the chemical shifts of nuclei A and X, respectively, and J is the homonuclear coupling constant. If a $(\frac{\pi}{2})_X$ pulse is applied to such a system at equilibrium, the nuclear magnetization is brought to the y-axis and precesses in the xy plane to the angle ϕ from the y-axis such that directly before the $(\pi)_y$ pulse,

$$\phi_{A_1}(t_{1/2}) = \pi/2 - 2\pi\ (\eta_A + J/2)\ (t_{1/2})$$

$$\phi_{A_2}(t_{1/2}) = \pi/2 - 2\pi\ (\eta_A - J/2)\ (t_{1/2})$$

and similarly for the X_1 and X_2 spins. Now let us concentrate on A_1 as

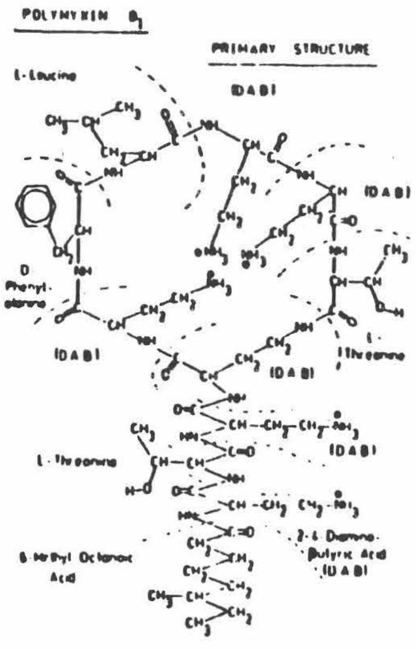

Figure 3

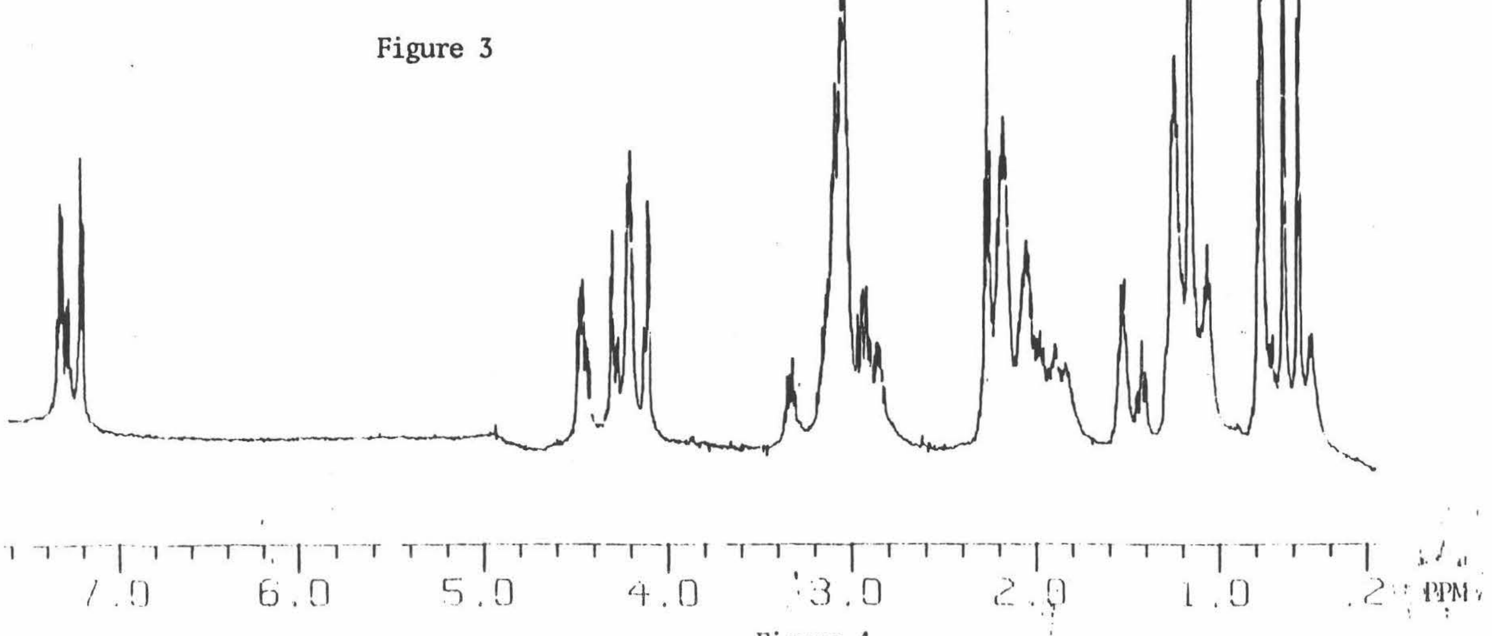

Figure 4

representative of the system. With application of the $(\pi)y$ pulse, A_1 is rotated about the y axis to A_1' (Figure 2). A_1 now rotates at frequency $\eta_{A_1} = (\eta_{A_1} - J/2)$ rather than $(\eta_A + J/2)$ because $|X>$ is reversed by the $(\pi)y$ pulse. Now the phase of A_1 $t_{1/2}$ seconds after the $(\pi)y$ excitation is given by

$$\phi_{A_1}(t_1) = {}^{\pi}/_{2} + \pi J\, t_1$$

By this relationship, it is apparent that at ω_2 frequency η_A we have phase modulation along the t_1 axis at frequency πJ, and thus, disregarding further mathematics, it is clear that two-dimensional Fourier transformation will yield peaks at the two-dimensional frequencies (J, η_A) and $(-J, \eta_A)$. Hence, we have separated chemical shift (η_A) and coupling constant (J) information among two distinct frequency axes and can now measure coupling constants unambiguously, at a glance.

The foregoing discussion has illustrated the utility of one form of 2D-NMR in the simplification of NMR spectra of complex spin systems. This paper deals with the application of various forms of 2D-NMR to the nuclear resonances of Polymyxin B, a naturally occurring cyclic dodecapeptide antibiotic with a single 6-methyl octanoic acid prosthetic group (Figure 3). The biological significance of this molecule will be expounded upon later in the manuscript.

Figure 4 shows the one-dimensional proton magnetic resonance spectrum of Polymyxin B. It is observed that many resonances overlap, and hence multiplet structure is obscured, hindering assignment of the spectrum. For assignment of this spectrum two-dimensional scalar J-correlated spectroscopy (COSY) was used. COSY is performed with the pulse sequence $(\text{RD}-\pi/2-t_1-\pi/2-\text{FID})_n$ and gives rise to a spectrum $F(\omega_1,\omega_2)$ in which the chemical shift axis lies along the diagonal. A "cross-peak" at (ω_1, ω_2) indicates that resonances at one-dimensional frequencies ω_1 and ω_2 have energy levels in common and are J-coupled. The COSY spectrum of Polymyxin B appears in Figure 5 with the connectivities of the 6-methyl octanoic acid spin system indicated. In this experiment, a pulse sequence giving mainly cross-peaks between protons of vicinal coupling was used, allowing one to simply "follow" the protons down the fatty acid chain. As an example of resonance assignment via COSY we will use the labelled spin system. Polymyxin B has six methyl groups derived from L-leucine, L-threonine, and 6-methyl octanoic acid. The two methyl resonances at 0.55 and 0.65 ppm are characteristic of the magnetically inequivalent leucine methyls, whereas the overlapping resonances at 1.16 ppm show J-connectivity with resonances in the α-proton region, and hence can be unambiguously assigned as constituents of the threonine residues. Hence, the methyl groups resonating with near perfect chemical shift degeneracy at 0.77 ppm must be those of 6-methyl octanoic acid. As can be seen from the COSY spectrum (Figure 5) this resonance is coupled to two resonances at 1.0 and 1.21 ppm corresponding to the ω-CH_2 and ε-CH resonances, respectively, which are coupled with each other as expected by the chemical structure. A cross-peak is noted at (1.21 ppm, 1.44 ppm) connecting the ε-CH resonance with that of the α-CH_2 protons. Cross-peaks at (1.44 ppm, 2.23 ppm), (2.23 ppm, 3.06 ppm) and (3.06 ppm, 3.39 ppm) complete the assignment of this spin system with the shifts being as follows: α-CH_2 = 3.39 ppm, β-CH_2 = 3.06 ppm, γ-CH_2 = 2.23 ppm, α-CH_2 = 1.44 ppm, ε-CH = 1.21 ppm, ω-CH_2 = 1.0 ppm. It should be noted that peptides readily exchange their amide protons in protic solvents, and hence if deuterated solvents are employed vicinal couplings will exist only between protons on the

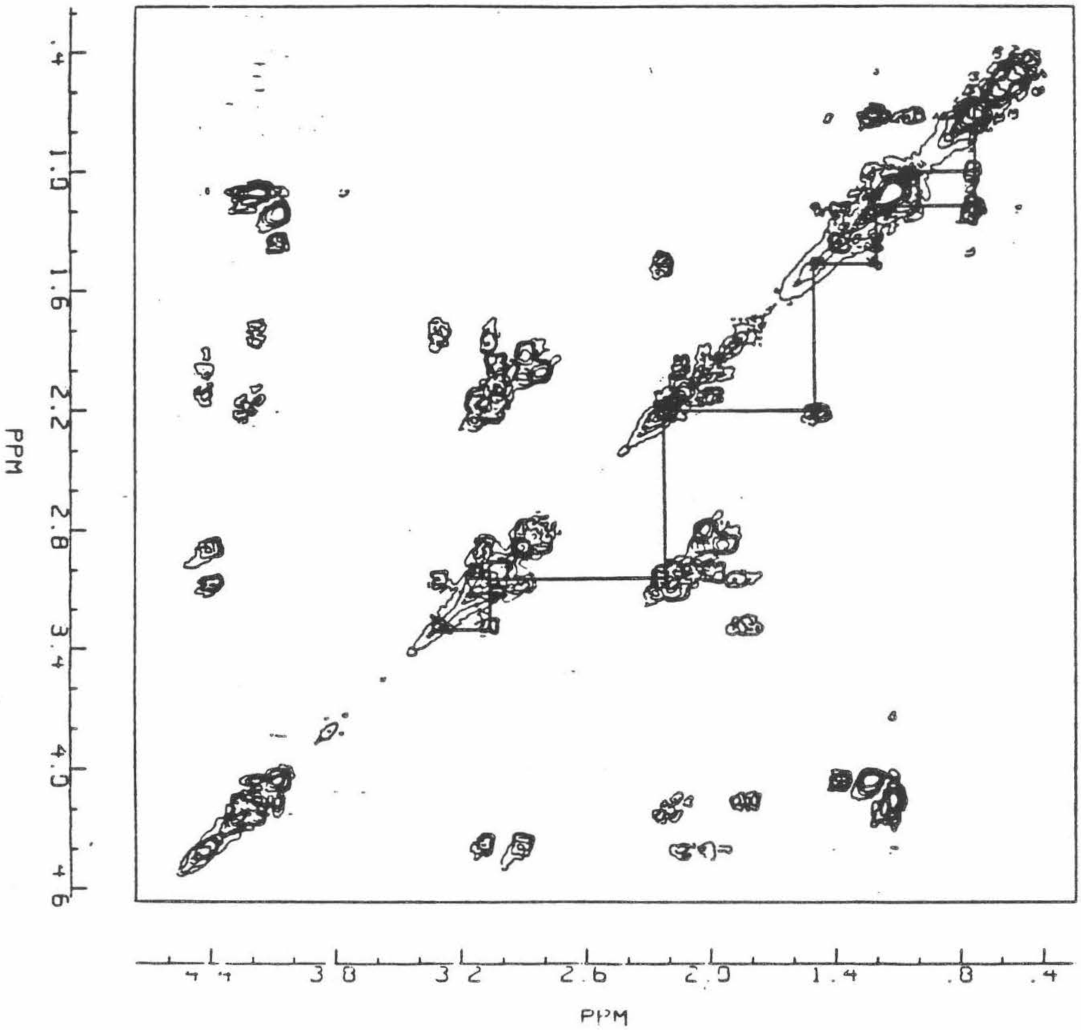

Figure 5

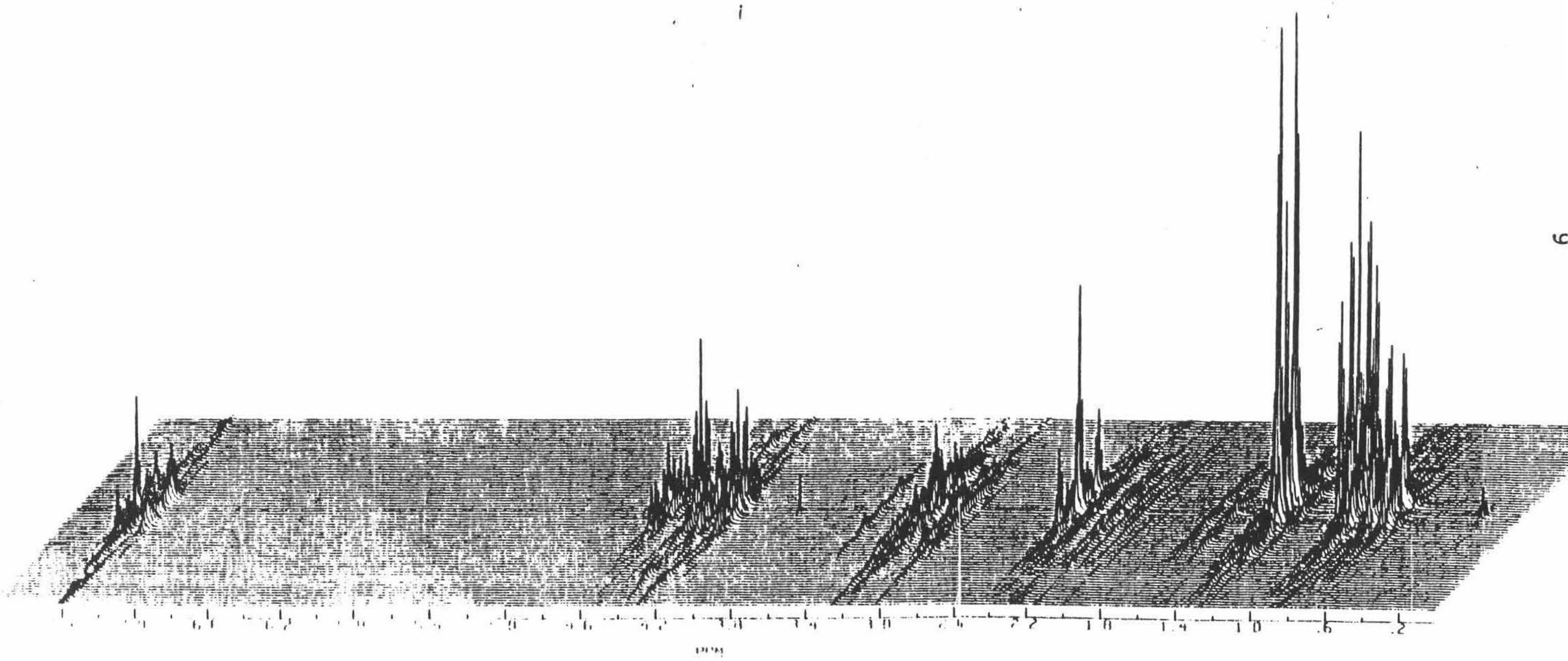

Figure 6

Table 1

Amino Acid; Functional Group	δ(PPM)
Leucine	
CH_3	0.55, 0.62
γ-CH	1.21
β-CH_2	1.4
α-CH	4.09
6-methyl octanoic acid	
CH_3	0.77
ω-CH_2	1.06
ε-CH	1.23
δ-CH_2	1.55
γ-CH_2	2.24
β-CH_2	3.07
α-CH_2	3.32
Threonine (1)	
CH_3	1.24
β-CH	4.19
α-CH	4.08
Threonine (2)	
CH_3	1.24
β-CH	4.19
α-CH	4.22
Phenylalanine	
Ring protons:	
ortho	7.32
meta	7.26
para	7.18
β-CH_2	2.91
α-CH	4.43

Table 1, continued

Diaminobutyric acid	
α-CH (1,5)	4.42
α-CH (3)	4.40
α-CH (4)	4.31
α-CH (2)	4.46
γ-CH_2 (3)	3.15
γ-CH_2 (4,5)	3.03
γ-CH_2 (2)	2.93
γ-CH_2 (1)	2.82
β-CH_2 (5)	2.18
β-CH_2 (1)	2.13
β-CH_2 (2,3)	1.96
β-CH_2 (4)	1.87

same amino acid, i.e., the spectrum in figure 5 achieves a separation of spin systems to individual amino acids, greatly simplifying analysis. If one can identify a single resonance of a spin system (e.g., the methyl groups of 6-methyl octanoic acid), one can assign all the resonances of the amino acid by inspection of the COSY connectivity map. If assignment is ambiguous due to insufficient resolution of cross-peaks, the two-dimensional proton J-resolved spectrum (figure 6) may be employed as a means to discern observed multiplet structures and compare these with spin-spin splittings predicted by the chemical structure. The 2D-J-resolved spectrum of Polymyxin B is too complex to evaluate in its three-dimensional representation, and hence "slices" parallel to the ω_1 axis have been projected in two dimensions, and coupling constants can be read directly from the plotted axis (figure 7).

It has long been known that the resonance of nuclei other than protons can yield significant information of peptide conformation. For example, ^{13}C spectra may lend great insight to the nature of hydrogen-bonding along the peptide backbone and among certain amino acid R-groups. Unfortunately, ^{13}C-NMR spectra of organic molecules as large as Polymyxin B are extremely complicated (figure 8), and due to this as well as other factors such as the low natural abundance of the I = 1/2 isotope, few of these spectra have been assigned. In this study, the ^{13}C assignment problems have been largely circumvented with, to our knowledge, the first use of heteronuclear shift-correlation spectroscopy in the assignment of a peptide ^{13}C spectrum. The pulse sequence for this experiment is shown in figure 9. This two-dimensional spectroscopy shows similarities to both COSY and homonuclear-J-resolved spectroscopy. The 2D-^{13}C-^{1}H shift-correlated spectrum of Polymyxin B is shown in figure 10. The proton chemical shift axis lies in the ω_1 direction whereas the ^{13}C axis is along ω_2. As with COSY, a cross-peak at (ω_1, ω_2) is indicative of scalar

Figure 8

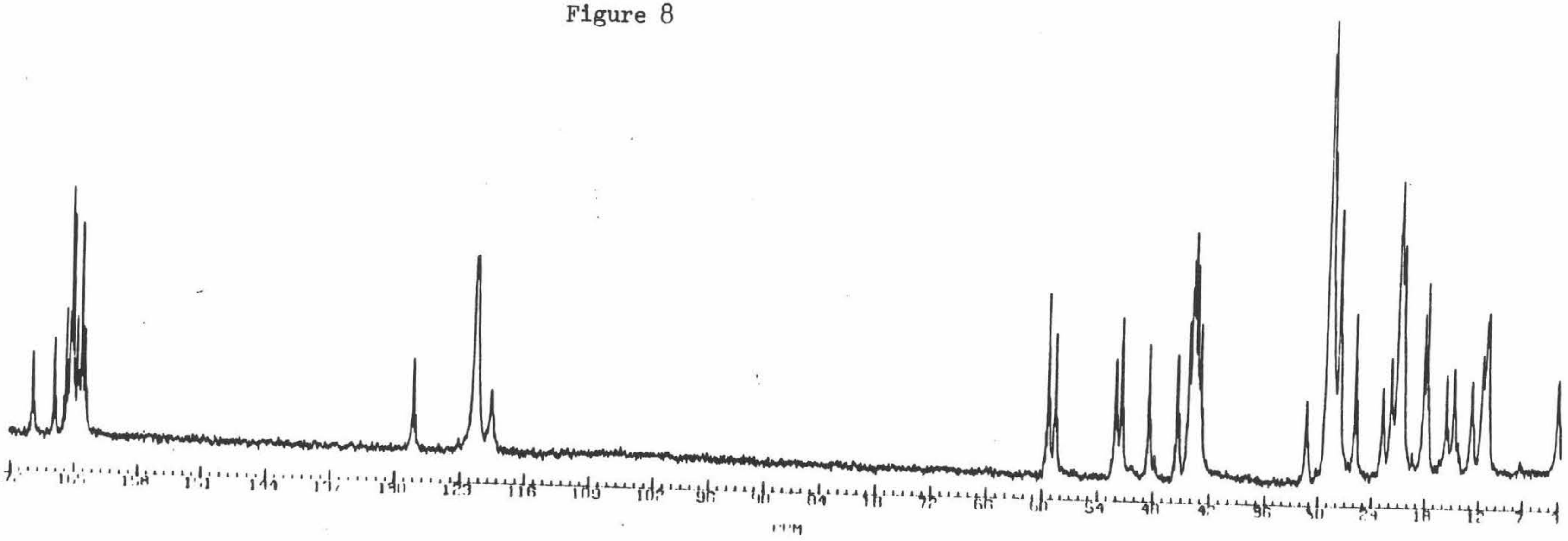

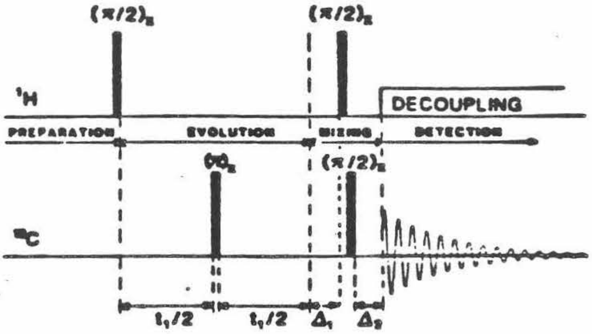

Figure 9

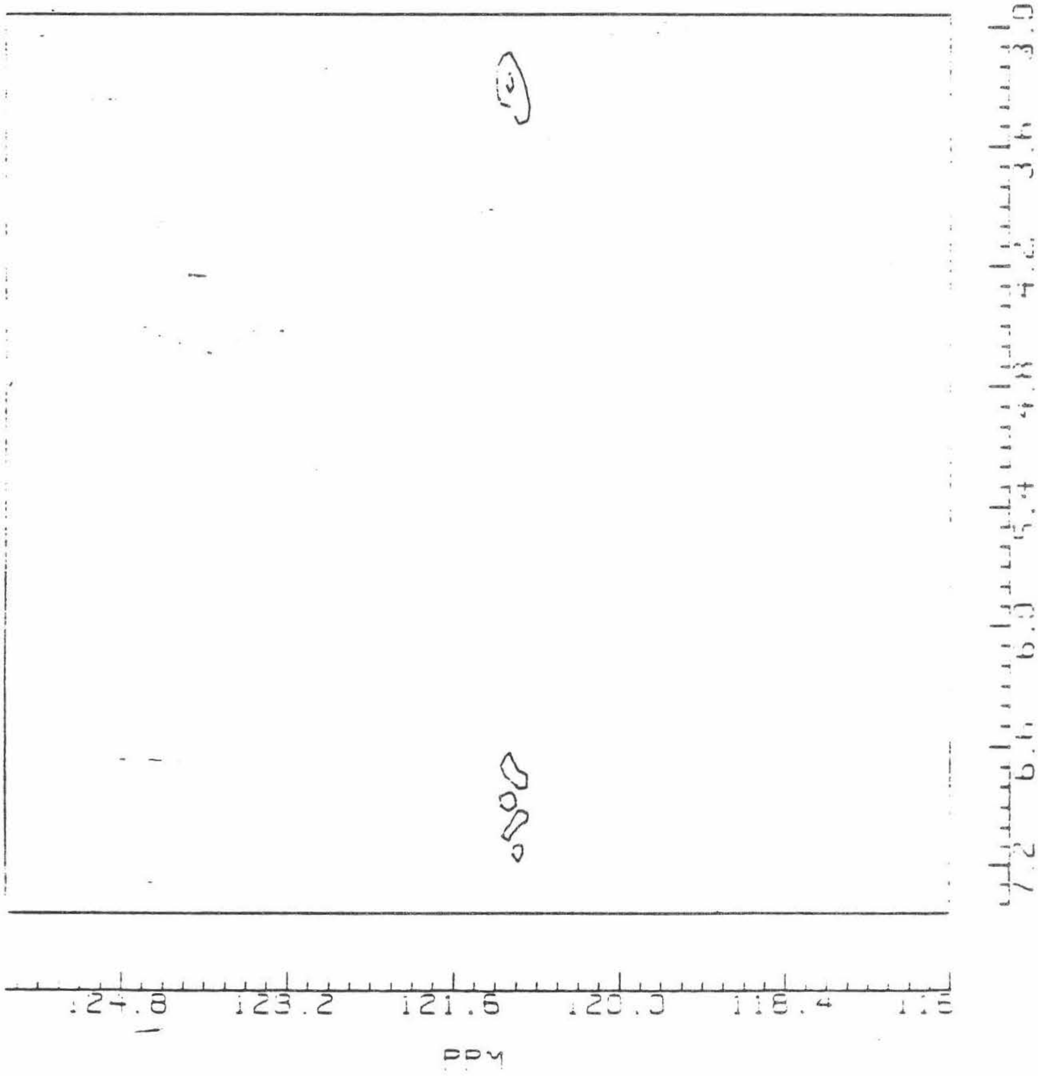

Figure 10a

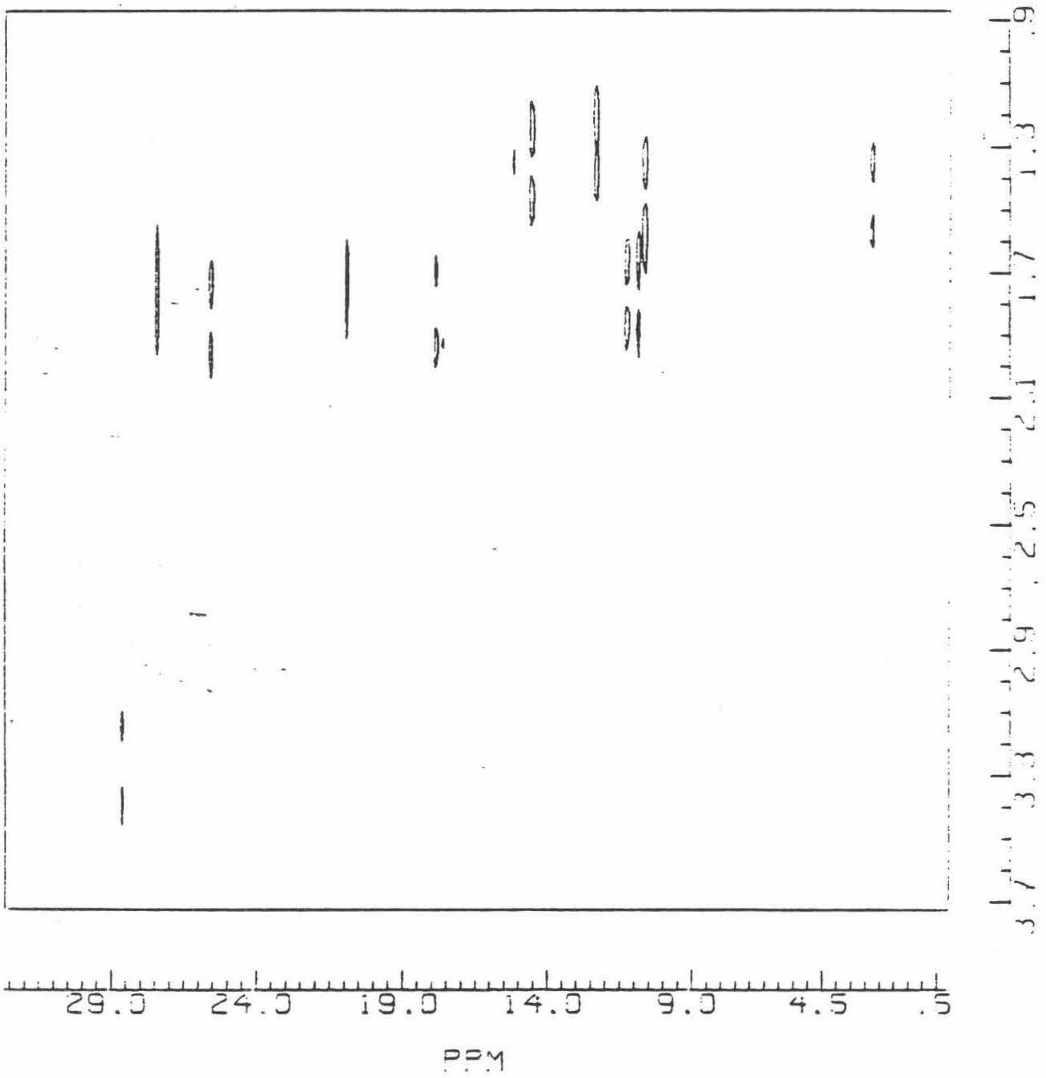

Figure 10b

coupling between nuclei with Larmour precession frequencies ω_1 and ω_2. Thus, simply by inspection of the spectrum, with knowledge of the assignments of the proton spectrum, the ^{13}C resonances can easily be assigned (Table 2). The correlation experiment shown in figure 10 was performed with Δ_1 and Δ_2 set for ^{1}H-^{13}C couplings on the order of J = 100 Hz. Hence, only couplings involving aromatic and β-resonances are manifest, whereas α-nuclei, with J ~ 250 Hz do not correlate. Assignment of these ^{13}C nuclei can be achieved by resetting Δ_1 - $(2J)^{-1}$ and $\Delta_2 = (4J)^{-1}$ for J = 250 Hz.

Consider two I = 1/2 spins in close spatial proximity. This system will have energy levels characterized by the following state diagram

which will have single quantum transitions αβ ← αα, βα ← αα, ββ ← αβ, ββ ← βα, Δm = 2 transition ββ ← αα, and zero quantum transition βα ← αβ. If we now saturate one of these spins with rf at its Larmour frequency, we equalize the probability of its two spin states with respect to the external field. Now βα and αβ are now more favorable levels, and the system is now characterized by a correspondingly new partition function. Hence, the non-irradiated nucleus will have a spin state population <u>different</u> from the case with no selective saturation, and thus the intensity of this nucleus' NMR signal will decrease or increase depending on the nature of this population transfer. This is a greatly simplified explanation of the nuclear Overhauser effect, which has gained wide use in NMR studies for elucidating thru-space dipolar coupling between nuclei. Moreover, since NOE's are dependent upon distance, "proximity maps" may be constructed, and through model-building, a three-dimensional structure obtained. NOE's may also be observed in two dimensions with the pulse sequence of figure 1. As with COSY, a cross-peak at (ω_1, ω_2) is indicative of coupling between peaks at these one-dimensional frequencies; however, in the case of NOESY the coupling is dipolar rather than scalar. The fractional intensity enhancement of the nuclear resonance of a spin I upon irradiation of a proximal spin S is a function of the NMR frequency ω and the correlation time τ_c:[†]

$$f_I(S) = \frac{5 + \omega^2\tau_c^{\,2} - 4\omega^4\tau_c^{\,4}}{10 + 23\omega^2\tau_c^{\,2} + 4\omega^4\tau_c^{\,4}}$$

For Polymyxin B in aqueous solution, τ_c is on the order of 10^{-9}S, making $f_I(S) \sim 0$, giving no Overhauser effect. To remedy this situation, the correlation time of the molecule was increased by an indeterminate factor by bringing the sample to 30% ethylene glycol concentration to increase the viscosity of the solvent. Indeed, in this sample NOE is observed (figure 11) and leads to some possibly exciting structural insight. Notable cross-peaks appear between the 6-methyl octanoic acid methyl and α protons, and these methyls with the methyl protons of a threonine residue, most probably in the acyclic portion of the molecule. These results point toward restricted conformation of the fatty acyl moiety, folding back on itself in, most probably, a hydrophobic interaction. Model-building studies are now under way

---

[†] Balaram, P., Bothner-By, A. A., and Breslow, E., Biochemistry 12, (1973), pp. 4695-4704.

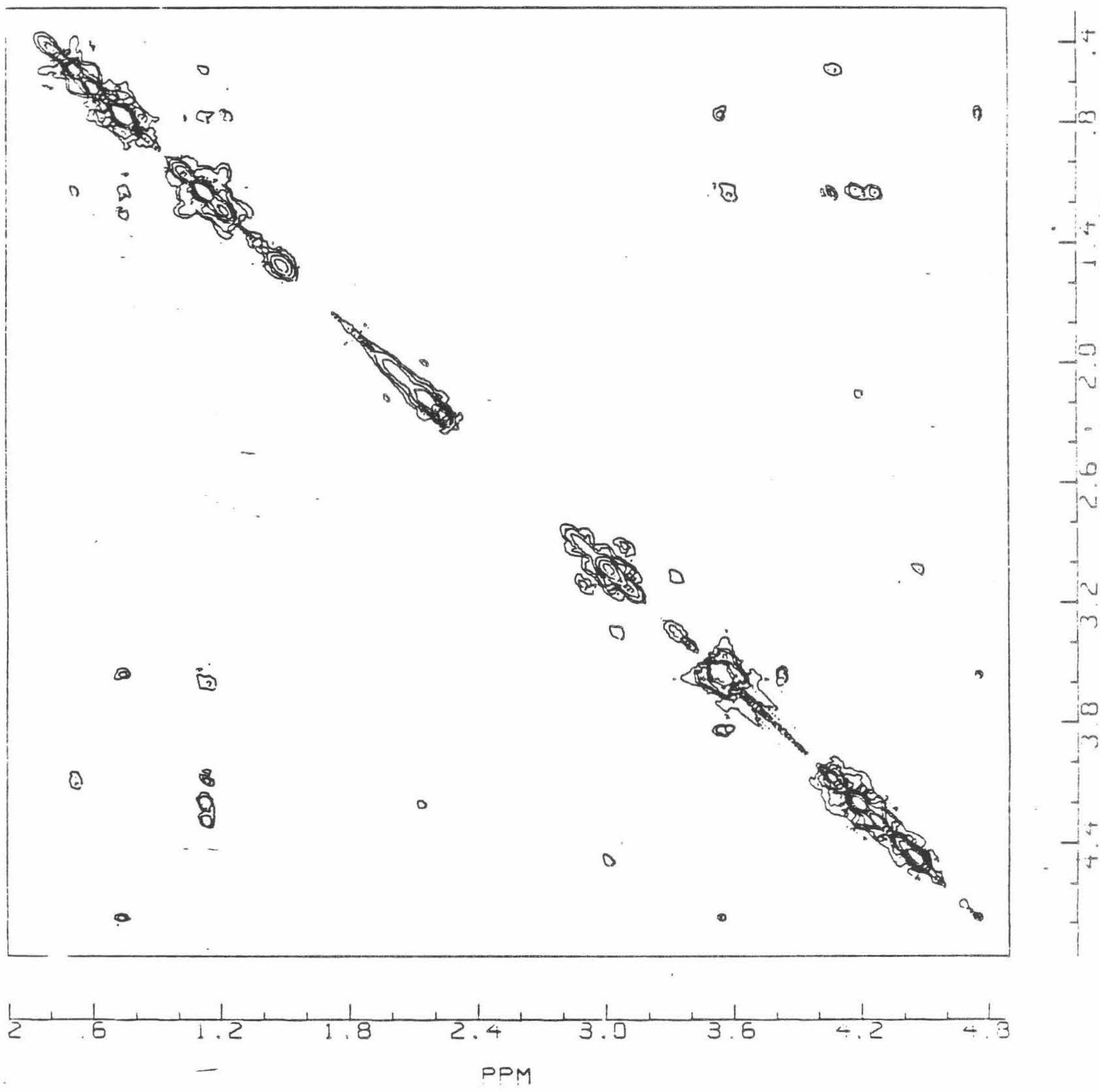

Figure 11

to lend insight to these and other Overhauser data.

It has long been known that Gram-negative bacteria resistant to lysis by complement cause about one-third of bacteriaemic infections in humans. Polymyxin B kills most of these bacteria, but is far too toxic to eukaryotic cells to gain clinical application. Vaara and Vaara[‡] have recently reported that enzymatic excision of the terminal diamino butyric acid and 6-methyl octanoic acid groups of Polymyxin B reduces the antibiotic's toxicity to virtually nil, however, Gram-negative bacteria are no longer killed. These investigators found that the cyclic degradation product with a terminal acyclic threonine residue sensitizes the bacteria to lysis by human complement. The authors propose that the nonapeptide exposes hydrophobic regions of the bacterial membrane allowing insertion of complement. Polymyxin B nonapeptide may now become a drug of great pharmaceutical importance. The present study, though still in progress, has illustrated that the acyclic residues of Polymyxin B most probably exist in a constrained configuration, an understanding of which may help to explain not only Polymyxin B action, but also the interaction of complement with the bacterial membrane. I am soon to embark upon a coincident investigation of the structure of Polymyxin B nonapeptide.

[‡] Vaara, M., and Vaara, T., Nature <u>303</u>, (1983), pp. 526-528.

Figure Legends

Figure 1. The pulse sequences of the four homonuclear two-dimensional spectroscopies are illustrated. All are discussed in the text with the exception of SECSY which leads to the same information as COSY in a different representation.

Figure 2. This figure shows spin behavior in the 2D-homonuclear J-resolved experiment described in the manuscript.

Figure 3. The chemical structure of Polymyxin B.

Figure 4. One-dimensional proton magnetic resonance spectrum of Polymyxin B with saturation of the HDO resonance. The decoupler was set at the HDO frequency at -16 dB and was gated off during aquisition. An 8-phase cycling was used with a relaxation delay of one second (16 scans).

Figure 5. COSY spectrum of Polymyxin B (1.5 mM in D_2O solution, pD 7.0) with solvent supression as in Figure 4. The J-connectivities of the 6-methyl octanoic acid spin system are indicated. A matrix size of 1024 x 1024 points was used (32-phase cycling, 32 scans per point in the ω_1 direction).

Figure 6. 2D-J-resolved spectrum of 1.5 mM polymyxin B (8192 x 128 point matrix, 32 scans per point).

Point 7. ω_1 slices of spectrum in Figure 6.

Figure 8. Proton decoupled ^{13}C spectrum of 0.15 M Polymyxin B in D_2O, pD 7.0, with complete NOE (4096 scans).

Figure 9. Pulse sequence for heteronuclear shift-correlation spectroscopy with decoupling along ω_2.

Figure 10. Expansions of ^{13}C-^{1}H-correlated spectrum: A) aromatic carbons, B) β-carbons (4096 x 256 point matrix, 256 scans per point).

Figure 11. 2D-NOE coutour plot of Polymyxin B, 1.5 mM in 30% ethylene glycol, pD 7.0 (1024 x 1024 point matrix, 32 scans per point).

Solving Problems in Classical Physics with Microcomputers

Anthony Skjellum

California Institute of Technology, Pasadena, California 91125

ABSTRACT

The main use for microcomputers has not traditionally been for the solution of scientific problems. New microcomputers overcome many limitations of previous units and are more suitable in this regard. This paper discusses a project in which a new generation microcomputer was set up to solve classical physics problems.

September 2, 1983

Prof. Geoffrey C. Fox was the advisor for this ten week project.

Solving Problems in Classical Physics with Microcomputers

Anthony Skjellum
California Institute of Technology, Pasadena, California 91125

I. Introduction

The number of personal computers and microcomputers is skyrocketing. Many of these systems are used in wordprocessing, accounting, and various other business pursuits. The latest generation microcomputers have faster execution speed, more memory capacity, better numerical processing ability and faster peripherals. Hence, they are also suitable for performing various types of scientific calculations. The purpose of this project was to set up a microcomputer system and to equip it with optional hardware and software so that it could be used to solve problems in classical physics. As an end result, the effectiveness of the system in solving problems could be determined in a qualitative sense. The quality of the software products available would be determined through evaluation, before any problems were posed, coded and solved.

While the problems to be chosen were in a well-developed area of physics, it was intended that they be non-trivial. By the end of the project, it was hoped that several examples with graphical output could be completed. Furthermore, a firm understanding of how to approach real problems with the computer system was also to be gained in the process.

Prof. Geoffrey C. Fox was the advisor for this ten week project.

II. Procedure

Before the project could really get underway, it was necessary to select and obtain a suitable microcomputer system. Because of an agreement with IBM, IBM XT computers were to have been available by the starting date of this project and so were chosen as the target machines. Unfortunately, IBM was not able to deliver computers until late in the fifth week of this project. Therefore, the author's own IBM PC was used in the interim. With the exception of one quickly corrected hardware malfunction, this computer proved suitable for software evaluation, testing, and production. Furthermore, all testing of the 8087 mathematical co-processor and associated software was done with this machine.

When the IBM XT systems did arrive, a configuration process was required prior to use. This configuration process involved both software and hardware. At the hardware level, additional memory and graphics hardware were installed. At the software level, the hard disk system was prepared and loaded with the appropriate system software. This was immediately possible, since the system software had already been selected through evaluation on the IBM PC unit.

The selection of the system software, including the disk operating system, was based on three factors. The primary factor was the availability of suitable language systems to accompany the operating system chosen. The secondary factor was the ability of the operating system to handle large numbers of data and program files effectively and hence provide a convenient programming environment. The tertiary factor was the ability of the system to provide support for IBM products such as the graphics hardware. After evaluation and testing on the IBM PC, the standard IBM operating system (PCDOS 2.0) was selected. Based also on this evaluation, additional system software was acquired to remove some of the perceived limitations of the standard operating system environment. This included a full-screen editor program to replace the rather primitive IBM editor.

Since the main point of this project was to solve problems with the computer systems, evaluation of programming languages was undertaken next. The selection of appropriate software development languages was based on the following criteria: first, that the language support double precision data types required for some types of problems (due to rounding errors). Second, the language should support the 8087 mathematical co-processor, since this co-processor significantly enhances computer performance for numerical calculations. Third, the language should produce reasonably optimal code to realize reasonable execution speeds in programs produced. Fourth, the language should support the IBM graphics products so that graphics output could be used to visually illustrate results.

The evaluation was performed in two stages. The IBM BASIC compiler and interpreter were evaluated with the IBM PC. While the BASIC systems supported graphics and provided double precision, no 8087 package was immediately identifiable for use with them. The BASIC language was therefore rated acceptable for those problems where execution speed was not a major factor. (Since BASIC co-processor supplements have since been located, this restriction need no longer hold.) Additionally, a C language compiler (Computer Innovations) was evaluated. It provided 8087 support but average code quality and so was also considered acceptable, but offered no real speed incentive over compiled BASIC, except when the 8087 co-processor was available.

After the IBM XT systems were received, the IBM FORTRAN and PASCAL systems were evaluated. IBM FORTRAN received more than a week of use, and was found to be completely unusable due to bugs in the release we received. PASCAL was not carefully examined, mostly because the PASCAL language lacks a double precision data type. Neither of these languages supported the 8087, although support software is now known to exist.

At the same time, another C compiler was obtained (Aztec C). This language offered slightly better code output than the previous C compiler product, but did not support the co-processor. Nevertheless, it offered a more complete runtime library implementation than the previous C compiler and hence was subsequently chosen for use in coding an actual problem. While the BASIC compiler system was considered as useful as Aztec C for the coding of problems, C was chosen for programming convenience.

With the extensive system software and language evaluation complete, it was possible to consider a problem to be solved. Several factors entered into the decision. The first was that the problem should be an interesting calculation in classical physics. The second was that there should be a ready means of verifying the results produced and the algorithm used.

The problem chosen for solution was a nine-body problem in three dimensions. In this problem, up to nine point masses experience mutual attraction through the gravitational force. The problem seemed sufficiently interesting, and an analogous program was available on a VAX/VMS system (in FORTRAN) for the purpose of verifying the results produced.

The coding of this example was done in C, because of the author's greater programming experience with this language. Debugging of the program was accomplished by comparing results with the VAX/VMS FORTRAN analog.

Programming in C also made it possible to test out performance with the 8087 co-processor. Roughly, the calculations proceeded at ten times the speed afforded without the co-processor. This proved significant since an example calculation with three bodies and three hundred time steps required about three point five minutes without the co-processor. It is interesting to note that on a

VAX-11/780 system under average load, the same calculation requires less than a second to complete.

It was originally intended to solved several problems in classical physics and interface IBM graphics output to them. Due to the delays, it was only possible to complete the one example and to use ASCII (text) output to illustrate a two-dimensional projection of the motion of the masses.

III. Results

The main goals of this project were to set up a microcomputer environment suitable for the solution of physics problems, to solve problems of interest, and to gauge the quality and effectiveness of available software/hardware in solving problems. In this project, we were able to complete the goals, but delays beyond our control prevented the completion of several planned software programs. Nevertheless, a great deal was learned and is presented in summary here.

In any project, there is always a potential for hardware malfunction and delivery delays. This project suffered from hardware and software delivery delays, some hardware malfunctions and some nasty bugs within IBM's software. We learned that this type of delay must be accounted for. Making the assumption that your program is incorrect and the language compiler correct is not always valid either. This leads to tremendous difficulties which can only be resolved by testing your software with more than one computer type and/or compiler product.

Figure I. is the two-dimensional projection produced by the FEQMA.C program in its example mode. In this case, only three bodies were included. They are labelled 'a', 'b', and 'c' respectively.

After running programs with and without the 8087 mathematical co-processor, it became obvious that the IBM XT is extremely slow (relative to a large minicomputer) even with the co-processor. Our example program, which was trivial for a VAX-11/780, took several minutes without the 8087. Execution time with the 8087 was more reasonable.

We were able to gauge the quality and effectiveness of the hardware and software. The hardware was essentially sound, but the software needed for scientific calculations was not that good. Standard IBM language products are, by and large, useless for this purpose. Other software required careful selection.

IV. Conclusions

The purpose of this project was not to solve a new problem in physics but to use a microcomputer to solve one or more worthwhile traditional problems. For many problems, microcomputers such as the IBM XT are suitable. However, extremely careful software selection must be performed in order to avoid painful compiler bugs, poor code generation (resulting in slow execution,) and lack of 8087 co-processor support. Additionally, efficient coding techniques must be employed. Furthermore, problems must be carefully evaluated to see if they can be reasonably handled with a microcomputer, before any coding is attempted.

We were able to solve problems with the IBM XT with reasonable speed. Delivery delays, hardware problems and language bugs notwithstanding, we solved an interesting problem and created an environment in which more sophisticated problems can be solved.

FIGURE I.

```
SCALE= 0.64E+10, DT= 0.70E+04, NOS PTS=  30.
Ma:X,Y,Z,VX,VY,VZ=  0.00E+00  0.00E+00  0.00E+00  0.00E+00  -12.      0.00E+00
Mb:X,Y,Z,VX,VY,VZ=  0.38E+09  0.00E+00  0.00E+00  0.00E+00  0.10E+04  0.00E+00
Mc:X,Y,Z,VX,VY,VZ=  0.42E+09  0.00E+00  0.00E+00  0.00E+00  0.14E+04  0.00E+00
```

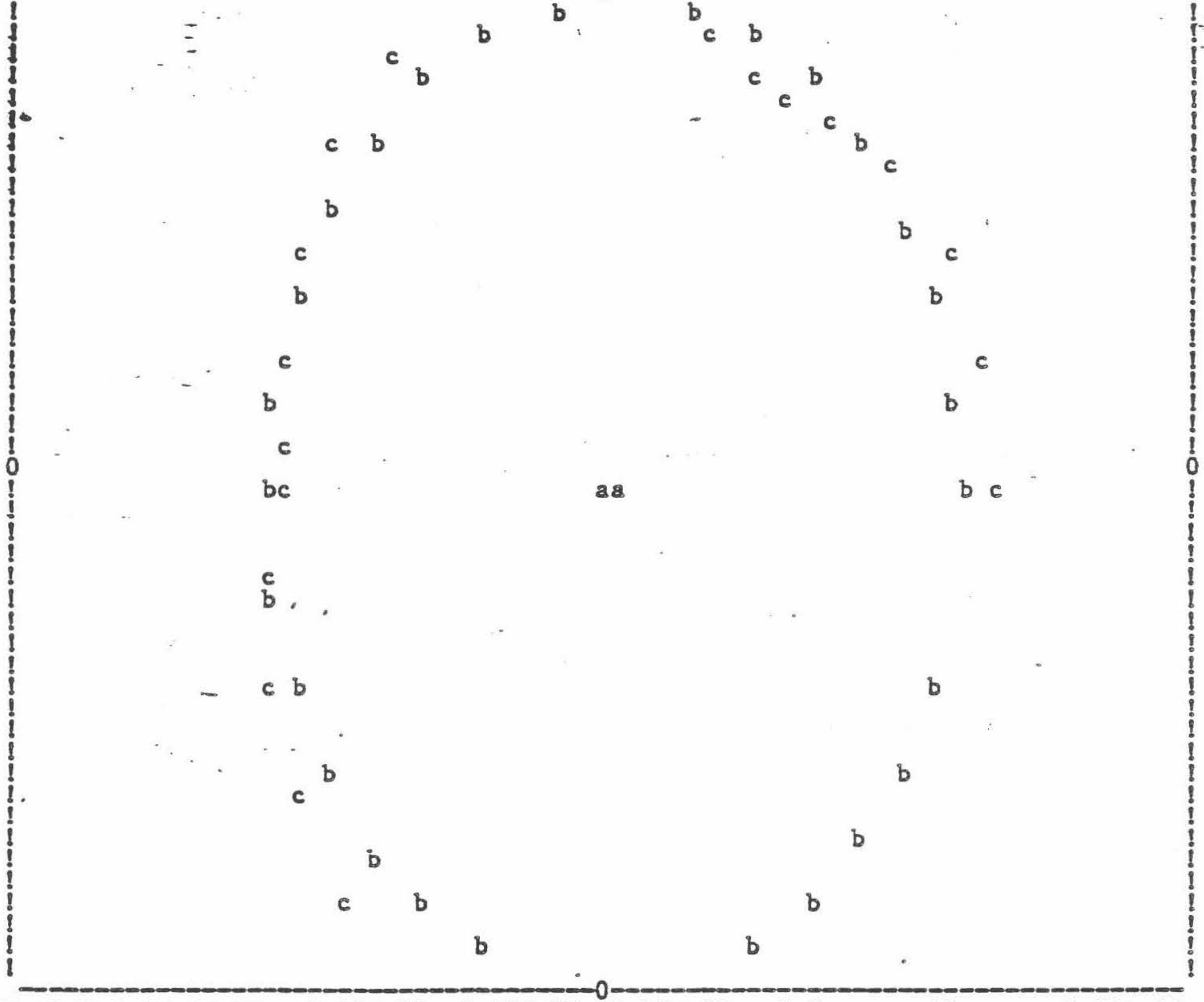

```
Ma:X,Y,Z,VX,VY,VZ=  0.39E+06  0.18E+07  0.00E+00  -4.9      -11.      0.00E+00
Mb:X,Y,Z,VX,VY,VZ=  0.35E+09 -0.14E+09  0.00E+00  0.39E+03  0.92E+03  0.00E+00
Mc:X,Y,Z,VX,VY,VZ=  0.48E+09 -0.37E+09  0.00E+00  0.90E+03  0.45E+03  0.00E+00
SCALE= 0.64E+10, DT= 0.70E+04, NOS PTS=  30.
```

Example Output Created by
FEQMA.C program.

Synthesis of Methidiumpropyl EDTA (MPE)

Teresa Solberg
Dr. Peter Dervan

Abstract

The project consisted of synthesizing a chemical called methidiumpropyl EDTA, using a series of eight reactions. The chemical consists of a DNA intercalator tethered to an iron compound which randomly breaks bonds between the base pairs of DNA. It is useful in determining bonding sites of various drugs to DNA.

Introduction

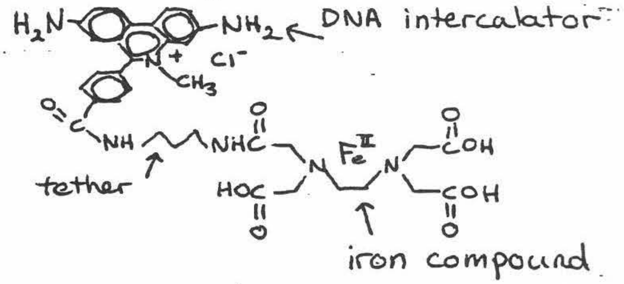

Methidiumpropyl EDTA consists of three parts as shown below. The intercalator sits between the base pairs of DNA, bringing the iron compound into close enough proximity to break the bonds between the base pairs. This is accomplished through the change in oxidation states between FeII and FeIII when added to  as shown below.

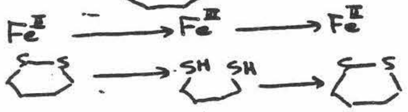

It is unknown exactly how this transition causes the bonds to break.

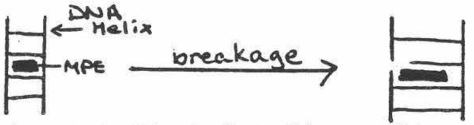

A drug is attached to a DNA helix which has been built in a predetermined way. The drugs block the MPE from working at that bonding site, since they keep the intercalator from entering. The MPE is introduced, and breaks the DNA into little pieces, except where the drug is. In this way the bonding site of the drug can be determined.

Results: Preparation of MPE

1. Distillation of 2-aminobiphenyl

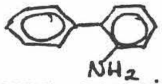

Distillation of 2-aminobiphenyl was carried out under vacuum at 129°C to remove purple and brown impurities present in the compound which was obtained from Aldrich Co.

Yield: 1rst run: 112.7 gms 2nd run: 127 gms white crystal

Impurities:  , 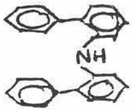

2. 4,4'-dinitro-2-aminobiphenyl

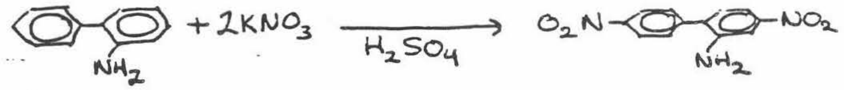

The 2-aminobiphenyl was added to sulfuric acid at 0°. The KNO_3 was added over a period of two hours maintaining temperature at 2-5°. The reaction was then stirred for 15 hrs. at 2°, poured over ice, filtered, neutralized, and recrystallized from 2-ethoxyethanol.

Yield: 1st: 103.91 gms 2nd: 150 gms orange powder

3. 4,4'-dinitro-2-(p-cyanobenzamide)biphenyl

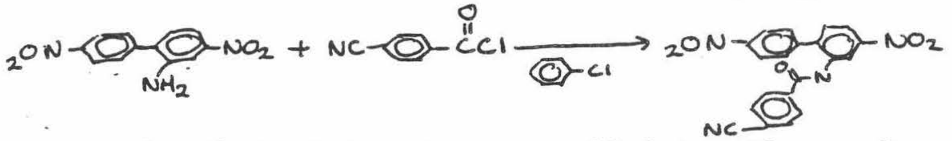

The three reagents were added together under argon, brought to reflux, and stirred for 7 hours. It was then cooled, filtered, and recrystallized from pyridine and ethanol. There was a small yield on the first try due to a blockage of the argon gas halfway through the reaction.

Yield: 1st: 72.11 gms 2nd: 143 gms yellow crystal

4. 6-(4-cyanophenyl)-3,8-dinitrophenanthridine

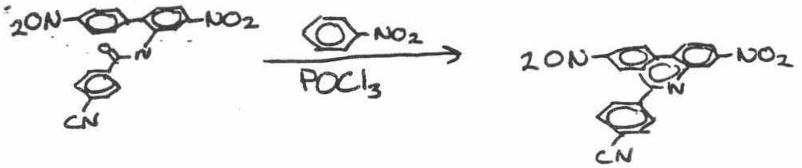

The reagents were added together under argon, brought to reflux, and stirred for 3 hours. It was then cooled, filtered, and recrystallized from nitrobenzene. This is where I got during the second try by the end of the summer.

Yield: 1st: 41.8 gms 2nd:120 gms yellow-white crystal

5. 6-(4-carboxyphenyl)-3,8-dinitro-5-methyl phenanthridinium methosulfate

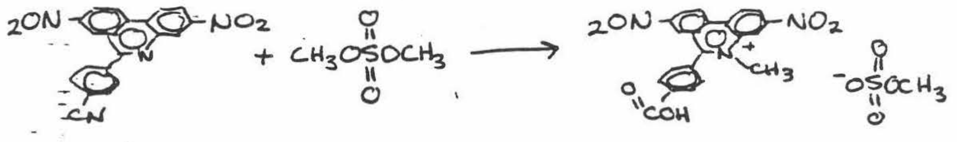

The reagents were added together and stirred at 160° for 1 hr. It was then cooled to 50°, added to water, and refluxed for 4 hrs. It was then hot filtered, cooled, and filtered again. This step is very difficult since it has never worked in the same way twice, and at this point the chemical did not come out. Various other methods were tried, according to what had worked in the past, but there was not a sufficient amount of the chemical to get through this step, so the reaction was started over at this time.

The rest of the reaction looks like this:

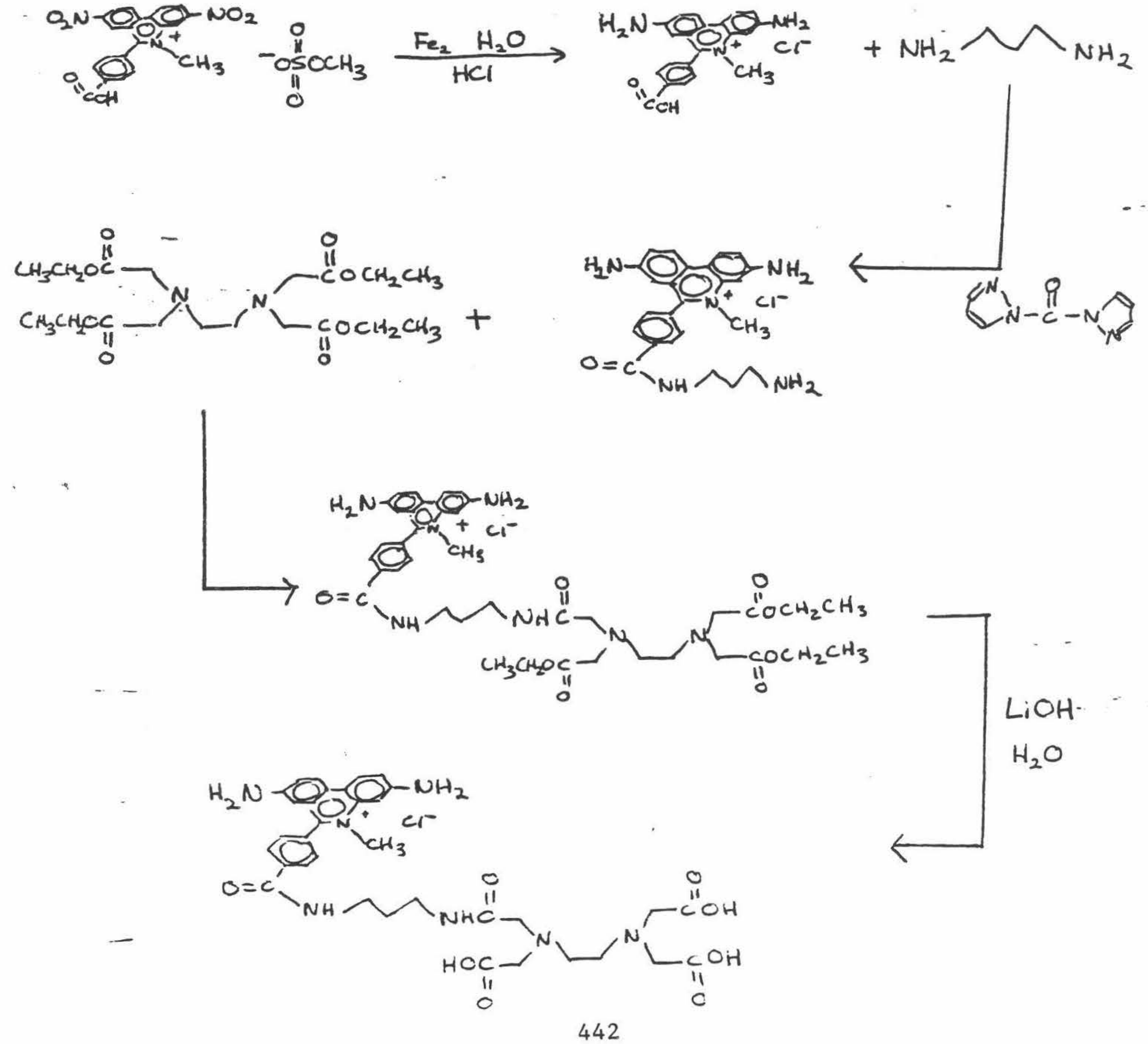

Conclusions

There are no real conclusions to be made in a project of this sort, other than that this chemical is more difficult to make than it appeared to be!

Bibliography

1. Cleavage of Double Helical DNA by (Methidiumpropyl-EDTA)iron(II) Robert P. Hertzberg and Peter B. Dervan, Journal of the American Chemical Society,1982.
2. Richard Ikeda, grad. student, Ch.

SURF 83 - FINAL REPORT

Investigation of the Feasibility of Fabricating Porous Electrodes for the AMTEC Project

Aditya Srinivasan

Faculty Sponsors: Dr. S. Khanna, JPL
Dr. J. Lambe, JPL

Abstract:

The aim was to fabricate Molybdenum electrodes (for the AMTEC project) capable of simultaneously collecting sufficient current and offering acceptable porosity to sodium ions. A CF_4 plasma etcher with 500 W, R.F. supply was built and used successfully to etch 30 to 40 micron wide fingers with 400 micron spacings in a 4 micron thick layer of Molybdenum on a beta"-Alumina substrate, this being sufficient to achieve the stated goal.

Introduction:

It would be appropriate to start with a brief description of the requirements of the Alkali Metal Thermo Electric Converter (AMTEC) project, which accomplishes direct conversion of thermal energy into electric energy with no moving parts, in a closed system. The device [also known as a Sodium Heat Engine (S.H.E.)] involves heating Sodium to 800°C in a tube of Sodium-Beta" Alumina (a ceramic) which offers a high impedence to electrons but is porous to Na+ ions. Current is collected on the outside of the tubes by electrodes of a suitable geometric configuration -- strands of Mo wire twisted around the tube collect only a small fraction of the current and offer no resistance to the diffusing sodium ions. On the other hand, deposition of a few microns of Molybdenum (Mo) film on the Na-beta"-Alumina tube using magnetron sputtering, while though more than sufficient for current collection, is not porous enough to Na atoms and does not offer the flexibility to control porosity which lithography does. The purpose of this project was to demonstrate the feasibility of depositing refractory metal such as Mo lithographically on B"Alumina to achieve acceptable current collection with sufficient porosity. The problem was complicated by the fact that the roughness of the Na-beta"-Alumina surface is of the order of microns, as should be the thickness of the Mo layer. Previous work on the AMTEC devices has indicated that a single strand of wire wrapped around the outside of the tube had an effective collection area greater than the physical collection area. This "spreading distance" of such a "line electrode" was estimated to be about 100 microns. This meant that a pattern of long thin metal fingers with large spaces between them would be suitable for current collection while allowing the required porosity. The overall purpose of this work was to see whether patterns of such dimensions could be etched through a few microns of Mo on a surface whose roughness was of the order of microns.

Discussion of Results:

The first step towards accomplishing this result was the construction of a suitable dry Plasma etcher. When Na-beta"-Alumina is exposed to water or moisture, Na is displaced from the material causing it to become structurally unstable. Consequently any process involving aqueous solutions was not acceptable (though one involving non-aqueous solutions would be). Plasma etching using a CF_4/Ar mixture was proposed. A schematic diagram of the system is shown in Figure 1. The mechanical flanges chosen to connect components in the evacuation path were of the "K-F" variety for easy and repeatable use. Following a copper trap, a main valve (A) and a fine control valve (B) were placed along with 2 thermocouple guages to monitor pressure. The etching chamber consists of a 2" o.d. pyrex tube around which two 1.5" x 3" copper electrodes were affixed. The output of a R.F. power supply (13.56 MHz) was connected across these plates. CF_4 and Ar were fed into this chamber from regulated cylinders through a needle valve facilitating very fine flow control. The R F generator was composed of three stages. The first stage consisted of the dc power supply and main switches. The second stage comprised a Colpitts oscillator, buffer and output stage while the third was an optional control box with remote control capability and a VSWR trip switch and alarm. A photograph of the dry etching facility is shown in Figure 2(a).

Preliminary etching tests were performed on 800 A° Mo, deposited by magnetron sputtering on a glass substrate. Patterns of 1/2 mm interspaced lines were deposited lithographically on the sample by using spin-deposited positive photoresist followed by a 15-second exposure to ultra-violet radiation through the pre-fabricated mask. The resist was then developed and hardened and the sample placed in the etcher. Etching took five minutes with the chamber at 250 microns and incident power (Pi) = 100W, reflected power (Pr) = 20W. The pattern was successfully transferred. Subsequently, samples of magnetron sputter-deposited Mo of 0.1 micron thickness on beta"-Alumina substrates were etched with no superimposed pattern to determine the etching time required. Table 1 shows the typical values of gas pressure, power and the etching time.

Table 1

S.No.	Gas Pressure µm	Incident Power Watts	Reflected Power Watts	Etching Time Min.
1	400	50	3	5
2	150	55	29	17
3	60	150	40	4

Finally, a mask was designed with alternating 28 and 40 micron-wide lines separated by 400 micron spacings and transferred onto 4 micron-thick Mo on a beta"-Alumina substrate. Etching of this pattern at a chamber pressure of 500 microns, Pi = 90W, Pr = 20W took 35 minutes. The samples were studied by Scanning Electron Microsopy (SEM). Figure 2(b) shows a typical SEM photograph of plasma etched lines on alumina.

The roughness of the surface is extreme as can be seen in Figures 2(c) and 2(d), and is of the order of microns, and because of the surface roughness the edges of the 4-micron Mo layer cannot be clearly seen. However, the clarity of the etched pattern is evident. Some residual Mo is visible in small disjoint patches and in one instance a fragment of photoresist which has reacted in the CF_4 plasma and so become insoluble in acetone is also observable.

Conclusions

In conclusion, these results indicate that lithographic fabrication of Mo electrodes a few microns thick on rough Na-beta"-Alumina substrates is feasible. A full size mask (1.5" x 3") with 30 micron lines and 300 micron spacings has been prepared and will be etched on a Na-beta"-Alumina tube coated with Mo. Consequently, it is feasible to fabricate lithographically metallic electrodes for the AMTEC project which are capable of collecting sufficient current and achieving the necessary porosity to Na ions.

Bibliography:

1. Thin Film Processes: John L. Vossen, Werner Kern. AP, 1978.

2. "Plasma etching and Reactive Ion Etching:" J. W. Coburn. American Vacuum Society, 1982.

3. "Plasma etching of sputtered Mo and $MoSi_2$ thin flims in NF_3 gas mixtures:" T.P. Chow, A. J. Steckl. J. Appl. Phys. Vol. 53, No. 8, Aug. 1982.

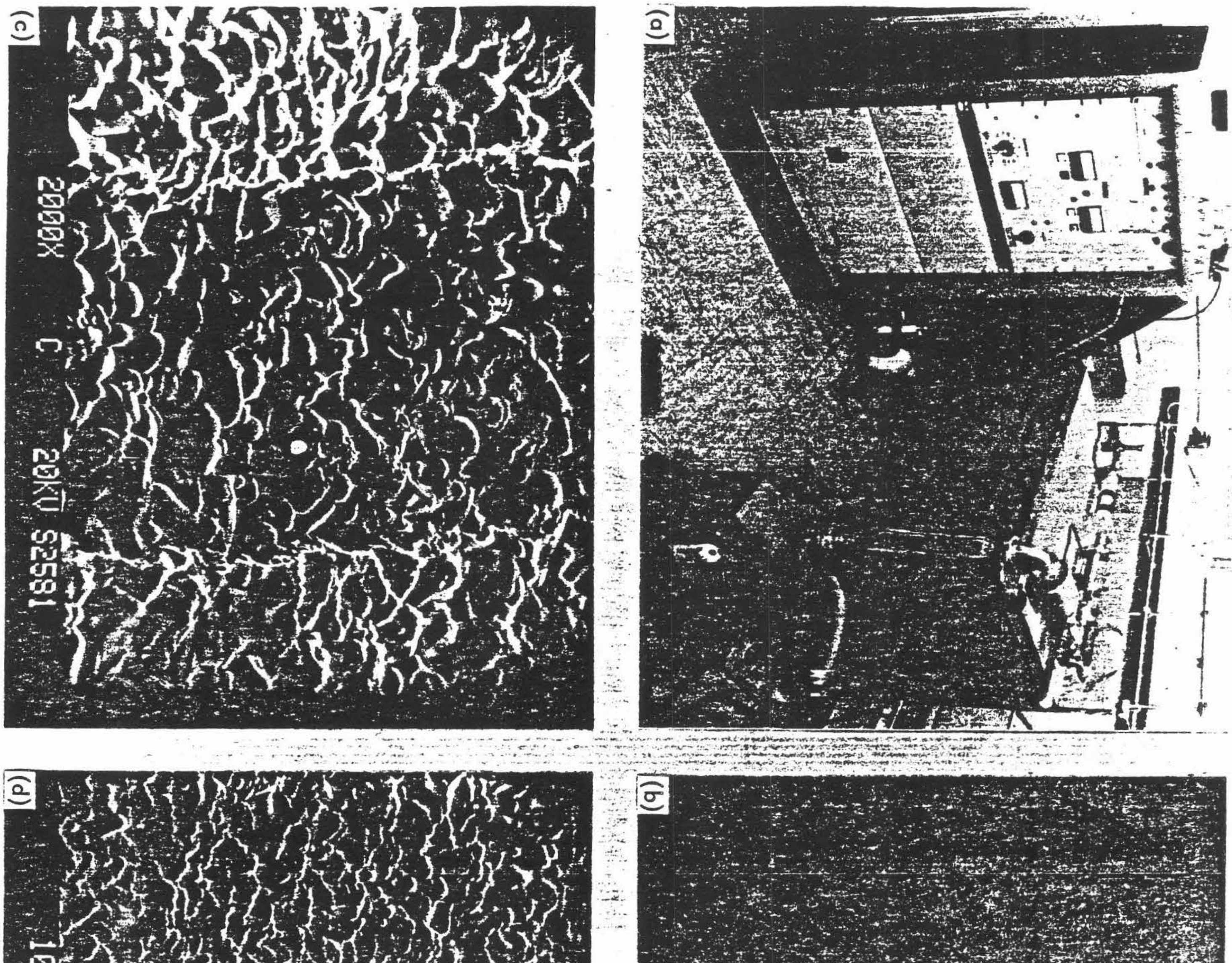
(a)
(b)
50X C 20KV S2581
(c)
2000X C 20KV S2581
(d)
1000X C 20KV S2581

Schematic of Plasma Etcher.

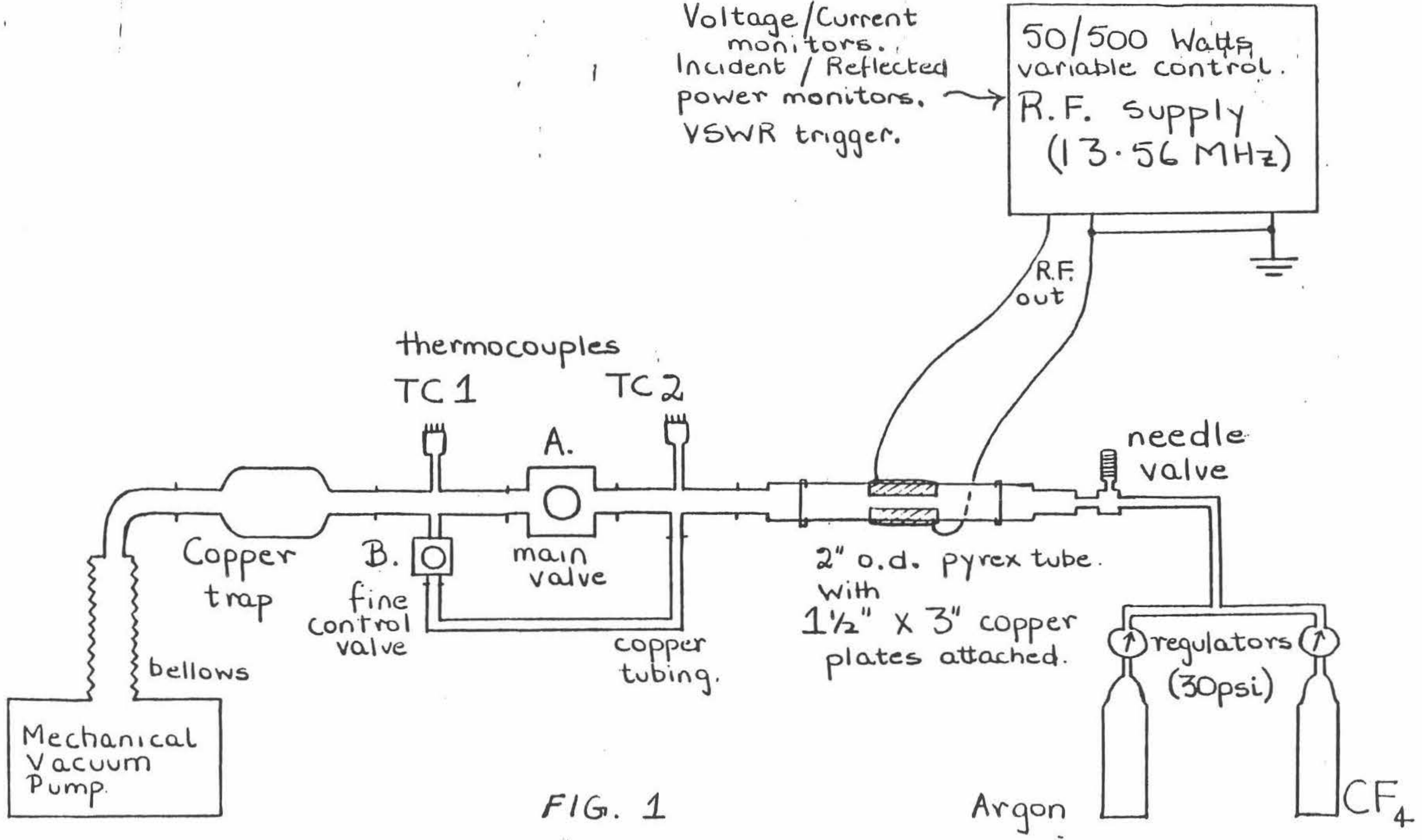

FIG. 1

A Method of Creating Three-dimensional Computer Generated Holograms

Clare W. Stassen
Faculty Sponsor: *Demetri Psaltis*
California Institute of Technology
Pasadena, CA 91125
Submitted September 2, 1983

ABSTRACT

Calculations of three-dimensional Fresnel computer-generated holograms are demonstrated and, with advancing technology, are shown to be potentially commercially feasible in the near future. Applications to computer-aided design are a possibility.

Introduction

This report will focus on methods of calculating holograms of three-dimensional objects. Generating holograms digitally was first demonstrated by Brown and Lohmann[1] in 1966. The holograms they created were Fourier-transform holograms, and the image that they formed upon "reconstruction" was two-dimensional. Computer generated Fresnel holograms (Fresnel CGH's) were largely ignored due to the great complexity of the Fresnel calculations when compared with the great simplifications that the Fraunhofer approximation afforded. Fourier-transform CGH's found such applications as pattern recognition, testing of aspheres, and coherent optical data processing. Some tried to adapt the Fourier-transform method to creating holograms of three-dimensional objects, but the best that could be produced was planes of two-dimensional objects. The CGH of a solid object, or a line drawing, could not be computed that way.

The possibility of three-dimensional display of objects that may or may not physically exist can create some very interesting possibilities, and attempts were made to create such holograms.[2] These CGH's were clumsy to make, however, and did not become as good as had been hoped. Back in 1966, another researcher published a method of making CGH's that has been largely overlooked since then.[3] Waters showed in this paper the "reconstruction" of a CGH of a fully three-dimensional tetrahedron. Keeton published a paper a year later that used a method similar to that of Waters to create a CGH on a line printer![4] I plan to show in this paper that the method of Keeton can be used with today's technology to create a three-dimensional image that is quite viable.

Method for calculating the CGH

Suppose we have a hologram plane located in the $x-y$ plane at $z=0$, and an object with amplitude distribution $F(x,y,z)$ on its surface located in the $+z$ direction. The electromagnetic disturbance E at the hologram plane is given by:[5]

$$E(x,y) = \frac{-i}{2\lambda}\iint_{-\infty}^{\infty} F(x_0,y_0)(1+\cos\vartheta)\frac{e^{ikr}}{r}dx_0dy_0 \quad (1)$$

This calculation can be simplified a great deal if we assume we are dealing with a collection of point sources. The integrals become a sum, and the possibility of calculating this sum on a computer becomes conceivable. Let us look at a collection of N point sources. If $\mathbf{r}$ is a point in the plane, and $\mathbf{r}_j$ is the distance from an object point to $\mathbf{r}$, then

$$E(\mathbf{r}) = A(\mathbf{r})e^{i\varphi(\mathbf{r})} = \sum_{j=1}^{N} A_j e^{ik\mathbf{r}_j} \qquad (2)$$

is the field at the hologram plane. Solving for $\varphi(\mathbf{r})$ and $A(\mathbf{r})$ gives the following equations:

$$\varphi(r) = arctan\left[\frac{\mathbf{sinsum}}{\mathbf{cossum}}\right]. \qquad (3a)$$

$$A(r) = \sqrt{\mathbf{sinsum}^2+\mathbf{cossum}^2}. \qquad (3b)$$

where

$$\mathbf{sinsum} = \sum_{i=0}^{N} sin(kr_i);\ \mathbf{cossum} = \sum_{i=0}^{N} cos(kr_i).$$

These are the basic equations used to create the 3-d CGH. Both Waters and Keeton have shown that the phase information $\varphi(\mathbf{r})$ is sufficient for creation of the desired image. However, if Lohmann-type or Lee-type[6] cells are desired, one needs the amplitude information also. Using the Keeton method, only the phase need be plotted, as black when $cos(\varphi)<0$ and white otherwise (or vice versa). Keeton introduced this method to be used on line printers, whereas most other methods worked on pen plotters. Keeton's method is more suited to a raster plotter which is useful since it is desired to output these plots on a Versatec plotter.

Results of This Method

The actual details of the technique as I have carried it out are as follows: The computer used was the VAX 11-780 of the Computer Science Department at Caltech. This computer was given a file describing the location of several point sources (as many as 31 were given) in relation to the hologram plane. The phase was calculated for every point on a 2112x2112 pixel hologram. Computations took on the order of a few hours of CPU time on the VAX (ran as batch jobs at night). This was plotted in binary fashion on the Versatec on continuous roll paper to allow plots that were 10.5x10.5 inches. (The Versatec has a resolution of 200 dots per inch and prints much faster than any pen plotter trying to plot a similar amount of data.)

The Versatec plots were then photographed onto Kodak Technical Pan Film (35mm) and developed for maximum contrast. The physical size of the CGH after this photoreduction varied from 1 to 2 cm. A He-Ne laser with collimating lenses was used to illuminate these CGH's, and quite satisfactory results were achieved. As a test, a zone plate was made — being the binary CGH of a point source, and it worked beautifully (fig. 1). Other test runs were made: 9 point sources arranged at the corners of a cube with one source in the center were observed to appear as if they were positioned behind the piece of film and shifted perspective appropriately as the angle of viewing changed (fig. 2); 31 point sources positioned along the 4 diagonals of a cube also seemed to work fine, except that some point sources were positioned too close to the plane of the hologram and could not be resolved (fig. 3). It appears that the resolution of the plot was not enough to display those close points.

The holograms that were made were in-line holograms, and thus had real images located along the axis in front of the CGH. These images were observed to be quite sharp, and distinctly separated in space. One CGH curiosity was made; it was a zone plate that had been split in two, separated and the pattern connected so that lines of constant phase had the shape of a track (like a jogging track perhaps?). This CGH (fig. 4) would form the real image of a line parallel to the plane of the hologram, but only looked like a point source with a streak through it when the virtual image was viewed.

Conclusions

The Keeton/Waters method of calculating Fresnel CGH's has been shown to be much more viable than when it was first investigated. The resolution now available in plotters, and the raster pattern rather than vector plotting both contribute greatly to the feasiblity of this method. There are two things, that are now being worked on at various places that, if they are perfected, could lead to this method being useful for creating CGH's for computer-aided design or the like.

The first useful advance, already in very limited use (by a team of researchers at Stanford[7] among others), is adapting the e-beam lithography that is currently used for creating VLSI integrated circuits to use as the plotter of the CGH. This method has tremendous advantages, since it can plot the CGH at the desired size. There is no need for further reduction, which is one of the major problems that computer-generated holography has always faced.

The other advance is that of computer architecture. Parallel processors can perform the simple calculations on huge arrays of data, and the time factor in computing the CGH can go way down. The points on a hologram are essentially independent from one another, since it is possible to determine whether a pixel should be black or white without knowing anything about the neighboring pixels. The lack of any need to communicate between cells (pixels) on the hologram will make this method much faster than the other processes that physicists are contemplating using parallel processors for.

The method invented by Case and Dallas[8] to convert a CGH into what they call a CGVH (a computer-generated volume hologram), can be used to make a CGH that can be viewed in white light. This technique, along with the two technologies described above that should soon be realized, will make possible realistic use of the CGH for three-dimensional display purposes such as computer-aided design (CAD) or for the illustration of complex organic molecules without the need to build bulky and awkward models.

Acknowledgements

I would like to thank Dr. Psaltis for his help and support, and Jim Campbell for his help in arranging for SURF students to use the CS-VAX.

References

1. B. R. Brown and A. W. Lohmann, "Complex Spatial filtering with Binary Masks," *Appl. Optics*, **5**, pp. 967-969, June 1966.
2. M. C. King, A. M. Noll, D. H. Berry, "A New Approach to Computer Generated Holography," *Appl. Optics*, **9**, pp. 471-475, June 1966.
3. J. P. Waters, "Holographic Image Synthesis Utilizing Theoretical Methods," *Appl. Phys. Letters*, **9**, pp. 405-407, Dec. 1966.
4.

S. C. Keeton, "A Sampled Computer-Generated Binary Hologram," *Proc. IEEE*, **56**, pp. 325-327, March 1968.

5. H. M. Smith, *Principles of Holography*, New York: Wiley, 1969.
6. W. - H. Lee, "Sampled Fourier Transform Hologram Generated by Computer," *Appl. Optics*, **9**, pp. 639-643, March 1970.
7. G. L. Freyer, R. J. Perlmutter, J. W. Goodman, "Digital Holography: Algorithms, e-beam Lithography, and Three-Dimensional Display," 1983 International Conference on Computer Generated Holography (SPIE), San Diego, CA, Aug 25 1983.
8. S. K. Case and W. J. Dallas, "Volume Holograms Constructed from Computer Generated Masks," *Appl. Optics*, **17**, pp. 2537-2540, Aug. 1978

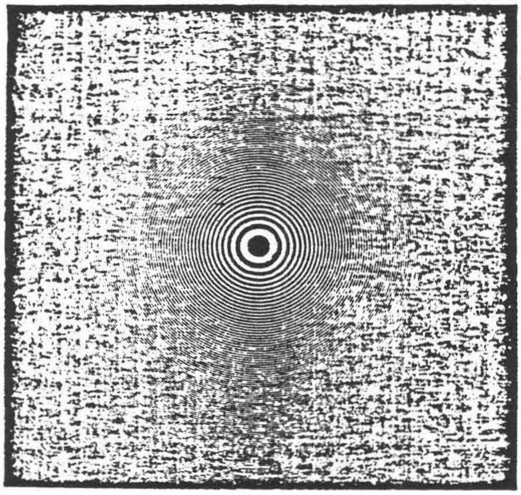

Figure 1

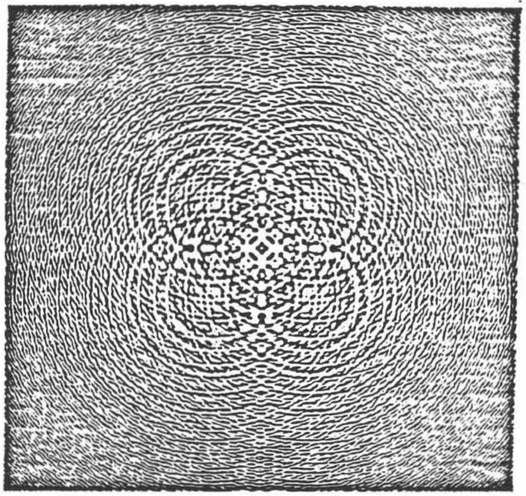

Figure 2

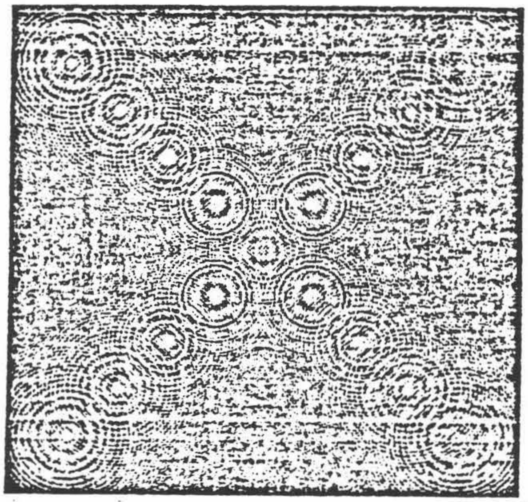

Figure 3

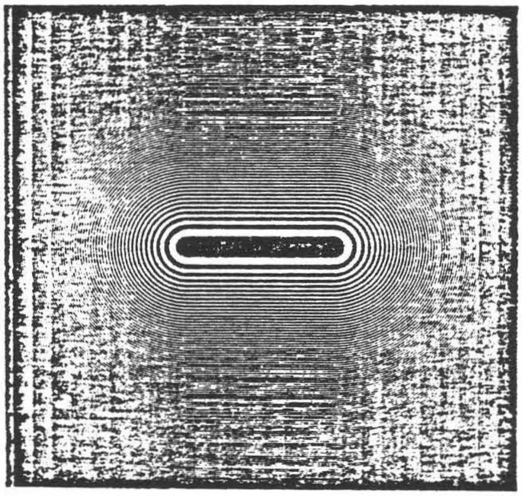

Figure 4

Investigator: Eliza L. Sutton
Advisor: Peter B. Dervan
September, 1983

Manipulation of DNA in Intact Phage

I. Crosslinking in T7 II. Cleavage in λ

I. A method for probing viral DNA structure by crosslinking selects for mutant viruses in T7. II. Sequence dependent cleavage of λ DNA inside and outside the viral head by a synthetic cutting agent is examined.

I. The higher order structure of DNA packaged in viruses remains largely a mystery, due both to the size and very dense packing of the nucleic acid and to the protective protein coat. Standard optical techniques have failed to give any definitive structure, although they do indicate that the packaging is ordered (1). Models have been proposed (1,2), but until recently no method existed to support or disprove these models.

Last year a method was described for probing the packaging of DNA in viruses (3). Bis(monoazidomethidium)octaoxahexacosanediamine (BAMO), a DNA-DNA crosslinker designed and synthesized by the Dervan group at Caltech (4), is introduced into the intact phage through the protein coat; the protein is then disrupted and the position of the crosslinks in the DNA mapped to show which regions neighbor each other in the intact phage. The protocol had been worked out for samples of T7 and λ phage.

Work since last summer, however, has indicated that the initial sample of T7 used to determine the protocol and to to gather data contained only about 90% wild type T7. The other 10% was mutant T7 with about 10% of its DNA missing. Deletion mutants seem to be more loosely packaged than wild type viruses and seem to take up invasive molecules like BAMO more easily (5). In addition, crosslinked wild type DNA runs as a smear on a preparative agarose gel, while mutant DNA concentrates in discrete bands. The crosslinking procedure, then, <u>selects</u> for the <u>mutant</u> viral DNA.

A new sample of T7 was grown up, determined to be wild type, and used this summer to correct the conditions for mapping. Compilation of an interhelical nearest neighbors map of wild type T7 should now be possible.

II. Restriction endonucleases are enzymes which recognize specific 4-6 base pair sequences in DNA and cleave at these sites. No artificial cutter has yet been made which cleaves DNA with as high specificity as enzymes, but a few do recognize, bind to, and cleave at fairly discrete sites. Penta-N-methylpyrrolecarboxamide-EDTA•Fe(II) (P5E; Figure 1) was designed and synthesized in the Dervan group and is one such molecule (6). P5E, an iron chelator attached to a pentapeptide, recognizes strings or 5-6 or more adenines (A) and thymines (T) and, in the presence of oxygen and dithiothreitol, cleaves the DNA at these sequences. Hydrogen bonding between the amide N-H of P5E and the O(2) of T or the N(3) of A is probably the cause of P5E's binding to these regions (7). Research this summer examined cleavage of λ DNA by P5E both inside and outside the protein head.

The plasmid pBR 322 has 4362 base pairs and is cleaved specifically at two sites by P5E to yield discrete fragments (6). In contrast, λ is 48,502 bp long and contains about 300 sequences of 5 A's and T's and 500 sequences of 6 or more. Because of the multitude of P5E cleavage sites, λ DNA run on an agarose gel appears randomly cut. Some structure does appear from cleavage of naked DNA, however; banding shows that some areas of the DNA have high frequencies of AT strings. Examination of the entire DNA sequence of λ (8) suggests this is true (Figure 2). P5E can enter the viral head and cleave the DNA inside the intact protein coat; however, in addition to lower overall levels of cutting (which are expected), less cleavage seems occur at the "hot spots" than in naked DNA. Conformation changes in the DNA or burial of those areas deep in the DNA packaged structure could explain this phenomenon.

P5E, a small organic molecule, can perform a feat no enzyme can: it can enter an intact virus and cleave the DNA. P5E does cleave DNA inside and outside the head differently, and while this might indicate that pieces of the DNA are hidden within the packaged genome, P5E seems to cut λ DNA in too many places to be an effective tool for studying the virus.

Figure 1

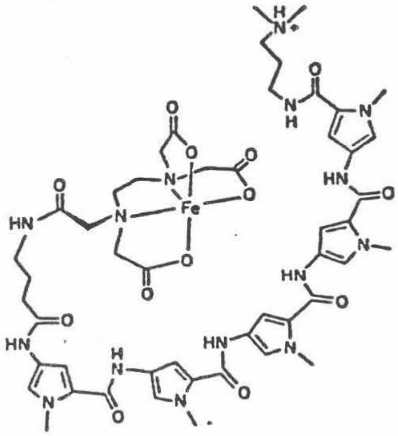

P5E·Fe(II)

References

(1) Earnshaw, W.C. and S.C. Harrison, Nature, 268, 598 (1977).

(2) Kosturko, L.D., M. Hogan, and N. Dattagupta, Cell, 16, 515 (1979). Kilkson, R. and M.F. Maestre, Nature, 195, 494 (1962). Richards, K.E., R.C. Williams, and R. Calendar, J. Mol. Biol., 78, 255 (1973).

(3) Sutton, E.L. and P. B. Dervan, Summaries of SURF Seminar Presentations, 313 (1982). Mitchell, M.A., Ph.D. Dissertation, California Institute of Technology, 1983.

(4) Mitchell, M.A., and P.B. Dervan, J. Amer. Chem. Soc., 104, 4265 (1982).

(5) Hall, S.B. and J.A. Schellman, Biopolymers, 21, 2011 (1982).

(6) Schultz, P.G., and P.B. Dervan, Proc. Nat. Acad. Sci., in press.

(7) Zasedatelev, A.S., A. L. Zhuze, C. Zimmer, S.L. Grokovshy, G.V. Tumanyan, G.V. Gursky, and B.P. Gottikh, Dokl. Acad. Nauk. SSSR, 231, 1006 (1976). Krylov, A.S., S.L. Grokhovsky, A.S. Zasedatelev, A.L. Zhuze, G.V. Gursky, and B.P. Gotthik, Nucleic Acids Research, 6, 289 (1979).

(8) Sanger, F., A.R. Coulson, G.F. Hong, D.F. Hill, G.B. Petersen, J. Mol. Biol., 162, 729 (1982).

Figure 2

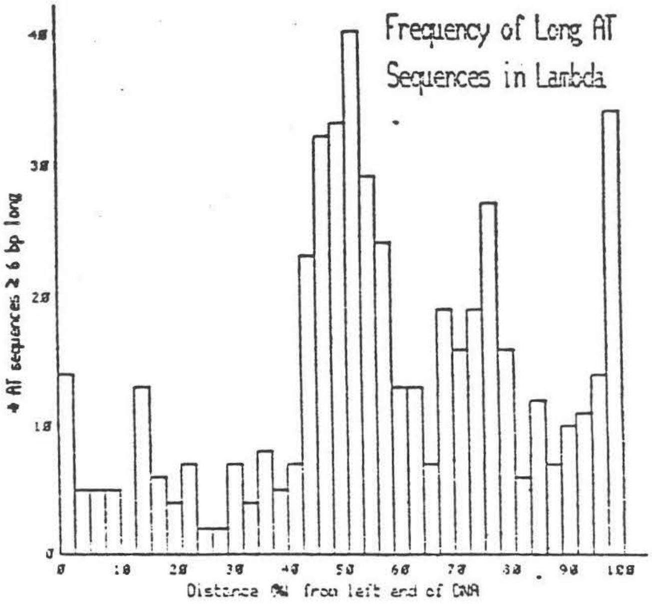

Near-Earth and Non-main Belt
Asteroid Search and Survey

by

Steven R. Swanson

Sponsored by: E. F. Helin (J.P.L.)

The Planet Crossing Asteroid Survey looks for unusual asteroids with orbits that cross inside those of Mars and/or Earth. The search is conducted with the 48" Schmidt telescope at Mt. Palomar and the 18" Schmidt telescope, also at Mt. Palomar. Finding these special asteroids is important in many ways, including the search for possible spacecraft mission candidates. This summer, we found two Earth-crossing asteroids and one Mars-crosser. Bringing the total number of Earth-crossing asteroids to 55.

Introduction

The search for near-Earth asteroids has only been really going well for the past decade. There was a large increase in the number of discoveries during the 1970's. However, the discovery has been slowing down recently. There are three types of near-Earth asteroids. Apollo asteroids have orbits which regularly cross inside the Earth's orbit. As of May 1983, there were a total of 31 Apollo asteroids known. The other two types are "Atens" and "Amors". Aten asteroids have orbits which are completely within the Earth's orbit. Thus, they never actually "cross" the orbit of the Earth. The other type, Amors,are asteroids which cross inside of Mars' orbit, but do not cross Earth's regularly. However, not all Mars crossers are of the Amor type. The classification is determined by the "perihelion" distance. The distance from the sun at closest approach. If the perihelion distance is less than 1.3 astronomical units (AU), then it is an Amor. It is possible for an Amor to be classified as an Earth-crosser. Some Amors are affected by planetary perturbations which cause there orbits to occasionally cross the Earth's. Once an orbit is determined, it is projected forward and backward abot 700 years in time. Planetary perturbations are included, and if it comes in close enough, it is classified as an "Earth-crossing Amor". The number of Amors, as of May 1983 was 33 and the number of Atens is only 4. Currenly, the total number of all asteroids known is about 5000. Thus, the 68 near-Earth asteroids comprise less than 1.5% of all asteroids.

The purpose of my project was to assist in the search for these unusual object in various capacities. These included two trips to Mt. Palomar to use the 18" Schmidt telescope. Also, the inspection of plates taken with the 48" Schmidt telescope. Another goal was to learn a computer language in order to make use of newly aquired computers. And to write useful scientific programs to speed up the data reduction needed in determining the orbits of the asteroids.

Presentation and Discussion

The search and survey program is done using photographic plates taken at Mt. Palomar. The method using the 48" Schmidt involves taking a 40 minute exposure on a 14"x14" plate, then the shutter is closed for 10 minutes, and then reopened for another 10 minutes. This type of exposure is called "gated". The asteroid is then seen as a long streak followed by the shorter one. This is done in order to distinguish faint trails from galaxies and to determine the direction of motion. The other telescope used (the 18") uses a different method. The 18" Schmidt had a larger field af view (about 50 sq. degrees as compared with 36 sq. degrees for the 48") but it has a smaller plate size (6"). Thus long exposures cannot be used, since by the time the trail was significant, the plate would be fogged by over-exposer. Therfore, what is done is that a set of 4 different fields are taken with 4-5 minute exposures each. Then the series is repeated. This gives a pair of identical fields separated by 30-45 minutes. The asteroids are then detected by viewing both plates simultaneously through a stereoscopic viewer. And while the stars will remain unchanged, the asteroid will appear as a pair of slightly shifted points.

It was while scanning a plate taken with the 48", that I found an asteroid with a motion of 1.4° per day. The plate was taken on the note of June 12. Also, on the same plate, my advisor, E. Helin, found an asteroid moving at 0.8° per day. The faster one was given the designation 1983 LB and the second became 1983 LC. Since the plate was taken on the last nite of the observing run, it was not till J. Gibson provided follow-up observations that an orbit was determined a few days later. It was found that 1983 LB was an Earth-crossing Amor with a highly inclined orbit. And by mid-August, it had quickly moved south to a declination of -85°. 1983 LB passed within 29 million miles of the Earth.

1983 LC was an Apollo asteroid. It's motion speeded up after discovery until it was moving 8-9° per day. On July 6, 1983 LC passed within 5.9 million miles of Earth at a speed of roughly 80,000 m.p.h. It is suspected that the orbit of 1983 LC is unstable because of perturbation effects caused by Jupiter. The discovery of two Earth-crossing asteroids on the same photographic plate is unprecedented. In addition, these discoveries ended six month period during which no near-Earth asteroids were found anywhere in the world.

Next, during a run on the 18" Schmidt at Palomar, on August 7, A. Graps and myself found 1983 PA. This asteroid was determined to be a Mars-crosser. But it does not come in close enough to make it an Amor. It was a bright asteroid and was observed with photometry by other observatories.

The following chart gives the orbital data for these three asteroids. "a" is the semi-major axis in A.U.s, "e" is the eccentricity, "i" is the inclination, "P" is the orbital period, "q" is the perihelion distance in A.U.s, and "T" is the date at which it reaches perihelion.

	1983 LB	1983 LC	1983 PA
a	2.3101	1.7828	2.2345
e	0.4826	0.5456	0.3493
i	25°.510	01°.264	19°.054
P	3.51yr	2.38yr	3.34yr
q	1.1952	0.8102	1.4539
T	Aug 2	Aug 19	Oct 26

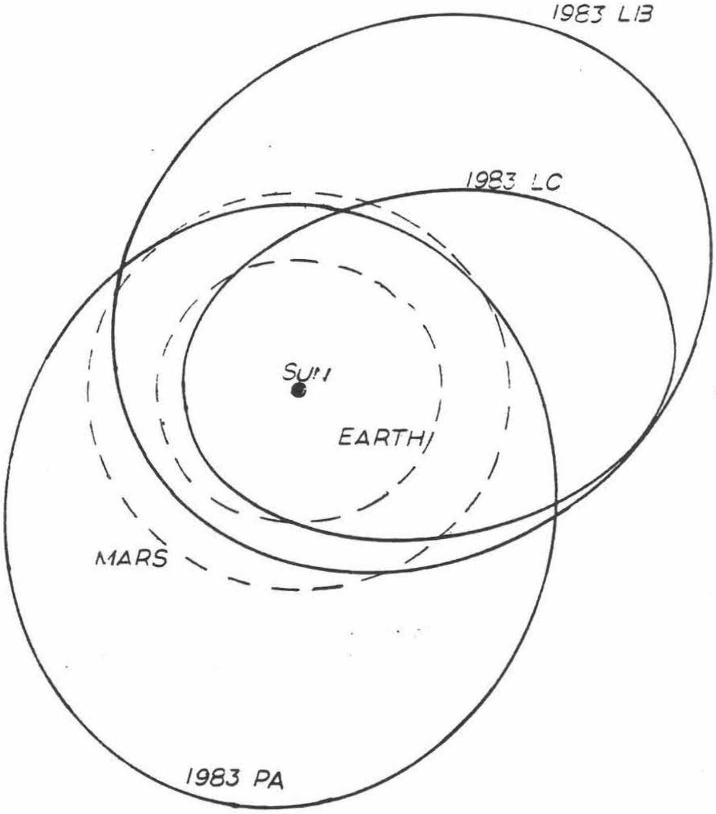

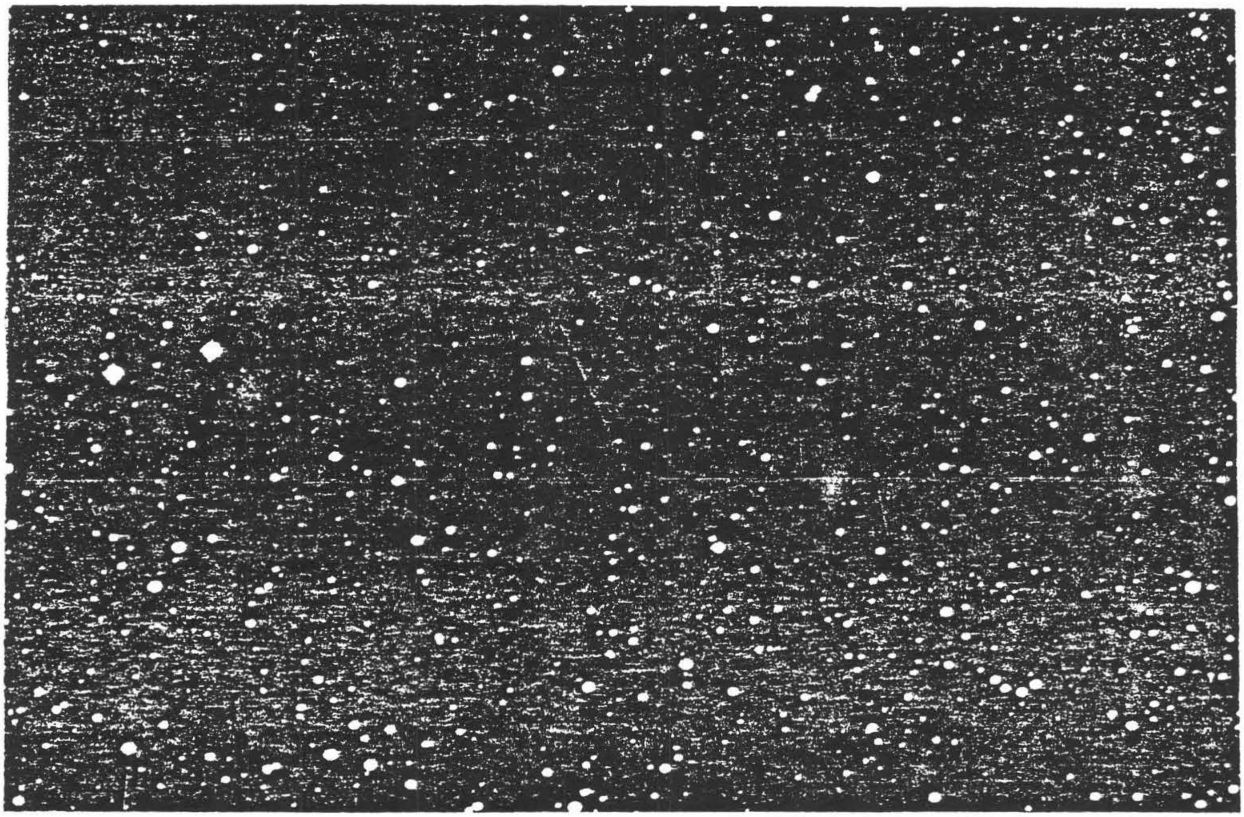

Discovery Photo of 1983 LB

Conclusion

There are two major reasons for searching for near-Earth asteroids. One is trying to find possible rendezvous mission candidates. Spacecraft missions to asteroids would yield valuable information about the composition of the early solar system. Since the material in asteroids have not been subjected to the geological evolution found in larger planets. Plus a retrieval mission could supply many valuable raw materials. The reason is to determine the population statistics to an accurate degree. This would give us a better understanding of the impact rates on the inner planets.

References

"Asteroid Issue"; Planetary Report; July/Aug. 1983, Vol. III No. 4

E. F. Helin, R. S. Dunbar, S. R. Swanson; "Two Near-Earth Asteroids, Apollo 1983 LC and Amor 1983 LB"; American Astronomical Society Abstract for 1983 D.P.S. meeting.

E. F. Helin, R. S. Dunbar, S. R. Swanson; "Discovery of Two Near-Earth Asteroida, Apollo 1983 LC and Amor 1983 LB"; Earth and Space Sciences Division, Scientific and Technical Achievements; 1 April - 30 June 1983; NASA,JPL.

E. F. Helin, E. Shoemaker, R. S. Dunbar; "Palomar Asteroid Search Program"; JPL Highlights 1983; JPL July 1983

B. Marsden; International Astronomical Union; "Astrograms", #3828, June 17, 1983; #3829, June 24, 1983; #3839, July 18, 1983; #3836, July 5, 1983; #3853, August 17,1983; Smithsonian Astronomical Observatory, Cambridge, MA

"JPL Team Sights Close-Approach Asteroid"; JPL Universe; July 15, 1983; Vol. 13; No. 26.

THE STUDY OF THE PERMEABILITY CHARACTERISTICS OF CORDIERITE CERAMICS AND POLYMER MEMBRANES

By

Christine Tiller

Sponsor: Professor G. Stephanopoulos

ABSTRACT:

The main objective of my project was to study the permeability characteristics of materials which might be used in the structure of bioreactors to facilitate simultaneous product formation and separation. Although my research is not yet complete, an experimental procedure has been developed and preliminary studies have been made of Cordierite ceramics and polymer membranes.

INTRODUCTION:

My project is just one part of an effort to develop a process which will make possible continuous, simultaneous product formation and separation in bioreactors. A cross-flow monolithic structure will be used for the reactor. The channels in one direction will be populated by microorganisms immobilized in a polymeric gel by adsorbtion, cross linking or entrapment. The feedstream will flow through these channels bringing nutrients to the microorganisms. The product will diffuse through the walls and be removed by a solvent stream flowing through the channels in the other direction.

The particular process under consideration is the production of ethanol by immobilized *Saccharomyces cerevisiae*. Air will be used as the solvent.

An important part of this research is the development of a wall material which is preferentially permeable to ethanol. Cross-flow monoliths can be made from Cordierite ceramic. A way must be found to modify this ceramic so that it will selectively allow ethanol to pass through but will withhold water and the other nutrients and wastes.

PRESENTATION AND DISCUSSION OF RESULTS:

The main component of my experimental setup is a National Bureau of Standards cell. With a ceramic plate clamped between the two halves of the cell, air can be circulated above and below and 10% ethanol water solution through the channels of the ceramic, thus approximating the conditions that would exist inside a cross-flow monolith reactor (See Figure 1). Figure 2 illustrates the experimental setup. The ethanol solution is circulated using a peristaltic pump and a gravity feed system to ensure a steady flow

Figure 1 Actual size illustration of one half of the 6 X 4 X 2.25" assembled NBS cell in cross-section

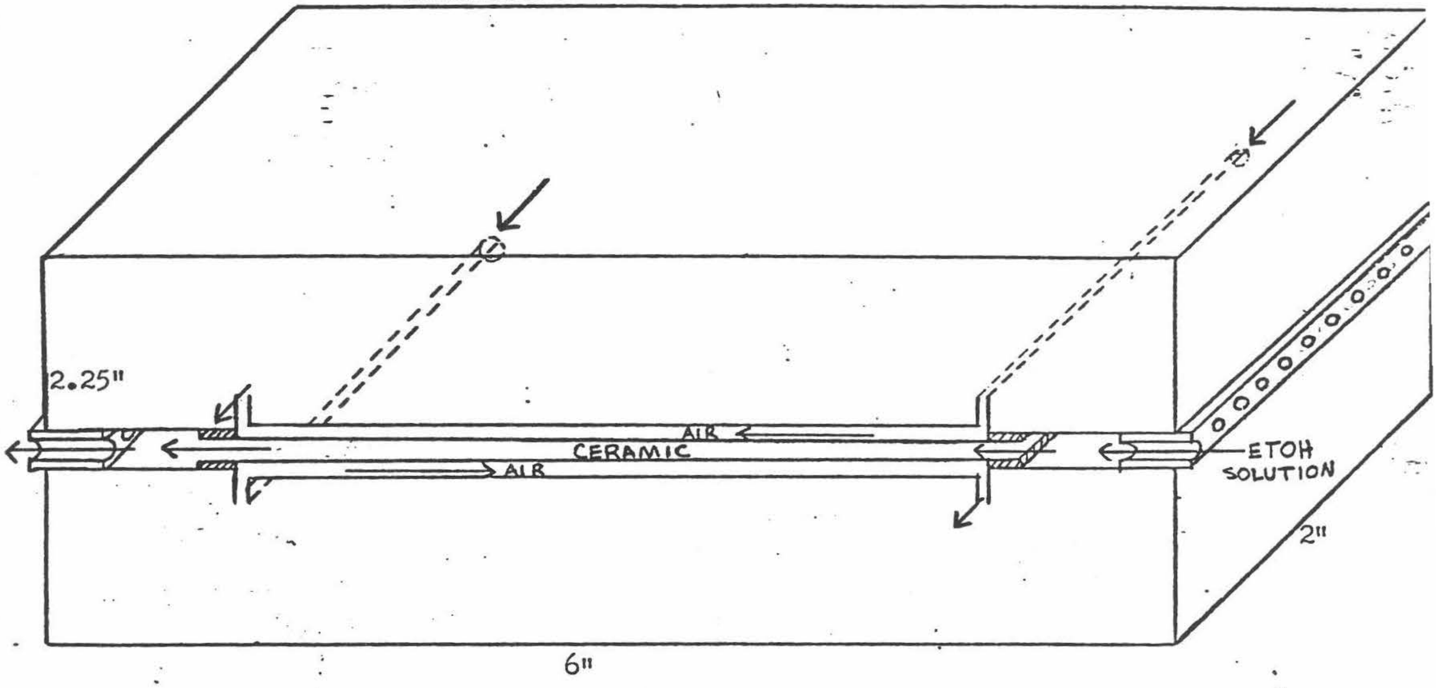

Figure 2 The experiment setup

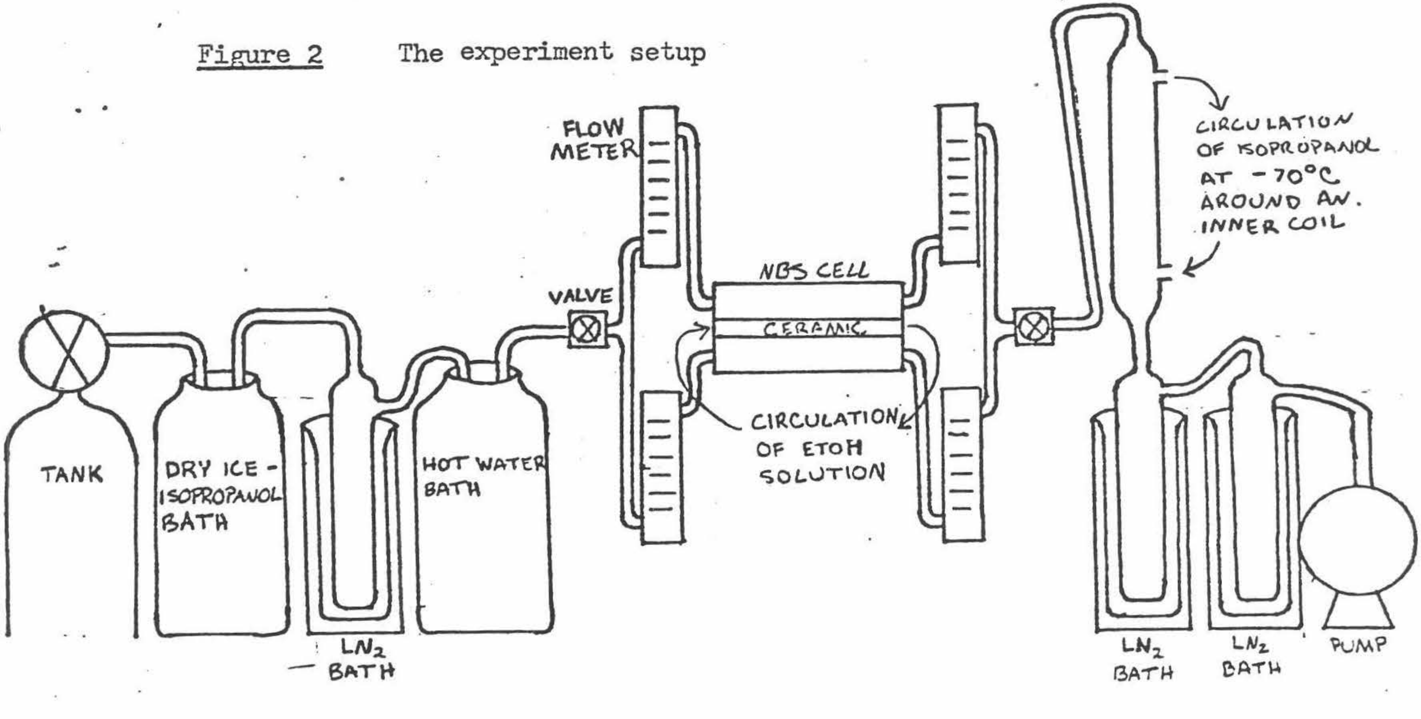

rate. The air is drawn from a tank and any moisture is condensed out by taking it through a coil immersed in a dry ice - isopropanol mixture and a cold finger immersed in liquid nitrogen. The air is warmed back up to room temperature and enters the NBS cell. The dry air flows over the ceramic and picks up ethanol or water which passes through the ceramic and vaporizes. The air then exits the cell and is passed through another cold trap to collect the sample of ethanol and water. This sample could then be analyzed with a gas chromatograph to determine the proportions of ethanol and water that the ceramic allowed to pass through.

In order not to interfere with the collected sample of ethanol and water the air which enters the NBS cell must be dry. This can be achieved using two cold traps as described above. The success of the drying procedure can be tested running the experiment with the air circulating but with no ethanol solution. Initially the results were not satisfactory and varied widely. One hour runs which pulled approximately three cubic feet of air through the system resulted in from 0.1 to 0.6 grams of water remaining in the air. Modifications have improved the system and two such runs, pulling six cubic feet of air each, have resulted in 0.07 and 0.06 grams of water remining in the air. These results are quite good and may be improved when all of the leaks are eliminated from the system.

The ceramic plates were prepared from pieces of existing monoliths. The pieces had to be ground by hand to the required size of 3 X 4 inches and one channel thickness because the ceramic is very fragile. Because of their delicacy the plates were cast in a supporting structure of polyethylene resin before they could be clamped into the NBS cell. Some problems still exist with this procedure however. The resin often leaks onto the actual sample area of the plate and clogs some channels and pores. Either these problems must be solved or another way must be found to prevent breakage of the ceramic plates when they are clamped into the NBS cell.

One possibility for modification of the ceramic to affect its permeability characteristics is direct chemical modification of the molecular structure. A first step is salinization of the ceramic. Two attempts were made to achieve a saline - cordierite reaction after which the amount of amino groups attached to the ceramic was determined by placing the washed and dried ceramic pieces in 0.100 N HCl, stirring over night and back titrating with 0.001 N NaOH. No amino groups were detected. As the salinization is a first step in a series of reactions needed to significantly affect permeability, this does not seem to be a promising approach.

Another possibility for modification is coating the ceramic with a polymeric material which has the appropriate permeability properties. One problem with this approach is that the polymer tends to leak into the channels during the coating process and block them. So far, no experiments have been run to test the permeability characteristics of any polymer coated ceramics.

CONCLUSIONS:

The primary conclusion of my research to date is that direct molecular modification of the cordierite ceramic does not promise to be able to significantly affect the permeability characteristics. Polymer coating of the ceramic does seem to have possibilites.

MIRA TODOROVICH

NO REPORT SUBMITTED

CROSS-CULTURAL ATTITUDES TOWARD THE USE OF RECLAIMED WASTEWATER IN SWA/NAMIBIA

Barbara Turpin

Dr. Ned Munger, Faculty Sponsor

ABSTRACT

Supplying water to the world's growing population has become a major concern to many. This paper examines attitudes toward the use of reclaimed wastewater through a survey conducted in Windhoek, Namibia. Results are compared with two California surveys conducted by Dr. Bruvold in 1972 and 1979. Overall the results were quite similar. However, within Windhoek those aware that the supply contained reclaimed water were considerably more positive about its use. A massive public relations campaign seems to have had a major positive effect on attitudes. In contrast, those people raised in areas of higher rainfall were found to be less receptive to the use of reclaimed water than those from more arid locations.

In Southern California, supplying water to the large and ever increasing population has been a growing concern. The influence of public opinion upon the financing of water supply projects cannot be overlooked. For this reason Dr. Bruvold at the University of California, Berkeley, has conducted two surveys (1972 and 1979) on California residents to examine their attitudes toward the use of reclaimed water[†]. Windhoek, the capital of South West Africa/Namibia, has been using reclaimed water since 1969. This study examines the attitudes of Windhoek's residents toward their water supply, their future supply options, and reclaimed water in general.

Over the course of 26 days in Namibia I conducted personal interviews in Windhoek and administered written surveys in the schools and the adult education center. With questions similar to those used in the California surveys I hoped to make some comparisons. How do California attitudes differ from those in an area where reclaimed water is used? How do responses compare between those raised in southern Namibia, and those raised in the northern areas where water is more abundant? Twenty-seven percent of respondents

---

[†] Reclaimed water is municipal wastewater which has been purified for re-use. Wastewater is water discharged from sinks, toilets, and drains in homes, industries, and commercial establishments.

were unaware that they were drinking reclaimed water at all. The effects this had on their viewpoint could be very interesting as well.

Windhoek averages about 13 inches of rain per year. However, extreme deviations are common. Yearly precipitation can be as high as 28 inches or as low as 6 inches per year. Drought conditions have brought only 8 inches for each of the last two years. To encourage conservation during this time of drought, Windhoek residents were subjected to a graduated tariff. Each household was allowed 30 cubic meters per month at the standard price of $0.38 per liter. Those exceeding that limit were charged $0.68 for each additional liter. Complementing this economic incentive was a massive public awareness campaign. The success of the conservation effort is mainly attributed to this publicity. On the average, Windhoek residents saved more than 30 percent of their total consumption for a two year period.

The importance of public attitudes has been recognized by the Department of Water Affairs since the beginning of their water reclamation project. In 1964 the South African Council of Scientific and Industrial Research, CSIR, began experimentation with a reclamation pilot plant in Windhoek. From then until its opening in 1969, publicity was given such a high priority that at one point many people believed the plant was already in operation. Water Affairs began to get complaints regarding the water quality of this reclaimed water before production began. Several of these water quality problems, Water Affairs argued, would be eliminated with the addition of reclaimed water to the present blend of storage dam and borehole waters. Upon completion of the plant, Water Affairs held "open days" for the public to tour the facilities. Given a taste test to compare dam water and reclaimed water, they were nearly always fooled by the extra clarity of the reclaimed water.

Currently Windhoek's reclamation plant supplies approximately 15 percent of the 12 million cubic meters consumed each year. While only 35 percent of the water supply reaches the sewers, 60 percent of that is fully reclaimed. This water goes through primary settling, activated sludge treatment (fermentation and first anoxic, aeration, second anoxic, and re-aeration), clarifiers, and maturation ponds. Secondary settling follows the addition of alum, chlorine, and lime. The effluent then proceeds through a third settling basin, sand filtration, a chlorine contraction tank, and a series of two activated carbon adsorption treatments. Chlorine is also added after secondary settling. Breakpoint chlorination is achieved after filtration and additional chlorine is added as a disinfectant just prior to distribution. The final product has a total dissolved solids content of 800. However, when blended with borehole and dam water this level is brought below the World Health Organization standards of 500. Industrial effluent remains separate and is not treated for re-use. This allows for a simpler treatment.

Although these facilities could be expanded to reclaim 100 percent of the municipal effluent, this option is not currently being considered. Instead, the development of a pipeline to the north will bring additional water at less expense. The pipeline will eventually extend to the Okavango River, a perennial river on the Angola-Namibia boarder. By diverting water from the swamps of Botswana it will provide a supply capable of carrying the slowly growing population through times of drought without danger of running out.

The blending of reclaimed water in the supply has changed the popular complaint about water quality. High concentrations of fluoride in the borehole water were causing mottling and discoloration of the teeth in the previous supply. With the present blend (reclaimed water, borehole water, and run-off), concentrations of fluoride have been contained to a reasonable level. However, sustaining disinfection to the end of the supply line results in a distinct chlorine taste in the tap water, particularly near the beginning of the line. This is the overwhelming complaint about the present supply.

To combat water shortages brought on by the drought, a top level decision was made to retain the 40 percent of wastewater effluent that was not fully reclaimed. This water is treated in primary settling tanks, single stage biofilters, and humus tanks. After maturation in a series of ponds, the effluent is deposited behind Goreangab Dam, where it is mixed with the water supply as necessary. In addition to bypassing activated carbon adsorption, the biological process used is poor compared to the activated sludge treatment given to fully reclaimed water. The effluent behind the dam was rich enough to smell. Noticing the decreased water quality, the public blamed it on an increased percentage of reclaimed water in their supply. However, few citizens were aware of this effluent use policy.

My limited visit provided insight into the treatment process, and a fair understanding of attitudes toward water and its re-use in an arid environment. With a survey sample of 70 the exact statistics do not have a solid base. Two limitations should be considered when examining the survey sample. I spoke with some respondents — mostly whites — in English. With others I used a translator who spoke in Afrikaans, the European language best known by most black Namibians. I had no access to Africans who spoke no European languages. This constraint excluded a few recent migrants from the North. As most of my work was done through educational facilities, I spoke to a good cross-section of people between the ages of 10 and 40, but few older than 40. Despite these limitations I have developed some insight into the questions raised.

Serious thought is given to the availability of water in this arid environment. It is a frequent topic of conversation at the dinner table. The drought has made an impact on people's day-to-day lives. School hostels limit the length of showers and do not allow students to take baths. Swimming pools are left dry, and gardens wither to nothing. Overgrazing has been a serious problem, turning pasture into desert and destroying cattle. Even the mice suffer, as evidenced by holes in the plastic tubing of automobiles made by mice looking for water. In the North, elephants tear off borehole plumbing rather than drink from the remaining brackish puddles. The people demonstrate a concern for the scarcity of water and an understanding of their dependence on it. When asked if they felt Windhoek had a severe water shortage, 86 percent of the respondents said Yes.

Severe Water Shortage

	yes	no	uncertain
California	25%	25%	50%
Windhoek	86	11	3

In times of drought, such as the present, the importance of conservation is widely acknowledged. However, this attitude does not encompass an environmental concern. When there is enough water they see no reason to conserve; if the residents don't use the water, it will just run into the sea. Not much thought is given to the value this river water could have to the environment downstream of Windhoek.

Bruvold's survey showed California respondents as disfavoring the release of untreated wastewater into the environment with no accompanying re-use. This is also very clearly true for Windhoek respondents. However, in California, the major reason stated was environmental concern, whereas Windhoek respondents disliked the option because it was throwing away needed water. Given three matters related to wastewater treatment and re-use, Windhoek residents listed their concerns as follows:

health	73%
cost of treatment	45
environmental factors	11

Both Windhoek and California surveys listed several possible uses of reclaimed water. These included: industrial manufacture, drinking, irrigation of pasture lands, irrigation of food crops, mining, bathing and laundry. The outcomes were quite similar. California residents opposed drinking reclaimed water by 56 percent and Windhoek residents by 58 percent. However, when Windhoek respondents were divided between those who knew Windhoek used reclaimed water and those who did not, the difference was remarkable. THOSE WHO KNEW THEY WERE DRINKING RECLAIMED WATER WERE FAR MORE ACCEPTING OF IT THAN THOSE WHO DIDN'T KNOW!

Opposition to Various Uses of Reclaimed Water

	Windhoek		California
	Know	Don't know	
Drinking	47%	94%	56%
Cooking	33	69	55
Bathing	40	50	39
Irrigation of food crops	29	47	14
Laundry	20	44	23
Irrigation of pasture land	18	12	14
Industrial manufacture	18	12	-
Mining	18	*	-

Some Windhoekers prefer to drink reclaimed water and let any leftover be used for industry. This contradicts conventional assumptions. The majority see drinking reclaimed water as perhaps necessary, but not desirable. However, some people believe that its quality is superior to that of the borehole and dam water which is given less intensive treatment. These individuals would first like to see this reclaimed water applied for drinking and other quality oriented uses. Then, only if supplies remain, should industry and mining interests benefit from its use. The major concern voiced by these respondents is the high cost of treatment.

A correlation was also observed between opposition to reclamation and the region in which respondents were raised. Not surprisingly, those coming from areas where there is more water, in northern Namibia and abroad, were much less receptive to drinking reclaimed water than those from the Windhoek area and from the south of the country.

	North & Foreign	Central	South
Opposed to drinking reclaimed water	73%	50%	55%

Despite the difficulties one has trying to get water at a restaurant -- and, to editorialize, the apparent aversion people have to drinking anything but alcohol and fruit juices – 56 percent of respondents rated the water's taste between very good and fair. Again a correlation can be made between this response and the area in which the respondents were raised. The overwhelming complaint was the chlorine taste and smell. However, borehole water throughout Namibia tends to be very brackish and contains large amounts of fluoride. This borehole water is often the only source respondents had for comparison.

	North & Foreign	Central	South
Water tastes fair to very good	33%	69%	80%

The results also show that those who know they are using reclaimed water have a much more favorable opinion of the water taste than those who do not.

	Know	Don't know
Water tastes fair to very good	67%	41%

Given the option of reclaimed water, demineralized water, desalinated water, or imported surface water, both California and Windhoek respondents preferred the use of imported surface water over all. The Windhoek results show the other three options much more equally valued than the California survey, which highly favors desalinization over reclaimed and demineralized waters. However, the order of preference is identical.

Preference For Additional Supply

	California	Windhoek
Imported surface water	36%	34%
Desalinated water	35	26
Reclaimed wastewater	11	21
Demineralized water	7	17

CONCLUSION

Water is the King and Queen of Namibia. It is recognized not only as a control on the economy, but as the sustainer of life. "A drop of water can save a life." This phrase is part of a publicity campaign which was indispensable for the success of water conservation efforts in Windhoek. This publicity impacted attitudes toward the use of reclaimed water. The statistics show that those who know they are using reclaimed water are substantially more in favor of its use than those who have not been reached by the publicity and are thus unaware. A correlation was also found between attitudes toward re-use and geographic location. Those raised in areas with plenty of water were less pleased with the water quality and less receptive to the use of reclaimed water than those from Windhoek and drier locations. Extraordinarily, some citizens claim that reclaimed water is the purest available and should be used for quality-oriented uses; Leave less costly waters to be used for mining and industry. Windhoek citizens accept that they are faced with a severe water shortage. Thus, those who are aware of the use of reclaimed water are easily convinced of its necessity. And when respondents are convinced of the necessity of its use, reclaimed water receives a more favorable response.

BIBLIOGRAPHY

Bruvold, William H.
Public Attitudes Toward Community Wastewater Reclamation and Reuse Options. California Water Resources Center, University of California, Contribution No. 179, Aug. 1979.

Bruvold, William H.
Public Attitudes Toward Reuse of Reclaimed Water. University of California Water Resources Center, Contribution No. 137, Aug. 1972.

Clayton, A.J., L.R.J. van Vuuren and B. Roux
Development of Water Reclamation Technology in South Africa. City Engineer's Department, Windhoek Municipality, and National Institute for Water Research, Council of Scientific and Industrial Research. **Wat. Sci. Tech.** Vol 14 (1982), pp. 339-353, Capetown.

Personal Interview with Dr. Helvick
Council of Scientific and Industrial Research, CSIR, Windhoek Regional Office, Windhoek, SWA/Namibia, July 20, 1983.

Personal Interview with Mr. Salmon
City Engineering Department, Municipal Bldg, Windhoek, SWA/Namibia, July 12, 1983.

Pitman, W.V.
A Depth-Duration-Frequency Diagram for Point Rainfall in SWA-Namibia. University of Witwatersrand, Johannesburg, Hydrological Research Unit. **Water S.A.**, Vol 6, No 4 (1980), pp. 157-162.

Wolmarans, A.D.W.
Power and Water for South West Africa S.W. Africa Water & Electricity Corporation, (Pty) Ltd. Windhoek. **The Professional Engineer**, Vol 4, No 4 (1975), pp. 5-11.

POLOIDAL SPACE-TIME MAPPING OF MICROTURBULENCE AT THE PLASMA EDGE IN THE CALTECH TOKAMAK

Jesus Noel Villasenor

California Institute of Technology, Pasadena, California USA

Abstract

A poloidal probe array is used to map the space-time plasma density fluctuations in the edge region of the Caltech Tokamak ($B_T = 3.5$ kG, $T_{edge} \leq 30$eV, $n_{edge} \leq 10^{12}$cm^{-3}, R=45cm, a=15cm). Localized structures are found along the poloidal direction with correlation lengths of about 2 cm and phase velocities of $.45-.60 \times 10^6$ cm/sec.

Supported by a 1983 Caltech SURF Grant

September 22,1983

POLOIDAL SPACE-TIME MAPPING OF MICROTURBULENCE AT THE PLASMA EDGE IN THE CALTECH TOKAMAK

Jesus Noel Villasenor

California Institute of Technology, Pasadena, California USA

1. Introduction

One of the problems of plasma confinement in tokamaks is the presence of microturbulence, which apparently causes anomalous levels of particle and energy transport. This degrades the confinement necessary for achieving sustained nuclear fusion.

Classically, heat and particle diffusion in plasmas is explained by Coulombic collisional interactions. Tokamak plasmas, however, exhibit high levels of particle and energy transport which classical diffusion cannot explain. Instead, an anomalous diffusion occurs which is orders of magnitude larger than that predicted.

It is estimated that microturbulent fluctuations in plasma density near the edge region are sufficient to produce this anomalous transport. Much has yet to be learned about the nature of microturbulence, though it is generally accepted that it is composed of non-linear modes with a broad-band frequency and wavenumber spectrum. Further, it is also known that the wavelengths of the fluctuations associated with the toroidal direction (i.e. along the long way around the torus) are long compared to the wavelengths around the poloidal direction (or around the side of the torus). This gives a qualitative picture of a relatively isotropic two-dimensional turbulence in the plane perpendicular to the toroidal axis.

Hence, the space-time mapping of the instabilities along the poloidal direction by a probe array should enable us to `see´ what is occurring at the plasma edge.

2. Experimental Setup

For this experiment, metal probe techniques are used to measure the fluctuating plasma density. A poloidal array of 32 probes was constructed to provide better resolution than the 8 by 8 2-dimensional probe array already built.

The 32 probes are made of tungsten electrodes .1 cm in diameter, and are spaced .25 cm along an arc describing a circle of radius 15 cm (corresponding to the minor radius a). Each probe has an exposed length of .3 cm. The probes are insulated by ceramic tubing, while being held in place by a stainless steel housing.

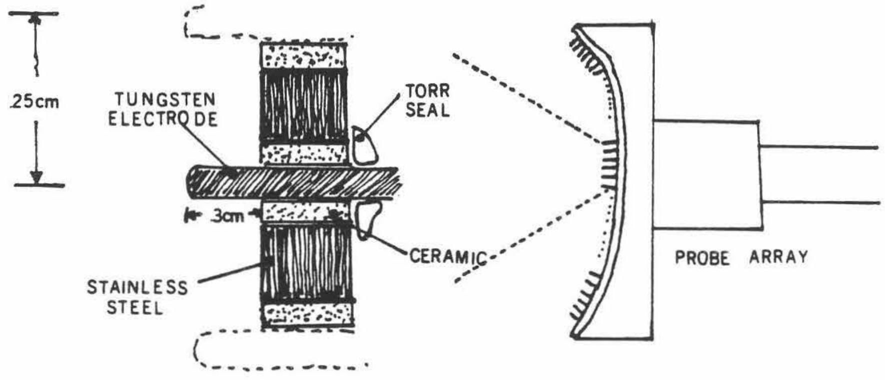

Fig. 1 The Probe Array

In order to collect the ion saturation current, the probes were negatively biased by a common power supply. The signals from the probes are measured as the voltage drop across a known load resistor. Each probe signal passes through a one stage 200 kHz low-pass filter to minimize aliasing in the LeCroy waveform digitizers. The digitizers have a sampling rate of 2.5 microseconds and are capable of resolving 200 kHz.

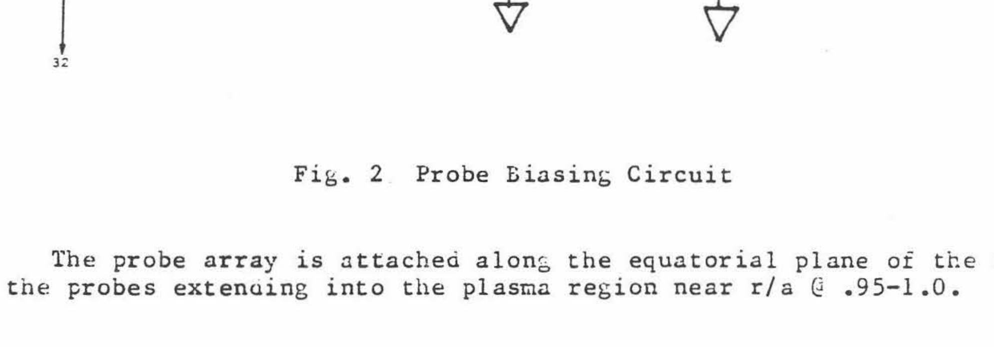

Fig. 2 Probe Biasing Circuit

The probe array is attached along the equatorial plane of the tokamak, with the probes extending into the plasma region near r/a @ .95-1.0.

3. Experiment

3.1 Analysis and Computational Technique

Deterministic (i.e., Fourier) and spectral analysis techniques are used to analyze the data. The signals are analyzed for the power, phase and coherence spectra, and also for the auto and cross correlations.

A function f(t) has as its Fourier transform

$$F(\omega) = \int_{-\infty}^{\infty} f(t)e^{-i\omega t}dt$$

The finite length of the data modifies the transform in two ways. If sampling is done at time intervals Δt for a period of T, the maximum resolvable frquency will then be $\omega_{max} = \pi/\Delta t$. This is the phenomena called aliasing, and arises from the fact that signals with frequency higher than ω_{max} are indistinguishable from waveforms with frequencies lower than ω_{max}. Another problem is that the transform we get is not an unbounded function f(t), but rather that of $f'(t)u(t)$ where u(t) is called a window function. The transform is modified by convolving $F_\epsilon(\omega)$ with $U_\epsilon(\omega)$, where $U_\epsilon(\omega)$ is the transform of some suitable window function. In our case, this is the Hanning function given by:

$$\begin{aligned} u(t) &= 0 && |t| > T \\ &= 1 + \tfrac{1}{2}\cos[2\pi t/T] && |t| < T/2 \end{aligned}$$

with $$H(\omega) = \frac{1}{\omega}\sin[\omega T/2| + \frac{T}{4}\left[\frac{\sin[\pi+\omega T]}{\pi+\omega T} + \frac{\sin[\pi-\omega T]}{\pi-\omega T}\right]$$

The resultant transform is:

$$F_e(\omega_i) = \tfrac{1}{4}\left[F_e(\omega_{i-1}) + F_e(\omega_{i+1})\right] + \tfrac{1}{2}F_e(\omega_i)$$

This gives a better resolution than that of the unconvoluted transform.

The power spectral density is given by:

$$P(\omega) = \lim_{T\to\infty}\frac{1}{T}\ F_T^*(\omega)F_T(\omega) = \lim_{T\to\infty}\frac{1}{T}|F_T^2(\omega)|$$

and the phase is recovered by:

$$\Theta = \arctan\left[\frac{\mathrm{Im}\,(F(\omega))}{\mathrm{Re}\,(F(\omega))}\right]$$

Another useful gauge in qualitatively checking the similarity of two signals is the cross power spectrum, given by:

$$P_{12}(\omega) = \lim_{T\to\infty}\frac{1}{T}\left[\int_{-T/2}^{T/2} f(t)e^{-i\omega t}dt\int_{-T/2}^{T/2} g(t')e^{-i\omega t'}dt'\right]$$

A better way of comparing two waveforms is made by taking the cross correlation formula, or:

$$C(\tau) = \frac{\lim_{T\to\infty} \frac{1}{T} \int_{-T/2}^{T/2} f[t]\, g[t+\tau]\, dt}{\left[\lim_{T\to\infty} \frac{1}{T} \int_{-T/2}^{T/2} f^2[t]\, dt \cdot \lim_{T\to\infty} \frac{1}{T} \int_{-T/2}^{T/2} g^2[t]\, dt \right]^{1/2}}$$

where f(t) and g(t) are two signals. When f(t)=g(t), C(τ) is then called the autocorrelation function. The autocorrelation function indicates the broadness of the frequency bandwidth; for a wide bandwidth noise a slight shift sharply reduces any similarity between f(t) and f(t+τ).

4. Results

A raw signal plot is shown in fig. 3, with the degree of intensity being proportional to plasma density and a temporal segment length of .45 msec. The width of the plot here is equivalent to 8 cm along the poloidal direction. The plot indicates some structure moving across the array, while at the same time demonstrates the turbulent nature (i.e., no regular space or time dependence) of the edge plasma density.

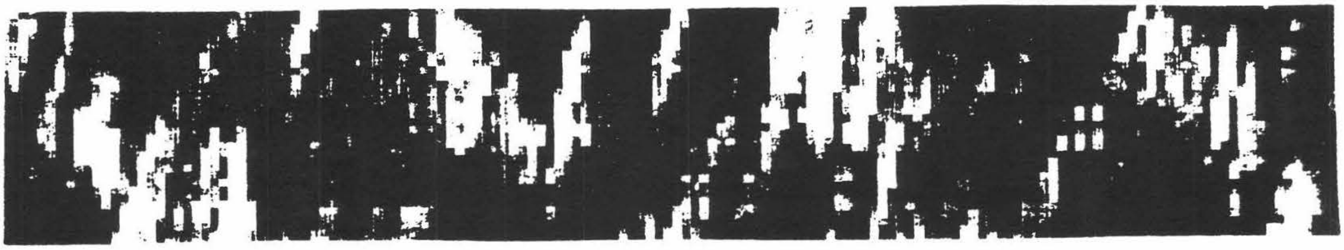

fig. 3 Raw Signal Plot

Typical results for the power and phase spectra are shown in fig. 4. The power spectra for the individual probes are relatively flat for regions between 0 and 25 KHz, but falls like f for higher frequencies, with ranging from 1 to 1.5. The phase spectrum presents a fairly linear relation between the phase and frequency.

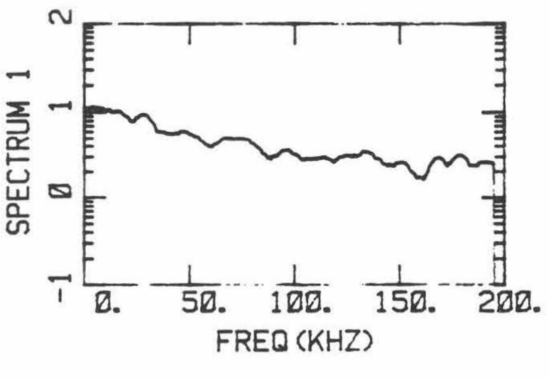

fig. 4a Power Spectrum

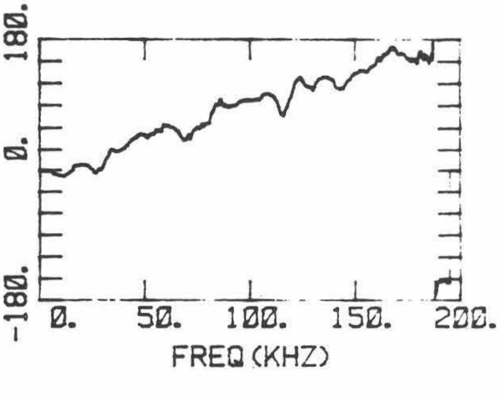

fig. 4b Phase Spectrum

Using the equation $\Delta\theta = \omega\Delta t + k\Delta x$
and seeing that t=0 for a set of spectra with the same reference probe, then for a certain frequency f we can associate a wavenumber $k = \Delta\theta/\Delta x$. Thus, we get a dispersion plot for the edge plasma medium. The plot in fig. 5 is taken from an ensemble of plots with different reference points. For higher frequencies, there is correspondingly a higher spread of k values.

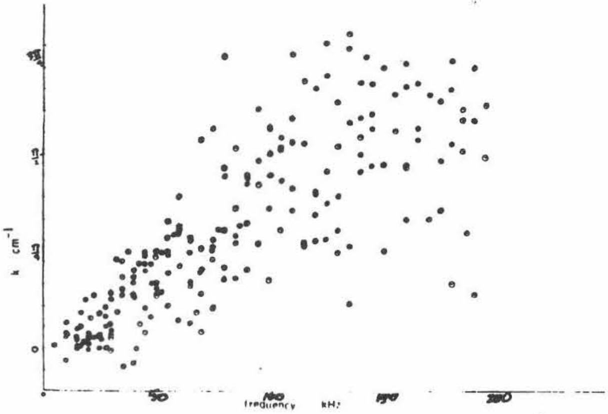

fig. 5 Dispersion Plot

With one probe designated as a reference point, the cross- and autocorrelation functions are plotted out. The correlation length, which is the distance over which the peak of $C(\tau)$ decays by 1/e, is found to be on the order of 2 cm. Typical results are shown in fig. 6, with the autocorrelation function at the bottom and the successive crosscorrelation functions arranged in order of increasing distance from the reference probe. τ varies from ±100 microseconds. The phase velocity of the structure is obtained from the slant of the peaks, or $v = .5 \times 10^6$ cm/sec.

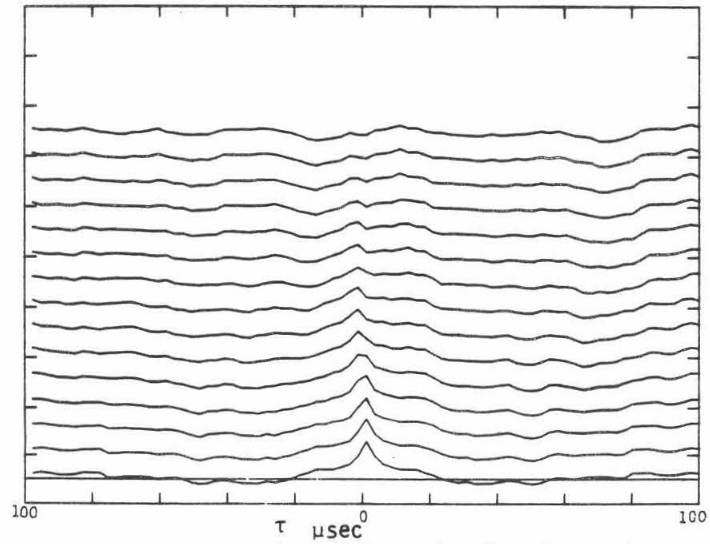

fig. 6 Auto and Cross Correlation Functions

5. Discussion

The raw signal plot along with the correlation functions show movement of coherent structures along the poloidal direction. This is reminiscent of the drift waves associated with fluctuating electric fields. The relationship between these observed patterns and drift wave turbulence theory is presently under investigation.

References

1) S.J. Zweben and R.W. Gould, Nuclear Fusion 21,2 (1983)

2) M. Hedemann, Ph.D. thesis, Plasma Physics Laboratory, California Institute of Technology (1980)

3) A. Hasegawa, Physical Review Letters 50,9 (1983)

4) S.J. Zweben and R.J. Taylor, Nuclear Fusion 23,4 (1983)

5) C.M. Surko and R.E. Slusher, J. Nucl. Mat.

Studies of a Large V_H Family in Balb/c Mice

by John Wall

Advisor L. Hood

Forty-five clones with 5' flanking sequence homology to the J558 V_H gene have been isolated. When digested with PstI and PvuII they fall into four large subfamilies. Six contain the 267 nucleotide PstI-PvuII fragment found in the J558 V_H gene. Six were J558-like. At least two fixed gene differences between the JAX and CRGL substrains of Balb/c mice have been indicated.

INTRODUCTION

Dextran is the bacterial, storage polysaccharide that contains a-1,3, a-1,4 and a-1,6 linked glucose in varying proportions (6). Balb/c mice exhibit a large response when immunized with dextran (1). The murine dextran antibody has been studied genetically, structurally and serologically (4). The heavy chain variable sequence is encoded in three separate gene segments: V_H, D and J_H (5).

One of the five different heavy chain V_H segments produced by the murine dextran response, denoted J558, is produced by a myeloma. The J558 V_H sequence was found in the V_H chains of antibodies produced by 15 of 21 hybridomas formed when the spleen cells of Balb/c mice were immunized with dextran (2). The J558 V_H gene was therefore defined as the prototype for the J558 gene family. The other six V_H regions were variants of this sequence. It is unknown whether they were produced by germ line genes or by somatic mutants.

In order to isolate the J558 gene family from the Balb/c germline, approximately 1.5×10^6 clones from the Balb/c sperm DNA library were screened (3). Ninety-seven clones were picked into two pools based on the intensity of their hybridization to a probe (pV558.1) containing the 558 V_H gene plus 400 nucleotides of 5' flanking sequence homology to the

J558 gene: the (++) pool contains the 20 most homologous and the (+) pool the 70 second most homologous clones.

The J558 gene was sequenced and PstI and PvuII sites indicated at either end of a 267 nucleotide fragment located in the V_H region (D. Livant, unpublished data)

PRESENTATION AND DISCUSSION OF RESULTS

The 90 clones were amplified for further study. Mini lysates of the clones were used to innoculate the host bacteria, E.Coli strain DP50sup F. The preps were grown until lysis occurred. The bacterial debris was removed by centrifugation and the phage precipitated with PEG. The phage were then spun in a CsCl gradient and the phage bands dialysed in EDTA to further purify the phage.

Several of the clones had to be plaque-purified because of the absence of a phage band or the presence of two in the CsCl gradient. Plaque positives were picked using pV558.1 probe. The purified phage were then regrown by the technique just described.

Calibration of Eco-RI conditions for each clone was necessary in order to get complete digestion. To accomplish this objective, several concentrations of Eco-RI were used in digestions of varying duration. The enzyme was thus calibrated for each clone.

When cloned J558 DNA was cut with Bam-HI + Eco-RI, six fragments between 1.0 and 1.9kb in length were present. The 1.9, 1.6 and 1.2kb fragments indicated J_H, Bam-HI ended and V_H fragments of the J558 gene respectively. This had been shown by mapping and hybridization to J_H and V_H probes. The 1.7, 1.1 and 1.0kb fragments were labeled A,B and C respectively and made into probes. To determine which fragment contained the J558 5' flanking sequence, three clones known to contain 5' flanking sequence homology to J558 were hybridized to the probes. J558 DNA was used as a positive control and pBR322 as a negative control. Fragment B contained the 5' flanking sequence of J558.

Hybridization of the 90 clone DNAs to the B fragment DNA indicated that 48 of the 90 clones had 5' flanking sequence homology to the J558 gene: 17 of the 20 members of the (++) pool and 31 of the 70 members of the (+) pool.

To verify the presence of the 267 nucleotide fragment with PstI and PvuII site ends, J558 DNA was cut with PstI and PvuII. HinfI cut pBR322 was used as a standard. The 267 nucleotide fragment was present.

PvuII and PstI digests were run on the remaining clones with 5' flanking sequence homology. The 48 clones fall into four subfamilies containing 6-8 clones each, as well as several small families having 1-2 clones. Six clones were contained in the J558-like subfamily and were analyzed further. The six J558 clones were digested with HaeIII + Sau3A, Sau3A + RsaI and HinfI. One clone resembled J558 and two Hdex8, one of the V_H chains produced in the murine response to immunization with dextran. These two subfamilies were separated based on the lack of a HinfI site in two of the clones, as predicted by the Hdex8 protein sequence.

To see if the 267 nucleotide fragment was contained in the genome, 5micro-grams of PstI-PvuII cut DNA from the JAX and CRGL substrains of Balb/c mice were run. PstI-PvuII cut m104E DNA and HinfI cut pBR322 were run as positive and negative standards respectively. Hybridization to the pV558.1 probe showed a strong 267 nucleotide fragment (at least 4-5 V_H) in m104E, CRGL and JAX. Thus nothing can be said about the chance of somatic mutation in the V_H of Balb/c at this locus. At least two differences between CRGL and JAX indicate the presence of fixed gene variances between these two substrains. This could be due to contamination of the CRGL substrain or large variance at separation of the two substrains after only 30 generations of inbreeding.

CONCLUSION

The original 90 clones were reduced to six with homology to J558 V_H, the prototype for the J558 gene family. Three of these clones resembled J558 and Hdex8. These clones will be sequenced in further work.

At least two fixed gene differences have been indicated between the JAX and CRGL substrain of Balb/c mice. The cause of this difference will be investigated during the next year.

BIBLIOGRAPHY

Blomberg, B., W.R. Geckler, and M. Weigart.1972.Genetics of the Antibody Response to Dextran in Mice.Science.177:178-180.

Clevinger, B., Thomas, J., Davie, J., Schilling, J., Bond, M., Hood,L. and Kearney, J. (1981) In:Immunoglobulin Idiotypes. ICN-UCLA Symposium on Molecular and Cellular Biology.C. Janeway,E.E. Sercarz, H. Wigzell and C. Fred Fox (Eds.),Vol.XX, 159-168. Academic Press,New York.

Davis, M., Calame,K., Early, P., Livant, D., John, R., Weissman, I. and Hood, L. (1980).Nature.283,733-739.

Schilling, J., Clevinger, B., Bond, M., Davie, J. and Hood, L. (1982). Manuscript in preparation.

Schilling, J., B. Clevinger, J. Davie and L. Hood.1980.Amino Acid Sequence of Homogeneous Antibodies to Dextran and DNA Rearrangements in Heavy Chain V-region Gene Segments.Nature.283:35-40.

Sugii, S., Kabot, E., Shapiro, M. and Potter, M. (1981).J. Exp. Med.153: 166-181.

TIME DEPENDENT RADIATION TRAPPING

N. S. Wingreen

Faculty Sponsor:
Dr. William B. Bridges

Abstract

Following the work of T. Holstein, C. van Trigt, and R. Bartman, a computer program was written to determine the spatial and time dependence of excitation in a system of atoms that can reabsorb its own resonance radiation (a "radiation-trapped" system). Results appropriate for a slab geometry and a doppler spectrum in the limit of large optical thickness are given.

Introduction

Radiation trapping is the name given to the process in which an enclosed gas reabsorbs resonance photons emitted by its own excited atoms. These emitted photons can be so strongly reabsorbed that excitation energy remains in the gas orders of magnitude longer than the isolated-atoms' spontaneous decay time. A few of the situations where radiation trapping occurs are in stellar objects, in flourescent lighting tubes, and in gas laser discharges. A better understanding of radiation trapping might lead to increased efficiency of the latter two and to a better overall understanding of the former.

Early work on this phenomenon was done by K. T. Compton[1], E. A. Milne[2], and C. Kenty[3]. The first really successful theoretical treatment was accomplished by T. Holstein[4,5]. He determined the probability $G(\vec{r}', \vec{r})d\vec{r}$ that a photon emitted at $\vec{r}'$ is absorbed in a volume $d\vec{r}$ about $\vec{r}$. Then for excited state density $N(\vec{r})$ and spontaneous decay rate γ, he observed

$$(1) \quad \frac{\partial N(\vec{r}, t)}{\partial t} = -\gamma N(\vec{r},t) + \gamma \int_{\substack{\text{Volume}\\ \text{of Gas}}} N(\vec{r}')\, G(\vec{r}', \vec{r})\, d\vec{r}'.$$

He assumed solutions of the form

$$(2) \quad N(\vec{r}, t) = N(\vec{r})\, e^{-\beta t},$$

leading him to the homogeneous integral equation

$$(3) \quad (1 - \beta/\gamma)\, N(\vec{r}) = \int N(\vec{r}')\, G(\vec{r}', \vec{r})\, d\vec{r}'.$$

Using the Ritz variational technique, Holstein solved for the smallest eigenvalue β_0 (slowest decay rate) and the corresponding fundamental eigenfunction. He observed that after sufficient time had passed, only this eigenfunction would remain and so excitation would continue to decay as $e^{-\beta_0 t}$.

Holstein's calculations were greatly extended by C. van Trigt in a series of papers[6, 7, 8, 9]. His primary result was a Fourier transformation of Eq. 3 which leads to a new integral equation in the limit of large optical thickness ($k_0 R >> 1$, where $e^{-k_0 R}$ is the probability of a photon with frequency at the center of the resonance line traversing the characteristic dimension of the enclosure, R). This new equation can be solved analytically and the results used to generate eigenvalues and eigenfunctions of Holstein's original Eq. 3, for both slab and cylindrical geometries.

What has not been addressed correctly to date in the theory of radiation trapping is the short-range time dependence and the dependence on an externally-applied time dependent excitation of the atomic system. Consider the time excitation rate equation with such a term $A(\vec{r}, t)$

$$(4)\quad \frac{\partial N(\vec{r},\, t)}{\partial t} = A(\vec{r},\, t) - \gamma N(\vec{r},\, t) + \gamma\int N(\vec{r}\,')\; G(\vec{r},\, \vec{r}\,')\; d\vec{r}\,' .$$

When faced with this equation, several researchers have cited Holstein and incorrectly set.

$$(5)\quad - \beta_0 N(\vec{r}) = - \gamma N(\vec{r}) + \gamma\int N(\vec{r}\,')\; G(\vec{r},\, \vec{r}\,')\; d\vec{r}\,'.$$

This, of course, is only true for a system freely decaying after a sufficient time has passed.

I have followed an approach suggested by R. Bartman[10] to solve Eq. 4. Let

$$(6)\quad N(\vec{r},\, t) = \sum_{i=0}^{\infty} f_i(\vec{r})\; T_i(t),$$

where the $f_i(\vec{r})$ are the eigenfunctions of the system and $T_i(t)$ is the as-yet undetermined time function with which the ith eigenmode decays. Expanding the pumping function

$$(7)\quad A(\vec{r},\, t) = \sum_{i=0}^{\infty} f_i(\vec{r})\; a_i(t)$$

leads to the trivial differential equations

$$(8)\quad \frac{\partial T_i(t)}{\partial t} = a_i(t) - \beta_i\; T_i(t),$$

from which $T_i(t)$ and hence the excited state density $N(\vec{r},\, t)$ can be found for all time.

My objective was to write a computer routine which would quickly generate and display solutions, $N(\vec{r},\, t)$, for arbitrary original densities, $N(\vec{r},\, o)$, and pumping functions $A(\vec{r},\, t)$.

Execution

The first stage of the project was an extensive search through the literature of radiation trapping. At the start, I was familiar only with Holstein's work. Following a recommendation from R. Bartman, I tracked down the papers by C. van Trigt. These proved invaluable in designing the mathematical structure of the program.

Computing was done on the VAX 11/780 timesharing machine at Booth Computing Center. Programming was done in FORTRAN 77 since the available subroutine libraries link best to this language.

The computer code was designed for maximum flexibility. It consists of a calling program which accepts input, traps errors in input, calls subroutines, and prints output. The various algorithms to calculate eigenvalues, expand density functions in terms of eigenfunctions, and evolve these eigenfunctions over time are all performed in specific subroutines. This modular approach made it possible to test and debug the algorithms independently. It also allowed major changes to be made in parts of the program without disrupting other parts.

Whenever possible, different approaches to a calculation were tested against each other for efficiency. In one case, substituting a recursion type calculation for a direct evaluation of a function produced an order of magnitude improvement in speed. Care was taken to document the program and its subroutines thoroughly.

Results

The results produced by the computer are, first of all, physically reasonable. Any initial excitation density, allowed to decay without pumping, evolves smoothly to Holstein's fundamental mode. The high-frequency spatial wiggles die out first. This agrees with physical intuition that fine structure in the energy distribution will be rapidly smoothed out by radiative transfer of excitation.

Comparison of these results with those of N. N. Bezuglov[11] and of Yu. B. Golubovskiĭ and R. I. Lyagushchenko[12], who used numerical finite-element techniques to solve transient radiation trapping problems, is reassuring. Figure 1 shows the density of excited atoms after continuous excitation by a pumping function of the form

$$A(r) = \begin{cases} A & \text{for } r < r_0 \\ 0 & \text{for } r \geq r_0 \end{cases}$$

obtained by Golubovskiĭ and Lyagushchenko for a cylindrical geometry. Figure 2 shows the density predicted by the eigenfunction method for a slab geometry with a similar pumping function.

$$A(r) = \begin{cases} A & \text{for } |r| < r_0 \\ 0 & \text{for } |r| \geq r_0 \end{cases}$$

The agreement in spatial shape and time evolution is excellent despite the difference in geometries. A quantitative comparison between the eigenfunction and finite-element techniques will be pursued in further work. (I was unable to complete the code for the cylindrical geometry this summer, and the Russians did not publish results for the slab geometry.

The improvement offered by the eigenfunction method over the naive use of Holstein is indicated in figures 3 and 4. Figure 3 shows an original density of excited atoms which is sharply peaked. Figure 4 shows the decay of this density with time. Curve A is the logarithm of the total excited state population vs. time. It is identical to the straight line (exponential decay as $e^{-\beta_0 t}$) predicted by Holstein. Curve B is the logarithm of the density of excited atoms at the center of the slab. Note that the density here starts out decreasing much faster than $e^{-\beta_0 t}$. The interpretation is as follows:

The original distribution is a superposition of several eigenfunctions. All but the first of these have spatial wiggles such that the individual functions are negative over some regions. The density of excited atoms must of course remain positive at all points at all times. The negative contributions just make the density smaller. As time passes the higher order eigenfunctions die out. Since these functions oscillate in space, the net number of excited atoms they represent is small. Therefore as they disappear the total excited state population is essentially unchanged. However, losing the high order eigenfunctions changes the distribution of the excitation drastically. The density at a specific point in the enclosure is only guaranteed to follow $e^{-\beta_0 t}$ when the fundamental eigenfunction dominates all others. Since some gas laser systems, for example the pulsed copper vapor laser, operate on time scales short compared to the decay time of the higher order eigenfunctions, it is important to be able to determine the short-term decay rate at all points in an enclosure.

Conclusion

The eigenfunction method appears to be a useful tool in studying time dependent radiation trapping. It makes it possible to observe the short time scale behavior of excitation energy, as well as to determine the effects of pumping. Further work is planned to extend the method to cylindrical geometry and to optically-thin media. This project will be continued as a senior thesis.

References

[1] Compton, K. T., Phys. Rev., 20, (283), (1922).

[2] Milne, E. A., J. Lond. Math. Soc., 1, (1), (1926).

[3] Kenty, C., Phys. Rev., 42, (823), (1932).

[4] Holstein, T., "Imprisonment of Resonance Radiation in Gases", Phys. Rev., 72, (12), 1212-1233, (1947).

[5] Holstein, T. "Imprisonment of Resonance Radiation in Gases. II", Phys. Rev., 83, (6), 1159-1168, (1951).

[6] van Trigt, C., "Analytically Solvable Problems in Radiative Transfer. I", Phys. Rev., 181, (1), 97-114, (1969).

[7] van Trigt, C., "Analytically Solvable Problems in Radiative Transfer. II", Phys. Rev. A, 1, (5), 1298-1314, (1970).

[8] van Trigt, C., "Analytically Solvable Problems in Radiative Transfer. III", Phys. Rev. A, 4, (3), 1303-1316, (1971).

[9] van Trigt, C., "Analytically Solvable Problems in Radiative Transfer, IV", Phys. Rev. A, 13, (2), 726-733, (1976).

[10] Bartman, R. (private communication).

[11] Bezuglov, N. N., "Radiation Capture in Cylindrical Volumes of Finite Dimensions", Opt. Spectrosc., (USSR), 43, (3), 246-249, (1977).

[12] Golubovskiĭ, Yu. B. and R. I. Lyagushchenko, "Population of Resonance Levels in a Cylindrical Volume", Opt. Spectrosc., 40, (2), 124-127, (1976).

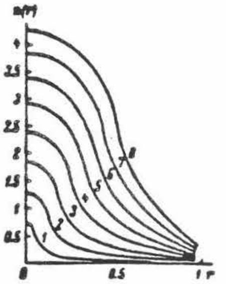

FIG. 1

Density of excited atoms over the cross section of a cylinder, calculated by the finite-element method of Ref. 12. The parameters r_0 (r_0 is the fraction of the total radius which is pumped) for the various curves are given by: (1) = 0.0333, (2) = 0.1, (3) = 0.167, (4) = 0.233, (5) = 0.3, (6) = 0.367, (7) = 0.433, (8) = 0.5.

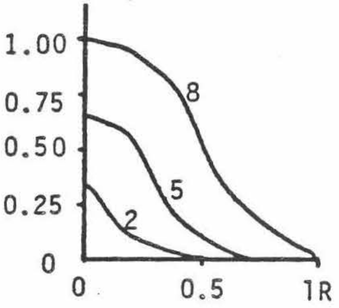

FIG. 2

Density of excited atoms over the cross section of a slab, calculated by the eigenfunction method of this paper. The parameters of the curves r_0 (here r_0 is the fraction of the slab from the center line which is pumped) are given in Fig. 1. The difference in numerical scale is a matter of normalization.

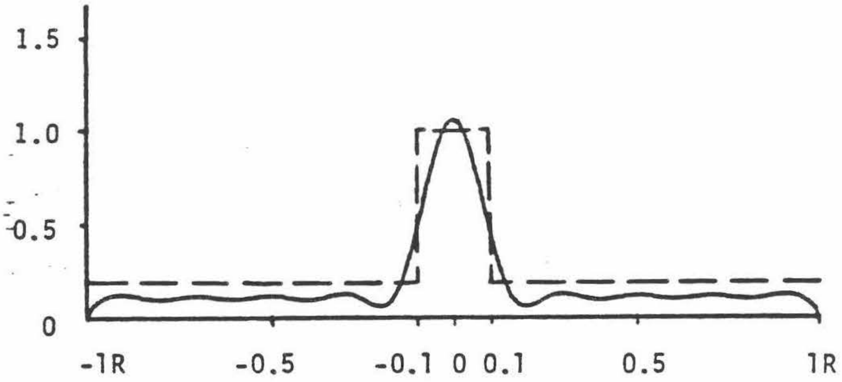

FIG. 3

Dashed curve is an idealized rectangle-on-a-pedestal initial distribution of excited atoms. Solid curve is the representation of the rectangular distribution in terms of the first 20 eigenfunctions, and this is actual initial distribution used in the computation.

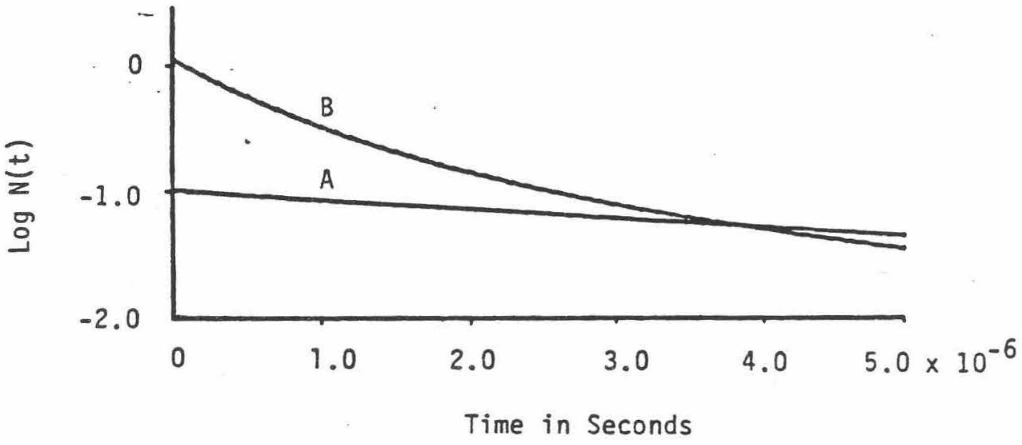

FIG. 4

Decay of excited state densities with time. Curve A - Log of total excited state population. Curve B - Log of excited state density at center of slab.

1983 SURF FINAL REPORT

Preparation Techniques and Surface Area of Supported Sorbents

By

Kriengkrai Wisanrakkit

Faculty Sponsor: Prof. G. Gavalas

Abstract:

The BET flow-adsorption technique is employed to obtain measurements of surface area, pore volume and pore-size distribution of porous sorbents used in H_2S removal from coal gasification gas. The results seem to correlate well with the expected physical change of the sorbents over the course of reaction.

Introduction:

The project is designed to work together with the high-temperature H_2S removal from coal gasification gas project which is being carried out at JPL. H_2S is removed from coal gasification gas by reacting with metal oxides to form metal sulfide and water. The metal oxide is regenerated by reacting the metal sulfide with oxygen.

Reactions: $MO + H_2S \rightleftharpoons MS + H_2O$

$$MS + O_2 \longrightarrow MO + S + SO_2$$

The metal oxide is impregnated on a porous support material in order to maximize its catalytic activity per unit volume of reactor. A basic problem is how to correlate sorbent behavior with physical and chemical structure of the supports. In other words, in comparing different catalytic metal oxides or the effect of different impregnation methods on catalytic activity, it is important to know the extent to which a change in activity is caused by a change in the area and structure of the support, in contrast to a change in intrinsic reactivity of the metal. Few standardized methods of characterization are determination of total surface area by the Brunauer-Emmett-Teller (BET) method, pore volume, and pore-size distribution. The purpose of the project is to obtain measurements of surface area and pore volume of various porous supports before and after impregnations, after reaction with H_2S, and after regeneration. Also, to obtain some information about the pore structure of the porous support from its pore-size distribution.

Presentation and Discussion of Results:

Theoretical approach:

Surface area: The basic principle of determining total surface area of porous materials is by adsorption of a particular gaseous species from a gas mixture of that adsorbate and a non-adsorbable carrier gas onto the surface. If the condition for monolayer coverage is established and the area covered by one adsorbed molecule is known, then the total quantity of adsorbed gas gives directly the total surface area of the material.

The equation commonly used to describe adsorption of gases is the BET equation,

$$\frac{P}{x(P_0-P)} = \frac{(C-1)}{x_m C} \frac{P}{P_0} + \frac{1}{x_m C}$$

where

x = weight of adsorbate adsorbed at relative pressure P/P_0

P = partial pressure of adsorbate

P_0 = saturated vapor pressure of adsorbate

x_m = weight of adsorbate adsorbed at a coverage of one monolayer

C = a constant related exponentially to the heats of adsorption and liquefaction of the gas

Many adsorption data show good agreement with the BET equation over the range of P/P_0 values from 0.05 to 0.3 and this range is usually used for surface area measurements.

According to the BET equation, the plot of $P/x(P_0-P)$ vs. P/P_0 should give a straight line with S = Slope = $(C-1)/x_m C$ and I = Intercept = $1/x_m C$. Solving for x_m yields $\underline{x_m = 1/(S + I)}$

The surface area of the porous material can then be calculated from x_m if the area occupied by an adsorbed molecule is known.

Nitrogen is generally used as an adsorbate because it is relatively cheap and readily available in high purity and nitrogen liquid is readily available as a coolant. The cross-sectional area of nitrogen molecule has been well established which has the value of $16.2*10^{-20}$ m^2/molecule.

Pore volume:

At a sufficiently high relative pressure, all pores will be filled by condensed adsorbate vapor. The equivalent liquid volume of the adsorbed gas yields directly the total pore volume, since the amount of gas adsorbed on the exterior of the pores is negligible for high surface material. The value of relative pressure P/P_0 in the range 0.96-0.99 will adequately serve on this purpose for most samples.

Pore-size distribution:

The basic principle used in determining pore-size distribution is that the pressure at which capillary condensation will occur depends on the curvature of the miniscus of the condensed liquid in the capillaries. This is given by the Kelvin equation

$$\ln \frac{P}{P_0} = \frac{-2sV_m \cos \theta}{r_k RT}$$

where

P = vapor pressure of liquid over the curved surface

P_0 = vapor pressure of liquid over a plane surface

s = surface tension of the liquid adsorbate

V_m = molar volume of the liquid adsorbate

θ = wetting angle (usually taken to be 0°)

r_k = the Kelvin radius of the capillary or pore (indicates the radius of a capillary in which condensation will occur at relative pressure P/P_0)

R = gas constant

T = absolute temperature

Some adsorption will take place before condensation occurs, so there will be a layer of adsorbate of thickness t, on the wall of an unfilled pore. Therefore the actual pore radius (r_p) is

$$\begin{aligned} r_p &= r_k + t \\ &= \frac{-2sV_m}{RT \ln(P/P_0)} + t \end{aligned}$$

Nitrogen has been universally used as an adsorbate and the value of t has been estimated as a function of P/P_0, independent of the nature of the adsorbent.

$$t = 3.54 \left[\frac{5}{RT \log(P/P_0)}\right]^{1/3}$$

The Kelvin equation indicates that adsorbate gas will condense into pores whose critical value of P/P_0 has been exceeded. Thus, by varying P/P_0 the equivalent amount of liquid adsorbate condensed in pores of radii less than some critical value can be determined which in turn gives the pore-size distribution.

Experimental Procedure:

The measurement is done using a flow BET apparatus. A gas mixture of adsorbate (N_2) and a non-adsorbable carrier gas (He) at fixed adsorbate partial pressure, is flown over the adsorbent sample. A thermal conductivity-cell (TCD) recorder records the change in gas composition in the effluent stream by detection the change in thermal conductivity of the gas stream. When steady flow is established, the adsorbent cell is immersed in a dewar of liquid nitrogen causing physical adsorption of the flowing nitrogen onto the surface of the adsorbent. After the adsorption is complete which is indicated by the return of the recorder to the zero base line, the dewar is lowered from the sample cell, causing desorption of the adsorbed gas.

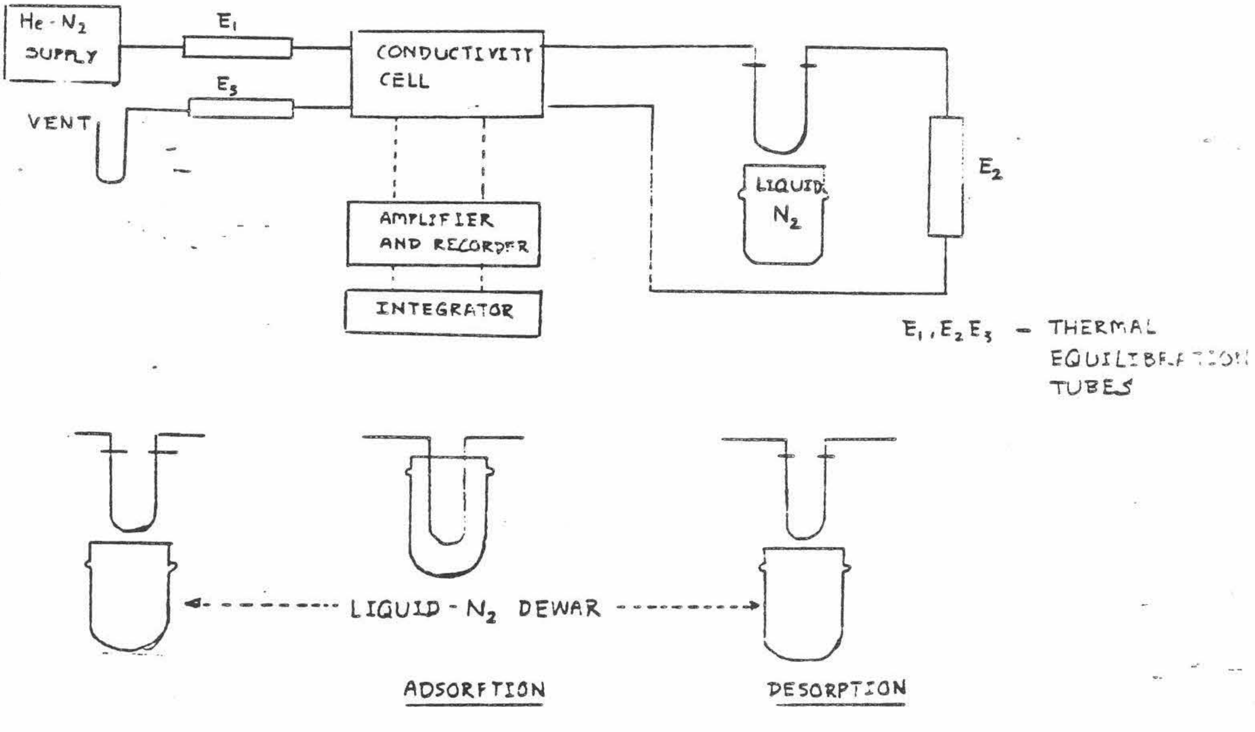

The adsorption and desorption cause a time-compositional change in the stream passing through the TCD. An integrator connected to the TCD will integrate the area of the recorded effluent concentration vs. time curves of both events. Calibration is done by introducing a known volume of adsorbate into the stream.

The integrated desorption area, together with the calibration area of known volume of adsorbate yields the volume of gas adsorbed at the prevailing adsorbate pressure. By varying adsorbate partial pressure, a series of volume vs. pressure data can be obtained to yield an isotherm over a limited pressure range which is used to construct the pore-size distribution.

Table 1: Surface area and pore volume of sorbents

Sample	surface area (cm^2/g sample)	pore volume (cm^3/g sample)	average pore$^{(b)}$ radius (A°)	most$^{(c)}$ probable radius (A°)
$Al_2O_3$$^{(a)}$(I)	91.43	0.2200	48	30
Al_2O_3(I)/ZnO	76.13	0.1842	48	30-35
Al_2O_3(I)/ZnO/V_2O_5	88.93	0.1886	42	
After reaction				
ZnO ⟶ ZnS	77.58	0.1870	48	35-40
$Al_2O_3$$^{(a)}$(II)	91.73	0.2159	47	30
Al_2O_3(II)/ZnO	68.90	0.1788	52	
Al_2O_3(II)/ZnO/V_2O_5	89.92	0.1977	44	
$Al_2O_3$$^{(a)}$(III)	101.21	0.2227	44	30
Al_2O_3(III)/ZnO/V_2O_5	97.94	0.2097	43	
After reaction				
ZnO ⟶ ZnS	84.69	0.2068	49	
Regenerated sorbent				
ZnS ⟶ ZnO	86.89	0.2089	48	

(a) Al_2O_3(I),(II) have been prepared by heating activated alumina in air 850°F for 2 hours. Al_2O_3(III) has been prepared the same way but at 800°F for 2 hours.

(b) The average radius is calculated by assuming all pores are cylindrical of total length L and radius r_{av}

$$\frac{\text{surface area}}{\text{pore volume}} = \frac{S}{V_p} = \frac{2}{r_{av}} . \quad \text{Therefore, } r_{av} = \frac{2V_p}{S}$$

(c) The most probable radius is obtained from the pore-size distribution.

Discussion

Due to tedious nature of elemental analysis using atomic adsorption, only one such result was obtained for the Al_2O_3(I)/ZnO/V_2O_5. It was found that the zinc constant of this material is 0.88% weight. Assuming that all the ZnO gets converted to ZnS after reaction with H_2S, the expected volume change calculated from the molar volumes of ZnO and ZnS would be 0.0014 cm^3/8 sorbent. From the measurements, the volume change is 0.0016 cm^3/8 sorbent. But since the amount of ZnO deposited on the surface is very small, the agreement of these results is not very significant.

For Al_2O_3(I) and Al_2O_3(II), we used a repeated-impregnation method, i.e. V_2O_5 was impregnated after ZnO had been impregnated. The results show the same pattern, surface area and pore volume decrease after Zn impregnation and increase after V_2O_5 impregnation. The pattern is surprising. We would expect the surface area and pore volume of the sorbent to decrease further after V_2O_5 impregnation since more material is added to the surface of the supports. At this point, we do not know the reason for this pattern. However, some possible explanations are:

(a) There is a blockage of small pores after ZnO impregnation which accounts for the decrease in surface area and pore volume. During the second impregnation with V_2O_5, ZnO dissolves in the solution and some ZnO blockage is removed, reopening the small pores, which accounts for the increase of surface area and pore volume.

(b) The porosity of V_2O_5 itself could have contributed for the increase of the surface area of the sorbents after V_2O_5 was impregnated. However, the pore volume could not increase in this way.

From the results both surface area and pore volume increase after V_2O_5 impregnation. Thus, explanation (a) is more likely than (b).

Conclusions

1. A simple model of uniform coating of active materials on the surface of a porous support is not adequate to describe the physical properties of the sorbent. The changes seem to be specific to the chemical composition of impregnated materials, irregularity and pore blocking by the deposited crystals. Thus repeated impregnation by two materials can lead to non-additive results.

2. In particular, it was found that deposition of ZnO by impregnation and calcining results in pore blockage. The pore blockage can be largely

removed by further impregnation by a ammoniacal solution of V_2O_5.

3. This complex behavior needs further study in view of the importance of high surface area in absorption and catalysis.

Bibliography

Carberry, James J.	Chemical and Catalytic Reaction Engineering, McGraw-Hill, 1976.
Satterfield, Charles N.	Heterogeneous Catalysis in Practice, McGraw-Hill, 1980.
Thomas, J. M. and Thomas, W. J.	Introduction to the Principles of Heterogeneous Catalysis, Academic Press, 1967.

The Control and Interface of a Robot Arm by Microcomputer

Sven Andreas Wolf
Dr. Peter M. Thomps

Abstract: The two main purposes of my research were: 1) to develop a microcomputer program to manipulate polynomial transfer functions, evaluate them at representative frequencies, and display the results graphically, and 2) to interface the microcomputer to a robot arm and develop some control programs important to useful operation. Both tasks are accomplished and, although they stand alone, will hopefully provide valuable building blocks in further researches.

My summer research was divided into two distinct areas. The initial part involving the writing of a program to work with polynomial transfer functions and the second part involving the interfacing of the robot arm. The first stage also served to familiarize me with the particular computer I was to use. Both tasks relied on my previous experience with computers and digital electronics.

The function manipulation program allows several operations. After the entry of the transfer function in rational polynomial form, a file of points can be created by evaluating over specified frequency ranges, at specified intervals. The method of display is then an option between a Bode plot, both frequency and magnitude, or a Nyquist plot. This program should prove useful in various control applications. More complex programs can be built around this basic structure, as my faculty adviser has proven with an expansion and refinement far beyond the scope of the original.

The second phase, the robot arm, involved several steps. It was necessary for me to learn machine language and also the theory of operation of stepper motors, used in the robot arm, as a prelude to further work. The next step was to investigate the arm by itself to determine what type of input it needed. An investigation of the computer's architecture, necessary to determine how to control the parallel output port that ultimately would connect to the robot arm, preceded the last step consisting of the physical connection and the final development of controlling software.

To understand the nature of the robotarm's circuitry one must first cover some of the basic ideas governing the operation of stepper motors. An ordinary motor creates a rotating magnetic field to drive its core by means of an oscillating input current. The stepper motor, on the other hand, has a number, generally four, of electromagnets, called poles, spaced evently around the core of the motor. Thus the motor is directly towards whichever magnets are on. Getting the motor to rotate is simply a matter of activating the poles in a circular sequence. The big advantages are that this is inherently a digital operation, involving either on or off, and that the stepper motor only turns a measured amount corresponding exactly to a change in the pole activation pattern.

Thus it is possible, theoretically, to know exactly where a motor is located, in terms of its rotation, without any type of feedback. All that is needed is one known starting point.

There are several distinct levels of control that the robot arm operates under. At the lowest level, wires to the individual stepper motor poles provide current to activate the magnets. This is a relatively high current beyond the capabilities of regular digital electronics so power transistors must be used. At the next level are the low power inputs to these transistors. These inputs are maintained, when nothing is accessing a particular motor directly, by special IC's called latches.

The next higher level requires an input of a motor number and a binary phase pattern corresponding to which poles of that particular motor to activate. Further up, after more circuitry and/or software, the required input is a motor number and a number of steps in either direction.

The highest controls want as input a location in space or even a particular curve to follow. These require far, far, too much processing to have been included with the arm. As it turned out, the manufacturer provided circuitry to a point a little bit above the motor number/phase pattern level. However, the little bit extra was not usable on the particular computer to be used and it was necessary to make circuit card modifications to make the desired input simply a number, corresponding to a motor, and a phase pattern for the poles.

The microcomputer has a parallel printer output port. Parallel means it has the capability to send 8 bits at once. The lines along which these bits are sent go directly to the robot arm. Obtaining the desired output for the arm involved discovering how the computer controls this port and also eliminating the computer's provision for "handshaking" signals which printers provide but robot arms don't.

The computer must deliver eight signal lines of digital one or zero. Three of these eight determine which motor is to be accessed while four correspond to the poles of that motor. The final one is simply a clock signal which instructs the arm when to accept information encoded on the other seven.

The next step in the chain of control, getting something which takes as input one of the motor numbers and a number of steps with a direction, then puts out the correct phase patterns, was the main focus of my final weeks' researches.

The first program, intended to work out the details of the interface without involving big challenges in actual programming, was written in BASIC. The arm moved as desired, though with insufficient speed for any useful work. This indicated the need for an assembly language program, which, although much more laborious to write, would provide the speed necessary for satisfactory operation.

This program now operates successfully, taking the required input of a motor number, a number of steps, and a direction, and providing the correct output to move the motor the corresponding amount.

This program now stands by itself as a success though it is an important staple for any further work with the robot arm. The first program, too, stands alone and has already been used as a building block.

VISUAL SYSTEM OF JUMPING SPIDERS

Author : Christopher Yo
Sponsor : John Allman

I. ABSTRACT

Different histological techniques have been used to study the visual system of jumping spiders. Paraffin sections (10μm thick)are fruitful in tracing visual pathways under the light microscope.Epoxy sections (0.5-1.0μm thick) cut by the ultramicrotome are unsuitable for looking at connections between different visual areas under the light microscope because of the small tissue block surface requirement.Thin epoxy sections (40-60nm) are cut to investigate the ultrastructure of photoreceptors under the electron microscope.

Abbreviations:
AME= anteromedial eye
ALE= anterolateral eye
PME= posteromedial eye
PLE= posterolateral eye
AMEn1= primary neuropile of the AME
AMEn2= secondary nueropile of the AME
ALEn1= primary neuropile of the ALE
PMEn1= primary neuropile of the PME
PLEn1= primary neuropile of the PLE
CP= corpora pedunculata
PC= protocerebrum

fig 1

II. INTRODUCTION

Jumping spiders rely heavily on vision for their predatory, locomotory, threat and courtship behaviors.Four pairs of eyes (Fig1) are situated on the dorsal surface of the carapace which covers the cephalothorax. The following is a summary of the visual pathways simplified from D.E.Hill's thesis (3).

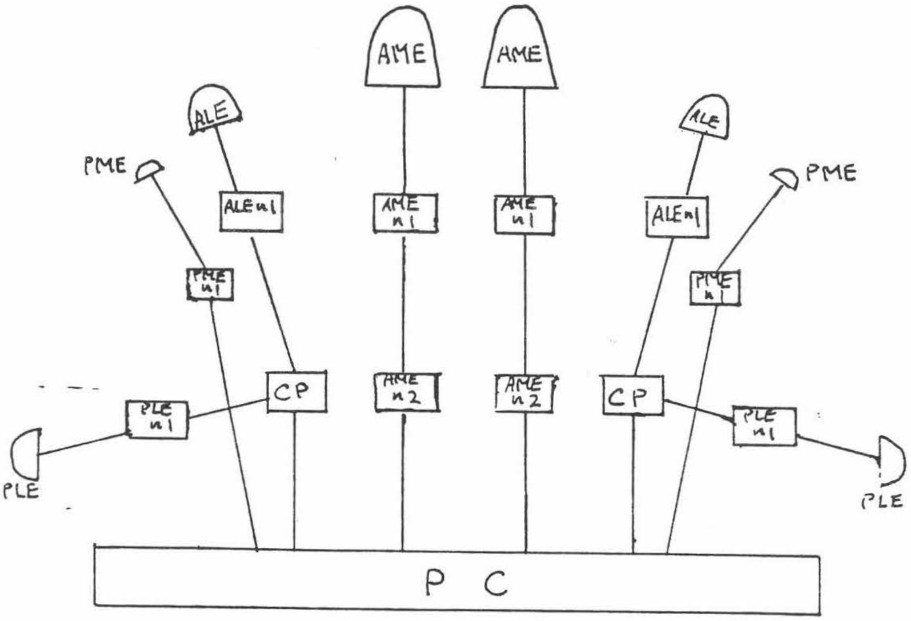

III. MATERIALS , METHODS & OBSERVATIONS

Two species of jumping spiders - Phidippus johnsoni and Phidippus rimator were used for these experiments. They were bought from Chuck Kristensen's spider farm ; kept in petri dishes and fed weekly with fruit flies or meal worms.

A. PARAFFIN SECTIONS (10µm) FOR LIGHT MICROSCOPY

1) METHOD:

Spiders were anaesthetized with carbon dioxide sublimated from dry ice. Appendages, pedipalps, chelicerae and the opisthosoma were then taken off under fixation medium.

a. Fixation: 24 hrs. in Bouin-Duboseq
b. Chromatization: 24 hrs. in 3% aqueous potassium dichromate solution
c. Washing: 5 mins. in 50% ethanol
d. Dehydration and Clearing: (i) 90 mins. in 3/4 dioxane 1/4 water
(ii) 60 mins. in dioxane
(iii) 2 hrs. in fresh dioxane
e. Infiltration: (i) 5 hrs. in 1/2 dioxane 1/2 paraffin(m.p.62°C)
(ii) 12hrs. in paraffin
f. Embed
g. Sectioning: use rotary microtome
h. Staining: Harri's Alum Hematoxylin
i. Counterstaining: Eosin

2) RESULTS:
fig. 2,3,4

3) OBSERVATIONS:

The convoluted primary neuropile of the PLE can be seen in Fig. 2f while the primary neuropile of the ALE is revealed in Fig. 2i,j,k,l,m. From Fig. 2f,g,h,i it can be seen that the corpora pedunculata receives input from the primary neuropile of the PLE. Fig. 2i,j,k and Fig. 3 show that the corpora pedunculata also receives input from the primary neuropile of the ALE. The primary and secondary neuropile of the AME can be seen in Fig. 2 l,m and they also show that the protocerebrum receives input from the secondary neuropile of the AME and the corpora pedunculata.Fig. 4 is a magnified view of Fig.2b, one can clearly see the cone cells, cone cell nuclei and the rhabdomeres surrounded by densely packed pigment granules.

B. EPOXY SECTIONS (0.5-1.0µm) FOR LIGHT MICROSCOPY

1) METHOD:

Spiders were dissected as in A 1), the cephalothorax was cut into smaller pieces by using razor blades because of the small block surface required.

a. Fixation: 12 hrs. in 2% glutaraldehyde, 1% formaldehyde 0.1M pH7.4
cacodylate buffer

b. Postfixation: 2-3 hrs. in 1% osmium tetoxide in 0.1M cacodylate buffer
c. Dehydration: 50%, 70%, 80%, 90%, 95%, 100%, 100%, 100% ethanol (20 mins. each)
d. Clearing: 30 mins. in propylene oxide
e. Infiltration: (i) 3 hrs. in 1/2 EPON 1/2 propylene oxide
(ii) 8 hrs. in 2/3 EPON 1/3 propylene oxide
(iii) 8 hrs. in 1/1 EPON
f. Embed
g. Stain: Toluidine Blue

2) RESULTS:
Fig. 6,7

3) OBSERVATIONS:

Breakage of the exoskeleton is common in paraffin sections e.g. Fig. 2b,c,d, h,i,j, etc, but this problem is eliminated in epoxy sections. However, large epoxy sections like those in Fig.6 show enormous chattering and knife marks can be seen in Fig.6b,e,h. Smaller epoxy sections like those in Fig.7 show much better quality and one can even see the rhabdomeres of the AME. Unlike the rhabdomeres of the lateral eyes, the rhabdomeres along the optical axis of the AME are not surrounded by pigment granules and probably this feature allows the rhabdomeres of the AME to be densely packed for enhanced acuity.

C. EPOXY SECTIONS (40-60nm) FOR ELECTRON MICROSCOPY

1) METHOD:

Same as for cutting thick epoxy sections excepts that the sections are stained with uranyl acetate and lead citrate.

2) RESULTS:
Fig. 8,9,10

3) OBSERVATIONS:

Unlike the rhabdomeres in the AME, those in the ALE (and those in the PLE(Fig.4)) are surrounded by dense pigment granules and form star shaped structures as shown in Fig.8a. At closer scrutiny (Fig.8b), one can see the microvilli inside the rhabdomere and the nonpigmented supportive cell encompassing the rhabdomere as reported by Eakin and Brandenburger in the PLE (1). Fig.9 shows sections of the same spider through the same eye, the structure of the rhabdomeres is clearly different from those shown in Fig.8. This may be due to different plane of sectioning, histological artifact (unlikely) or the existence of 2 kinds of rhabdomeres in the ALE.

IV. DISCUSSION

Cutting epoxy sections is extremely time consuming and is limited by the small cutting surface and the variety of stains applicable. Therefore the paraffin method is recommended for tracing visual pathways in the jumping spider.In the present study, a great deal of efforts have been spent in experimenting with HRP. However, as shown in Fig.5 reaction product was not seen in areas other than the opticoel. This may be due to a variety of factors such as injection site, survival time, stabilization of the reaction product, etc. Future experimentations with HRP on the spider visual system should also be done using the paraffin method.

ACKNOWLEDGEMENTS:

I am indebted to Drs. J. Allman and E.McGuinness for their support and advice.I would like to thank D.Sivertsen for sharing his knowledge, help in interpreting various structures and giving valuable criticisms of this paper.I would also like to thank Drs. S.Benzer and J-P.Revel.

V. REFERENCES

1 Eakin,R.M.,and Brandenburger,R.L. 1971 Fine structure of the eyes of jumping spiders. J. Ultrastructure Res.,37:618-663
2 Foelix,R.F. 1982 Biology of Spiders. Harvard Univ. Press
3 Hill,D.E. 1975 The structure of the CNS of jumping spiders of the genus Phidippus (Araneae:Salticidae).M.S.Thesis,Oregon State Univ., Corvallis, Oregon.
4 Humason,G.L. 1972 Animal Tissue Techniques
5 Mesulam,M-M.(ED) 1982 Tracing Neural Connections with Horseradish Peroxidase. John Wiley & Sons Ltd.

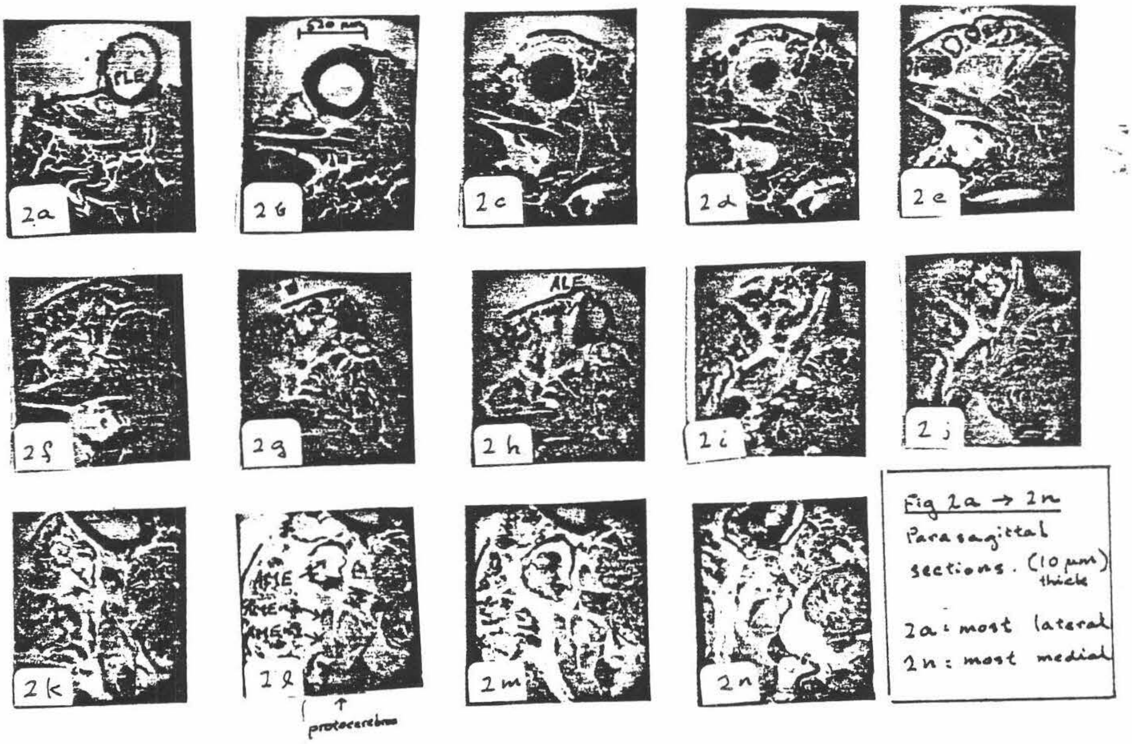

Fig 2a → 2n
Parasagittal
sections. (10 µm) thick

2a: most lateral
2n: most medial

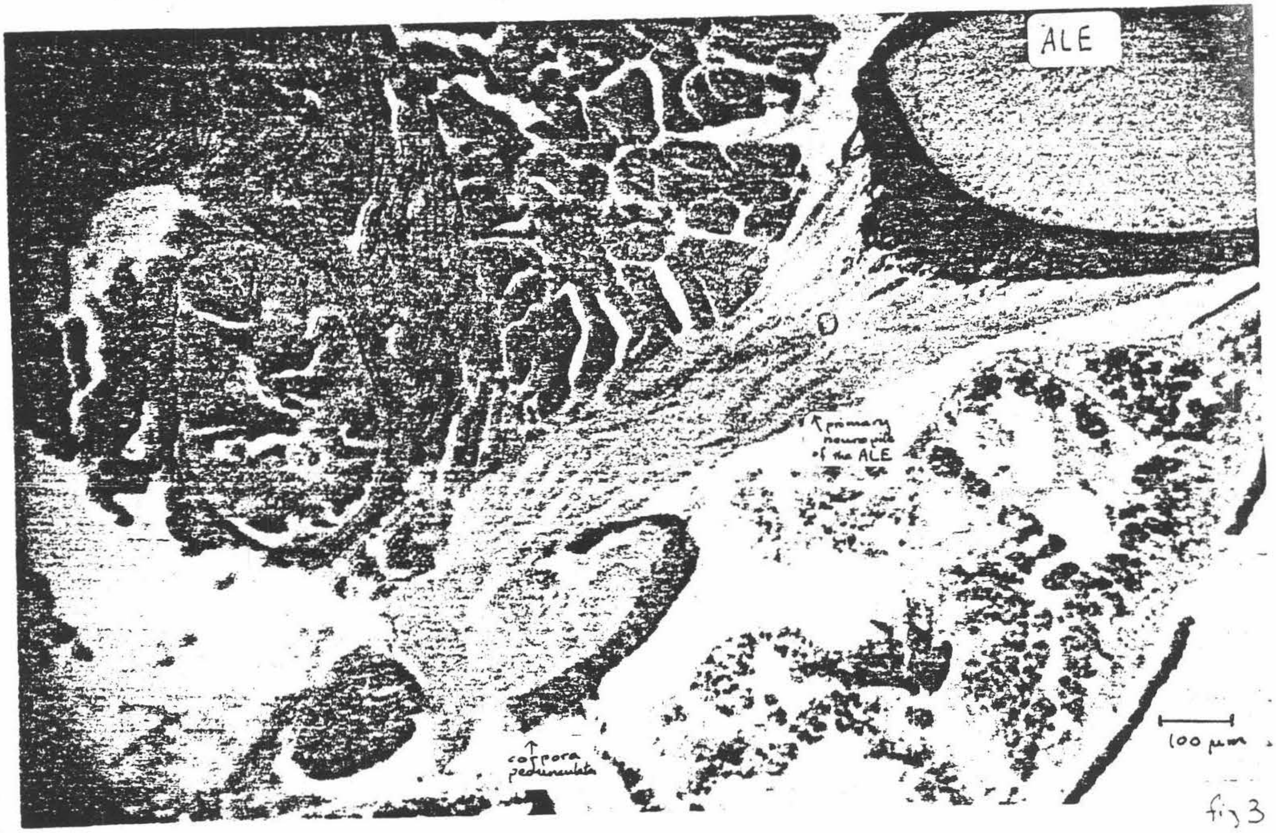

fig 3

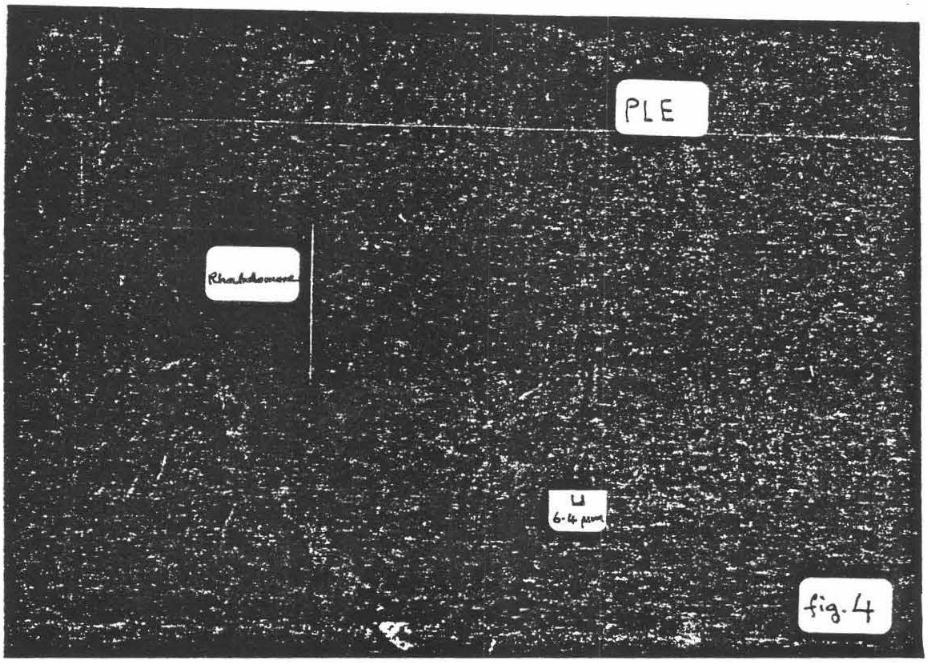

fig. 4

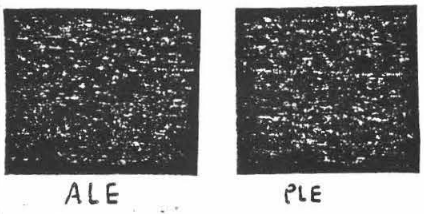

fig 5

Horseradish Peroxidase was also used to look at visual connections. Reaction product can be seen in the core cells but not in other areas.

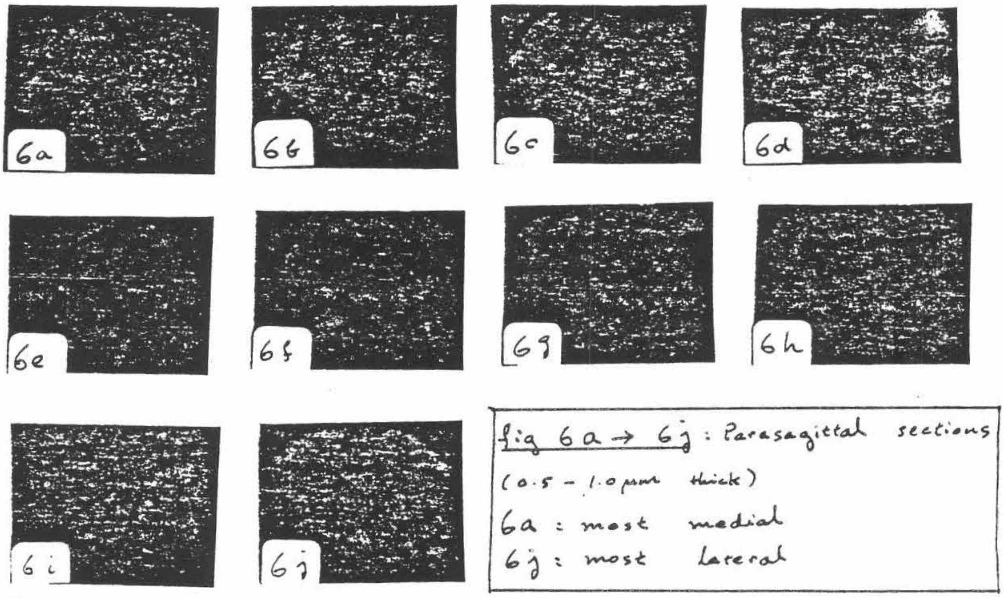

fig 6a → 6j: Parasagittal sections
(0.5 – 1.0 µm thick)
6a: most medial
6j: most lateral

fig 7 : Parasagittal sections (1.0 µm thick) of the AME
7a : most lateral
7d : most medial

100 µm

fig 8 : cross sectional view of rhabdomeres in the ALE.
Rh : rhabdomere
Npsc : nonpigmented supportive cell.

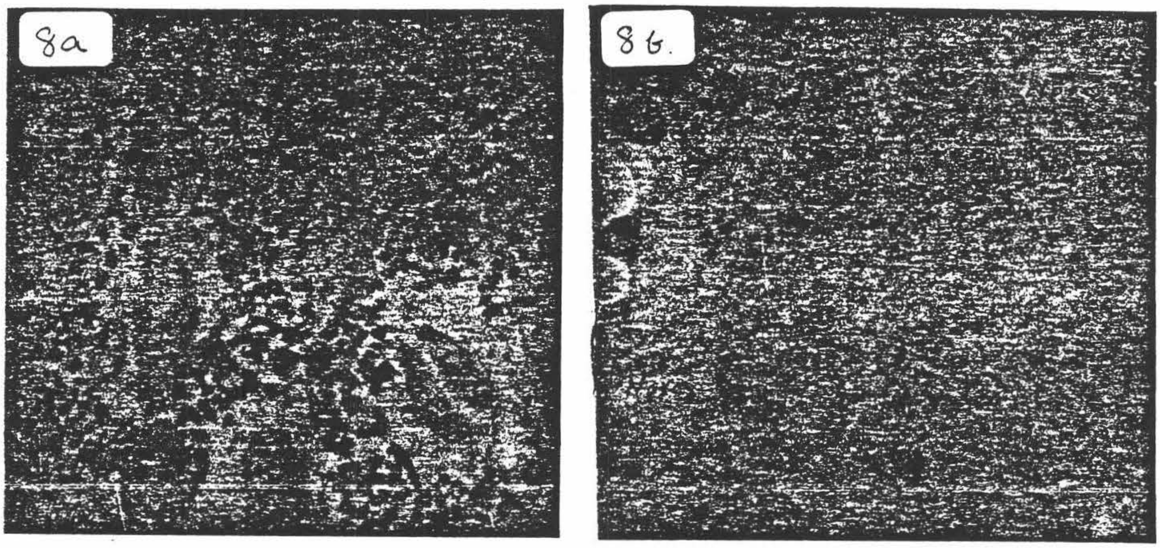

9a

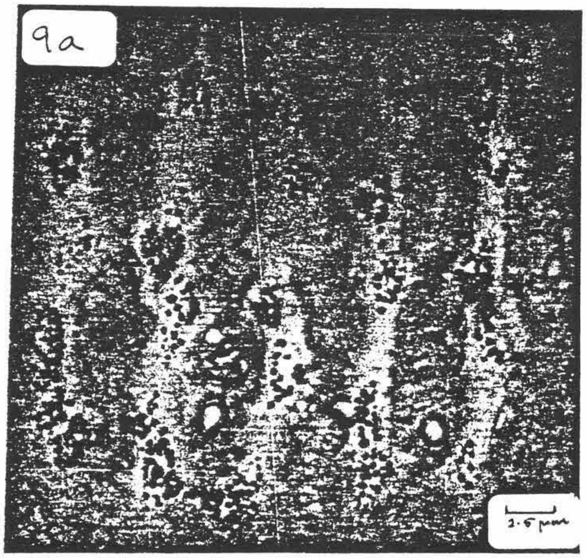

9b

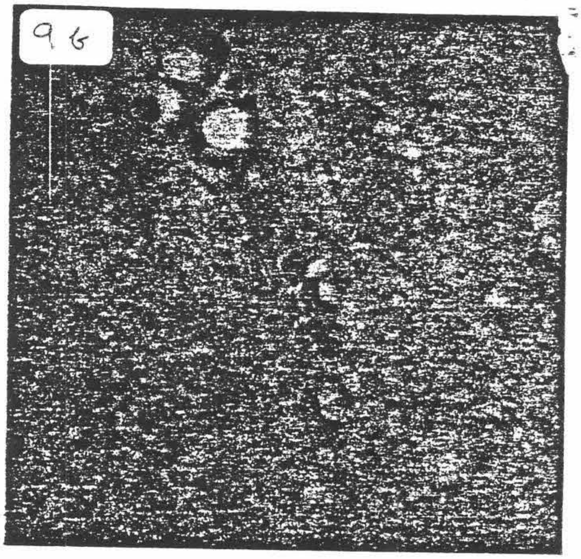

9c

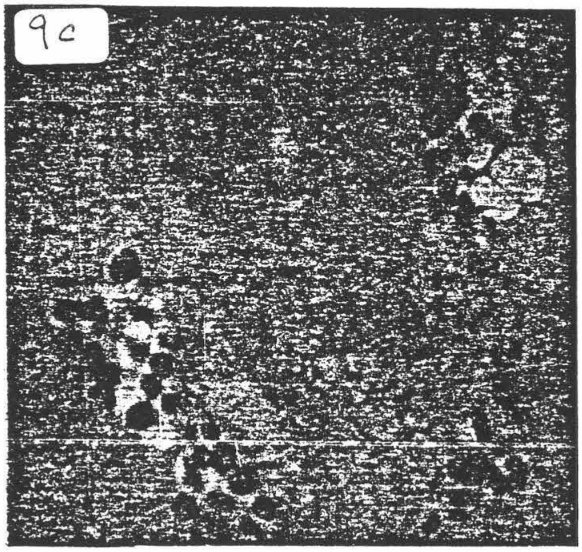

fig. 9 rhabdomeres of the ALE

10

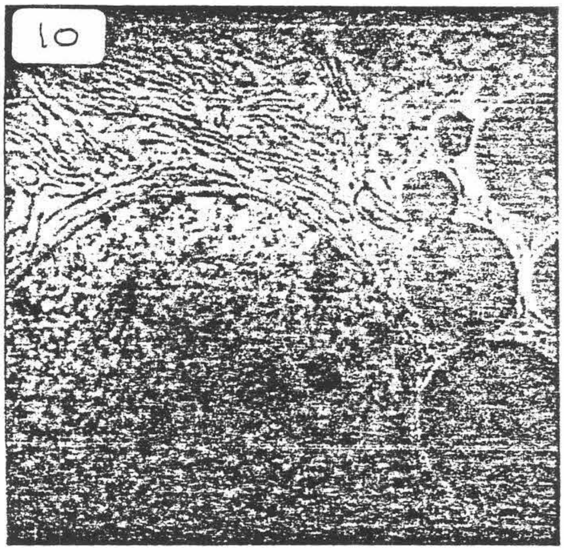

fig. 10 sensory cell nucleus

1 µm

CONTACT ANGLES OF VARIOUS LIQUIDS ON GLASS AND PLEXIGLASS MEASURED BY A NEW METHOD

SURF Student: Minami Yoda
SURF Sponsor: Prof. Donald Coles, Aeronautical Engineering

We measured the contact angles of about ninety liquids on glass, and about thirty liquids on plexiglass using a new method based on the Concus and Finn theory (1). We found liquids with very consistent contact angles, and relations between chemical structure and contact angles.

INTRODUCTION

About 150 years ago, Thomas Young proposed a theory that the contact angle (the angle that a droplet of a liquid makes with a smooth solid surface) could be calculated by looking at the mechanical equilibrium of a drop resting on a plane solid surface under the influence of three surface tensions--SV at the solid-vapor interface, SL at the solid-liquid interface, and LV at the liquid-vapor interface (2). Therefore, if γ is the contact angle,

$$SV - SL = LV\cos\gamma. \quad \text{(Young Equation of Wetting).}$$

Unfortunately, SV and SL cannot be measured, and so this equation is not useable (2).

Since then, many scientists have proposed theories about contact angles--Laplace, Rayleigh, and Wenzel, for example (2)--but there are still many unanswered questions on the subject. In 1969, P. Concus and R. Finn devised a new theory which enabled us to easily measure contact angles (1) (Fig. 2b). According to their theory, there exists a discontinuity in the height of a liquid in a corner above some reference level. The liquid rises continuously in the corner when the corner angle 2α is decreased, and falls continuously when the corner angle is increased. As long as $\alpha + \gamma \leqq \pi/2$ (γ contact angle), then the height of the liquid is bounded. However, as soon as $\alpha + \gamma > \pi/2$, there exists no solution for the height of the liquid, and the height becomes unbounded. In other words, the shape of the liquid meniscus should develops a discontinuity at $\alpha + \gamma = \pi/2$. The surface developed a sharp tip for the rising (decreasing α) liquid, and lost the sharp tip and went flat for the receding (increasing α) liquid (Fig. 3).

METHODS

All of our contact angle measurements on glass and plexiglass were taken using a special apparatus (Fig. 1). Two slides (25 x 75 mm, 1 to 2 mm thick) were kept in contact lengthwise by springs. The angle between the two slides can be smoothly changed from 180 to about 20°, i.e. contact angles from 0 to about ±80° can be measured ($\gamma = \pi/2 - \alpha$). The slides are placed in a Petri dish (60 mm diameter, 15 mm deep) containing five to twenty-five grams of liquid--enough to keep the slides at least one mm deep in liquid. The experimental setup was lighted by a diffuse fluorescent light source from behind, and a concentrated incandescent light source from the front. The meniscus was magnified about thirty times by a binocular microscope. All experiments were conducted in a fume hood to avoid harmful vapors.

We spent the first week of the summer deciding on a cleaning method for our glass slides. We tested various methods--soaking in concentrated nitric acid, boiling in distilled water, washing with Dichrol (a potassium dichromate-concentrated sulfuric acid solution), and washing with 1,1,2-trichloro-1,2,2-trifluoroethane--by measuring the contact angle of water, one of our most consistent liquids, on slides cleaned by the various methods. The methods were rated by the reproducibility of the contact angle measurements. We decided on a one to three minute ultrasonic bath in 1,1,2-trichloro-1,2,2-trifluoroethane (Freon TF). After going through a similar testing procedure with plexiglass using: 409 (a detergent solution), MS-260 (a commercial cleaner), and various soaps (Labtone, Ivory soap, Palmolive liquid), we chose MS-260 (65% water, 5% 2-butoxyethanol, 30% various alcohols and additives) for cleaning our plexiglass slides. The glass slides used were VWR plain 25 x 75 x 1 mm Micro Slides or Corning plain 1" x 3 " x 1 mm Gold Label Micro Slides; the plexiglass slides were made by the Aeronautical Engineering shop from 1/16" thick plexiglass (dimensions 1" x 3").

After the slides were clamped to the apparatus, adjusted, and put in the liquid, the contact angle was estimated by the droplet method on a clean slide (Fig. 2a). Then the angle between the two slides, 2α, was slowly decreased until a discontinuity--the development of a sharp tip by the liquid profile--was observed. The rising contact angle was recorded, and then after a couple minutes' wait the angle was slowly increased until the sharp tip disappeared and the surface went flat at the receding contact angle.

RESULTS

All of our contact angle measurements are presented in Table 1.

DISCUSSION

As with most new methods, our method had some problems. Our biggest problem was that we seldom saw any "jumps"--we ended up defining our rising and receding contact angles as the angles when the liquid profiles looked like they had just "jumped." We saw "jumps" only with water, dibromomethane, formic acid benzyl ester, and benzoic acid butyl ester. (We defined liquids that "jumped" as Type I liquids) (Fig. 3).

There are many possible reasons for our not seeing "jumps"--the slides may not have been clean enough, the liquids may not have been pure enough, and a lot of the liquids were hard to see because the liquid was constantly evaporating and condensing at the surface. The surface of liquids with indices of refraction close to those of glass or plexiglass were also hard to see. Some of the liquids, especially the glycols, were very hygroscopic; their contact angles consistently decreased with time as the liquid absorbed more and more water. (We usually only looked at the first reading.) Some liquids were very viscous and would not drain off the slides; it was impossible to measure the receding angles of liquids such as glycerin and triethylene glycol on glass. And even if the liquids weren't very viscous, none drained off completely--the contact angle of a liquid could decrease significantly between the first and second readings because of slide wetting. The liquid meniscuses often were very rough and ragged, making it difficult to tell what the profile really looked like. It was very hard to take the contact angles of liquids with low boiling points, like acetone or ethanol--as soon as the surface developed a sharp tip, it evaporated off, and a lot of the volatile liquids would evaporate condense on the slides a couple millimeters above the surface, and drip back down, making it extremely difficult to distinguish the meniscus. Liquids with high indices of refraction and high boiling points (100°C and above) gave us fairly consistent measurements, however.

We were also unable to control either the temperature or humidity, since we conducted our experiments in a fume hood open to the air. The temperature varied from 22 to 27°C, and we did not measure the humidity. If we could put our apparatus in a glovebox, we would be able to control the temperature, thereby controlling the volatility of the liquids, and the amount of water vapor, enabling us to reproducibly measure the contact angles of hygroscopic liquids. We plan to build another apparatus, consisting of a glass-bottomed cylindrical tank (capacity 5 to 30 ml liquid) with a slide at an adjustable angle in it and put it in a glovebox. A laser beam would be passed over the tank perpendicular to the liquid surface; the contact angle would be defined as the angle the slide was at when the light intensity beneath the slide was uniform over the bottom of the tank. This tank apparatus will enable us to check our measurements by a different method. We will also be able to work with "difficult" liquids--hygroscopic, volatile, or hazardous liquids. The glovebox will also minimize contamination of the slide and liquid.

While we do not have the contact angle measurements of very many liquids with similar chemical structures, we believe that there are some correlations between contact angles and chemical structures. Among the straight-chain α-carbon alcohols (ethanol, 1-propanol, 1-butanol, 1-pentanol, 1-hexanol, and 1-octanol) there seems to be a pretty clear trend of the contact angle increasing with the number of carbon atoms in the chain, both on glass and on plexiglass. The contact angle values for the straight-chain ketones (2-propanone, 2-butanone, 3-pentanone, and 2-octanone) are all about the same-- 5.7 to 8.2°, ±20%. The glycols as a family seem to have uniformly high contact angles (10 to 27° on glass, 37 and 67° on plexiglass). Among the straight-chain aldehydes (butanal, pentanal, heptanal) there also is a trend of increasing contact angle with chain length. It is difficult to really see very many trends, since we have so many chemicals with radically different chemical structures, but there does seem to be some relation between chemical structure and contact angle values.

CONCLUSIONS

Despite all out problems with the Concus and Finn method, our new method is a simple, reproducible way of measuring contact angles. It is quick--a measurement takes no more than ten minutes--and it can be used pretty much on any liquid-solid combination, as long as the solid can be made into a planar surface. It works best on liquids with a high index of refraction and a high boiling point--i.e. liquids which are easy to see and have very little condensation--but most liquids can be used if the apparatus is put in a glovebox, where volatility, temperature, pressure, humidity, and contamination would be controllable.

From the data obtained using this method, there appear to be some correlations between contact angles and chemical structures. The contact angles of straight-chain carbon compounds seem to increase with the length of the chain, and certain families of chemicals seem to have generally larger contact angles than others.

BIBLIOGRAPHY

1. Concus, R., and P. Finn, "On the behavior of a capillary surface in a wedge," Proc. N. A. S.: Applied Mathematical Sciences 69, 292-9 (1969).

2. J. J. Bikerman, Physical Surfaces (New York: Academic Press, 1970).

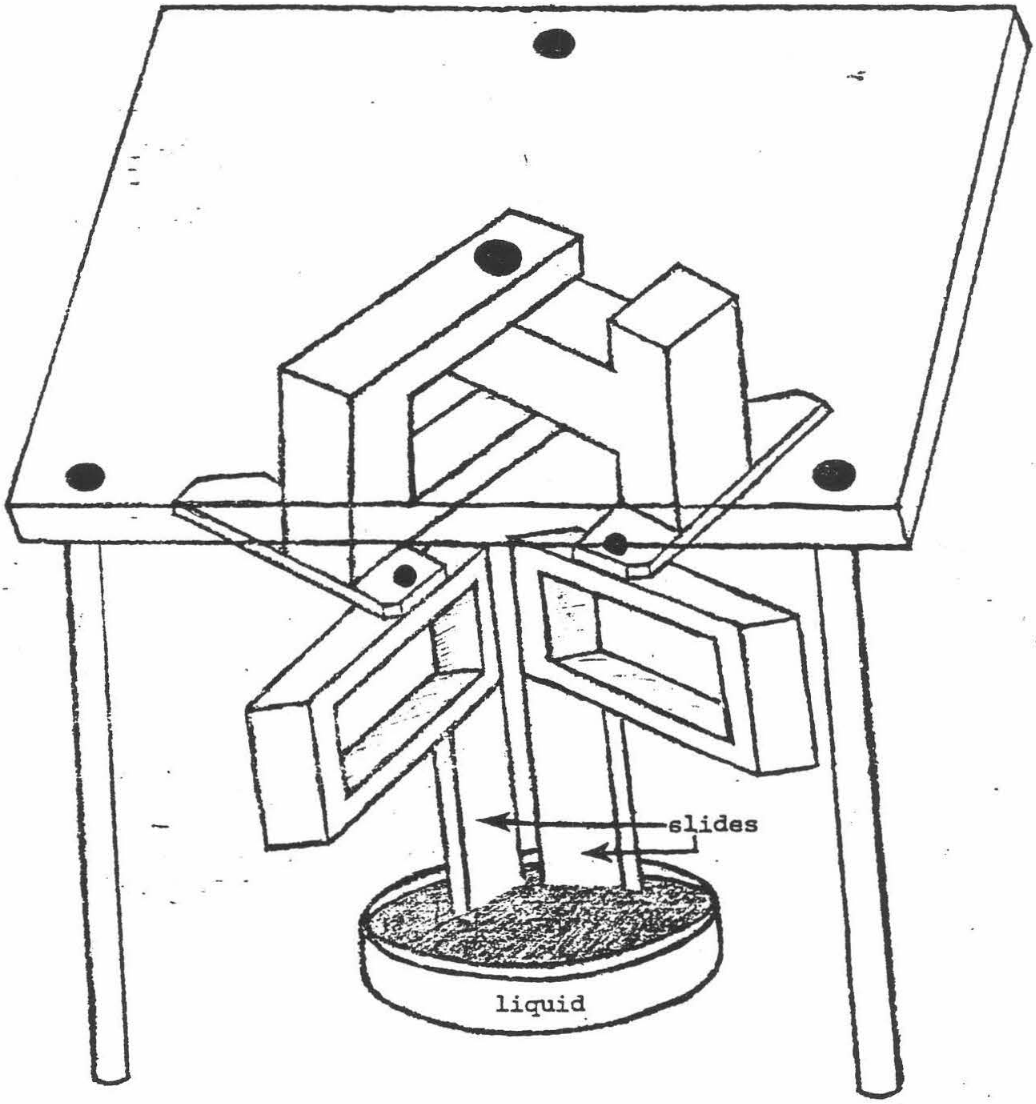

Fig. 1. Apparatus for Measuring Contact Angles Using Concus and Finn Theory

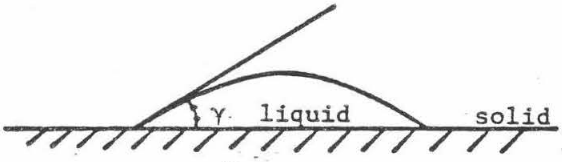

a) Droplet technique

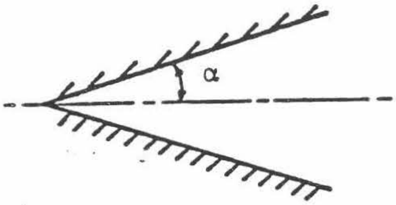

b) Technique using Concus and Finn theory

$\gamma = \pi/2 - \alpha$ at discontinuity

Fig. 2. Two Techniques Used for Measuring Contact Angles (γ contact angle)

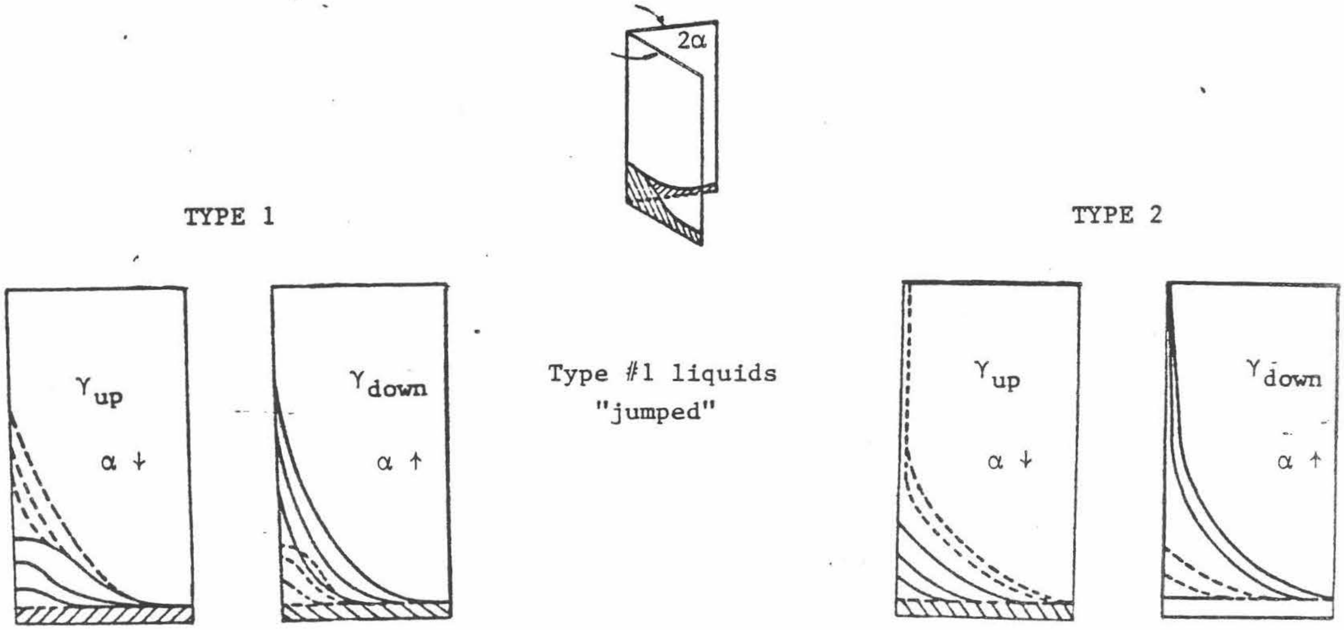

Fig. 3. Observed Meniscus Profiles (γ_{up} rising contact angle; γ_{down} receding contact angle)

CONTACT ANGLES OF VARIOUS LIQUIDS ON GLASS

Chem. Service No.	Liquid	#	$\gamma_{up} \pm \sigma$	$\gamma_{down} \pm \sigma$	$\gamma_{est.}$	T (°C)
-	Water	5	38±1°	15±0.8°	30°	24°
	HALOGEN-SUBSTITUTED HYDROCARBONS					
633	Dibromomethane	4	12.4±1°	7±0°	12°	26°
		2	13.5±0.7°	4.5±0.7°		
		3	13.8±0.3°	5.7±0.6°		
618	2-bromopropane	7	9.8±2°	9.1±1°	10°	26°
3110	2-chloropropane	7	16.1±1°	13.6±1°	10°	26°
601	1-bromobutane	8	10.9±1°	9.6±1°	5°	25°
621	Chlorobutane	5	7.9±0.4°	3.5±0.7°	5°	24°
3040	Isobutyl chloride	6	8±0.7°	2.3±0.5°	2°	23°
2385	1-bromooctane	5	8±2°	4±1°	5°	26°
		5	7.9±1°	3.6±1°		
666	Bromobenzene	4	9.8±1°	5.5±0.6°	20°	25°
		5	17.2±2°	4.4±1°		
2450	2-bromotoluene	5	13.8±0.8°	2.8±1°	10°	26°
		5	13.6±2°	1.6±1°		
672	2-chlorotoluene	5	8.8±2°	1.3±0.3°	10°	25°
		5	11.6±0.9°	2±1°		
	ALCOHOLS					
151	Ethanol	5	7.2±0.4°	4.4±0.4°	-	24°
161	1-propanol	5	9.1±0.9°	3.3±1°	5°	25°
		5	9.3±0.4°	2.8±0.8°		
142	1-butanol	5	13.1±2°	2.6±0.9°	5°	25°
		5	12±1°	2.2±0.8°		
139	1-pentanol	5	12.4±1°	6.9±0.4°	12°	25°
		5	12.5±1°	2.4±0.5°		
155	1-hexanol	6	10±0°	8.4±2°	5°	26°
166	1-octanol	5	28.2±3°	4.1±0.7°	30°	26°
		4	30.8±1°	3.8±1°		
213	α-hydroxytoluene	5	13.5±2°	6.1±0.9°	5°	-
218	2-phenylethanol	6	13±2°	6.5±1°	15°	25°
		6	13.3±1°	7.3±1°		
168	2-propanol	5	9.7±0.4°	2.4±0.5°	5°	25°
		5	9.8±0.3°	4±0.8°		

CONTACT ANGLES ON GLASS (cont.)

	ALCOHOLS (cont.)					
6788	3-pentanol	5	7.8±0.4°	4.2±0.8°	3°	25°
		5	9.7±1°	3.3±0.6°		
143	2-methyl-1-propanol	5	17.4±0.9°	7.1±0.7°	6°	25°
		5	10.9±0.7°	3.8±2°		
158	2-methyl-3-butyn-2-ol	5	8.9±1°	3.9±1°	10°	24°
		4	9.5±0.6°	3.1±0.6°		
153	2-ethyl-1-hexanol	5	6.1±0.7°	3.5±0.5°	5°	24°
3310	Cyclohexylmethanol	5	16.6±1°	6.2±1°	15°	24°
		6	12.4±0.8°	4.5±1°		
188	2-mercaptoethanol	5	22.6±2°	---	-	-
		5	19.1±2°	5±0°		
	GLYCOLS*					
7990	2,2'-dihydroxydiethyl sulfide	-	27°	---	25°	24°
205	1,2-propanediol	-	10°	---	8°	24°
195	Glycerin	-	23°	2°	25°	23°
210	Triethylene glycol	-	20°	---	8°	25°
5880	2-methyl-2,4-pentanediol	10	16.9±1°	13.1±1°	18°	26°
	ESTERS					
396	Carbonic acid dimethyl ester	6	7.7±1°	6.8±0.8°	7°	25°
395	Carbonic acid diethyl ester	5	8.5±0.7°	6.4±0.4°	10°	23°
		4	11±1°	6.3±0.3°		
4135B	Malonic acid dimethyl ester	5	23.5±1°	6.8±2°	25°	26°
4646E	Malonic acid diethyl ester	6	5.3±0.5°	2.3±0.5°	5°	24°
421	Acetic acid methyl ester	7	6.9±1°	2.9±0.7°	-	24°
412	Acetic acid ethyl ester	5	7.4±0.5°	3±0.8°	4°	25°
443	Acetic acid 2-ethoxyethyl ester	2	10.5±0.7°	6.8±0.4°	5°	24°
		6	9.3±2°	6.2±0.9°		
438	Acetic acid isopropyl ester	5	12.4±2°	7.2±1°	5°	26°
		5	14.4±2°	7.8±1°		
436	Acetic acid isopropenyl ester	5	9.9±2°	9.2±2°	5°	26°
		4	13±1°	8.5±2°		
416	Acetic acid 2-ethylhexyl ester	5	6±2°	1.3±0.4°	5°	25°
		5	3.1±0.9°	2.3±1°		
418	Propanoic acid ethyl ester	5	10.3±1°	9.4±0.5°	10°	26°
1004	Propenoic acid butyl ester	5	10.6±0.9°	4.9±0.4°	5°	26°
		4	11±0.8°	4.8±0.5°		
413	Butanoic acid ethyl ester	6	4.2±0.8°	0.7±0.7°	5°	26°
		5	1.8±0.3°	1±0.1°		

CONTACT ANGLES ON GLASS (cont.)

	ESTERS (cont.)					
1965B	Butanoic acid 3-methylbutyl ester	6	13.7±0.8°	5.3±0.4°	5°	26°
		6	7.8±3°	3.7±1°		
PZ5	Tetradecanoic acid isopropyl ester	3	9±0°	8±0°	-	-
919	Phosphoric acid triethyl ester	5	9.6±0.4°	5.1±0.5°	8°	25°
		4	11.5±1°	4.4±0.5°		
916	Phosphoric acid tributyl ester	5	15.9±4°	2.4±0.5°	7°	25°
		5	13.2±0.6°	2.7±0.8°		
463	Malonic acid monoethyl ester mononitrile	5	11.2±0.8°	6.8±0.4°	15°	25°
		5	12.2±0.8°	7±0°		
5740A	Chloroacetic acid methyl ester	5	5.3±1°	2.6±1°	5°	26°
2145B	Formic acid benzyl ester	5	8.3±0.4°	3±1°	10°	24°
		4	9±0.7°	3.5±2°		
1980	2-hydroxybenzoic acid 3-methylbutyl ester	5	23.4±1°	2.1±0.9°	20°	-
486	Succinic acid diethyl ester	5	9.3±0.3°	---	10°	-
		4	9.3±0.5°	6±0.5°		
465	3-oxobutanoic acid ethyl ester	10	17.1±2°	11.9±2°	15°	26°
482	Maleic acid diethyl ester	6	11.4±2°	4.7±2°	15°	24°
		5	10.3±2°	5±0°		
534	Benzoic acid methyl ester	4	13±1°	9±0.4°	10°	25°
		4	14±0.8°	8±0°		
		4	9.9±0.3°	5.8±1°		
531	Benzoic acid ethyl ester	6	5.3±1°	4.6±1°	5°	25°
517	Benzoic acid butyl ester	4	10.5°	---	-	-
492	1,2-ethanediol diacetate	4	10±0°	5.3±0.5°	10°	25°
			5.9±3°	2.4±1°		
	HYDROCARBONS					
741	2,2,4-trimethylpentane	5	5.5±0.4°	2±0.4°	3°	25°
		3	8.3±0.6°	5.7±0.6°		
6781B	Pentane	3	14.7±2°	3.5±2°	7°	25°
733	Heptane	5	9.5±2°	3.8±0.8°	-	25!
		5	8.6±0.5°	4±0.4°		
740	Octane	5	9.4±0.9°	6.8±0.8°	10°	26°
		6	10±0.6°	7.5±2°		
756	1-octene	6	8.2±2°	6.8±2°	5°	25°
		6	9±1°	7.3±1°		
748	Cyclohexene	5	8.6±1°	8.4±0.5°	7°	25°
744	Decalin	6	16±1°	9.7±2°	15°	26°
	KETONES					
798	2-propanone	5	8.1±2°	1.8±1°	5°	24°
810	2-butanone	5	5.7±0.4°	2.8±1°	2°	23°

CONTACT ANGLES ON GLASS (cont.)

	KETONES (cont.)					
813	3-pentanone	6	7.6±0.8°	4.3±0.4°	2°	25°
		5	7.3±0.8°	3.5±0.6°		
811	2-octanone	5	7.7±0.8°	7.2±1°	5°	25°
		5	8.2±1°	6.3±0.4°		
5895B	4-methyl-2-pentanone	11	9.5±0.5°	6.1±1°	5°	26°
7121F	3,3-dimethyl-2-butanone	5	8.1±1°	3.4±0.7°	3°	26°
		5	9.2±0.4°	3.4±0.8°		
808	4-methyl-3-penten-2-one	5	6.4±2°	2.5±0.5°	2°	-
		5	5.7±0.8°	3.2±0.8°		
815	2,4-pentanedione	5	12.9±2°	11.8±3°	5°	27°
		4	12±4°	---		
	ALDEHYDES					
225	Butanal	5	9.6±2°	6.3±2°	5°	25°
		5	12.5±0.5°	8.1±0.5°		
234	Pentanal	4	13±0.8°	4.3±1°	5°	25°
231	Heptanal	4	14.8±2°	2.3±1°	17°	23°
		5	13.8±0.8°	1.3±0.7°		
240	Cinnamaldehyde	5	15.4±0.5°	6.8±1°	15°	-
	ETHERS					
172	Diethylene glycol monobutyl ether	5	14.6±0.5°	5.8±0.8°	12°	24°
		5	10.7±1°	4.8±0.4°		
8280	Triglyme	5	6.2±0.4°	3.6±0.5°	5°	25°
		5	6.4±0.7°	3.2±0.8°		
173	Diethylene glycol monoethyl ether	5	16.8±0.8°	6.3±0.6°	3°	-
		2	17.5±0.7°	5±0°		
3	Methylal	5	4±0.5°	2.4±0.5°	5°	25°
177	2-ethoxyethanol	5	6.7±0.4°	4.4±0.5°	2°	24°
221	2-phenoxyethanol	6	17.8±1°	10.5±2°	15°	25°
		5	17±1°	9.8±0.8°		
	AROMATICS					
764	Isopropylbenzene	5	15.6±0.5°	4±0.6°	2°	24°
		5	18.2±1°	7.9±0.7°		
771	1,3,5-trimethylbenzene	6	8.5±0.5°	7.8±2°	7°	-
		5	7.8±0.6°	7.2±2°		
	MISCELLANEOUS					
297	Triethylamine	5	9.4±2°	5.6±1°	5°	26°
856	1-nitropropane	4	9.8±0.5°	3±1°	3°	25°
		5	11.6±1°	3.6±0.5°		

CONTACT ANGLES ON GLASS (cont.)

	MISCELLANEOUS (cont.)					
7727F	Perhydrosqualene	6	18±0.9°	13.5±1°	20°	26°
		6	17.5±1°	11.8±2°		
6	2-methylpropanoic acid	5	13.9±1°	4.4±0.8°	7°	24°
		5	13.7±1°	4.1±1°		

Table 1. Contact Angles of Various Liquids on Glass

Chem Service No.--an identification number for each chemical
Liquid--name of liquid, and chemical family of liquid
#--number of measurements taken per pair of slides
$\gamma_{up} \pm \sigma$-- γ_{up} is the rising contact angle average for each pair of slides; σ is the standard deviation
$\gamma_{down} \pm \sigma$--γ_{down} is the receding contact angle average
$\gamma_{est.}$--the contact angle estimated by the droplet method (Fig. 2b)
T--temperature in degrees Centigrade

All liquids are divided into families by chemical structure, and are ordered by chemical structure, i.e. the chemicals that are most similar chemically are next to each other.

*Since glycols are hygroscopic except for 2-methyl-2,4-pentanediol, only the first measurement taken is recorded for all other glycols.

CONTACT ANGLES OF VARIOUS LIQUIDS ON PLEXIGLASS *

Chem. Service No.	Liquid	#	$\gamma_{up} \pm \sigma$	$\gamma_{down} \pm \sigma$	$\gamma_{est.}$	T (°C)
	HALOGEN-SUBSTITUTED HYDROCARBONS					
618	2-bromopropane	3	23.7±2	9.3±1	-	25°
601	1-bromobutane	5	19.4±0.9°	5.6±0.4°	-	23°
		5	17.1±1°	5.6±0.7°		
666	Bromobenzene	5	14±4°	3.6±2°	-	26°
672	2-chlorotoluene	5	11.2±1°	6±0.7°	8°	25°
		5	12±1°	5.9±0.6°		
	ALCOHOLS					
142	1-butanol	5	17.5±1°	6.4±1°	5°	25°
		5	19.1±1°	7±1°		
139	1-pentanol	5	15.4±1°	6.6±1°	5°	25°
		5	15.5±1°	6.6±1°		
155	1-hexanol	5	18.6±1°	7.1±1°	-	24°
		5	18.4±2°	5.6±1°		
166	1-octanol	5	20.4±1°	5.7±1°	5°	24°
		5	21.4±1°	6.4±1°		
213	α-hydroxytoluene	5	18±2°	1.9±0.2°	-	25°
		5	19.4±2°	2.6±0.6°		
218	2-phenylethanol	5	12.6±1°	6±1°	-	-
		5	19.8±1°	6.4±1°		
	GLYCOLS*					
7990	2,2'-dihydroxydiethyl sulfide	-	37°	5°	40°	24°
195	Glycerin	-	67°	5°	60°	25°
	ESTERS					
2145B	Formic acid benzyl ester	3	21.7±2°	5.3±1°	15°	26°
		5	20.2±1°	6.2±0.8°		
412	Acetic acid ethyl ester	4	12.3±0.7°	4.3±1°	8°	26°
		3	17±3°	3.8±0.3°		
418	Propanoic acid ethyl ester	5	18.2±1°	4.9±0.7°	-	25°
		5	16.2±0.5°	5.4±0.6°		
1004	Propenoic acid butyl ester	5	9.1±0.8°	2.8±0.8°	5°	25°
		5	12.8±1°	6.2±1°		
4135B	Malonic acid dimethyl ester	5	23.2±2°	6.4±1°	28°	26°
		5	20.3±0.7°	6±1°		

*We were unable to measure the contact angle of water on plexiglass.

CONTACT ANGLES ON PLEXIGLASS (cont.)

	ESTERS (cont.)					
463	Malonic acid mono-	5	13.2±1°	4.6±2°	-	25°
	ethyl ester	5	16.4±1°	5.4±0.6°		
	mononitrile					
517	Benzoic acid butyl	5	16.1±0.7°	6±0.4°	-	25°
	ester	5	12.3±0.5°	6±0.7°		
492	1,2-ethanediol	5	20.1±0.7°	5.6±2°	20°	26°
	diacetate	5	22±2°	6.2±2°		
	HYDROCARBONS					
741	2,2,4-trimethyl-	3	16±2°	5.7±2°	5°	26°
	pentane	5	17±2°	5.4±1°		
733	Heptane	5	23.8±0.8°	8.6±1°	2°	24°
		5	19.4±0.9°	5.8±1°		
740	Octane	5	9.8±0.6°	2.4±0.6°	-	26°
		5	10.8±1°	4.1±0.2°		
744	Decalin	5	14.3±0.7°	4.4±0.6°	8°	26°
		5	13.5±0.5°	3.6±0.6°		
	ALDEHYDES					
231	Heptanal	5	14±0.7°	5.1±0.7°	5°	26°
		5	13.3±1°	4.9±0.9°		
	AROMATICS					
764	Isopropylbenzene	5	12.6±2°	5±1°	4°	25°
		5	9.4±1°	3.8±1°		
	MISCELLANEOUS					
7727F	Perhydrosqualene	5	16.6±0.6°	5.9±0.6°	-	24°
		5	15.5±1°	5.4±0.9°		
6	2-methylpropanoic	5	18.2±3°	4.4±1°	5°	25°
	acid	5	17.5±3°	4.8±0.5°		

An Interactive Graphics Editor for the HP 9836/9826 Computer

Christine H. Yu

SURF Final Report

ABSTRACT

This paper is meant to introduce a graphics editor GRED. It includes:

I. Getting Started on GRED

II. The Editor

III. The Filer

IV. Problems Encountered

September 1, 1983

An Interactive Graphics Editor for the HP 9836/9826 Computer

Christine H. Yu

SURF Final Report

INTRODUCTION

GRED is a graphics editor which creates,modifies,saves and plots pictures of various shapes for various purposes. GRED is written in Pascal and runs on the HP Chipmunk series (9826/9836). The black and white machine (chipmunk) is used with a color monitor and a HP 9111 graphics tablet. GRED is easy to learn and use: NO programming is needed and it is as easy to use as drawing pictures by hand.

I. GETTING STARTED ON GRED

TO use GRED, execute (X) the program /BIN/GRED on the SRM (Shared Resource Manager) system. A welcome sign and a listing of commands on the screen will then indicate that you are in the filer mode of GRED. The prompt in GRED is '$'. Input a command after a prompt by typing the capitalized character of the command listed on the screen and then pressing the < ENTER> key. When using GRED, a command will be executed only after the < ENTER> key is pressed. An UPPER CASE command and lower case command achieve the same functions.

II. THE EDITOR

To get into the editor, type 'E" or "e". The editor prompts a name of a file to edit, which can be an existing one or a new one. Input the file name after the question 'Edit what file?" and press the < ENTER> key, or just press the < ENTER> key to edit the previous file. Now you are in the editor and are ready to "draw" a pretty picture.

The user can generate or modify a picture by pressing the stylus attached to the graphics tablet onto the tablet board to determine the location of a shape and can detect the entire picture on the color monitor screen.

A row of 16 small squares will appear at the top of the color monitor screen. These squares correspond to the 16 menu boxes at the top of the graphics tablet. Labels inside the small squares are the abbreviations for the available drawing modes, drawing shape styles and functions. The current functions in use are indicated by different colored borders. For example, right now the borders of the first square from the left [red] and the tenth square [lin] are colored in red to indicate that the current color is red and the current drawing shape style is a line. There are two menu command levels. Pressing the last menu square [mor] allows access to the other menu command level.

Always press the stylus inside the corresponding menu boxes on the tablet board to select menu commands. A little cursor [+] on the color monitor will tell you the location of the stylus. Now let's get acquainted with those menu commands.

< FIRST MENU COMMAND LEVEL >

There are six choices of colors:

[red]:	RED
[grn]:	GREEN
[yel]:	YELLOW
[blu]:	BLUE
[pur]:	PURPLE
[cyn]:	CYAN

There are five regular shape styles:

[arw]: SINGLE-POINTED ARROW

[dbl arw]: DOUBLE-POINTED ARROW

[lin]: LIN

[box]: BOX

[cir]: CIRCLE

After selecting one of the above shape styles, you can start "drawing". First, select a starting point, press the stylus down, and then move the stylus on the tablet board. Notice the change of the shape as the stylus moves. Be sure that the stylus is ALWAYS pressed down while drawing the shape. The size and the location of the shape are determined when the stylus is lifted from the board. You can keep on drawing shapes of the same style and color until another shape, color, or mode is selected.

There are three specialized functions:

[pol]: To draw one polygon at a time. First, select a starting point and then move the stylus around to vary the length and the direction of a side the same way as you draw a line. Lifting up the stylus determines the location and length of one side of the polygon. This procedure can be repeated as desired for different sizes and number of sides. A polygon is created when one side ends at the starting point of the first side .

[tex]: To input one text at a time. After [tex] is selected, you will be asked to input a message, which can be any word or sentence composing 200 characters or less (spaces also count). First, type a message after the instruction "Input a message: " and press the < ENTER> key. Then select the location of the first character of the message by pressing the styluson the tablet board. The message should now appear on the color screen. To input another message, you have to select the menu commmand "tex" again.

[ckt fon]: To draw one circuit symbol at a time. You do not need to draw the irregular circuit shapes; just select them. You have an option of displaying all the available circuit symbols on the color monitor. This display is always helpful since you select one symbol by inputing the number associated with that symbol. Finally, select the location for the symbol as usual by pressing the stylus on the tablet board.

[ful arw]: To be able to draw arrows and double-arrows with width. It toggles every time it is pressed.

[mor]: OTHER MENU OF COMMANDS

< SECOND MENU COMMAND LEVEL >

[ext]: To stop editing the picture. The file will be updated and saved the way it is displayed on the color monitor.

[clr]: To clear the monitor screen and empty the file.

[frh]: To refresh the screen so that all the existing shapes in the file will be redrawn again clearly.

[plt]: To plot all the shapes shown on the monitor screen. A standard HP plotter should be connected by a HP IB (interface bus) to the computer and a piece of graphics paper needs to be loaded into the plotter.

There are four editing modes for modifying a picture:

[edt]: To alter the size of a shape.

[cpy]: To make a new copy of a shape at another location.

[mov]: To move a shape from one location to another.

[del]: To delete a shape.

While in one of the modes above, you need to select a shape by pressing the stylus inside the shape's BODY (not arrow heads, if the shape style is arrow or double-pointed arrow).

Except for "del", keep pressing the stylus while moving it and notice the changes. When the stylus is lifted, the shape is updated on the monitor screen.

[un- del]: To return all the shapes deleted since last time the [del] mode was selected.

The following two commands are to select two different graphics character fonts, which are not completely finished at this time. The user should skip the following two commands for the present time.

[fon]: Incomplete.

[fon]: Incomplete.

[oth]: Orthoganality is valid while drawing or editing an arrow, a double-arrow or a line. It toggles every time it is pressed.

[win]: To set a new view window so that certain shapes in the picture can be enlarged on the screen. Press the stylus at two different points which will become the two opposite corners of the window which contains the shapes to be enlarged. All shapes will be rescaled and new shapes will be scaled accordingly. It toggles every time it is pressed.

[chg col]: To change the colors of shapes to the current color in use by pressing the stylus inside the shapes. You may keep changing colors of different shapes until another mode is selected.

[chg fon]: This mode does not function yet because there are no other available character fonts besides the standard HP character fonts.

After finishing editing the picture, select the command [ext] to get out. Your picture will automatically be saved in its last form. Now you are back to the filer of GRED again.

III. THE FILER

PLOT (P/p) The same as the command [plt]: to plot all the shapes shown on the screen.

In the method of averaging one usually assumes $R_0 \equiv R$, $\Phi_0 \equiv \Phi$; however, the more general form given here will be convenient. In the linear problems dealt with, R_k will contain R only as a multiplicative factor and Φ_k will be independent of R. The slow time τ may or may not be given a priori.

To determine the functions R_k and Φ_k we first compute the (substantial) time derivative in two ways and equate the results. One way is to apply d/dt to (2.5), the other way is to insert (2.5) into the right-hand side of (2.1) and develop into powers of ε: $\sum \varepsilon^k \begin{pmatrix} f_k \\ g_k \end{pmatrix}$ Rearranging the equality gives

$$\frac{d\tau}{dt}\frac{\partial}{\partial\tau}\sum_{k=0}\varepsilon^k\begin{pmatrix} R_k \\ \Phi_k \end{pmatrix} = \sum_{k=0}\varepsilon^k\left[\begin{pmatrix} f_k \\ g_k \end{pmatrix} - J_k\begin{pmatrix} 0 \\ 1 \end{pmatrix} - \frac{\partial}{\partial t}\begin{pmatrix} R_k \\ \Phi_k \end{pmatrix}\right], \qquad (2.6)$$

where

$$J_k = \begin{pmatrix} \dfrac{\partial R_k}{\partial R} & \dfrac{\partial R_k}{\partial \Phi} \\ \dfrac{\partial \Phi_k}{\partial R} & \dfrac{\partial \Phi_k}{\partial \Phi} \end{pmatrix}.$$

In the second term of the right-hand side we have used (2.2). Another consequence of (2.2) is that, within an irrelevant constant of integration

$$\Phi = t. \qquad (2.7)$$

This leads to various different-looking but equivalent formalisms. For instance, we may treat Φ and t as different variables in a functional expression, form $\frac{\partial}{\partial \Phi}$ and $\frac{\partial}{\partial t}$ as separate derivatives and then use (2.7), or we may use (2.7) immediately.

We shall now use (2.6) to determine the R_k and Φ_k. These functions are not unique; we shall try to choose them so as to give convenient coordinate

4. Jacques Tiberghien, *HP Computer Systems, The Pascal Handbook*, Hewlett-Packard Company, 1981.

Signature of Sponsor

Christine H. Yu

Signature of Fellow

SURF Seminar Day Schedule
Saturday, October 8, 1983

12:00 - 1:30 PM	Buffet Luncheon in Dabney Garden
1:30 - 4:30 PM	SURF Student Presentations (See Schedule Below)
4:30 - 5:30 PM	President´s Reception President and Mrs. Goldberger´s Garden 415 South Hill, Pasadena

Session I

Room 102 Spalding Laboratory
Dr. Marc-Aurele Nicolet
Professor of Electrical Engineering

1:25 PM	Introduction	Dr. Nicolet
1:30-1:50	Perturbation Methods for Autonomizing Ordinary Differential Equations (Sponsor: Dr. P. Lagerstrom)	Stephen Anco Sr Physics/ Applied Math (GM-SURF)
1:50-2:10	Combinatorial Designs (Sponsor: Dr. H. Ryser)	Bradley Brock Sr Physics/ Applied Math (Richter-SURF)
2:10-2:30	On Moufang Loops of Even Order $\underline{pq}^2$ (Sponsor: Dr. R. Wilson)	Mark Purtill Sr Mathematics (Richter-SURF)
2:30-2:50	A Determination of the Solar Period in the Calcium K-line and the Sun as a Star (Sponsor: Dr. H. Zirin)	Aaron Roodman Jr Physics
2:50-3:10	Near Earth and Non-mail Belt Asteroid Search and Survey (Sponsor: Dr. E. Helin [JPL])	Steven Swanson Sr Astronomy
3:10-3:30	Death and Disappearance in Gasconade County (Sponsor: Dr. W. Kamphoefner)	Jeff Freymueller Jr Mathematics
3:30-3:50	The Influence of the Eighteenth Century Novel on the Writings of Lord Byron (Sponsor: Dr. J. McGann)	Catherine Hayes Jr Mathematics/ Literature
3:50-4:10	Development of a Composer´s Amanuensis (Sponsor: Dr. F. Thompson)	Craig Minor Sr Computer Science (IBM-SURF)

Session II

Room 104 Spalding Laboratory
Dr. Charles D. Babcock
Professor of Aeronautics and Applied Mechanics

1:25	Introduction	Dr. Babcock
1:30-1:50	An Experimental Study of Soil Slope Failure Using a Centrifuge (Sponsor: Dr. R. Scott)	Lisa Nikodym Sr Engineering and Applied Science
1:50-2:10	Structural Design and Analysis of a Space Shuttle Payload (Sponsor: Dr. C. Babcock)	Norman Princen Sr Aeronautics (GM-SURF)
2:10-2:30	Unidirectional Crystal Growth from Solution with Negligible Convection (Sponsor: Dr. D. Wood)	Darrell Schlom Sr Materials Science
2:30-2:50	Investigation of the Feasibility of Fabricating Porous Electrodes for the AMTEC Project (Sponsor: Dr. J. Lambe/ Dr. S. Khanna)	Aditya Srinivasan Electrical Engineering
2:50-3:10	Contact Angles of Various Liquids on Glass and Plexiglass Measured by a New Method (Sponsor: Dr. D. Coles)	Minami Yoda Jr Engineering and Applied Science
3:10-3:30	An Interactive Graphics Editor for the HP 9836/9826 Computer (Sponsor: Dr. C. Mead)	Christine Yu Jr Engineering and Applied Science (Ford-SURF)
3:30-3:50	Water Channel Tests of Trapped Vortex High-Lift Airfoils (Sponsor: Dr. A. Roshko)	Robert Anderson Sr Engineering and Applied Science (GM-SURF)
3:50-4:10	Theoretical Model for the Study of Coagulation of Particles (Sponsor: Dr. J. List)	Alex Bouzari Sr Electrical Engineering (IBM-SURF)
4:10-4:30	Design and Construction of Screen Based Jet Impaction Fog Collector (Sponsor: Dr. R. Flagan)	Mehrdad Haghi Sr Applied Physics/ Engineering and Applied Science (GM-SURF)

Session III

Room 106 Spalding Laboratory
Dr. William Bridges
Professor of Electrical Engineering and Applied Physics

1:25	Introduction	Dr. Bridges
1:30-1:50	Acousto-Optic Experiments with BSO Crystals (Sponsor: Dr. D. Psaltis)	Praveen Asthana Jr Electrical Engineering (IBM-SURF)
1:50-2:10	The Electron Runaway Phenomenon (Sponsor: Dr. N. Corngold)	Pang-Chieh Chen Sr Applied Math/ Engineering
2:10-2:30	Hot Electron Transport in a Proposed GaAs-Al-GaAs Transistor (Sponsor: Dr. A. Yariv)	Ze-Hua Chen Sr Applied Physics
2:30-2:50	Microstrip Transmission Losses at Millimeter Frequencies (Sponsor: Dr. D. Rutledge)	David Fun Sr Electrical Engineering
2:50-3:10	Measuring the Copper Isotope Shift and HFS Using Opto-Galvanic Spectroscopy (Sponsor: Dr. W. Bridges)	Stephen Jones Sr Physics (GM-SURF)
3:10-3:30	Poloidal Space-Time Mapping of Microturbulence at the Plasma Edge in the Caltech Tokamak (Sponsor: Dr. S. Zweben)	Jesus N Villasenor Sr Physics
3:30-3:50	A Method for Creating Three-Dimensional Computer Generated Holograms (Sponsor: Dr. D. Psaltis)	Clare Stassen Sr Applied Physics/ Computer Science
3:50-4:10	Time Dependent Radiation Trapping (Sponsor: Dr. W. Bridges)	Ned Wingreen Sr Physics
4:10-4:30	The Control and Interface of a Robot Arm by Microcomputer (Sponsor: Dr. P. Thompson)	Sven A Wolf Jr Electrical Eng./ Applied Mathematic

Session IV

Room 125 Donald E. Baxter, M.D. Hall
Dr. Thomas Tombrello
Professor of Physics

1:25	Introduction	Dr. Tombrello
1:30-1:50	Growth of Sympathetic Neurons in Culture (Sponsor: Dr. J. Pine)	John Butman Jr Physics
1:50-2:10	An Electrostatic Lens for Focusing High Energy Ions in the Solar Wind (Sponsor: Dr. D. Burnett Dr. T. Tombrello)	Glen Crawford Jr Biology/ Chemical Eng. (Richter-SURF)
2:10-2:30	Conductivity Changes in Carbon Films Induced by Ion Irradiation (Sponsor: Dr. T. Tombrello/ Dr. D. Burnett)	Eric Grannan Sr Physics (IBM-SURF)
2:30-2:50	Hydration of Sodium Silicate Glasses: Dependence on Sodium Content (Sponsor: Dr. T. Tombrello)	John McGowan Jr Physics (IBM-SURF)
2:50-3:10	An Analysis of Satellite Observations of Ozone and Related Species (Sponsor: Dr. Y. Yung)	Stanley Berman Jr Physics
3:10-3:30	Hartree-Fock Calculations of Neutron-rich Nuclei in the s-d Shell (Sponsor: Dr. S.E. Koonin)	Joe Chung-Yee Chang Sr Physics (IBM-SURF)
3:30-3:50	Io´s Atmospheric Density as a Function of Aura´s Density Distribution (Sponsor: Dr. P. Haff)	Joe Cheng Jr Applied Physics
3:50-4:10	Investigations of the Sputtering Processes in Semi-Conductors and Insulators (Sponsor: Dr. T. Tombrello)	Kelly Cherrey Jr Applied Physics (IBM-SURF)
4:10-4:30	Environmental Effects on Subsurface Radon: A Lytle Creek Rainfall Anomally Model and a Pacoima Signal Model (Sponsor: Dr. T. Tombrello)	Dennis Fatland So Physics (Richter-SURF)

Session V

Room 127 Donald E. Baxter, M.D. Hall
Dr. Ward Whaling
Professor of Physics

1:25	Introduction	Dr. Whaling
1:30-1:50	Solving Problems in Classical Physics with Microcomputers (Sponsor: Dr. G. Fox)	Anthony Skjellum Sr Physics/Chemical Eng. (IBM-SURF)
1:50-2:10	Design of Apparatus to Detect ^{16}O from the $^{12}C(\alpha,\gamma)^{16}O$ Reaction (Sponsor: Dr. C. Barnes)	Brett Garrett Jr Physics
2:10-2:30	Determination of the Nuclear Proximity Function from Sub-barrier Fusion Data for p-shell (Sponsor: Dr. S.E. Koonin)	Masahiko Inui Sr Physics (Richter-SURF)
2:30-2:50	Study of Charge Asymmetry in the Reaction $e^+e^- \to \mu^+\mu^-$ with the Forward Counters of the MARK J Detector at PETRA (Sponsor: Dr. H. Newman)	Tak Leuk Kwok Sr Physics (Richter-SURF)
2:50-3:10	Gamma-ray Background Suppression in Detection of Polarization Asymmetry of Nuclear Beta Rays (Sponsor: Dr. F. Boehm)	Mark Lindsay Sr Physics
3:10-3:30	Geomagnetic Positions of Various Cratons (Sponsor: Dr. J. Kirschvink)	Paul Filmer Jr Geophysics
3:30-3:50	Atomic Abundances in a Hollow Cathode Discharge (Sponsor: Dr. W. Whaling)	Matthew Penn So Astronomy (Richter-SURF)
3:50-4:10	Argon Drift Calorimetry (Sponsor: Dr. D. Hitlin)	Janet Saylor Sr Physics (Richter-SURF)
4:10-4:30	Laser Beam Cleaning with Single Mode Optical Fibers (Sponsor: Dr. S. Whitcomb)	Josef Frisch Sr Physics (Richter-SURF)

Session VI

Room 128 Donald E. Baxter, M.D. Hall
David C. Van Essen
Associate Professor of Biology

1:25	Introduction	Dr. Van Essen
1:30-1:50	DHFR Gene Expression Controlled by Anti-Sense DNA (Sponsor: Dr. L. Hood/ Dr. B. Wold)	Susanna Chan Jr Biology
1:50-2:10	Studies of a Large V_H Family in Balb/c Mice (Sponsor: Dr. L. Hood)	John Wall Jr Biology
2:10-2:30	Comparative Sequence Analysis of Embryonic Actin Genes of the Sea Urchin (Sponsor: Dr. R. Shott/ Dr. E. Davidson)	Ted George Jr Biology
2:30-2:50	Neuronal Connectivity in the Song System Control Nuclei of the Zebra Finch (_Poephila Guttata_) Brain (Sponsor: Dr. M. Konishi)	Daniela Bonafede Sr Biology
2:50-3:10	Mathematical Representations of Transformations of the Visual Field in the Visual Pathway (Sponsor: Dr. D. Van Essen)	John Houde Sr Electrical Engineering (IBM-SURF)
3:10-3:30	Hemispheric Differences in Preference and Response in Split-Brain Monkeys (Sponsor: Dr. C. Hamilton)	Catherine Ifune Jr Biology
3:30-3:50	Purification of Murine Interleukin-2 (Sponsor: Dr. E. Rothenberg)	Santosh Krishnan So Biology
3:50-4:10	Applications of Soundspectrogram Analysis to Birdsong (Sponsor: Dr. M. Konishi)	Misha Mahowald Jr Biology

Session VII

Room 104 Watson Laboratories of Applied Physics
Dr. Jean-Paul Revel
Albert Billings Ruddock Professor of Biology

1:25	Introduction	Dr. Revel
1:30-1:50	Cloning the Murine Terminal Transferase Gene Using λgt11, a Unique Phage Expression Vector (Sponsor: Dr. E. Rothenberg)	Candice McCoy Sr Biology
1:50-2:10	Association of Gap Junctions with Endoplasmic Reticulum (Sponsor: Dr. J-P. Revel)	James Dunn Jr Biology/ Chemical Eng.
2:10-2:30	Visual System of Jumping Spiders (Sponsor: Dr. J. Allman)	Christopher Yo Jr Biology
2:30-2:50	The Phase III Crystal Structure of Hexamethylbenzene (Sponsor: Dr. S. Samson)	Michael Bronikowski So Chemical Engineering
2:50-3:10	Testing of the Cluster Model Approach to Desorption Problems (Sponsor: Dr. W. Goddard)	Kenneth Hui Sr Physics (Ford-SURF)
3:10-3:30	Photochemistry of Ozone on GaAs Surfaces (Sponsor: Dr. K. Janda)	Steven Kong Jr Applied Physics/ Applied Math (Ford-SURF)
3:30-3:50	Cross-Cultural Attitudes Toward the Use of Reclaimed Wastewater in SWA/Namibia (Sponsor: Dr. E. Munger)	Barbara Turpin Sr Mechanical Engineering

Session VIII

Room 142 Keck Laboratories
Dr. Eric Herbolzheimer
Assistant Professor of Chemical Engineering

1:25	Introduction	Dr. Herbolzheimer
1:30-1:50	The Reduction of Sulfur Dioxide to Elemental Sulfur (Sponsor: Dr. G. Gavalas)	Robert Murphy Sr Chemical Engineering (GM-SURF)
1:50-2:10	Modeling of Indoor Air Quality (Sponsor: Dr. F. Shair)	Glayde Myers Jr Chemical Engineering
2:10-2:30	Sedimentation in Sheared Suspensions (Sponsor: Dr. E. Herbolzheimer)	Thomas Remmers Sr Chemical Engineering (Carnation-SURF)
2:30-2:50	Isolating the Gene for a Drosophila Transcription Factor (Sponsor: Dr. C. Parker)	Doug Ruden Sr Biology/ Chemistry
2:50-3:10	Activity of β-Lactamase and Mutant R2 (Sponsor: Dr. J. Richards)	Brian Mapes Jr Chemistry
3:10-3:30	Description of the Luminescent Excited State of the Ionic Cluster Species $W_6Br_{14}^{-2}$ (Sponsor: Dr. H. Gray)	Behzad Sadeghi Jr Mathematics
3:30-3:50	Work on a Synthetic Sequence in the Synthesis of Tirandamycin (Sponsor: Dr. P. Bartlett [Berkeley])	John Schaeck Sr Chemistry
3:50-4:10	Activity of Fluorescent Mevinolin Derivitives in Human Cells in Tissue Culture (Sponsor: Dr. B. Wold)	James Mayhugh So Chemistry

Session IX

Room 102 Steele Laboratory
Christopher E. Brennen
Professor of Mechanical Engineering

1:25	Introduction	Dr. Brennen
1:30-1:50	The Study of Permeability Characteristics of Cordierite Ceramics and Polymer Membranes (Sponsor: Dr. G. Stephanopoulos)	Christine Tiller Jr Engineering and Applied Science (Ford-SURF)
1:50-2:10	Preparation Techniques and Surface Area of Supported Sorbents (Sponsor: Dr. G. Gavalas)	Kriengkrai Wisanrakkit Sr Chemical Engineering
2:10-2:30	Isolation of the Low Density Lipoprotein Receptor Gene (Sponsor: Dr. B. Wold)	Charles Reel Sr Biology
2:30-2:50	Verbs in a Simple Knowledgeable System (Sponsor: Dr. F. Thompson/ Dr. B. Thompson)	Timothy Fernando Jr Computer Science
2:50-3:10	Synthesis of Methidiumpropyl EDTA (MPE) (Sponsor: Dr. P. Dervan)	Teresa Solberg Jr Chemistry
3:10-3:30	Two-Dimensional Nuclear Magnetic Resonance Studies of Polymyxin B at 11.75 Tesla (Sponsor: Dr. S. Chan)	Lawrence Shapiro So Chemistry
3:30-3:50	Study of Flagellar Motility Inhibition (Sponsor: Dr. C. Brokaw)	Mira Todorovich Jr Biology
3:50-4:10	Manipulation of DNA in Intact Phage (Sponsor: Dr. P. Dervan)	Eliza Sutton Sr Chemistry/ Biology

CALIFORNIA INSTITUTE OF TECHNOLOGY

1983 SURF Summer Seminar Series
12:00-1:00 PM, 153 Noyes

Friday, June 17: Charles J. Brokaw, Professor of Biology

Searching for the Flagellar Oscillator

Flagella are the motile organelles of spermatozoa and many unicellular organisisms. They generate bends that propagate along the flagellum, causing propulsion. We know that the bending of a flagellum is generated by active sliding between the parallel "microtubules" inside the flagellum. We are still trying to understand how this active sliding process is controlled to produce oscillatory bending and bend propagation.

Friday, June 24: Joseph L. Kirschvink, Assistant Professor of Geobiology

Biogenic Magnetite: The Smallest Fossils and the Debate about Magnetic Sensitivity

Although living organisms are known to precipitate biochemically over 40 different minerals, magnetite (Fe_3O_4) is the only one which is permanently magnetic (ferromagnetic). Despite low concentrations in individual organisms, magnetite is now known to be one of the most common biogenic precipitates, and has been found in organisms ranging from bacteria to vertebrates. Sub-micron sized crystals of bacterial magnetite have recently been discovered as microfossils in deep sea sediments and are clearly responsible for much of their stable magnetic remanence. The presence of biogenic magnetite in a variety of vertebrates is also at the center of the current debate concerning the geomagnetic sense in terrestrial animals.

Monday, June 27: Sally Asmundson, Director, Placement and Career Planning Services

Preparing for your Career

An overview of the resources and services available to both students who plan to attend graduate school and those who plan to seek career employment after their BS degree will be presented. Strategies for gaining both the experience and the information needed in order to effectively plan your career and to be successful in attaining your goals will be discussed. Various handouts will be made available.

Thursday, June 30: Terry Cole, Senior Research Associate in Chemistry and Chemical Engineering, Caltech, and Technology Advisor to the Technical Divisions, JPL

Energy Conversion with Solid Electrolytes

Solid electrolytes are a new class of materials which selectively conduct ions but not electrons. The Alkali Metal Thermoelectric Converter (AMTEC) is a sodium gas expansion engine based on beta-alumina solid electrolyte. The new device has no moving parts, with the sodium ions being expanded against an electric field within the solid electrolyte; and the output work is electrical only. The efficiency and power density of the new device may be comparable to internal combustion engines. Applications in aerospace power and solar to electric energy conversion are foreseen.

Friday, July 8: Geoffrey C. Fox, Professor of Theoretical Physics

Use of Computers in Physics Research

We will describe the impact of large scale computing in physics research covering algorithms, software and hardware. Reference: Physics Today, May, 1983, p. 23.

Monday, July 11: Shirley Thomas, Technical Writer and Consultant

The Oral Report

Oral presentations usually are based on written reports, but are an individual form. They are spoken, largely, not read. They contain visuals (slides or overhead projections), and are adjusted in length and technical depth according to the audience. Generally, the author prepares the written report first.

The process of adapting the latter to the former involves this general process: The report is scrutinized, marked with a highlighter pen, analyzed for short passages so detailed they must be read, and appropriate places for visuals marked. A script is prepared, using key words for most passages that are to be talked and complete text for passages to be read.

Rehearsal for the oral presentation is essential. Preferably, tape recordings should be made, replayed, and critiqued by associates. Keen attention must be paid to clarity of speech, pacing, tone, and emphasis.

Visuals require great attention. They should be simple, diverse, and colorful. (Slides that contain a mass of information and are left on for long liperiods are guaranteed to be sleep-inducing.) These are types of visuals: block diagrams, schematics and logistics, graphs, prespective illustrations, pictorial or line art, exploded drawings, cutaways, and overlays (where progression may be shown on a basic visual). They may be prepared from hand-sketched material, rub-ons, paste-ups, typewritten material, lettering systems, and computer images.

Friday, July 15: Rudolph A. Marcus, Arthur Amos Noyes Professor of Chemistry

Chemical Dynamics

There have been many exciting experimental developments in this field and a number of parallel theoretical advances. These include studies of intramolecular redistribution of vibrational energy in isolated molecules, using laser techniques particularly, and the study of fast and slow electron transfer reactions in solution. Illustrations and long range objectives will be discussed.

Monday, July 18: Shirley Thomas, Technical Writer and Consultant

The Written Report

Professional scientific and engineering reports possess certain features and characteristics. This presentation summarizes some of them so that students may prepare their reports in a more professional manner.

The format specified for SURF reports is that designated by the American Institute of Physics. Beyond the format, students need to understand the principles underlying good report writing.

Material must be organized so that a logical outline may be prepared. Relative importance of specific points must be designated through use of headings, subheadings, second level subheadings, third level subheadings, and listings. A report must be written in proper order; for example, the Introduction is not written first, though it appears at the first of the report.

The writing style must be simple, unambiguous, clear, and devoid of deadwood. Reports must accommodate a diverse readership; all readers will not be specialists in the report discipline. The language must be specific and accurate. Necessary data must support the conclusion.

Tables and figures must be properly prepared. Graphics should be used extensively, whether they be photographs, hand drawings, photocopied drawings, or photocopies of parts. Correct use of abbreviations characterize a professional report. Use of checklists is valuable. Correct grammar is imperative.

Friday, July 22: Demetri Psaltis, Assistant Professor of Electrical Engineering

Optical Methods in Radar Imaging

The resolution of an imaging system is proportional to λ/A, where λ is the wavelength of the radiation used and A is the aperture of the lens (or antenna) that forms the image. At radio frequencies the wavelength is over a thousand times longer than optical frequencies. In order to get fine resolution at these relatively low frequencies a very large aperture would be required. Synthetic Aperture Radar (SAR) is a technique, analogous to optical holography, that allows radars to form low resolution images with a small antenna. The optical analogy can be exploited to construct optical systems that form SAR images from the radar returns. Recent images of the earth taken by space shuttle radars and focused optically will be presented, along with a tutorial discussion on SAR.

Monday, July 25: Larry J. Howell, Engineering and Mechanics Department, General Motors Research Laboratories

Applied Mechanics Research at General Motors Research Laboratories

An overview of applied mechanics research in progress at GMRL's Engineering Mechanics Department will be given. Current activities in structural mechanics, with particular attention given to applications to product design, will be discussed. This work spans the use of conventional finite element methods to more recently developed techniques in structural optimization.

A particularly complex applied mechanics problem, that of predicting vehicle crashworthiness, is a topic which has been under investigation for more than 15 years. The current state-of-the-art in predictive methods will be reviewed, and needed research will be discussed.

Another application of advanced numerical techniques is the use of finite element methods in predicting cavity acoustic response. This analytical approach is currently being used to assess the influence of body panel vibration on passenger compartment noise.

The opportunities for applications of alternate materials in the automobile have never been greater, particularly with recent emphasis on weight reduction. However, the unique requirements of the automobile industry for low cost materials suitable for high-volume manufacturing create some new research needs for the industry. An example of how analytical procedures were used to improve manufacturing cycle time for plastic body panels will be discussed.

Friday, July 29: John E. Bercaw, Professor of Chemistry

Synfuels and Chemicals from Coal

In view of the dwindling supply and unstable price of petroleum, coal is becoming increasingly attractive as a feedstock for the chemical industry. Many chemical processes utilize "synthesis gas", a mixture of carbon monoxide and hydrogen obtained by heating coal with water vapor, to produce synthetic liquid fuels and commodity chemicals. The nature and function of the metal catalysts used in such reactions will be discussed.

Monday, August 1: Paul Hu, Senior Engineer, IBM General Products Division

Non-impact Printing Products and Technologies

Current products in the non-impact printing market will be described. These will include Laser, Ink Jet, and electrophotographic printing. Technologies involving these printing processes will be described. Technical challenges involving process and materials are outlined.

Friday, August 5: Jerome Pine, Professor of Physics

Microcircuits in Neurobiology

It is possible to grow nerve cells in culture dishes, where they form two-dimensional networks on the bottom of the dish. By utilizing modern integrated circuit techniques it is possible to interact with these cultures in a variety of ways, including electrical stimulation of selected cells, or the recording of signals generated by action potentials in specific cells.

Monday, August 8: Roger A. Clemens, Senior Research Nutritionist, Carnation Company

Today's Nutrition - Tomorrow's Health

Biochemistry, human physiology, cell and molecular biology, genetics, microbiology, endocrinology, toxicology, histology, pharmacology, research methodology, food chemistry, computer science and social sciences characterize the types of disciplines represented in the science of nutrition.

Nutrition research, then, involves investigations to examine and understand the interrelationships between these disciplines.

The twentieth century represents an era of important discoveries and advances in nutrition: vitamins were discovered, essential amino acids identified, certain minerals determined essential, nutrient quantitative techniques improved, and human nutrient needs defined.

Research in human nutrition and modern engineering technology are combining forces to provide answers to heretofore unresolved problems regarding the inadequate or excessive intake and subsequent metabolism of six fundamental nutrients: protein, carbohydrate, fat, vitamins, minerals, and water.

It is through quality research by professional scientists that today's nutritionists, dietitians, physicians, pharmacists and nurses can provide sound practical nutrition information for everyone.

Friday, August 12: Christopher E. Brennen, Professor of Mechanical Engineering

Mechanics of Flowing Granular Materials

Flows of granular, bulk materials are widespread not only in industrial processes but also in nature. Yet, until recently very little attention was given to understanding the fundamental mechanics of such flows. This lecture will present some of the recent ideas on the modelling of granular material flows and will demonstrate some phenomena you may or may not have noticed while playing in the sand.

Monday, August 15: Robert Mink, Technical Manager, Sodium Sulfur Battery Program, Ford Motor Company

The Sodium Sulfur Battery - An Update

The Sodium Sulfur Battery is now entering its engineering phase of development after fifteen years in the laboratory. Performance continues to look promising for many diverse applications although cost and lifetime must be improved to send to the commercial market.

Friday, August 19: Ray D. Owen, Professor of Biology, Emeritus

Immunogenetics — Past, Present, Future

Immunology and Genetics are two components of biological science in which remarkable progress is being made. Working in the common territory at the margins of these two active disciplines is especially rewarding. The talk will survey highlights of the development, present status, and future promise of this interdisciplinary field.

SURF BIBLIOGRAPHY

1. "Crustal Structure Near the Eastern Transverse Ranges", Am. Geophys. Union Trans. Eos, 60 p. 876 (Abstract), N.W. Clayton*, J.B. Minster**.

2. "Coulomb Distortion of Pion Spectra from Heavy-Ion Collisions", Phys. Rev. Letters, Vol. 43, p. 1581 (1979), K.G.Libbrecht*, S.E. Koonin**.

3. "Flux Pinning by Magnetic Impurities in an Amorphous Superconducting Alloy", Report to the Department of Energy, (1980) D.L. Whiting*, (worked with W. Johnson**).

4. "IUE and Visual Spectrophotometry of Markarian 9, Markarian 10, and 3C 390.3", Astrophysical Journal, Vol. 243, p. 445 (1981), R.W. Goodrich*, J.B. Oke**.

5. "Structure and Transcription of Normal and Abnormal Globin Genes", J. Supermolecular Structure of Cellular Biochem., supp. 5, 381 (1981). N. Proudfoot, M. Shander, S. VandeWoude*, T. Maniatis**.

6. "Repetitive Sequences of the Sea Urchin Genome II. Subfamily Structure and Evolutionary Conservation", Journal of Molecular Biology (1981) 149, 15-39. R.H. Scheller, D.M. Anderson, J.W. Posakony, L.B. McAllister*, R.J. Britten, E.H. Davidson**.

7. "Repetitive Sequences of the Sea Urchin Genome, Distribution of Members of Specific Repetitive Families", Journal of Molecular Biology (1981) 145, 5-28. D.M. Anderson, R.H. Scheller, J.W. Posakony, L.B. McAllister*, S.G. Trabert, C. Beall, R.J. Britten, E.H. Davidson**.

8. "Molecular Basis of Genetic Defects in Human Globin Genes", J. Supermolecular Structure of Cellular Biochem., Supp. 5, 229 (1981). M. Shander, S. VandeWoude*, N. Proudfoot, T. Maniatis**.

9. "Organization and Expression of Multiple Actin Genes in the Sea Urchin", Molecular and Cellular Biology, July 1981, p. 609-628. R.H. Scheller, L.B. McAllister*, W.R. Crain, Jr., D.S. Durica, J.W. Posakony, T.L. Thomas, R.J. Britten, E.H. Davidson**.

10. "Infrared Photometric Observation of BL Lac Object BL Lacertae (2200-42)" Annual Report of the Mount Wilson and Las Companas Observatories, 1981-1982, R. Pogge* (worked with G. Neugebauer**).

11. "Absolute Spectrophotometry of Very Large Redshift Quasars", Astrophysical Journal, Vol. 255, p. 11 (1982), D. Korycansky*, J.B. Oke**.

12. "Experimental Study of Autorotation with Flow Visualization", Received Third Place Certificate of Merit at American Institute of Aeronautics and Astronautics Minta Martin Student Competition for presentation of a technical paper, University of California, Irvine, April, 1982. I. Sugioka* (worked with F.E.C. Culick**).

13. "Electrical Characteristics of Thin Ni_2Si, NiSi, and $NiSi_2$ Layers Grown on Silicon", Paper presented at the Electronic Materials Conference 1982, June 23-25, Colorado State University, Ft. Collins, CO, and a manuscript to be published in the *Journal of Electronic Materials*. E. Colgan* (worked with M-A. Nicolet**).

14. "Erosion of Frozen Sulfur Dioxide by Ion Bombardment: Applications to IO", *Geophysical Research Letters*, Vol. 9, No. 10, Oct. 1982, pp 1151-54, C.L. Melcher, D.J. LePoire*, B.H. Cooper, T.A. Tombrello**.

15. "Shock Compaction of Ferrous Alloy Powders", to appear in Third Conference on Rapid Solidification Processing at the National Bureau of Standards, Gaithersburg, MD, December 6-8, 1982, T.J. Ahrens, D. Kostka*, P. Kasiraj, T. Vreeland**.

16. "Interspersed Sequence Organization and Developmental Representation of Cloned Poly(A) RNAs from Sea Urchin Eggs" *Journal of Molecular Biology*, In Press. J.W. Posakony, C.N. Flytzanis, R.J. Britten, E.J. Davidson** (Gary Mockli* helped with this work though not an author on the paper).

17. "Sputtering of SO_2 by High Energy Ions", *Radiation Effects*, To be Published in 1983. D.J. LePoire*, B.H. Cooper, C.L. Melcher, T.A. Tombrello**.

18. "Two-Phase Gravitational Instabilities in Thin Disks with Application to the Origin of the Moon", To be published in *Lunar & Planetary Science Abstracts*, XIV (1983). A.C. Thompson*, D.J. Stevenson**.

19. "Study of Ni-Nb System by Ion Mixing," Submitted to *physica status solidi* (*a*). K.T. Kung*, B.X. Liu, M-A. Nicolet**.

20. "Electrical Characteristics of Amorphous Iron-Tungsten Contacts on Silicon" *Applied Physics Letters* *42* (11). M. Finetti, E. T-S. Pan*, I. Suni, M-A. Nicolet**.

21. "Rapid Grain Flow in a Vertical Chamber", in preparation, K. Hui*, P. Haff**.

22. "A Possible Phase Transition in $(Zr_2Ni)_{1-x}B_x$ Metallic Glasses" To be submitted to *J Non-Cryst Solids*, A.Y.L. Mak*, W.L. Johnson**.

23. "Atomic Level Populations in the Hollow Cathode Discharge", To be submitted to *Journal of Quantitative Spectroscopy*, J.N. Humphrey*, D.L. Adams, W. Whaling**.

24. "Shock Wave Consolidation of an Amorphous Alloy", Proc. of Liquid Amorphous Metals V, August 15-19, 1983, UCLA, P. Kasiraj, D. Kostka*, T. Vreeland, Jr.**, and T.J. Ahrens.

25. "Isolation of New Yeast DNA Replicaton Mutants Using Permeabilized Cells", Proc. Natl. Acad. Sci., *80*, in press, C-L Kuo, N-H Huang*, J.L. Campbell**.

26. "Suppressors of a Temperature-Sensitive Copy-Number Mutation in Plasmid NTP1", Molec. Gen. Genet., in press, D.R. Moser, C.D. Moser, E. Sinn*, J.L. Campbell**.

27. "Beta Decay Phenomenology of Nuclear Fission Products", submitted to <u>Nuclear Physics A</u>, J.A. Behr* and P. Vogel**.

* - SURF student
** - Faculty Sponsor